

申 报	系列：教师系列 教学科研并重 型
	专业：应用化学
	职称：副教授

业绩成果材料

（申报人的业绩成果材料包括论文、科研项目、获奖以及其他成果等）

单 位（二级单位） 材料与化学工程学院

姓 名 刘维

材料核对人：

单位盖章：

核对时间：

华南农业大学制

目 录

一、教学研究业绩

1.主持教学研究项目

- 1.1 关于雨课堂在公共《物理化学》课程教学中的应用项目有关佐证材料.....7
- 1.2.关于课程内容上线新华网新华思政平台展播有关佐证材料.....8
- 1.3.关于第四届全国农林院校课程思政联盟优秀视频案例有关佐证材料.....9
- 1.4.关于材料科学基础 II 线下一流课程有关佐证材料.....10
- 1.5.关于物理化学校级课程示范课堂有关佐证材料.....12
- 1.6.关于华南农业大学第二批卓越教师百人计划项目有关佐证材料.....18

2.第一作者教改论文

- 2.1.具有荧光和抗菌双重功能的苦味酸吡啶季铵盐的制备综合实验（C类，附检索证明） 20
- 2.2. 雨课堂在公共《物理化学》课程教学中的应用初探...32
- 2.3. 离子型镍配合物的制备及其电催化产氢性能综合性实验设计（中国核心期刊数据库，附检索证明）38

3.创新创业训练项目结题证书

- 3.1 柑橘口罩—PLA/CNF 复合纳米纤维的制备及性能研究 46
- 3.2 半导体材料-生物杂化增强型光催化系统的产氢优化 47

4.教学成果奖证书

- 4.1. “四位一体”生物化工与制药实践平台的探究与实践（校

级二等奖，第 4)	48
4.2. 科创引领产业面向的材料科学与工程本科人才培养体系的探索与实践（校级二等奖，第 9）	49

二、科研项目

1.主持的科研项目

1.1. 国家自然科学基金项目：基于自旋交叉的手性分子探针的定向构筑与研究项目的立项通知（合同）及有关佐证材料	50
1.2. 广东省自然科学基金项目：基于金属还原菌的生物质纳米铂及其电催化氧还原研究的立项合同	52
1.3. 广州市科技项目：铁还原菌的质子传递机制解析与合成生物学调控的立项合同	53

2.主持的科研项目

2.1. 杂原子掺杂对氧化硼基质-碳点余辉能量传递的调控机理研究的立项合同	54
2.2. 面向农业病害即时诊断的 DNA 水凝胶自供能传感器构建的立项合同	56
2.3. 泡沫金属基光电极增强光电耦合全解水制氢研究的立项合同	58
2.4. 绿色环保型抗菌膜的制备及应用的立项合同	60
2.5. 高性能电芯粘结剂产业化关键技术开发的立项合同	62

三、论文、著作等

1. 检索证明	70
2. 以第一作者发表本专业论文情况	
2.1. Influence of Incubation Temperature on 9,10- Anthra	

quinone-2-Sulfonate (AQS)-Mediated Extracellular Electron Transfer	77
2.2. Tuning the Net Topology of Ternary Ag(I)-1,2,4,5-Tetra(4-pyridyl)benzene-Carboxylate Framework: Structures and Photoluminescence	89
3. 以通讯作者发表本专业论文情况	
3.1. Hematite enhances microbial autotrophic nitrate removal in carbonate and phosphate-rich environments by increasing Fe(II) activity.....	96
3.2. Three Silver(I) Coordination Polymers Based on Pyridyl Ligands and Auxiliary Carboxylic Ligands: Luminescence and Efficient Sensing Properties.....	107
3.3. Effects of different dithiolate ligands on electrocatalytic hydrogen production of nickel complexes in acetic acid or water	120
3.4. Synthesis, characterization, DNA/HSA interactions and in vitro cytotoxic activities of two novel water-soluble copper(II) complexes with 1,3,5-triazine derivative ligand and amino acids	131
3.5. Distinct biofilm formation regulated by different culture media: Implications to electricity generation.....	145
3.6. Revealing the underestimated role of Gram positive bacteria in Iron reduction within paddy soils.....	156
3.7. A solid state Ag(I) complex with excellent stability, luminescent and sensing properties.....	166
3.8. Cobalt- based Metalloporphyrins As Efficient Electrocatalysts for Hydrogen Evolution From Acetic Acid and Water	

.....	175
3.9. Enhancing the photocatalytic hydrogen production performance of CdS by introducing a co-catalyst CoTPPBr ₄ (7,8,17,18-tetrabromo-5,10,15,20-tetraphenylporphyrin).....	188

四、科研成果

1. 知识产权

1.1. 专利授权证书：一种多功能性荧光识别 Ag 配位聚合物及其制备方法与应用.....	199
1.2. 专利授权证书：配位聚合物晶体材料及其制备方法与荧光应用.....	201
1.3. 专利授权证书：一种温度诱导的三维自旋交叉配位聚合物及其制备方法和应用.....	203
1.4. 专利授权证书：一种新型 Ag 配位聚合物晶体材料及其制备方法与应用.....	205
1.5. 专利授权证书：一种四氯合钴复合双季磷盐、缓释薄膜材料及其制备方法和应用.....	207

五、其他业绩

1. 指导学生学科竞赛

1.1. 第十届广东省材料创新大赛三等奖.....	208
1.2. 第五届广东省大学生金相技能大赛一金相大会二等奖.....	209
1.3. 第十四届广东省材料创新大赛三等奖.....	210
1.4. 第六届广东省大学生金相技能大赛三等奖.....	211
1.5. 第六届广东省大学生金相技能大赛一等奖.....	212
1.6. 第十四届全国大学生金相技能大赛三等奖.....	213
1.7. 第十四届全国大学生金相技能大赛二等奖.....	214

2. 个人荣誉

2.1. 广东省第七届高校（本科）青年教师教学大赛理科组一等奖证书.....	215
2.2. 第四届全国高等农林院校课程思政优秀案例证书.....	216
2.3. 华农十佳教师证书.....	217
2.4. 华农十佳班主任证书.....	218
2.5. 校级“优秀班主任”证书.....	219
2.6. 第二批卓越青年教师百人证明材料.....	220
2.7. 校级“2018 年度考核优秀”证书.....	223
2.8. 校级“2020 年度考核优秀”证书.....	224
2.9. 校级“2022 年度考核优秀”证书.....	225
2.10. 校级“2024 年度考核优秀”证明.....	226
2.11. 华南农业大学 2019-2020 年度青年教师教学效果优秀奖（校青教赛）三等奖证书.....	227
2.12. 华南农业大学 2022-2023 年度青年教师教学效果优秀奖（校青教赛）二等奖证书.....	228
2.13. 优秀指导教师获奖证书.....	229
2.14. 2022 年度教学效果优秀奖一等奖证书.....	230
2.15. 2020 年度教学效果优秀奖一等奖证书.....	231
2.16. 院优秀党员示范岗称号.....	232
2.17. 学院就业积极分子证书.....	233
2.18. 材能学院第二届青年教师教学观摩比赛一等奖证书.....	234
2.19. 材能学院第四届青年教师教学观摩比赛一等奖证书.....	235
2.18. 材能学院第五届青年教师教学观摩比赛二等奖证书.....	236

3. 生产实践单位证明.....	237
------------------	-----

附件 1

广东省质量工程项目 验收登记表

项目类别：

教改项目

项目名称：

雨课堂在公共《物理化学》课程教学中的应用研究

所在学校：

华南农业大学

项目负责人：

刘维

项目参与人：

(限前 5 人，不含
项目负责人)

陈明洁，邓延平，曹巧英

立项时间：

2018 年 12 月 05 日

填表时间：

2022 年 02 月 15 日

广东省教育厅 制

二〇二一年

首页

热点发布

育人品牌

名师讲坛

示范课程

专题资源

课程思政联盟

院校专区

师资培训

所在位置: 首页 - 示范课程 - 课程详情

《物理化学》课程

第四章 相平衡

物理化学

学 校 华南农业大学



节段: 单组分系统两相平衡- Clapeyron方程

授课对象: 理工科专业 本科二年级学生

授课教师: 刘维 (华南农业大学)

授课教师

刘维

讲师

分享

累计学习人数 132 人

课程简介

- 教学设计
- 教学视频
- 教学课件

课程简介

物理化学这门课是针对理工科专业本科二年级的学生开设的一门公共基础课程。物理化学是整个化学学科的理论基础,是以物理的原理和实验技术,结合数学演绎的方法为基础,研究化学体系的性质和行为,发现并建立化学体系中特殊规律的一门科学。它研究的不是一个化学反应,也不是一类化学反应,而是所有化学反应化学体系的规律性,物理化学对理工农等相关专业起着重要支撑作用。课程讲授的知识点理论性强,概念多、推理多、公式多,抽象难学,学生在学习过程中畏难情绪较重。如何将专业知识与科研、生产紧密联系,如何让学生有效地掌握理论,将理论联系实际,深化所学知识并实际为解决专业问题所用,是物理化学课程教学遇到的问题和挑战。



高等农林院校
课程思政联盟

获奖证书

刘维 老师：

您主讲的课程思政教学案例在第四届全国高等农林院校课程思政联盟研讨会
案例征集评选中被评为优秀案例。

特发此证，以资鼓励。

课程名称：物理化学

案例名称：克拉佩龙方程

所在高校：华南农业大学

获奖组别：视频案例

全国高等农林院校课程思政联盟

(华中农业大学代章)

二〇二四年十二月



关于2024年度校级一流课程（金课）拟认定名单的公示

来源单位及审核人： 编辑： 审核发布：本科生院（招生办公室） 发布时间：2024-04-30

各学院（部）、各相关单位：

根据《关于开展2024年度校级一流课程（金课）遴选认定工作的通知》精神，本科生院组织开展了2024年校级一流本科课程申报和遴选工作。经本人申报、所在单位审核、公示并推荐、学校组织专家评审等程序，遴选出我校一流本科课程49门（包含线下一流课程37门、线上线下混合式一流课程12门）。现将遴选结果予以公示，详细名单见附件。

公示时间为2024年4月30日至2024年5月6日，共7天。在公示期内如有异议，请在5月6日17:30前邮件或直接送本科生院教研科（行政楼329），反馈情况时要签署真实姓名，要有具体事实依据，否则不予受理。

联系人：孙航
联系电话：85280052
邮 箱：gjyj@scau.edu.cn

本科生院（招生办公室）
2024年4月30日

2024年度校级一流课程（金课）拟认定名单

序号	课程名称	课程类别	所属单位	课程负责人	课程团队其他主要成员
1	材料科学基础II	线下一流课程	材料与能源学院	刘维	胡航、梁业如、董汉武、刘彦祺
2	区域规划	线上线下混合式一流课程	公共管理学院	李玮	吴顺辉、孙传谭、王玉琳、刘卓君
3	数值分析	线下一流课程	数学与信息学院	李娇娇	张昕、赵峰、梁艳影、何艳玲
4	数学I	线下一流课程	数学与信息学院	周裕中	湛秋辉、张昕、尤雪莲、曾庆茂

- 2025-07-04
转发《广东省教育厅关于征集2025年数字化赋能教育管理高质量发展...
- 2025-07-15
关于中国高等教育学会“高等教育科学研究课题”评审专家库拟推荐...
- 2025-07-10
关于第四批“全国高校黄大年式教师团队”拟推荐团队的公示
- 2025-07-10
关于明确2024年度职称评审本科教学工作量填报相关问题的通知
- 2025-07-09
转发广东省高等教育学会关于推荐“高等教育科学研究课题”评审专...

附件 4

华南农业大学线下一流本科课程申报书

课程名称：材料科学基础 II

课程负责人：刘维

课程类型：☐公共课平台课程 ☒专业核心课程

申报课程学院：材料与能源学院

所属专业名称（仅专业核心课填写）：材料科学与工程

申报日期：2024.03.14

华南农业大学本科生院制

二〇二四年三月

华南农业大学文件

华南农教〔2025〕7号

关于公布华南农业大学 2024 年度 课程思政示范项目立项名单的通知

各学院、部处、各单位：

根据《关于开展 2024 年度校级课程思政示范建设项目申报工作的通知》，学校组织开展了 2024 年度课程思政示范项目评选工作。经项目负责人申请、所在单位遴选推荐、学校组织专家评审、校内公示等程序，决定立项建设华南农业大学 2024 年度课程思政示范项目 91 项，包括课程思政试点学院 4 个、课程思政示范团队 6 个、课程思政示范课程 14 门、课程思政示范课堂 25 个、课程思政典型案例 42 个（名单详见附件），现予以公布。

本次立项的课程思政示范项目建设期至 2026 年 12 月，建设期内，示范项目原则上不允许更换负责人或变更项目团队成员。各项目负责人要严格按照 2024 年度申报通知要求，及时开展工作，加

- 1 -

快推进课程思政改革，确保高质量完成建设目标和任务。

请各学院充分认识课程思政改革的重要意义，认真贯彻《华南农业大学课程思政实施方案》，加强对教师的相关培训、指导、引领和支持，带动教师全员积极参与课程思政教学改革，持续深入抓典型、树标杆、推经验，全面提升本科人才培养质量。

附件：华南农业大学 2024 年度课程思政示范项目立项名单

华南农业大学
2025 年 1 月 24 日

公开方式：主动公开

华南农业大学党政办公室 2025 年 1 月 24 日印发

附件

华南农业大学 2024 年度课程思政示范项目立项名单

序号	类别	项目名称	所属单位	项目负责人	团队成员（不含负责人）
kcsz2024001	试点学院	课程思政试点学院	动物科学学院	王文策	
kcsz2024002	试点学院	课程思政试点学院	艺术学院	张艳河	
kcsz2024003	试点学院	课程思政试点学院	数学与信息学院、软件学院	陈文艺	
kcsz2024004	试点学院	课程思政试点学院	公共管理学院	蔡茂华	
kcsz2024005	示范团队	《公共管理学》课程思政示范团队	公共管理学院	史传林	唐斌、姜国兵、方敏、曾小龙、吴彦
kcsz2024006	示范团队	藏粮于“技”，“数”说农业：数字化转型课程思政教学团队	数学与信息学院、软件学院	熊俊涛	黄文玲、韩方珍、古万荣、邓金、张建桃、宋歌、韦婷婷、邓成剑、黄丽清
kcsz2024007	示范团队	农业昆虫学课程群思政示范团队	植物保护学院	陆永跃	王磊、齐易香、岑伊静、黄振、程代凤、桑文、洗继东、吴建辉、潘慧鹏、何晓芳、汪萃萃、何娜芬
kcsz2024008	示范团队	大数据与机器学习类课程思政	经济管理学院	陈有华	何勤英、伍敬文、文乐、

		示范团队			李景荣
kcsz2024009	示范团队	水利工程类专业课程群课程思政示范团队	水利与土木工程学院	齐龙	韦未、王慧琳、杨海燕、卢玉华、余长洪、张巍
kcsz2024010	示范团队	光电信息类课程群思政团队	电子工程学院（人工智能学院）	林芳	刘金龙、欧阳强强、胡旭波、刘建斌、翁嘉文、徐初东、杨初平、林上港、曾应新
kcsz2024011	示范课程	水污染控制工程	资源环境学院	余光伟	梁瑜海、种云霄、陈澄宇、仲海涛、黄柱坚
kcsz2024012	示范课程	行政法与行政诉讼法	人文与法学学院	李燕	杨正喜、欧仁山、左卫霞、孙梦
kcsz2024013	示范课程	森林培育学	林学与风景园林学院	何茜	邱权、陈祖静、刘效东、潘澜、苏艳
kcsz2024014	示范课程	植物学实验	生命科学学院	梁祥修	白玫、李雁群、张荣京、何韩军
kcsz2024015	示范课程	瑜伽	体育教学研究部	何灵捷	田甜、周文英、王顺熙、姚叶戴、戴金明
kcsz2024016	示范课程	乒乓球（国球）	体育教学研究部	陈华东	钞飞侠、张波、李嘉鹏、赵东升、王一
kcsz2024017	示范课程	数据挖掘与大数据分析	经济管理学院	文乐	李琴、陈有华、何勤英、李景荣
kcsz2024018	示范课程	翻译理论与实践	外国语学院	陈喜华	王之杰、张欢、杨敏、严晓蓉、周戬丰

kcsz2024019	示范课程	咨询心理学	公共管理学院	钟向阳	何小芹、唐晓容、卓彩琴、吕玲玲、李锦顺、韩丽
kcsz2024020	示范课程	大学英语 IV（学术英语）	外国语学院	刘玉花	钟志英、柳青、李莉
kcsz2024021	示范课程	西方园林史	林学与风景园林学院	潘建非	夏宇、陈意微、李晓雪
kcsz2024022	示范课程	金融工程	经济管理学院	周丽云	陈标金、王雄志、林伟芬、陈晓洁
kcsz2024023	示范课程	民事诉讼法	人文与法学学院	刘万洪	张艳琼、王琳、杜国明
kcsz2024024	示范课程	农业技术经济学	经济管理学院	蔡键	薛春玲、周伟、苏柳方、易智敏，蔡轶
kcsz2024025	示范课堂	《物理化学》第四章第 4 节（单组元系统两相平衡）	材料与能源学院	刘维	陈明洁、胡航
kcsz2024026	示范课堂	《生态工程学》第五章第 1 节（湿地保护与生态修复）	资源环境学院	田纪辉	蔡昆争
kcsz2024027	示范课堂	《食品分析》第八章第 2 节（蛋白质的测定）	食品学院	徐振林	温棚、罗林
kcsz2024028	示范课堂	《生态农业工程》第七章 第 1 节（碳中和与农业绿色低碳）	资源环境学院	秦俊豪	赵本良
kcsz2024029	示范课堂	《篮球》--传接球与挡拆技术专题	体育教学研究部	郭城	张波、于江杨、黄燕玲
kcsz2024030	示范课堂	《大学生心理健康教育》第七	经济管理学院	何凯	刘思蓓、崔翱鸽

华南农业大学

课程思政示范课堂申报书

学院名称（盖章）材料与能源学院

所属课程名称《物理化学》

课堂所在章节第四章相平衡第4节单组元系

统两相平衡

课堂主讲人刘维

申报日期2024年11月06日

本科生院制

二〇二四年

华南农业大学文件

华南农教〔2021〕25 号

关于公布华南农业大学第二批卓越青年教师 百人计划人选的通知

各学院、部处、各单位：

为贯彻落实《华南农业大学高水平本科教育实施意见》（华南农办〔2019〕62 号），进一步加强我校青年教师队伍建设，重点培育一批卓越青年教师，整体提升我校青年教师教育教学能力，根据《华南农业大学卓越青年教师百人计划实施方案》，学校开展了第二批卓越青年教师百人计划遴选工作，经教师自愿报名、单位推荐、学校资格审查、校内公示无异议等程序，共遴选出王小龙等 42 位教师入选第二批卓越青年教师百人计划（详见附件），现予以公布。

附件：华南农业大学第二批卓越青年教师百人计划人选名单

华南农业大学
2021 年 5 月 12 日

- 1 -

附件

华南农业大学第二批卓越青年教师 百人计划人选名单

序号	单位名称	姓名	序号	单位名称	姓名
1	农学院	王小龙	22	水利与土木工程学院	杨雨冰
2	农学院	金 晶	23	水利与土木工程学院	卢小圣
3	植物保护学院	郑 正	24	材料与能源学院	刘 维
4	植物保护学院	徐春玲	25	材料与能源学院	袁 腾
5	植物保护学院	孔广辉	26	材料与能源学院	刘海峰
6	植物保护学院	刘家莉	27	数学与信息学院、软件学院	王雪琴
7	植物保护学院	陈少华	28	数学与信息学院、软件学院	金玲玉
8	林学与风景园林学院	吴道铭	29	数学与信息学院、软件学院	李娇娇
9	林学与风景园林学院	单体江	30	数学与信息学院、软件学院	周 燕
10	林学与风景园林学院	李 培	31	经济管理学院	董 莹
11	园艺学院	赵杰堂	32	公共管理学院	曾永辉
12	动物科学学院	谭成全	33	公共管理学院	王 枫
13	动物科学学院	蔺文成	34	公共管理学院	徐 强
14	动物科学学院	李耀坤	35	公共管理学院	曲 霞
15	动物科学学院	孙宝丽	36	人文与法学学院	李 颖
16	资源环境学院	李荣华	37	外国语学院	林 绿
17	资源环境学院	张 池	38	外国语学院	郭圣琳
18	海洋学院	黄玉妹	39	外国语学院	侯丽娴
19	海洋学院	孙红岩	40	艺术学院	栾志弘
20	海洋学院	曾 芳	41	艺术学院	欧阳文昱
21	食品学院	宋明月	42	马克思主义学院	梁 娟

公开方式：主动公开

华南农业大学党政办公室

2021年5月12日印发

检索证明

根据委托人提供的论文材料, 委托人华南农业大学材料与能源学院刘维 (Liu, Wei) 2篇论文收录情况如下表。

序号	论文名称	发表刊物及发表的年月卷期/页码等	作者排名	论文等级	作者文中单位	收录情况	影响因子	中科院大类分区
1	A solid state Ag(I) complex with excellent stability, luminescent and sensing properties	POLYHEDRON 出版年: 2022 NOV 15 卷期: 227 文献号: 116148 文献类型: Article	共同通讯作者	B类	华南农业大学	SCI	IF2-year=2.975 IF5-year=2.389 (2021)	化学 3区 Top期刊: 否 (2022)
2	具有荧光和抗菌双重功能的苦味酸吡啶季铵盐的制备综合实验	化学通报 出版年: 2022 卷期: 85 4 页码: 505-511 文献类型:	第一作者		华南农业大学	已在线发表		

说明: 论文等级和中科院大类分区按《华南农业大学学术论文评价方案(试行)》划分。

报告免责声明: 如未盖章, 报告无效

检索员: 杨穗旒
华南农业大学图书馆
2023-02-28

SCAULIB202625680

检索证明

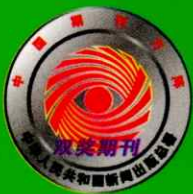
根据委托人提供的论文材料，委托人华南农业大学材料与化学工程学院 刘维(学科类型:自然科学) 2 篇论文收录情况如下表。

序号	论文名称	发表刊物及发表的年月卷期/页码等	作者排名	论文等级	作者文中单位	收录情况	影响因子	中科院大类分区
1	离子型银配合物的制备及其电催化产氢性能综合性实验设计	实验科学与技术 出版年：2025 卷期： 页码： - 文献号： 文献类型：	第一	普刊类	华南农业大学材料与能源学院	CNKI	无	无
2	Revealing the underestimated role of Gram-positive bacteria in iron reduction within paddy soils	Science of the Total Environment 出版年：2025 卷期： 页码： - 文献号： 文献类型：	共同通讯作者	A 类	华南农业大学材料与能源学院	已发表，暂未被SCI 收录	IF2-year=8.0 IF5-year=8.7 (2024)	环境科学与生态学 2 区 Top 期刊：是 0A 期刊：否 标注：Mega-Journal (2025)

说明：论文等级和中科院大类分区按《华南农业大学学位论文评价方案（试行）》划分。

报告免责声明：如未盖章，报告无效





ISSN 0441-3776

CN 11-1804/O6

<http://www.hxtb.org>

化学通报

CHEMISTRY

4

第85卷
2022

中国科学院化学研究所
中国化学会

主 办



2022 年 4 月 第 85 卷 第 4 期



CHINESE
CHEMICAL
SOCIETY

目 次

进展评述

- 防冰材料研究进展及其在风电领域的应用 梁镇宇 朱志成 韩毅平 李存义 龚 伟 李嘉鑫 王占辉 张宏强 贺志远 王健君 (386)
- 自修复超疏水涂层材料研究进展 李 彪 李康康 陈香李 (401)
- 超高温 (200~250℃) 聚合物电解质膜燃料电池的机遇与挑战 王慧萍 杨楚杰 Felix Kwofie 张爱京 江胜娟 唐浩林 蒋三平 程 义 (410)
- 金属有机骨架材料在气体分离膜中的应用 高 明 朱元璐 闫江毅 王北福 (425)
- 脂质纳米颗粒的制备及在基因治疗中的应用 张庭瑜 唐紫晴 李 庆 覃勇莎 苏 玉 支德福 (432)
- 天然糖类纳米药物传递系统的研究进展 吴 怡 王新敬 尚宏周 孙晓然 (441)
- 7-位取代的甾体类化合物生物活性研究进展 陈华龙 刘钦洲 黄燕敏 崔建国 陈小凤 甘春芳 (446)
- 工业固废资源化过程中组分“分离-转化-定向制备”研究进展 刘红盼 倪海涛 段亨攀 杨仲卿 (452)

研究论文

- 基于乙酰胆碱酯酶和丁酰胆碱酯酶靶标的查尔酮衍生物的合成及生物活性 杨 燕 陈旭飞 张 前 袁旭芳 何希瑞 (460)
- 槲皮素-3-O-丙基衍生物的合成及生物活性 冯 爽 李阳杰 刁冉冉 王昭阳 冯亚莉 颜子童 翟广玉 (470)
- 7-羟基-3-乙酰基香豆素曼尼希碱衍生物的合成及抗血小板聚集活性 尚飞扬 丁 乐 何黎琴 顾宏霞 徐路安 (480)
- 类查尔酮氟喹诺酮衍生物的合成及抗肿瘤活性 冯亚莉 李 珂 黄文龙 崔红艳 胡国强 (485)
- 金纳米花的合成及其与人血清白蛋白相互作用的研究 张钊维 宋雨欣 王艺蓉 鲁钊瑛 王一名 何 硕 杜中玉 徐香玉 (490)
- 连翘酯苷 A 与弹性蛋白酶相互作用的研究 付金凤 姚红柳 尹广婷 周雪健 苏丽红 (496)

研究简报

- meso-四苯基-2,3-二氢卟啉-2,3-二醇的合成 崔春雨 秦云珍 蒋旭亮 (501)

化学教学

- 具有荧光和抗菌双重功能的苦味酸吡啶季铵盐的制备综合实验 刘 维 徐奕琳 陈梓莹 倪春林 (505)

读者·作者·编者

- 本期部分研究论文和研究简报的图文摘要 (385)

本期责任编辑 邬 慧 田艳文

化学教学

具有荧光和抗菌双重功能的苦味酸吡啶季铵盐的制备综合实验

刘 维 徐奕琳 陈梓莹 倪春林*

(华南农业大学生物基材料与能源教育部重点实验室 华南农业大学材料与能源学院 广州 510642)

摘 要 介绍了一项涉及苦味酸吡啶季铵盐制备与性能研究的综合性实验。以吡啶、苦味酸、4-溴苄基溴和碳酸钾等为原料,合成了苦味酸-4-溴苄基吡啶季铵盐([4BrBzPy][PIC]),利用红外光谱、紫外-可见光谱、电喷雾质谱、粉末 X-射线衍射和单晶 X-射线衍射技术进行了表征,并对其固态荧光和抗菌性能进行研究。该实验项目来源于科研,涵盖多个学科的知识点和实验操作技术,具有综合性和研究性,有利于增强学生勇于探索的创新精神,培养学生解决实际问题的能力,适用于应用化学、材料化学、材料科学与工程和制药工程等本科专业综合实验教学。

关键词 苦味酸季铵盐 固态荧光 抗菌 综合实验 能力培养

DOI:10.14159/j.cnki.0441-3776.2022.04.012

Comprehensive Experiment on Synthesis of Pyridine Quaternary Ammonium Salt Picric Acid with Fluorescent and Antibacterial Dual Functions

Liu Wei, Xu Yilin, Chen Ziyang, Ni Chunlin*

(Key Laboratory for Biobased Materials and Energy of Ministry of Education, College of Materials and Energy, South China Agricultural University, Guangzhou, 510642)

Abstract A comprehensive experiment on the preparation and properties of pyridine quaternary ammonium salt picric acid was introduced. 4-Bromobenzyl pyridine quaternary ammonium salt picric acid ([4BrBzPy][PIC]) is synthesized by using 4-bromobenzyl bromide, pyridine, picric acid and potassium carbonate as raw materials. It has been characterized by IR spectrum, UV-Vis spectrum, electrospray mass spectrometry, powder X-ray diffraction and single crystal X-ray diffraction. The fluorescent properties in solid state and antibacterial properties of the salt are investigated. The experiment project covers the multi-disciplinary knowledge and experiment operation technology, and is comprehensive and research-oriented. The project helps students to cultivate their comprehensive experimental ability and creative ability, and is suitable for undergraduate majors such as applied chemistry, material chemistry and materials science and engineering as comprehensive experiment project.

Keywords Picric acid quaternary ammonium salt, Fluorescence in solid state, Antibacterial properties, Comprehensive experiment, Ability cultivation

教育部发布的《关于一流本科课程建设的实施意见》中提出了增加课程的挑战度的具体要求^[1]。将科研成果融入本科实验教学,增加研究性、创新性和综合性内容,是“一流专业”建设背景下深化实验教学改革,提高实验教学质量的重要途径之一^[2,3]。

有机光学材料作为化学和物理光学的交叉研究领域,近几十年来引起了科学家广泛的兴

趣^[4,5]。与无机材料比较,有机光学材料具有响应时间快、电光系数大、介电常数小、光学效应显著、热稳定性强等特点,并呈现出良好的光学性能,在荧光探针、光学数据存储、太阳能电池等方面有着广泛的应用前景^[6,7]。特别是苦味酸与吡啶类化合物展现出良好的二阶非线性光学性和抗菌性能^[8,9]。近几年来,笔者等将取代苄基异喹啉季铵盐阳离子和取代苄基三苯基季磷盐与苦味

* 联系人,倪春林 男,博士,教授,主要从事配位化学研究。E-mail: niclchem@scau.edu.cn

广东省科技计划项目(2016A010103025)、广东省本科高校教学质量与教学改革工程建设项目(2019516)和广东省高等教育教学改革项目(粤教高函[2020]20号)资助

2021-08-03 收稿,2021-08-28 接受

酸阴离子自组装,获得了一些非线性光学性能优于磷酸二氢钾(KDP)参考晶体的有机苦味酸盐材料^[10-12]。如果将该类材料的合成、表征、性能测定应用于本科教学,可设计集化学合成、结构分析、物理光学性质测定、生物抗菌分析于一体的综合性教学实验。

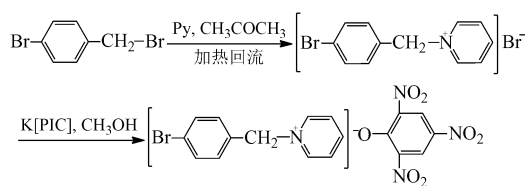
本文详细阐述了苦味酸 4-溴苄基吡啶季铵盐([4BrBzPy][PIC])的制备方法,介绍了通过元素分析、电喷雾质谱、红外光谱、紫外-可见光谱和 X-射线单晶粉末衍射对该材料进行表征与分析的方法,并测定了材料的固体荧光和抗菌性能。目的在于将科研成果融入本科实验教学,提出一套具有研究性、创新性和综合性的教学实验,培养大学生的综合实验能力和创新能力。

1 实验目的

(1) 通过查阅文献了解有机材料、季铵盐和苦味酸盐的制备、应用领域及研究进展。(2) 学习一种苦味酸苄基吡啶季铵盐的制备方法及其单晶体的生长方法,熟练磁力搅拌器、旋转蒸发仪和真空干燥箱等常规仪器的使用。(3) 熟悉傅里叶红外光谱仪、紫外-可见分光光度计、荧光分光光度计、液相-质谱联用仪和粉末 X-射线衍射仪等表征仪器的工作原理和操作方法,学会独立分析实验数据与绘制图谱。(4) 了解固态紫外-可见漫反射光谱测定的方法和积分球的作用原理,学会用作图法计算半导体禁带宽度。(5) 了解单晶 X-射线衍射的原理、单晶结构解析的过程和晶系、空间群等晶体学知识;通过教师的演示,了解运用 SHELX-97 程序进行晶体结构解析的过程,学会用解析后的晶体学文件绘制晶体结构图和堆积图。(6) 学会用平板纸片扩散测试季铵盐抗菌性能的原理、过程与方法,掌握超净工作台、恒温培养箱的使用方法及无菌操作技术。

2 实验原理

以 4-溴苄基溴和吡啶为原料,通过 SN1 亲核取代反应合成溴化 4-溴苄基吡啶季铵盐([4BrBzPy]Br),再以苦味酸(2,4,6-三硝基苯酚)和碳酸钾为原料合成苦味酸钾(K[PIC])。在此基础上,用[4BrBzPy]Br和K[PIC]在甲醇中反应制备苦味酸 4-溴苄基吡啶季铵盐([4BrBzPy][PIC])(图式 1)。



图式 1 苦味酸吡啶季铵盐的合成路线
Scheme 1 Synthetic route of picric pyridine quaternary ammonium salt

3 试剂与仪器

3.1 实验试剂

4-溴苄基溴、吡啶、苦味酸、碳酸钾、N,N-二甲基甲酰胺、甲醇等试剂均为市售分析纯级,未经纯化处理直接使用。金黄色葡萄球菌和大肠杆菌由华南农业大学生物化工与制药实验中心提供,使用前活化。

3.2 实验仪器

电子天平,恒温磁力搅拌器,真空干燥烘箱,循环水式真空泵,旋转蒸发仪,超净工作台,恒温培养箱,AVATAR360 FT-IR 红外光谱仪(美国 Nicolet 公司),UV2550 紫外-可见分光光谱仪(日本 Shimadzu 公司),Rigaku-Ultima IV 粉末 X-射线衍射仪(日本 Rigaku 公司),API-3200 液相色谱串联质谱联用仪(新加坡 AB Sciex 公司),RF-5301 荧光分光光度计(日本 Shimadzu 公司),Smart APEX 单晶 X-射线衍射仪(德国 Bruker 公司)。

3.3 溴化 4-溴苄基吡啶季铵盐的合成

称取 2.50g(0.01mol) 4-溴苄基溴和 0.87g(0.011mol) 吡啶溶于 30mL 丙酮中,磁力搅拌下加热回流反应 6h。冷却、减压过滤,用冷的丙酮洗涤,真空干燥,得白色固体 2.32g,产率为 81.4%。

3.4 苦味酸 4-溴吡啶季铵盐的合成

称取 0.46g(2.0mmol) 苦味酸溶于 10mL 甲醇中,在搅拌下,滴加到含有 0.14g(1.0mmol) K₂CO₃ 的 10mL 甲醇中的溶液中,继续搅拌 2h,得黄色苦味酸钾溶液。将 0.66g(2.0mmol) 溴化 4-溴苄基吡啶季铵盐[4BrBzPy]Br 溶于 20mL 甲醇中,搅拌下滴加到上述苦味酸钾溶液中,搅拌 1h,旋转蒸发浓缩,静置,减压过滤,甲醇洗涤,真空干燥,得到黄色粉状固体。用甲醇重结晶,得黄色晶状产物 0.67g,产率为 77.9%。用于晶体结构分析的晶体通过冷却结晶法得到。

3.5 抗菌性能测试

采用平板纸片扩散法测定苦味酸季铵盐的抑

菌圈直径大小^[13],其中金黄色葡萄球菌和大肠杆菌菌液浓度分别为 5.0×10^6 CFU/mL 和 2.0×10^6 CFU/mL,苦味酸吡啶季铵盐二甲亚砷溶液浓度为 5.0×10^{-3} mol/L。分别吸取 20 μ L 金黄色葡萄球菌与 20 μ L 大肠杆菌菌液于培养基平板,使用涂布棒将菌液均匀涂布在培养基表面,将已晾干的滤纸片紧贴于各个琼脂培养皿表面并密封,置于 37℃ 的恒温恒湿培养箱中培养 24 h 后,测量抑菌圈的直径,取三次平行实验的平均值。

4 结果与讨论

4.1 晶体结构分析

苦味酸季铵盐晶体衍射数据用德国 Bruker 公司 Smart APEX CCD X-射线衍射仪收集,以石墨单色化的 Mo K α ($\lambda = 0.071073$ nm) 作辐射源。晶体结构通过 SHELX-97 软件^[14]采用直接法进行解析,利用全矩阵最小二乘法 F^2 对所有数据进行优化。学生根据获得的晶体学信息文件(.cif 文件)通过 Diamond 软件画图。苦味酸吡啶季铵盐的晶体学数据列于表 1 中,晶体结构如图 1 所示。可以看出,所制备的晶态材料属于单斜晶系 $P2(1)/n$ 空间群。一个不对称单元中含有 2 个 4-溴苄基吡啶阳离子 [4BrBzPy]⁺ 和 2 个苦味酸阴离子 [PIC]⁻。在其中一个 [PIC]⁻ 阴离子中,三个硝基 O2-N1-O3、O4-N2-O5 和 O6-N3-O7 所在平面与苯环 C1-C2-C3-C4-C5-C6 平面之间的二面角分别为 135.4°、5.4° 和 2.5°,在另外一个 [PIC]⁻ 阴离子中,三个硝基 O9-N4-O10、O11-N5-O12、O13-N6-O14 所在平面与苯环 C7-C8-C9-C10-C11-C12 平面之间的二面角分别为 20.5°、1.2° 和 24.9°。两个 [4BrBzPy]⁺ 阳离子均显现“ Λ ”构型,在含 N7 的阳离子中吡啶环与苯环之

间的二面角分别为 91.5.2°,而在含 N8 的阳离子中该二面角为 101.3°。从图 2 可以看出,晶体中 4-溴苄基吡啶 [4BrBzPy]⁺ 阳离子和苦味酸 [PIC]⁻ 阴离子均沿 b 方向呈柱状堆积,阴、阳离子之间通过 C—H \cdots O 氢键^[15] 形成网络结构,这些氢键的键长和键角列于表 2 中。

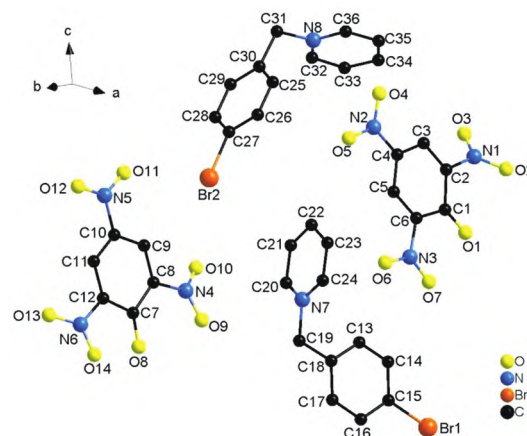


图 1 苦味酸季铵盐的晶体结构

Fig.1 The Crystal structure of picric acid pyridine quaternary ammonium salt

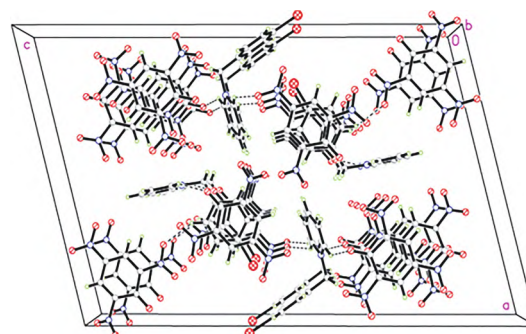


图 2 苦味酸季铵盐的沿 b 方向的堆积图(虚线表示 C—H \cdots O 氢键作用)

Fig.2 The stacking diagram of quaternary ammonium salt (Dashed lines indicate C—H \cdots O hydrogen bonds)

表 1 苦味酸吡啶季铵盐的主要晶体学数据

Tab.1 Crystallographic data for picric acid pyridine quaternary ammonium salt

参数	数据	参数	数据
化学式	C ₁₈ H ₁₃ BrN ₄ O ₇	吸收系数(mm ⁻¹)	2.221
分子量	477.23	单胞中电子数 $F(000)$	1920
晶系和空间群	Monoclinic, $P2(1)/n$	晶胞大小(mm ³)	0.07×0.11×0.16
a (nm)	1.9162(1)	收集衍射点数目	35398
b (nm)	0.6896(1)	独立衍射点数目(R_{int})	7041(0.061)
c (nm)	2.9656(1)	拟合优度 S	1.020
β (°)	104.74(1)	残差因子	0.0510, 0.0921
晶胞体积(Å ³)	3789.9(3)	加权残差因子	0.1157, 0.1317
密度计算值(g·cm ⁻³)	1.673	最小和最大残余密度/e·nm ⁻³	-690, 680

表 2 季铵盐晶体中的氢键作用

Tab.2 Hydrogen bonds in picric acid pyridine quaternary ammonium salt

氢键(D-H...A)	键长与键角			
	D-H 键长/nm	H...A 键长/nm	D...A 键长/nm	<DHA 键角/(°)
C(5)-H(5)...O(6)	0.0930	0.2280	0.2604(5)	100.0
C(13)-H(13)...O(6 ^a)	0.0930	0.2300	0.3128(5)	147.0
C(24)-H(24)...O(1 ^b)	0.0930	0.2470	0.3322(6)	152.0
C(26)-H(26)...O(13 ^c)	0.0930	0.2590	0.3425(5)	150.0
C(32)-H(32)...O(4)	0.0930	0.2460	0.3218(6)	138.0
C(36)-H(36)...O(8 ^b)	0.0960	0.2350	0.3115(5)	139.0

注: 对称操作代码: $a = -x+1/2, y-1/2, z+1/2$; $b = x, y-1, z$; $c = -x+1, -y+1, z+1$.

4.2 ESI-MS 分析

苦味酸季铵盐 [4BrBzPy] [PIC] 的电喷雾质谱以色谱纯甲醇为溶剂, 采用正离子和负离子模式分别在液相色谱-质谱联用仪测定。[4BrBzPy] [PIC] 的阳离子和阴离子电喷雾质谱如图 3 所示。图 3(a) 其中相对丰度为 100%、43.75%、65.62% 和 18.75% 的分子离子峰分别对应于 [4BrBzPy+H]⁺、[4BrBzPy+2H]⁺ 和 [4BrBzPy+3H]⁺, 其中 [4BrBzPy]⁺ 与理论值 249.1 接近。从图 3(b) 可以得知, 苦味酸季铵盐样品中阴离子 [PIC]⁻ 最强峰位于 227.7, 与理论值 228.1 接近。

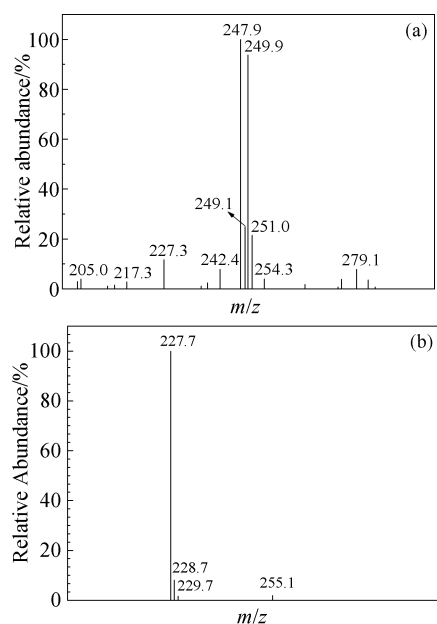


图 3 苦味酸吡啶季铵盐中阳离子 (a) 和阴离子 (b) 的 ESI-MS 谱图

Fig.3 ESI-MS of the cation (a) and the anion (b) of picric acid pyridine quaternary ammonium salt

4.3 红外光谱

取少量干燥的 [4BrBzPy] [PIC] 样品与 KBr 研磨成粉末压片, 用红外光谱仪在 400 ~ 4000 cm⁻¹ 范围内扫描测定其红外光谱 (图 4)。3089 和

3058 cm⁻¹ 为苯环和吡啶环上 =C—H 的伸缩振动吸收峰; 2925 和 2857 cm⁻¹ 的吸收峰为阳离子 [4BrBzPy]⁺ 中亚甲基的 C—H 伸缩振动峰; 1631 和 1505 cm⁻¹ 的峰为苯环和吡啶环上 C=C 骨架的伸缩振动吸收峰; 1492 cm⁻¹ 处为吡啶环上 C=N 骨架上的伸缩振动吸收峰; 1306 和 1248 cm⁻¹ 处分别为亚甲基上 C—H 不对称和对称变形振动吸收峰; 769 cm⁻¹ 处为苯环上 =C—H 面外变形振动吸收峰; 682 cm⁻¹ 处为 C—Br 伸缩振动的特征吸收峰^[16]; 阴离子苦味酸根中硝基不对称和对称伸缩振动位于 1555 和 1336 cm⁻¹ 处, 786、743 和 712 cm⁻¹ 处分别为硝基的面内弯曲振动、面外摇摆振动、剪切振动和平面摇摆振动的峰^[17]。

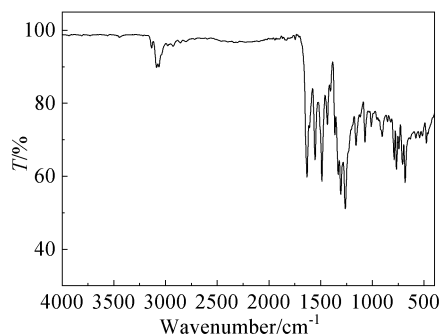


图 4 苦味酸季铵盐的红外光谱图

Fig.4 IR spectrum of the quaternary ammonium salt

4.4 紫外-可见吸收光谱与漫反射光谱

以色谱纯甲醇为溶剂, 将样品配制为 1.0 × 10⁻⁴ mol/L 的溶液, 装入 1 cm 的石英比色皿中, 扫描 200 ~ 500 nm 范围的 UV-Vis 光谱。季铵盐 [4BrBzPy] [PIC] 在紫外区有 3 个吸收峰, 分别位于 203、253 和 353 nm (图 5)。其中 203 nm 的吸收峰归属于 [4BrBzPy] [PIC] 的 [4BrBzPy]⁺ 中苯环或吡啶环的 $\pi \rightarrow \pi^*$ 电子跃迁^[17], 253 和 353 nm 的吸收峰主要来源于 [4BrBzPy] [PIC] 的苦味酸根中的苯环和硝基之间的 $\pi \rightarrow \pi^*$ 电子跃迁^[11, 18]。

以 BaSO₄ 作为空白背景, 用紫外-可见光谱在

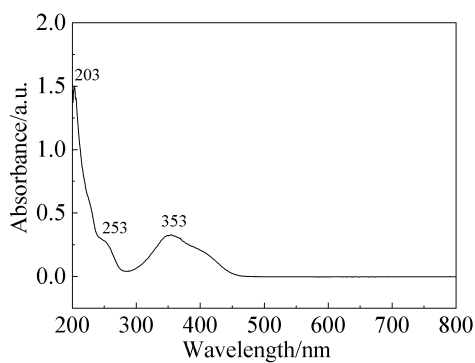


图 5 苦味酸季铵盐的紫外-可见光谱

Fig.5 UV-Vis spectrum of the quaternary ammonium salt

200~800 nm 波长范围测定样品的固体紫外-可见漫反射光谱,了解其吸收情况,计算样品的带隙。对于间接带隙型半导体材料,其带隙和吸收系数之间存在如下关系(式(1)):

$$(ah\nu)^{1/2} = B(h\nu - E_g) \quad (1)$$

其中 a 为摩尔吸收系数, h 为普朗克常数, ν 为入射光子频率, B 为比例常数, E_g 为材料带隙。因此,以 $(ah\nu)^{1/2}$ 对 $h\nu$ 做图,将直线部分外推至横坐标交点,交点数值即为带隙宽度值。苦味酸季铵盐的带隙图谱见图 6,求得的光学带隙为 2.40 eV,对可见光有一定的吸收能力,属于典型半导体材料的范围。

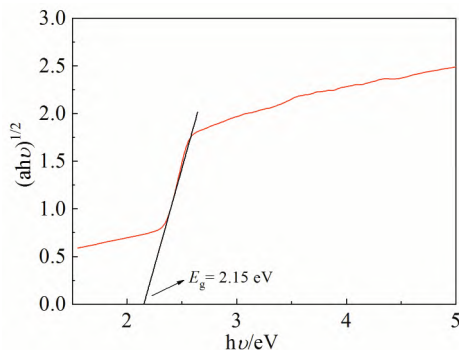


图 6 苦味酸季铵盐的带隙能图

Fig.6 The band gap energy (E_g) of the salt

4.5 粉末 X-射线衍射

取适量苦味酸季铵盐样品在 Rigaku-Ultima IV 型粉末 X-射线衍射仪上进行 XRD 表征。测试条件为辐射源 Cu 靶,射线的波长 $\lambda = 0.154056\text{nm}$,扫描角度 2θ 为 $5^\circ \sim 80^\circ$,扫描速率为 $10^\circ/\text{min}$,实验电压为 40kV,测试电流为 40mA。样品的 XRD 图谱如图 7 所示,其中模拟 XRD 图谱由精修后得到的晶体学信息文件(cif 文件)通过 Mercury 软件计算拟合得到。可以看出,实验

观察到的 XRD 峰与由晶体结构数据拟合的 XRD 图谱吻合得很好,表明所合成的苦味酸吡啶季铵盐粉末样品具有高的纯度,可以用于固态荧光光谱的测试^[19]。其中 2θ 为 $7.28^\circ, 7.89^\circ, 9.06^\circ, 11.89^\circ, 13.24^\circ, 15.74^\circ, 16.56^\circ, 17.02^\circ, 17.72^\circ, 19.06^\circ, 21.08^\circ, 22.57^\circ, 23.87^\circ, 15.17^\circ$ 和 28.20° 处出现了特征衍射峰,对应的晶面分别为 (011) , (100) , (101) , $(1\bar{1}0)$, $(10\bar{2})$, (113) , $(20\bar{1})$, (220) , $(10\bar{3})$, $(22\bar{1})$, $(2\bar{1}2)$, $(20\bar{3})$, $(2\bar{2}1)$, (015) 和 $(3\bar{1}2)$ 。

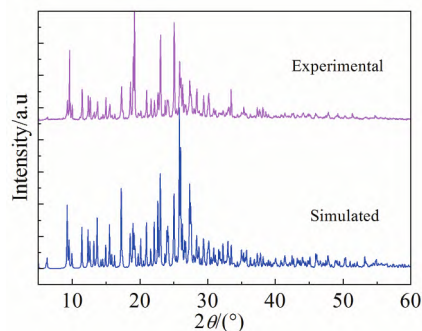


图 7 苦味酸季铵盐实验和拟合的 PXRD 图

Fig.7 Experimental and simulated PXRD patterns of the salt

4.6 荧光光谱

苦味酸吡啶季铵盐的外观如图 8 所示,样品的固体荧光光谱(图 9)用荧光分光光度计测定,以 350nm 作为激发波长,扫描波长范围为 370~650 nm,狭缝宽度为 5nm。



图 8 苦味酸季铵盐的外观图

Fig.8 The appearance of the salt

从图 8 可以看出,苦味酸吡啶季铵盐 $[4\text{BrBzPy}][\text{PIC}]$ 晶体为黄色条状。当用 350nm 的紫外光激发时,分别在 389、469 和 517 nm 出现了发射峰(图 9),其中两个强发射峰为 $[4\text{BrBzPy}][\text{PIC}]$ 的紫色和绿色荧光发射峰,归属于苯环或吡啶环之间的 $\pi \rightarrow \pi^*$ 能级跃迁^[12,18]。

4.7 抗菌活性

两种季铵盐的抑菌圈直径列于表 3。从表 3

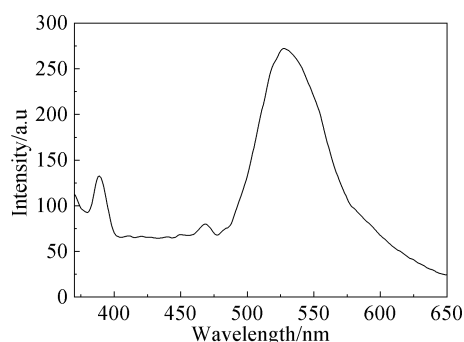


图 9 苦味酸季铵盐的荧光光谱

Fig.9 Fluorescence spectra of the salt

可以看出,中间体和苦味酸季铵盐对大肠杆菌和金葡萄球菌均具有一定的抗菌活性。对大肠杆菌的抗菌活性优于对金葡萄球菌的活性,且含有苦味酸阴离子的吡啶季铵盐对所选菌种的抗菌作用明显比单纯的溴化吡啶季铵盐的强。

表 3 苦味酸吡啶季铵盐的抗菌活性

Tab.3 Antimicrobial activity of quaternary ammonium salts

季铵盐	抑菌圈直径 D/mm	
	金葡萄球菌	大肠杆菌
[4BrBzPy] ⁺ Br ⁻	3.1	4.3
[4BrBzPy] ⁺ [PIC] ⁻	6.8	10.1

5 教学安排

5.1 实验内容安排

本实验项目用于制药工程、应用化学、材料化学和材料科学与工程等相关专业本科生三年级开设综合设计性实验,实验时间为 3 周,2 人一组。其中每个专业学生都需要完成苦味酸吡啶季铵盐的制备、晶体结构、红外光谱、质谱和紫外-可见光谱分析等实验内容,制药工程和应用化学专业学生完成季铵盐抗菌实验内容,而材料化学和材料科学与工程的学生完成粉末 X-射线衍射、紫外-可见漫反射光谱和荧光光谱的实验内容。

由于综合实验较为复杂,对学生能力要求较高,在实验过程中,可针对不同专业的学生,将本实验拆分为“材料制备实验”、“结构表征实验”以及“性能测试实验”三大部分。其中,材料制备实验设置为 6 学时,主要完成图式 1 所示的苦味酸 4-溴苄基吡啶季铵盐合成,得到外观与图 8 对应的产物即完成实验,锻炼学生的化学合成能力;结构表征实验每项表征为 2 学时,由老师提供已合成的苦味酸吡啶季铵盐材料,由学生完成 ESI-MS、红外光谱、粉末 XRD 等结构分析实验,锻炼

学生的仪器分析和谱图分析能力;性能测试实验为 4 学时,包括带隙测试、荧光测试以及抑菌圈测试,锻炼学生对样品构效关系的分析能力。

5.2 实验教学方式

实验项目设计苦味酸吡啶季铵盐的制备包括回流反应、浓缩结晶、减压过滤与真空干燥等过程,材料的表征与性能测试涉及多种现代化仪器分析技术,因此,在具体的实施过程中主要采取“四个结合”的方式:

(1) 线上与线下教学相结合。实验前,学生根据综合性实验的具体要求,通过查阅 CNKI(中国知网)期刊、博士、硕士论文全文库,维普中文科技期刊全文库,Elsevier 期刊全文库,ACS(美国化学学会)期刊库,Springer 电子期刊库,Wiley 电子期刊全文库等电子资源,了解苦味酸盐和季铵盐研究进展,拟定实验方案,撰写预习报告;通过广东省化学实验教学示范中心和生物化工与制药实验教学示范中心网站,预习傅里叶红外光谱仪、紫外-可见分光光度计、荧光分光光度计、液相与-质谱联用仪和粉末 X-射线衍射仪等仪器的工作原理。通过观看视频,学习恒温磁力搅拌器、压片机、真空干燥箱、超净工作台等仪器的操作方法。

(2) 教师讲授、演示与学生现场操作结合。单晶数据的收集、单晶结构解析与精修等耗时长,是本实验项目的难点,学生在短时间内难以掌握。通过教师讲授,让学生了解晶系、空间群等晶体学知识,单晶 X-射线衍射的原理,晶体的培养、选择与安放、衍射数据收集等测试过程;通过演示,让学生了解 SHELX-97 程序进行晶体结构解析的过程,子程序 XPREP、XS、XL 和 XP 等程序的使用,指导学生用晶体学信息文件(cif)和 Diamond 或 Mercury 绘图软件绘制晶体结构图和堆积图。让学生观察合成的苦味酸吡啶季铵盐结构单元、原子之间的连接方式、结构单元 [4BrBzPy]⁺ 阳离子和 [PIC]⁻ 阴离子空间排布方式以及它们之间的弱相互作用。

(3) 集中实验与分散实验相结合。根据实验项目的特点和实验室仪器设备的分布情况,其中苦味酸吡啶季铵盐的制备、纯化、干燥和单晶的培养等内容进行集中实验,季铵盐的 IR、ESI-MS、UV-Vis 和 PXRD 表征,荧光光谱、漫反射光谱和抗菌性能测试等内容在学院两个省级教学示范中心的开放实验平台上由实验技术人员具体指导下完成。

(4) 分组实验与集中讨论相结合。根据不同专业特点,将学生分为应化与制药组和材化与材工两个大组。其中应化与制药组主要完成苦味酸吡啶季铵盐的制备、表征和抗菌性能测试,材化与材工组主要完成苦味酸吡啶季铵盐的制备、表征和荧光性能测试等。实验结束后,一方面要求学生进行数据处理与分析,按照科技论文的形式撰写综合实验报告;另一方面,要求学生制作 PPT,从实验结果的展示与分析、Excel 和 Origin 等软件的使用与绘图、实验报告的规范撰写、实验中出现的与改进措施等方面集中汇报、讨论与总结,进行师生互动、生生互动,提高实验教学效果。

6 教学效果

教学实践证明,该实验项目具有以下特点:

(1) 制备过程简单,操作性强。学生通过回流反应、浓缩结晶、减压过滤与真空干燥等过程获得苦味酸吡啶季铵盐目标产物;(2) 具有综合性和研究性。实验内容涵盖化学、材料、结晶学和微生物学等多个学科的知识点,表征与性能测试涉及到液相-质谱、液体紫外-可见光谱、红外光谱、粉末 X-射线衍射、单晶 X-射线衍射、紫外-可见漫反射光谱、荧光光谱等多种现代化仪器分析技术。(3) 具有系统性和一定的挑战度。实验项目所涉及的制备、表征和性能测试等实验环节紧密关联,学生通过线上线下、教师讲授与演示、集中与分散实验、分组实验与集中讨论等教学方式,提高了综合运用知识的能力和团结协作的精神;学生通过紫外-可见漫反射光谱的测定,根据吸光度计算所合成季铵盐的带隙,判断典型半导体材料类型;通过晶体结构分析获得的晶体学信息文件和相关拟合 XRD 图谱与实验测的 XRD 图谱进行对比分析,判断所合成的苦味酸吡啶季铵盐粉末样品的纯度,提高了学生理论分析水平。(4) 具有前沿性与实用性。学生在了解苦味酸盐有机光学材料和季铵盐抗菌材料的相关前沿知识和应用同时,

测定所制备苦味酸季铵盐的固态荧光发射光谱和对大肠杆菌和金葡萄球菌的抗菌性能,激发了科学研究兴趣,开拓了学生的视野,培养了学生的创新精神,提高了学生综合实验能力和解决实际问题的能力。

参 考 文 献

- [1] 教育部. 关于一流本科课程建设的实施意见: 教高[2019]8 号[Z]. 2019.
- [2] 吴娟娟, 孙慧, 王筱虹, 等. 实验室研究与探索, 2020, 39(12): 208~211.
- [3] 张立春, 吕戈, 衣晓凤, 等. 实验技术与管理, 2019, 36(12): 191~196.
- [4] Scott J C, Bozano L D. Adv. Mater., 2007, 19(11): 1452~1463.
- [5] 李亮, 尹建红, 曹璐, 等. 化学通报, 2011, 74(5): 402~407.
- [6] Samal M, Valligatla S, Saad N A, et al. Chem. Commun., 2019, 55(74): 11025~11028.
- [7] Thirumurugan R, Babu B, Anitha K, et al. Opt. Laser Technol., 2018, 105(9): 106~113.
- [8] Kirubavathi K, Selvaraju K, Vijayan N, et al. Spectrochim. Acta A, 2008, 71(2): 288~291.
- [9] Whitesides G M, Grzybowski B. Science, 2002, 295(5564): 2418~2421.
- [10] Zhang Z, Zhou Y H, Zheng W Q, et al. Synth. Met., 2016, 222(B): 267~263.
- [11] Man L, Li T, Wu X, et al. J. Mol. Struct., 2019, 1175(1): 971~978.
- [12] Li T, Gan Z, Liu C, et al. J. Mol. Struct., 2019, 1180(3): 163~169.
- [13] Munusamy S, Krishnan S, Vedavati G P, et al. Spectrochim. Acta A, 2014, 118(1): 399~406.
- [14] Sheldrick G M. SHELXTL-97, Programs for crystal structure refinements. University of Göttingen, Germany, 1997.
- [15] Kumar V S S, Pigge F C, Rath N P. Cryst. Growth Des., 2004, 4(4): 651~653.
- [16] 赵瑶兴, 孙祥玉. 有机分子结构光谱鉴定(第二版). 北京: 科学出版社, 2010.
- [17] Kumar V K, Nagalakshmi R. Spectrochim. Acta A, 2007, 66(2): 924~934.
- [18] Srinivasan P, Kanagasekaran T, Gopalakrishnan R, et al. Cryst. Growth Des., 2006, 6(7): 1663~1670.

《化学通报》第十六届编委会名单

主 编:张德清

副主编(以姓氏拼音为序):

葛茂发 李亚栋 刘会洲 毛兰群 乔金樑 涂永强 吴 凯 杨振忠

编 委(以姓氏拼音为序):

安立佳 蔡 倩 陈道勇 戴志晖 东为富 段昊泓 范青华 冯长根 付志峰
高栓虎 宫勇吉 郭子建 何林涛 胡憾石 黄 佳 蒋健晖 江 浪 李攻科
李晓娜 李艳梅 梁福鑫 梁文平 林金明 刘虎威 刘鸣华 刘世勇 刘应亮
刘 铮 刘正平 任定成 申 茜 史林启 田中群 万立骏 王吉德 汪 成
王少华 汪 勇 王 煜 魏子栋 吴 菲 郭 慧 杨 柏 杨 帆 杨国强
杨良嵘 杨文胜 姚建年 于 萍 俞书宏 曾小庆 张关心 赵华章 郑南峰
周 峰 周仁贤 周 雄 庄仲滨

本刊采用中国科学院化学研究所纳米材料绿色制版技术制版印刷

化 学 通 报

(月刊·1934年创刊)

2022年4月18日 第85卷第4期 <http://www.hxtb.org>

主 管 中 国 科 学 院
主 办 中国科学院化学研究所
中 国 化 学 会
主 编 张 德 清
编辑出版 《化学通报》编辑部
(地址:北京市海淀区中关村北一街2号
邮政编码:100190)
E-mail: hxtb@iccas.ac.cn

赞 助 单 位 长兴材料工业股份有限公司

印刷装订 北京市泰锐印刷有限责任公司
总发行处 北京报刊发行局
订 购 处 全 国 各 邮 电 局
国外总发行 中国国际图书贸易总公司
国内统一刊号:CN 11-1804/O6
广告发布登记:京海工商广登字 20170209号

公开发行

国内邮发代号: 2-28

国外发行代号: M55

定价 50.00 元

Copyright © 2022 《化学通报》编辑部

ISSN 0441-3776



国际标准连续出版物号: ISSN 1007-1865

国内统一连续出版物号: CN44-1238/TQ

半月刊 创刊于1974年

广东化工

Guangdong Chemical Industry

全国石油和化工行业优秀期刊一等奖

《中国核心期刊(遴选)数据库》全文收录期刊

中国学术期刊综合评价数据库统计源期刊

美国《化学文摘》(CA)重点收录期刊

《中国学术期刊(光盘版)》收录期刊

广东省优秀科学技术期刊

2019 **15**
8月上半月刊

第46卷 (总第401期)

主办单位: 广东省石油与精细化工研究院

佛山市华联有机硅有限公司

FOSHAN HUALIAN ORGANOSILICON CO., LTD



本公司是一家专业从事有机硅产品研究、开发、生产的股份合作企业, 曾是国内第一家中外合资的有机硅公司, 为我国的有机硅事业的发展做出了卓有成效的贡献。为了确保最终的产品满足顾客的要求, 我们已于2001年成功导入ISO9001:2000质量管理体系, 对原材料选购到成品出厂以及售后服务整个过程进行持续的监控, 确保最终的产品满足顾客的要求。

ISSN 1007-1865



地址: 广东省佛山市三水区乐平镇三水中心科技工业园B区13号

电话: 0757-87388188 传真: 0757-87381986

华东地区总代理: 上海海谊化工有限公司

电话: 021-52915425

E-mail: fos757@vip.163.com http://www.hlyjg.com

Guangdong Chemical Industry

第46卷 第15期 8月上半月刊
(总第401期)

1974年创刊 (半月刊)

刊号 ISSN 1007-1865
CN 44-1238/TQ

- 全国石油与化工行业优秀期刊一等奖
- 高、中级化工职称资格评审认定刊物
- 中国核心期刊(遴选)数据库收录期刊

主 管: 广东省科学院

主 办: 广东省石油与精细化工研究院

社 长: 麦裕良

出版发行: 《广东化工》编辑部

发行范围: 国内外公开发行

地 址: 广州市越秀区越华路116号

邮 编: 510030

电话/传真: (020) 83302517 83336009

在线投稿: <http://www.gdchem.com>

电子邮箱: gdcic200@163.com

广告经营许可证号: 440000100138

印 刷: 广州一龙印刷有限公司

订 购: 全国各地邮局、所

邮发代号: 46-211

出版日期: 2019年8月15日

邮局全年定价:

国内480元; 国外384美元

公告: 经广东省新闻出版局批准同意,
本刊从2012年7月开始变更为半月刊。

◆ 试验与研究

- 1 生物填料床去除低温低污染河水中硝态氮及其微生物群落结构特征研究 任海腾, 左剑恶, 黄帅辰, 等
- 5 Cu-V/TiO₂的制备及其催化苯羟基化反应性能研究 赵振龙, 贾丽华, 李良
- 7 聚丙烯纤维改性及应用研究 刘治球, 杨毅, 黄梅欢, 等
- 9 响应曲面法优化蜡状芽孢杆菌 ZW1 去除电镀废水有机物的研究 刘裕华, 戴江汇, 陈寿昆, 等
- 13 FBRM、PVM 在低钠光卤石制取氯化钾结晶中的应用 齐美玲, 王刚, 张莉媛, 等
- 16 某高校 2018 年果蔬农残检测及质量安全情况分析 林瑾
- 18 基于 SWMM 模型的城市低影响开发水文水质效应模拟分析 王宏杰, 董文艺, 吴建立, 等
- 21 不同产地元胡质量的灰色关联及聚类分析 时培东, 周莲
- 23 不同厂家加味逍遥丸电化学指纹图谱的研究 王聪, 韩璐, 吴迪, 等
- 24 基于碳纳米片修饰电极检测水体中的对苯二胺 姚凤, 毛灵苑, 林露, 等
- 26 7075 铝合金微弧氧化陶瓷膜摩擦性能 夏袁昊
- 28 烧结温度对 0.525Bi_{0.5}Na_{0.5}TiO₃-0.475Ba_{0.85}Ca_{0.15}TiO₃ 陶瓷电性能的影响 胡晨曦
- 30 微发泡聚丙烯材料发泡性能影响因素研究 李振华, 彭莉, 杨波, 等
- 33 多功能汽车挡风玻璃清洗剂的研制 王勇军, 叶少林, 何远华, 等
- 36 苯扎氯铵消毒剂的抗菌性能研究 钟瑜, 林少婷, 覃芳敏, 等
- 39 蛋黄磷脂 PC 和 PE 比例对脂肪乳灭菌稳定性的影响 关伟键, 牛亚伟, 唐顺之, 等
- 42 三黄糖肾康颗粒对糖尿病小鼠炎症因子的影响 吴培臻, 余万霖
- 44 耐溶剂改性的聚碳酸酯材料的制备与性能的探讨 黎子宇, 刘冉, 钟志伟
- 47 溶剂对测定烷基醇酰胺值的影响 杨培滨
- 48 不同稳定剂对浓缩胶乳及其硫化胶膜性能的影响 宁家胜, 潘俊任, 蒋一帆
- 51 玻纤增强聚丙烯的纵向热膨胀行为研究 龚文幸, 唐孝芬, 余豪杰, 等
- 53 磺化季铵盐两性表面活性剂合成及研究 冉光友
- 56 不饱和 PDMS-PCL 嵌段共聚物的合成及其在不饱和聚酯树脂中的应用 余桐柏, 黄贵明, 符若文
- 60 磷酸铁锂正极匀浆工艺研究 刘范芬, 黄斯, 杜双龙, 等
- 63 二氧化硅负载硫酸钛催化合成水杨酸正丁酯 班智华, 蔡敏
- 65 TSMR 处理渗滤液纳滤浓缩液影响因素及效果验证 夏俊方
- 70 基于纤维床聚结分离技术的柴油脱水研究 于吉平, 齐庆轩, 胡晓雪
- 73 光学 BOPET 产线抑制纵拉蹭伤的方法研究 程新星, 刘长丰
- 75 喷雾干燥制备托伐普坦固体分散体及其评价 黄健
- 77 QuEChERS 结合 LC-MS/MS 法用于消字号乳膏产品中糖皮质激素的研究测定 傅小红, 李芳, 姜伟
- 80 银离子对白色念珠菌菌丝形成的影响 张梦翔
- 82 miR-497、miR-210 在非小细胞肺癌中的表达及意义研究 徐雷, 宋碧莹, 曹文杰, 等
- 84 还原萃制制备高纯黄金新工艺研究 黄勇, 范义春, 陈静静
- 86 香椿不同部位总黄酮含量比较及生物活性研究 张家俊, 刘玉梅, 胡美忠, 等

◆ 专论与综述

- 88 化学氧化修复氧化剂的选择算法研究 杨坤, 李尤
- 91 电石生产节能降耗优化的研究 熊文杰, 胡伟, 王全勇, 等
- 93 内荆河“一河一策”技术思路及实施途径 向超, 王景芸, 李瑞, 等
- 95 液相剥离法制备石墨烯进展 姜昊, 秦登雪, 汪贞贞, 等
- 97 以标准体系建设促进电子商务质量供给侧改革 李春燕, 顾虎

- 190 检验电导率仪电极性能的一些新思路 周敏倩
191 水中氟离子的测量不确定度评定 朱雯佳
193 土壤中氯乙酸的高效液相色谱分析方法探讨 胡佩雷, 刘绿叶, 刘成霞
195 高效液相色谱法测定艾曲波帕片有关物质及含量 胡蝶
197 火焰原子吸收分光光度法测定化妆品祛痘霜中铅含量的不确定度评估 邱红燕, 廖海伟, 李泽夏琼
199 土壤中多环芳烃的测量不确定度评定 胡志猛

◆ 教学教改

- 201 有机化学全英文教学中的思考与改革 赵红, 郭玲香, 刘安然, 等
203 突出特色、理工融合的应用化学专业实践教学探索 张光华, 李俊国, 朱军峰, 等
204 酒类风味化学课程教学改革与探索 戴怡凤, 邱树毅
205 一流专业建设背景下化工专业实验教学模式探讨 王军
206 浅谈物理化学实验课程的教学改革 何田, 胡自强, 边界, 等
207 提高物理化学教学成效的方法与分析 张谱, 张英
208 工科专业无机及分析化学课程教学体系的优化与探索 殷成阳, 陈庆阳, 程鹏
210 科研成果在无机化学 II 实验教学中的探索应用 张红丹, 程鹏, 陈庆阳, 等
212 关于化学专业研究生导师团队建设的思考 张岩
213 “雨课堂”在天然药物化学课程教学中的运用 邓春梅, 余传明, 张国光, 等
214 基于微信订阅号的碎片化学习在普通化学中的探讨 程作慧, 杨美红, 高春艳, 等
216 专业认证背景下无机及分析化学课程教学改革 李俊国, 张光华, 李运涛, 等
217 大型仪器设备服务于本科实验教学的初探 宋娟
219 发酵工艺原理课程教学探讨与思考 智楠楠, 梁娟, 宗凯
220 制药工程专业计算机辅助药物设计课程的探索 杨兆琪, 朱景宇, 秦兰, 等
222 重点实验室开放项目管理信息系统分析与设计 张燕, 林美芳, 徐惠民
224 中药学专业《中药炮制学》课程教学改革与实践 刘润南, 杨洁, 石继连, 等
225 《实验设计分析与数据处理》课程课堂教学的研究探索 侯向阳, 王潇
227 以增强实践性为目的《环境仪器分析》教学改革探讨 孙彩丽
229 应用型本科院校无机化学课程教学探索 吴云, 高飞, 吴义平, 等
231 基于提高学生自主主动性的化学专业英语教学探索 刁贵强, 林铮, 解芳, 等
233 新工科背景下配位化学课程的教学改革初探 李金燕, 侯得健, 董建宏
234 以应用型人才为导向的化工原理实验教学改革探究 耿莉莉, 何伟, 周婷婷, 等
235 核心素养下中学化学实验教学探讨 陈丽东, 刘江月
237 三重表征下化学学科职前教师 PCK 能力的培养 韩银凤, 胡艳艳
238 关于化学工程与工艺专业应用型人才培养方案的探讨 王允威, 马光强, 朱学军, 等
240 转型期应用型人才培养模式的探索与实践 曾志红, 林授锴, 黄建辉
242 浅谈专业认证下的机械设计教学探索 徐厚昌
244 光伏专业产教融合型新工科应用人才培养探析 李明华
246 《材料分析与表征技术》教学改革探究 张丽
247 药物制剂专业开设《药物毒理学》课程的探索与实践 钱一鑫, 罗乙凯, 王鲁, 等
249 能源化学工程专业创新实验—煤焦油沥青的催化裂解 钟梅
251 雨课堂在公共《物理化学》课程教学中的应用初探 刘维, 何若琳, 陈丛丛

◆ 其它

《广东化工》投稿须知(前插一) 广告索引(69)

本期基金项目论文(共 48 篇)

- P1 生物填料床去除低温低污染河水中硝态氮及其微生物群落结构特征研究
P7 聚丙烯纤维改性及应用研究
P9 响应曲面法优化蜡状芽孢杆菌 ZW1 去除电镀废水有机物的研究
P13 FBRM、PVM 在低钠光卤石制取氯化钾结晶中的应用
P18 基于 SWMM 模型的城市低影响开发水文水质效应模拟分析
P21 不同产地元胡质量的灰色关联及聚类分析
P23 不同厂家加味逍遥丸电化学指纹图谱的研究
P24 基于碳纳米片修饰电极检测水体中的对苯二胺
P39 蛋黄磷脂 PC 和 PE 比例对脂肪乳灭菌稳定性的影响
P42 三黄糖肾康颗粒对糖尿病小鼠炎症因子的影响
P56 不饱和 PDMS-PCL 嵌段共聚物的合成及其在不饱和聚酯树脂中的应用
P65 TSMM 处理渗滤液纳滤浓缩液影响因素及效果验证
P77 QuEChERS 结合 LC-MS/MS 法用于消字号乳膏产品中糖皮质激素的研究测定
P86 香椿不同部位总黄酮含量比较及生物活性研究
P91 电石生产节能降耗优化的研究
P102 基于生物质合成气的固体氧化物燃料电池研究进展
P106 近红外光谱在物料混合均匀度判定中的应用进展
P125 壳聚糖及其改性材料在降低卷烟烟气有害成分上的应用
P127 超高效液相色谱在不同领域的应用
P165 微波消解-ICP-OES 法测定不同产地柿饼中的矿物质元素
P170 近红外光谱技术快速测定清开灵胶囊中 3 种成分及总氮含量
P201 有机化学全英文教学中的思考与改革
P203 突出特色、理工融合的应用化学专业实践教学探索
P204 酒类风味化学课程教学改革与探索
P206 浅谈物理化学实验课程的教学改革
P208 工科专业无机及分析化学课程教学体系的优化与探索
P210 科研成果在无机化学 II 实验教学中的探索应用
P212 关于化学专业研究生导师团队建设的思考
P213 “雨课堂”在天然药物化学课程教学中的运用
P214 基于微信订阅号的碎片化学习在普通化学中的探讨
P216 专业认证背景下无机及分析化学课程教学改革
P219 发酵工艺原理课程教学探讨与思考
P220 制药工程专业计算机辅助药物设计课程的探索
P222 重点实验室开放项目管理信息系统分析与设计
P224 中药学专业《中药炮制学》课程教学改革与实践
P225 《实验设计分析与数据处理》课程课堂教学的研究探索
P227 以增强实践性为目的《环境仪器分析》教学改革探讨
P229 应用型本科院校无机化学课程教学探索
P231 基于提高学生自主主动性的化学专业英语教学探索
P233 新工科背景下配位化学课程的教学改革初探
P234 以应用型人才为导向的化工原理实验教学改革探究
P237 三重表征下化学学科职前教师 PCK 能力的培养
P238 关于化学工程与工艺专业应用型人才培养方案的探讨
P240 转型期应用型人才培养模式的探索与实践
P242 浅谈专业认证下的机械设计教学探索
P244 光伏专业产教融合型新工科应用人才培养探析
P247 药物制剂专业开设《药物毒理学》课程的探索与实践
P251 雨课堂在公共《物理化学》课程教学中的应用初探

雨课堂在公共《物理化学》课程教学中的应用初探

刘维, 何若琳, 陈丛丛
(华南农业大学 材料与能源学院, 广东 广州 510642)

[摘 要]信息时代的到来分散了学生在课堂上的注意力, 导致课程教学产出成果不理想。公共《物理化学》是一门重要的基础必修理论课, 但是存在一定的学习门槛, 学生普遍反映该门课的学习难度大。如何提高物理化学课堂教学质量和效果迫在眉睫。雨课堂作为一款免费教学工具, 或许可以有效地提高物理化学的教学质量, 但目前还缺乏其在公共《物理化学》课程中的应用实例可借鉴。本文通过传统的辅助教学方法相比较, 确定了雨课堂的应用能够为课程带来益处, 明确了雨课堂与传统教学辅助方法之间相辅相成的关联, 为雨课堂《物理化学》教学中的使用提供了指导依据。

[关键词]雨课堂; 物理化学; 课程教学

[中图分类号]G4

[文献标识码]A

[文章编号]1007-1865(2019)15-0251-02

The Application of Rain Classroom in the Teaching of Public Physical Chemistry

Liu Wei, He Ruolin, Chen Congcong
(College of Materials and Energy, South China Agricultural University, Guangzhou 510642, China)

Abstract: The arrival of the information-age distracts the students' attention in the classroom which leads to the unsatisfactory output of the course teaching. Physical chemistry is an important basic compulsory theoretical course, but there is a certain learning threshold, students generally feedback the difficulties in the process of learning. Thus, to improve the quality and effect of physical chemistry classroom teaching becomes urgent. Rain classroom, as a free teaching tool, throws light on it. However, there is still lack of cases in this curriculum. Compared with the traditional auxiliary teaching method, this paper determines that the application of rain classroom can bring benefits to the curriculum, and clarifies the complementary relationship between rain classroom and traditional teaching auxiliary method, which provides a guiding basis for the use of rain classroom physical chemistry teaching.

Keywords: Rain Classroom; Physical chemistry; Course teaching

一流本科、一流专业建设离不开一流课程教学。可是, 随着信息时代的到来, 学生面对更多的诱惑, 手机等通讯工具分散学生课堂注意力, 缺课率不断升高, 课后学生自主学习意识不强, 这些方面的原因导致课程教学产出成果不理想。如何在新形势下, 能吸引每一个学生的注意力, 让学生在轻松愉快的氛围中完成学习任务, 打造魅力课堂, 成为了课程教学改革的重要研究课题。

公共《物理化学》, 是高等农业院校中生物技术、生物工程、食品科学与工程、环境科学、土壤农学等专业的一门重要的基础必修理论课^[1-3]。但是, 由于物理化学的学习涉及到高等数学和物理学相关的基础知识, 存在一定的学习门槛, 加之课时有限, 物理化学课程的讲解存在很大的挑战, 学生普遍反映该门课的学习难度大, 在私下里更是调侃“物化生化必有一挂”。如何能够让学生更轻松的掌握知识, 提高物理化学课堂教学质量和效果, 让学生从心理上主动学习进而培养学生的创新能力和科学素质, 是任课教师必须解决的问题^[4-7]。

雨课堂(Rain Classroom)是由清华大学在线教育办公室组织研发的供学校教师免费使用的教学工具^[8-11]。它将 PPT、MOOC 与手机微信融为一体, 使手机从“低头的工具”变为了“抬头的利器”, 对于改善公共《物理化学》的教学效果有着可观的前景。但目前

为止, 对于如何将雨课堂应用于公共《物理化学》教学并没有详细的报道^[12], 在使用雨课堂协助教学时缺乏可参考的文献。

因此, 本研究旨在研究如何将雨课堂应用于公共《物理化学》课程教学。通过传统的辅助教学方法(如建立答疑教室、组建 QQ 群、建立公共邮箱、设置章节考试、进行期末答疑等)进行比较, 阐明雨课堂能够为课程带来的益处, 明确雨课堂与传统教学辅助方法之间的关系, 为利用雨课堂教学提供指导依据。

1 传统辅助教学方法在《物理化学》公共课中的应用

在传统教学中, 除了正常的教学以外, 多种辅助手段可帮助师生提高教学效果, 如建立答疑教室、组件 QQ 群或进行期末答疑等。因此, 我们将上述方法在课程中进行了实际应用, 得到的总体教学效果如表 1 所示。结果表明, 不同的教学尝试均起到了一定的效果, 如 QQ 群能够为学生提供完整的复习资料等。但是这些效果主要是有助于学生提高复习效率, 并不能在预习、课堂教学上起到很好的作用。

表 1 不同辅助教学手段的优点和弊端

Tab.1 Advantages and disadvantages of different auxiliary teaching methods

教学尝试	尝试时间	结果	弊端
借教室每周答疑	2017下	只有三四个学生参与	缺乏约束力
组建QQ群	2016下	学生比较活跃, 群内	临近期末QQ信息量太大, 扰乱正常的工作, 很
	2017下	资料下载频繁	多回复, 学生要翻很久才能找到答案
建公共邮箱	2016下	学生很少登录邮箱下	手机发邮件没那么方便, 学生用的极少
	2017下	载资料或咨询问题	
章节考试题	2016下	最后汇总为平时作业	有个别学生会抄; 当周发下去, 次周收, 再下一周才能返作业, 此时的课程已经早过去了
	2017下	成绩	
期末答疑	2016下	大部分学生会来	临时抱佛脚
	2017下		

[收稿日期] 2019-07-20

[基金项目] 广东省高等教育教学改革项目, 粤教高函【2018】180号

[作者简介] 刘维(1988-), 女, 商丘人, 博士, 主要研究方向为分子磁性材料。

2 雨课堂在《物理化学》公共课中的应用

图1是雨课堂app的教学页面,它有着整套的教学辅助工具,除了像传统方法在复习上为学生提供帮助以外(图1b),雨课堂还能够提供学生学习情况统计数据(图1a),在预习时为学生

推送资料,在课堂教学时进行随堂测验(图1c),从而大幅提高学生的学习效率。同时,雨课堂界面友好,学生参与度高,对于提高学生课堂兴趣也很有帮助。



图1 雨课堂 app 用于教学的界面
Fig.1 The interface of Rain Classroom

3 小结

实际上,传统辅助教学手段和雨课堂教学并不冲突。在传统辅助教学的基础上引入雨课堂,不仅能够让老师与学生形成更好的互动,更加有效地激发学生的学习兴趣,还能够方便老师掌握学生信息、统计学生的成长情况,实现因材施教。雨课堂在公共《物理化学》教学中具有重要的应用前景,值得化学教师尝试并使用。

参考文献

- [1]陈永东,朱元强,赖南君.安全工程专业物理化学课堂教学的改革和探索[J].教育现代化,2016,3(6):64-66.
- [2]王春华,马丽英,武小清,等.药学专业化学课程教学改革探索[J].药学教育,2017,33(3):59-61.
- [3]徐佳.化工专业物理化学课程的教学改革与实践[J].教育现代化,2018,5(5):129-131.
- [4]余刚,谢祥林,董奇志,等.物理化学“讲授加导修”教学模式的研究与实践[J].中国大学教学,2013(11):27-29.
- [5]白杨,张秀辉.物理化学教学中的师生多途径交流[J].大学化学,2016,

31(1):28-32.

- [6]李志军.案例式教学在物理化学课程教学中的应用[J].科教文汇(中旬刊),2018(1):69-70.
- [7]马献力,刘汉甫,李芳耀,等.翻转课堂在《物理化学》课程教学中的应用思考[J].教育教学论坛,2017(6):237-239.
- [8]臧晶晶,郭丽文.滴水成雨——走进雨课堂[J].信息与电脑(理论版),2016(8):235-236.
- [9]王帅国.雨课堂:移动互联网与大数据背景下的智慧教学工具[J].现代教育技术,2017,27(5):26-32.
- [10]徐盛夏.教学方式与时俱进:“雨课堂”教学[J].教育现代化,2016,3(35):191-192.
- [11]王瑞娟,印志鸿.雨课堂在翻转课堂教学中的应用研究[J].现代计算机(专业版),2018(1):38-40.
- [12]陈海玲.雨课堂+PPT教学在物理化学中的应用[J].广州化工,2017,45(20):163-164.

(本文文献格式:刘维,何若琳,陈丛丛.雨课堂在公共《物理化学》课程教学中的应用初探[J].广东化工,2019,46(15):251-252)

国家级高新技术企业
国家火炬计划产品
2010年制药装备十佳创新企业
I、II类压力容器制造企业

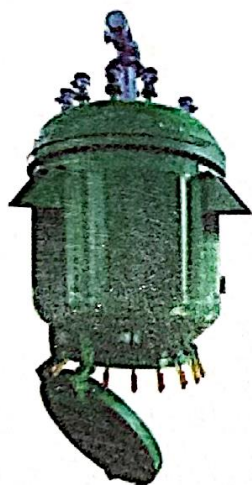


过滤、洗涤、压干精密微孔过滤机



用于超细粉末活性炭、超细固体催化剂、超细结晶体等的过滤、洗涤、压干

全国已有几千台在成功应用；
高精度(0.3微米)、高效率(>99.9%)；
长寿命、低能耗与低物耗；
密闭、安全、占地面积小



新型强化离子交换柱

树脂交换效果好，避免了常规离子交换柱的短路、沟流和树脂破碎后液体流动阻力大等弊端；

树脂利用率高，破碎的树脂可继续使用，绝无树脂穿漏现象；

吸附均匀，确保每一粒树脂最大限度发挥作用，节约洗水，再生酸、碱用量大大减少；

树脂吸附速度快，且更换方便；

因自动化程度高，可实现无人操作。



原料液、中间液（包括中药提取液）与成品液精密微孔过滤机

过滤精度(0.3微米)，高效率(>99.9%)；

长寿命，低能耗，低物耗；

密闭、安全、占地面积小；

过滤面积：从5米²到200米²；

全国已有上千台在成功应用。



工业用层析柱

柱内径：0.5至1.6米。

十多台大型工业层析柱已在制药企业成功应用一年以上。

采用东瓯公司的核心技术使工业用大直径层析柱结构简化、操作方便、效率高。

浙江东瓯过滤机制造
有限公司

温州市东瓯微孔过
滤有限公司

浙江省丽水市水阁工业园区石牛
路85-2号

邮编：323000

电话：0577-88130119 88130813

0578-2695199 2975888

传真：0577-88138523

0578-2695198

网址：www.chinadongou.com

E-mail: chinadongou@126.com

Chinadongou@sina.com

上海市东瓯微孔过
滤技术研究所

上海市长寿路396号7楼

邮编：200060

电话：021-62778862

62275792

传真：021-52520537

E-mail:

xianhong@public4.net.cn



离子型镍配合物的制备及其电催化产氢性能 综合性实验设计

刘 维, 胡宝怡, 余家瑜, 陈克来, 倪春林*

(华南农业大学 材料与化学工程学院, 广州 510642)

摘要: 通过科研成果提炼, 将具有电催化产氢活性配合物的制备引入本科综合性实验教学, 以 2,2'-联吡啶 (bpy)、1,2-二氰基-1,2'-二硫烯 (mnt) 和氯化镍为原料, 制备一种离子型镍配合物($[\text{Ni}(\text{bpy})_3][\text{Ni}(\text{mnt})_2]$), 用单晶 X 射线衍射仪(XRD)、红外光谱、电喷雾质谱和紫外-可见光谱对配合物进行了表征, 研究了其在有机相和水相的电催化产氢性能。结果表明, 在电解电压为 -1.15 V 的磷酸盐缓冲溶液中, 配合物在 4 h 内的产氢量为 0.386 mmol , 电催化效率 (TON 值) 为 2922.13, 且具有良好的稳定性。该实验项目合成步骤简单, 具有前沿性和综合性, 涵盖的知识点和实验技术丰富, 有利于学生树立绿色低碳理念, 提高创新能力和科学研究的能力。

关键词: 二硫烯镍配合物; 电催化; 产氢; 综合实验; 创新能力

中图分类号: O627.51, O642.423

文献标志码: A

DOI: 10.12179/1672-4550.20240393

Comprehensive Experimental Design of Preparation and Electrocatalytic Hydrogen Evolution Performance of Ionic Nickel Complex

LIU Wei, HU Baoyi, YU Jiayu, CHEN Kelai, NI Chunlin*

(College of Materials and Chemical Engineering, South China Agricultural University, Guangzhou 510642, China)

Abstract: By refining scientific research results, the preparation of a nickel complex with electrocatalytic hydrogen evolution activity was introduced into undergraduate comprehensive experimental teaching. An ionic nickel(II) complex ($[\text{Ni}(\text{bpy})_3][\text{Ni}(\text{mnt})_2]$) was prepared using 2,2'-bipyridine (bpy), 1,2-dicyano-1,2'-dithiolene (mnt) and nickel chloride as raw materials. The complex was characterized by single crystal X-ray diffraction, infrared spectroscopy, electrospray ionization mass spectrometry, and ultraviolet-visible spectroscopy. Its electrocatalytic hydrogen evolution performance in both organic and aqueous phases was investigated. The results show that in a phosphate buffer solution at an applied voltage of -1.15 V , the complex produces 0.386 mmol of hydrogen over 4 h, with a turnover number (TON) of 2922.13, and exhibits good stability. This experimental project features simple synthetic procedures, combines cutting-edge and comprehensive aspects, covers numerous knowledge points and experimental technologies, and helps foster students' awareness of green and low-carbon development while enhancing their innovation ability and scientific research skills.

Key words: dithiolene nickel complex; electrocatalysis; ; hydrogen evolution; comprehensive experiment; innovation ability

在“科技融合”的理念下, 将学科前沿研究相关的难点和热点以及现代科学技术有机融入本科实验教学体系是“一流课程”建设的必然要求, 是提升实验课程的高阶性、创新性和挑战度^[1-2], 提高一流专业建设水平和人才培养质量的

重要途径^[3]。氢气由于具有清洁、高效、安全、高热值、环境友好等特点, 已成为最有发展前景的新能源^[4-5]。目前制取氢气的方法主要有化石燃料制氢、电解水制氢、光解水制氢和生物制氢等^[6-7]。其中电解水制氢可以直接得到纯的氢气, 没有污

收稿日期: 2023-11-30

基金项目: 广东省本科高校教学质量与教学改革工程建设项目(粤教高函〔2024〕9号); 广东省本科高校课程思政改革示范项目(粤教高函〔2021〕21号)。

作者简介: 刘维, 博士, 讲师, 主要从事功能金属配合物方面的研究。E-mail: 550919971@qq.com

*通信作者: 倪春林, 博士, 教授, 主要从事分子基功能材料的制备与应用研究。E-mail: niclchem@scau.edu.cn

染,水储量丰富,但耗能大、成本高。因此,在“碳达峰、碳中和”目标的指引下,如何通过简单、高效的途径从储量丰富的水资源中获取氢气已成为全球科学家们的研究目标^[4,8-10]。

离子型的二硫烯过渡金属配合物由于其阴离子 $[M(dit)_2]^{n-}$ (M 为过渡金属离子, $n = 1$ 或 2) 具有高度离域化的平面共轭结构,使这类配合物展现出了电化学、电导、磁学、电催化和光催化等优良的性能^[11-13]。依托团队的科研成果^[14-16],将“离子型镍(II)配合物制备及其电催化产氢性能”设计成面向应用化学、材料化学等本科一流专业高年级学生的综合实验,采用改进的方法制备了一种离子型镍配合物—双(1,2-二氰基-1,2'-二硫烯)镍(II)酸三(2,2'-联吡啶) $[\text{Ni}(\text{bpy})_3][\text{Ni}(\text{mnt})_2]$, 通过一个完整的“合成—结构—性能—用途”实验项目的实施过程,引导学生发现问题、提出问题、分析问题和解决问题,树立绿色低碳理念,提升学生的综合素质和解决复杂问题的思维能力。

1 实验目的

1) 了解氢能的特点和应用前景以及金属镍配合物在电催化制氢方面的研究进展。

2) 掌握离子型金属镍配合物的制备和采用溶液结晶法获得单晶的方法与技术。

3) 了解单晶 X 射线衍射仪(X-ray diffraction, XRD)的原理和收集晶体数据的过程、SHELX-2018 程序中 XPREP、XS、XL 和 XP 等子程序的

使用和晶体结构解析的全过程。

4) 熟悉紫外-可见光谱、傅立叶红外光谱仪和电化学工作站的原理和使用方法,学习用气相色谱仪测定电解产生的氢气含量的方法。

5) 掌握利用循环伏安和控制电位电解法测定配合物电催化制氢性能的原理和方法,根据实验结果,结合相关文献,推断出可能的离子型镍配合物电催化产氢机理。

2 实验原理

离子型镍配合物 $[\text{Ni}(\text{bpy})_3][\text{Ni}(\text{mnt})_2]$ 的制备通过 2 个步骤完成:首先以无水乙醇为溶剂,2,2'-联吡啶和氯化镍发生配位反应,合成中间体二氯联吡啶镍配合物 $[\text{Ni}(\text{bpy})_3]\text{Cl}_2$;其次,将中间体 $[\text{Ni}(\text{bpy})_3]\text{Cl}_2$ 与马来二氰基二硫烯二钠盐 (Na_2mnt) 反应,然后过滤、洗涤和重结晶得到最终产物,合成路线如图 1 所示。所得产物通过单晶 XRD、傅立叶红外光谱、紫外-可见光谱等手段表征,电催化效率的高低(TON 值)用转换数 T 表示,即催化底物发生化学变化的分子数,公式如(1)所示。

$$T = \Delta C \times 3600 / (F \times n_1 \times n_2) \quad (1)$$

式中: ΔC 指扣除空白后的电解电量,单位为 C; F 指法拉第常数, $96480 \text{ C} \cdot \text{mol}^{-1}$; n_1 指转化为 1 mol 氢气所需要的电子数; n_2 指催化剂的物质的量,单位为 mol。

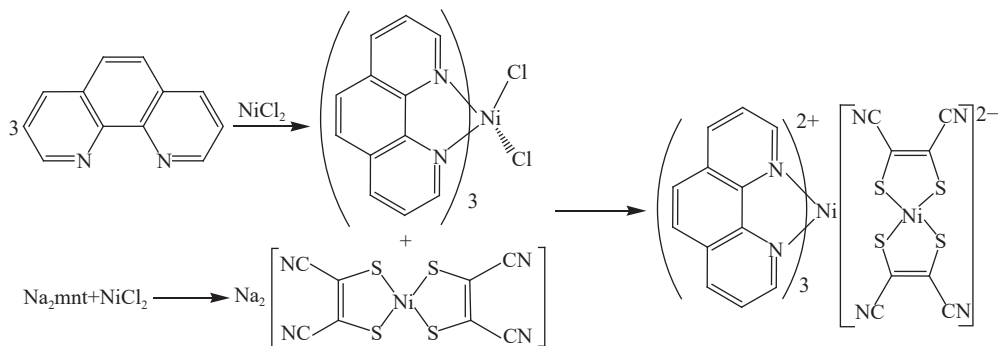


图 1 $[\text{Ni}(\text{bpy})_3][\text{Ni}(\text{mnt})_2]$ 的合成路线图

3 实验内容

3.1 实验试剂

2,2'-联吡啶、六水合氯化镍($\text{NiCl}_2 \cdot 6\text{H}_2\text{O}$)、甲醇、乙醇、二氯甲烷、乙腈等试剂均为市售分析

纯,使用前未经进一步处理。马来二氰基二硫烯二钠盐(Na_2mnt)由华南农业大学无机功能材料研究室提供。

3.2 实验仪器

单晶 XRD (Bruker Smart APEX CCD, 德国

Bruker 公司); 液相色谱串联质谱联用仪 (API 3200, 美国 AB Sciex 公司); 紫外-可见分光光度计 (UV 2600i 型, 日本 Shimadzu 公司); 气相色谱 (FuLi 9790 Plus, 浙江福立分析仪器股份有限公司); 电化学工作站 (CHI660E, 上海辰华仪器有限公司); 恒温磁力搅拌器 (B11-3, 上海司乐仪器有限公司); 真空干燥烘箱 (DZF-6051, 上海一恒科学仪器有限公司); 循环水式真空泵 (SHZ-D(III), 河南省予华仪器有限公司)。

3.3 配合物的合成

称取 2,2'-联吡啶 (0.72 g, 0.3 mmol) 和 $\text{NiCl}_2 \cdot 6\text{H}_2\text{O}$ (0.24 g, 0.1 mmol) 于 100 mL 的锥形瓶中, 加入 50 mL 无水乙醇, 80 °C 回流反应 2 h。将绿色沉淀减压过滤, 无水乙醇洗涤 3 次, 60 °C 真空干燥, 得到绿色的三(2,2'-联吡啶)氯化镍固体。

称取 $\text{Na}_2(\text{mnt})$ (0.19 g, 0.1 mmol) 溶于 20 mL 的甲醇溶液, 加入含 $\text{NiCl}_2 \cdot 6\text{H}_2\text{O}$ (0.12 g, 0.05 mmol) 的 10 mL 的甲醇溶液, 磁力搅拌 20 min 得到红色的 $\text{Na}_2[\text{Ni}(\text{mnt})_2]$ 溶液。将三(2,2'-联吡啶)氯化镍固体 (0.30 g, 0.05 mmol) 用 20 mL 二氯甲烷溶解后加入到上述溶液中, 有红色沉淀生成, 继续搅拌 0.5 h 后, 减压过滤, 用甲醇洗涤, 真空干燥后用少量乙腈溶解, 置于冰箱中冷却, 得到红色针状晶体, 产率 55.1%。

3.4 晶体结构测定与 Hirshfeld 表面分析

选取适当尺寸的晶体置于 Bruker Smart CCD 单晶 XRD 上, 用经石墨单色器单色化的 $\text{Mo K}\alpha$ 辐射为光源 ($\lambda = 0.071073 \text{ nm}$), 常温下以 φ - ω 扫描方式在 5°~50° 范围内收集衍射数据。全部数据还原和结构解析用 SHEXTL-2018 程序^[17]。

3.5 电催化性能测试

电化学性能测试采用三电极系统在电化学工作站上完成, 其中工作电极为玻碳电极, 参比电极分有机相电极 Ag (0.1 mol/L 的 $\text{n-Bu}_4\text{NClO}_4$ 和 0.01 mol/L 的 AgNO_3 乙腈溶液) 和水相电极 Ag/AgCl (内充饱和氯化钾溶液), 辅助电极为铂丝电极, 有机相电解质为四丁基高氯酸铵 ($\text{n-Bu}_4\text{NClO}_4$), 水相电解质为 KCl , 溶剂主要是乙腈和水。循环伏安测试在单槽电解槽中进行, 使用的玻碳电极直径为 1 mm, 内标物为二茂铁。控制电位电解测试在 H 型双槽电解槽中进行, 两槽中间通过聚四氟乙烯薄膜进行隔离, 使用的工

作电极为玻碳片 (面积为 0.45 cm^2), 在进行电解产氢测试时, 工作电极一侧的电解槽经过密封处理, 并用 N_2/CH_4 (体积比 4:1) 的混合气排除电解槽内的空气, 电解产生的氢气含量用气相色谱仪进行测定。

4 结果与讨论

4.1 红外光谱分析

配合物红外光谱如图 2 所示, 其中 $[\text{Ni}(\text{bpy})_3]^{2+}$ 中联吡啶苯环上的 C—H 伸缩振动出现在 3074 cm^{-1} , C=C 和 C=N 骨架伸缩振动出现在 1604 cm^{-1} 和 1441 cm^{-1} , 1315 cm^{-1} 是 C—N 伸缩振动, 759 cm^{-1} 归属于吡啶环上 C—H 面外弯曲振动, 649 cm^{-1} 来自于 C—C 面内弯曲振动; $[\text{Ni}(\text{mnt})_2]^{2-}$ 中 C≡N 的伸缩振动吸收出现在 2194 cm^{-1} , C=C 的伸缩振动吸收峰在 1480 , 1152 , 1022 cm^{-1} 归属于 C—S 和 C—C 的伸缩振动, 511 cm^{-1} 是环的变形振动峰, 448 cm^{-1} 归属于 Ni—S 伸缩振动和 C—C≡N 面内弯曲振动^[18]。

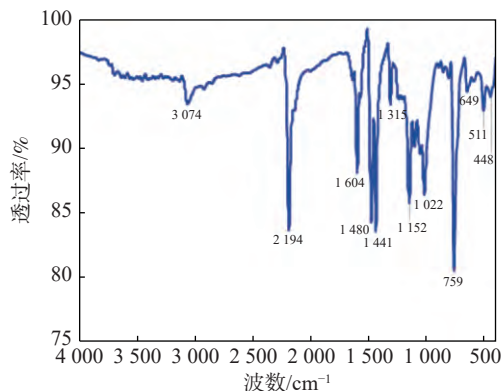


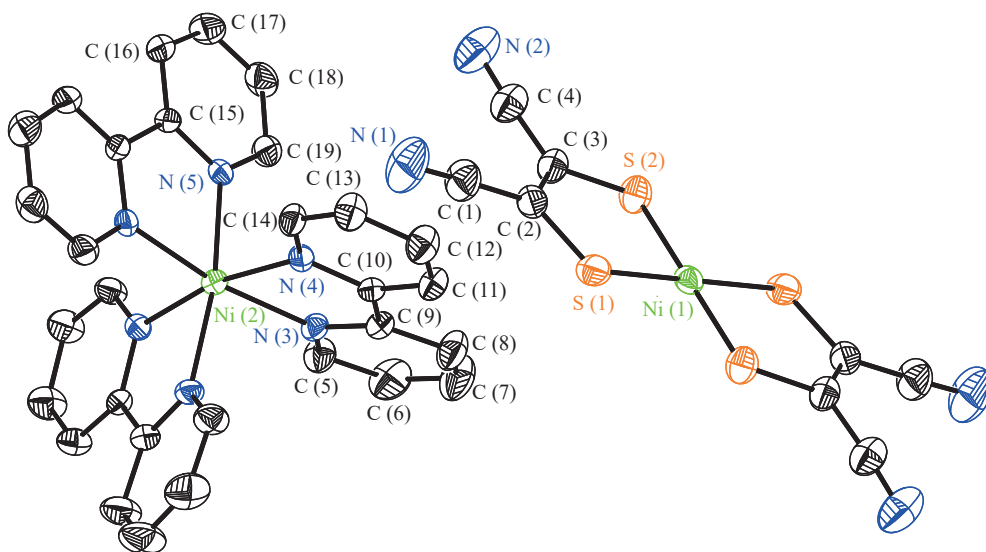
图 2 $[\text{Ni}(\text{bpy})_3][\text{Ni}(\text{mnt})_2]$ 的红外光谱图

4.2 晶体结构的比较分析

在 293 K 下经 XRD 测得的配合物的主要晶体学数据和键参数列于表 1。可以得知, 配合物属于单斜晶系 $\text{C}2/c$ 空间群, 不同于文献^[15]报道的空间群 ($\text{P}2_1/a$)。晶胞参数为 a, b, c, β 和 V 与文献^[15]报道的 193 K 下的略有不同。晶体结构如图 3 所示, 可以看出, 配合物的一个不对称单位中含有半个 $[\text{Ni}(\text{bpy})_3]^{2+}$ 阳离子和半个 $[\text{Ni}(\text{mnt})_2]^{2-}$ 阴离子, 不同于文献^[19]报道的组成; 配合物中 Ni—S 和 Ni—S 键长、S—Ni—S 和 N—Ni—N 键角等键参数与文献^[19]的键参数基本一致。

表 1 配合物的主要晶体学数据和键参数

项目	参数(实验)	参数(文献)	化学键	键参数(实验)	键参数(文献)
测试温度	291	193	Ni(1)—S(1)	0.2174	0.2174
晶系	Monoclinic	Monoclinic	Ni(1)—S(2)	0.2169	0.2172
空间群	$C2/c$	$P2_1/a$	Ni(1)—N(3)	0.2103	0.2094
a/nm	1.5498(2)	1.3799(8)	Ni(1)—N(4)	0.2083	0.2071
b/nm	2.3327(2)	2.3630(10)	Ni(1)—N(5)	0.2089	0.2019
c/nm	1.3534(2)	1.4884(10)	S(1)—Ni(1)—S(1)	92.3300	92.7000
$\beta/^\circ$	118.273(2)	115.382(9)	N(3)—Ni(2)—N(4)	171.0000	170.4000
晶胞体积/ nm^3	4.3092(9)	4.3856(5)	N(3)—Ni(2)—N(5)	171.0000	169.1000

图 3 $[\text{Ni}(\text{bpy})_3][\text{Ni}(\text{mnt})_2]$ 的晶体结构图

4.3 紫外-可见光谱分析

配合物在 200~800 nm 范围内的紫外-可见光谱(溶剂为乙腈)结果如图 4(a)所示, 其中 250 nm 处为配体上苯环的 $\pi \rightarrow \pi^*$ 跃迁; 285 nm 处为配体间的 $\text{L} \rightarrow \text{L}^*$ 跃迁; 384 nm 处为配体 π 轨道到中心金属 d_{xy} 分子轨道的 $\text{L}(\pi) \rightarrow \text{M}$ 跃迁; 406 nm 处为

中心金属的 $d \rightarrow d^*$ 跃迁^[16]。图 4(b) 展示了配合物在不同醋酸量条件下的紫外-可见光谱的曲线变化情况, 随着酸量的增大, 紫外-可见吸收曲线吸收峰没有明显的变化, 说明配合物在酸中可以保持很好的稳定性^[16]。

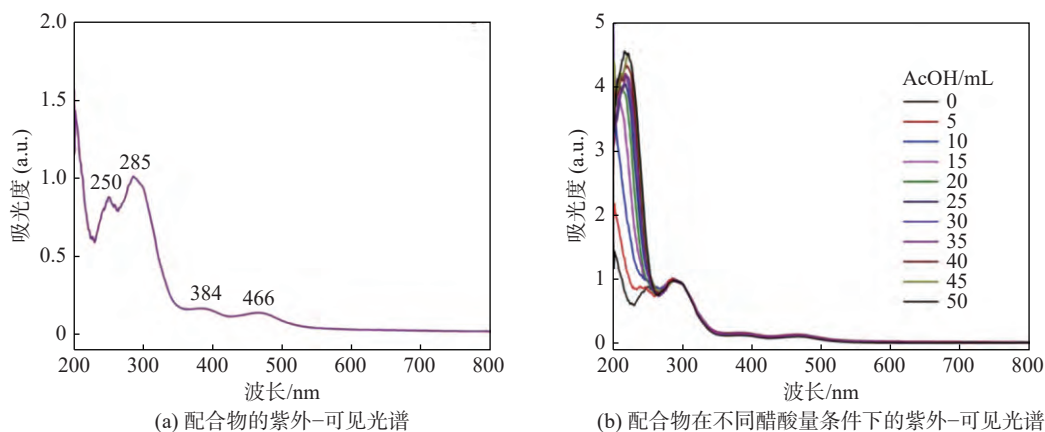


图 4 紫外-可见光谱图

4.4 循环伏安测试

在以乙腈为溶剂的有机相中进行循环伏安测试, 结果如图 5 所示。图中用符号“*”标明的是二茂铁内标峰, 从图 5(a)可以看出配合物有

两对可逆的氧化还原峰, 对应的是 -0.11 V ($\Delta E_p = 49\text{ mV}$) 和 -2.04 V ($\Delta E_p = 66\text{ mV}$), 分别归属于 $\text{Ni}^{\text{II}}/\text{Ni}^{\text{I}}$ 氧化还原峰和 $\text{Ni}^{\text{I}}/\text{Ni}^0$ 氧化还原峰^[14-15]。

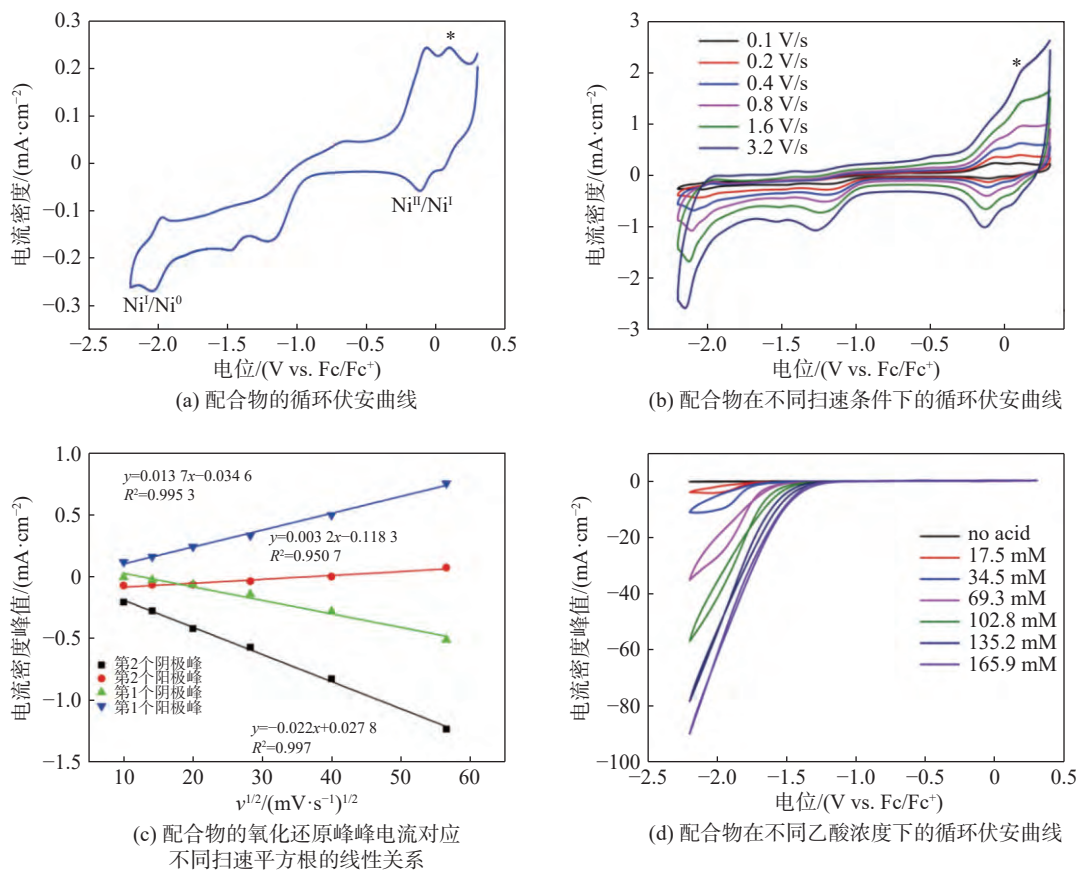


图 5 循环伏安测试结果曲线图

为了进一步探究配合物在溶液中的传输形式, 保持其他条件不变, 通过改变循环伏安测试中的扫速, 来观察氧化还原峰峰电流与扫速的平方根的线性关系。从图 5(b)可以看出随着扫速的增大, 配合物的氧化还原峰峰电流也在相应增大, 而且氧化还原峰峰电流与扫速的平方根呈良好的线性关系, 如图 5(c)所示, 可以表明配合物迁移到工作电极表面进行得失电子的过程是自由扩散控制过程^[18]。为了探究这种配合物电催化活性, 通过添加冰乙酸, 来观察随着酸浓度增大循环伏安曲线氧化还原峰峰电流的变化情况, 结果如图 5(d)所示。可见配合物在 $\text{Ni}^{\text{I}}/\text{Ni}^0$ 氧化还原峰处峰电流随酸浓度的增大而增大, $\text{Ni}^{\text{II}}/\text{Ni}^{\text{I}}$ 氧化还原峰处峰电流无明显变化, 说明催化产氢的过程是 $\text{Ni}^{\text{I}}/\text{Ni}^0$ 氧化还原起主导作用, 而且随着酸浓度增大催化

电流显著增加, 揭示配合物具有良好的催化活性。

4.5 电催化产氢活性测试

在 H 型双槽电解槽中, 首先以乙腈为溶剂, 冰乙酸为氢质子源, 使用控制电压电解法对配合物的电催化产氢效果进行检测, 电解电压为 -1.50 V 。相关结果如图 6(a)和图 6(b)所示, 配合物的 4 h 电解产氢量为 0.068 mmol , 对应的电荷转移数为 14.8 C , T 值达 315.56 。然后以磷酸缓冲溶液为溶剂, 控制电解电压为 -1.15 V , 进行 4 h 电解产氢实验, 结果如图 7(c)和图 7(d)所示。配合物的 4 h 电解产氢量为 0.386 mmol , 对应的电荷转移数为 36.6 C , T 值达 2922.13 。由此可见配合物无论在弱酸环境还是水溶液中都有优良的电催化产氢效果, 其中在水溶液中能实现更高的催化产氢能力。

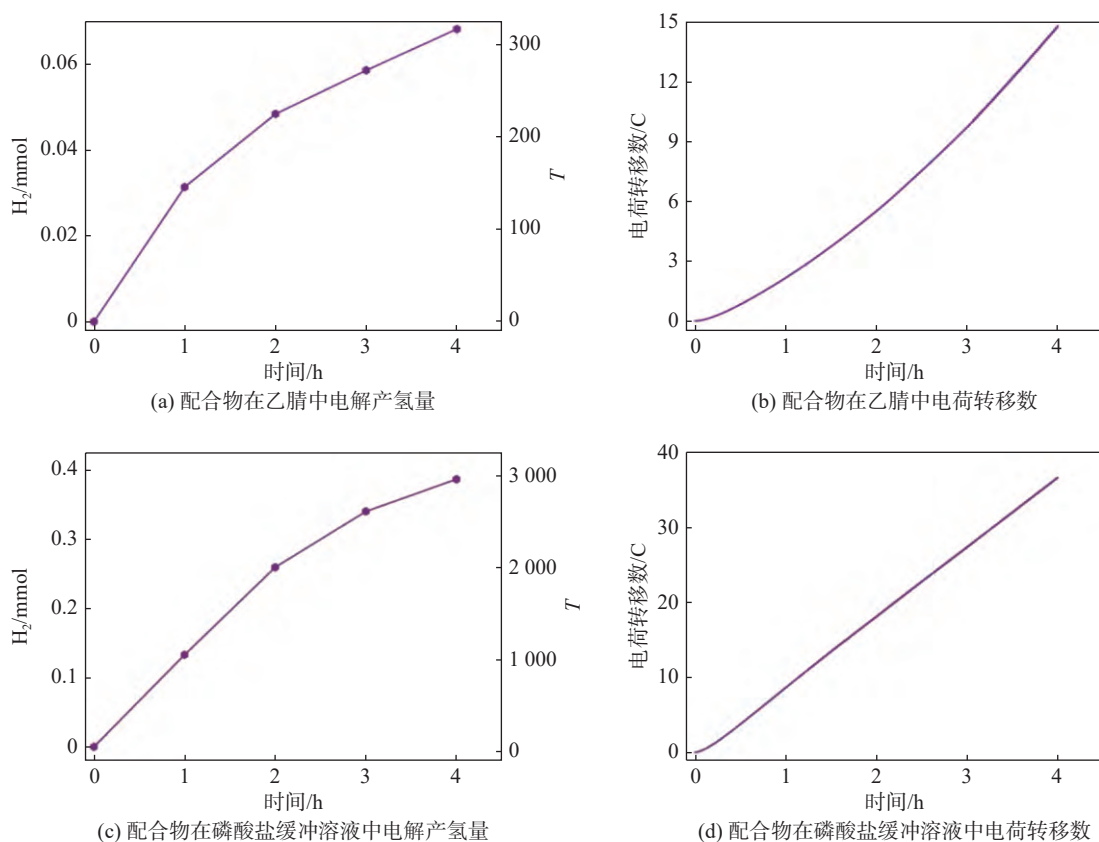


图 6 配合物电解产氢实验结果曲线图

4.6 电催化剂的稳定性测试

为了探究配合物的电催化产氢的稳定性,测定了在磷酸缓冲溶液中进行 2 h 催化电解产氢实验后溶液中 $[Ni(bpy)_3]^{2+}$ 阳离子和 $[Ni(mnt)_2]^{2-}$ 阴离子的电喷雾质谱 (ESI-MS)。从图 7(a) 和图 7(b) 可以看出,电解后溶液中仍然存在镍(II)

配合物的催化中心。由于电解时间较长,产氢量较大,所以保持双槽电解槽两端液面水平,测定了 4 次电解 1 h 的产氢量,从图 7(c) 可以看出,经过 4 次循环电解,配合物仍能保持一定的产氢量,说明所制备的配合物具有较好的电催化活性和稳定性。

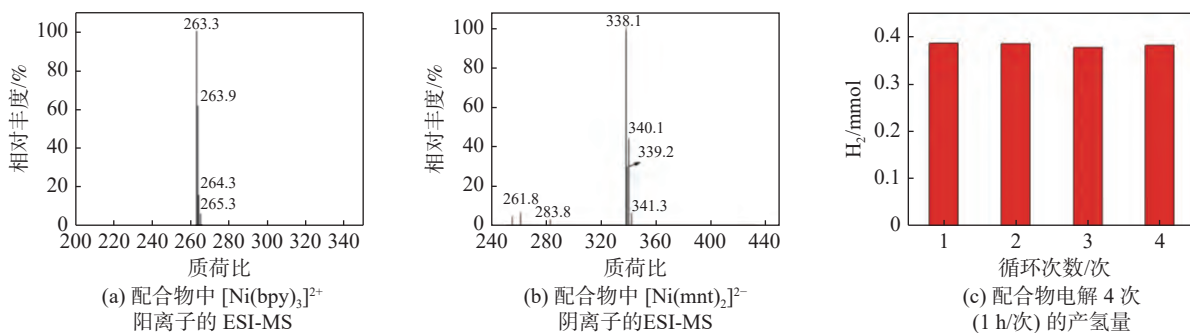


图 7 配合物稳定性测试结果图

5 实验组织与教学效果

该实验项目作为化学类专业学生高年级的综合创新型实验,安排在学生主修完成培养方案中的无机化学实验、分析化学实验、有机化学实

验、物理化学实验、现代仪器分析实验和计算化学实验等课程后,在大学四年级上学期开设,两人 1 组,总学时数为 24 学时。其中配合物的制备与纯化 4 学时;红外光谱和紫外-可见光谱和循环伏安测试 4 学时;电催化产氢活性和催化剂的稳

定性测试 10 学时, 其中催化活性测定分为两个大组, 一部分学生测定配合物在非水溶剂中的活性, 另一部分学生测定配合物在水溶液中的活性, 便于比较分析; 单晶 XRD 和 Hirshfeld 表面分析 4 学时, 采用线上教学形式; 实验结果汇报与交流 2 学时。教学实践的效果如下。

1) 通过实验前预习, 了解氢能作为最有发展前景的新能源的特点和金属镍配合物在电催化制氢方面的研究进展, 树立“绿色低碳”和“绿色制造”理念; 通过离子型金属镍配合物的制备实验, 掌握利用溶液结晶法获得单晶的方法与技术。

2) 通过教师的视频教学, 了解单晶 XRD 的原理; 了解晶体数据收集的过程, 包括晶体的选择与安置、晶胞参数的测定、衍射强度的测定、还原与校正等; 了解晶体结构解析的过程(SHEXTL-2018 程序安装, 结构解析方法的选择, 结构模型的精修, 子程序 XPREP、XS、XL 和 XP 等程序的应用以及晶体结构的表达等); 根据晶体学数据, 判断配合物所属的晶系和空间群, 并绘制晶体结构图, 获得晶胞参数和主要键参数并与文献对比分析。

3) 通过配合物红外光谱的测定, 掌握常见傅立叶红外光谱仪的原理和使用方法, 根据实验测定的 IR 图, 分析归属 $[\text{Ni}(\text{bpy})_3]^{2+}$ 阳离子中联吡啶苯环上的 C—H 伸缩振动和面外弯曲振动, C=C 和 C=N 骨架伸缩振动, 以及 $[\text{Ni}(\text{mnt})_2]^{2-}$ 中 C≡N、C=C 的伸缩振动吸收和 C—S 和 Ni—S 伸缩振动等特征谱带。

4) 通过紫外-可见光谱分析实验, 学习紫外-可见分光光度计的基本原理和使用方法, 了解配合物中电子跃迁的类型, 并对配合物在 200~800 nm 范围内的紫外-可见光谱进行归属; 通过测试配合物在不同醋酸量条件下的紫外-可见光谱的曲线变化图, 分析说明配合物在酸性介质中可以保持良好的稳定性。

5) 通过电催化性能测试实验, 掌握电化学工作站的工作原理, 三电极系统中玻碳电极、Ag/AgCl(内充饱和氯化钾溶液)电极和铂丝电极的功能与作用, 循环伏安测试和控制电位电解测试方法, 利用气相色谱法测定电解产生的氢气含量的方法, 学会电催化效率的计算方法。

6) 根据离子型镍(II)配合物电喷雾质谱(ESI-

MS)确定配合物中 $[\text{Ni}(\text{bpy})_3]^{2+}$ 和 $[\text{Ni}(\text{mnt})_2]^{2-}$ 的具体存在形式和配合物电催化活性随冰乙酸的酸浓度变化等实验结果, 再结合相关文献, 推断出可能的离子型镍(II)配合物电催化产氢机理。

6 结束语

本实验项目包含离子型镍(II)配合物的制备与纯化、结构表征与分析、电催化水解制氢性能与机理分析等内容, 涵盖有机化学、材料化学、配位化学和现代仪器分析化学等实验的原理和操作方法, 可以使学生了解材料科学和能源科学的研究在促进人类社会可持续发展、人与自然和谐共生等方面的重要作用; 初步掌握离子型配合物的合成和表征手段, 熟悉利用电化学工作站进行电催化性能研究的基本研究方法; 掌握采用三电极测试系统进行循环伏安和不同相中电解产氢量的测定方法和过程。实验涉及单晶 XRD 的原理、单晶结构解析的过程、晶体结构解析程序 SHELX-2018 的运用和晶体结构图的绘制等内容, 具有一定“高阶性”“创新性”和“挑战度”。本实验内容丰富, 可操作性强, 反映了材料科学与能源科学研究的最新成果, 有利于激发学生的实验热情, 培养学生的创新能力和实践能力, 是一个适用于应用化学和材料化学等专业的综合实验项目。在今后的实验改进与拓展中, 通过改变氢质子源、有机相溶剂和缓冲溶液等条件进行测试电催化活性, 探究不同催化条件对离子型镍(II)配合物电催化产氢活性的影响。

参考文献

- [1] 教育部. 关于一流本科课程建设的实施意见[Z/OL]. (2019-01-30) [2023-11-01]. http://www.moe.gov.cn/src/site/A08/s7056/201901/t20190130_368447.html.
- [2] 施佳欢, 蔡颖蔚, 郑昱. 一流本科课程建设的实践路径: 以南京大学优质课程建设为例[J]. 中国大学教学, 2021(4): 49-53.
- [3] 张树永, 朱亚先. 高等学校化学类本科一流专业建设标准和建设重点浅析[J]. 大学化学, 2021, 36(5): 1-6.
- [4] ZHU J, HU L S, ZHAO P X, et al. Recent advances in electrocatalytic hydrogen evolution using nanoparticles[J]. *Chemical Reviews*, 2020, 120(2): 851-918.
- [5] MAZLOOMI K, GOMES C. Hydrogen as an energy carrier: Prospects and challenges[J]. *Renewable and Sustainable Energy Reviews*, 2012, 16(5): 3024-3033.

- [6] FENG W S, PANG W B, XU Y, et al. Transition metal selenides for electrocatalytic hydrogen evolution reaction[J]. *ChemElectroChem*, 2020, 7(1): 31–54.
- [7] ZANG N, WU Z X, WANG J, et al. Rational design of Cu–Co thiospinel ternary sheet arrays for highly efficient electrocatalytic water splitting[J]. *Journal of Materials Chemistry A*, 2020, 8(4): 1799–1807.
- [8] GREELEY J, JARAMILLO T F, BONDE J, et al. Computational high-throughput screening of electrocatalytic materials for hydrogen evolution[J]. *Nature Materials*, 2006, 5(11): 909–913.
- [9] HANAN A, NAZIM LAKHAN M, WALVEKAR R, et al. Heteroatom-doped MXenes as electrocatalysts for hydrogen evolution reaction: A review on the recent advances, mechanisms and prospects[J]. *Chemical Engineering Journal*, 2024, 483: 149107.
- [10] FEIDENHANS' L A A, REGMI Y N, WEI C, et al. Precious metal free hydrogen evolution catalyst design and application[J]. *Chemical Reviews*, 2024, 124(9): 5617–5667.
- [11] DUAN H B, REN X M, MENG Q J. One-dimensional (1D)[Ni(mnt)₂]-based spin-Peierls-like complexes: Structural, magnetic and transition properties[J]. *Coordination Chemistry Reviews*, 2010, 254(13/14): 1509–1522.
- [12] ROBERTSON N, CRONIN L. Metal bis-1, 2-dithiolene complexes in conducting or magnetic crystalline assemblies[J]. *Coordination Chemistry Reviews*, 2002, 227(1): 93–127.
- [13] PENG Q X, XUE D, ZHAN S Z, et al. Visible-light-driven photocatalytic system based on a nickel complex over CdS materials for hydrogen production from water[J]. *Applied Catalysis B: Environmental*, 2017, 219: 353–361.
- [14] LEI J M, PENG Q X, LUO S P, et al. A nickel complex, an efficient cocatalyst for both electrochemical and photochemical driven hydrogen production from water[J]. *Molecular Catalysis*, 2018, 448: 10–17.
- [15] NIU Z C, YANG L M, XIAO Y X, et al. Novel dithiolene nickel complex catalysts for electrochemical hydrogen evolution reaction for hydrogen production in nonaqueous and aqueous solutions[J]. *Electrocatalysis*, 2022, 13(3): 230–241.
- [16] YIN H J, GAN Z H, WANG Z, et al. Effects of different dithiolate ligands on electrocatalytic hydrogen production of nickel complexes in acetic acid or water[J]. *Journal of Molecular Structure*, 2023, 1287: 135659.
- [17] SHELDRICK G M. Crystal structure refinement with SHELXL[J]. *Acta Crystallographica Section C Structural Chemistry*, 2015, 71(1): 3–8.
- [18] JOHNSON M K. Progress in inorganic chemistry[M]. New York: John Wiley & Sons, Inc. 2004.
- [19] ZHANG J S, ZHU Q Y, JIA D X, et al. Synthesis and structural characterization of bimetallic Salt [Ni(phen)₃] [Ni(mnt)₂] and [Ni(bpy)₃] [Ni(mnt)₂][J]. *Synthesis and Reactivity in Inorganic, Metal-Organic, and Nano-Metal Chemistry*, 2005, 35(8): 633–637.

编辑 王燕

(上接第 45 页)

- [14] 胡维鑫, 尹佳, 田辉. 基于双目视觉的航空复杂结构件机器人制孔研究[J]. *工具技术*, 2023, 57(12): 101–105.
- [15] ULRICH M, LUX G, PIPREK T. Analysis and visualisation of the positioning accuracy and underlying effects of industrial robots[J]. *Advanced Materials Research*, 2014, 3467: 1018–1018.
- [16] 吴锦辉, 陶友瑞. 工业机器人定位精度可靠性研究现状综述[J]. *中国机械工程*, 2020, 31(18): 2180–2188.
- [17] LI Z, LI S, LUO X. An overview of calibration technology of industrial robots[J]. *IEEE/CAA Journal of Automatica Sinica*, 2021, 8(1): 23–36.
- [18] 齐飞, 平雪良, 刘洁, 等. 关于工业机器人标定方法的研究[J]. *机床与液压*, 2015, 43(21): 32–36.
- [19] 王郑拓, 杨波, 林志伟, 等. 机器人三维视觉实验平台坐标系标定实验设计[J]. *实验室研究与探索*, 2024, 43(8): 52–56.

编辑 钟晓

2024年华南农业大学大学生创新创业训练计划项目

结题证书

项目编号： 2024105641161

项目级别： 校级

项目类型： 创新训练项目

项目名称： 柑橘口罩——PLA/CNF复合纳米纤维的制备及性能研究

项目主持人： 李芷妍

指导老师： 刘维

项目组成员： 常紫妍、施若锴、邓芷婧、郭薇、莫俊东

该项目已完成，经专家组评审准予结题，验收结果为 合格，特发此证。

华南农业大学创新创业学院
二〇二五年十一月



2024年华南农业大学大学生创新创业训练计划项目

结题证书

项目编号：S202410564133

项目级别：省级

项目类型：创新训练项目

项目名称：半导体材料-生物杂化增强型光催化系统的产氢优化

项目主持人：苏黄盛

指导老师：刘维

项目组成员：鹿辰璐、胡慧娥、刘文君

该项目已完成，经专家组评审准予结题，验收结果为合格，特发此证。

华南农业大学创新创业学院
二〇二五年十二月





華南農業大學

本科教學成果獎

獲獎證書

獲獎成果：“四位一體”生物化工
與制藥實踐平台的探究與
實踐

獲獎者：周武藝、倪春林、鄭文旭、
劉維、胡洋、王磊、
張耀謀

獲獎等級：二等獎

證書編號：JXCG24062





華南農業大學

教學成果獎
獲獎證書

獲獎成果:

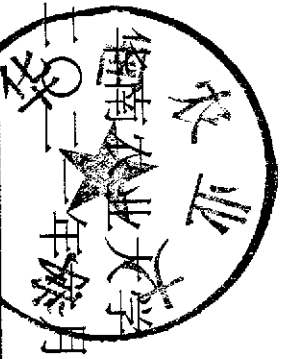
料創引領產業面向的材
料科學與工程本科人才
培養體系的探索與實踐

獲獎者:

雷炳富、董漢武、
鄭明濤、劉應亮、
梁業如、盧其明、
張學杰、胡航、
劉超維、胡健、
胡超凡

獲獎等級: 二等獎

證書編號: JXCG21054



关于国家自然科学基金资助项目批准及有关事项的通知

与原件相符

刘维 先生/女士:

根据《国家自然科学基金条例》的规定和专家评审意见,国家自然科学基金委员会(以下简称自然科学基金委)决定批准资助您的申请项目。项目批准号:

21701045, 项目名称: 基于自旋交叉的手性分子探针的定向构筑与研究, 直接费用: 25.00万元, 项目起止年月: 2018年01月至 2020年12月, 有关项目的评审意见及修改意见附后。

请尽早登录科学基金网络信息系统(<https://isisn.nsfc.gov.cn>), 获取《国家自然科学基金资助项目计划书》(以下简称计划书)并按要求填写。对于有修改意见的项目, 请按修改意见及时调整计划书相关内容; 如对修改意见有异议, 须在计划书电子版报送截止日期前提出。**注意: 请严格按照《国家自然科学基金资助项目资金管理办法》填写计划书的资金预算表, 其中, 劳务费、专家咨询费科目所列金额与申请书相比不得调增。**

计划书电子版通过科学基金网络信息系统(<https://isisn.nsfc.gov.cn>)上传, 由依托单位审核后提交至自然科学基金委进行审核。审核未通过者, 返回修改后再行提交; 审核通过者, 打印为计划书纸质版(一式两份, 双面打印), 由依托单位审核并加盖单位公章后报送至自然科学基金委项目材料接收工作组。计划书电子版和纸质版内容应当保证一致。

向自然科学基金委提交和报送计划书截止时间节点如下:

- 1、提交计划书电子版截止时间为**2017年9月11日16点**(视为计划书正式提交时间);
- 2、提交计划书电子修改版截止时间为**2017年9月18日16点**;
- 3、报送计划书纸质版截止时间为**2017年9月26日16点**。

请按照以上规定及时提交计划书电子版, 并报送计划书纸质版, 未说明理由且逾期不报计划书者, 视为自动放弃接受资助。

附件: 项目评审意见及修改意见表

国家自然科学基金委员会
化学科学部
2017年8月17日



项目批准号	21701045
申请代码	B0308
归口管理部门	
收件日期	



20201121701045

国家自然科学基金 资助项目结题/成果报告

资助类别： 青年科学基金项目

亚类说明： _____

附注说明： _____

项目名称： 基于自旋交叉的手性分子探针的定向构筑与研究

负责人： 刘维 电话： 020-85280319

电子邮件： liuwei97@scau.edu.cn

依托单位： 华南农业大学

联系人： 倪慧群 电话： 020-85280070

直接费用： 25.0000（万元） 执行年限： 2018.01-2020.12

填表日期： 2021年01月28日

国家自然科学基金委员会制（2016年）

项目编号： 202201010559

基础与应用基础研究项目 合同书

项目名称： 基于金属还原菌的生物质纳米铂及其电催化氧还原研究

承担单位： 华南农业大学

项目负责人： 刘维

计划类别： 基础研究计划

专题名称： 基础与应用基础研究项目

支持方向： 一般项目（博士青年科技人员类）

组织单位： 华南农业大学

起止时间： 2022年04月01日 至 2024年03月31日

主管处室： 基础研究处

广州市科学技术局
(二〇二二年制)

受理编号：c24140500001001

项目编号：2024A1515010293

文件编号：粤基金字（2024）7号

广东省基础与应用基础研究基金项目 任务书

项目名称：铁还原菌的质子传递机制解析与合成生物学调控

项目类别：广东省自然科学基金-面上项目

项目起止时间：2024-01-01 至 2026-12-31

管理单位（甲方）：广东省基础与应用基础研究基金委员会

依托单位（乙方）：华南农业大学

通讯地址：广东省广州市天河区五山路483号

邮政编码：510642

单位电话：020-85283435

项目负责人：刘维

联系电话：020-85287100



（广东科技微信公众号）



（查看任务书信息）



（受理纸质材料二维码）

广东省基础与应用基础研究
基金委员会
二〇二〇年制

受理编号: c23140500000319

项目编号: 2023A1515012003

文件编号: 粤基金字(2023)2号

广东省基础与应用基础研究基金项目 任务书

项目名称: 杂原子掺杂对氧化硼基质-碳点余辉能量传递的调控机理研究

项目类别: 广东省自然科学基金-面上项目

项目起止时间: 2023-01-01 至 2025-12-31

管理单位(甲方): 广东省基础与应用基础研究基金委员会

依托单位(乙方): 华南农业大学

通讯地址: 广东省广州市天河区五山路483号

邮政编码: 510642

单位电话: 020-85283435

项目负责人: 胡超凡

联系电话: 15521501455



(广东科技微信公众号)



(查看任务书信息)



(受理纸质材料二维码)

广东省基础与应用基础研究
基金委员会
二〇二〇年制

五、人员信息

项目负责人

姓名	证件号码	年龄	性别	职称	学历	在项目中承担的任务	所在单位	签名
胡超凡	43102719840809001X	39	男	副教授	博士研究生	项目负责人	华南农业大学	

项目组主要成员

姓名	证件号码	年龄	性别	职称	学历	在项目中承担的任务	所在单位	签名
刘维	411424198809230940	35	女	讲师	博士研究生	材料的发光性能表征	华南农业大学	
刘金坤	440785199712276617	26	男	未取得	本科	材料的合成和反应条件优化	华南农业大学	
陈春锦	440882199805100713	25	男	未取得	本科	材料组成和结构分析	华南农业大学	
万芷君	441625199705215022	26	男	未取得	本科	材料的发光机理分析	华南农业大学	

受理编号: c23140500002974

项目编号: 2023A1515012871

文件编号: 粤基金字(2023)2号

广东省基础与应用基础研究基金项目 任务书

项目名称: 面向农业病害即时诊断的DNA水凝胶自供能传感器构建

项目类别: 广东省自然科学基金-面上项目

项目起止时间: 2023-01-01 至 2025-12-31

管理单位(甲方): 广东省基础与应用基础研究基金委员会

依托单位(乙方): 华南农业大学

通讯地址: 广东省广州市天河区五山路483号

邮政编码: 510642

单位电话: 020-85283435

项目负责人: 刘伟鹏

联系电话: 15521270102



(广东科技微信公众号)



(查看任务书信息)



(受理纸质材料二维码)

广东省基础与应用基础研究
基金委员会
二〇二〇年制

五、人员信息

项目负责人

姓名	证件号码	年龄	性别	职称	学历	在项目中承担的任务	所在单位	签名
刘伟鹏	230103198709291954	36	男	副教授	博士研究生	项目负责人	华南农业大学	

项目组主要成员

姓名	证件号码	年龄	性别	职称	学历	在项目中承担的任务	所在单位	签名
刘维	411424198809230940	35	女	讲师	博士研究生	模拟酶和电极材料设计	华南农业大学	
敖日其冷	150102199203303610	31	男	未取得	硕士研究生	金属模拟酶合成	华南农业大学	
郑纯	44522119970906730X	26	女	未取得	本科	DNA水凝胶合成	华南农业大学	
陈梦婷	42098319960824402X	27	女	未取得	硕士研究生	材料合成，表征及传感器的构建	华南农业大学	
梁弘志	441402199702260738	26	男	未取得	硕士研究生	材料合成，表征及传感器的构建	华南农业大学	

受理编号: c23140500000648

项目编号: 2023A1515012033

文件编号: 粤基金字(2023)2号

广东省基础与应用基础研究基金项目 任务书

项目名称: 泡沫金属基光电极增强光电耦合全解水制氢研究

项目类别: 广东省自然科学基金-面上项目

项目起止时间: 2023-01-01 至 2025-12-31

管理单位(甲方): 广东省基础与应用基础研究基金委员会

依托单位(乙方): 华南农业大学

通讯地址: 广东省广州市天河区五山路483号

邮政编码: 510642

单位电话: 020-85283435

项目负责人: 杨思源

联系电话: 02085285565



(广东科技微信公众号)




(查看任务书信息)



(受理纸质材料二维码)

广东省基础与应用基础研究
基金委员会
二〇二〇年制

五、人员信息

项目负责人								
姓名	证件号码	年龄	性别	职称	学历	在项目中承担的任务	所在单位	签名
杨思源	210701198709159212	36	男	副研究员	博士研究生	项目负责人	华南农业大学	

项目组主要成员								
姓名	证件号码	年龄	性别	职称	学历	在项目中承担的任务	所在单位	签名
刘维	411424198809230940	35	女	讲师	博士研究生	催化剂设计	华南农业大学	刘维
卫孟	410522199010026822	33	女	未取得	硕士研究生	催化剂表征与制氢性能评价	华南农业大学	卫孟
张倩倩	622826199611101923	27	女	未取得	本科	催化剂制备与光电性能测试	华南农业大学	张倩倩
杨甜珍	522631199802028366	25	女	未取得	本科	光伏与光电性能测试	华南农业大学	杨甜珍
毛昊宁	372301199906041415	24	男	未取得	本科	光电耦合制氢装置设计与评价	华南农业大学	毛昊宁
徐超	34082319970411491X	26	男	未取得	本科	催化剂制备与光电性能测试	华南农业大学	徐超

技术合作协议

甲方：广州美颂化妆品有限公司

乙方：华南农业大学

广州美颂化妆品有限公司（简称甲方）和华南农业大学（简称乙方）根据《中华人民共和国合同法》的规定，就《绿色环保型抗菌膜的制备及应用》开展合作研究，经平等协商，达成如下协议，双方共同遵守。

一、合作双方分工

甲方：

- (1) 提供项目研发所需原材料；
- (2) 负责对研发试验样品进行应用性试验及评价；
- (3) 负责研发产品的市场推广及销售；
- (4) 提供项目所需的研发经费。

乙方：

- (1) 负责提供项目研发所需的场地和仪器设备；
- (2) 负责抗菌膜制备条件的探索和抗菌等性能测试，提供 2 种抗菌膜样品，申请相关发明专利 2 件（甲方为第一完成单位），撰写相关科技论文 1 篇；
- (3) 根据甲方的实际情况和要求，选派技术人员到甲方进行现场指导，每年不少于 2 次，培训科研人员 2-3 名，推荐并协助甲方引进技术专才；
- (4) 负责联合双方就该项目申报各类科技计划项目，并在甲方申报高新技术企业和研究平台等过程中提供相关的咨询服务。

二、投入经费与使用

1、本项目由甲方提供给乙方科研经费 15.00 万元，按照以下方式支付给乙方。具体支付方式和时间如下：

- (1) 签订合同 7 天内甲方通过银行转帐至乙方帐户；
- (2) 签订合同一周内先支付 10.00 万元；2022 年 2 月前支付余下 5.00 万元。

乙方开户银行名称、地址和帐号为：

开户银行：中国工商银行广东分行五山分理处

地 址：华南农业大学

帐 号: 3602002609000310520

2、任何一方不得将协议中约定的部分或全部工作转交第三方承担。

3、项目合作期限为: 2021 年 01 月 01 日-2022 年 12 月 31 日。

三、成果归属

1. 项目实施过程中所产生的知识产权归属如下:

(1) 各方独立完成的所有权归各自所有, 对方有使用权; 双方共同完成的, 按照双方的贡献大小进行分配。

(2) 项目成果的转让, 须双方同意的前提下进行, 任何一方不得私自开展。

2. 阶段性成果研究, 各方可独立组织成果鉴定; 阶段性成果各方独立完成的所有权归各自所有; 双方共同完成的, 归双方共享。

3. 成果应用后所产生的收益, 由双方根据贡献大小进行协商分配。

4. 项目成果申报各级奖项, 奖项应根据甲、乙两方贡献大小排名。

5. 乙方利用研发经费所购置与研究开发工作有关的设备、器材、资料等财产, 归乙方所有。

四、合作方确定因履行本协议应遵守的保密义务如下:

(1) 保密内容为有关本项目的技术研究信息。

(2) 涉密人员范围: 参与本项目的研究、管理和协调人员。

(3) 保密期限: 自签字盖章之日起至2023年3月31日。

五. 本协议一式四份, 自甲、乙双方签字盖章之日起即具有法律效力。

甲方: 广州美颂化妆品有限公司

(盖章)

法人或委托代理人签字: 梁嘉宏

日期: 2020-11-26

乙方: 华南农业大学

(盖章)

法人或委托代理人签字: 刘韩红

日期: 2020-11-26

合同编号:

技术开发（合作）合同

项目名称: 高性能电芯粘结剂产业化关键技术开发

甲 方: 艾迪天目（常州）新材料科技有限公司

乙 方: 苏州艾迪亨斯胶粘技术有限公司

丙 方: 华南农业大学

签订时间: 2024 年 4 月 25 日

签订地点: 广州市天河区五山路 483 号华南农业大学

有效期限: 2024 年 4 月 25 号至 2029 年 4 月 24 号

中华人民共和国科学技术部印制

填 写 说 明

一、本合同为中华人民共和国科学技术部印制的技术开发(合作)合同示范文本,各技术合同认定登记机构可推介技术合同当事人参照使用。

二、本合同书适用于当事人各方就共同进行新技术、新产品、新工艺或者新材料及其系统的研究开发所订立的技术开发合同。

三、本合同书未尽事项,可由当事人附页另行约定,并可作为本合同的组成部分。

四、当事人使用本合同书时约定无需填写的条款,应在该条款处注明“无”等字样。

高性能电芯粘结剂产业化关键技术开发

甲方：艾迪天目（常州）新材料科技有限公司

地址：溧阳市昆仑街道创智路 29 号 313 室

乙方：苏州艾迪亨斯胶粘技术有限公司

地址：苏州市吴中区木渎镇木东路 317 号 17 幢 101 室三四楼

丙方：华南农业大学

地址：广州市天河区五山路 483 号

本合同合作各方就共同参与研究开发高性能电芯粘结剂产业化关键技术开发项目事项，经过平等协商，在真实、充分地表达各自意愿的基础上，根据《中华人民共和国民法典》的规定，达成如下协议，并由合作各方共同恪守。

第一条 合作宗旨

本合同合作研究开发项目的要求如下：各方本着相互支持、合作共赢的基本原则，进一步发挥各自合作领域的优势，围绕推荐电芯粘结剂产业化，满足性能要求，开发性能优性价比高的电芯粘结剂可产业化产品，包括正极、负极、隔膜及固态电池相关胶粘剂。

第二条 经费分配

1、研究开发经费总额为人民币100 万元整，项目执行期限为 5 年，自 2024 年 3 月 26 日至 2029 年 3 月 25 日。

2、研究开发经费由甲方分五期支付给丙方，甲方首次支付拾伍(15)万元整，第二次支付拾伍(15)万元整，第三次支付贰拾五(25)万元整，第四次支付贰拾伍(25)万元整，第五次支付贰拾(20)万元整。具体支付方式和时间为：第一次支付为签订本合同 30 天内，甲方通过银行转账至丙方指定账户；第二次支付为签订本合同 1.5 年内，经甲方审核满足乙方指标要求后，给予划拨，甲方通过银行转账至丙方指定账户；第三次支付为签订本合同 2.5 年内，经甲方审核满足甲方指标要求后，给予划拨，甲方通过银行转账至丙方指定账户；第四次支付为签订本合同 3.5 年内，经甲方审核满足甲方指标要求后，给予划拨，甲方通过银行转账至丙方指定账户；第五次支付为签订本合同 4.5 年内，经甲方审核满足甲方指标要求后，给予划拨，甲方通过银行转账至丙方指定账户。

3、丙方开户银行名称、单位和账户为：

开户银行： 中国工商银行广州五山支行

户 名： 华南农业大学

账 户： 3602002609000310520

第三条 研究开发的风险承担

在本合同履行期间，因出现在现有技术水平和条件下难以克服的技术困难，导致研究开发失败或部分失败，并造成合作一方或三方损失的，三方各自承担损失。

三方确定，本合同项目的技术风险按 各方协商第三方权威机构进行认定 的方式认定。认定技术风险的基本内容应当包括技术风险的存在、范围、程度及损失大小等。认定技术风险的基本条件是：

1. 本合同项目在现有技术水平条件下具有足够的难度；
2. 丙方在主观上无过错且经认定研究开发失败为合理的失败。

第四条 研究开发成果交付的形式及数量

1、 丙方与甲方联合申请国家发明专利 1 件，申请费用由甲方承担；

2、 根据甲方技术指标要求，丙方为甲方分别在正极胶粘剂、负极胶粘剂、隔膜胶粘剂以及固态电池胶粘剂四个方向上各提供一个可满足甲方技术指标要求的可产业化产品的配方及工艺；

3、 配合甲方和乙方开展其他形式的技术合作，包括竞争对手产品分析、人才引进与培养、产品测试分析、平台建设以及知识产权布局等。

第五条 知识产权及技术成果产生的收益

甲乙丙三方确定，因履行本合同所产生的研究开发成果及其相关知识产权权利归属，按如下方式处理：三方共同研究产生的技术成果（包括但不限于专利权、专利申请权、著作权等）由三方共同享有。未经甲方和乙方允许，丙方不得将此技术成果应用于其他项目，此条永久有效。技术成果应用后所产生的收益，由甲方和乙方根据丙方的贡献大小及权利义务另行协商制定具体的收益分配方法。

第六条 研究开发的财产归属

丙方利用研究开发经费所购置与研究开发工作有关的设备、器材、资料等财产，归丙方所有。

未经甲方和乙方同意，丙方不得将本合同研究开发工作或研究成果转让第三人。

丙方完成本合同项目的研究开发人员在经甲方和乙方同意后享有在有关技术成果文件上写明技术成果完成者权利和取得有关荣誉证书、

奖励的权利。

第七条 合同解除情形

甲乙丙三方确定，出现下列情形，致使本合同无法继续履行或继续履行将成为不必要或不可能的，一方可以通知另一方解除本合同：

- 1、因发生不可抗力或技术风险；
- 2、乙方无法按本合同规定时间提供研究开发经费的，丙方有权解除本合同。
3. 丙方无法按照技术要求开发出满足甲方和乙方要求的产品，甲方和乙方有权解除本合同。

第八条 项目联系人

甲乙丙三方确定，在本合同有效期内，甲方指定柯海岚（联系方式：13795372698）为甲方的项目联系人；乙方指定李吉明（联系方式：15915759763）为乙方的项目联系人；丙方指定杨宇（联系方式：15920111230）为丙方的项目联系人。任何一方需变更项目联系人的，应当及时以邮件或是书面形式通知其他各方。若出现任何一方未及时通知并影响本合同履行的情形，导致另外两方损失的，未通知的一方应承担相应的赔偿责任。

第九条 争议解决

甲乙丙三方因履行本合同而产生争议纠纷的，三方应友好协商解决，协商不成的，任何一方均有权提交至广州仲裁委员会申请仲裁。

第十条 其他

1、本合同未尽事宜，经三方共同协商一致，可另行签订书面补充协议。

2、经甲乙丙三方共同协商一致，可变更本合同中的部分条款，凡对本合同中的任何条款作出变更，应当签订书面变更协议。

3、丙方根据甲方乙方要求，须在签订合同一个月内在广东省科技厅备案该技术合同并提供备案号。

4、本合同一式陆份，甲乙丙三方各执贰份，经三方签字盖章后生效，具有同等法律效力。

5、本合同签署地点：广州市

(以下无正文)

甲方：艾迪天目（常州）新材料科技有限公司

(盖章)

(盖章)

法定代表人 / 委托代理人：

柯阿波

(签名)

2024 年 4 月 25 日

乙方：苏州艾迪亨斯胶粘技术有限公司

法定代表人 / 委托代理人：

李吉明

(签名)

2024 年 4 月 25 日

丙方： _____ 华南农业大学 _____ (盖章)

法定代表人 / 委托代理人： _____ (签名)

2024 年 4 月 25 日



检索证明

根据委托人提供的论文材料, 委托人华南农业大学材料与能源学院 刘维 2 篇论文收录情况如下表。

序号	论文名称	发表刊物及发表的年月卷期/页码等	作者排名	论文等级	作者文中单位	收录情况	影响因子	中科院大类分区
1	Influence of Incubation Temperature on 9,10-Anthraquinone-2-Sulfonate (AQS)-Mediated Extracellular Electron Transfer	FRONTIERS IN MICROBIOLOGY 出版年: 2019 卷期: 10 页码: - 文献号: 464 文献类型: Article	第一作者	A 类	华南农业大学材料与能源学院	SCI	IF2-year=4.236 IF5-year=4.927 (2019)	生物学 2 区 Top 期刊: 否 (2019)
2	Tuning the net topology of a ternary Ag(i)-1,2,4,5-tetra(4-pyridyl)benzene-carboxylate framework: structures and photoluminescence	CRYSTENGCOMM 出版年: 2019 卷期: 21 42 页码: 6446-6451 文献号: 文献类型: Article	第一作者	A 类	华南农业大学材料与能源学院	SCI	IF2-year=3.117 IF5-year=2.933 (2019)	化学 2 区 Top 期刊: 否 (2019)

说明: 论文等级和中科院大类分区按《华南农业大学学术论文评价方案(试行)》划分。

报告免责声明: 如未盖章, 报告无效



检索证明

根据委托人提供的论文材料, 委托人华南农业大学材能学院刘维3篇论文收录情况如下表。

序号	论文名称	发表刊物及发表的年月卷期/页码等	作者排名	论文等级	作者文中单位	收录情况	影响因子	中科院大类分区
1	Tuning the net topology of a ternary Ag(i)-1,2,4,5-tetra(4-pyridyl)benzene-carboxylate framework: structures and photoluminescence	CRYSTENGCOMM 出版年: 2019 NOV 14 卷期: 21 42 页码: 6446-6451 文献类型: Article	通讯作者	A类	华南农业大学	SCI	IF2-year=3.117 IF5-year=2.933 (2019)	化学 2区 Top期刊: 否 (2019)
2	Influence of Incubation Temperature on 9,10-Anthraquinone-2-Sulfonate (AQS)-Mediated Extracellular Electron Transfer	FRONTIERS IN MICROBIOLOGY 出版年: 2019 MAR 6 卷期: 10 文献号: 464 文献类型: Article	第一作者	A类	华南农业大学	SCI	IF2-year=4.236 IF5-year=4.927 (2019)	生物学 2区 Top期刊: 否 (2019)
3	Synthesis, characterization, DNA/HSA interactions and in vitro cytotoxic activities of two novel water-soluble copper (II) complexes with 1,3,5-triazine derivative ligand and amino acids	MATERIALS SCIENCE & ENGINEERING C-MATERIALS FOR BIOLOGICAL APPLICATIONS 出版年: 2018 OCT 1 卷期: 91 页码: 414-425 文献类型: Article	共同通讯作者	A类	华南农业大学	SCI	IF2-year=4.959 IF5-year=4.708 (2018)	工程技术 2区 Top期刊: 否 (2018)

说明: 论文等级和中科院大类分区按《华南农业大学学术论文评价方案(试行)》划分。

报告免责声明: 如未盖章, 报告无效

检索证明

根据委托人提供的论文材料, 委托人华南农业大学材料与能源学院刘维2篇论文收录情况如下表。

序号	论文名称	发表刊物及发表的年月卷期/页码等	作者排名	论文等级	作者文中单位	收录情况	影响因子	中科院大类分区
1	Distinct biofilm formation regulated by different culture media: Implications to electricity generation	BIOELECTROCHEMISTRY 出版年: 2021 AUG 卷期: 140 文献号: 107826 文献类型: Article	共同通讯作者	A类	华南农业大学	SCI	IF2-year=5.373 IF5-year=4.827 (2020)	化学 2区 Top期刊: 否 (2021)
2	Three Silver(I) Coordination Polymers Based on Pyridyl Ligands and Auxiliary Carboxylic Ligands: Luminescence and Efficient Sensing Properties	INORGANIC CHEMISTRY 出版年: 2021 APR 19 卷期: 60 8 页码: 5463-5473 文献类型: Article	通讯作者	A类	华南农业大学	SCI	IF2-year=5.165 IF5-year=4.815 (2020)	化学 2区 Top期刊: 是 (2021)

说明: 论文等级和中科院大类分区按《华南农业大学学术论文评价方案(试行)》划分。

报告免责声明: 如未盖章, 报告无效



检索证明

根据委托人提供的论文材料，委托人华南农业大学材料与能源学院 刘维 2 篇论文收录情况如下表。

序号	论文名称	发表刊物及发表的年月卷期/页码等	作者排名	论文等级	作者文中单位	收录情况	影响因子	中科院大类分区
1	Effects of different dithiolate ligands on electrocatalytic hydrogen production of nickel complexes in acetic acid or water	JOURNAL OF MOLECULAR STRUCTURE 出版年：2023 卷期：1287 页码：- 文献号：135659 文献类型：Article,Early Access	共同通讯作者（倒数第一）	A 类	华南农业大学材料与能源学院	SCI	IF2-year=3.8 IF5-year=3.2 (2022)	化学 2 区 Top 期刊：否 (2023)
2	Cobalt-based Metalloporphyrins As Efficient Electro-catalysts for Hydrogen Evolution From Acetic Acid and Water	ELECTROCATALYSIS 出版年：2023 卷期：14 5 页码：752-762 文献号： 文献类型：Article,Early Access	共同通讯作者（倒数第一）	B 类	华南农业大学材料与能源学院	SCI	IF2-year=3.1 IF5-year=2.7 (2022)	化学 4 区 Top 期刊：否 (2023)

说明：论文等级和中科院大类分区按《华南农业大学学术论文评价方案（试行）》划分。

报告免责声明:如未盖章,报告无效



检索证明

根据委托人提供的论文材料，委托人华南农业大学材料与能源学院 刘维 1 篇论文收录情况如下表。

序号	论文名称	发表刊物及发表的年月卷期/页码等	作者排名	论文等级	作者文中单位	收录情况	影响因子	中科院大类分区
1	Hematite enhances microbial autotrophic nitrate removal in carbonate and phosphate-rich environments by increasing Fe(II) activity	SCIENCE OF THE TOTAL ENVIRONMENT 出版年: 2024 出版日期: NOV 1 卷期: 949 页码: - 文献号: 175002 文献类型: Article	共同通讯作者	T2 类	华南农业大学材料与能源学院	SCI	IF2-year=8.2 IF5-year=8.6 (2023)	环境科学与生态学 1 区 Top 期刊: 是 (2023)

说明: 论文等级和中科院大类分区按《华南农业大学学术论文评价方案(试行)》划分。

报告免责声明: 如未盖章, 报告无效



检索证明

根据委托人提供的论文材料，委托人华南农业大学材料与能源学院 刘维 1 篇论文收录情况如下表。

序号	论文名称	发表刊物及发表的年月卷期/页码等	作者排名	论文等级	作者文中单位	收录情况	影响因子	中科院大类分区
1	Enhancing the photocatalytic hydrogen production performance of CdS by introducing a co-catalyst CoTPPB ₄ (7, 8, 17, 18-tetrabromo-5, 10, 15, 20-tetraphenylporphyrin)	NEW JOURNAL OF CHEMISTRY 出版年: 2024 出版日期: MAY 14 卷期: 48 19 页码: 8868-8876 文献类型: Article	共同通讯作者 (倒数第一)	B 类	华南农业大学	SCI	IF2-year=2.5 IF5-year=2.7 (2024)	化学 3 区 Top 期刊: 否 (2025)

说明: 论文等级和中科院大类分区按《华南农业大学学位论文评价方案(试行)》划分

报告免责声明: 如未盖章, 报告无效

检索员: 邓智心
华南农业大学图书馆

2025-07-16

SCAULIB202625680

检索证明

根据委托人提供的论文材料，委托人华南农业大学材料与化学工程学院 刘维(学科类型:自然科学) 2 篇论文收录情况如下表。

序号	论文名称	发表刊物及发表的年月卷期/页码等	作者排名	论文等级	作者文中单位	收录情况	影响因子	中科院大类分区
1	离子型银配合物的制备及其电催化产氢性能综合性实验设计	实验科学与技术 出版年：2025 卷期： 页码： - 文献号： 文献类型：	第一	普刊类	华南农业大学材料与能源学院	CNKI	无	无
2	Revealing the underestimated role of Gram-positive bacteria in iron reduction within paddy soils	Science of the Total Environment 出版年：2025 卷期： 页码： - 文献号： 文献类型：	共同通讯作者	A 类	华南农业大学材料与能源学院	已发表，暂未被SCI 收录	IF2-year=8.0 IF5-year=8.7 (2024)	环境科学与生态学 2 区 Top 期刊：是 OA 期刊：否 标注：Mega-Journal (2025)

说明：论文等级和中科院大类分区按《华南农业大学学位论文评价方案（试行）》划分。

报告免责声明：如未盖章，报告无效



Frontiers in Microbiology

5.2
Impact Factor

7.8
CiteScore

701,873
Citations

Submit →



doi 10.3389/fmicb.2018.02816

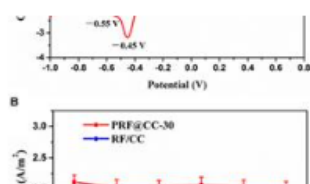
3,398 views 16 citations

ORIGINAL RESEARCH

Published on 15 Jan 2019

Promoting *Shewanella* Bidirectional Extracellular Electron Transfer for Bioelectrocatalysis by Electropolymerized Riboflavin Interface on Carbon Electrode

Long Zou · Xian Wu · Yunhong Huang · Haiyan Ni · Zhong-er Long



doi 10.3389/fmicb.2019.00293

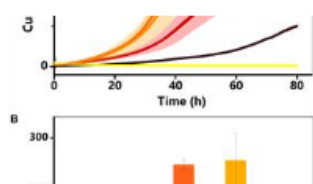
5,283 views 38 citations

ORIGINAL RESEARCH

Published on 06 Mar 2019

Influence of Incubation Temperature on 9,10-Anthraquinone-2-Sulfonate (AQS)-Mediated Extracellular Electron Transfer

Wei Liu · Yundang Wu · Tongxu Liu · Fangbai Li · Hui Dong · Meiqing Jing



doi 10.3389/fmicb.2018.02883

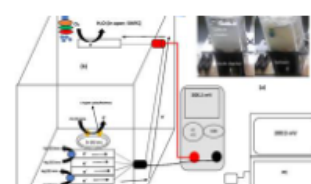
3,065 views 21 citations

ORIGINAL RESEARCH

Published on 14 Jan 2019

Bioremediation and Electricity Generation by Using Open and Closed Sediment Microbial Fuel Cells

Syed Zaghun Abbas · Mohd Rafatullah · Moonis Ali Khan · Masoom Raza Siddiqui





Influence of Incubation Temperature on 9,10-Anthraquinone-2-Sulfonate (AQS)-Mediated Extracellular Electron Transfer

Wei Liu^{1†}, Yundang Wu^{2†}, Tongxu Liu^{2*}, Fangbai Li², Hui Dong¹ and Meiqing Jing²

¹ College of Materials and Energy, South China Agricultural University, Guangzhou, China, ² Guangdong Key Laboratory of Integrated Agro-Environmental Pollution Control and Management, Guangdong Institute of Eco-Environmental Science and Technology, Guangzhou, China

OPEN ACCESS

Edited by:

Fanghua Liu,
Yantai Institute of Coastal Zone
Research (CAS), China

Reviewed by:

Souichiro Kato,
National Institute of Advanced
Industrial Science and Technology
(AIST), Japan
Liang Shi,
China University of Geosciences,
China

*Correspondence:

Tongxu Liu
txliu@soil.gd.cn

[†] These authors have contributed
equally to this work

Specialty section:

This article was submitted to
Microbiotechnology, Ecotoxicology
and Bioremediation,
a section of the journal
Frontiers in Microbiology

Received: 26 September 2018

Accepted: 21 February 2019

Published: 06 March 2019

Citation:

Liu W, Wu Y, Liu T, Li F, Dong H
and Jing M (2019) Influence
of Incubation Temperature on
9,10-Anthraquinone-2-Sulfonate
(AQS)-Mediated Extracellular Electron
Transfer. *Front. Microbiol.* 10:464.
doi: 10.3389/fmicb.2019.00464

The electron shuttling process has been recognized as an important microbial respiration process. Because the incubation temperature can influence both the reactivity of electron mediators and cell growth, it may also affect the electron-shuttle-mediated extracellular electron transfer (EET) process. Here, the effect of incubation temperature (22–38°C) was investigated in a bioelectrochemical system (BES) using *Shewanella oneidensis* MR-1 and 50 μ M of 9,10-anthraquinone-2-sulfonate (AQS). We found that current generation increased as the temperature was increased from 22 to 34°C and then decreased sharply at 38°C. The biofilm biomass, as indicated by the total protein extracted from the electrode, increased as the temperature increased from 22 to 34°C and then decreased at 38°C, mirroring the current generation results. These results were further confirmed by increasing the temperature slowly, step-by-step, in a single BES with a constant biofilm biomass, suggesting that the EET rates could be substantially influenced by temperature, even with the same biofilm. The effects of temperature on the AQS bioreduction rate, c-type cytochrome (c-Cyts)-bound-cofactor-mediated EET, the AQS mid-point potential, and the AQS diffusion coefficient were studied. From these results, we were able to conclude that temperature influenced the EET rates by changing the c-Cyts-bound-cofactor-mediated EET process and the AQS bioreduction rate, and that the change in biofilm formation was a dominant factor influencing the overall EET rates. These findings should contribute to the fundamental understanding of EET processes. Moreover, optimization of the operating parameters for current generation will be helpful for the practical application of bioelectrochemical techniques.

Keywords: extracellular electron transfer, temperature, redox transformation, mediator, biofilm

INTRODUCTION

Extracellular electron transfer (EET) is a key process of extracellular respiration, which is an important part of microbial anaerobic metabolism (Lovley et al., 1987; Shi et al., 2007, 2009, 2016; Calandra et al., 2016; Light et al., 2018). As this process is active in the epigeosphere, it has an impact on the fate of trace metals and nutrients and on the degradation of organic matter

(Ohtsuka et al., 2013; Zhou et al., 2016; Han et al., 2018). Owing to the EET ability of microbes, microbial fuel cells can be constructed to generate bioelectricity (Logan, 2009). Because some organic materials, such as quinone compounds, can act as electron shuttles to facilitate electron transfer in bioelectrochemical systems (BESs) (Klöpfer et al., 2014; Yuan et al., 2017), extensive attention has been paid to quinone-compound-mediated EET processes (Watanabe et al., 2009; Niedźwiecka et al., 2017; Wu et al., 2018; Yamamura et al., 2018).

Quinone-compound-mediated EET includes two steps, namely, bioreduction of quinone to hydroquinone and chemical oxidation of hydroquinone to quinone (Wu et al., 2014). The dynamics of the redox transformations of quinone compounds may directly affect EET rates (Li et al., 2013, 2014), thus indirectly affecting cell growth, by changing the metabolic rates of carbon sources (Gralnick and Newman, 2007). Hence, the biofilm in the BES, which determines current generation, may also be influenced by the dynamics of the quinone redox transformations. In addition, the understanding of the mechanism of *c*-type cytochrome (*c*-Cyts)-bound-cofactor-mediated EET has become better in recent years. It has been reported that flavins secreted by *Shewanella oneidensis* MR-1 primarily act as *c*-Cyts-bound cofactors to accelerate EET, rather than as free soluble shuttles (Okamoto et al., 2013; Xu et al., 2016). Hence, the effects of environmental factors on *c*-Cyts-bound-cofactor-mediated EET also need to be properly understood.

Temperature is an important environmental factor that affects microbial activity, and its effects on microbial growth have been extensively reported. For example, it has been shown that *S. oneidensis* MR-1 can survive in a wide temperature range (3–35°C) (Abboud et al., 2005), that the metabolism of *Shewanella* (i.e., fatty acid biosynthesis) changes with temperature (Wang et al., 2009), and that its iron bioreduction rate decreases when the temperature decreases from 37 to 4°C (Picard et al., 2014). However, few previous studies have considered the impact of temperature on the specifics of quinone-compound-mediated EET. It has been recognized that changes in environmental factors, such as pH, significantly impact biofilm growth and the quinone redox potential (Wu et al., 2016), resulting in large changes in the produced current. Nevertheless, it remains unclear whether, or how, transient or longer-term temperature differences affect the formation and redox properties of the biofilm, which could in turn influence the quinone-compound-mediated EET process.

Thus, to investigate these issues in detail, a BES was constructed with *S. oneidensis* MR-1 as a model strain. A quinone compound (9,10-anthraquinone-2-sulfonate, AQS), which has a similar structure to anthraquinone-2,6-disulfonate (AQDS), was chosen as the model mediator because our previous studies (Li et al., 2013, 2014; Wu et al., 2014) demonstrated that the enhancing effects of AQS on EET were higher than those of AQDS. The objectives of this study were to (1) clarify how transient temperature changes and long-term temperature differences affect current generation in a BES with AQS; (2) quantitatively investigate the factors that influence the AQS-mediated EET process; and (3) determine the underlying

mechanism responsible for the temperature effect on AQS-mediated EET.

MATERIALS AND METHODS

Materials and BES Setup

Shewanella oneidensis MR-1, purchased from the Marine Culture Collection of China (China), was aerobically incubated in lysogeny broth (LB) medium, at 30°C while being continuously shaken at 180 rpm. When the cell suspension was in the logarithmic phase, it was centrifuged, washed, and then diluted to the target concentration for the following experiments. Each BES, equipped with a carbon cloth (2 cm × 2 cm) working electrode, titanium counter electrode, and calomel reference electrode, was incubated anaerobically at a constant potential of 441 mV vs. Standard Hydrogen Electrode (SHE). Phosphate was used as the pH buffer (pH = 7.0). A solution of AQS (AR, 98.0%) was obtained from Acros (China). All other chemicals were purchased from the Guangzhou Chemical Reagent Factory (China).

Spectral Measurements

By using UV-visible diffuse-transmittance absorption spectroscopy, AH₂QS can be directly detected in living cell suspensions. A sealed cuvette was used as the reactor, to which AQS (50 μM), MR-1 (OD₆₀₀ = 1.0), and lactate (50 mM) were added. The spectra of AH₂QS were recorded *in situ* using a diffuse-transmittance spectrophotometer (UV-2600, Shimadzu) equipped with an integrating sphere. A standard solution of AH₂QS was prepared in an anaerobic chamber, with sodium hydrosulfite used to reduce AQS to AH₂QS. To calibrate the AH₂QS concentration, AH₂QS spectra (0–50 μM), with excess sodium hyposulfite as reducer, were collected, and each AH₂QS concentration was determined from the absorbance peak at 382 nm. The standard AH₂QS curve had a slope of 153.4 ($R^2 = 0.9996$). For the treatment with cell suspensions and AQS, the AH₂QS concentration was determined according to the difference between the spectrum of MR-1 with AH₂QS and that of MR-1 only.

Electrochemical Measurements

An electrochemical workstation (Autolab PGSTAT 302N, Metrohm, Switzerland) was used for electrochemical impedance spectroscopy (EIS) measurements. EIS spectra of the BESs were obtained by applying sinusoidal perturbations of ±10 mV over the open circuit voltage at frequencies from 10⁻² to 10⁵ Hz. Cyclic voltammetry (CV) and differential pulse voltammetry (DPV) tests were conducted using a potentiostat (CHI660D, Chenhua Co., Ltd., China). CV of AQS was performed at various scanning rates (50–400 mV s⁻¹). Carbon cloth (2 cm × 2 cm) electrodes were used as working electrodes in the electrochemical systems.

Biofilm Characterization

The morphologies of the biofilms on the electrodes were characterized using scanning electron microscopy (SEM; S-3000N, Hitachi, Japan) and fluorescence microscopy (Axio Scope

A1, Carl Zeiss, Germany). The carbon cloth electrodes with biofilms were removed after incubation for 3 days, gently washed in water, and then treated with glutaraldehyde (2.5%), osmic acid, and ethanol. After freeze-drying and coating with evaporated platinum, the washed biofilm samples were imaged using SEM. The cells were then dyed with 4',6-diamidino-2-phenylindole before fluorescence microscopy imaging.

The biofilm was then quantified by extracting the total biofilm protein with a boiling 0.2 M NaOH solution (Zhao et al., 2013). A carbon cloth sample (2 cm × 0.66 cm) was placed into a 2 mL sealed tube, together with 0.5 mL NaOH and some glass beads, and the tube was then subjected to a super high-speed vortex (6.5 m s^{-1} , 45 s) using a homogenizer (FastPrep-24, MP, United States). The mixture was then centrifuged at 8000 g for 3 min, and finally, the supernatant was collected for protein quantification. The supernatant was then quantified by Coomassie blue staining via a protein quantification kit (C503041-1000 Modified Bradford Protein Assay Kit, Sangon Biotech, China).

RESULTS

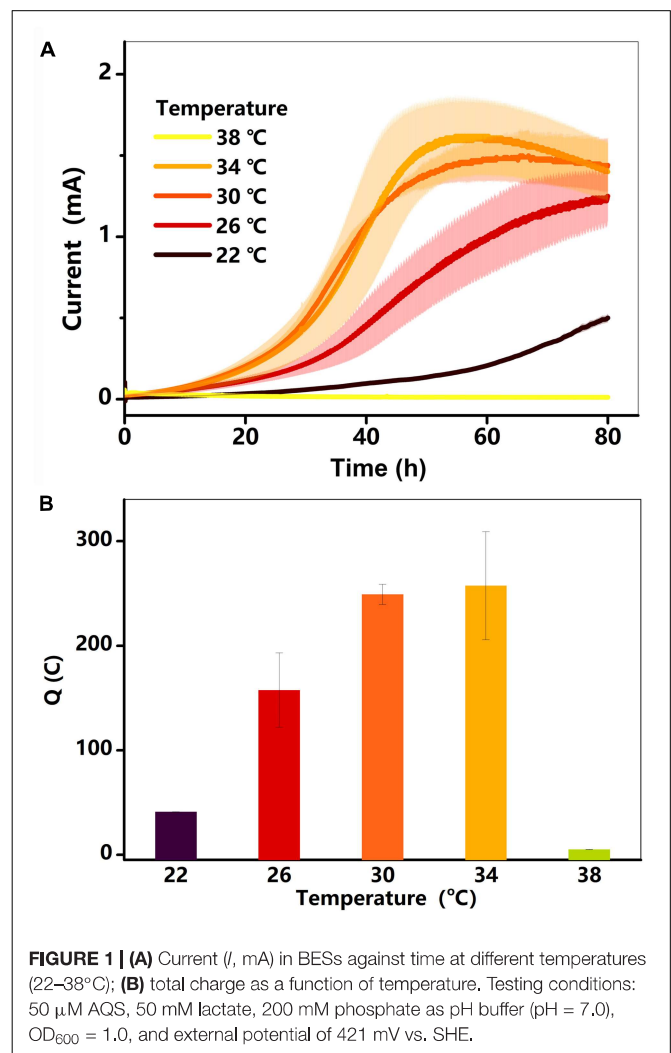
Electricity Generation at Different Temperatures

Electricity generation in the BES was examined at different temperatures. As shown in **Figure 1A**, the current in each treatment (22–34°C) started increasing after a hysteresis period of approximately 5 h, reaching a maximum value within 72 h. Electricity generation was extremely low at 38°C, lasting for 40 h before decreasing to near zero. The total charge (Q) for each treatment is shown in **Figure 1B**. The Q , which was only 41°C at 22°C, increased gradually to 257°C at 34°C, and then decreased substantially to 5°C at 38°C. As the current and charge changed, the rate of lactate consumption must have changed (Pinchuk et al., 2011; Saito et al., 2016).

Because the concentration of lactate can influence the physiology of *S. oneidensis* MR-1, the effect of lactate concentration (10, 20, 30, 40, and 50 mM) on current generation was examined in the BES at 34°C. The results (**Supplementary Figure S1**) suggested that the generated current was very similar for all lactate concentrations between 10 and 50 mM. It has previously been reported that the current generated without AQS is much lower than that generated with AQS (Wu et al., 2016). The treatments with and without exogenous AQS are very different. The main purpose of this study is to investigate the influence of temperature on the AQS-mediated EET process quantitatively.

Biofilm Formation at Different Temperatures

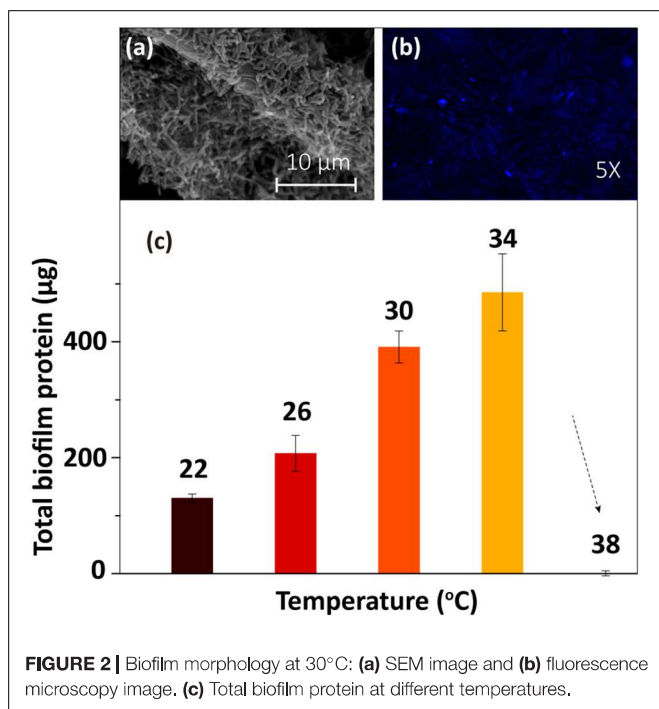
The SEM and fluorescence microscopy images of the biofilm sample at 30°C (**Figures 2a,b**) showed that the electrode surface was fully covered with biofilm cells. To determine the amount of biofilm formed under different temperatures, the total protein on the electrode was extracted and then quantified using Coomassie



blue staining via a protein quantification kit. The results (**Figure 2c**) showed that the total biofilm protein amount on the electrode increased gradually as the temperature rose from 22 to 34°C and then sharply decreased as the temperature increased further (from 34 to 38°C). The low concentration of protein at 38°C implied that the cells were dead at this temperature. Thus, this temperature is not suitable for the anaerobic survival of MR-1 cells (Abboud et al., 2005).

Electricity Generation at Different Temperatures With a Constant Biofilm

To examine the effect of temperature on electricity generation with the same biofilm, current generation was examined in a BES as the temperature was quickly reduced from 34 to 22°C and then gradually increased back to 34°C over a period of 3 h. As shown in **Figure 3A**, the current decreased sharply after the initial temperature decrease, suggesting that the BES electron transfer ability was very sensitive to temperature. Then, as the temperature was gradually restored back to 34°C, the current increased, step-by-step, with the increasing temperature.



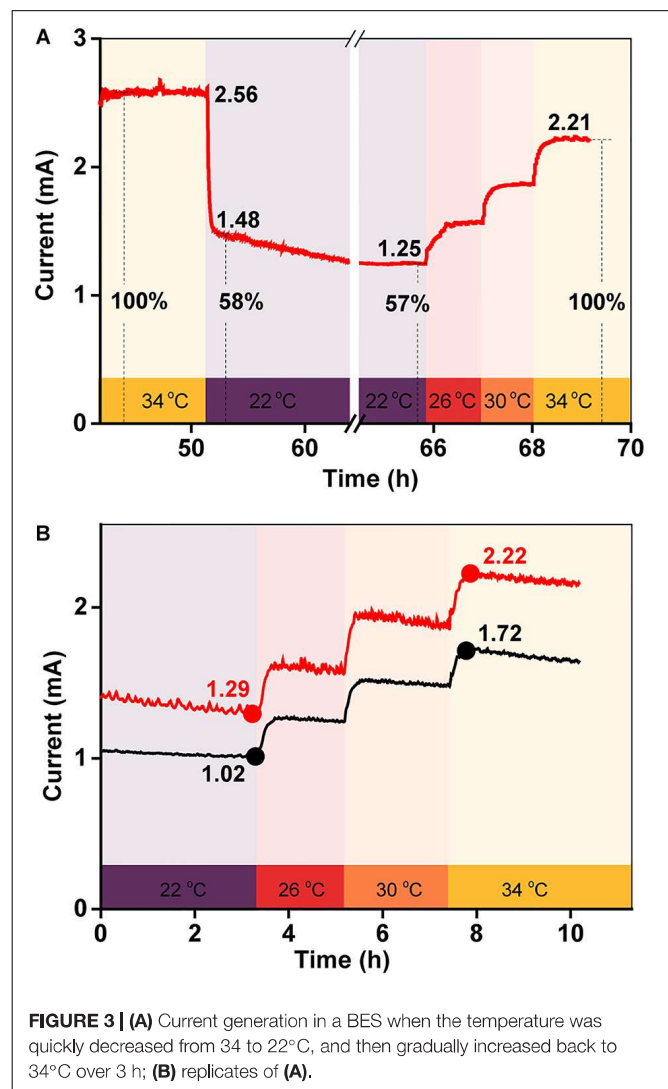
The percentage by which the current intensity decreased was consistent with the increased current intensity, which suggested that the temperature-dependent change in the current output was reversible. To confirm this phenomenon, this test was repeated twice. The results in **Figure 3B** show that the percentage by which the current increased with the step-by-step temperature increase was similar for each.

Quantitative Analysis of the Effect of Temperature on Current Generation

To quantify the influence of each factor on total current production, the maximum current at 34°C was defined as 100%, meaning that the current decreased by 58% when the temperature was rapidly reduced from 34 to 22°C (**Figures 3A,B**). As the biofilm biomass remained constant during this period, the decrease in current generation was mainly caused by a change in the redox reactivity of AQS and the metabolic activity of the cells. However, after long-term incubation, the maximum current intensity decreased to 31% when the temperature decreased to 22°C (**Figure 1A**). The biomass changed substantially during this period, indicating that the extra current decrease was caused by the decrease in biofilm biomass.

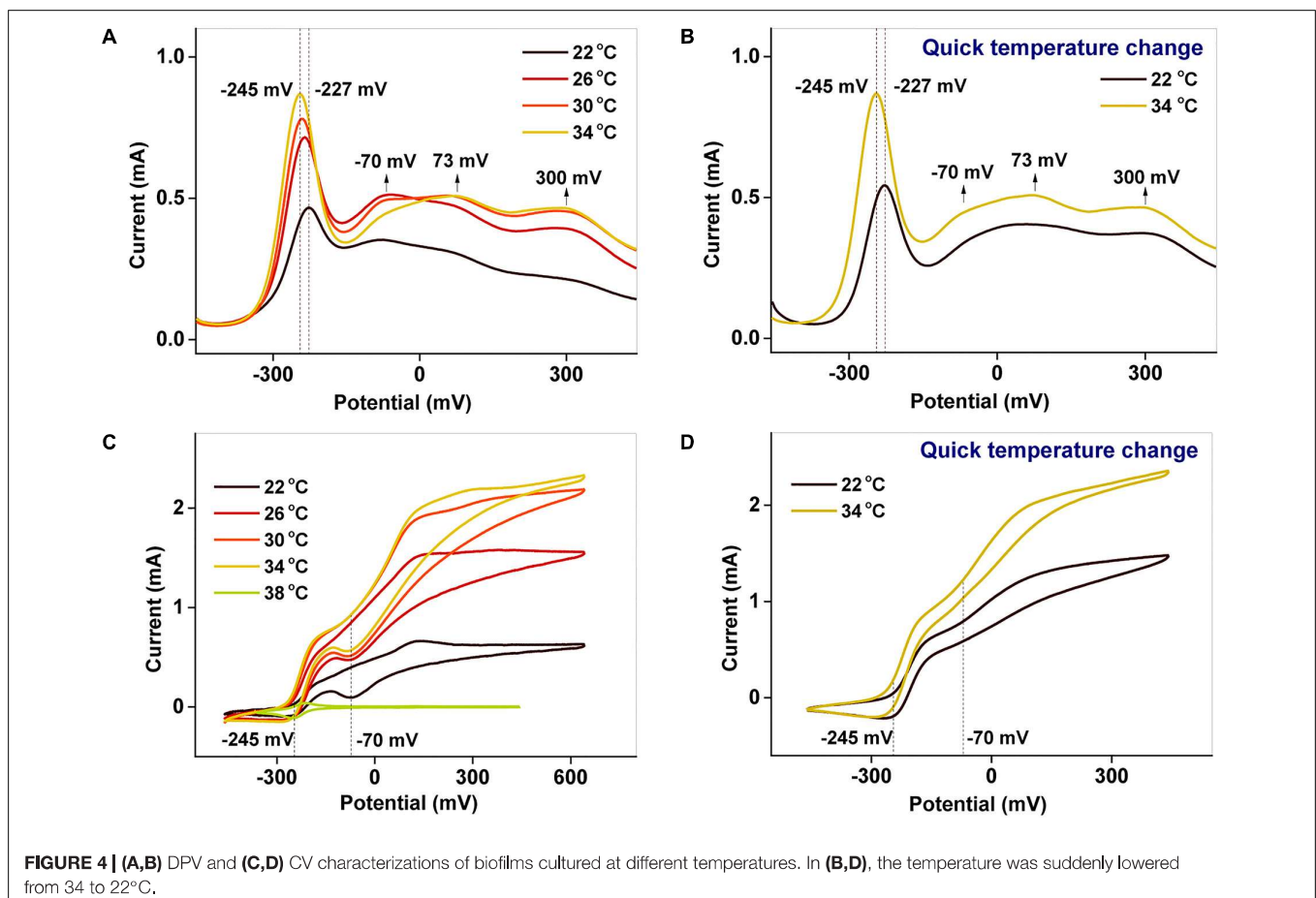
Electrochemical Properties of the Biofilm at Different Temperatures

To examine the redox properties of the biofilms, electrochemical characterizations were performed after potentiostatic incubation. The DPV results (**Figures 4A,B**) allow various processes occurring in the biofilm to be distinguished. The peaks around −227 to −245 mV and −70 mV correspond to



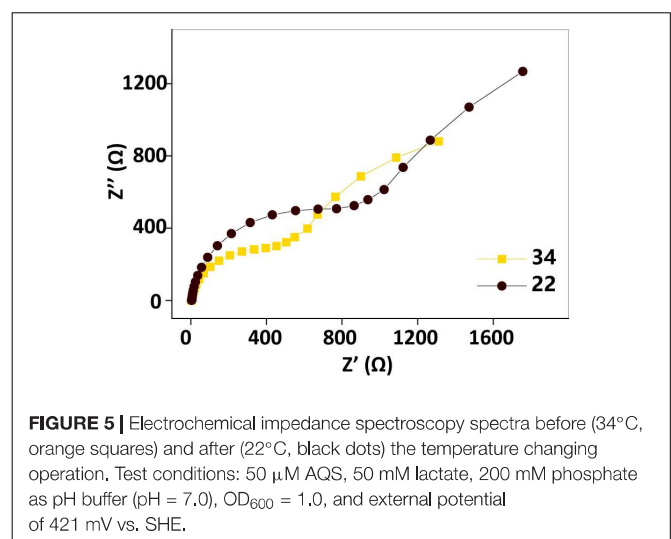
free AQS and *c*-Cyts-bound cofactor, respectively (Wu et al., 2016; Xu et al., 2016), whereas the peaks at 73 and 300 mV reflect direct *c*-Cyts redox reactions (Okamoto et al., 2013, 2014b; Xu et al., 2016). When the incubation temperature was reduced from 34 to 22°C, the peak potential of free AQS increased slightly from −245 to −227 mV, and the peak shapes of the *c*-Cyts-bound cofactor (−70 mV) and free *c*-Cyt (73 and 300 mV) showed obvious changes (**Figure 4A**). However, the shapes of these peaks remained stable when the temperature decreased from 34 to 22°C instantaneously (**Figure 4B**).

Using CV analysis, the catalytic current generated by each process could be studied and the contribution from each process to the catalytic current could be distinguished. From the CV results in **Figures 4C,D**, two significant current increases were observed at −245 and −70 mV, representing the free AQS mediation process and the *c*-Cyt-bound cofactor associated transport, respectively. Meanwhile, free *c*-Cyt (+73 mV) exhibited a very weak contribution



to the catalytic current. As shown in **Figure 4C**, as the temperature was decreased, the peak at -70 mV decreased significantly, whereas the peak at -245 mV decreased only slightly from 34 to 26°C before decreasing much more as the temperature decreased further (from 26 to 22°C). As shown in **Figure 4D**, the peak corresponding to the mediation process only decreased slightly when the temperature was suddenly lowered from 34 to 22°C, whereas the peak corresponding to *c*-Cyts-bound cofactor associated transport decreased significantly. This phenomenon was verified in triplicate. These results indicated that both the mediation process and *c*-Cyts-bound cofactor associated electron transfer were changed by temperature after long-term incubation, whereas only *c*-Cyts-bound cofactor associated electron transfer was changed significantly when the temperature decreased quickly from 34 to 22°C.

Electrochemical impedance spectroscopy tests performed before and after the temperature changing operation (**Figure 5**) showed that the impedance also increased as the temperature decreased. This observation also implied that factors other than the biofilm biomass, such as the AQS redox properties, the properties of the *c*-Cyt-bound cofactor, and the metabolic activity of the microbes, may also be temperature dependent, causing current generation in the BES with a fixed biofilm to change with temperature.



Redox Transformation of AQS at Different Temperatures

It has been documented that electron transport during AQS-mediated EET processes occurs via the redox cycling of AQS, including the reduction of AQS to AH₂QS by MR-1 and the

electrochemical oxidation of AH₂QS to AQS on the surface of the electrode. The *in situ* kinetics of quinone compound reduction can be studied in living bacterial suspensions using diffuse-transmittance spectroscopy (Nakamura et al., 2009; Han et al., 2016; Liu et al., 2017). Therefore, the bioreduction of AQS and the electrochemical oxidation of AH₂QS were investigated at different temperatures.

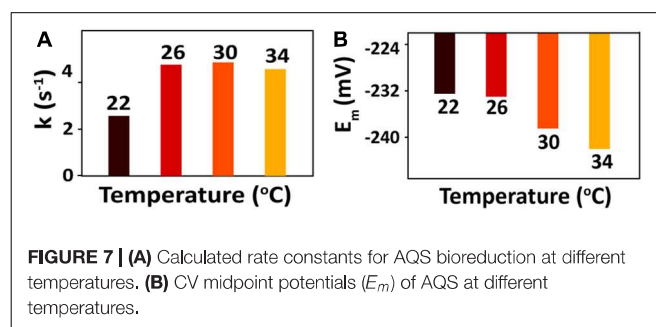
For the bioreduction of AQS to AH₂QS without an electrode, similar patterns were observed for the spectral kinetics at different temperatures de (Figures 6A–D). The peaks at 330 and 382 nm were attributed to AQS and AH₂QS, respectively. To demonstrate the kinetics of AQS reduction to AH₂QS clearly, the concentrations of AH₂QS at different temperatures were plotted as a function of time. As the concentration of lactate (50 mM) in the system was much higher than that AQS (50 μ M), the reduction of AQS can be considered a pseudo-first-order reaction. As shown in Figure 7A, the rate constants increased at temperatures of 22–26°C and then slightly decreased at higher temperatures (30–34°C).

After bioreduction of AQS to AH₂QS, electrochemical oxidation of AH₂QS will ultimately result in current generation. To examine the differences in the AQS redox reactions on the electrode surface at different temperatures, CV of AQS was conducted at various scan rates (50–400 mV s⁻¹). As shown in Figures 8A–D, an increase in the current as the scan rate increased was accompanied by, a positive shift of the oxidation peak and a negative shift of the reduction peak. The midpoint potential (Figure 7B) decreased slightly, from –232.5 to –242 mV, with increased temperature (22–34°C).

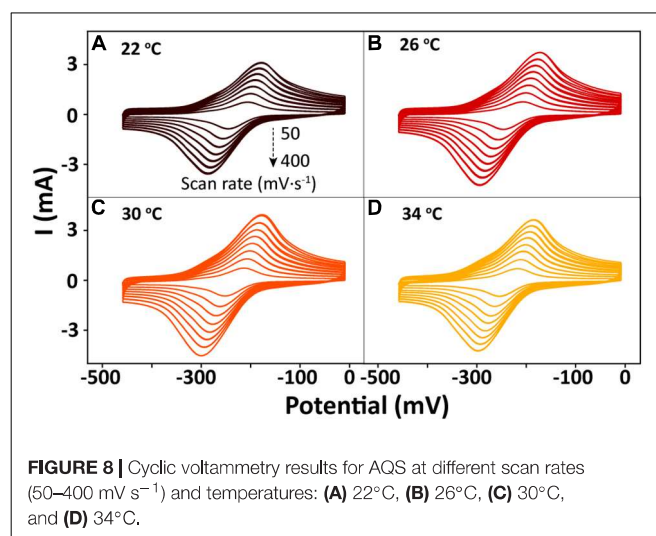
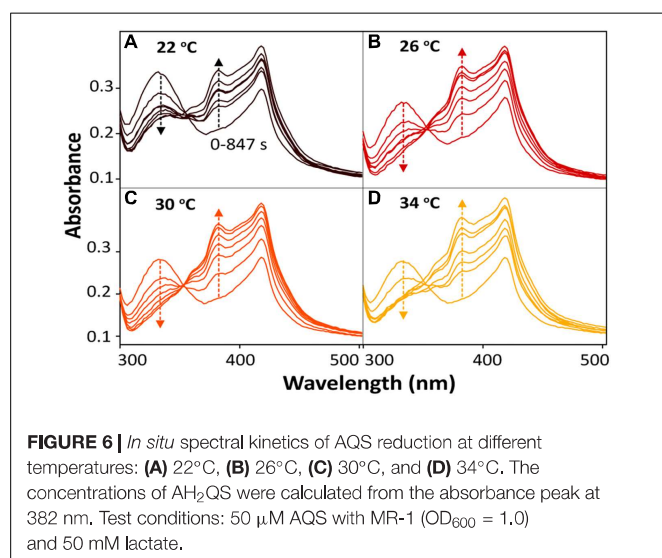
DISCUSSION

Role of Temperature-Dependent Biofilm Formation

The biofilm, as the driving force for EET, has been observed to be affected by the incubation temperature (Tango et al., 2018;



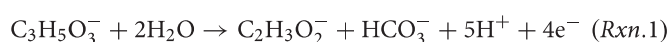
Zhang et al., 2018), and the changes in biofilm biomass may significantly influence the EET process. To examine the effect of temperature-dependent biofilm formation on electricity generation, the linear regression of total charge (Q) as a function of total biofilm protein was analyzed. A good linear relationship ($R^2 = 0.91$) was observed between the Q values and total biofilm protein, which implied that biofilm cell growth is an essential factor that affects EET at different temperatures. The amount of total biofilm protein increased as the temperature rose from 22 to 34°C, indicating a corresponding increase in the lactate consumption rate. As shown by Rxn. 1, high lactate consumption rates could increase the amount of available electrons, which would be favorable for AQS reduction (Rxn. 2 and Figure 8) and current generation (Rxns. 3 and 4). In addition, if the maximum current at 34°C was defined as 100% as shown in Supplementary Figure S3a, the maximum current decreased to 31% when the biofilm was incubated at a temperature of 22°C (Supplementary Figure S3c). This current intensity was almost two times lower than that obtained when the temperature was changed instantaneously (Supplementary Figure S3b). This difference in behavior might be caused by changes in the biofilm biomass in the former system. Notably, the current also decreased when the temperature was reduced from 34 to 22°C in a single BES with the same biofilm (Supplementary Figure S3b).



Therefore, factors other than the biofilm must contribute to the changes in current generation at different temperatures.

Free AQS-Mediated EET Processes in BESs

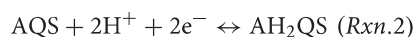
It is known that the reduction of an electron acceptor (i.e., AQS) can be coupled to an oxidizing electron donor (lactate) during current generation by MR-1 (Coursolle and Gralnick, 2010; Pinchuk et al., 2011), with the diffusion of reduced AQS to the anode electrode resulting in current generation. The potential losses can drive electron flow from the electron donor to the anode. For lactate oxidation, the following half-cell reaction (Rxn. 1) determines the electron production rates and the concomitant anode potential.



According to the Nernst equation, the specific theoretical redox potential of the electron donor can be determined using Eq. 1.

$$E_{\text{C}_3\text{H}_5\text{O}_3^-} = E_{\text{C}_3\text{H}_5\text{O}_3^-}^0 - \frac{RT}{4F} \ln \frac{[\text{C}_2\text{H}_3\text{O}_2^-][\text{HCO}_3^-][\text{H}^+]^5}{[\text{C}_3\text{H}_5\text{O}_3^-]} \quad (1)$$

As a result of the oxidation of lactate, the electrons generated can be captured by AQS to produce AH₂QS (Rxn. 2).



The redox potential of AQS (E_{AQS}) can be calculated using Eq. 2.

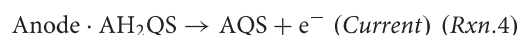
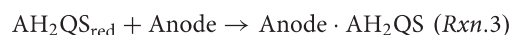
$$E_{\text{AQS}} = E_{\text{AQS}}^0 - \frac{RT}{2F} \ln \frac{[\text{AH}_2\text{QS}]}{[\text{AQS}][\text{H}^+]^2} \quad (2)$$

Hence, at a fixed pH, the driving force for lactate oxidation and AQS reduction ($\Delta E = E_{\text{C}_3\text{H}_5\text{O}_3^-} - E_{\text{AQS}}$) can be influenced by both the temperature and the concentrations of lactate and AQS, which is why the peak potentials of AQS changed, as shown in **Figures 4A,B, 7B**.

However, as a metabolic process determined by microbial activity, the oxidation of lactate by MR-1, as well as the biofilm biomass, was sensitive to temperature. The peak of the free AQS-mediated process at −245 mV exhibited a noticeable decrease when the temperature decreased gradually from 34 to 22°C (**Figure 4C**), but this only showed a slight decrease when the temperature was decreased rapidly (**Figure 4D**). This difference suggested that the change in the AQS bioreduction rate likely has an important effect on current generation in the long-term incubation system. The change in the AQS bioreduction rate constant (**Figure 7A**) showed a similar tendency as the change of the peak in **Figure 4C**, which confirmed the importance of the AQS bioreduction process.

After AQS was reduced to AH₂QS, it then diffused to the electrode surface and concomitantly transferred

electrons to the anode, resulting in the generation of current (Brutinel and Gralnick, 2012).



The peak current (**Figures 8A–D**) exhibited a linear relationship with the square root of the scan rate ($\nu^{1/2}$) (**Supplementary Figure S2**), indicating that a diffusion process (Rxn. 3) was the rate-determining step in the electrochemical oxidation of AH₂QS on the electrode (Richter et al., 2009).

The transport of soluble AH₂QS to the anode (Rxn. 3) is a diffusion process governed by Fick's law (Torres et al., 2009). As the diffusion coefficient at different temperatures follows the Einstein relation ($D = KT/6\pi\eta r$), Fick's law can be written as shown in Eq. 3.

$$j = nF \left(\frac{KT\Delta[\text{AH}_2\text{QS}]}{6\pi\eta r\Delta z} \right) \quad (3)$$

where j is the current density (A m^{-2}), nF is a conversion factor from moles to coulombs, K is Boltzmann's constant, T is the absolute temperature, $\Delta[\text{AH}_2\text{QS}]$ is the concentration gradient of AH₂QS (mol m^{-3}), π is the circumference ratio, η is the coefficient of viscosity of the solution (Pa s), r is the hydrodynamic radius (m), and Δz is the transport distance (m). Hence, it is clear that the current density (j) can be positively affected by temperature. However, based on the Einstein relation, a 1.05-fold change in the value of D should be observed between 22 and 38°C (295 K/311 K). Notably, we observed a larger difference in our current production values, indicating that the changes in the diffusion process probably have a very limited influence on current generation.

Cytochrome-Bound-Co-factor-Mediated EET in BESs

In addition to the free AQS-mediated process, the *c*-Cyts-bound cofactor can also be involved in electron transfer. As reported previously, low concentrations of flavin can be bound to *c*-Cyts, and as the *c*-Cyts-bound cofactor is obviously different from free flavin, it can be used to regulate the extent of EET processes (Okamoto et al., 2013, 2014a,c). Hence, the roles of temperature-dependent, *c*-Cyts-bound-cofactor-mediated electron transfer processes are considered further below.

Figures 4A,B exhibit peaks at −245 and −70 mV corresponding to free AQS and the *c*-Cyts-bound cofactor, respectively. Thus, the catalytic currents generated at −245 and −70 mV, as depicted in **Figures 4C,D**, were contributed from the free AQS-mediated process and the *c*-Cyts-bound-cofactor-mediated process, respectively. In the long-term incubation experiments, the catalytic current from both the free AQS-mediated process and the *c*-Cyts-bound-cofactor-mediated process decreased as the temperature decreased from 34 to 22°C

(Figure 4C). However, in the instantaneous temperature change experiments, the catalytic current from the *c*-Cyts-bound-cofactor-mediated EET process decreased significantly, whereas that from the free AQS-mediated process only decreased slightly (Figure 4D). These results suggested that the current variation in the instantaneous temperature change experiment was mainly caused by a decline in *c*-Cyts-bound-cofactor-mediated EET, whereas both weaker AQS-mediated and *c*-Cyts-bound-cofactor-mediated EET contributed to the total current decrease during the long-term incubation experiment.

The bioreduction rate of AQS is mainly limited by the metabolic rate of microbes. As changes in the rate of microbial metabolism probably require a certain period of time, the AQS reduction rate did not change much in the short-term incubation and instantaneous temperature change experiments. Hence, as shown in Figure 7A, the rate constants of AQS reduction only changed slightly. However, flavin as a bound cofactor for accelerating EET is involved in a biochemical process on the outer surface of the cell. It has been reported that this process can be regulated by the properties of *c*-Cyts, and *S. oneidensis* MR-1 has the capacity to use flavin as a regulator to control the extent of EET processes (Okamoto et al., 2013). Hence, the response of this biochemical process to changes in temperature may be faster than that of microbial metabolism, resulting in the *c*-Cyts-bound-cofactor-mediated EET process being more susceptible to sudden temperature changes.

Although MR-1 has been shown to grow slower at 34°C than at 30°C, the reported optimum temperature for manganese reduction by MR-1 is 35°C (Myers and Nealson, 1988). Hence, the optimum temperature of MR-1 in different system can be different. In this study, 34°C was the optimum temperature, probably because in the presence of exogenous AQS, the change in temperature not only changes the physiology of MR-1 but also changes the electron shuttling properties of AQS. Specifically, it can influence the AQS midpoint potential, the AQS bioreduction process, the AQS diffusion coefficient, and *c*-Cyts-bound-cofactor-mediated EET. These factors might contribute to the observation of a lower optimum temperature of 34°C in this study.

Here, the EET capacity increased as the temperature rose from 22 to 34°C and then decreased sharply at 38°C. Besides the cell death observed at 38°C, five key factors, namely, the biofilm biomass, *c*-Cyts-bound-cofactor-mediated EET, the AQS bioreduction rate, the AQS midpoint potential, and the AQS diffusion coefficient, could be affected by changing the incubation temperature. The temperature-dependent AQS midpoint potential and the AQS diffusion

coefficient contributed little to the variations in total electricity generation at different temperatures, whereas the temperature-dependent biofilm biomass, *c*-Cyts-bound-cofactor-mediated EET, and the AQS bioreduction rate dominated the observed electricity generation variation. As the ambient temperature changes often in natural environments, it is an important environmental factor that influences natural microbial processes such as biofilm formation and microbe-mineral electron transfer. Thus, our findings provide an improved fundamental understanding of EET processes and will aid in the practical application of bioenergy techniques via optimization of the operating parameters for current generation in relevant BESs such as microbial fuel cells.

AUTHOR CONTRIBUTIONS

WL, YW, FL, and TL conceived and designed the experiments. WL, YW, and TL were responsible for drafting the article. WL, YW, HD, and MJ were involved in the experiments preformation and data analysis. All authors approved the final version of the manuscript.

FUNDING

This work was funded by the GDAS Special Project of Science and Technology Development (2017GDASCX-0409), the National Natural Science Foundation of China (41701305, 41522105, and 21701045), and the Opening Fund of Key Laboratory for Water Quality and Conservation of the Pearl River Delta, Ministry of Education (201705).

SUPPLEMENTARY MATERIAL

The Supplementary Material for this article can be found online at: <https://www.frontiersin.org/articles/10.3389/fmicb.2019.00464/full#supplementary-material>

FIGURE S1 | The effect of lactate concentration (10, 20, 30, 40, and 50 mM) on current generation.

FIGURE S2 | The peak current in Figures 8A–D versus the square root of the scan rate.

FIGURE S3 | The normalized current output at different conditions: (a) Maximum current when the biofilm was incubated at a temperature of 34°C. It was defined as 100%. (b) Current after the temperature was changed instantaneously from 34 to 22°C. (c) Maximum current when the biofilm was incubated at a temperature of 22°C.

REFERENCES

- Abboud, R., Popa, R., Souza-Egipsy, V., Giometti, C. S., Tollaksen, S., Mosher, J. J., et al. (2005). Low-temperature growth of *Shewanella oneidensis* MR-1. *Appl. Environ. Microbiol.* 71, 811–816. doi: 10.1128/AEM.71.2.811-816.2005
- Brutinel, E. D., and Gralnick, J. A. (2012). Shuttling happens: soluble flavin mediators of extracellular electron transfer in *Shewanella*. *Appl. Microbiol. Biotechnol.* 93, 41–48. doi: 10.1007/s00253-011-3653-0
- Calandra, D. M., Mauro, D., Di Cutugno, F., and Martino, S. (2016). Navigating wall-sized displays with the gaze: a proposal for cultural heritage. *CEUR Workshop Proc.* 1621, 36–43.

- Coursolle, D., and Gralnick, J. A. (2010). Modularity of the Mtr respiratory pathway of *Shewanella oneidensis* strain MR-1. *Mol. Microbiol.* 77, 995–1008. doi: 10.1111/j.1365-2958.2010.07266.x
- Gralnick, J. A., and Newman, D. K. (2007). Extracellular respiration. *Mol. Microbiol.* 65, 1–11. doi: 10.1111/j.1365-2958.2007.05778.x
- Han, R., Li, F., Liu, T., Li, X., Wu, Y., Wang, Y., et al. (2016). Effects of incubation conditions on Cr(VI) reduction by c-type cytochromes in intact *Shewanella oneidensis* MR-1 cells. *Front. Microbiol.* 7:746. doi: 10.3389/fmicb.2016.00746
- Han, R., Liu, T., Li, F., Li, X., Chen, D., and Wu, Y. (2018). Dependence of secondary mineral formation on Fe(II) production from ferrihydrite reduction by *Shewanella oneidensis* MR-1. *ACS Earth Space Chem.* 2, 399–409. doi: 10.1021/acsearthspacechem.7b00132
- Klöpfer, L., Piepenbrock, A., Kappler, A., and Sander, M. (2014). Humic substances as fully regenerable electron acceptors in recurrently anoxic environments. *Nat. Geosci.* 7, 195–200. doi: 10.1038/ngeo2084
- Li, X., Liu, L., Liu, T., Yuan, T., Zhang, W., Li, F., et al. (2013). Electron transfer capacity dependence of quinone-mediated Fe (III) reduction and current generation by *Klebsiella pneumoniae* L17. *Chemosphere* 92, 218–224. doi: 10.1016/j.chemosphere.2013.01.098
- Li, X., Liu, T., Liu, L., and Li, F. (2014). Dependence of the electron transfer capacity on the kinetics of quinone-mediated Fe(III) reduction by two iron/humic reducing bacteria. *RSC Adv.* 4, 2284–2290. doi: 10.1039/C3RA45458D
- Light, S. H., Su, L., Rivera-lugo, R., Cornejo, J. A., Louie, A., and Iavarone, A. T. (2018). A flavin-based extracellular electron transfer mechanism in diverse Gram-positive bacteria. *Nature* 562, 140–144. doi: 10.1038/s41586-018-0498-z
- Liu, T., Wu, Y., Li, F., Li, X., and Luo, X. (2017). Rapid redox processes of c-type cytochromes in a living cell suspension of *Shewanella oneidensis* MR-1. *ChemistrySelect* 2, 1008–1012. doi: 10.1002/slct.201602021
- Logan, B. E. (2009). Exoelectrogenic bacteria that power microbial fuel cells. *Nat. Rev. Microbiol.* 7, 375–381. doi: 10.1038/nrmicro2113
- Lovley, D. R., Stolz, J. F., Nord, G. L., and Phillips, E. J. P. (1987). Anaerobic production of magnetite by a dissimilatory iron-reducing microorganism. *Nature* 330, 252–254. doi: 10.1038/330252a0
- Myers, C. R., and Nealson, K. H. (1988). Bacterial manganese reduction and growth with manganese oxide as the sole electron acceptor. *Science* 240, 1319–1321. doi: 10.1126/science.240.4857.1319
- Nakamura, R., Ishii, K., and Hashimoto, K. (2009). Electronic absorption spectra and redox properties of C type cytochromes in living microbes. *Angew. Chem. Int. Ed. Engl.* 48, 1606–1608. doi: 10.1002/anie.200804917
- Niedzwiecka, J. B., Drew, S. R., Schlautman, M. A., Millerick, K. A., Grubbs, E., Tharayil, N., et al. (2017). Iron and electron shuttle mediated (bio)degradation of 2,4-dinitroanisole (DNAN). *Environ. Sci. Technol.* 51, 10729–10735. doi: 10.1021/acs.est.7b02433
- Ohtsuka, T., Yamaguchi, N., Makino, T., Sakurai, K., Kimura, K., Kudo, K., et al. (2013). Arsenic dissolution from Japanese paddy soil by a dissimilatory arsenate-reducing bacterium *Geobacter* sp. OR-1. *Environ. Sci. Technol.* 47, 6263–6271. doi: 10.1021/es400231x
- Okamoto, A., Hashimoto, K., and Nealson, K. H. (2014a). Flavon redox bifurcation as a mechanism for controlling the direction of electron flow during extracellular electron transfer. *Angew. Chem. Int. Ed. Engl.* 53, 10988–10991. doi: 10.1002/anie.201407004
- Okamoto, A., Kalathil, S., Deng, X., Hashimoto, K., Nakamura, R., and Nealson, K. H. (2014b). Cell-secreted flavins bound to membrane cytochromes dictate electron transfer reactions to surfaces with diverse charge and pH. *Sci. Rep.* 4:5628. doi: 10.1038/srep05628
- Okamoto, A., Saito, K., Inoue, K., Nealson, K. H., Hashimoto, K., and Nakamura, R. (2014c). Uptake of self-secreted flavins as bound cofactors for extracellular electron transfer in *Geobacter* species. *Energy Environ. Sci.* 7, 1357–1361. doi: 10.1039/C3EE43674H
- Okamoto, A., Hashimoto, K., Nealson, K. H., and Nakamura, R. (2013). Rate enhancement of bacterial extracellular electron transport involves bound flavin semiquinones. *Proc. Natl. Acad. Sci. U.S.A.* 110, 7856–7861. doi: 10.1073/pnas.1220823110
- Picard, A., Testemale, D., Wagenknecht, L., Hazael, R., and Daniel, I. (2014). Iron reduction by the deep-sea bacterium *Shewanella profunda* LT13a under subsurface pressure and temperature conditions. *Front. Microbiol.* 5:796. doi: 10.3389/fmicb.2014.00796
- Pinchuk, G. E., Geydebrekht, O. V., Hill, E. A., Reed, J. L., Konopka, A. E., Beliaev, A. S., et al. (2011). Pyruvate and lactate metabolism by *Shewanella oneidensis* MR-1 under fermentation, oxygen limitation, and fumarate respiration conditions. *Appl. Environ. Microbiol.* 77, 8234–8240. doi: 10.1128/AEM.05382-11
- Richter, H., Nevin, K. P., Jia, H., Lowy, D. A., Lovley, D. R., and Tender, L. M. (2009). Cyclic voltammetry of biofilms of wild type and mutant *Geobacter sulfurreducens* on fuel cell anodes indicates possible roles of OmcB, OmcZ, type IV pili, and protons in extracellular electron transfer. *Energy Environ. Sci.* 2, 506–516. doi: 10.1039/b816647a
- Saito, J., Hashimoto, K., and Okamoto, A. (2016). Flavon as an indicator of the rate-limiting factor for microbial current production in *Shewanella Oneidensis* MR-1. *Electrochim. Acta* 216, 261–265. doi: 10.1016/j.electacta.2016.09.002
- Shi, L., Dong, H., Reguera, G., Beyenal, H., Lu, A., Liu, J., et al. (2016). Extracellular electron transfer mechanisms between microorganisms and minerals. *Nat. Rev. Microbiol.* 14, 651–662. doi: 10.1038/nrmicro.2016.93
- Shi, L., Richardson, D. J., Wang, Z., Kerisit, S. N., Rosso, K. M., Zachara, J. M., et al. (2009). The roles of outer membrane cytochromes of *Shewanella* and *Geobacter* in extracellular electron transfer. *Environ. Microbiol. Rep.* 1, 200–227. doi: 10.1111/j.1758-2229.2009.00035.x
- Shi, L., Squier, T. C., Zachara, J. M., and Fredrickson, J. K. (2007). Respiration of metal (hydr)oxides by *Shewanella* and *Geobacter*: a key role for multihaem c-type cytochromes. *Mol. Microbiol.* 65, 12–20. doi: 10.1111/j.1365-2958.2007.05783.x
- Tango, C. N., Akkermans, S., Hussain, M. S., Khan, I., Van Impe, J., Jin, Y. G., et al. (2018). Modeling the effect of pH, water activity, and ethanol concentration on biofilm formation of *Staphylococcus aureus*. *Food Microbiol.* 76, 287–295. doi: 10.1016/j.fm.2018.06.006
- Torres, C. I., Marcus, A. K., Lee, H., Parameswaran, P., Krajmalnik-Brown, R., and Rittmann, B. E. (2009). A kinetic perspective on extracellular electron transfer by anode-respiring bacteria. *FEMS Microbiol. Rev.* 34, 3–17. doi: 10.1111/j.1574-6976.2009.00191.x
- Wang, F., Xiao, X., Ou, H.-Y., Gai, Y., and Wang, F. (2009). Role and regulation of fatty acid biosynthesis in the response of *Shewanella piezotolerans* WP3 to different temperatures and pressures. *J. Bacteriol.* 191, 2574–2584. doi: 10.1128/JB.00498-08
- Watanabe, K., Manefield, M., Lee, M., and Kouzuma, A. (2009). Electron shuttles in biotechnology. *Curr. Opin. Biotechnol.* 20, 633–641. doi: 10.1016/j.copbio.2009.09.006
- Wu, Y., Li, F., Liu, T., Han, R., and Luo, X. (2016). pH dependence of quinone-mediated extracellular electron transfer in a bioelectrochemical system. *Electrochim. Acta* 213, 408–415. doi: 10.1016/j.electacta.2016.07.122
- Wu, Y., Liu, T., Li, X., and Li, F. (2014). Exogenous electron shuttle-mediated extracellular electron transfer of *Shewanella putrefaciens* 200: electrochemical parameters and thermodynamics. *Environ. Sci. Technol.* 48, 9306–9314. doi: 10.1021/es5017312
- Wu, Y., Liu, W., Liu, T., Li, F., Xiao, T., Wu, Q., et al. (2018). Sustainable electron shuttling processes mediated by in situ-deposited phenoxazine. *ChemElectroChem* 5, 2171–2175. doi: 10.1002/celec.201800470
- Xu, S., Jangir, Y., and El-Naggar, M. Y. (2016). Disentangling the roles of free and cytochrome-bound flavins in extracellular electron transport from *Shewanella oneidensis* MR-1. *Electrochim. Acta* 198, 49–55. doi: 10.1016/j.electacta.2016.03.074
- Yamamura, S., Sudo, T., Watanabe, M., Tsuboi, S., Soda, S., Ike, M., et al. (2018). Effect of extracellular electron shuttles on arsenic-mobilizing activities in soil microbial communities. *J. Hazard. Mater.* 342, 571–578. doi: 10.1016/j.jhazmat.2017.08.071
- Yuan, Y., Cai, X., Wang, Y., and Zhou, S. (2017). Electron transfer at microbe-humic substances interfaces: electrochemical, microscopic and bacterial community characterizations. *Chem. Geol.* 456, 1–9. doi: 10.1016/j.chemgeo.2017.02.020
- Zhang, J., Zhang, L., Miao, Y., Sun, Y., Li, X., Zhang, Q., et al. (2018). Feasibility of in situ enriching anammox bacteria in a sequencing batch biofilm reactor

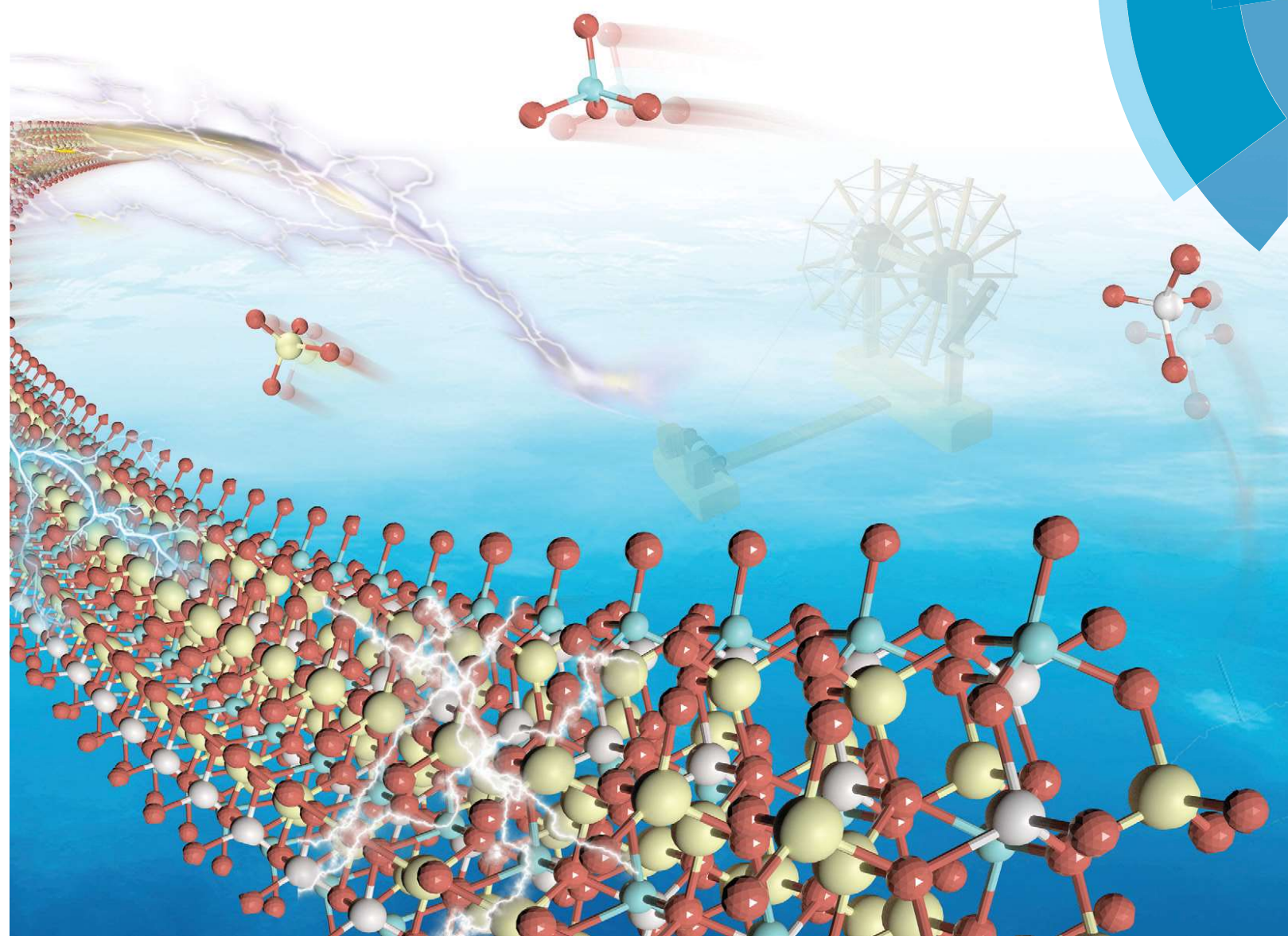
- (SBBR) for enhancing nitrogen removal of real domestic wastewater. *Chem. Eng. J.* 352, 847–854. doi: 10.1016/j.cej.2018.06.024
- Zhao, L., Dong, H., Kukkadapu, R., Agrawal, A., Deng, L., Jing, Z., et al. (2013). Biological oxidation of Fe(II) in reduced nontronite coupled with nitrate reduction by *Pseudogulbenkiania* sp. strain 2002. *Geochim. Cosmochim. Acta* 119, 231–247. doi: 10.1016/j.gca.2013.05.033
- Zhou, G. W., Yang, X. R., Li, H., Marshall, C. W., Zheng, B. X., Yan, Y., et al. (2016). Electron shuttles enhance anaerobic ammonium oxidation coupled to iron(III) reduction. *Environ. Sci. Technol.* 50, 9298–9307. doi: 10.1021/acs.est.6b02077

Conflict of Interest Statement: The authors declare that the research was conducted in the absence of any commercial or financial relationships that could be construed as a potential conflict of interest.

Copyright © 2019 Liu, Wu, Liu, Li, Dong and Jing. This is an open-access article distributed under the terms of the Creative Commons Attribution License (CC BY). The use, distribution or reproduction in other forums is permitted, provided the original author(s) and the copyright owner(s) are credited and that the original publication in this journal is cited, in accordance with accepted academic practice. No use, distribution or reproduction is permitted which does not comply with these terms.

CrystEngComm

rsc.li/crystengcomm



ISSN 1466-8033



ROYAL SOCIETY
OF CHEMISTRY

Celebrating
IYPT 2019

PAPER

Changzhou Yuan *et al.*

Efficient electrospinning fabrication and the underlying formation mechanism of one-dimensional monoclinic $\text{Li}_2\text{FeSiO}_4$ nanofibers

aromatic rings by C-H... π interactions: experimental evidence, computational criteria, and database analysis

Ali Samie, Alireza Salimi and Jared C. Garrison

In C-H... π interaction, the relative π -electron localization in aromatic ring led to the change of contact position from centre to edges of the ring (C-H... π_n) which was confirmed by experimental evidences, computational criteria, and database analysis.



The article was first published on 24 Sep 2019

CrystEngComm, 2019, **21**, 6432-6445

<https://doi.org/10.1039/C9CE00929A>

Download PDF

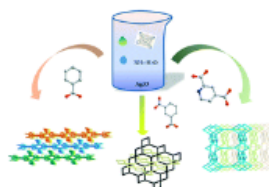
Article HTML

Paper

Tuning the net topology of a ternary Ag(I)-1,2,4,5-tetra(4-pyridyl)benzene-carboxylate framework: structures and photoluminescence

Wei Liu, Cong-Cong Chen, Ling-Ling Mao, Si-Guo Wu, Long-Fei Wang and Ming-Liang Tong

Changing of auxiliary ligands leads to the formation of 1D-3D coordination structures and the use of dye molecules provides a way to promote the luminescence properties of MOFs.



The article was first published on 12 Sep 2019

CrystEngComm, 2019, **21**, 6446-6451

<https://doi.org/10.1039/C9CE01155B>

Download PDF

Article HTML

Paper

Energetic transition metal salts of 5,5'-dinitramino-3,3'-methylene-1*H*-1,2,4-bis-triazole: syntheses, structures and properties

Yanna Wang, Xiaoming Yang, Weijing Zhang, Haibo Li, Zhimin Li, Lin Wang and Tonglai Zhang

Five energetic transition metal salts based on H₂DNAMT were synthesized. Meanwhile, H₂DNAMT was oxidized to H₂BNATO due to Fe³⁺ in [Fe(BNATO)(H₂O)₄]·2H₂O. All of the metal salts exhibit comparable thermal stability and insensitivity.





Cite this: *CrystEngComm*, 2019, 21, 6446
6446

Tuning the net topology of a ternary Ag(I)-1,2,4,5-tetra(4-pyridyl)benzene-carboxylate framework: structures and photoluminescence†

Wei Liu,^a Cong-Cong Chen,^a Ling-Ling Mao,^b Si-Guo Wu,^b Long-Fei Wang^b and Ming-Liang Tong^b

The dye molecule 1,2,4,5-tetra(4-pyridyl)benzene (bztpy), a tetradentate ligand, can be an excellent candidate for construction of coordination polymers with photoluminescence properties. Here, based on Ag(I) and bztpy, three novel complexes, namely [Ag₂(bza)₂(μ₄-bztpy)] (1), [Ag₂(μ-*ipa*)(μ₄-bztpy)]·EtOH·3H₂O (2) and [Ag₃(pda)(μ-pda)_{1/2}(μ₄-bztpy)₂]·3EtOH·6H₂O (3) (Hbza = benzoic acid, H₂*ipa* = isophthalic acid and H₂pda = 2,4-pyridinedicarboxylic acid), have been synthesized with the assistance of auxiliary carboxylates. The choice of carboxylates was found to have a pronounced effect on the framework topology. Structural analysis revealed that there are [Ag₂(bztpy)]_∞ chains as basic side groups and the change of interconnected auxiliary ligands from Hbza to H₂pda leads to the formation of 1D, 2D and 3D structures, respectively. They were further characterized by elemental analysis, IR, single-crystal X-ray diffraction and luminescence study.

Received 25th July 2019,
Accepted 12th September 2019

DOI: 10.1039/c9ce01155b

rsc.li/crystengcomm

Introduction

In recent decades, due to their intriguing structural diversities and potential applications in gas capture and storage,¹ separation,² molecular recognition,³ photoluminescence,⁴ catalysis,⁵ magnetism,⁶ biomedicine,⁷ etc., metal-organic frameworks (MOFs)⁸ have attracted intense attention in materials research. Considerable efforts have been devoted to assemble one-, two- and three-dimensional (1–3D) extended networks and predict theoretically the topology and geometries of frameworks to improve the performance of materials in order to realize their applications. However, the precise principles of the design and construction of desirable framework topologies with specific properties are still a challenge for chemists. In general, the choice of suitable organic ligands and the selection of appropriate metal centres are the main key.⁹

Resulting from the multifaceted nature of their structure, MOFs display a wide range of luminescence behaviours.⁴ As transition-metal ions with unpaired electrons exhibit a quenching effect, d¹⁰ type transition-metal centres can be

good candidates for generating luminescence in MOFs.^{4a} In this work, Ag(I) has been selected as a framework metal ion due to not only its intrinsic electronic configuration but also highly flexible coordination mode and geometry shape that result in multiple types of fascinating coordination architectures.¹⁰ On the other hand, MOFs' attractive physicochemical properties can be considered as the cooperative effect integrated from the subunits. For example, linker molecules play a critical role in MOF luminescence since organic linkers can absorb photon energies and transfer them to metal centres.^{4a} Thus, development of dye molecules as inorganic linkers can be excellent to construct coordination polymers with photoluminescence properties. Benefiting from more donor sites, multidentate ligands prove to be very useful for the synthesis of coordination polymers.¹¹ In recent years, the tetradentate ligand bztpy was successfully isolated from a hydrothermal system and has been found to exhibit distinct photoluminescence with a quantum efficiency of up to 42% in the solid state because of the special molecular packing and/or water molecules in the lattice.¹² Herein we are trying to extend this tetradentate ligand to d¹⁰ type metal centres for its potential applications as a luminescent material.¹³

Fortunately, with the assistance of auxiliary carboxylates, benzoic acid (Hbza), isophthalic acid (H₂*ipa*) and 2,4-pyridinedicarboxylic acid (H₂pda), three novel complexes based on Ag(I) atoms and bztpy, namely [Ag₂(bza)₂(μ₄-bztpy)] (1), [Ag₂(μ-*ipa*)(μ₄-bztpy)]·EtOH·3H₂O (2) and [Ag₃(pda)(μ-pda)_{1/2}(μ₄-bztpy)₂]·3EtOH·6H₂O (3), have been synthesized by

^a College of Materials and Energy, South China Agricultural University, Guangzhou 510640, P. R. China. E-mail: liuwei97@scau.edu.cn

^b Key Laboratory of Bioinorganic and Synthetic Chemistry of Ministry of Education, School of Chemistry, Sun Yat-Sen University, Guangzhou 510275, P. R. China

† Electronic supplementary information (ESI) available. CCDC 1922113–1922115. For ESI and crystallographic data in CIF or other electronic format see DOI: 10.1039/c9ce01155b

slow crystallization under ambient conditions. Single crystal X-ray diffraction measurements reveal that all the three structures are based on $[\text{Ag}_2(\text{bztpy})]_\infty$ chains in which every tetradentate bztpy ligand binds with four $\text{Ag}(\text{I})$ atoms. The change of interconnected auxiliary ligands on Ag^+ sites from Hbza to H_2pda further leads to the formation of 1D, 2D and 3D structures, respectively. And in particular, compound 1 exhibits a 1D $[\text{Ag}_2(\text{bztpy})]_\infty$ chain structure with bza^- mounted on Ag^+ sites, and the 1D chains expand into a 3D supramolecular structure by intermolecular $\text{Ag}\cdots\text{Ag}$ and $\pi\cdots\pi$ stacking interaction. For compound 2, adjacent parallel 1D $[\text{Ag}_2(\text{bztpy})]_\infty$ chains are bridged by ipa^{2-} on Ag^+ sites to show a 2D layer and further interpenetrate into a 3D structure. The framework can be simplified to a 2D interpenetrated (3,4)-connected topology with a point symbol of $(4\cdot6^2)_2(4^2\cdot6^2\cdot8^2)$.¹⁴ And 3, in which 1D $[\text{Ag}_2(\text{bztpy})]_\infty$ chains perpendicular to each other are bridged by ipa^{2-} on Ag^+ sites, has a novel 3D 3-fold interpenetrated (3,4)-connected net with a point symbol of $(4\cdot10^2)(4\cdot7^2)(4^2\cdot7^2\cdot9^2)(4^2\cdot7^4)$. The photoluminescence properties of the three complexes were also investigated. The solid samples of 1–3 exhibit intense emission with $\lambda_{\text{em}}^{\text{max}}$ at ca. 542 ($\lambda_{\text{ex}} = 395$), 539 ($\lambda_{\text{ex}} = 360$) and 498 nm ($\lambda_{\text{ex}} = 380$ nm), respectively, mainly assigned to linker-based luminescence as well as metal-to-linker charge transfer (MLCT).

Experimental section

Materials and general measurements

All the starting chemicals were commercially available, which were used as received without further purification. The bztpy ligand was prepared by the hydrothermal method reported in the literature.¹² Elemental analysis (C, H, and N) was performed with a Vario EL elemental analyser. The FT-IR spectra of KBr pellets were recorded on a Bruker-EQUINOX 55 FT-IR spectrometer in the range of 4000–400 cm^{-1} . The X-ray single-crystal structure was measured using a Rigaku R-Axis SPIDER IP diffraction instrument and Oxford diffraction Gemini R CCD instrument. The powder X-ray diffraction intensity of the polycrystalline samples was measured using a Bruker D8 Advanced diffractometer at room temperature. Thermogravimetric analyses (TGA) were carried out using a TG-209 analyser at ambient temperature to 900 °C with a heating rate of 10 K min^{-1} under a flowing N_2 atmosphere. The photoluminescence spectra and emission decay curves were recorded at room temperature using an Edinburgh FLS920 spectrofluorometer. The room temperature internal quantum efficiency (IQE) values of the three samples were measured using a barium sulfate coated integrating sphere attached to an FSP920. In the CIF file, the disordered guests have been squeezed using the Platon software, and the total potential solvent accessible void volume (1329 \AA^3 per cell) and the density of the squeezed electron (electron count voids per cell = 427), together with elemental analysis and TGA results have been taken to determine the proportion of the guest molecules.

Diffraction intensities data of 1 and 3 were collected on a Bruker D8 QUEST diffractometer at 120 K while those of 2 on a Rigaku R-Axis SPIDER IP diffractometer at 150 K using Mo-K α radiation ($\lambda = 0.71073$ \AA). The structures were solved by direct methods, and anisotropic thermal parameters were assigned to all non-hydrogen atoms, through least squares on F^2 using the SHELXTL program suite.¹⁶ The hydrogen atoms of the organic ligands were placed in idealised positions and refined using a riding model. The SQUEEZE program of PLATON¹⁷ was employed to deal with the disordered solvent molecules in the framework of 3. CCDC 1922113 (1), 1922114 (2) and 1922115 (3) contain the supplementary crystallographic data for this paper.

Synthesis of complexes 1–3

$[\text{Ag}_2(\text{bza})_2(\mu_4\text{-bztpy})]$ (1). A mixture of fresh $\text{NH}_3\cdot\text{H}_2\text{O}$ (0.1 mol L^{-1} , 2 mL), Ag_2O (11 mg, 0.05 mmol) and bztpy (19 mg, 0.05 mmol) in ethanol solution (6 mL) with stirring for 10 minutes was added to an ethanol solution (2 mL) of benzoic acid (12 mg, 0.1 mmol). After stirring for 30 minutes, the resulting solution was filtered to afford a colourless transparent filtrate. Yellow bulk crystals of 1 were obtained by slow evaporation after three days. Yield: about 40% based on bztpy. Anal. calcd. (%) for $\text{C}_{40}\text{H}_{28}\text{Ag}_2\text{N}_4\text{O}_4$: C, 56.90; H, 3.34; N, 6.64. Found: C, 56.67; H, 3.32; N, 6.54. IR (KBr, cm^{-1}): 3368 m, 3052 m, 2492 w, 1990 w, 1648 s, 1552 s, 1386 s, 1365 s, 1421 s, 1222 s, 1066 s, 1011 s, 832 s, 707 s, 563 s.

$[\text{Ag}_2(\mu\text{-ipa})(\mu_4\text{-bztpy})]\cdot\text{EtOH}\cdot 3\text{H}_2\text{O}$ (2). A mixture of fresh $\text{NH}_3\cdot\text{H}_2\text{O}$ (0.1 mol L^{-1} , 3 mL), Ag_2O (23 mg, 0.1 mmol), bztpy (19 mg, 0.05 mmol) and isophthalic acid (16 mg, 0.1 mmol) in ethanol solution (8 mL) was stirred for 30 minutes. The resulting solution was filtered to afford a colourless transparent filtrate. Yellow acicular crystals of 2 were obtained by slow evaporation after three days. Yield: about 47% based on bztpy. Anal. calcd. (%) for $\text{C}_{36}\text{H}_{34}\text{Ag}_2\text{N}_4\text{O}_8$: C, 49.91; H, 3.96; N, 6.47. Found: C, 49.90; H, 4.01; N, 6.38. IR (KBr, cm^{-1}): 3362 s, 3241 m, 2974 m, 2427 w, 1971 w, 1604 s, 1547 s, 1476 s, 1421 s, 1366 s, 1243 m, 1068 m, 1006 m, 823 s, 752 s, 704 m, 545 m, 497 m.

$[\text{Ag}_3(\text{pda})(\mu\text{-pda})_{1/2}(\mu_4\text{-bztpy})_2]\cdot 3\text{EtOH}\cdot 6\text{H}_2\text{O}$ (3). A mixture of fresh $\text{NH}_3\cdot\text{H}_2\text{O}$ (0.1 mol L^{-1} , 2 mL), Ag_2O (11 mg, 0.05 mmol) and dipicolinic acid (16 mg, 0.1 mmol) in ethanol solution (2 mL) with stirring for 10 minutes was added to an ethanol solution (6 mL) of bztpy (19 mg, 0.05 mmol). After stirring for 30 minutes, the resulting solution was filtered to afford a colourless transparent filtrate. Yellow bulk crystals of 3 were obtained by slow evaporation after three days. Yield: about 53% based on bztpy. Anal. calcd. (%) for $\text{C}_{68.5}\text{H}_{70.5}\text{N}_{9.5}\text{Ag}_3\text{O}_{15}$: C, 51.73; H, 4.47; N, 8.37. Found: C, 51.25; H, 4.71; N, 8.30. IR (KBr, cm^{-1}): 3374 s, 3079 m, 2443 w, 1957 w, 1599 s, 1546 s, 1575 m, 1417 s, 1365 s, 1219 m, 1066 m, 1004 m, 881 s, 780 m, 756 m, 701 m, 562 m, 541 m.

Results and discussion

General procedure for the synthesis of compounds 1–3

Complex 1 was synthesized by the reaction of $\text{NH}_3\cdot\text{H}_2\text{O}$, Ag_2O , bztpy and benzoic acid. When changing benzoic acid

into isophthalic acid and 2,4-pyridinedicarboxylic acid, complexes 2 and 3 were obtained. The ratios of the reactants were adjusted respectively for better yields. The detailed experimental schemes are described in the synthesis section.

The X-ray crystallography data shows that complex 1 is crystallized in the $P\bar{1}$ space group with an asymmetric unit containing one Ag(I) atom, half a bztpy and one bza^- . The Ag(I) atom is tetrahedrally coordinated by two nitrogen atoms from different bztpy ligands and two carboxylate oxygen atoms from bza^- (Fig. 1a). As illustrated in Fig. 1b, every tetradentate bztpy ligand connects with four Ag(I) atoms and thus forms the $[Ag_2(bztpy)]_\infty$ double chains with bza^- counterions chelating on Ag⁺ sites. The 1D double chains are stacked into layers (Fig. 1c) by ligand-unsupported Ag \cdots Ag interaction with a distance of 3.25 Å which is in accordance with the values reported in other Ag(I) complexes.¹⁵ Face to face π - π stacking interaction (3.94 Å) is also observed between the benzene ring on bza^- and the pyridine ring of bztpy at neighboring layers, thus resulting in a three-dimensional supramolecular network (Fig. 1d).

Complex 2 crystallizes in the monoclinic Cc space group. Each asymmetric unit contains two crystallographically unique Ag atoms, one ipa^- counterion, one bztpy ligand, one ethanol and three water molecules as guest molecules. The two Ag atoms per asymmetric unit have a similar trigonal planar coordination geometry ligated by two nitrogen atoms from bztpy and one oxygen atom from ipa^- (Fig. 2a). The basic side groups of the structure are also 1D $[Ag_2(bztpy)]_\infty$ chains that are formed by bztpy ligands and Ag(I) atoms and each pair of the adjacent 1D chains are linked into a 2D sheet by the two carboxyl groups on ipa^- . In this sheet, the tetradentate ligand bztpy acts as a four-connected framework node and Ag(I) as a three-connected framework node, and it

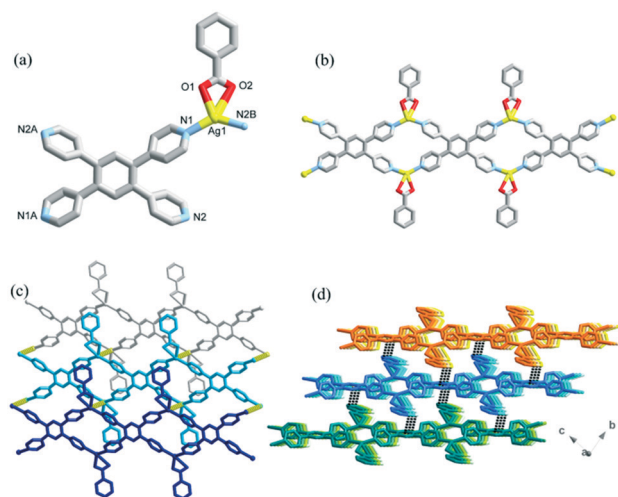


Fig. 1 For complex 1: (a) the coordination environment of the silver atom; (b) view of the 1D chain; (c) the two-dimensional plane, formed by weak Ag \cdots Ag interaction (yellow dashed lines) of 1D chains; (d) the three-dimensional framework formed by the interfacial π - π stacking (black dashed lines) interaction among the 2D plane. All H atoms have been omitted for clarity.

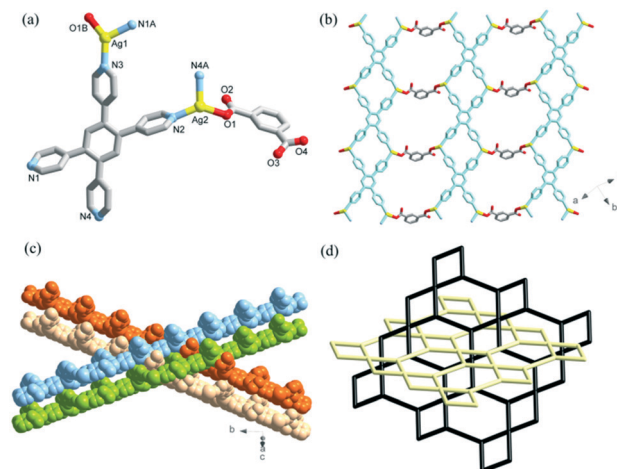


Fig. 2 For complex 2: (a) coordination environment of the silver atoms; (b) view of the two-dimensional plane; (c) space-filling representations of the adjacent layers; (d) 2D (3,4)-connected interpenetrated network. The lattice guest molecules and H atoms have been omitted for clarity.

can be simplified into a 2D topological network with a Schläfli symbol of $(4\cdot6^2)_2(4^2\cdot6^2\cdot8^2)$. Each sheet has enough “empty” room for the interpenetration with an infinite number of inclined sheets (40.8°) in a “diagonal-diagonal” fashion¹⁸ thus finally resulting in an inclined catenation 2D \rightarrow 3D framework (Fig. 2b and c).

The structure of 3 is found to be a 3D triple-intercalation framework in the space group $P\bar{1}$ with an asymmetric unit containing three crystallographically unique Ag atoms, two bztpy ligands, one and half a pda^- and several solvent molecules. Each Ag(I) atom is tetrahedrally coordinated: Ag1 is coordinated by two pyridine nitrogen atoms from different bztpy ligands and either the pyridine nitrogen atom and carboxylate oxygen atom or two carboxylate oxygen atoms from a pda^- ligand (pda^- bound with Ag1 turns out to exhibit positional disorder, Fig. 3a); Ag2 is coordinated with four pyridine nitrogen atoms from four different bztpy ligands; Ag3 is coordinated to two pyridine nitrogen atoms from different bztpy ligands as well as the pyridine nitrogen atom and carboxylate oxygen atom from a pda^- ligand. The whole frame can be viewed as a 3D structure composed of two kinds of $[Ag_2(bztpy)]_\infty$ chains. One chain (Fig. 3b and S1,[†] marked by blue) is composed of a bztpy ligand, Ag1 and Ag2, whereas the other chain (Fig. 3b and S1,[†] marked by green) is composed of a bztpy ligand, Ag2 and Ag3. The two chains are arranged vertically with each other and cross-assembled by Ag2 to form a 3D structure (Fig. 3b). With regards to Ag1 as a three connected node, Ag2 as a tetrahedral node, bztpy that links with Ag1 and Ag2 as a planar four-connected node, and bztpy that links with Ag2 and Ag3 as a three connected node, the whole framework is simplified into a novel 3D 3-fold interpenetrated net with a point symbol of $(4\cdot10^2)(4\cdot7^2)(4^2\cdot7^2\cdot9^2)(4^2\cdot7^4)$ (Fig. 3c). In spite of the interpenetration, there are still voids that accommodate disordered guests which

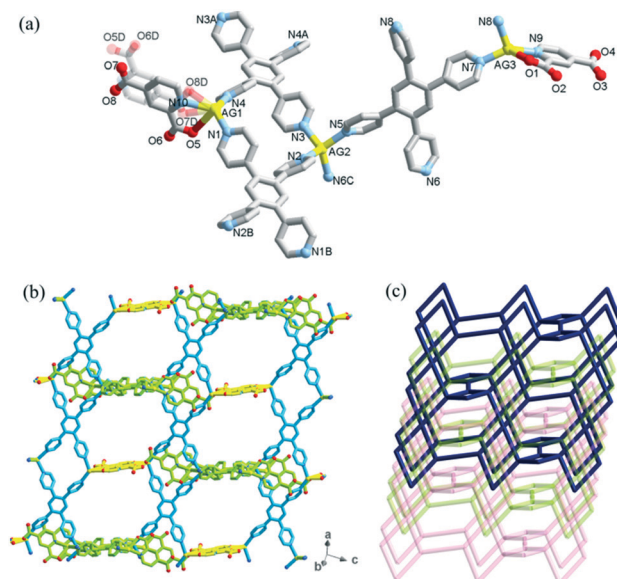


Fig. 3 For complex **3**: (a) coordination environment of the three silver atoms; (b) 3D structure cross-assembled by Ag2 atoms from two kinds of Ag-bztpy chains respectively marked by blue and green (the disordered pda[−] that bridges two Ag1 is marked by yellow); (c) 3D 3-fold interpenetrated topological network. The lattice guest molecules and H atoms have been omitted for clarity.

cannot be refined well in our crystallographic analysis, but can be determined by further assistance of thermogravimetric and elemental analyses as 3 EtOH and 6 H₂O of the formula.

The phase purity of compounds **1–3** was characterized by powder X-ray diffraction (PXRD) (Fig. S2†). The thermal stability of all the compounds was investigated by thermogravimetric analyses (TGA) (Fig. S3†). The TGA curve of **1** indicates its excellent thermal stability under heating up to 536 K. For **2**, it shows a weight loss of 10.7% in the temperature range of 337–480 K, which corresponds to the loss of three lattice water molecules and one lattice ethanol molecule (calcd.: 11.55%). Compound **3** reveals a total

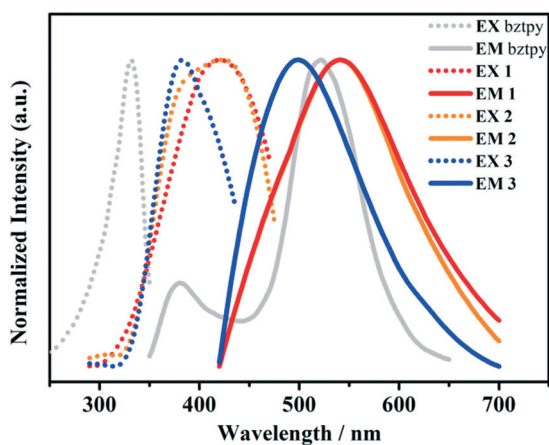


Fig. 4 Excitation and emission spectra of ligand bztpy and **1–3** in the solid state recorded at room temperature.

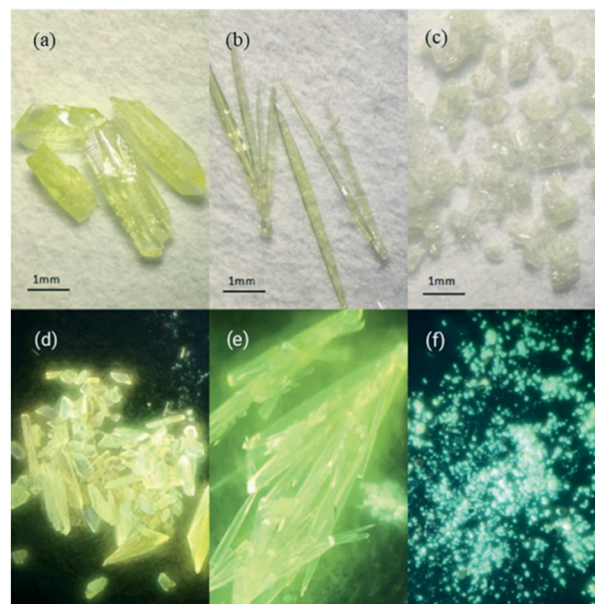


Fig. 5 The single crystal morphology of compounds **1–3** (a–c) and the observed luminescence of the crystals of compounds **1–3** irradiated with a standard laboratory UV lamp ($\lambda_{\text{exc}} = 365 \text{ nm}$) (d–f).

weight loss of 15.9% in the range of 300–373 K, which is approximately consistent with the calculated value of 15.48%.

As complexes **1–3** are a series of d¹⁰ coordination polymers based on Ag⁺, their photoluminescence properties are also studied. All the spectra were investigated in the solid state at room temperature (Fig. 4). The excitation peaks of **1–3** in the solid state at 395 nm, 360 nm and 380 nm exhibit strong luminescence with $\lambda_{\text{em}}^{\text{max}}$ at ca. 542 nm, 539 nm and 498 nm, respectively. The emission colors of the three compounds can be captured with the naked eye under UV light, with absolute quantum yields of 22.52%, 27.92% and 12.07% evaluated by using the ratio of the number of emission photon to the number of absorption photon.¹⁹ As shown in Fig. 5, illumination with a laboratory UV lamp (ca. 365 nm) results in bright emission from the samples with colors ranging from orange-yellow (sample **1**) to yellow and yellow-green (samples **2** and **3**), respectively. The radiative lifetimes are determined to be 4.43 ns for **1**, 5.59 ns for **2** and 3.62 ns for **3**, found in the same order of magnitude as nanoseconds. The free bztpy ligand as-synthesized exhibits a strong emission peak at about 521 nm upon excitation at $\lambda_{\text{max}} = 332 \text{ nm}$ (Fig. 4). Obviously, the photoluminescence properties of the three complexes should be mainly assigned to intraligand transition. The contribution of charge transfer from the silver centers to the dye molecule linker (MLCT) should also be taken into consideration, which is commonly observed in d¹⁰ Cu(I) and Ag(I) based MOFs.^{4a} Compared with complex **3**, the main emission peaks of **1** and **2** are both red-shifted and can be ascribed to the cooperative association relatively stronger intermolecular interaction among the structure.^{4a,20}

Conclusions

Resulting from the multifaceted nature of their structure, coordination polymers display a wide range of luminescence behaviours. Here, according to the principle of crystal engineering, we successfully design and synthesize three complexes (1–3) from 1D to 3D that are based on d^{10} metal centres (Ag^+) and a dye molecule (bztpy). Using interconnected auxiliary ligands plays an important role in the self-assembly process and the final structures. The intense luminescence of the solid samples indicates that dye molecules are proved to be excellent candidates for construction of coordination polymers with photochemical properties.

Conflicts of interest

There are no conflicts to declare.

Acknowledgements

This work was supported by the National Natural Science Foundation of China (21701045).

References

- (a) J. R. Li, R. J. Kuppler and H. C. Zhou, *Chem. Soc. Rev.*, 2009, **38**, 1477–1504; (b) K. J. Chen, D. G. Madden, T. Pham, K. A. Forrest, A. Kumar, Q. Y. Yang, W. Xue, B. Space, J. J. Perry IV, J. P. Zhang, X. M. Chen and M. J. Zaworotko, *Angew. Chem., Int. Ed.*, 2016, **55**, 10268–10272; (c) X. Cui, K. Chen, H. Xing, Q. Yang, R. Krishna, Z. Bao, H. Wu, W. Zhou, X. Dong, Y. Han, B. Li, Q. Ren, M. J. Zaworotko and B. Chen, *Science*, 2016, **353**, 141–144; (d) C. Gücüyener, J. van den Bergh, J. Gascon and F. Kapteijn, *J. Am. Chem. Soc.*, 2010, **132**, 17704–17706; (e) N. L. Rosi, J. Eckert, M. Eddaoudi, D. T. Vodak, J. Kim, M. O’Keeffe and O. M. Yaghi, *Science*, 2003, **300**, 1127–1129.
- (a) A. Cadiou, K. Adil, P. M. Bhatt, Y. Belmabkhout and M. Eddaoudi, *Science*, 2016, **353**, 137–140; (b) S. Yang, A. J. Ramirez-Cuesta, R. Newby, V. Garcia-Sakai, P. Manuel, S. K. Callear, S. I. Campbell, C. C. Tang and M. Schröder, *Nat. Chem.*, 2014, **7**, 121; (c) T. Rodenas, I. Luz, G. Prieto, B. Seoane, H. Miro, A. Corma, F. Kapteijn, F. X. Llabrés i Xamena and J. Gascon, *Nat. Mater.*, 2014, **14**, 48; (d) Z. R. Herm, B. M. Wiers, J. A. Mason, J. M. van Baten, M. R. Hudson, P. Zajdel, C. M. Brown, N. Masciocchi, R. Krishna and J. R. Long, *Science*, 2013, **340**, 960–964; (e) P. Q. Liao, N. Y. Huang, W. X. Zhang, J. P. Zhang and X. M. Chen, *Science*, 2017, **356**, 1193–1196.
- (a) K. Kishida, Y. Okumura, Y. Watanabe, M. Mukoyoshi, S. Bracco, A. Comotti, P. Sozzani, S. Horike and S. Kitagawa, *Angew. Chem., Int. Ed.*, 2016, **55**, 13784–13788; (b) S. Carrasco, *Biosensors*, 2018, **8**, 92; (c) Q. Li, W. Zhang, O. Š. Miljanić, C. H. Sue, Y. L. Zhao, L. Liu, C. B. Knobler, J. F. Stoddart and O. M. Yaghi, *Science*, 2009, **325**, 855–859; (d) A. Chidambaram and K. C. Stylianou, *Inorg. Chem. Front.*, 2018, **5**, 979–998; (e) B. Chen, S. Xiang and G. Qian, *Acc. Chem. Res.*, 2010, **43**, 1115–1124; (f) C. Li, J. Hai, S. Li, B. Wang and Z. Yang, *Nanoscale*, 2018, **10**, 8667–8676.
- (a) M. D. Allendorf, C. A. Bauer, R. K. Bhakta and R. J. T. Houk, *Chem. Soc. Rev.*, 2009, **38**, 1330–1352; (b) Y. C. Chang and S. L. Wang, *J. Am. Chem. Soc.*, 2012, **134**, 9848–9851; (c) B. Chen, Y. Yang, F. Zapata, G. Lin, G. Qian and E. B. Lobkovsky, *Adv. Mater.*, 2007, **19**, 1693–1696; (d) Z. Hu, B. J. Deibert and J. Li, *Chem. Soc. Rev.*, 2014, **43**, 5815–5840; (e) J. H. Jia, Q. W. Li, Y. C. Chen, J. L. Liu and M. L. Tong, *Coord. Chem. Rev.*, 2019, **378**, 365–381; (f) J. Heine and K. Müller-Buschbaum, *Chem. Soc. Rev.*, 2013, **42**, 9232–9242; (g) J. Rocha, L. D. Carlos, F. A. A. Paz and D. Ananias, *Chem. Soc. Rev.*, 2011, **40**, 926–940; (h) X. X. Zhao, S. L. Wang, L. Y. Zhang, S. Y. Liu and G. Z. Yuan, *Inorg. Chem.*, 2019, **58**, 2444–2453.
- (a) J. Lee, O. K. Farha, J. Roberts, K. A. Scheidt, S. T. Nguyen and J. T. Hupp, *Chem. Soc. Rev.*, 2009, **38**, 1450–1459; (b) C. D. Wu, A. Hu, L. Zhang and W. Lin, *J. Am. Chem. Soc.*, 2005, **127**, 8940–8941; (c) J. Liu, L. Chen, H. Cui, J. Zhang, L. Zhang and C. Y. Su, *Chem. Soc. Rev.*, 2014, **43**, 6011–6061; (d) Y. B. Huang, J. Liang, X. S. Wang and R. Cao, *Chem. Soc. Rev.*, 2017, **46**, 126–157; (e) Y. S. Kang, Y. Lu, K. Chen, Y. Zhao, P. Wang and W. Y. Sun, *Coord. Chem. Rev.*, 2019, **378**, 262–280; (f) G. Z. Yuan, H. Jiang, L. Y. Zhang, Y. Liu and Y. Cui, *Coord. Chem. Rev.*, 2019, **378**, 483–499.
- (a) M. Ferbinteanu, F. Cimpoeșu and S. Tanase, in *Lanthanide Metal-Organic Frameworks. Structure and Bonding*, ed. P. Cheng, Springer, Berlin, Heidelberg, 2014, vol. 163; (b) Q. Liu, C. H. Deng and N. Sun, *Nanoscale*, 2018, **10**, 12149–12155; (c) Z. P. Ni, J. L. Liu, M. N. Hoque, W. Liu, J. Y. Li, Y. C. Chen and M. L. Tong, *Coord. Chem. Rev.*, 2017, **335**, 28–43; (d) W. Liu, Y. Y. Peng, S. G. Wu, Y. C. Chen, M. N. Hoque, Z. P. Ni, X. M. Chen and M. L. Tong, *Angew. Chem., Int. Ed.*, 2017, **56**, 14982–14986; (e) Y. N. Wu, M. Zhou, S. Li, Z. Li, J. Li, B. Wu, G. Li, F. Li and X. Guan, *Small*, 2014, **10**, 2927–2936.
- (a) M. X. Wu and Y. W. Yang, *Adv. Mater.*, 2017, **29**, 1606134; (b) G. Chen, S. Huang, X. Kou, S. Wei, S. Huang, S. Jiang, J. Shen, F. Zhu and G. Ouyang, *Angew. Chem., Int. Ed.*, 2019, **58**, 1463–1467; (c) M. Giménez-Marqués, T. Hidalgo, C. Serre and P. Horcajada, *Coord. Chem. Rev.*, 2016, **307**, 342–360.
- (a) R. Batten Stuart, R. Champness Neil, X. M. Chen, J. Garcia-Martinez, S. Kitagawa, L. Öhrström, M. O’Keeffe, M. Paik Suh and J. Reedijk, *Pure Appl. Chem.*, 2013, **85**, 1715–1724; (b) B. Li, H. M. Wen, Y. Cui, W. Zhou, G. Qian and B. Chen, *Adv. Mater.*, 2016, **28**, 8819–8860; (c) H. Furukawa, K. E. Cordova, M. O’Keeffe and O. M. Yaghi, *Science*, 2013, **341**, 1230444.
- (a) Y. M. Zhang, S. Yuan, G. Day, X. Wang, X. Y. Yang and H. C. Zhou, *Coord. Chem. Rev.*, 2018, **354**, 28–45; (b) M. P. Suh, Y. E. Cheon and E. Y. Lee, *Coord. Chem. Rev.*, 2008, **252**, 1007–1026; (c) G. F. Swiegers and T. J. Malefetse, *Chem. Rev.*, 2000, **100**, 3483–3537.
- (a) E. M. Njogu, B. Omondi and V. O. Nyamori, *J. Coord. Chem.*, 2015, **68**, 1–43; (b) A. G. Young and L. R. Hanton,



Hematite enhances microbial autotrophic nitrate removal in carbonate and phosphate-rich environments by increasing Fe(II) activity

Mingliang Long^{a,b}, Jiayi Zhu^{a,b}, Xinxin Wang^{a,b}, Shiwen Hu^b, Juntao Zhang^c, Kuan Cheng^b, Tongxu Liu^b, Wei Liu^{a,*}, John R. Reinfelder^d, Yundang Wu^{b,*}, Fangbai Li^b

^a College of Materials and Energy, South China Agricultural University, Guangzhou 510642, China

^b National-Regional Joint Engineering Research Center for Soil Pollution Control and Remediation in South China, Guangdong Key Laboratory of Integrated Agro-Environmental Pollution Control and Management, Institute of Eco-Environmental and Soil Sciences, Guangdong Academy of Sciences, 808 Tianyuan Road, Guangzhou 510650, China

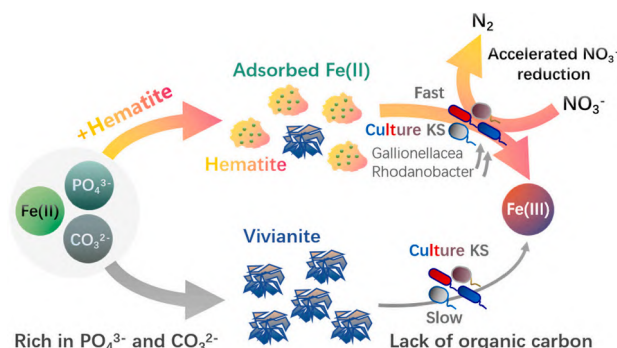
^c Guangzhou Institute of Forestry and Landscape Architecture, 428 Guangyuan Middle Road, Guangzhou 510405, China

^d Department of Environmental Sciences, Rutgers University, New Brunswick, NJ 08901, United States

HIGHLIGHTS

- Hematite enhances the rate of autotrophic nitrate reduction in NRFeOB community.
- The abundance of autotrophic Gallionellaceae and denitrifying Rhodanobacter increases.
- Hematite inhibits the formation of vivianite by maintaining Fe(II) in an adsorbed state.
- The transformation of mineral structure alters Fe(II)'s redox activity.

GRAPHICAL ABSTRACT



ARTICLE INFO

Editor: Baoliang Chen

Keywords:
Culture KS
Hematite
Fe(II) oxidation
Nitrate reduction
Autotrophic

ABSTRACT

Groundwater contamination by nitrates presents significant risks to both human health and the environment. In groundwater characterized as oligotrophic—low in organic carbon, but abundant in carbonate and phosphate—chemolithoautotrophic bacteria, including nitrate-reducing Fe(II)-oxidizing bacteria (NRFeOB), play a vital role in denitrification. The chemoautotrophic nitrate reduction is sensitive to environmental factors, including widespread iron oxides like hematite in nature. However, the specific mechanisms of this influence remain unclear. We examined the mechanism of how hematite impacts autotrophic nitrate reduction in a model NRFeOB community known as culture KS. We found that hematite enhances the rate of autotrophic nitrate reduction by promoting Fe(II) oxidation. Mössbauer spectroscopy detected a significant amount of adsorbed Fe(II) when hematite was present, leading to a reduction in dissolved ferrous iron. In conjunction with XRD data, it can be inferred that the formation of vivianite decreased, thereby increasing the Fe(II) activity in the reaction system. Within the culture KS bacterial consortium, hematite fosters the proliferation of autotrophic microorganisms, specifically Gallionellaceae, and amplifies the presence of denitrifying microbes, notably Rhodanobacter. This

* Corresponding authors.

E-mail addresses: liuwei97@scau.edu.cn (W. Liu), ydwu@soil.gd.cn (Y. Wu).

<https://doi.org/10.1016/j.scitotenv.2024.175002>

Received 26 February 2024; Received in revised form 1 July 2024; Accepted 22 July 2024

Available online 23 July 2024

0048-9697/© 2024 Elsevier B.V. All rights reserved, including those for text and data mining, AI training, and similar technologies.

dual enhancement improves Fe(II) utilization and nitrate reduction capabilities. Our findings highlight intricate interactions between hematite and a model NRFeOB community, offering insights into groundwater nitrate removal mechanisms and the ecological strategies of autotrophic bacteria in mineral-rich environments.

1. Introduction

The presence of nitrates in groundwater poses hazards to both drinking water and the environment (Organization, 2004; Ward et al., 2018). Denitrification is a critical natural process responsible for the removal of nitrate from natural waters (Peng and Zhu, 2006). However, denitrification in groundwater is limited by low concentrations of organic carbon. In oligotrophic ecosystems, chemolithoautotrophic bacteria may alleviate this limitation (Jakus et al., 2021). Indeed, under anoxic conditions and at circumneutral pH, chemolithoautotrophic microbial nitrate reduction, with Fe(II) as the electron donor, is catalyzed by nitrate-reducing Fe(II)-oxidizing bacteria (NRFeOB) (Straub et al., 1996). The chemoautotrophic nitrate reduction is sensitive to environmental factors, therefore, understanding how environmental factors affect the nitrate reduction behavior of NRFeOB is crucial for comprehending the self-purification processes in groundwater.

In the natural environment, the transformation of Fe(II) is influenced by various environmental factors. Geochemical conditions such as pH, the presence of oxyanions, humic matter, carbonate, phosphate and mineralogical nucleation sites have been found to impact the activity of Fe(II) (Cheng et al., 2022; Dippon et al., 2012; Liu et al., 2020). Hematite, a widely distributed iron mineral, often coexists with adsorbed and dissolved ferrous iron, which is available to microorganisms (Khare et al., 2006; Yanina and Rosso, 2008). However, there is a lack of in-depth research on its impact on the iron oxidation and nitrate reduction of the NRFeOB community. Karst regions are rich in carbonates (Tong et al., 2021), and in some areas, they also contain phosphates (Kogovšek, 2011). Due to the deposition of pollutants from distant agricultural, urban, and industrial sources, as well as natural geological processes and the internal nutrient cycling within the lake ecosystems, some oligotrophic lakes in high-altitude areas also exhibit the characteristics of coexistence of nitrogen and phosphorus (Heard and Sickman, 2016). Autotrophic microorganisms are easy to thrive in these environments. Nevertheless, the Fe(II) oxidation process in phosphorus-rich environments remains unexplored and requires clarification. In such environments, the impact of hematite on NRFeO and the underlying mechanisms remain unclear. Previous studies have demonstrated that hematite can adsorb Fe(II) to form highly active Fe(II) surface complexes (Li et al., 2019). Additionally, during the crystallization of dissolved Fe (II), hematite nucleation sites can influence the mineralogy of the iron-bearing precipitates that form (Dippon et al., 2012). Therefore, it can be reasonably hypothesized that, through its influence on the crystal structures of iron carbonates and phosphates, hematite affects the NRFeO process.

The establishment of autotrophic NRFeO microcosms to study their underlying mechanisms is challenging. Although numerous mixotrophic NRFeOB have been well-documented (Bryce et al., 2018; Jamieson et al., 2018), model autotrophic NRFeOB cultures are rare. Culture KS, which was isolated from a freshwater sediment, represents one of the very few examples of an autotrophic NRFeOB culture (Blöthe and Roden, 2009; Tominski et al., 2018a; Tominski et al., 2018b). At neutral pH, the rapid precipitation of iron minerals during NRFeO usually leads to cell encrustation, ultimately leading to cell death (Hedrich et al., 2011; Miot et al., 2011). However, the synergistic cooperation among multiple strains within the microbial communities of culture KS prevents cell encrustation (Nordhoff et al., 2017). Therefore, culture KS exhibits a remarkable ability to achieve autotrophic growth by oxidizing Fe(II) and simultaneously reducing nitrate: $10\text{Fe}^{2+} + 2\text{NO}_3^- + 24\text{H}_2\text{O} = 10\text{Fe}(\text{OH})_3 + \text{N}_2 + 18\text{H}^+$ (Jakus et al., 2021; Song et al., 2022). In addition, culture KS grows by using inorganic carbon for biomass synthesis: 4Fe^{2+}

$+ \text{HCO}_3^- + 10\text{H}_2\text{O} = 4\text{Fe}(\text{OH})_3 + <\text{CH}_2\text{O}> + 7\text{H}^+$ (Beller, 2005; Tominski et al., 2018b). Thus, culture KS has emerged as an ideal model microbial community for in-depth investigations into the mechanisms underlying autotrophic NRFeO processes.

In this study, we used culture KS to investigate the impact of hematite on the NRFeO process in environments rich in carbonates and phosphates. The aims of this study were to (i) elucidate the effects of hematite on the yields and kinetics of autotrophic nitrate reduction; (ii) clarify the influence of hematite on culture KS microbial community; (iii) reveal the mechanisms by which hematite influences the NRFeO process from both chemical and microbiological perspectives. The broader aims of this study are to improve our understanding of nitrate removal in groundwater and the role of natural minerals in the survival of NRFeOB communities.

2. Materials and methods

2.1. Reagents and culture KS information

All chemicals were analytical grade and were purchased from Guangzhou Chemical Co. (China). The Bradford assay kit was purchased from Sangin Biotech (China). The culture KS microbial community was isolated and cultivated by the team of Dr. Andreas Kappler (Tominski et al., 2018a; Tominski et al., 2018b). Our team obtained the bacterial community from Dr. Chao Peng at West China Normal University, originally gifted by Dr. Andreas Kappler. Culture KS is a community composed of various microorganisms such as Gallionellaceae, Burkholderiaceae, and Rhodanobacter. Its abundance can vary with changes in cultivation conditions and time (Huang et al., 2021). In our experiment, the initial community structure of KS is shown in Fig. S1. Detailed incubation medium information of culture KS is provided in Table S1. Hematite (CAS: 1309-37-1) used in this study was purchased from Sigma-Aldrich without purification. The purity of hematite was analyzed by X-ray diffraction (XRD) and the morphology of hematite was characterized by electron microscopy using a JEM 2100 TEM. All XRD peaks matched well those of hematite standards (JCPDS No. 33-0664) (Fig. S2) (Jang et al., 2007). TEM images showed that hematite crystals were short (100 nm) and had a rod-like morphology (Fig. S3), and that no other lattice fringes of Fe minerals were present, indicating that the hematite used in this study was of high purity.

2.2. NRFeOB microcosm experiments

To explore the effects of hematite on microbially mediated NO_3^- -reducing coupled to Fe(II) oxidation, microcosm experiments were conducted. In these microcosms, culture KS was grown in media with Fe (II) and NO_3^- and either without hematite (denoted as Fe(II)- NO_3^-), or with hematite (denoted as Hem-Fe(II)- NO_3^-). The complete recipe of this media is provided in Table S1. Briefly, all microcosm experiments were conducted in 100 mL serum bottles at pH 6.8 under anoxic conditions (with 80 % N_2 and 20 % CO_2 in the head space). The serum bottles contained 50 mL of mixed solutions, including 49 mL freshwater culture medium, 0.5 mL enriched culture KS, 4.5 mM NO_3^- , 5 mM Fe(II), and 4 mg mL^{-1} hematite. The pH was buffered at 6.8 by the addition of 22 mM NaHCO_3 (Blöthe and Roden, 2009; Straub et al., 1996). Phosphorus is a critical element for microorganisms during their growth. Concentration of phosphate is 4.4 mM. The carbonate concentration is 264 mg/L, representing a typical karst groundwater environment. For comparison, two abiotic control experiments, one with sterilized culture KS, Fe(II), and NO_3^- (denoted as Fe(II)- NO_3^- (sterilized)), and another with

sterilized culture KS, hematite, Fe(II), and NO_3^- (denoted as Hem-Fe(II)- NO_3^- (sterilized)), were also incubated under the same conditions. Live microcosms without Fe(II) (Hem- NO_3^- and NO_3^-) were also included. Triplicates microcosms were prepared for each treatment in an anaerobic chamber. Furthermore, we adjusted the NO_3^- concentration to 1 mM to test the kinetics of iron oxidation and nitrate reduction under low nitrate conditions. Except for the nitrate concentration, the other reaction conditions were consistent with the aforementioned experiments.

All serum bottles were crimp-sealed with butyl rubber stoppers, placed on a rotary shaker at 220 rpm in the dark at 28 °C, and sampled at selected times (0, 2, 4, 6, 8, and 11 d). All serum bottles were shaken to ensure that they were well mixed and whole suspension samples from each serum bottle were collected for batch extraction experiments, X-ray diffraction (XRD), and transmission electron microscope (TEM) analyses. Whole suspension samples were immediately filtered through a 0.22 μm nylon filter membrane, and the filtrate was collected for aqueous Fe(II), NO_3^- , NO_2^- , and NH_4^+ analyses. The aqueous Fe(II) in the filtrate was immediately analyzed using the 1,10-phenanthroline method (Hu et al., 2022; Li et al., 2016). To measure NO_3^- , NO_2^- , and NH_4^+ concentrations in the filtrate, we first conducted a pre-treatment to remove Fe(II) (Baethgen and Alley, 2008; Chen et al., 2018). Under the uncovered condition, we agitated the sample to allow Fe(II) to come into contact with air, leading to oxidation and precipitation. Subsequently, we removed Fe(III) by filtering through 0.22 μm nylon membrane filters. The obtained filtrates were used for NO_3^- , NO_2^- , and NH_4^+ quantification. NO_3^- and NO_2^- concentrations in the filtrate were analyzed by ion chromatography (ICS-500, Thermo Fisher Scientific, MA, USA) after acidification (Cheng et al., 2022). NH_4^+ concentrations were measured by a colorimetric method using a mixture of salicylate and nitroprusside (Paul et al., 2007). For N_2O quantification, on days 2, 4, 6, 8, and 11, 5.0 mL of headspace gas was sampled from each serum bottle using gastight syringes, and subsequently transferred into an evacuated gastight tube before whole suspension sample collection. The collected gas was immediately used for N_2O analysis by GC7900 gas chromatograph (Liu et al., 2014).

Furthermore, we have constructed two special treatments for study. One approach taken was to conduct a reaction without solid Fe(II) to investigate the impact of hematite on dissolved Fe(II). In this treatment, solid-phase Fe(II) in the system was filtered in an anaerobic glove box, and only the soluble fraction was utilized as the culture medium for analysis. The second objective was to establish a pre-precipitation reaction system to investigate how important hematite affects the chemical mineralization process of Fe(II). In this special treatment, Fe(II) and hematite were mixed with a culture medium containing carbonate and phosphate, and allowed to pre-precipitate for 48 h to form relatively stable minerals before adding culture KS community.

2.3. Quantification of adsorbed Fe(II) and protein concentrations

In order to quantify the total Fe(II), 0.5 mL of whole suspension was added to a polypropylene centrifuge tube, which contained 2 mL of deoxygenated 1 M HCl (Cheng et al., 2022). Subsequently, the centrifuge tube was placed on a shaker at 220 rpm for 1 h in the anaerobic chamber. Then, the suspension was centrifuged at 6000 rpm for 12 min and filtered through 0.22 μm nylon membrane filters. The Fe(II) concentration in the filtrate was determined by the 1,10-phenanthroline method (Li et al., 2010). Owing to the difficulty of counting cells in the presence of Fe minerals, changes in microbial biomass in the Fe(II)- NO_3^- (the treatment with Fe(II) and NO_3^- but without hematite), Hem-Fe(II)- NO_3^- (the treatment with hematite, Fe(II) and NO_3^-), and Hem- NO_3^- (the treatment with hematite and NO_3^- but without Fe(II)) were quantified as variations in total protein (Liu et al., 2019b; Liu et al., 2018; Zhao et al., 2013). On days 0, 4, 11, 22 and 33, protein was extracted from microcosm solids by centrifuging 10 mL of whole suspension at 8000 rpm for 5 min to remove the supernatant and subsequent addition of 1 mL 0.2 M NaOH. The resuspended pellet was boiled at 105 °C for 10

min to solubilize bacterial protein, and subsequently, the mixture was centrifuged at 8000 rpm for 5 min to obtain a total protein extract in the supernatant (Liu et al., 2019b; Zhao et al., 2013). The total concentration of protein in the supernatant was quantified at 595 nm by the Bradford assay using bovine serum albumin as the standard (Wu et al., 2023).

2.4. Morphology and composition of mineral phases

To characterize the morphology and composition of mineral phases, all samples were analyzed using X-ray diffraction (XRD) and transmission electron microscopy (TEM). For XRD analysis, whole suspension samples collected at 0, 2, 4, and 11 d from the Fe(II)- NO_3^- and Hem-Fe(II)- NO_3^- treatments were centrifuged at 8000g for 10 min and washed five times with deoxygenated deionized water. The wet precipitates were dried in an anaerobic chamber and the collected solid powders were sealed in brown glass vials before XRD analysis. All samples were characterized using a powder X-ray diffractometer (Bruker D8 Advance), equipping with Cu K α radiation and operating at 40 kV and 40 mA (Hu et al., 2022). All data were collected from 10 to 70° 2 θ , and step size and scan speed were set to 0.02° and 2° min⁻¹, respectively (Hu et al., 2021). For mineral TEM analysis, whole suspension samples collected at 11 d from the Fe(II)- NO_3^- and Hem-Fe(II)- NO_3^- treatments were diluted with ethanol and sonicated for 12 min under an N₂ atmosphere to disaggregate cells and mineral particles. Treated samples were dropped onto 3–5 nm thick ultrathin carbon film, supported by lacey formvar on 200 mesh copper TEM double folding grids (Shelobolina et al., 2012). Grids were air-dried for 15 min and stored in an anaerobic chamber before TEM characterization. Selected-area electron diffraction (SAED) was also used to characterize selected samples and analyze the compositions of Fe minerals after 11 days of incubation (Chen et al., 2020). The Mössbauer spectroscopy was conducted at 13 Kelvin utilizing a conventional spectrometer model (Germany, Wissel MS-500). The measurements were taken in a transmission setup, employing a constant acceleration method. A ⁵⁷Co(Rh) radioactive source with a specific activity of 25 mCi was deployed for the experiment. Velocity calibration was executed using an α -Fe absorber at room temperature. The spectral data were subsequently analyzed and fitted with the Recoil software, employing Voigt-based Fitting (VBF) methodology.

2.5. Electrochemical analysis

The redox activity of iron in the Hem-Fe(II)- NO_3^- and Fe(II)- NO_3^- treatments during the reaction was characterized using cyclic voltammetry (CV). CV scans were obtained using an electrochemistry workstation (CHI660D, Chenhua Co. Ltd., Shanghai, China) with a three-electrode system at 28 °C under anoxic conditions (Liu et al., 2020). The workstation was equipped with three electrodes including a calomel reference electrode, a carbon cloth working electrode (2 cm × 2 cm), and a carbon cloth counter electrode (2 cm × 2 cm). During CV analysis, all data were collected over a potential range of -0.8 (vs SCE, versus Saturated Calomel Electrode) to 0.6 V (vs SCE) (Li et al., 2019). To obtain representative data, the scan rate was set to 0.01 V s⁻¹ for CV analysis, and the potential increment, pulse interval, pulse period, and sampling interval were set to 0.005 V, 0.05 V, 0.05 s, 5 s, and 0.0167 s, respectively, for DPV analysis.

2.6. Microbial characterization

The microbial community structure of culture KS was analyzed by high-throughput sequencing of 16 s rDNA. Samples were collected on days 11, 22 and 33, centrifuged at 8000g, and the resulting pellet was subjected to DNA extraction and amplicon sequencing to reveal changes in the microbial community structure. The cell morphology was analyzed by biological TEM (Cheng et al., 2022). Samples are first fixed with a 1 % osmium tetroxide solution. Following fixation, they undergo

a dehydration series with ethanol at concentrations of 30 % to 100 %, and finally with pure acetone. Subsequently, the samples are embedded in epoxy resin and sectioned using an ultramicrotome to produce 70–90 nm thin sections. These sections are stained with lead citrate and a 50 % ethanol saturated solution of uranyl acetate for 5–10 min each. Once dried, the sections are ready for examination under a transmission electron microscope.

3. Results and discussion

3.1. Effect of hematite on nitrate reduction by culture KS

The addition of hematite significantly increased the rate of nitrate reduction by culture KS (Fig. 1a). After 11 days of reaction, the NO_3^- concentration in the Hem-Fe(II)- NO_3^- treatment decreased by 1.42 mM, whereas the reduction of nitrate in the Fe(II)- NO_3^- treatment was only 0.67 mM. NO_3^- concentrations in sterilized controls and controls without Fe(II) (Hem- NO_3^- and NO_3^-) barely changed, confirming that NO_3^- reduction was the result of microbial metabolism and that nitrate reduction by the culture KS community was coupled to Fe(II) oxidation (Huang et al., 2021).

In addition, all treatments showed little to no production of NO_2^- (Fig. 1b), but the generation of N_2O was detected (Fig. 1c). This is consistent with the reported metabolic behavior of culture KS, where NO_2^- may be rapidly metabolized by nitrite reductase within the cells producing N_2O (Huang et al., 2023). The presence of hematite significantly increased the production of N_2O . After 4 days of reaction, the concentration of N_2O in the Hem-Fe(II)- NO_3^- treatment reached 0.21 mM, whereas its concentration was only 0.12 mM in the Fe(II)- NO_3^- treatment. In comparison to the consumption of NO_3^- , N_2O accounts for only a small proportion. According to previous reports, nitrogen (N) is expected to primarily undergo transformation into N_2 (Huang et al., 2021; Tominski et al., 2018b). Additionally, no more NH_4^+ are produced other than those added to the culture medium, which is consistent with the literature indicating that this process does not produce NH_4^+ (Fig. S4) (Huang et al., 2023).

In our microcosms, which initially contained 4.5 mM NO_3^- and 5 mM Fe(II), nitrate was not completely removed over 11 d (Fig. 1a). However, nitrate can be completely reduced by culture KS when the concentration of Fe(II) is higher than that of nitrate, such as in the case where NO_3^- is 1 mM and Fe(II) is 5 mM (Fig. S5). Consistent with Fe: NO_3^- stoichiometry for the production of N_2O (4:1) or N_2 (5:1) coupled to the oxidation of Fe (II), this suggests that, as long as there is enough Fe(II) to provide energy, culture KS can completely remove nitrate from environments lacking organic carbon, but rich in inorganic carbon.

3.2. Effects of hematite on growth and composition of culture KS

The biomass in each system was examined. Total protein was extracted in this study (Fig. 2a). Results showed that hematite significantly increased the biomass of the culture KS, with the total protein in the hematite treatment group being 1.6 times higher than that of the group without hematite at 11 d. Additionally, we tested the growth curves under various hematite addition conditions and found that during the 11-day cultivation period, the rate of microbial growth increased with the rising hematite concentration (Fig. S6). This suggests that hematite has an impact on the survival and reproduction of the microbes in culture KS.

Moreover, to gain insights into how hematite influences the community metabolism of culture KS, we conducted a thorough examination of changes in the community composition within our microcosms. Principal component analysis of beta diversity shows that there were significant differences between treatments with and without hematite (Fig. 2b). Therefore, we further analyzed differences in microbial community structure (Fig. 2c). Previous studies have shown that members of the Gallionellaceae are the dominant autotrophic Fe(II) oxidizers in

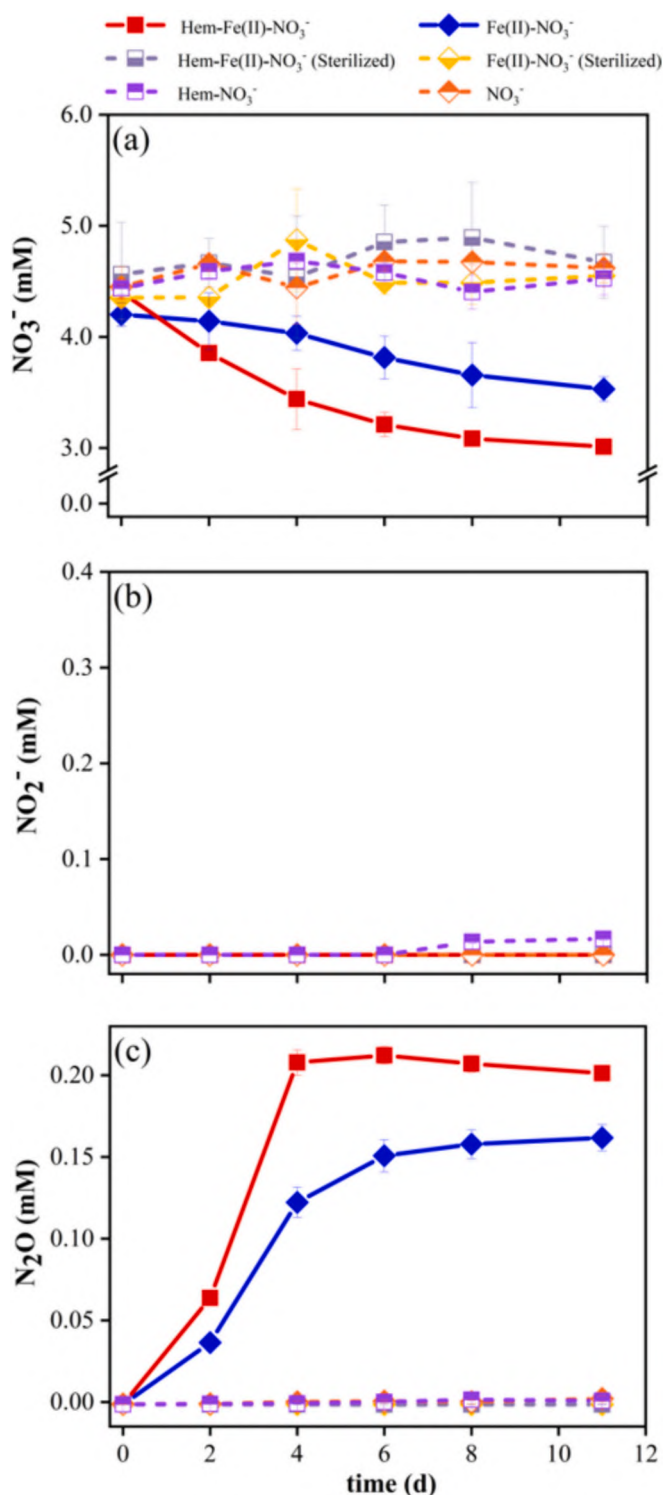


Fig. 1. Time-dependent concentrations of (a) NO_3^- , (b) NO_2^- , and (c) N_2O during culture KS-mediated Fe(II) oxidation and nitrate reduction in microcosms containing 4.5 mM NO_3^- and 5 mM Fe(II) with and without hematite (Hem), and in various controls.

culture KS (He et al., 2016), while Rhodanobacter is the key group of denitrifying bacteria that perform nitrate reduction through interspecies interactions with Gallionellaceae (Huang et al., 2021). The most abundant family of bacteria in both Fe(II) treatments, with or without hematite, was Gallionellaceae, accounting for 47 % and 20 % of bacterial families, respectively. The presence of hematite significantly increased

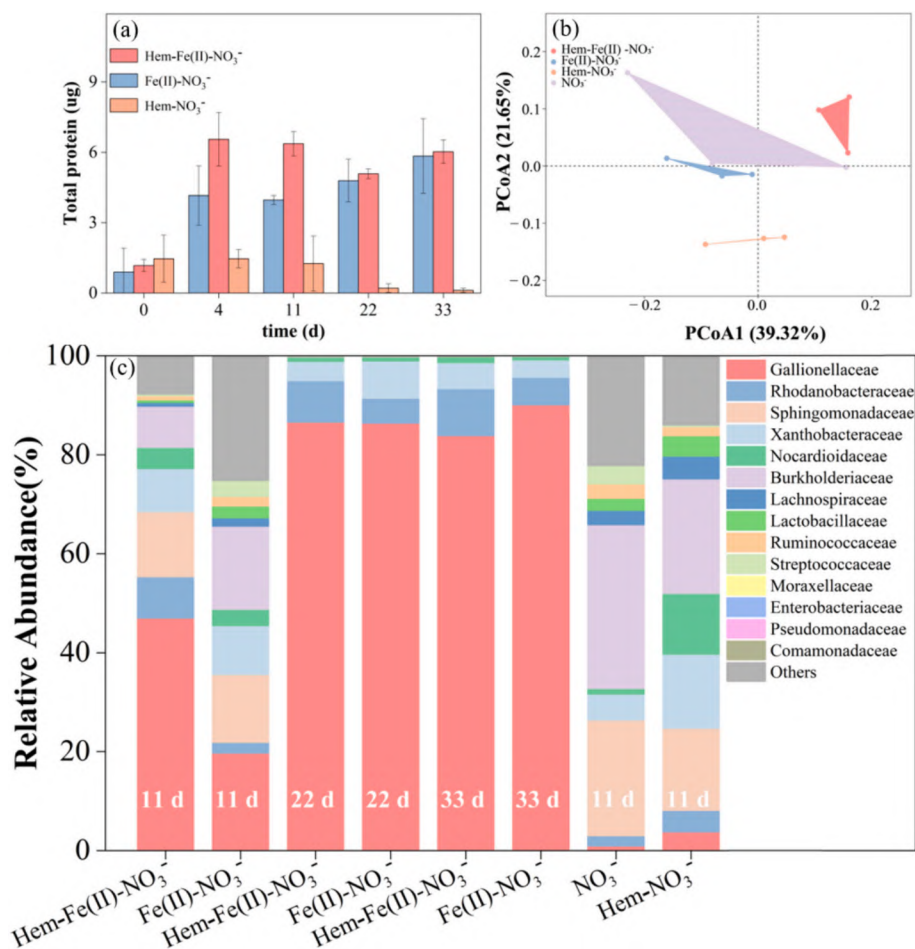


Fig. 2. (a) Total protein during the culture KS mediated the Fe(II) oxidation and nitrite reduction process. Samples were collected on days 0, 4, 11, 22 and 33; (b) principal component analysis (PCA). Samples were collected on day 11; (c) microbial community structure analysis. Samples were collected on days 11, 22 and 33. Samples from the sterile control groups, namely group NO₃⁻ and group Hem-NO₃⁻, were collected on day 11.

the abundance of Gallionellaceae. In addition, the abundance of the family of denitrifying bacteria, Rhodanobacter, also increased from 2.2 % to 8.4 % with the addition of hematite to Fe-oxidizing microcosms. This is probably because organic carbon produced by Fe oxidizing bacteria supported denitrifying bacteria (Huang et al., 2021; Tominski et al., 2018b), which in turn led to an increase in their abundance.

After 11 days, we performed the second and third generation transfers and continued the cultivation. The results from the 22nd and 33rd days indicated that Gallionellaceae had become the dominant population, showing negligible differences in community structure between the treatments (Fig. 2c). Concurrently, on days 22 and 33, we observed no significant difference in protein content between treatments with and without hematite (Fig. 2a). This may be because, after long-term autotrophic transfer cultivation, the changes in the microbial community gradually reached a stable state, thus the impact of hematite on the community gradually weakened. Furthermore, since organic matter in nature may affect the microbial community, we also set up a control experiment with organic acids included. Fig. S7 shows that after adding a small amount of acetate to the above system, the abundance of Gallionellaceae sharply decreased after 11 days, indicating that if organic matter is provided as a carbon source, it will significantly alter the community structure.

3.3. Effect of hematite on Fe(II) oxidation by culture KS

Fe(II) oxidation is the source of energy, thus, effects of hematite on Fe(II) oxidation were examined. On day 0, dissolved Fe(II) only ranged

from 0.26 mM to 0.64 mM across various treatments (Fig. 3a), whereas the HCl-extracted Fe(II) (Chen et al., 2018; Hu et al., 2017) in each treatment was approximately 5 mM (Fig. 3b), indicating that Fe(II) was present mainly as precipitated and adsorbed species. The concentration of dissolved Fe(II) rapidly decreased within 2 days in the absence or presence of hematite and in microbially active and sterile controls (Fig. 3a). This shows that part of the dissolved Fe(II) was removed by abiotic processes. The loss of dissolved Fe(II) may have resulted from reaction with phosphate or carbonate to form precipitates (Blöthe and Roden, 2009; Ehrenreich et al., 1994). Note that since all added Fe(II) was recovered in the HCl extracts, HCl-insoluble Fe(II) minerals did not form during microcosm preparation.

The oxidation rate of HCl-extracted Fe(II), which includes dissolved plus adsorbed Fe(II), was significantly enhanced in the presence of hematite (Fig. 3b). Specifically, by day 4, the treatment with hematite had only 0.87 mM Fe(II)_{HCl} remaining, while the treatment without hematite still had 2.30 mM. This indicates that in the presence of hematite, Fe(II) becomes more accessible for utilization by culture KS. Hematite may have lowered the stability of Fe(II) precipitates, thereby increasing Fe(II) oxidation and nitrate reduction by culture KS. Due to the coupling of iron oxidation with carbon fixation (Tong et al., 2021), it is suggested that changes in iron oxidation may contribute to the promotion of inorganic carbon fixation and the acceleration of bacterial growth (Fig. 2).

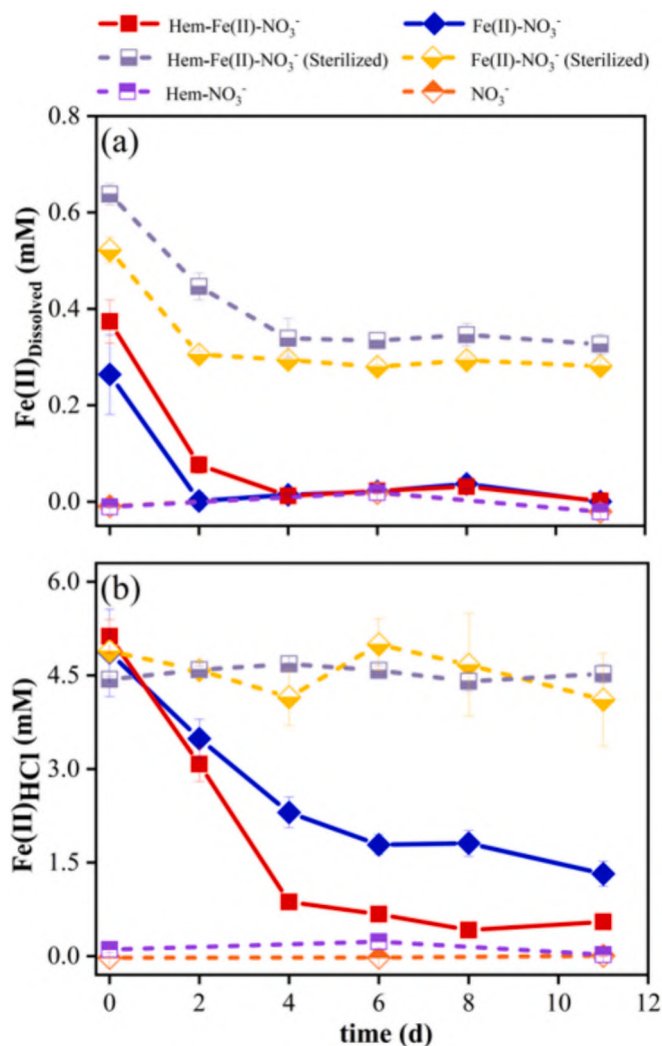


Fig. 3. Time-dependent concentrations of (a) aqueous Fe(II) ($\text{Fe(II)}_{\text{dissolved}}$), and (b) HCl-extracted Fe(II) ($\text{Fe(II)}_{\text{HCl}}$) during culture KS-mediated Fe(II) oxidation and nitrate reduction in microcosms containing 4.5 mM NO_3^- and 5 mM Fe(II) with and without hematite (Hem), and in various controls.

3.4. Mineral transformation during culture KS-mediated Fe(II) oxidation and nitrate reduction

According to SEM results, hematite was present in our microcosms in the form of micrometer-sized particles, consistent with a previous study (Fig. S8) (Liu et al., 2020). In the treatments without hematite, flocculent precipitates with a morphology similar to vivianite (Blöthe and Roden, 2009; Miot et al., 2009a) were observed on day 0 (Fig. 4a). However, such flocculent precipitates were relatively less abundant in treatments with hematite (Fig. 4b).

On day 0 in the treatments with hematite, XRD scans revealed distinctive hematite peaks (Fig. 4c). On the second day of the incubations, a very strong vivianite peak was observed in the group without hematite (Fig. 4c), while it was very weak in the hematite-containing group (Fig. 4d). In addition, it was also observed that hematite delayed the formation of vivianite in the sterile controls (Fig. S9). These observations all suggest that hematite slows down the transformation of dissolved Fe(II) into highly crystalline vivianite. It is reasonable to hypothesize that the suppression of vivianite mineralization by hematite may have had a critical effect on the iron oxidation rate, as previous studies have suggested that vivianite possesses high crystallinity and exceptional stability, making it difficult for culture KS

to utilize (Straub et al., 1996; Tominski et al., 2018a). As the incubations progressed, the peak of vivianite in the non-hematite treatments weakened slightly after 11 days. In contrast, in the hematite treatments, the initially tiny peak of vivianite could not be detected on day 11. Although carbonate was present in the reaction system, siderite was not detected. This may be because, due to the solubility product constant K_{sp} of vivianite being 1.71×10^{-36} , which is significantly lower than that of siderite with a K_{sp} of 1.28×10^{-11} at 25 °C (Al-Borno and Tomson, 1994; Sun, 2006), therefore, under conditions of pH 7.0, 4.4 mM phosphate, and 22 mM carbonate, the formation of vivianite is thermodynamically more favorable over siderite. (Kappler and Newman, 2004; Miot et al., 2009b).

TEM was also employed to further characterize the mineral morphology and structure at day 11 (Fig. 4e-f). In addition to detecting the clear diffraction patterns of vivianite and hematite, a large amount of amorphous oxides was observed (Fig. 4e and f). Based on the sampling time of 11 days and the kinetics of iron oxidation, it can be concluded that most of the Fe(II) in the system has been oxidized to Fe(III). These amorphous oxides could probably represent an amorphous form of ferric phosphate. In addition, bio-TEM revealed that cells of culture KS were not encrusted by iron (Fig. 4g). Previous pure culture studies have shown that during microbial Fe(II) oxidation, the resulting oxidized Fe(III) can encapsulate the microorganisms, forming an iron oxide cell crust and causing their death (Hedrich et al., 2011; Miot et al., 2011; Konhauser et al., 2011). The formed amorphous iron oxides in this study were separated from the cells, which is a key reason why the culture KS bacterial community can proliferate by oxidizing ferrous iron to obtain energy (Shelobolina et al., 2012; Weber et al., 2001). This is also a significant characteristic that distinguishes culture KS from pure cultures of Fe(II)-oxidizing bacteria. Mapping results revealed N and O enrichment in cells, which are the among the primary elements composing cells, while the amorphous iron oxide contained Fe, O, and P, consistent with the elements found in amorphous ferric phosphate (Fig. 4h) (Dippon et al., 2012; Miot et al., 2009b).

Based on the iron oxidation kinetics and XRD data, the variation in ferrous mineralogy during the initial two days of the reaction appears to significantly influence the overall ferrous oxidation activity. To further investigate, we performed Mössbauer spectroscopy on mineral samples treated with hematite (Fig. 5 and Table S2). The spectroscopy results showed a high-intensity hematite sextet peak (Wu et al., 2021) at both day 0 and day 2, which is consistent with the addition of hematite (Fig. 5a and b). After 2 days of reaction, in treatment without hematite, two quadrupole doublets were observed which were assigned to the ferrous sites I and II (Fig. 5c, Table S2). The hyperfine parameters were found to be for Fe_I^{2+} : $\text{IS} = 1.43 \text{ mm}\cdot\text{s}^{-1}$, $\text{QS} = 2.97 \text{ mm}\cdot\text{s}^{-1}$; for Fe_{II}^{2+} : $\text{IS} = 1.36 \text{ mm}\cdot\text{s}^{-1}$, $\text{QS} = 1.68 \text{ mm}\cdot\text{s}^{-1}$. This is consistent with the reported vivianite. However, only one pair of doublet peaks was observed in treatment with hematite (Fig. 5a and b). The peak position is comparable to the peaks of Fe(II) adsorbed on hematite as reported in the literature ($\text{IS} = 1.26 \text{ mm}\cdot\text{s}^{-1}$, $\text{QS} = 2.65 \text{ mm}\cdot\text{s}^{-1}$) (Laresse-Casanova and Scherer, 2007), suggesting substantial adsorption of Fe(II). By the second day of the reaction, the intensity of this peak has weakened, which is consistent with the results of the iron oxidation kinetics (Fig. 3). Given hematite's reported strong adsorptive capacity for Fe(II), and the substantial impact of Fe(II) adsorption on its behavior as documented (Friedrich et al., 2015), the increased adsorbed Fe(II) likely increases the reactivity of dissolved Fe(II) in the system. Additionally, an increase in adsorbed Fe(II) leads to a decrease in dissolved Fe(II), thereby probably reducing the transformation of dissolved ferrous iron into vivianite. Furthermore, on day 2, a doublet corresponding to ferric phosphate was detected (Okada et al., 2005), indicating that the predominant amorphous Fe(III) species formed is iron phosphate. This is also consistent with the results identified by X-ray absorption near edge structure (XANES) in previous reports (Miot et al., 2009a).

The results above confirm that in a system where Fe(II) is present with phosphates and carbonates, hematite mitigates the formation of

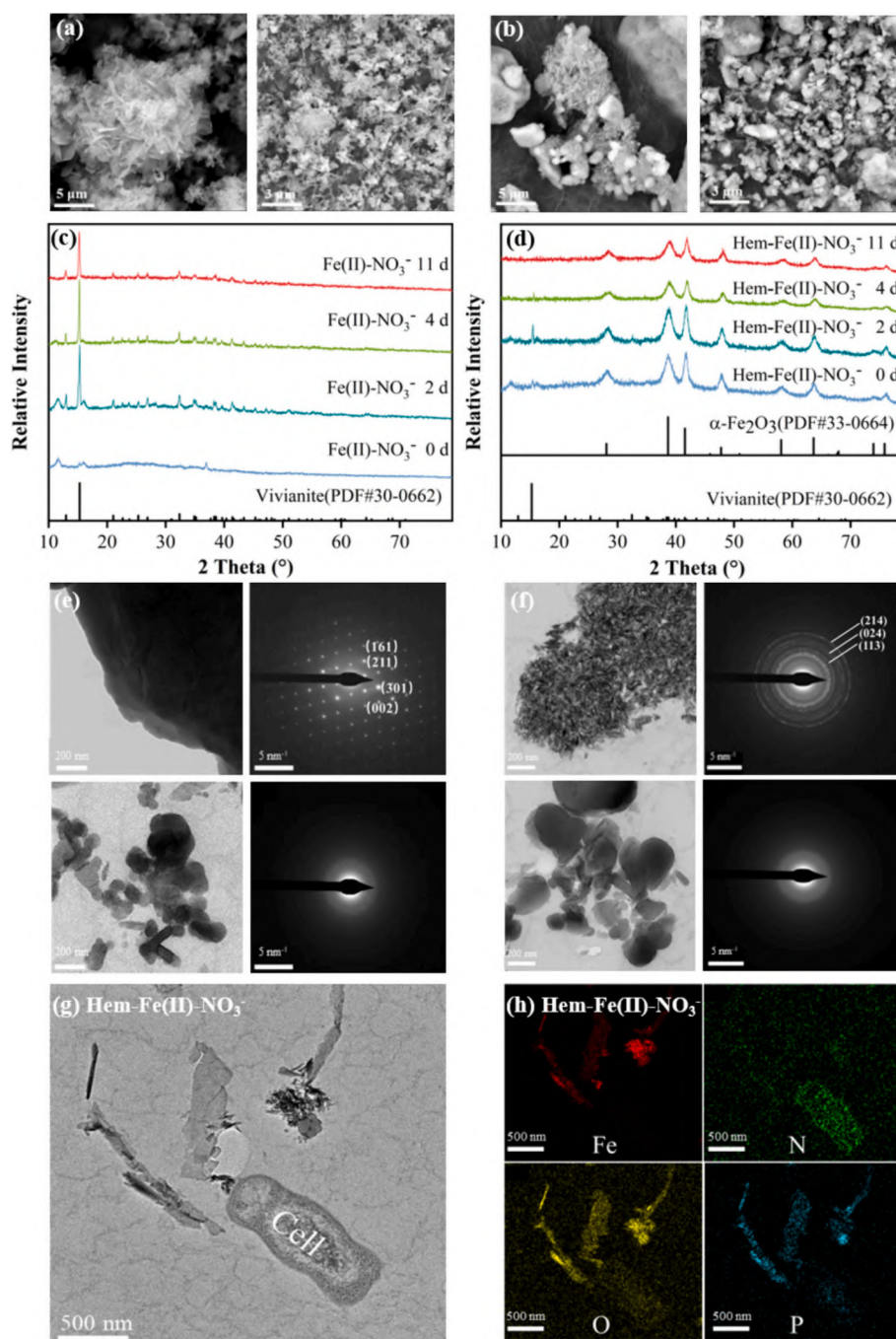


Fig. 4. Morphology and identification of minerals formed during culture KS-mediated Fe(II) oxidation and nitrate reduction in microcosms without (a,c,e) and with (b,d,f,g,h) hematite (Hem). (a-b) SEM morphology; (c-d) XRD characterization; (e-f) TEM imaging and SAED analysis; (g-h) Bio-TEM and element mapping of the iron oxides and a microorganism. TEM samples were collected after 11 days of incubation. XRD samples were collected on day 0, 2, 4, and 11.

vivianite by adsorbing dissolved ferrous iron. Since the adsorbed Fe(II) demonstrates high reactivity (Liu et al., 2020), the increase in adsorbed Fe(II) and decrease of vivianite is likely a critical factor enhancing Fe(II) oxidation by culture KS.

3.5. Effect of hematite on the Fe(II) activity

To further investigate the effect of hematite on changes in Fe(II) redox activity, we implanted electrodes into a separate set of identical microcosms (see Fig. S10) and recorded cyclic voltammetry (CV) scans at various times (Fig. 6). The results show that on day 0, strong redox peaks appeared in both treatments with and without hematite, which

were attributed to the redox peaks of Fe(II). However, the peak intensity in the treatment with hematite was substantially higher than that in the treatment without hematite, indicating a higher concentration of active Fe(II) in the Hem-Fe(II)-NO₃⁻ treatment (Fig. 6a). As time passed (Fig. 6b-c), the peak intensity of Fe(II) in the system with hematite decreased sharply, indicating that active Fe(II) was rapidly consumed, while the peak in the system without hematite decreased slowly, which is consistent with the oxidation kinetics of Fe(II) shown in Fig. 3. By day 11, there were no obvious redox peaks in either treatment (Fig. 6d). Although some adsorbed Fe(II) remained on day 11 (Fig. 3a), its oxidation rate had become very slow, indicating that it may have been present in an inactive form.

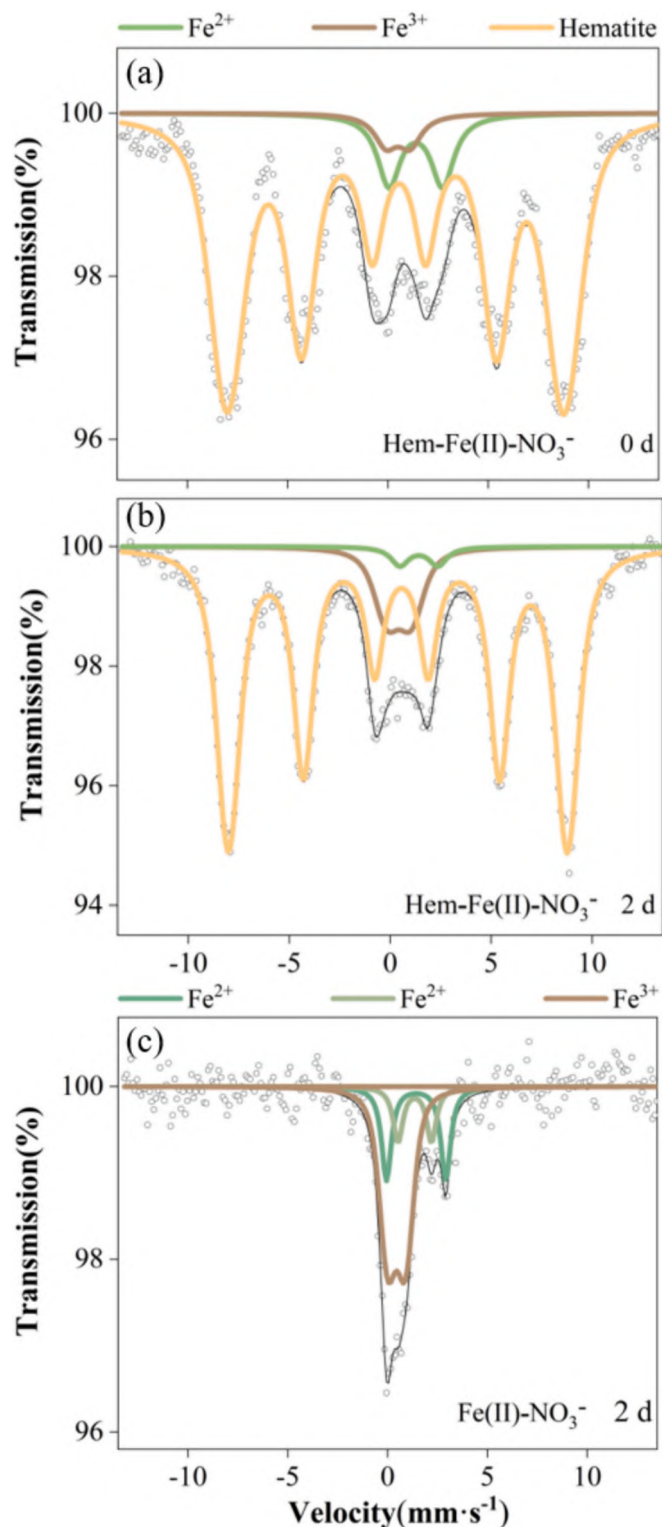


Fig. 5. Morphology and identification of minerals formed during culture KS-mediated Fe(II). (a) Hem-Fe(II)-NO₃⁻, day 0 sample; (b) Hem-Fe(II)-NO₃⁻, day 2 sample; (c) Fe(II)-NO₃⁻, day 2 sample.

To further determine which aspect of ferrous activity hematite enhances – whether it increases the activity of soluble ferrous or the solid-phase ferrous as analyzed above – we conducted two specially treated kinetic experiments. In the first special treatment, solid-phase Fe(II) in the system was filtered in an anaerobic glove box, and only the soluble fraction was utilized as the culture medium for analysis. Fig. S11a shows

that the remaining initial Fe(II) is approximately 4.5 mM. Results in Fig. S11a and b indicated that the promoting effect of hematite on the kinetics of Fe(II) oxidation and nitrate reduction was not significant in the presence of only dissolved Fe(II). Previous studies have shown that dissolved Fe(II) can be adsorbed onto hematite (Tai and Dempsey, 2009). Although adsorption occurred in the system, the reaction activity did not decrease, implies that adsorbed Fe(II) on hematite remains in a highly active form (Gorski et al., 2016; Stewart et al., 2018). In the second special treatment, Fe(II) and hematite were mixed with a culture medium containing carbonate and phosphate, and allowed to pre-precipitate for 48 h to form relatively stable minerals before adding culture KS community. The results of this treatment are presented in Fig. S11c and d. The residual concentrations of Fe(II)_{HCl} is 1.95 and 0.53 mM in the groups with and without hematite at day 11. Compared to the unprecipitated group in Fig. 2a, the rate of Fe(II) oxidation decreased. This is probably because, after 48 h of precipitation, the ferrous formed, with more vivianite, is more stable compared to that without precipitation (Xiong et al., 2023). However, the addition of hematite still increased the rates of Fe(II) oxidation and nitrate reduction in the pre-precipitated group, as hematite reduced the formation of vivianite (Fig. S11c and d). These data are consistent with the speculation from XRD data (Fig. 4), confirming that the alteration in solid-phase ferrous activity is crucial for hematite's influence on Fe(II) oxidation in culture KS.

3.6. Underlying mechanism and environmental implication

As shown in previous studies, the reduction of nitrate by NRFeO occurs primarily through direct enzymatic catalysis by NRFeOB (He et al., 2017; Klueglein and Kappler, 2012; Liu et al., 2019a) and abiotic reaction between Fe(II) and NO₂⁻ (Benz et al., 1998; Kappler et al., 2005; Muehe et al., 2009). Both of these processes are significantly influenced by the Fe(II) activity. Hence, the activity of Fe(II) plays a critical role in nitrate reduction by autotrophic microorganisms.

Our results show that greater redox activity of Fe(II) in the presence of hematite is attributed to the formation of highly reactive adsorbed Fe(II) species, as well as leading to a decrease in vivianite formation. In addition to the environment studied in this work, this study also reveals to some extent a universal mechanism: due to hematite's adsorption of Fe(II), the concentration of dissolved ferrous iron may be reduced, thereby decreasing the formation of iron minerals and enhancing microbial-mediated iron oxidation. The addition of hematite increases the supply of electrons from Fe(II) for autotrophic microorganisms, which convert inorganic carbon into biomass. Some of the newly produced organic carbon may then support the anaerobic respiration of denitrifying bacteria, which catalyze the conversion of nitrate to N₂O or N₂. As we observed in the culture KS bacterial community, hematite is expected to promote the growth of Fe(II) oxidizing autotrophs, such as members of the Gallionellaceae, and increase the abundance of denitrifying microorganisms, such as those in the Rhodanobacter family. Thus, as long as a sufficient amount of available Fe(II) is present, nitrate can be continuously reduced. In oligotrophic ecosystems, such as groundwater that is low in organic matter, hematite may enhance autotrophic iron(II) oxidation, which in turn plays a role in the reduction and removal of nitrate.

CRedit authorship contribution statement

Mingliang Long: Writing – original draft, Investigation, Data curation. **Jiayi Zhu:** Data curation, Investigation. **Xinxin Wang:** Writing – review & editing, Validation. **Shiwen Hu:** Methodology, Conceptualization. **Juntao Zhang:** Data curation, Investigation. **Kuan Cheng:** Methodology. **Tongxu Liu:** Funding acquisition, Conceptualization. **Wei Liu:** Writing – review & editing, Writing – original draft, Methodology, Investigation. **John R. Reinfelder:** Writing – review & editing. **Yundang Wu:** Writing – review & editing, Writing – original draft,

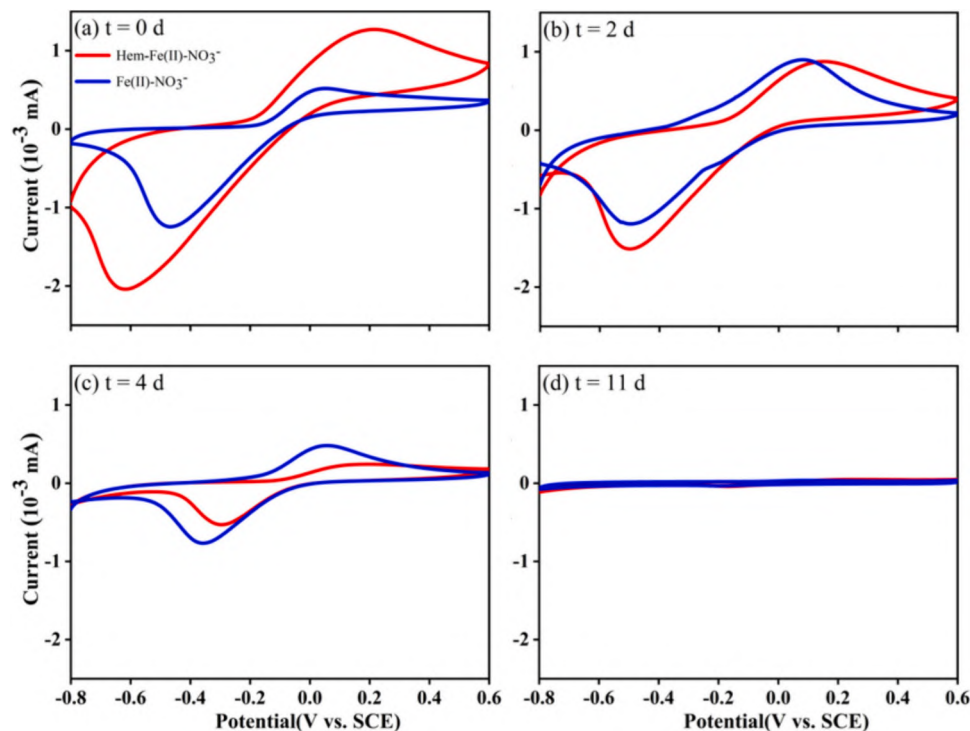


Fig. 6. CV characterization of the Fe(II)-NO₃⁻ and Hem-Fe(II)-NO₃⁻ treatments on (a) day 0, (b) day 2, (c) day 4, and (d) day 11 during culture KS-mediated Fe(II) oxidation and nitrite reduction.

Conceptualization. Fangbai Li: Writing – review & editing, Resources, Funding acquisition, Conceptualization.

Declaration of competing interest

The authors declare that they have no known competing financial interests or personal relationships that could have appeared to influence the work reported in this paper.

Data availability

The data proving the results of this study are available within the paper and related Supporting information.

Acknowledgments

This work was funded by the National Natural Science Foundation of China (42077020, 42377315 and 42077354), Guangdong Basic and Applied Basic Research Foundation (2024A1515010293), the National Key Research and Development Program (2023YFD1902100), the GDAS' Project of Science and Technology Development (2023GDASQNR-0202), the open competition program of top ten critical priorities of Agricultural Science and Technology Innovation for the 14th Five-Year Plan of Guangdong Province (2022SDZG09), the Chemical Synthesis and Pollution Control Key Laboratory of Sichuan Province (CSPC202307), and SAFEA: High-End Foreign Experts Project (G2023030071L); Guangdong Province Science and Technology Special Fund Project in Shaoguan City (220716096270196, 230225176275072); Agricultural and Social Development Project of Guangzhou Municipal Science and Technology Bureau (202206010058); Youth S&T Talent Support Program of Guangdong Provincial Association for Science and Technology (SKXRC202410).

Declaration of generative AI and AI-assisted technologies in the writing process

During the preparation of this work the authors used Chat GPT in order to check for grammatical errors. After using this tool, the authors reviewed and edited the content as needed and take full responsibility for the content of the publication.

Appendix A. Supplementary data

Supplementary data to this article can be found online at <https://doi.org/10.1016/j.scitotenv.2024.175002>.

References

- Al-Borno, A., Tomson, M.B., 1994. The temperature dependence of the solubility product constant of vivianite. *Geochim. Acta* 58 (24), 5373–5378. [https://doi.org/10.1016/0016-7037\(94\)90236-4](https://doi.org/10.1016/0016-7037(94)90236-4).
- Baethgen, W.E., Alley, M.M., 2008. A manual colorimetric procedure for measuring ammonium nitrogen in soil and plant Kjeldahl digests. *Commun. Soil Sci. Plant Anal.* 20 (9–10), 961–969. <https://doi.org/10.1080/00103628909368129>.
- Beller, H.R., 2005. Anaerobic, nitrate-dependent oxidation of U(IV) oxide minerals by the chemolithoautotrophic bacterium *Thiobacillus denitrificans*. *Appl. Environ. Microbiol.* 71 (4), 2170–2174. <https://doi.org/10.1128/AEM.71.4.2170-2174.2005>.
- Benz, M., Brune, A., Schink, B., 1998. Anaerobic and aerobic oxidation of ferrous iron at neutral pH by chemoheterotrophic nitrate-reducing bacteria. *Arch. Microbiol.* 169, 159–165. <https://doi.org/10.1007/s002030050555>.
- Blöthe, M., Roden, E.E., 2009. Composition and activity of an autotrophic Fe(II)-oxidizing, nitrate-reducing enrichment culture. *Appl. Environ. Microbiol.* 75 (21), 6937–6940. <https://doi.org/10.1128/aem.01742-09>.
- Bryce, C., Blackwell, N., Schmidt, C., Otte, J., Huang, Y.M., Kleindienst, S., Tomaszewski, E., Schad, M., Warter, V., Peng, C., Byrne, J.M., Kappler, A., 2018. Microbial anaerobic Fe(II) oxidation-ecology, mechanisms and environmental implications. *Environ. Microbiol.* 20 (10), 3462–3483. <https://doi.org/10.1111/1462-2920.14328>.
- Chen, D., Liu, T., Li, X., Li, F., Luo, X., Wu, Y., Wang, Y., 2018. Biological and chemical processes of microbially mediated nitrate-reducing Fe(II) oxidation by *Pseudogulbenkiania* sp. strain 2002. *Chem. Geol.* 476, 59–69. <https://doi.org/10.1016/j.chemgeo.2017.11.004>.
- Chen, D., Yuan, X., Zhao, W., Luo, X., Li, F., Liu, T., 2020. Chemodenitrification by Fe(II) and nitrite: pH effect, mineralization and kinetic modeling. *Chem. Geol.* 541 <https://doi.org/10.1016/j.chemgeo.2020.119586>.

- Cheng, K., Li, H., Yuan, X., Yin, Y., Chen, D., Wang, Y., Li, X., Chen, G., Li, F., Peng, C., Wu, Y., Liu, T., 2022. Hematite-promoted nitrate-reducing Fe(II) oxidation by *Acidovorax* sp. strain BoFeN1: roles of mineral catalysis and cell encrustation. *Geobiology* 20 (6), 810–822. <https://doi.org/10.1111/gbi.12510>.
- Dippon, U., Pantke, C., Porsch, K., Larese-Casanova, P., Kappler, A., 2012. Potential function of added minerals as nucleation sites and effect of humic substances on mineral formation by the nitrate-reducing Fe(II)-oxidizer *Acidovorax* sp. BoFeN1. *Environ. Sci. Technol.* 46 (12), 6556–6565. <https://doi.org/10.1021/es2046266>.
- Ehrenreich, A., Widdel, F.J.A., microbiology, e., 1994. Anaerobic oxidation of ferrous iron by purple bacteria, a new type of phototrophic metabolism. *Appl. Environ. Microbiol.* 60 (12), 4517–4526. <https://doi.org/10.1128/aem.60.12.4517-4526.1994>.
- Friedrich, A.J., Helgeson, M., Liu, C., Wang, C., Rosso, K.M., Scherer, M.M., 2015. Iron atom exchange between hematite and aqueous Fe. *Environ. Sci. Technol.* 49 (14), 8479–8486. <https://doi.org/10.1021/acs.est.5b01276>.
- Gorski, C.A., Edwards, R., Sander, M., Hofstetter, T.B., Stewart, S.M., 2016. Thermodynamic characterization of iron(II) oxide–aqueous Fe²⁺ redox couples. *Environ. Sci. Technol.* 50 (16), 8538–8547. <https://doi.org/10.1021/acs.est.6b02661>.
- He, S., Tominski, C., Kappler, A., Behrens, S., Roden, E.E., Voordouw, G., 2016. Metagenomic analyses of the autotrophic Fe(II)-oxidizing, nitrate-reducing enrichment culture KS. *Appl. Environ. Microbiol.* 82 (9), 2656–2668. <https://doi.org/10.1128/aem.03493-15>.
- He, S., Barco, R.A., Emerson, D., Roden, E.E., 2017. Comparative genomic analysis of neutrophilic iron(II) oxidizer genomes for candidate genes in extracellular electron transfer. *Front. Microbiol.* 8, 1584. <https://doi.org/10.3389/fmicb.2017.01584>.
- Heard, A.M., Sickman, J.O., 2016. Nitrogen assessment points: development and application to high-elevation lakes in the Sierra Nevada, California. *Ecosphere* 7 (11). <https://doi.org/10.1002/ecs2.1586>.
- Hedrich, S., Schlömann, M., Johnson, D.B., 2011. The iron-oxidizing proteobacteria. *Microbiology* 157 (6), 1551–1564. <https://doi.org/10.1099/mic.0.045344-0>.
- Hu, M., Chen, P., Sun, W., Li, F., Cui, J., 2017. A novel organotrophic nitrate-reducing Fe (II)-oxidizing bacterium isolated from paddy soil and draft genome sequencing indicate its metabolic versatility. *RSC Adv.* 7 (89), 56611–56620. <https://doi.org/10.1039/c7ra09328d>.
- Hu, S., Li, H., Wang, P., Liu, C., Shi, Z., Li, F., Liu, T., 2021. Interfacial photoreactions of Cr(VI) and oxalate on lepidocrocite surface under oxic and acidic conditions: reaction mechanism and potential implications for contaminant degradation in surface waters. *Chem. Geol.* 583, 120481. <https://doi.org/10.1016/j.chemgeo.2021.120481>.
- Hu, S., Liu, T., Zheng, L., Wang, P., Yang, Y., Li, F., Shi, Z., Liu, C., Li, H., 2022. Arsenate sequestration by secondary minerals from chemodenitrification of Fe(II) and nitrite: pH effect and mechanistic insight. *Geochim. Cosmochim. Acta* 336, 62–77. <https://doi.org/10.1016/j.gca.2022.09.008>.
- Huang, Y.-M., Straub, D., Blackwell, N., Kappler, A., Kleindienst, S., Semrau, J.D., 2021. Meta-omics reveal *Gallionellaceae* and *Rhodanobacter* species as interdependent key players for Fe(II) oxidation and nitrate reduction in the autotrophic enrichment culture KS. *Appl. Environ. Microbiol.* 87 (15). <https://doi.org/10.1128/aem.00496-21>.
- Huang, J., Mellage, A., Garcia, J.P., Glöckler, D., Mahler, S., Elsner, M., Jakus, N., Mansor, M., Jiang, H., Kappler, A.J.A., Microbiology, E., 2023. Metabolic Performance and Fate of Electrons During Nitrate-reducing Fe(II) Oxidation by the Autotrophic Enrichment Culture KS Grown at Different Initial Fe/N Ratios, 89(3). <https://doi.org/10.1128/aem.00196-23> e00196-23.
- Jakus, N., Blackwell, N., Osenbrück, K., Straub, D., Byrne, J.M., Wang, Z., Glöckler, D., Elsner, M., Lueders, T., Grathwohl, P., Kleindienst, S., Kappler, A., Stams, A.J.M., 2021. Nitrate removal by a novel lithoautotrophic nitrate-reducing, iron(II)-oxidizing culture enriched from a pyrite-rich limestone aquifer. *Appl. Environ. Microbiol.* 87 (16). <https://doi.org/10.1128/aem.00460-21>.
- Jamieson, J., Prommer, H., Kaksonen, A.H., Sun, J., Siade, A.J., Yusov, A., Bostick, B., 2018. Identifying and quantifying the intermediate processes during nitrate-dependent iron(II) oxidation. *Environ. Sci. Technol.* 52 (10), 5771–5781. <https://doi.org/10.1021/acs.est.8b01122>.
- Jang, J.-H., Dempsey, B.A., Burgos, W.D., 2007. Solubility of hematite revisited: effects of hydration. *Environ. Sci. Technol.* 41 (21), 7303–7308. <https://doi.org/10.1021/es070535t> (technology).
- Kappler, A., Newman, D.K., 2004. Formation of Fe(III)-minerals by Fe(II)-oxidizing photoautotrophic bacteria. *Geochim. Cosmochim. Acta* 68 (6), 1217–1226. <https://doi.org/10.1016/j.gca.2003.09.006>.
- Kappler, A., Schink, B., Newman, D.K., 2005. Fe (III) mineral formation and cell encrustation by the nitrate-dependent Fe (II)-oxidizer strain BoFeN1. *Geobiology* 3 (4), 235–245. <https://doi.org/10.1111/j.1472-4669.2006.00056.x>.
- Khare, N., Eggleston, C.M., Lovelace, D.M., Boese, S.W., 2006. Structural and redox properties of mitochondrial cytochrome c co-sorbed with phosphate on hematite (α-Fe₂O₃) surfaces. *J. Colloid Interface Sci.* 303 (2), 404–414. <https://doi.org/10.1016/j.jcis.2006.07.070>.
- Klueglein, N., Kappler, A., 2012. Abiotic oxidation of Fe(II) by reactive nitrogen species in cultures of the nitrate-reducing Fe(II) oxidizer *Acidovorax* sp. BoFeN1-questioning the existence of enzymatic Fe(II) oxidation. *Geobiology* 11 (2), 180–190. <https://doi.org/10.1111/gbi.12019>.
- Kogovšek, J., 2011. Impact of chlorides, nitrates, sulfates and phosphates on increased limestone dissolution in the karst vadose zone (Postojna Cave, Slovenia). *Acta Carsologica* 40 (2), 319–327. <https://doi.org/10.3986/ac.v40i2.16>.
- Konhauser, K.O., Kappler, A., Roden, E., 2011. Iron in microbial metabolisms. *Elements* 7 (2), 89–93. <https://doi.org/10.2113/gselements.7.2.89>.
- Larese-Casanova, P., Scherer, M.M., 2007. Fe (II) sorption on hematite: new insights based on spectroscopic measurements. *Environ. Sci. Technol.* 41 (2), 471–477. <https://doi.org/10.1021/es0617035>.
- Li, F.B., Li, X.M., Zhou, S.G., Zhuang, L., Cao, F., Huang, D.Y., Xu, W., Liu, T.X., Peng, C.H., 2010. Enhanced reductive dechlorination of DDT in an anaerobic system of dissimilatory iron-reducing bacteria and iron oxide. *Environ. Pollut.* 158 (5), 1733–1740. <https://doi.org/10.1016/j.envpol.2009.11.020>.
- Li, X., Zhang, W., Liu, T., Chen, L., Chen, P., Li, F., 2016. Changes in the composition and diversity of microbial communities during anaerobic nitrate reduction and Fe(II) oxidation at circumneutral pH in paddy soil. *Soil Biol. Biochem.* 94, 70–79. <https://doi.org/10.1016/j.soilbio.2015.11.013>.
- Li, X., Liu, L., Wu, Y., Liu, T., Chemistry, S., 2019. Determination of the redox potentials of solution and solid surface of Fe (II) associated with iron oxyhydroxides. *ACS Earth Space Chem.* 3 (5), 711–717. <https://doi.org/10.1021/acsearthspacechem.9b00001>.
- Liu, T., Li, X., Zhang, W., Hu, M., Li, F., 2014. Fe(III) oxides accelerate microbial nitrate reduction and electricity generation by *Klebsiella pneumoniae* L17. *J. Colloid Interface Sci.* 423, 25–32. <https://doi.org/10.1016/j.jcis.2014.02.026>.
- Liu, Y., Feng, C., Sheng, Y., Dong, S., Chen, N., Hao, C., 2018. Effect of Fe(II) on reactivity of heterotrophic denitrifiers in the remediation of nitrate- and Fe(II)-contaminated groundwater. *Ecotoxicol. Environ. Saf.* 166, 437–445. <https://doi.org/10.1016/j.ecoenv.2018.09.104>.
- Liu, T., Chen, D., Luo, X., Li, X., Li, F., 2019a. Microbially mediated nitrate-reducing Fe (II) oxidation: quantification of chemodenitrification and biological reactions. *Geochim. Cosmochim. Acta* 256, 97–115. <https://doi.org/10.1016/j.gca.2018.06.040>.
- Liu, W., Wu, Y., Liu, T., Li, F., Dong, H., Jing, M., 2019b. Influence of incubation temperature on 9,10-anthraquinone-2-sulfonate (AQS)-mediated extracellular electron transfer. *Front. Microbiol.* 10, 464. <https://doi.org/10.3389/fmicb.2019.00464>.
- Liu, T., Wang, Y., Liu, C., Li, X., Cheng, K., Wu, Y., Fang, L., Li, F., Liu, C., 2020. Conduction band of hematite can mediate cytochrome reduction by Fe(II) under dark and anoxic conditions. *Environ. Sci. Technol.* 54 (8), 4810–4819. <https://doi.org/10.1021/acs.est.9b06141>.
- Miot, J., Benzerara, K., Morin, G., Bernard, S., Beyssac, O., Larquet, E., Kappler, A., Guyot, F., 2009a. Transformation of vivianite by anaerobic nitrate-reducing iron-oxidizing bacteria. *Geobiology* 7 (3), 373–384. <https://doi.org/10.1111/j.1472-4669.2009.00203.x>.
- Miot, J., Benzerara, K., Morin, G., Kappler, A., Bernard, S., Obst, M., Féraud, C., Skouri-Panet, F., Guigner, J.-M., Posth, N., Galvez, M., Brown, G.E., Guyot, F., 2009b. Iron biomineralization by anaerobic neutrophilic iron-oxidizing bacteria. *Geochim. Cosmochim. Acta* 73 (3), 696–711. <https://doi.org/10.1016/j.gca.2008.10.033>.
- Miot, J., MacLellan, K., Benzerara, K., Boisset, N., 2011. Preservation of protein globules and peptidoglycan in the mineralized cell wall of nitrate-reducing, iron(II)-oxidizing bacteria: a cryo-electron microscopy study. *Geobiology* 9 (6), 459–470. <https://doi.org/10.1111/j.1472-4669.2011.00298.x>.
- Muehe, E.M., Gerhardt, S., Schink, B., Kappler, A., 2009. Ecophysiology and the energetic benefit of mixotrophic Fe(II) oxidation by various strains of nitrate-reducing bacteria. *FEMS Microbiol. Ecol.* 70 (3), 335–343. <https://doi.org/10.1111/j.1574-6941.2009.00755.x>.
- Nordhoff, M., Tominski, C., Halama, M., Byrne, J., Obst, M., Kleindienst, S., Behrens, S., Kappler, A., 2017. Insights into nitrate-reducing Fe (II) oxidation mechanisms through analysis of cell-mineral associations, cell encrustation, and mineralogy in the chemolithoautotrophic enrichment culture KS. *Appl. Environ. Microbiol.* 83 (13), e00752-17. <https://doi.org/10.1128/AEM.00752-17>.
- Okada, S., Yamamoto, T., Okazaki, Y., Yamaki, J.-i., Tokunaga, M., Nishida, T., 2005. Cathode properties of amorphous and crystalline FePO₄. *J. Power Sources* 146 (1–2), 570–574. <https://doi.org/10.1016/j.jpowsour.2005.03.200>.
- Organization, W.H., 2004. *Guidelines for Drinking-Water Quality*. World Health Organization.
- Paul, T., Miller, P.L., Strathmann, T.J., 2007. Visible-light-mediated TiO₂ photocatalysis of fluoroquinolone antibacterial agents. *Environ. Sci. Technol.* 41 (13), 4720–4727. <https://doi.org/10.1021/es070097q>.
- Peng, Y., Zhu, G., 2006. Biological nitrogen removal with nitrification and denitrification via nitrite pathway. *Appl. Microbiol. Biotechnol.* 73 (1), 15–26. <https://doi.org/10.1007/s00253-006-0534-z>.
- Shelobolina, E., Xu, H., Konishi, H., Kukkadapu, R., Wu, T., Blöthe, M., Roden, E., 2012. Microbial lithotrophic oxidation of structural Fe(II) in biotite. *Appl. Environ. Microbiol.* 78 (16), 5746–5752. <https://doi.org/10.1128/aem.01034-12>.
- Song, X., Wang, P., Van Zwieten, L., Bolan, N., Wang, H., Li, X., Cheng, K., Yang, Y., Wang, M., Liu, T., Li, F., 2022. Towards a better understanding of the role of Fe cycling in soil for carbon stabilization and degradation. *Carbon Res.* 1 (1). <https://doi.org/10.1007/s44246-022-00008-2>.
- Stewart, S.M., Hofstetter, T.B., Joshi, P., Gorski, C.A., 2018. Linking thermodynamics to pollutant reduction kinetics by Fe²⁺ bound to iron oxides. *Environ. Sci. Technol.* 52 (10), 5600–5609. <https://doi.org/10.1021/acs.est.8b00481>.
- Straub, K.L., Benz, M., Schink, B., Widdel, F., 1996. Anaerobic, nitrate-dependent microbial oxidation of ferrous iron. *Appl. Environ. Microbiol.* 62 (4), 1458–1460. <https://doi.org/10.1128/aem.62.4.1458-1460.1996>.
- Sun, W., 2006. *Kinetics of Iron Carbonate and Iron Sulfide Scale Formation in CO₂/H₂S Corrosion*. Diss. Ohio University.
- Tai, Y.-L., Dempsey, B.A., 2009. Nitrite reduction with hydrous ferric oxide and Fe(II): stoichiometry, rate, and mechanism. *Water Res.* 43 (2), 546–552. <https://doi.org/10.1016/j.watres.2008.10.055>.
- Tominski, C., Heyer, H., Lösekann-Behrens, T., Behrens, S., Kappler, A., 2018a. Growth and population dynamics of the anaerobic Fe(II)-oxidizing and nitrate-reducing

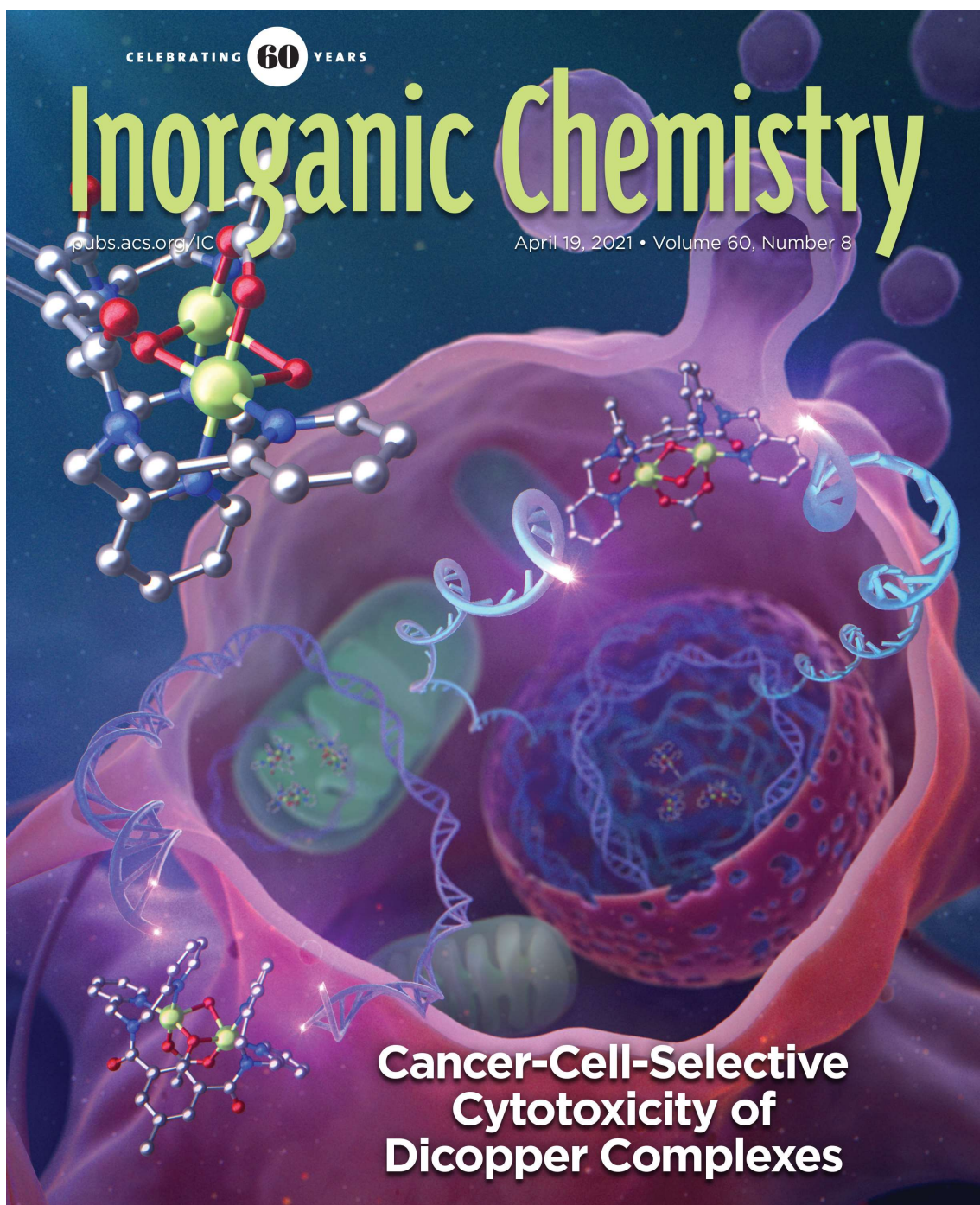
- enrichment culture KS. Appl. Environ. Microbiol. 84 (9), e02173-17 <https://doi.org/10.1128/AEM.02173-17>.
- Tominski, C., Lösekann-Behrens, T., Ruecker, A., Hagemann, N., Kleindienst, S., Mueller, C.W., Höschen, C., Kögel-Knabner, I., Kappler, A., Behrens, S., Löffler, F.E., 2018b. Insights into carbon metabolism provided by fluorescence in situ hybridization-secondary ion mass spectrometry imaging of an autotrophic, nitrate-reducing, Fe(II)-oxidizing enrichment culture. Appl. Environ. Microbiol. 84 (9), e02166-17 <https://doi.org/10.1128/aem.02166-17>.
- Tong, H., Zheng, C., Li, B., Swanner, E.D., Liu, C., Chen, M., Xia, Y., Liu, Y., Ning, Z., Li, F., Feng, X., 2021. Microaerophilic oxidation of Fe(II) coupled with simultaneous carbon fixation and As(III) oxidation and sequestration in karstic paddy soil. Environ. Sci. Technol. 55 (6), 3634–3644. <https://doi.org/10.1021/acs.est.0c05791>.
- Ward, M., Jones, R., Brender, J., de Kok, T., Weyer, P., Nolan, B., Villanueva, C., van Breda, S., 2018. Drinking water nitrate and human health: an updated review. Int. J. Environ. Res. Public Health 15 (7), 1557. <https://doi.org/10.3390/ijerph15071557>.
- Weber, K.A., Picardal, F.W., Roden, E.E., 2001. Microbially catalyzed nitrate-dependent oxidation of biogenic solid-phase Fe (II) compounds. Environ. Sci. Technol. 35 (8), 1644–1650. <https://doi.org/10.1021/es0016598>.
- Wu, F., Hua, J., Zhou, J., Liu, Y., Long, S., Fei, Y., Liu, C., 2021. Facet-specific reactivity of hematite nanocrystals during Fe(II)-catalyzed recrystallization. Chem. Geol. 583, 120460 <https://doi.org/10.1016/j.chemgeo.2021.120460>.
- Wu, Y., Zhu, X., Wang, X., Lin, Z., Reinfelder, J.R., Li, F., Liu, T., 2023. A new electron shuttling pathway mediated by lipophilic phenoxazine via the interaction with periplasmic and inner membrane proteins of *Shewanella oneidensis* MR-1. Environ. Sci. Technol. 57 (6), 2636–2646. <https://doi.org/10.1021/acs.est.2c07862>.
- Xiong, Y., Guilbaud, R., Peacock, C.L., Krom, M.D., Poulton, S.W., 2023. Phosphorus controls on the formation of vivianite versus green rust under anoxic conditions. Geochim. Cosmochim. Acta 351, 139–151. <https://doi.org/10.1016/j.gca.2023.04.032>.
- Yanina, S.V., Rosso, K.M., 2008. Linked reactivity at mineral-water interfaces through bulk crystal conduction. Science 320 (5873), 218–222. <https://doi.org/10.1126/science.1154833>.
- Zhao, L., Dong, H., Kukkadapu, R., Agrawal, A., Liu, D., Zhang, J., Edelmann, R.E., 2013. Biological oxidation of Fe(II) in reduced nontronite coupled with nitrate reduction by *Pseudogulbenkiania* sp. strain 2002. Geochim. Cosmochim. Acta 119, 231–247. <https://doi.org/10.1016/j.gca.2013.05.033>.

CELEBRATING **60** YEARS

Inorganic Chemistry

pubs.acs.org/IC

April 19, 2021 • Volume 60, Number 8



 **ACS Publications**
Most Trusted. Most Cited. Most Read.

www.acs.org



Expanding the Toolbox of Octahedral Molybdenum Clusters and Nanocomposites Made Thereof: Evidence of Two-Photon Absorption Induced NIR Emission and Singlet Oxygen Production

Soumaya Khelifi, Gregory Taupier, Maria Amela-Cortes, Noée Dumait, Stéphane Freslon, Stéphane Cordier, and Yann Molard*

Inorganic Chemistry 2021, 60, 8, 5446-5451

(Communication)

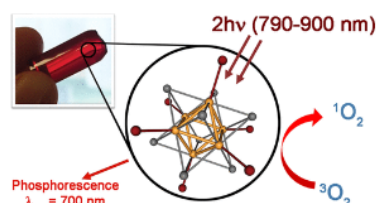
Publication Date (Web): March 31, 2021

Abstract

Full text

PDF

▼ ABSTRACT



ARTICLES

Effect of the Molecular Conformation on Excitation Energy Transfer in Conformationally Constrained Boryl-BODIPY Dyads

Rajendra Prasad Nandi, Chinna Ayya Swamy P*, Pandi Dhanalakshmi, Santosh Kumar Behera, and Pakkirisamy Thilagar*

Inorganic Chemistry 2021, 60, 8, 5452-5462 (Article)

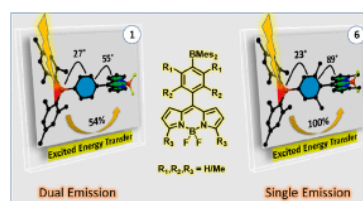
Publication Date (Web): April 8, 2021

Abstract

Full text

PDF

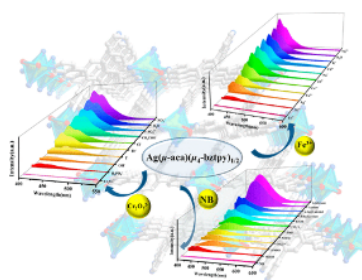
▼ ABSTRACT



Three Silver(I) Coordination Polymers Based on Pyridyl Ligands and Auxiliary Carboxylic Ligands: Luminescence and Efficient Sensing Properties

Cong-Cong Chen, Yue Cai, Long-Fei Wang, Yun-Dang Wu, Hao-Jun Yin, Jia-Rong Zhou, Chun-Lin Ni*, and Wei Liu*

Inorganic Chemistry 2021, 60, 8, 5463-5473 (Article)



Three Silver(I) Coordination Polymers Based on Pyridyl Ligands and Auxiliary Carboxylic Ligands: Luminescence and Efficient Sensing Properties

Cong-Cong Chen, Yue Cai, Long-Fei Wang, Yun-Dang Wu, Hao-Jun Yin, Jia-Rong Zhou, Chun-Lin Ni,* and Wei Liu*

Cite This: *Inorg. Chem.* 2021, 60, 5463–5473

Read Online

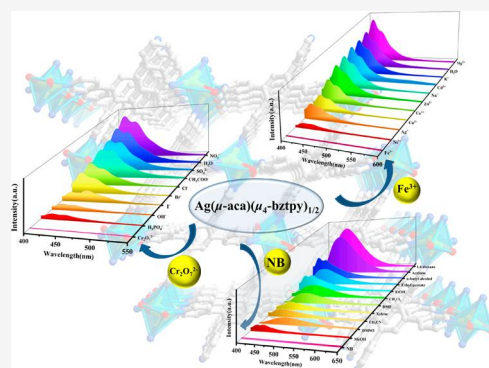
ACCESS |

Metrics & More

Article Recommendations

Supporting Information

ABSTRACT: Easily producible sensors for harmful industrial waste compounds are of significant interest for both human health and the environment. Three novel coordination polymers, $[\text{Ag}(\mu\text{-aca})(\mu_4\text{-bztpy})_{1/2}]$ (**1**), $[\text{Ag}(\mu\text{-bza})(\mu\text{-bpa})]$ (**2**), and $[\text{Ag}_2(\mu\text{-aca})_2(\mu\text{-bpa})_2] \cdot \text{EtOH} \cdot 2\text{H}_2\text{O}$ (**3**), were assembled in this study by reactions using Ag^+ as a node with the pyridyl ligand 1,2,4,5-tetrakis(4-pyridyl)benzene (bztpy) or 9,10-bis(4-pyridyl)anthracene (bpa) and an auxiliary chelating carboxylic ligand. Single-crystal X-ray structural analyses revealed that compound **1** has a 3D framework consisting of 1D $[\text{Ag}(\text{aca})]_\infty$ chains and bztpy linkers, while **2** and **3** have 2D layered structures consisting of binuclear Ag–carboxylate units and bpa linkers, respectively. Topological studies revealed that **1** has a **bbf** topology, while **2** and **3** are 2D $[4,4]$ rhombic grids. The compounds were further characterized by powder X-ray diffraction, IR, elemental analysis, thermogravimetric analysis, and a luminescence study. The solids of **1–3** exhibited intense photoluminescent emission with $\lambda_{\text{em}}^{\text{max}}$ at ca. 493, 472, and 500 nm, respectively. Remarkably, due to their excellent framework stability, **1** and **2** can act as multiresponsive luminescent sensors for nitrobenzene, Fe^{3+} , and $\text{Cr}_2\text{O}_7^{2-}$ with a high selectivity and sensitivity ascribed to their quenching effect.



INTRODUCTION

Built by the inherently strong coordination bonds that form between the abundant junction points of organic ligands and metal centers, functional coordination polymers (CPs)¹ have gained immense scientific interest for the construction of novel geometrical architectures for stable crystalline functional materials amenable to applications in gas storage² and separation,³ catalysis,⁴ fluorescence,⁵ sensing,⁶ and so on. Among the diverse applications, proposals for fluorescence sensing based on luminescent CPs have arisen on account of their excellent optical properties, quick responses, operability, and high selectivity, allowing them to serve as sensors for probing small organic molecules and contaminant ions.⁷ However, compounds with poor solvent resistances have limited research in fluorescence sensing. Accordingly, the fabrication of luminescent CP-based multifunctional sensors with tunable luminescence properties and favorable structural stabilities remains a challenge for chemists.

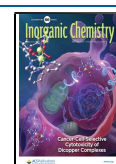
The rapid growth of modern society and industry has resulted in the release of toxic small molecules and pollutant ions, which have caused critical damage to the health of human beings and the environment.⁸ Among them, nitrobenzene (NB), the most basic constituent of explosives, can result in momentous safety problems. Furthermore, the harm caused by the high toxicity, accumulation, and nondegradability of such

contaminants to health and the environment is also unpredictable. In recent years, the development of sensing and detection methods for these chemicals has played a significant role in terms of ecological and safety considerations, and luminescent CPs have been reported as promising sensors for the detection of NB.^{7b,d,9}

It is well-known that Fe^{3+} is an essential ion in living organisms, as it plays a key role in crucial processes related to electron transfer in various bodily processes and the formation of genetic material. Iron deficiency and excess can both lead to severe health issues such as sleep loss, iron deficiency anemia, and decreased immunity.¹⁰ Additionally, anion pollutants such as $\text{Cr}_2\text{O}_7^{2-}$ cause growing damage to the environment and human health and have thus become a severe problem. Industrial wastewater usually contains some amount of $\text{Cr}_2\text{O}_7^{2-}$, causing critical harm to the ecosystem; meanwhile, excess $\text{Cr}_2\text{O}_7^{2-}$ in the body will interfere with proper cell

Received: September 30, 2020

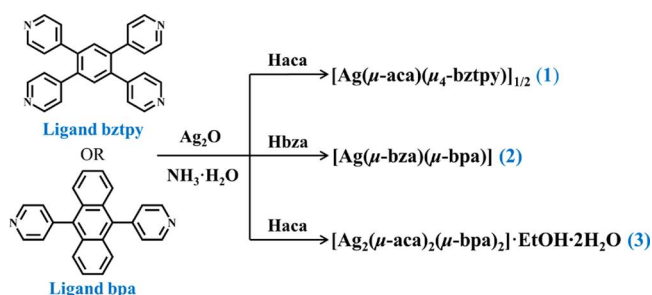
Published: April 1, 2021



functioning, leading to diseases such as rhinitis, skin cancer, lung cancer, embryo malformation, renal failure, and so on.¹¹ Many valuable analytical techniques have been proposed to detect these ions, including voltammetry,¹² X-ray dispersion,¹³ and atomic absorption spectroscopy,¹⁴ but some are limited in their characteristics. Hence, the convenient and sensitive detection of trace amounts of destructive chemicals is an essential research focus.

Aromatic-based CPs have gained interest in the construction of photoactive CPs with photoluminescent properties. In this respect, dye molecules such as 1,2,4,5-tetrakis(4-pyridyl)-benzene (bztpy) and 9,10-bis(4-pyridyl)anthracene (bpa) are perfect candidates for organic linkers.¹⁵ In this study, three compounds, namely $[\text{Ag}(\mu\text{-aca})(\mu_4\text{-bztpy})]_{1/2}$ (**1**), $[\text{Ag}(\mu\text{-bza})(\mu\text{-bpa})]$ (**2**), and $[\text{Ag}_2(\mu\text{-aca})_2(\mu\text{-bpa})_2]\cdot\text{EtOH}\cdot 2\text{H}_2\text{O}$ (**3**), were prepared with the assistance of two auxiliary carboxylates, benzoic acid and 9-anthracenecarboxylic acid (Scheme 1). Compound **1** consists of 1D $[\text{Ag}(\text{aca})]_\infty$ chains

Scheme 1. Synthetic Routes of Compounds 1–3^a



^aAbbreviations: Haca, 9-anthracenecarboxylic acid; Hbza, benzoic acid.

linked by bztpy ligands to form an interesting 3D framework, while **2** and **3** have 2D-layered structures that form 3D supermolecular networks via rich π – π interactions. The three compounds exhibited notable solid-state photoluminescence. Remarkably, luminescence studies illustrated that CPs **1** and **2** may serve as highly selective multiresponsive luminescence sensors for NB , Fe^{3+} , and $\text{Cr}_2\text{O}_7^{2-}$ in aqueous solutions.

EXPERIMENTAL SECTION

Materials and General Procedures. All solvents and reagents, as well as the bpa ligand, for syntheses were obtained commercially and used without further purification. The bztpy ligand was prepared by a reported hydrothermal method.^{15b} Compounds **1–3** were synthesized by a solution method, which is more facile and conducive to large-scale synthesis. In addition, the use of silver ammonia solution to reduce the interference of other coordination atoms can make the coordination of silver atoms more flexible, which is beneficial to obtain more interesting structures.^{5,15,18} Powder X-ray diffraction (PXRD) was conducted on an Ultima IV diffractometer with $\text{Cu K}\alpha$ radiation in the range of $2\theta = 5$ – 50° at room temperature. IR spectra of KBr pellets were measured on a NICOLET 6700 instrument in the range of 4000 – 400 cm^{-1} . Elemental analyses of C, H, and N were carried out a Vario EL elemental analyzer. Thermogravimetric analysis (TGA) was performed using a TG 209 F1 Libra micro thermal analyzer with a heating rate of 10 K min^{-1} under an N_2 flow. UV–vis absorption spectra were obtained using a Spectro UV-2550 spectrophotometer.

Fluorescence Measurements. The solid fluorescence spectra and emission decay curves were acquired on an Edinburgh FLS920 spectrofluorometer, and the internal quantum efficiencies of the three samples were measured at room temperature using a barium sulfate

coated integrating sphere attached to the FSP920 apparatus. Fluorescence lifetimes were detected using an EPLED 360 ps pulsed light emitting diode and EPL 445 ps pulsed diode laser as excitation sources. The liquid fluorescence spectra were recorded on a Hitachi F-7000 fluorescence spectrometer. Emulsions were prepared by adding 2 mg of powder samples of **1** and **2** to 5 mL of diverse organic solvents and ultrasonication for 10 min. For the detection of cations and anions, 3 mg of **1** and **2** was dispersed in 0.01 mol L^{-1} $\text{M}(\text{NO}_3)_x$ (5 mL, $\text{M} = \text{Ag}^+$, K^+ , Na^+ , Co^{2+} , Ni^{2+} , Cu^{2+} , Cd^{2+} , Zn^{2+} , Mg^{2+} , Fe^{3+}) and/or 0.01 mol L^{-1} $\text{K}_n(\text{A})$ (5 mL, $\text{A} = \text{SO}_4^{2-}$, CH_3COO^- , Br^- , I^- , Cl^- , OH^- , H_2PO_4^- , NO_3^- , $\text{Cr}_2\text{O}_7^{2-}$), followed by ultrasonication for 0.5 h to obtain a stable suspension with a uniform dispersion.

Synthesis of Compounds 1–3. $[\text{Ag}(\mu\text{-aca})(\mu_4\text{-bztpy})]_{1/2}$ (**1**). The mixture resulting from the successive addition of fresh $\text{NH}_3\cdot\text{H}_2\text{O}$ (0.1 mol L^{-1} , 2 mL), Ag_2O (23 mg, 0.1 mmol), bztpy (19 mg, 0.05 mmol), and 9-anthracenecarboxylic acid (22 mg, 0.1 mmol) to ethanol (10 mL) was stirred for 30 min. The resulting solution was filtered to afford a colorless transparent filtrate and kept undisturbed at room temperature. Yellow bulk crystals of **1** were obtained by slow evaporation after 3 days in ca. 57% yield based on bztpy. Anal. Calcd for $\text{C}_{28}\text{H}_{18}\text{AgN}_2\text{O}_2$: C, 64.39; H, 3.47; N, 5.36. Found: C, 64.52; H, 3.36; N, 5.71. IR (KBr, cm^{-1}): 3415w, 3032w, 1599s, 1572m, 1553s, 1473w, 1419m, 1382w, 1315m, 1275w, 1216w, 1062w, 1006w, 877w, 842w, 827m, 759m, 733w, 561w.

$[\text{Ag}(\mu\text{-bza})(\mu\text{-bpa})]$ (**2**). The mixture resulting from the successive addition of fresh $\text{NH}_3\cdot\text{H}_2\text{O}$ (0.1 mol L^{-1} , 2 mL), Ag_2O (11 mg, 0.05 mmol), bpa (8 mg, 0.025 mmol), and benzoic acid (6 mg, 0.05 mmol) to ethanol (10 mL) was stirred for 30 min. The resulting solution was filtered to afford a colorless transparent filtrate and kept undisturbed at room temperature. Yellow bulk crystals of **2** were obtained by slow evaporation after 7 days in ca. 42% yield based on bpa. Anal. Calcd for $\text{C}_{31}\text{H}_{21}\text{AgN}_2\text{O}_2$: C, 66.32; H, 3.77; N, 4.99. Found: C, 66.24; H, 3.91; N, 4.85. IR (KBr, cm^{-1}): 3430w, 3058w, 1594s, 1552s, 1442w, 1419w, 1392m, 1368s, 1215m, 1065w, 1023w, 1009w, 830w, 814m, 767m, 740w, 711s, 689w, 642m, 611m, 535w.

$[\text{Ag}_2(\mu\text{-aca})_2(\mu\text{-bpa})_2]\cdot\text{EtOH}\cdot 2\text{H}_2\text{O}$ (**3**). The preparation of compound **3** was similar to that of **2**, except that 9-anthracenecarboxylic acid (11 mg, 0.05 mmol) was used instead of benzoic acid (6 mg, 0.05 mmol). Pale yellow flake crystals were obtained by slow evaporation after 7 days in ca. 15% yield based on bpa. Anal. Calcd for $\text{C}_{80}\text{H}_{60}\text{Ag}_2\text{N}_4\text{O}_7$: C, 68.38; H, 4.30; N, 3.99. Found: C, 68.36; H, 4.51; N, 3.93. IR (KBr, cm^{-1}): 3408m, 3045w, 1594m, 1551s, 1441w, 1428m, 1392s, 1318s, 1273m, 1215w, 1064w, 949w, 878m, 814m, 769s, 735m, 677w, 643m, 611m, 537m.

Crystal Structure Determination. The X-ray single-crystal structures of compounds **1–3** were recorded on a Rigaku R-Axis SPIDER IP diffractometer equipped with graphite-monochromated Mo $\text{K}\alpha$ radiation ($\lambda = 0.71073\text{ \AA}$) at 120 K (compounds **1–3**) and 298 K (compound **2**), and the unit cell dimensions were determined by the least-squares remnants. The structures were solved by direct methods, and anisotropic thermal parameters were assigned to all non-hydrogen atoms using the SHELXTL program suite by least squares on F^2 .¹⁶ The hydrogen atoms of organic ligands were placed in idealized positions and refined by a riding model. A summary of the crystallographic details is given in Table S1. CCDC 2027402–2027404 contain supplementary crystallographic data for this paper. The data can be obtained free of charge from The Cambridge Crystallographic Data Centre via www.ccdc.cam.ac.uk/data_request/cif.

RESULTS AND DISCUSSION

Synthetic Chemistry of Compounds 1–3. Compound **1** was synthesized by the reaction of Ag_2O , $\text{NH}_3\cdot\text{H}_2\text{O}$, bztpy, and 9-anthracenecarboxylic acid at room temperature. Switching bztpy and 9-anthracenecarboxylic acid for bpa and benzoic acid, respectively, yielded compound **2**, while the preparation of compound **3** was the same as that for **2** with benzoic acid

instead of 9-anthracenecarboxylic acid. The quantity of the reactants was adjusted for better yields.

Crystal Structure. A single-crystal X-ray structural analysis revealed that compound **1** crystallizes in the monoclinic system with space group $P2_1/c$ and consists of one Ag(I) ion, a half bztpy ligand, and one aca^- ligand in an asymmetric unit. The Ag(I) center adopts a distorted $[AgO_2N_2]$ tetrahedral geometry, which is surrounded by two oxygen atoms from two aca^- ligands and two nitrogen atoms from two bztpy ligands (Figure 1a). The basic side pieces of the structure are

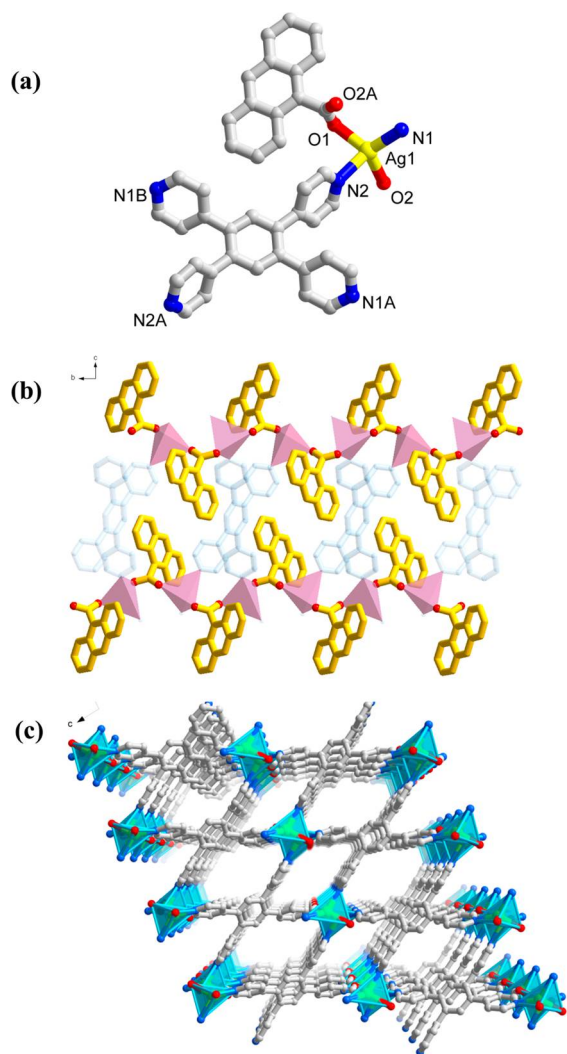


Figure 1. (a) View of the coordination environment of the Ag(I) center in **1**. (b) 2D structure formed by linked bztpy and 1D $[Ag(aca)]_\infty$ chains along the a axis. (c) 3D framework of **1** along the $[010]$ direction (part of the structure of anthracene acid has been omitted). All H atoms are omitted for clarity.

1D $[Ag(aca)]_\infty$ chains (Figure 1b) formed by the carboxyl groups on the aca^- ligand extending as bridges to connect two adjacent Ag atoms, thus forming a 3D structure linked by the tetradentate bztpy ligand (Figure 1c). When the Ag atom is considered as a tetrahedral node and bztpy linking Ag as a four-connected node, the whole 3D framework can be simplified into the **bbf** topology with the Schläfli point symbol $\{6^4;8^2\}\{6^6\}_2$ by the TOPOS4.0 software¹⁷ (Figure S1).

Compound **2** crystallizes in the triclinic system with space group $P1$, and the asymmetric unit comprises one crystallo-

graphically independent Ag(I) ion, two half bpa ligands, and one bza^- counterion. The basic structural motif is a binuclear Ag unit, in which two Ag centers are linked by two μ -O atoms from the bza^- ligand and two nitrogen atoms from two bpa ligands (Figure 2a). In comparison with the Ag...Ag distance

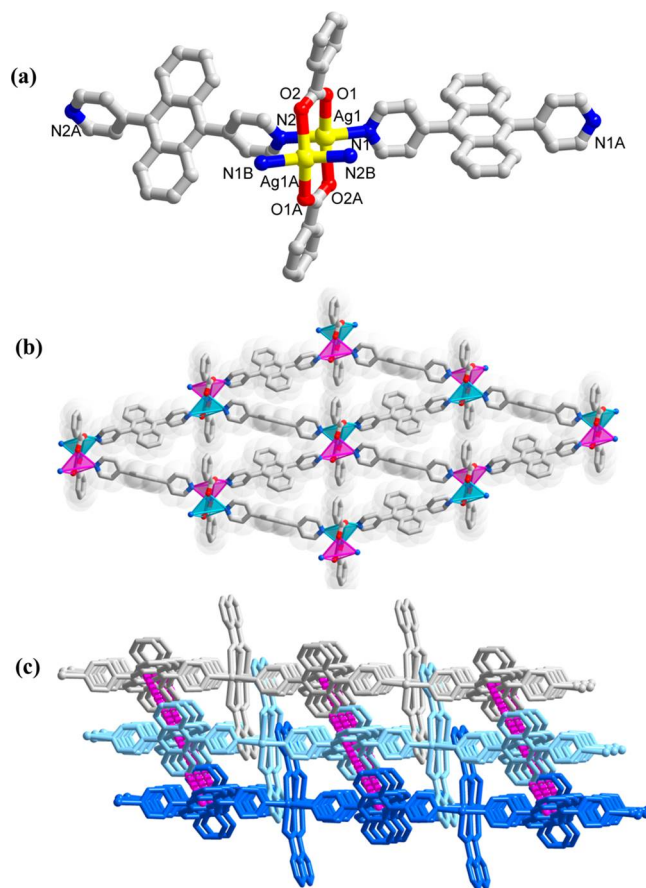


Figure 2. (a) Coordination environment of the Ag(I) center in **2**. (b) View of the 2D grid configuration of **2**. (c) 3D framework formed by interfacial $\pi \cdots \pi$ stacking (purple-red dotted lines) interactions between 2D layers. All H atoms are omitted for clarity.

(3.01 Å) in metallic silver,¹⁸ the Ag1...Ag1A distance of 2.86 Å suggests a stronger metal–metal interaction. The Ag atoms adopt a distorted-tetrahedral geometry, where the equatorial plane is constructed from nitrogen atoms from the bpa ligand, while the axial orientation is coordinated by the oxygen atoms of the bza^- auxiliary ligand. Thus, it can be regarded as a metal double-cluster secondary unit linked by bpa to construct a $[2 \times 2]$ 2D grid (Figure 2b). On the basis of these connection modes, the adjacent layers further assemble into a 3D supramolecular network (Figure 2c) via abundant $\pi \cdots \pi$ interactions between anthracene rings on nearby bpa ligands at a distance of 3.51 Å.

Compound **3** crystallizes in the monoclinic space group $P2_1/n$ and contains two crystallographically independent Ag(I) ions, two bpa ligands, two aca^- counterions of distinct coordination modes, and two water molecules and one ethanol molecule as guests in an asymmetric unit. As portrayed in Figure 3a, compound **3** consists of binuclear Ag(I) units connected by oxygen atoms. The Ag1 centers are tetradentate to two oxygen atoms from two aca^- ligands and two nitrogen atoms from two bpa ligands, generating a distorted-tetrahedral

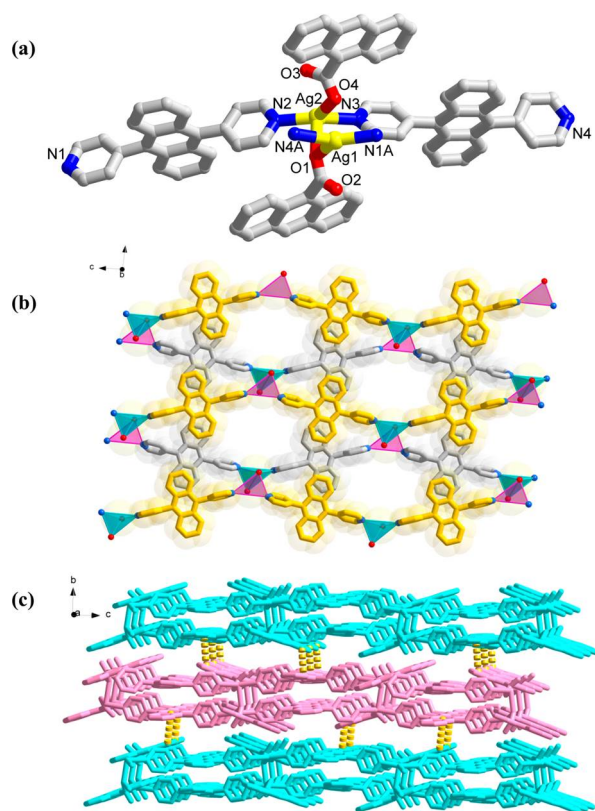


Figure 3. (a) Coordination environment of the Ag(I) ion in 3. (b) View of the 2D double-layer structure of 3 along the *b* axis. (c) 3D supramolecular framework formed via interlayer $\pi \cdots \pi$ stacking (orange dashed lines). All H atoms and lattice guest molecules are omitted for clarity.

configuration. On the other hand, the Ag2 centers adopt a trigonal-planar coordination geometry ligated by one oxygen atom from the aca⁻ ligand and two nitrogen atoms from the bpa ligand. There are weak interactions for both Ag1 \cdots Ag2 with a distance of 3.89 Å and Ag1 \cdots O4 with a distance of 2.67 Å. The basic side pieces of the structure are 1D [Ag₂(bpa)]_∞ chains formed by bpa ligands and Ag(I) atoms, which are further linked into 2D double sheets through the carboxyl groups on the aca⁻ ligand between each pair of adjacent 1D chains (Figure 3b). These layers are connected by interlayer $\pi \cdots \pi$ interactions at a distance of 3.53 Å, thereby forming a 2D \rightarrow 3D supramolecular open framework (Figure 3c).

PXRD and Thermal Analysis. The PXRD analyses of the synthesized crystalline samples of 1–3 were in good agreement with the simulated patterns, demonstrating the phase purity of the synthesized products (Figure S2). To determine the thermal stability of the three compounds, a TGA study was carried out on the crystalline samples under N₂, as depicted in Figure S3. The TGA curves of compounds 1 and 2 indicate their favorable thermal stability on heating up to 505 and 500 K, respectively. For compound 3, the observed weight loss (%) was ascribed to the loss of the one lattice ethanol molecule and two lattice water molecules (observed 5.62%, calculated 5.84%) in the temperature range of 302–456 K, followed by gradual stabilization up to 504 K.

Luminescence Properties. Encouraged by the luminescent properties of d¹⁰-based CPs containing electron-rich π -conjugated organic ligands,¹⁹ we investigated the photoluminescent properties of CPs 1–3 and those of the free

bztpy and bpa ligands in the solid state at room temperature (Figure 4). Upon excitation at 332 nm for bztpy and 395 nm

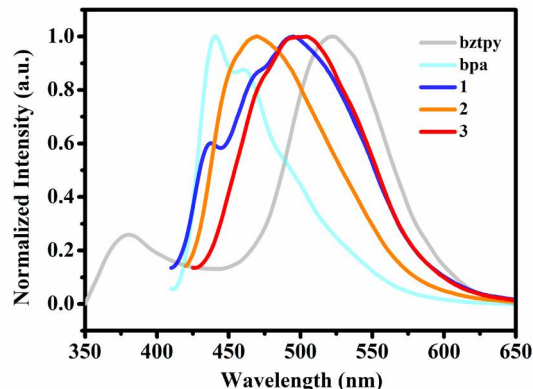


Figure 4. Solid-state luminescent emission spectra of 1–3 and the free ligands bztpy and bpa at room temperature.

for bpa, corresponding strong emission peaks at 521 and 440/475 nm, respectively, were observed. In comparison with free anthracene, the 9,10-positions of anthracene replaced by pyridine groups in bpa will produce electron delocalization with the anthracene ring, which will reduce the potential energy between the ground state and the first electron excited state.²⁰ Thus, for the free ligand bpa, emission peaks are obviously red shifted in comparison with anthracene (Figure S5). Strong emission bands for 1–3 were observed at 493, 472, and 500 nm (λ_{ex} = 390, 394, and 394 nm), with CIE coordinates of (0.192, 0.327), (0.166, 0.251), and (0.197, 0.391), respectively, which are similar to those of Ag polymers in the literature.^{5e,f,15,18} Obviously, these emission bands should mainly come from intraligand-based charge transfer ($\pi \rightarrow \pi^*$) transitions.^{5b,21} In comparison with the spectra of their free homologous ligands, compound 1 exhibited a blue shift (28 nm), while the strong emission peaks of 2 and 3 corresponded to notable red shifts (32 and 60 nm, respectively). The wavelength shift of emission maxima is mainly the result of changes in the packing modes after coordination, and the contribution of charge transfer from the silver center to the organic ligands (MLCT) should also be taken into consideration.^{5,22} Extensive interactions, such as Ag(I) \cdots Ag(I) interactions and $\pi \cdots \pi$ stacking, exist in compounds 2 and 3 and play a part in decreasing the energy gaps.²² Unfortunately, no Ag(I) \cdots Ag(I) interactions were observed in 1. For compound 1, as the free bztpy ligand exhibits multiple conformations under different crystallization conditions and shows different fluorescence properties,^{15b} less conjugated bztpy conformations may be the reason for the slight wavelength shift of the emission maxima of 1 (Figure S1).

To further understand the fluorescence properties of CPs 1–3, the fluorescence lifetimes and quantum yields were measured in the solid state at ambient temperature. The fluorescence decays of 1–3 were fitted by double-exponential decay laws with the following formula: $I = A_1 \exp(-t/\tau_1) + A_2 \exp(-t/\tau_2)$, where τ_1 and τ_2 are the fast and slow components of the fluorescence lifetimes, respectively, and A_1 and A_2 are the corresponding pre-exponential factors.^{7d} Therefore, the average decay time (τ^*) can be determined by the equation $\tau^* = (A_1\tau_1 + A_2\tau_2)/(A_1 + A_2)$, which gives the corresponding average lifetimes of 2.10, 3.34, and 3.83 ns for 1–3,

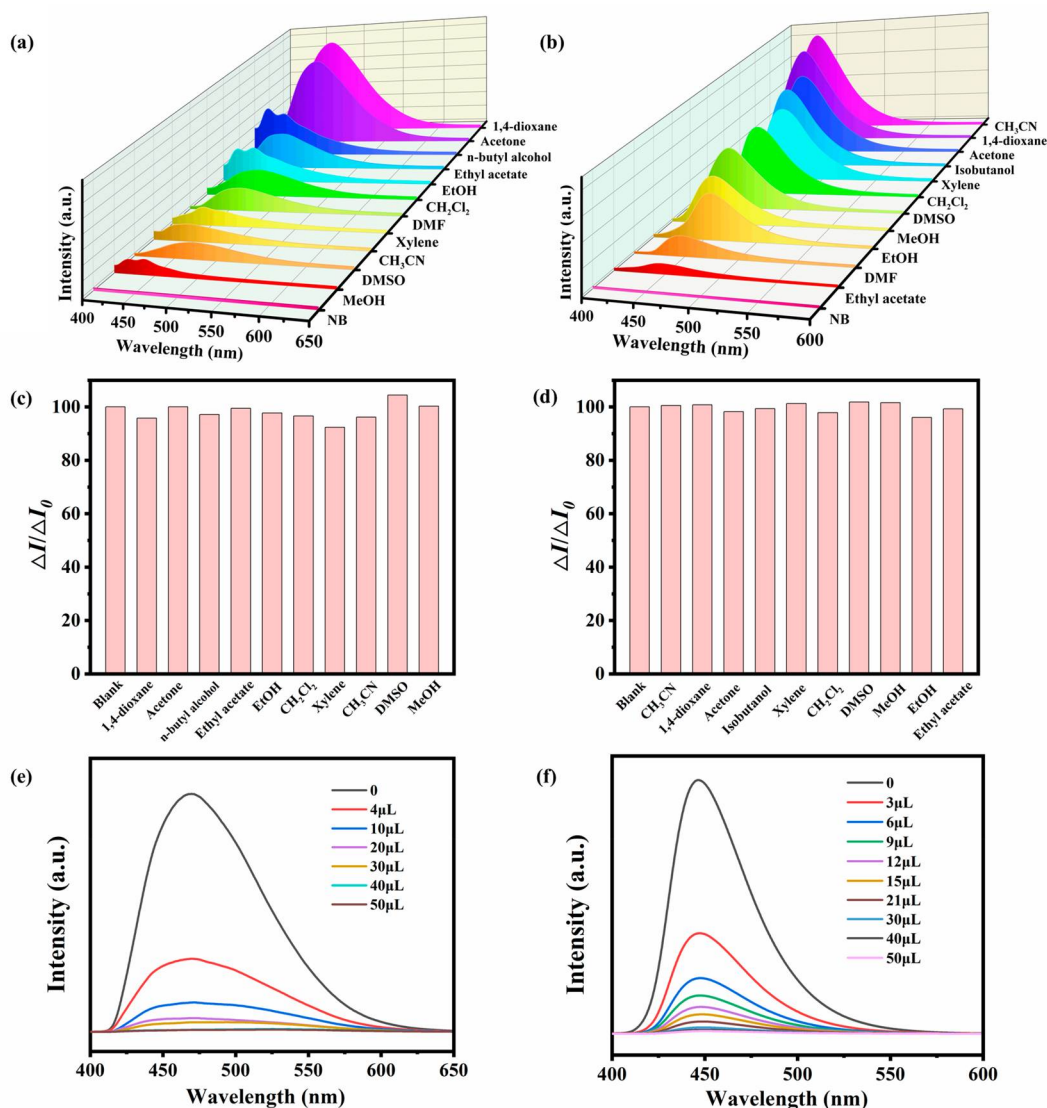


Figure 5. Emission spectra of (a) 1 and (b) 2 dispersed in different solvents, fluorescence change ratio ($\Delta I/\Delta I_0$) histograms of (c) 1 and (d) 2 in the presence of various solvents containing NB in DMF, and emission spectra of (e) 1 and (f) 2 dispersed in DMF with different concentrations of NB.

respectively. These are on the same order of magnitude of nanoseconds (Figure S8), suggesting that all three complexes are potential candidates for luminescent materials. The emission colors of the three compounds can also be observed by the naked eye under ultraviolet light (Figure S7). Absolute quantum yields of 9.70%, 14.15%, and 14.66% for 1–3 (λ_{ex} = 390, 394, and 394 nm), respectively, were determined according to the ratio of emitted to absorbed photons.²³ In particular, in comparison with 3, compounds 1 and 2 exhibited more stable frameworks. Therefore, they were chosen as luminescent probes to explore in detail their ability to sense small solvent molecules and diverse metals and anions.

Sensing of Organic Small Molecules. To further explore the potential sensing properties of compounds 1 and 2, stable suspensions for luminescence measurements were prepared by introducing sample 1 or 2 into diverse organic solvents, including methanol (MeOH), ethanol (EtOH), acetonitrile (MeCN), dichloromethane (CH₂Cl₂), dimethyl sulfoxide (DMSO), *N,N*-dimethylformamide (DMF), xylene, ethyl acetate, 1,4-dioxane, *n*-butyl alcohol, isobutanol, acetone, and

NB. As portrayed in Figure 5a,b and Figure S10, the fluorescence emission intensity and position of the emission bands of 1 and 2 were largely regulated by the different organic pure solvents, especially for NB, which exhibited the most significant quenching effect. Such solvent-dependent quenching behavior is highly valuable for sensing NB molecules. In addition to a high selectivity toward NB, the anti-interference ability of sensors is also essential. The interference of other organic reagents in the fluorescence responses of 1 and 2 containing NB was extremely limited in the observed systems, which demonstrates that NB can be sensitively detected in the presence of other solvents (Figure 5c,d).

The sensing properties toward NB were further investigated by measuring a series of emulsions of 1 and 2 in DMF with gradually increasing NB concentration (Figure 5e,f). The luminescence intensity of the suspensions showed a particularly marked decrease with increasing microscale NB concentration. The quenching efficiency (%), defined as $(I_0 - I)/I_0 \times 100\%$, where I_0 is the original fluorescence intensity and I is the fluorescence intensity with the addition of analytes,

Table 1. Comparison among Various Fluorescent Sensors Based on CPs for NB, Fe³⁺, and Cr₂O₇^{2−} ^a

CP-based fluorescent sensing material	analyte	solution	K _{sv} (M ^{−1})	detection limit (M)	ref
[Tb(L ¹)(H ₂ O) ₂].guest	NB	hexane	5.90 × 10 ²		26a
[Tb(L ²)(H ₂ O) ₂].guest	NB	hexane	4.46 × 10 ²		
{[Cd ₂ (L ³)(DMA)]·[H ₂ N(Me) ₂]} _n	NB	DMA	2.7 × 10 ³	2.54 × 10 ^{−3}	26b
	Fe ³⁺	DMA	4.90 × 10 ³	1.2 × 10 ^{−3}	
{[Zn ₃ (mtrb) ₃ (btc) ₂]·3H ₂ O} _n	Fe ³⁺	water	6.50 × 10 ³	1.78 × 10 ^{−6}	27a
	Fe ³⁺	water		1 × 10 ^{−4}	5a
[Zn ₂ L ⁴] ₂ ·2DMF·2MeOH	Fe ³⁺	water			30c
[Cd ₂ (L ⁵)(bipb) ₃] _n	Fe ³⁺	water	5.14 × 10 ³		
{[Cd ₃ (HL ⁶)(H ₂ O) ₃]·3H ₂ O·2CH ₃ CN} _n	Cr ₂ O ₇ ^{2−}	water	6.69 × 10 ³		
	Cr ₂ O ₇ ^{2−}	water	6.99 × 10 ³	1.17 × 10 ^{−4}	7e
	Fe ³⁺	water	1.04 × 10 ⁴	9.06 × 10 ^{−5}	
{[Eu ₂ Na(Hpddb)(pddb) ₂ (CH ₃ COO) ₂]·2.5(DMA)} _n compound 1	Cr ₂ O ₇ ^{2−}	DMF	6.45 × 10 ³	5.35 × 10 ^{−6}	30a
	NB	DMF	2.47 × 10 ²	2.02 × 10 ^{−3}	this work
	Fe ³⁺	water	1.25 × 10 ⁴	6.85 × 10 ^{−6}	
	Cr ₂ O ₇ ^{2−}	water	7.33 × 10 ³	3.68 × 10 ^{−5}	
compound 2	NB	DMF	1.63 × 10 ²	4.57 × 10 ^{−3}	this work
	Fe ³⁺	water	3.93 × 10 ³	5.17 × 10 ^{−5}	
	Cr ₂ O ₇ ^{2−}	water	4.37 × 10 ⁴	1.03 × 10 ^{−5}	

^aAbbreviations: H₃L¹, [1,1':4',1''-terphenyl]-3,4'',5-tricarboxylic acid; H₃L², [1,1':4',1'':4'',1'''-quaterphenyl]-3,4'',5-tricarboxylic acid; H₅L³, 2,4-di(3',5'-dicarboxylphenyl)benzoic acid; mtrb, 1,3-bis(1,2,4-triazole-4-ylmethyl)benzene; btc, 1,3,5-benzenetricarboxylate; H₂L⁴, (E)-2-[2-(4-carboxy)ethenyl]-8-hydroxyquinoline; H₄L⁵, 5,5'-(1,4-phenylenebis(methoxy))diisophthalic acid; bipb, 4,4'-bis(imidazolyl)biphenyl; H₄L⁶, 1-(3,5-dicarboxylatobenzyl)-3,5-pyrazoledicarboxylic acid; H₂pddb, 4'-(pyridine-2,6-diyl)dibenzoic acid.

was estimated to be 99.13% for **1** and 98.97% for **2** by the addition of 50 μL of NB, indicating that the fluorescence intensity was almost completely quenched. In order to explicate the fluorescence quenching effect of NB, time-resolved fluorescence decay analyses in the absence and presence of NB were performed. It could be found that the fluorescence lifetime obviously decreased after contact with NB (Figure S16), which implied that the fluorescence quenching of a sample triggered by NB could be mainly due to a dynamic quenching effect.²⁴ To further quantitatively investigate the quenching effect, the data were analyzed using the Stern–Volmer equation, $I_0/I = 1 + K_{sv}[M]$, where $[M]$ is the molar concentration of the analyte. The Stern–Volmer curve shows an almost linear relationship over the concentration ranges 13.03–96.91 and 14.66–72.86 mM for **1** and **2**, respectively. The calculated quenching constant, K_{sv} , was $2.47 \times 10^2 \text{ M}^{-1}$ for **1** and $1.63 \times 10^2 \text{ M}^{-1}$ for **2** (Figure S13). On the basis of the reported formula of $3\delta/k$ (δ and k are the standard deviation of three replicate fluorescence measurements in a blank solution and the slope of the calibration curve, respectively),²⁵ the detection limits were calculated to be approximately $2.02 \times 10^{-3} \text{ M}$ for **1** and $4.57 \times 10^{-3} \text{ M}$ for **2**, which are equivalent to or better than those of previously reported well-designed MOFs for sensing NB (Table 1).²⁶ The extremely high detection selectivity and sensitivity toward NB of **1** and **2** indicate that they are highly promising for use as chemical sensors for trace NB.

Sensing of Metal Ions. The potential ability of compounds **1** and **2** to sense metal ions was also evaluated in water. Suspensions of **1** and **2** with metal ions were prepared by dispersing the powder samples in $M(\text{NO}_3)_x$ ($M = \text{Ag}^+$, K^+ , Na^+ , Co^{2+} , Ni^{2+} , Cu^{2+} , Cd^{2+} , Zn^{2+} , Mg^{2+} , or Fe^{3+}) aqueous solutions. Most interestingly, as shown in Figure 6a,b and Figure S11, the luminescence intensity of the water suspensions with different metal ions largely depended on the metal species, especially Fe^{3+} , which had a drastic quenching effect on the two compounds. Furthermore, to demonstrate that other common competing metal ions have no

significant influence on the sensing behavior for Fe^{3+} , an anti-interference sensing test was performed under the same conditions. Notably, the interfering metal ions exerted little influence on the luminescence of emulsions of **1** and **2** containing Fe^{3+} , indicating that Fe^{3+} can still be sensitively detected in spite of the presence of different metal ions in the solution (Figure 6c,d).

To further explore the sensitivity of **1** and **2** as luminescent probes for Fe^{3+} , the fluorescence intensities of the aqueous suspensions were measured with the addition of different concentrations of Fe^{3+} (Figure 6e,f). The emission intensity gradually weakened with increasing Fe^{3+} concentration and was almost completely quenched at 2.5 mM Fe^{3+} for **1** and 8.3 mM Fe^{3+} for **2**, corresponding to excellent quenching efficiencies of 99.66% and 98.90%, respectively. According to Figure S17, the fluorescence lifetime decreases obviously with the addition of Fe^{3+} ; thus, the fluorescence quenching can also be attributed to the dynamic quenching effect. In addition, the linear fit between $(I_0/I - 1)$ and the millimolar concentration of Fe^{3+} in the low-concentration range (0.05–0.25 mM for **1** and 0.12–1.10 mM for **2**) also revealed a favorable linear relationship, with K_{sv} values calculated to be approximately $1.25 \times 10^4 \text{ M}^{-1}$ for **1** and $3.93 \times 10^3 \text{ M}^{-1}$ for **2** (Figure S14), which are comparable to the values for some reported compounds (Table 1).²⁷ The detection limits for **1** and **2** were estimated to be 6.85×10^{-6} and $5.17 \times 10^{-5} \text{ M}$, respectively, which imply that **1** and **2** have tremendous potential application value for detecting Fe^{3+} ions. Surprisingly, the Fe^{3+} detection limit for both compounds is lower than that of other reported sensors such as $[(\text{CH}_3)_2\text{NH}_2] \cdot [\text{Tb}(\text{bptc})] \cdot x(\text{solvent})$ ($1.801 \times 10^{-4} \text{ M}$),²⁸ $\{[\text{Cd}_3(\text{HL})_2(\text{H}_2\text{O})_3] \cdot 3\text{H}_2\text{O} \cdot 2\text{CH}_3\text{CN}\}_n$ ($9.06 \times 10^{-5} \text{ M}$),^{7e} and $[\text{Zn}_5(\text{hfipbb})_4(\text{trz})_2(\text{H}_2\text{O})_2]$ ($2.0 \times 10^{-4} \text{ M}$).²⁹

Sensing of Anions. Considering their outstanding luminescent properties and favorable stability in aqueous solutions, it seems feasible and promising to use compounds **1** and **2** as fluorescence sensors to detect aqueous $\text{Cr}_2\text{O}_7^{2-}$. To explore the sensing properties of **1** and **2** toward $\text{Cr}_2\text{O}_7^{2-}$, the

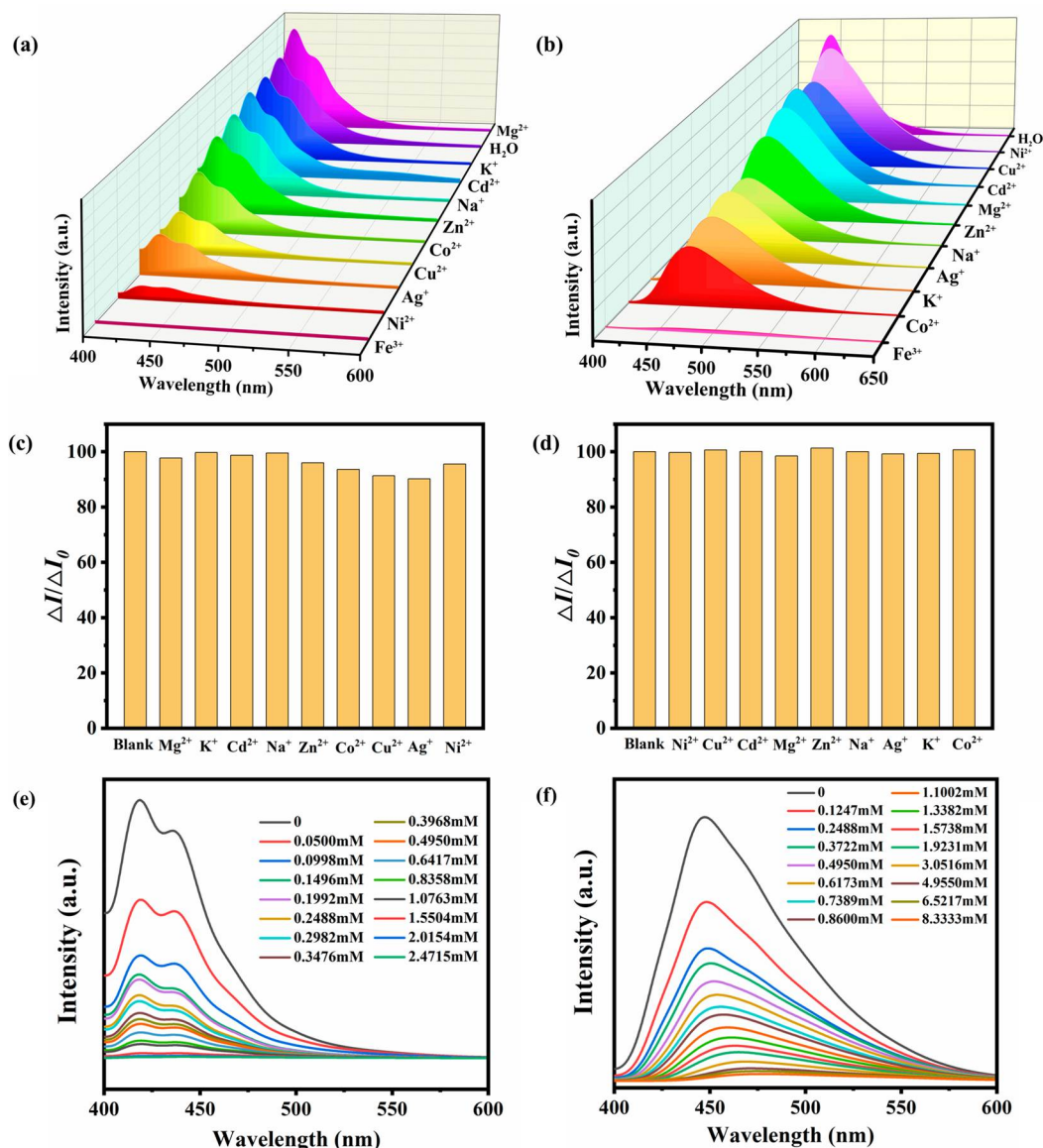


Figure 6. Emission spectra of (a) 1 and (b) 2 dispersed in aqueous solutions of various metal ions, fluorescence change ratio ($\Delta I/\Delta I_0$) histograms of (c) 1 and (d) 2 in the presence of aqueous Fe^{3+} and various interfering substances, and emission spectra of (e) 1 and (f) 2 dispersed in water with different concentrations of Fe^{3+} .

synthetic samples were dispersed in different $\text{K}_n(\text{A})$ ($\text{A} = \text{SO}_4^{2-}$, CH_3COO^- , Br^- , I^- , Cl^- , OH^- , H_2PO_4^- , NO_3^- , or $\text{Cr}_2\text{O}_7^{2-}$) solutions for luminescence analysis. The results indicated that the luminescence intensity of 1 and 2 largely depends on the type of anion, especially $\text{Cr}_2\text{O}_7^{2-}$, which caused distinct fluorescence quenching (Figure 7a,b and Figure S12). In addition, to prove the high selectivity toward $\text{Cr}_2\text{O}_7^{2-}$ versus other common competitive anions, anti-interference sensing experiments were implemented under the same conditions (Figure 7c,d). The luminescence intensity was almost completely quenched only by the addition of a certain amount of $\text{Cr}_2\text{O}_7^{2-}$, demonstrating that $\text{Cr}_2\text{O}_7^{2-}$ can be detected even in the presence of other anions.

To further assess the sensitivity of 1 and 2, two groups of titration experiments were performed by adjusting the concentration of $\text{Cr}_2\text{O}_7^{2-}$ (Figure 7e,f). Interestingly, the fluorescence intensity of $\text{Cr}_2\text{O}_7^{2-}$ -incorporated 1 and 2 was heavily dependent on the anion concentration. The luminescence intensities gradually weakened with an increasing

concentration of $\text{Cr}_2\text{O}_7^{2-}$, with the most complete quenching at 1.57 mM for 1 and 0.69 mM for 2 corresponding to quenching efficiencies of 99.77% and 99.85%, respectively. In addition, the fluorescence lifetime was shortened after contact with $\text{Cr}_2\text{O}_7^{2-}$, which indicated that the fluorescence quenching is a dynamic quenching effect (Figure S18). It is remarkable that 1 and 2 are highly sensitive and selective toward $\text{Cr}_2\text{O}_7^{2-}$ ions in aqueous suspensions. As shown in Figure S15, the fluorescence intensity and $\text{Cr}_2\text{O}_7^{2-}$ concentration for 1 and 2 are nearly linear below 0.62 mM and 0.20 mM, respectively. The calculated K_{sv} values were $7.33 \times 10^3 \text{ M}^{-1}$ for 1 and $4.37 \times 10^4 \text{ M}^{-1}$ for 2, and the detection limits of the assays calculated with $3\sigma/k$ were approximately 3.68×10^{-5} and $1.03 \times 10^{-5} \text{ M}$, respectively. These are comparable to or even better than those of other compounds for sensing $\text{Cr}_2\text{O}_7^{2-}$ ions (Table 1).^{30,7e,6d} Therefore, these results support that 1 and 2 have a good sensitivity and anti-interference ability, which are expected to allow the detection of $\text{Cr}_2\text{O}_7^{2-}$ anions in realistic environments.

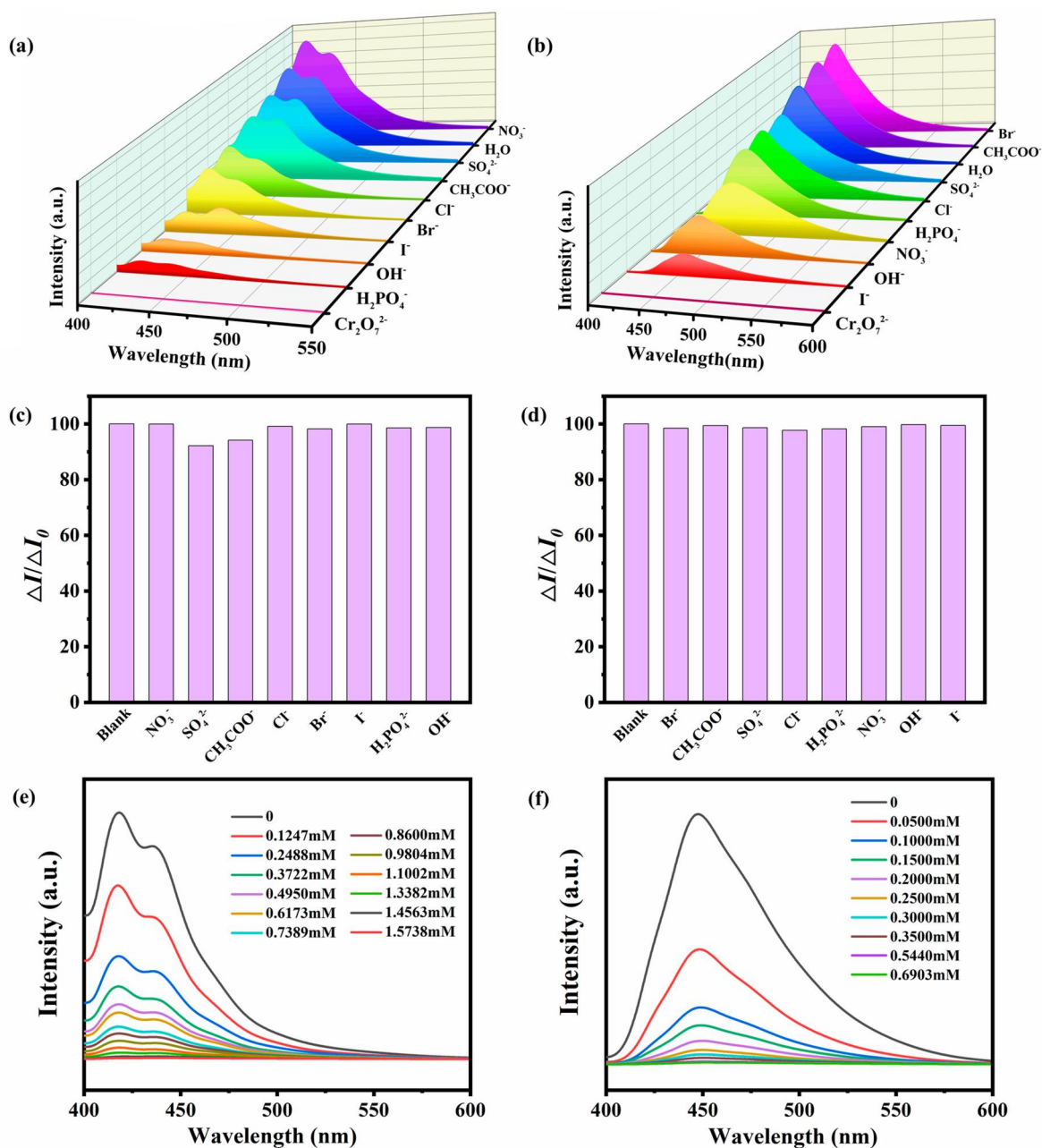


Figure 7. Emission spectra of (a) **1** and (b) **2** dispersed in aqueous solutions of various anions, fluorescence change ratio ($\Delta I/\Delta I_0$) histograms of (c) **1** and (d) **2** in the presence of aqueous Cr₂O₇²⁻ and various competing substances, and emission spectra of (e) **1** and (f) **2** dispersed in water with different concentrations of Cr₂O₇²⁻.

Sensing Mechanism. In comparison with the cited references (Table 1), the quenching constants in this work are shown to be greater than or equal to those in the literature, and the detection limits are less or equal, which is beneficial for the detection of low concentrations of harmful chemicals. Moreover, our compounds can also detect three harmful substances. In summary, these substances are excellent multiresponsive fluorescent sensing functional materials.

To gain deeper insight into the mechanisms of luminescence quenching induced by NB, Fe³⁺, and Cr₂O₇²⁻, further characterizations including PXRD and UV–visible absorption spectroscopy were performed. The PXRD patterns revealed that the frameworks of compounds **1** and **2** did not change after sensing in comparison with the original framework (Figure S9), suggesting that the luminescence quenching

cannot be ascribed to framework collapse. When the structural features of **1** and **2** are considered, incorporation of NB molecules into the framework pores is impossible due to the lack of porosity. Consequently, the sensing mechanisms of **1** and **2** would not be guest-induced quenching where the analyte molecules exist in the pores as a guest and interact directly with the fluorophore.³¹ It is noteworthy that the finely ground particles of **1** and **2** could be well dispersed in the analyte solution, which enables the NB molecules to closely adsorb onto the particle surfaces and facilitate possible host–guest interactions to a large extent. As a result, the fluorescence responses of **1** and **2** toward NB may be ascribable to an electron transfer quenching mechanism, where the excited electrons in the framework transfer to the strongly absorbent electron nitro group in NB.³²

The fluorescence quenching caused by Fe^{3+} ions can be mainly ascribed to metal cationic exchange, collapse of the framework, or competitive absorption between Fe^{3+} ions and the framework. Apparently, it is extremely difficult for the neutral frameworks of **1** and **2** to capture Fe^{3+} ions through cationic exchange according to the discussed PXRD results. Aqueous solutions with different metal ions $[\text{M}(\text{NO}_3)_x]$ were investigated by UV–visible absorption spectra (Figure S19). Notably, the spectra showed partial overlap between the excitation spectra of the compounds and the broad absorption band of Fe^{3+} from 240 to 600 nm, while no overlap was observed in the same wavelength range for other metal ions. For $\text{Cr}_2\text{O}_7^{2-}$ ions, as shown in Figure S20, the UV–visible absorption spectra of $\text{Cr}_2\text{O}_7^{2-}$ solutions also partially overlap with the excitation spectra of compounds **1** and **2**, while there was no clear overlap for solutions of other anions. Thus, these results indicate that the fluorescence quenching induced by Fe^{3+} and/or $\text{Cr}_2\text{O}_7^{2-}$ ions could be caused by a competitive absorption mechanism, as reported in the literature.³³

CONCLUSIONS

In summary, three luminescent CPs (**1–3**) based on d^{10} metal centers (Ag^+), dye molecules (bztpy and bpa), and auxiliary ligands were successfully synthesized and structurally characterized. The framework stability and fluorescence properties of the three synthetic compounds were investigated. Importantly, **1** and **2** can retain their intrinsic crystal structures under different conditions and exhibit obvious fluorescence quenching with a highly selective and sensitive effect toward NB, Fe^{3+} , and $\text{Cr}_2\text{O}_7^{2-}$ in aqueous solutions. Overall, the successful assembly of these compounds provides valuable guidelines for the design of Ag-CPs for excellent multiresponsive fluorescence-sensing functional materials.

ASSOCIATED CONTENT

Supporting Information

The Supporting Information is available free of charge at <https://pubs.acs.org/doi/10.1021/acs.inorgchem.0c02853>.

PXRD and TGA measurements, emission decay curves and IR spectra, observed luminescence of the crystals, diagram and table showing structural details of **1–3**, and supplementary fluorescence-sensing data for **1** and **2** (PDF)

Accession Codes

CCDC 2027402–2027404 contain the supplementary crystallographic data for this paper. These data can be obtained free of charge via www.ccdc.cam.ac.uk/data_request/cif, or by emailing data_request@ccdc.cam.ac.uk, or by contacting The Cambridge Crystallographic Data Centre, 12 Union Road, Cambridge CB2 1EZ, UK; fax: +44 1223 336033.

AUTHOR INFORMATION

Corresponding Authors

Chun-Lin Ni – Key Laboratory for Biobased Materials and Energy of Ministry of Education, College of Materials and Energy, South China Agricultural University, Guangzhou 510642, People's Republic of China; Email: niclchem@scau.edu.cn

Wei Liu – Key Laboratory for Biobased Materials and Energy of Ministry of Education, College of Materials and Energy, South China Agricultural University, Guangzhou 510642,

People's Republic of China; orcid.org/0000-0003-0101-5792; Email: liuwei97@scau.edu.cn

Authors

Cong-Cong Chen – Key Laboratory for Biobased Materials and Energy of Ministry of Education, College of Materials and Energy, South China Agricultural University, Guangzhou 510642, People's Republic of China

Yue Cai – Key Laboratory for Biobased Materials and Energy of Ministry of Education, College of Materials and Energy, South China Agricultural University, Guangzhou 510642, People's Republic of China

Long-Fei Wang – Key Laboratory of Bioinorganic and Synthetic Chemistry of Ministry of Education, School of Chemistry, Sun Yat-Sen University, Guangzhou 510275, People's Republic of China

Yun-Dang Wu – National-Regional Joint Engineering Research Center for Soil Pollution Control and Remediation in South China, Guangdong Key Laboratory of Integrated Agro-environmental Pollution Control and Management, Institute of Eco-environmental and Soil Sciences, Guangdong Academy of Sciences, Guangzhou 510650, People's Republic of China; orcid.org/0000-0003-2996-5407

Hao-Jun Yin – Key Laboratory for Biobased Materials and Energy of Ministry of Education, College of Materials and Energy, South China Agricultural University, Guangzhou 510642, People's Republic of China

Jia-Rong Zhou – Key Laboratory for Biobased Materials and Energy of Ministry of Education, College of Materials and Energy, South China Agricultural University, Guangzhou 510642, People's Republic of China

Complete contact information is available at: <https://pubs.acs.org/doi/10.1021/acs.inorgchem.0c02853>

Notes

The authors declare no competing financial interest.

ACKNOWLEDGMENTS

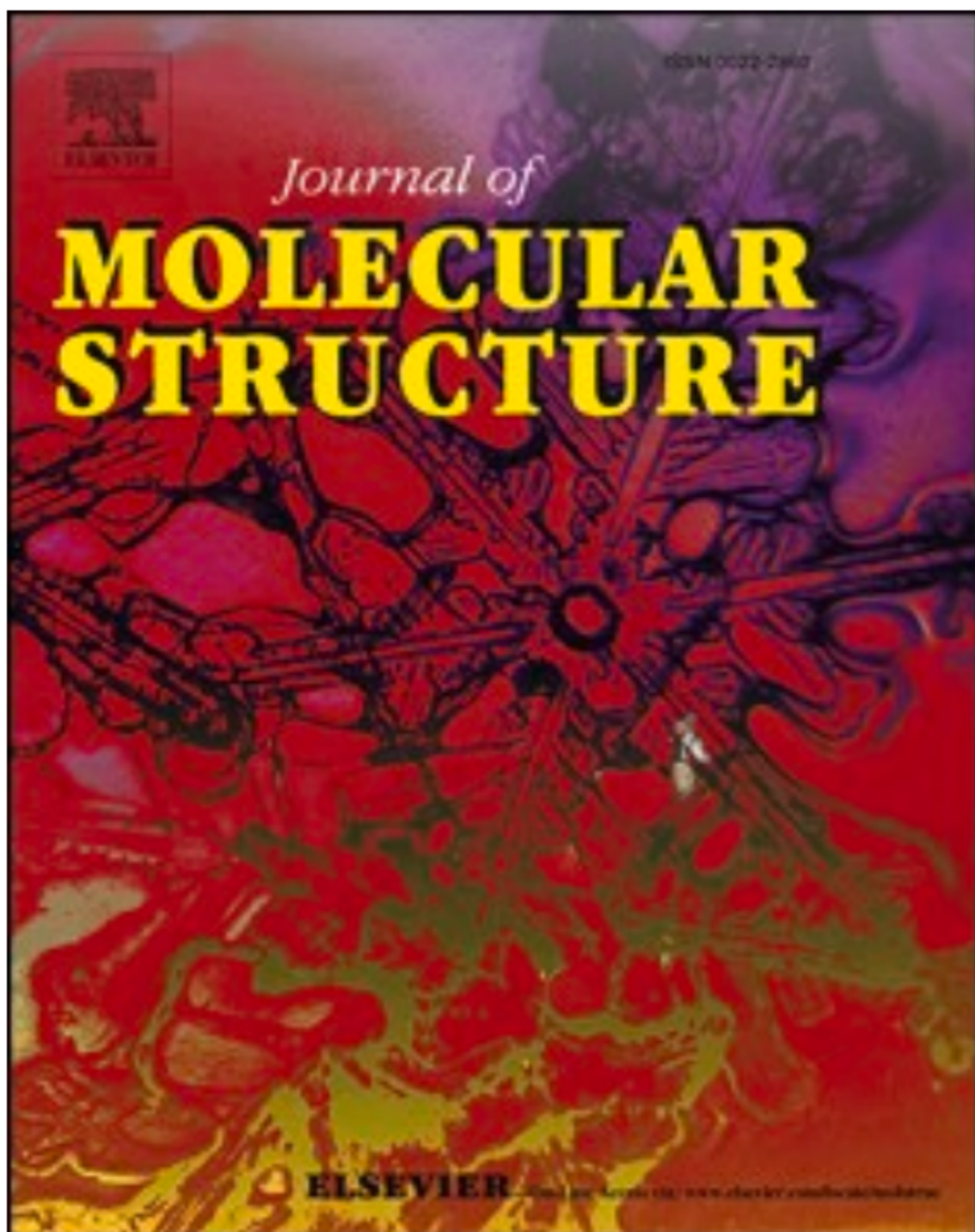
This work was supported by the NSFC (Grant No. 21701045).

REFERENCES

- (1) (a) Canary, J. W.; Mortezaei, S.; Liang, J. Transition metal-based chiroptical switches for nanoscale electronics and sensors. *Coord. Chem. Rev.* **2010**, 254, 2249–2266. (b) Li, B.; Wen, H.; Cui, Y.; Zhou, W.; Qian, G.; Chen, B. Emerging multifunctional metal-organic framework materials. *Adv. Mater.* **2016**, 28, 8819–8860. (c) Li, X.; Li, Y.; Yang, Y.; Hou, L.; Wang, Y.; Zhu, Z. Efficient light hydrocarbon separation and CO_2 capture and conversion in a stable MOF with oxalamide-decorated polar tubes. *Chem. Commun.* **2017**, 53, 12970–12973.
- (2) (a) Gücüyener, C.; Den Bergh, J. V.; Gascon, J.; Kapteijn, F. Ethane/ethene separation turned on its head: selective ethane adsorption on the metal-organic framework ZIF-7 through a gate-opening mechanism. *J. Am. Chem. Soc.* **2010**, 132, 17704–17706. (b) Chen, K.; Madden, D.; Pham, T.; Forrest, K.; Kumar, A.; Yang, Q.; Xue, W.; Space, B.; Perry, J., IV; Zhang, J.; Chen, X.; Zaworotko, M. Tuning pore size in square-lattice coordination networks for size-selective sieving of CO_2 . *Angew. Chem., Int. Ed.* **2016**, 55, 10268–10272. (c) Baumann, A. E.; Burns, D. A.; Liu, B.; Thoi, V. S. Metal-organic framework functionalization and design strategies for advanced electrochemical energy storage devices. *Commun. Chem.* **2019**, 2, 86. (d) Lin, R.; Xiang, S.; Xing, H.; Zhou, W.; Chen, B. Exploration of porous metal-organic frameworks for gas separation and purification. *Coord. Chem. Rev.* **2019**, 378, 87–103.

- (3) (a) Cadiau, A.; Adil, K.; Bhatt, P. M.; Belmabkhout, Y.; Eddaoudi, M. A metal-organic framework-based splitter for separating propylene from propane. *Science* **2016**, 353, 137–140. (b) Liao, P.; Huang, N.; Zhang, W.; Zhang, J.; Chen, X. Controlling guest conformation for efficient purification of butadiene. *Science* **2017**, 356, 1193–1196. (c) Ban, Y.; Zhao, M.; Yang, W. Metal-organic framework-based CO₂ capture: From precise material design to high-efficiency membranes. *Front. Chem. Sci. Eng.* **2020**, 14, 123–126.
- (4) (a) Yoon, M.; Srirambalaji, R.; Kim, K. Homochiral metal-organic frameworks for asymmetric heterogeneous catalysis. *Chem. Rev.* **2012**, 112, 1196–1231. (b) Kang, Y.; Lu, Y.; Chen, K.; Zhao, Y.; Wang, P.; Sun, W. Metal-organic frameworks with catalytic centers: From synthesis to catalytic application. *Coord. Chem. Rev.* **2019**, 378, 262–280. (c) Yuan, G.; Jiang, H.; Zhang, L.; Liu, Y.; Cui, Y. Metallosalen-based crystalline porous materials: Synthesis and property. *Coord. Chem. Rev.* **2019**, 378, 483–499. (d) Wu, J.; Hou, S.; Zhang, X.; Xu, M.; Yang, H.; Cao, P.; Gu, Z. Cathodized copper porphyrin metal-organic framework nanosheets for selective formate and acetate production from CO₂ electroreduction. *Chem. Sci.* **2019**, 10, 2199–2205.
- (5) (a) Zhao, X.; Wang, S.; Zhang, L.; Liu, S.; Yuan, G. 8-Hydroxyquinolate-based metal-organic frameworks: Synthesis, tunable luminescent properties, and highly sensitive detection of small molecules and metal ions. *Inorg. Chem.* **2019**, 58, 2444–2453. (b) Heine, J.; Müller-Buschbaum, K. Engineering metal-based luminescence in coordination polymers and metal-organic frameworks. *Chem. Soc. Rev.* **2013**, 42, 9232–9242. (c) Wu, Z.; Tan, B.; Velasco, E.; Wang, H.; Shen, N.; Gao, Y.; Zhang, X.; Zhu, K.; Zhang, G.; Liu, Y.; Hei, X.; Huang, X.; Li, J. Fluorescent in based MOFs showing “turn on” luminescence towards thiols and acting as a ratiometric fluorescence thermometer. *J. Mater. Chem. C* **2019**, 7, 3049–3055. (d) Mi, X.; Sheng, D.; Yu, Y.; Wang, Y.; Zhao, L.; Lu, J.; Li, Y.; Li, D.; Dou, J.; Duan, J.; Wang, S. Tunable light emission and multiresponsive luminescent sensitivities in aqueous solutions of two series of lanthanide metal-organic frameworks based on structurally related ligands. *ACS Appl. Mater. Interfaces* **2019**, 11, 7914–7926. (e) Li, B.; Zang, S.; Ji, C.; Hou, H.; Mak, T. C. W. Syntheses, structures, and properties of silver-organic frameworks constructed with 1,1-biphenyl-2,2',6,6'-tetracarboxylic Acid. *Cryst. Growth Des.* **2012**, 12, 1443–1451. (f) Gan, X.; Yu, R.; Chen, X.; Yang, M.; Lin, L.; Wu, X.; Lu, C. Unique tetranuclear Ag(I) complex emitting efficient thermally activated delayed fluorescence with a remarkably short decay time. *Dalton Trans.* **2018**, 47, 5956–5960. (g) Liu, X.; Guo, G. C.; Fu, M. L.; Liu, X. H.; Wang, M. S.; Huang, J. S. Three novel silver complexes with ligand-unsupported argentophilic interactions and their luminescent properties. *Inorg. Chem.* **2006**, 45, 3679–3685. (h) Li, T.; Huang, X.; Zhao, Y.; Li, H.; Wu, S.; Huang, C. An unusual double T5(2) water tape trapped in silver(I) coordination polymer hosts: influence of the solvent on the assembly of Ag(I)-4,4'-bipyridine chains with trans-cyclohexanedicarboxylate and their luminescent properties. *Dalton Trans.* **2012**, 41, 12872–12881.
- (6) (a) Zhao, H.; Ni, J.; Zhang, J.; Liu, S.; Sun, Y.; Zhou, H.; Li, Y.; Duan, C. A trichromatic MOF composite for multidimensional ratiometric luminescent sensing. *Chem. Sci.* **2018**, 9, 2918–2926. (b) Zhan, Z.; Liang, X.; Zhang, X.; Jia, X.; Hu, M. A water-stable europium-MOF as a multifunctional luminescent sensor for some trivalent metal ions (Fe³⁺, Cr³⁺, Al³⁺), PO₄³⁻ ions, and nitroaromatic explosives. *Dalton Trans.* **2019**, 48, 1786–1794. (c) Wu, S.; Min, H.; Shi, W.; Cheng, P. Multicenter metal-organic framework-based ratiometric fluorescent Sensors. *Adv. Mater.* **2020**, 32, 1805871. (d) Zhang, M.; Zheng, Y.; Liu, M.; Ren, Y.; Wang, Z.; Cao, J.; Wang, J. Two zinc(II) coordination polymers based on flexible co-ligands featuring assembly imparted sensing abilities for Cr₂O₇²⁻ and o-NP. *RSC Adv.* **2019**, 9, 21086–21094. (e) Zhang, Q.; Wang, J.; Kirillov, A.; Dou, W.; Xu, C.; Xu, C.; Yang, L.; Fang, R.; Liu, W. Multifunctional Ln-MOF luminescent probe for efficient sensing of Fe³⁺, Ce³⁺, and acetone. *ACS Appl. Mater. Interfaces* **2018**, 10, 23976–23986.
- (7) (a) Chen, B.; Wang, L.; Xiao, Y.; Fronczek, F. R.; Xue, M.; Cui, Y.; Qian, G. A luminescent metal-organic framework with Lewis basic pyridyl sites for the sensing of metal ions. *Angew. Chem., Int. Ed.* **2009**, 48, 500–503. (b) Wang, J.; Gao, L.; Zhang, J.; Zhao, L.; Wang, X.; Niu, X.; Fan, L.; Hu, T. Syntheses, gas adsorption, and sensing properties of solvent-controlled Zn(II) pseudo-supramolecular isomers and Pb(II) supramolecular isomers. *Cryst. Growth Des.* **2019**, 19, 630–637. (c) Dutta, P.; Chakravarty, S.; Sarma, N. S. Detection of nitroaromatic explosives using pi-electron rich luminescent polymeric nanocomposites. *RSC Adv.* **2016**, 6, 3680–3689. (d) Yang, L.; Lian, C.; Li, X.; Hang, Y.; Yang, L.; Cai, T.; Shao, C. Highly selective bifunctional luminescent sensor toward nitrobenzene and Cu²⁺ ion based on microporous metal-organic frameworks: synthesis, structures, and properties. *ACS Appl. Mater. Interfaces* **2017**, 9, 17208–17217. (e) Tong, W.; Liu, W.; Cheng, J.; Zhang, P.; Li, G.; Hou, L.; Wang, Y. A new stable luminescent Cd(II) metal-organic framework with fluorescent sensing and selective dye adsorption properties. *Dalton Trans.* **2018**, 47, 9466–9473. (f) Han, Z.; Wang, K.; Guo, Y.; Chen, W.; Zhang, J.; Zhang, X.; Siligardi, G.; Yang, S.; Zhou, Z.; Sun, P.; Shi, W.; Chen, P. Cation-induced chirality in a bifunctional metal-organic framework for quantitative enantioselective recognition. *Nat. Commun.* **2019**, 10, 5117. (g) Lv, R.; Li, H.; Su, J.; Fu, X.; Yang, B.; Gu, W.; Liu, X. Zinc metal-organic framework for selective detection and differentiation of Fe(III) and Cr(VI) ions in aqueous solution. *Inorg. Chem.* **2017**, 56, 12348–12356.
- (8) Hao, Z.; Song, X.; Zhu, M.; Meng, X.; Zhao, S.; Su, S.; Yang, W.; Song, S.; Zhang, H. One-dimensional channel-structured Eu-MOF for sensing small organic molecules and Cu²⁺ ion. *J. Mater. Chem. A* **2013**, 1, 11043–11050.
- (9) Nagarkar, S. S.; Joarder, B.; Chaudhari, A. K.; Mukherjee, S.; Ghosh, S. K. Highly selective detection of nitro explosives by a luminescent metal-organic framework. *Angew. Chem.* **2013**, 125, 2953–2957.
- (10) (a) Andrews, N. C. Medical progress: Disorders of iron metabolism. *N. Engl. J. Med.* **1999**, 341, 1986–1995. (b) Haas, J. D.; Brownlie, T. Iron deficiency and reduced work capacity: A critical review of the research to determine a causal relationship. *J. Nutr.* **2001**, 131, 676S–688S.
- (11) (a) Wen, L.; Zheng, X.; Lv, K.; Wang, C.; Xu, X. Two amino-decorated metal-organic frameworks for highly selective and quantitatively sensing of Hg-II and Cr-VI in aqueous solution. *Inorg. Chem.* **2015**, 54, 7133–7135. (b) Guo, X.; Zhao, F.; Liu, J.; Liu, Z.; Wang, Y. An ultrastable zinc(II)-organic framework as a recyclable multi-responsive luminescent sensor for Cr(III), Cr(VI) and 4-nitrophenol in the aqueous phase with high selectivity and sensitivity. *J. Mater. Chem. A* **2017**, 5, 20035–20043.
- (12) Elrod, V. A.; Johnson, K. S.; Coale, K. H. Determination of subnanomolar levels of iron (II) and total dissolved iron in seawater by flow injection and analysis with chemiluminescence detection. *Anal. Chem.* **1991**, 63, 893–898.
- (13) Tesfaldet, Z. O.; van Staden, J. F.; Stefan, R. I. Sequential injection spectrophotometric determination of iron as Fe(II) in multivitamin preparations using 1,10-phenanthroline as complexing agent. *Talanta* **2004**, 64, 1189–1195.
- (14) Akatsuka, K.; McLaren, J. W.; Lam, J. W.; Berman, S. S. Determination of iron and ten other trace elements in the Open Ocean Seawater reference material NASS-3 by inductively coupled plasma mass spectrometry. *J. Anal. At. Spectrom.* **1992**, 7, 889–894.
- (15) (a) Liu, W.; Chen, C.; Mao, L.; Wu, S.; Wang, L.; Tong, M. Tuning the net topology of a ternary Ag(i)-1,2,4,5-tetra(4-pyridyl)-benzene-carboxylate framework: structures and photoluminescence. *CrystEngComm* **2019**, 21, 6446–6451. (b) Chang, Y.; Wang, S. From stimuli-responsive polymorphic organic dye crystals to photoluminescent cationic open-framework metal phosphate. *J. Am. Chem. Soc.* **2012**, 134, 9848–9851. (c) Meneses-Sánchez, M.; Piñero-López, L.; Delgado, T.; Bartual-Murgui, C.; Muñoz, M. C.; Chakraborty, P.; Real, J. A. Extrinsic vs. intrinsic luminescence and their interplay with spin crossover in 3D Hofmann-type coordination polymers. *J. Mater. Chem. C* **2020**, 8, 1623–1633.

- (16) Sheldrick, G. M. SHELXT-Integrated space-group and crystal-structure determination. *Acta Crystallogr.* **2015**, *C71*, 3–8.
- (17) Blatov, V. Nanocluster analysis of intermetallic structures with the program package TOPOS. *Struct. Chem.* **2012**, *23*, 955–963.
- (18) Liu, B.; Lin, X.; Li, H.; Li, K.; Huang, H.; Bai, L.; Hu, H.; Liu, Y.; Kang, Z. Luminescent coordination polymers for highly sensitive detection of nitrobenzene. *Cryst. Growth Des.* **2015**, *15*, 4355–4362.
- (19) (a) Zhao, J.; Wang, Y.; Dong, W.; Wu, Y.; Li, D.; Zhang, Q. A robust luminescent Tb(III)-MOF with Lewis basic pyridyl sites for the highly sensitive detection of metal ions and small molecules. *Inorg. Chem.* **2016**, *55*, 3265–3271. (b) Wei, Z.; Gu, Z.; Arvapally, R. K.; Chen, Y.; McDougald, R. N.; Ivy, J. F.; Yakovenko, A. A.; Feng, D. W.; Omary, M. A.; Zhou, H. Rigidifying fluorescent linkers by metal-organic framework formation for fluorescence blue shift and quantum yield enhancement. *J. Am. Chem. Soc.* **2014**, *136*, 8269–8276. (c) Chen, B.; Wang, L.; Zapata, F.; Qian, G.; Lobkovsky, E. B. A luminescent microporous metal-organic framework for the recognition and sensing of anions. *J. Am. Chem. Soc.* **2008**, *130*, 6718–6719.
- (20) Nakatsui, S.; Matsuda, K.; Uesugi, Y.; Nakashima, K.; Akiyama, S.; Fabian, W. Synthesis and absorption/emission spectroscopic properties of bis(phenylethynyl)benzenes and 9,10-bis(phenylethynyl)anthracenes. *J. Chem. Soc., Perkin Trans. 1* **1992**, 755–758.
- (21) (a) Zhang, L.; Ma, J.; Yang, J.; Pang, Y.; Ma, J. Series of 2D and 3D coordination polymers based on 1,2,3,4-benzenetetracarboxylate and N-donor ligands: Synthesis, topological structures, and photoluminescent properties. *Inorg. Chem.* **2010**, *49*, 1535–1550. (b) Yang, Y.; Shen, K.; Lin, J.; Zhou, Y.; Liu, Q.; Hang, C.; Abdelhamid, H. N.; Zhang, Z.; Chen, H. A Zn-MOF constructed from electron-rich pi-conjugated ligands with an interpenetrated graphene-like net as an efficient nitroaromatic sensor. *RSC Adv.* **2016**, *6*, 45475–45481. (c) Vogler, A.; Kunkely, H. Ligand-to-ligand and intraligand charge transfer and their relation to charge transfer interactions in organic zwitterions. *Coord. Chem. Rev.* **2007**, *251*, 577–583.
- (22) (a) Chen, Z.; Zhao, N.; Fan, Y.; Ni, J. Luminescent groups 10 and 11 heteropolynuclear complexes based on thiolate or alkynyl ligands. *Coord. Chem. Rev.* **2009**, *253*, 1–20. (b) Che, C.; Lai, S. Structural and spectroscopic evidence for weak metal–metal interactions and metal–substrate exciplex formations in d10 metal complexes. *Coord. Chem. Rev.* **2005**, *249*, 1296–1309. (c) Valeur, B.; Berberan-Santos, M. N. *Molecular Fluorescence: Principles and Applications*, 2nd ed.; Wiley-VCH: 2012. (d) Allendorf, M. D.; Bauer, C.; Bhakta, R.; Houk, R. Luminescent metal-organic frameworks. *Chem. Soc. Rev.* **2009**, *38*, 1330–1352.
- (23) Zhang, S.; Liang, H.; Liu, C. Increased D-1(2) red emission of Pr³⁺ in NaGdTiO₄:Pr³⁺ due to temperature-assisted host sensitization and its color variation. *J. Phys. Chem. C* **2013**, *117*, 2216–2221.
- (24) Jin, S.; Son, H.; Farha, O. K.; Wiederrecht, G. P.; Hupp, J. T. Energy transfer from quantum dots to metal-organic frameworks for enhanced light harvesting. *J. Am. Chem. Soc.* **2013**, *135*, 955–958.
- (25) (a) Wang, B.; Lv, X.; Feng, D.; Xie, L.; Zhang, Z.; Li, M.; Xie, Y.; Li, J.; Zhou, H. Highly stable Zr(IV)-based metal-organic frameworks for the detection and removal of antibiotics and organic explosives in water. *J. Am. Chem. Soc.* **2016**, *138*, 6204–6216. (b) Lazarovici, D.; Pickl, P. A mean field limit for the Vlasov-Poisson system. *Arch. Ration. Mech. Anal.* **2017**, *225*, 1201–1231.
- (26) (a) Wang, H.; Cheng, F.; Zou, C.; Li, Q.; Hua, Y.; Duan, J.; Jin, W. Design and synthesis of luminescent porous coordination polymers for chromaticity modulation, sensing of nitrobenzene and iodine encapsulation. *CrystEngComm* **2016**, *18*, 5639–5646. (b) Yan, Y.; Liu, J.; Yang, G.; Zhang, F.; Fan, Y.; Zhang, W.; Wang, Y. Highly selective luminescence sensing for the detection of nitrobenzene and Fe³⁺ by new Cd(II)-based MOFs. *CrystEngComm* **2018**, *20*, 477–486. (c) Wang, S.; Cao, T.; Yan, H.; Li, Y.; Lu, J.; Ma, R.; Li, D.; Dou, J.; Bai, J. Functionalization of microporous lanthanide-based metal-organic frameworks by dicarboxylate ligands with methyl-substituted thieno[2,3-*b*]thiophene groups: Sensing activities and magnetic properties. *Inorg. Chem.* **2016**, *55*, 5139–5151.
- (27) (a) Zhang, Y.; Blatov, V. A.; Zheng, T.; Yang, C.; Qian, L.; Li, K.; Li, B.; Wu, B. A luminescent zinc(II) coordination polymer with unusual (3,4,4)-coordinated self-catenated 3D network for selective detection of nitroaromatics and ferric and chromate ions: a versatile luminescent sensor. *Dalton Trans.* **2018**, *47*, 6189–6198. (b) Liu, Z.; Zhao, Y.; Zhang, X.; Kang, Y.; Lu, Q.; Azam, M.; Al-Resayes, S. I.; Sun, W. Metal-organic frameworks with 1, 4-di(1 H-imidazol-4-yl)benzene and varied carboxylate ligands for selectively sensing Fe(III) ions and ketone molecules. *Dalton Trans.* **2017**, *46*, 13943–13951. (c) Xu, N.; Zhang, Q.; Hou, B.; Cheng, Q.; Zhang, G. A novel magnesium metal-organic framework as a multiresponsive luminescent sensor for Fe(III) ions, pesticides, and antibiotics with high selectivity and sensitivity. *Inorg. Chem.* **2018**, *57*, 13330–13340.
- (28) Zhao, X.; Tian, D.; Gao, Q.; Sun, H.; Xu, J.; Bu, X. A chiral lanthanide metal-organic framework for selective sensing of Fe(III) ions. *Dalton Trans.* **2016**, *45*, 1040–1046.
- (29) Hou, B.-L.; Tian, D.; Liu, J.; Dong, L.-Z.; Li, S.-L.; Li, D.-S.; Lan, Y.-Q. A water-stable metal-organic framework for highly sensitive and selective sensing of Fe³⁺ ion. *Inorg. Chem.* **2016**, *55*, 10580–10586.
- (30) (a) Xu, S.; Shi, J.; Ding, B.; Liu, Z.; Wang, X.; Zhao, X.; Yang, E. A heterometallic sodium(I)-europium(III)-organic layer exhibiting dual-responsive luminescent sensing for nitrofurantoin antibiotics, Cr₂O₇²⁻ and MnO₄⁻ anions. *Dalton Trans.* **2019**, *48*, 1823–1834. (b) Yao, Z.; Li, G.; Xu, J.; Hu, T.; Bu, X. A water-stable luminescent Zn^{II} metal-organic framework as chemosensor for high-efficiency detection of Cr^{VI}-Anions (Cr₂O₇²⁻ and CrO₄²⁻) in aqueous solution. *Chem. - Eur. J.* **2018**, *24*, 3192–3198. (c) Zhu, Z.; Wang, M.; Xu, C.; Zong, Z.; Zhang, D.; Bi, S.; Fan, Y. A multifunctional three-fold interpenetrated coordination polymer showing excellent luminescent sensing for Cr(VI)/Fe(III) and photocatalytic properties. *J. Solid State Chem.* **2017**, *256*, 176–183.
- (31) (a) Nagarkar, S. S.; Joarder, B.; Chaudhari, A. K.; Mukherjee, S.; Ghosh, S. K. Highly Selective Detection of Nitro Explosives by a Luminescent Metal-Organic Framework. *Angew. Chem., Int. Ed.* **2013**, *52*, 2881–2957. (b) Pramanik, S.; Zheng, C.; Zhang, X.; Emge, T. J.; Li, J. New microporous metal-organic framework demonstrating unique selectivity for detection of high explosives and aromatic compounds. *J. Am. Chem. Soc.* **2011**, *133*, 4153–4155.
- (32) (a) Tian, D.; Li, Y.; Chen, R.; Chang, Z.; Wang, G.; Bu, X. A luminescent metal-organic framework demonstrating ideal detection ability for nitroaromatic explosives. *J. Mater. Chem. A* **2014**, *2*, 1465–1470. (b) Sun, Z.; Sun, J.; Xi, L.; Xie, J.; Wang, X.; Ma, Y.; Li, L. Two novel lanthanide metal-organic frameworks: selective luminescent sensing for nitrobenzene, Cu²⁺, and MnO₄⁻. *Cryst. Growth Des.* **2020**, *20*, 5225–5234. (c) Zheng, H.; Deng, Y.; Ye, M.; Xu, Q.; Kong, X.; Long, L.; Zheng, L. Lanthanide-titanium Oxo clusters as the luminescence sensor for nitrobenzene detection. *Inorg. Chem.* **2020**, *59*, 12404–12409.
- (33) (a) Li, Y.; Song, H.; Chen, Q.; Liu, K.; Zhao, F.; Ruan, W.; Chang, Z. Two coordination polymers with enhanced ligand-centered luminescence and assembly imparted sensing ability for acetone. *J. Mater. Chem. A* **2014**, *2*, 9469–9473. (b) Wei, R.; Wei, Z.; Sun, L.; Zhang, J.; Liu, J.; Ge, X.; Shi, L. Nile red derivative-modified nanostructure for upconversion luminescence sensing and intracellular detection of Fe³⁺ and MR imaging. *ACS Appl. Mater. Interfaces* **2016**, *8*, 400–410. (c) Goswami, R.; Mandal, S.; Pathak, B.; Neogi, S. Guest-induced ultrasensitive detection of multiple toxic organics and Fe³⁺ ions in a strategically designed and regenerative smart fluorescent metal-organic framework. *ACS Appl. Mater. Interfaces* **2019**, *11*, 9042–9053. (d) Xu, M.; Kong, X.; He, T.; Wu, X.; Xie, L.; Li, J. A stable Zr(IV)-based metal-organic framework constructed from C≡C bridged di-isophthalate ligand for sensitive detection of Cr₂O₇²⁻ in Water. *Inorg. Chem.* **2018**, *57*, 14260–14268.



Actions for 1 selected article

[Select all](#) / [Deselect all](#)

Download PDF



Export citation



Show all article previews

Contents

Articles

Elaine Aktebramm-Denkora, Hamed Ghoshdini, Pooneh Koochaki, Monser Estima-Denkora, ... Nina Rezaei

Article 135642

[View PDF](#)

Article preview ▾



Research article • Full text access

Synthesis of 2,3-dihydroquinazolin-4(1H)-one derivatives as potential inhibitors of TNF- α

G. Dhananjaya, Rapolu Venkateshwarlu, M.V. Madhubabu, Akula Raghunadh, ... Manojit Pal

Article 135668

[View PDF](#)

Article preview ▾



Research article • Full text access

Effects of different dithiolate ligands on electrocatalytic hydrogen production of nickel complexes in acetic acid or water

Hao-Jun Yin, Zhi-Hao Gan, Zong Wang, Xiao-Ting Zheng, ... Wei Liu

Article 135659

[View PDF](#)

Article preview ▾



Research article • Full text access

Identification of potential N-substituted 5-benzylidenethiazolidine-2,4-dione derivatives as α -amylase inhibitors: Computational cum synthetic studies

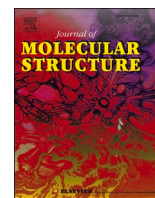
Shankar Gupta, Gurkaran Singh Baweja, GD Gupta, Vivek Asati

Article 135596

[View PDF](#)

Article preview ▾





Effects of different dithiolate ligands on electrocatalytic hydrogen production of nickel complexes in acetic acid or water

Hao-Jun Yin, Zhi-Hao Gan, Zong Wang, Xiao-Ting Zheng, Li-Yuan Huang, Yi-Chun Chen, Jia-Rong Zhou*, Chun-Lin Ni, Wei Liu*

Key Laboratory for Biobased Materials and Energy of Ministry of Education, College of Materials and Energy, South China Agricultural University, Guangzhou 510642, PR China

ARTICLE INFO

Keywords:

Nickel complexes
Dithiolate ligands
Catalytic activity
Water splitting
Hydrogen generation

ABSTRACT

In order to solve the problems of fossil energy depletion and environmental pollution, it is necessary to find new energy sources that are recyclable and environmentally friendly. Among them, hydrogen is a high calorific value, clean and sustainable energy. At present, hydrogen is mainly obtained by electrolysis of water. The use of electrocatalysts in this process can effectively reduce the consumption of electrical energy. In this study, three molecular electrocatalysts based on nickel complexes, $[\text{BzTPP}]_2[\text{Ni}(\text{mnt})_2]$ (1), $[\text{BzTPP}]_2[\text{Ni}(\text{i-mnt})_2]$ (2), and $[\text{BzTPP}]_2[\text{Ni}(\text{tdas})_2]$ (3) ($[\text{BzTPP}]^+ = 1$ -benzyltriphenylphosphonium, $\text{mnt} = 1,2$ -dicyanoethylene-1,2-dithiolate, $\text{i-mnt} = 1,1$ -dicyanoethylene-2,2-dithiolate and, $\text{tdas} = 1,2,5$ -thiadiazole-3,4-dithiolate), were systematically investigated. Electrochemical study showed three complexes can electrocatalyze hydrogen generation from acetic acid or aqueous buffer solution, and afford a turnover frequency (TOF) of 504.76, 591.52 and 1022.93 mol of hydrogen per mole of catalyst per hour at an overpotential (OP) of 0.838 V from a neutral buffer. It is shown that $[\text{Ni}^{\text{II}}(\text{tdas})_2]^{2-}$ exhibits higher electro-catalytic hydrogen production activity than $[\text{Ni}^{\text{II}}(\text{mnt})_2]^{2-}$ and $[\text{Ni}^{\text{II}}(\text{i-mnt})_2]^{2-}$. This provides a new chemical paradigm for the design and fabrication of efficient molecular catalysts for water reduction.

1. Introduction

Since the 21st century, the issue of energy crisis and environmental pollution has been the focus of global attention, the reduction of fossil resources and the resulting waste can cause extremely serious environmental problems [1]. Therefore, the development of pollution-free green new energy has become an important issue. Hydrogen energy has attracted widespread attention because its by-product is only water, which is environmentally friendly. At present, industrial hydrogen production is mainly through three methods: water splitting, methane steam reforming and coal gasification. Among them, the latter two methods still consume fossil fuels and emit large amounts of carbon dioxide. Only the method of producing hydrogen by splitting cheap water is considered as the lowest cost, environmentally friendly and most promising as a sustainable energy option [2]. However, water splitting is an energy-consuming reaction, and its energy conversion efficiency is very low, so catalysts are needed to increase the rate of hydrogen evolution reaction and reduce energy consumption. One of the

challenges in this direction is the development of catalysts with excellent stability and high catalytic efficiency [3,4]. Therefore, people strive to develop various effective metal-center complex catalysts such as manganese [5], nickel [6–9], cobalt [10–12] and copper [13–15] for the reduction of protons or water to form H_2 . They undergo proton reduction, in which proton shuttling by the ligand increases the reaction rate and reduces the overpotential [16]. With ligand-mediated electron transfer, it can enhance the catalysis and electron transfer of redox-active metal centers. Metal ions transfer electrons to the substrate and interact with the substrate during bond formation and breaking [17].

Among the highly efficient and stable catalysts, metal disulfide complexes are a promising electrocatalyst [18]. Disulfide refers to a molecular group in which two adjacent thiocarbonyl groups or a carbene are connected in sequence with two negatively charged sulfur atoms, and has delocalized π -electron characteristics. The negatively charged sulfur atom makes the dithione ligand have a strong coordination ability, which can form a planar stable structure with the transition

* Corresponding authors.

E-mail addresses: scauchem534@126.com (J.-R. Zhou), liuwei97@scau.edu.cn (W. Liu).

<https://doi.org/10.1016/j.molstruc.2023.135659>

Received 28 November 2022; Received in revised form 22 April 2023; Accepted 24 April 2023

Available online 29 April 2023

0022-2860/© 2023 Elsevier B.V. All rights reserved.

metal. Dithioene ligands enable reversible electron transfer with minimal structural perturbation and suppress hydrogenation. With these excellent properties, they are potential electron transfer catalysts in the proton reduction of H_2 [19]. Currently, nickel-based bis(benzenedithiocarbamate) (bdt) complexes and related Co complexes have been shown to be active for light-driven and electrocatalytic hydrogen production. There are a few reports on the donor type and the nature of the ligand that play an important role in determining the structure and reactivity of the corresponding metal complexes [20–22]. However, there is not much research on the catalytic properties of different complexes of the same metal with the same oxidation state. Due to its highly delocalized π -electron system and special planar structure, and the diversity of disulfide ligands in the anionic part, combined with the properties of the central metal, the disulfide metal complex shows good performance in catalysis. Based on the above results, in this paper, three nickel complexes with different dithioene ligands and identical organic cation, $[BzTPP]_2[Ni(mnt)_2](1)$, $[BzTPP]_2[Ni(i-mnt)_2](2)$, and $[BzTPP]_2[Ni(tdas)_2](3)$ were used as molecular electrocatalysts to investigate electrocatalytic hydrogen production properties in acetic acid and water and the influence of different dithioene ligands on the catalytic efficiency in buffer solution.

2. Experimental

2.1. Materials and physical measurements

1-Benzyltriphenylphosphonium bromide was purchased from Aldrich and used without further purification. Disodium maleonitriledithiolate (Na_2mnt), dipotassium isomaltonitriledithiolate ($K_2(i-mnt)$) and disodium 1,2,5-thiadiazole-3,4-dithiolate (Na_2tdas) were synthesized following the literature procedures [23,24].

Elemental analyses (C, H and N) were recorded on a PerkinElmer PE 2400II CHNS/O organic element analyzer. Electrospray mass spectra (ESI-MS) were measured on AB SCIEX, API3200. Infrared spectra were recorded on a Nicolet Nexus 670 FT-IR spectrophotometer in the range 4000–400 cm^{-1} with the samples in the form of KBr pellets. UV–Vis spectra in CH_3CN were measured on a Japan Shimadzu Corporation UV-2550 spectrometer.

Electrochemical measurements were conducted on a CHI-660E electrochemical analyzer under N_2 using a three-electrode cell in which a glassy carbon electrode was the working electrode, an Ag/AgNO₃ (organic media) or a saturated Ag/AgCl (aqueous media) electrode was the reference electrode, and platinum wire was the auxiliary electrode. In organic media, a ferrocene/ferrocenium (1+) couple was used as an internal standard, and 0.10 mol·L⁻¹ [(n-Bu)₄N]ClO₄ was used as the supporting electrolyte. Controlled-potential electrolysis (CPE) in aqueous media was conducted using an air-tight glass double compartment cell separated by a glass frit. The working compartment was fitted with a glassy carbon plate and an Ag/AgCl reference electrode. The auxiliary compartment was fitted with a Pt gauze electrode. The working compartment was filled with 0.025 L of 0.25 mol·L⁻¹ phosphate buffer, the same auxiliary compartment. After adding 1, 2 or 3, cyclic voltammograms were recorded. After electrolysis, a 5.0×10^{-4} L aliquot of the headspace was removed and replaced with 5.0×10^{-4} L of CH_4 . The headspace sample was injected into the gas chromatograph (GC). GC experiments were carried out with an Agilent Technologies 7890A gas chromatography instrument.

2.2. Syntheses of complexes

$[BzTPP]_2[Ni(mnt)_2](1)$, $[BzTPP]_2[Ni(i-mnt)_2](2)$ and $[BzTPP]_2[Ni(tdas)_2](3)$ (mnt^{2-} = maleonitriledithiolate, $i-mnt^{2-}$ = isomaltonitriledithiolate, $tdas^{2-}$ = 1,2,5-thiadiazole-3,4-dithiolate) were prepared according to the reported methods [25–27]. Typically, the direct combination of 1:2:2 mol equiv of $NiCl_2 \cdot 6H_2O$, and the salt of dithiolate (Na_2mnt , $K_2(i-mnt)$ and Na_2tdas) and

1-benzyltriphenylphosphonium bromide in methanol affords three nickel(II) complexes (Scheme 1).

Yield: 87.6% for complex 1. Anal. calc. for $C_{58}H_{44}N_4NiP_2S_4$: C, 66.61; H, 4.24; N, 5.36%. Found: C, 66.54%; H, 4.32%; N, 5.27%.

Yield: 86.7% for complex 2. Anal. calc. for $C_{58}H_{44}N_4NiP_2S_4$: C, 66.61; H, 4.24; N, 5.36%. Found: C, 66.48%; H, 4.34%; N, 5.42%.

Yield: 85.4% for complex 3. Anal. Calc. for $C_{54}H_{44}N_4NiP_2S_6$: C, 61.08; H, 4.18; N, 5.28%. Found: C, 60.96; H, 4.27; N, 5.21%.

3. Results and discussion

3.1. General characterization

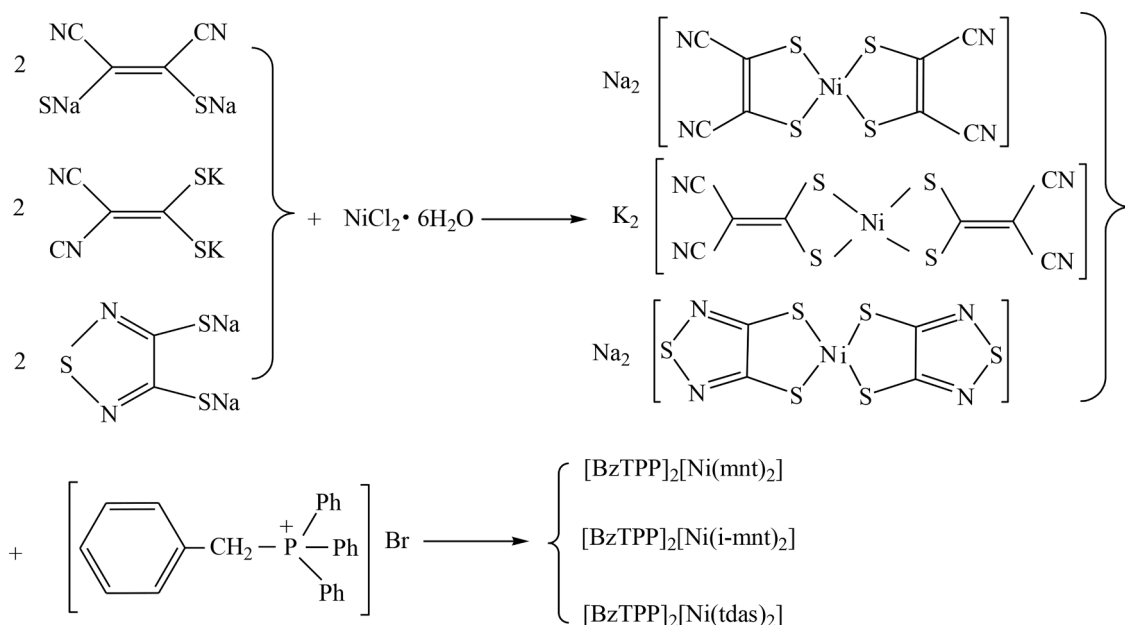
Three molecular catalysts, $[BzTPP]_2[Ni(mnt)_2](1)$, $[BzTPP]_2[Ni(i-mnt)_2](2)$ and $[BzTPP]_2[Ni(tdas)_2](3)$ were prepared by the direct reaction of $NiCl_2 \cdot 6H_2O$, Na_2dit (dit = maleonitriledithiolate, isomaltonitriledithiolate and 1,2,5-thiadiazole-3,4-dithiolate) and $[BzTPP]Br$ with molar ratio of 1: 2: 2 in methanol [25–27]. The three molecular catalysts were characterized by elemental analyses, FTIR, ESI-MS and UV–Vis spectra to confirming their formation.

It can be seen from the results given in the experimental section that the experimental values of elemental analysis (C, H and N) are in good agreement with the theoretical values by calculating from the corresponding molecular formula.

The FTIR spectra of complexes 1, 2 and 3 are shown Fig. S1. It can be seen that the C–H stretching vibrations of aromatic rings are at 3050 cm^{-1} (complex 1), 3060 cm^{-1} (complex 2), and 3059 cm^{-1} (complex 3). The asymmetric and symmetric C–H stretching vibrations of methylene are seen at 2931 and 2890 cm^{-1} (complex 1), 2928 and 2883 cm^{-1} (complex 2), as well as 2925 and 2885 cm^{-1} (complex 3), respectively. The $C \equiv N$ stretching vibration absorption peaks in the anions of 1 and 2 appear at 2192 cm^{-1} and 2200 cm^{-1} , respectively. The stretching vibrations of the C=C skeleton bond from benzene rings are at 1585 cm^{-1} and 1481 cm^{-1} (complex 1), 1595 cm^{-1} and 1492 cm^{-1} (complex 2), 1583 cm^{-1} and 1487 cm^{-1} (complex 3). The C=C stretching vibration peaks from the anion mnt^{2-} , $i-mnt^{2-}$ and $tdas^{2-}$ are at 1437 cm^{-1} , 1420 cm^{-1} , and 1439 cm^{-1} , respectively.

The negative-ion and positive-ion ESI-MS spectra of complexes 1, 2 and 3 in MeOH solution are shown in Figs. S2–S4. It is seen that the mass spectra in 1 (Fig. S2) are dominated by the peaks at 353.3(positive-ion) and 169.4(negative-ion), which are consistent with the calculated values (353.4 and 169.5) from corresponding chemical formula, and due to $[Ni(mnt)_2]^{2-}$ anion and $[BzTPP]^+$ cation. The ESI-MS spectra of 2 (Fig. S3) dominated by 353.3 (positive-ion) and 168.8(negative-ion) are attribute to $[BzTPP]^+$ and $[Ni(i-mnt)_2]^{2-}$. In complex 3, the peaks at 353.2 and 177.4 (Fig. S4) are assigned to $[BzTPP]^+$ and $[Ni(tdas)_2]^{2-}$.

To test properties of complexes 1, 2 and 3 in liquid, electronic spectra were measured in both organic and aqueous media. Fig. S5 is the UV–Vis spectra of the three complexes and their respective reactants. It can be seen from the figure that the absorption peaks of the functional groups of the three complexes roughly correspond to the absorption peaks of the respective reactants. The UV–Vis spectrum of 1 shows an absorption peak at 474 nm, which corresponds to a ligand-metal-charge-transition (LMCT) between the ligands and nickel ion. Complex 2 exhibits a LMCT at 453 nm. And complex 3 exhibits a LMCT at 440 nm. As shown in Fig. S6, in aqueous buffer at the pH range 2.0–11.0, the intensities of the absorption bands of complex 1 at 379 and 473 nm indeed changes, suggesting there are new components appear under these conditions, such as $[H-Ni(mnt)_2]^-$ or $[HO-Ni(mnt)_2]^{3-}$. From Fig. S7, the intensities of the absorption bands of complex 2 at 338 and 454 nm also changes with varying pH values, indicating there are new components appear under these conditions, such as $[H-Ni(i-mnt)_2]^-$ or $[HO-Ni(i-mnt)_2]^{3-}$. From Fig. S8, the intensities of the absorption bands of complex 3 at 315 and 430 nm also changes with varying pH values, indicating there are new components appear under these conditions, such as



Scheme 1. Schematic representation of the synthesis of 1, 2 and 3.

$[\text{H}-\text{Ni}(\text{tdas})_2]^-$ or $[\text{HO}-\text{Ni}(\text{tdas})_2]^{3-}$.

The molecular structures of the organic $[\text{BzTPP}]^+$ cation and $\text{Ni}(\text{mnt})_2^{2-}$, $[\text{Ni}(\text{i-mnt})_2]^{2-}$, $[\text{Ni}(\text{tdas})_2]^{2-}$ anions are shown in Fig. 1. Selected crystal data are listed in Table 1 according to our previous study [25–27]. It was found that compound 1 crystallized in monoclinic crystal system with a $P2_1/n$ space group, while compounds 2 and 3 belonged to the triclinic crystal system with $P-1$ or $C2/c$ space group. The NiS_4 core of the $[\text{Ni}(\text{mnt})_2]^{2-}$, $[\text{Ni}(\text{i-mnt})_2]^{2-}$, and $[\text{Ni}(\text{tdas})_2]^{2-}$ anion existed in a slightly distorted square-planar geometry in which Ni is coordinated by four S atoms from two mnt, i-mnt and tdas ligands, and provided the active center for hydrogen evolution reaction (HER).

3.2. Linear sweep voltammetry

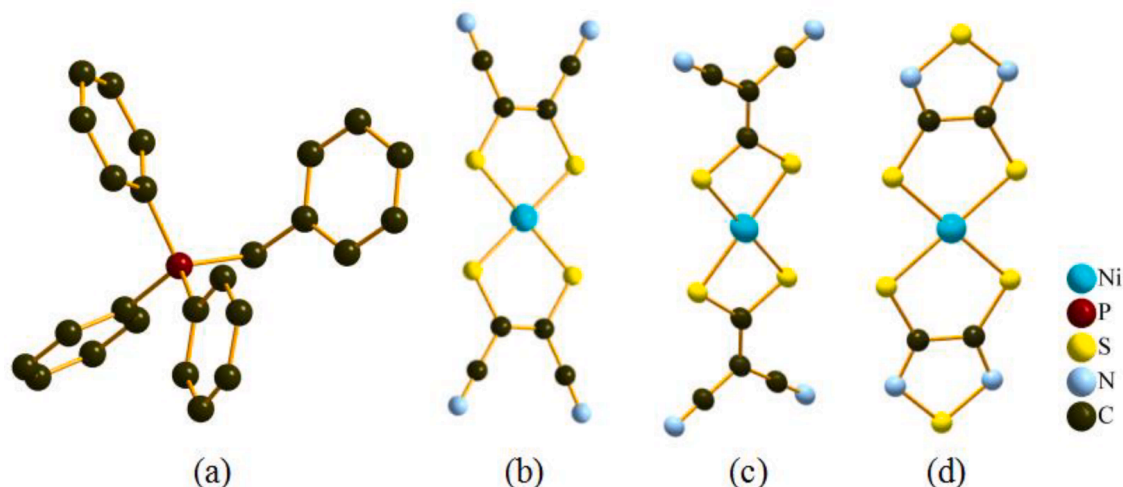
In order to investigate if these three nickel complexes have electrocatalytic activity, first we used linear sweep voltammetry (LSV) to study their electrochemical behaviors. As described in Fig. 2a, the onset potential of 1 is the same as the background potential in the early stage (ca. -1.25 V versus Ag/AgCl), suggesting that no proton is lost during the initial reduction. Similar to that of complex 1, no proton is lost during

Table 1

Main crystallographic data for 1, 2, and 3*.

Compound	1	2	3
Empirical formula	$\text{C}_{58}\text{H}_{44}\text{N}_4\text{NiP}_2\text{S}_4$	$\text{C}_{58}\text{H}_{44}\text{N}_4\text{NiP}_2\text{S}_4$	$\text{C}_{54}\text{H}_{44}\text{N}_4\text{NiP}_2\text{S}_6$
Formula weight	1045.86	1045.88	1061.94
Description	Red, block	Yellow, block	Brown, block
Space system	Monoclinic	Triclinic	Triclinic
Space group	$P2_1/n$	$P-1$	$C2/c$
a (Å)	9.3845(1)	9.466(1)	9.098(1)
b (Å)	14.683(1)	10.196(1)	9.666(1)
c (Å)	18.875(1)	29.252(3)	29.573(3)
α (°)	0	99.28(1)	83.811(1)
β (°)	99.44(1)	93.96(1)	81.97(1)
γ (°)	0	106.34(1)	78.826(1)
Volume (Å ³)	2565.5(3)	2654.3(4)	2517.5(4)
Z	2	2	2

$R_1 = \Sigma(|F_o| - |F_c|) / \Sigma|F_o|$, $wR_2 = [\Sigma w(|F_o|^2 - |F_c|^2)^2 / \Sigma w(|F_o|^2)^2]^{1/2}$. *Refs. [26–27].

Fig. 1. Structures of the cation and three anions: (a) $[\text{BzTPP}]^+$, (b) $[\text{Ni}(\text{mnt})_2]^{2-}$, (c) $[\text{Ni}(\text{i-mnt})_2]^{2-}$, (d) $[\text{Ni}(\text{tdas})_2]^{2-}$.

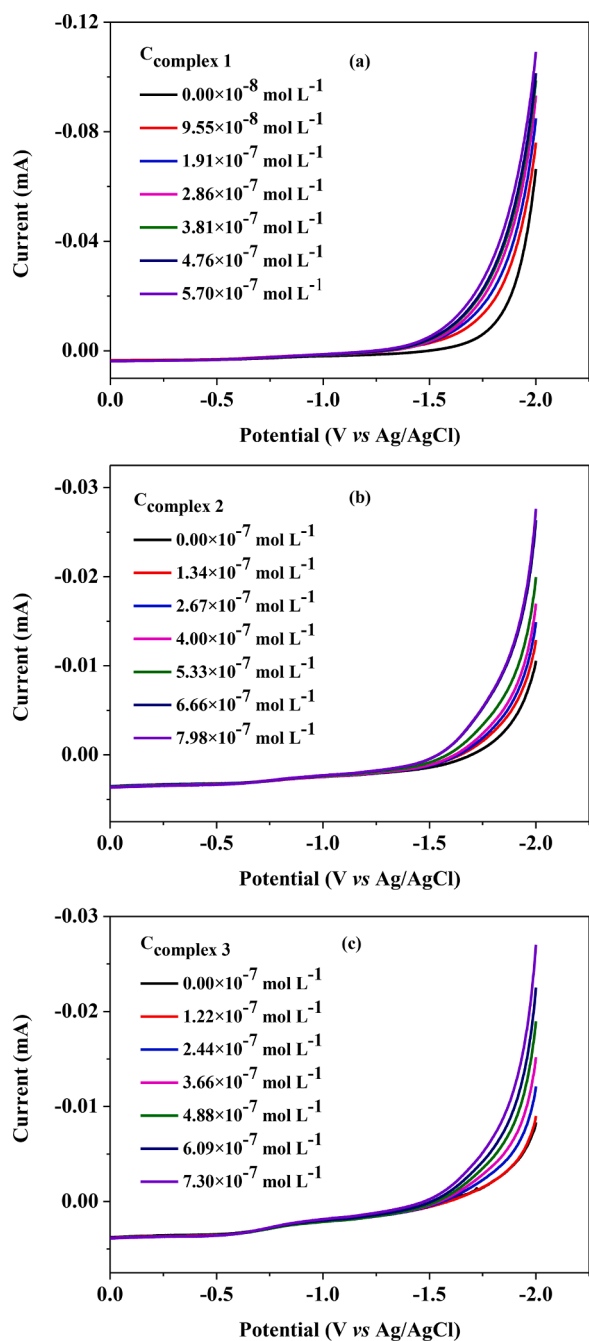


Fig. 2. Linear scan voltammograms (LSVs) of a neutral buffer solution (pH 7.0) without and with complexes 1(a), 2(b) and 3(c). Conditions: glassy carbon working electrode, Pt counter electrode, Ag/AgCl reference electrode, scan rate $0.10 \text{ V}\cdot\text{s}^{-1}$.

the initial reduction for complex 2 and 3 (Fig. 2b,c). On the basis of Fig. 2, the peak current increase continually with increasing complex 1, 2 or 3 concentration from 0.0 to $7.98 \times 10^{-7} \text{ mol}\cdot\text{L}^{-1}$, and no turning point is found, expressing that 1, 2 or 3 undergoes redox cycling during the electrochemical experiments. From Fig. S9, the catalytic current increases obviously with decrease of pH from 7.0 to 3.0, disulfide bonds are stable in acid, so indicating that there is a protonation step in the catalytic reaction.

3.3. Cyclic voltammetry

In a glass carbon as the working electrode in an acetonitrile solution,

complex 1, 2, and 3 exhibit rich redox electrochemistry. No obvious change was discovered after several scans, suggesting that the catalysts are stable under these conditions (Fig. S10, S13 and S14). Scan rate analysis of the voltammograms of the three catalysts showed linear dependence in the current versus $\nu^{1/2}$ curves (Fig. S12, S14 and S16), as expected for diffusing species in all observed redox events. As shown in Fig. 3a, the cyclic voltammogram of $3.31 \times 10^{-4} \text{ mol}\cdot\text{L}^{-1}$ complex 1 shows one reversible couple at 0.32 V versus Ag/AgNO₃ and one quasi-reversible redox couple at 0.80 V versus Ag/AgNO₃. For comparison, [BzTPP]Br exhibits one quasireversible redox peak at 0.79 V and one

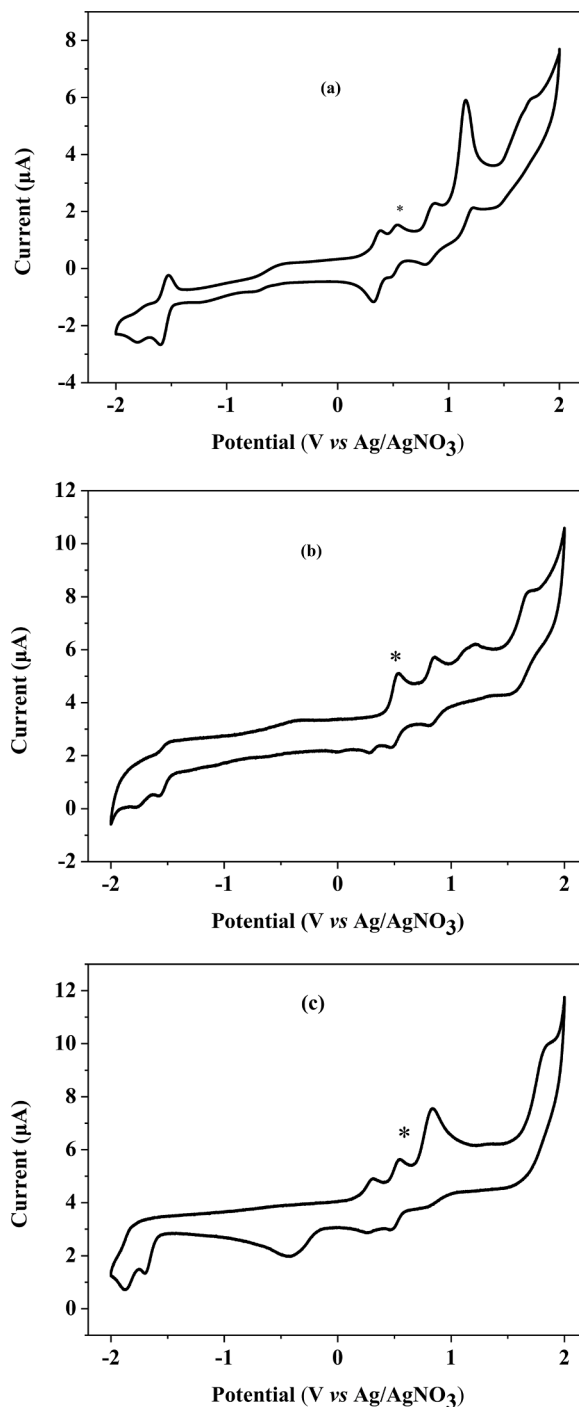


Fig. 3. CVs of $3.31 \times 10^{-4} \text{ mol}\cdot\text{L}^{-1}$ complex 1 (a), 2 (b) and $3.03 \times 10^{-4} \text{ mol}\cdot\text{L}^{-1}$ 3 (c) in CH₃CN with $0.10 \text{ mol}\cdot\text{L}^{-1}$ of [n-Bu₄N]ClO₄. Ferrocene internal standard(*). Glassy carbon working electrode ($1.0 \times 10^{-2} \text{ m}$ diameter), Pt counter electrode, Ag/AgNO₃ reference electrode, scan rate $0.10 \text{ V}\cdot\text{s}^{-1}$.

reversible redox couple at 1.20 V versus Ag/AgNO₃ (Fig. S11). These two oxidation waves of 1, approaching to the oxidations of [BzTPP]Br, are assigned to [BzTPP]Br. Scanning to cathodic potentials reveals an irreversible redox event at a cathodic peak potential of $E_{p,c} = -1.60$ V followed one irreversible wave at -1.80 V versus Ag/AgNO₃. The two redox peaks are assigned in turn to the Ni^{II/I} and Ni^{I/0} couples, respectively. Comparing of S12(a) and S12(b), it can be seen that the complex 2 has a pair of reversible redox peaks at 0.28 V. After adding ferrocene, the oxidation peak coincides with the oxidation peak of ferrocene. From Fig. 3b, complex 2 appears one reversible couple at 0.28 V versus Ag/AgNO₃, and one quasireversible redox couple at 0.80 V versus Ag/AgNO₃. These two oxidation waves of 2, approaching to the oxidations of [BzTPP]Br, are assigned to [BzTPP]Br. Scanning to cathodic potentials reveals one quasireversible couple at -1.56 V and one irreversible wave at -1.76 V versus Ag/AgNO₃, which are attributed to the couples of Ni^{II/I} and Ni^{I/0} couples, respectively. As described in Fig. 3c, complex 3 shows one reversible couple at 0.26 V and one quasireversible redox couple at 0.79 V versus Ag/AgNO₃. For comparison, [BzTPP]Br exhibits one quasireversible redox peak at 0.79 V and one reversible redox couple at 1.20 V (Fig. S11). These two oxidation waves of 3, approaching to the oxidations of [BzTPP]Br, are assigned to [BzTPP]Br. Scanning to cathodic potentials reveals an irreversible redox event at a cathodic peak potential of $E_{p,c} = -0.43$ V followed by two irreversible wave at -1.70 and -1.87 V versus Ag/AgNO₃. The second and third redox peaks are assigned to the couples of Ni^{II/I} and Ni^{I/0} couples, respectively.

3.4. Electrocatalytic activity from acetic acid in acetonitrile

In the exploration process, we use acetic acid as proton resource to experiment whether these three nickel complexes can be used as hydrogen production of electrocatalysts. As exhibition in Fig. 4a, with the addition of varied amounts of acetic acid (from 0.0 to 6.6×10^{-3} mol L⁻¹), apparent voltammetric currents occurs at -1.73 V and increase with increasing proton concentration. This phenomenon shows that hydrogen evolution electro-catalyzed by 1 requires the reduction of Ni (II) to Ni(I) and protonation. Interestingly, with the acetic acid concentration increased from 0.0 to 6.6×10^{-3} mol L⁻¹, the onset of the catalytic wave moves positive ca. 0.16 V from -1.43 to -1.27 V versus Ag/AgNO₃. Differently, the addition of varied amounts of acetic acid (from 0.0 to 6.6×10^{-3} mol L⁻¹) led to current strength increase at -1.71 V and 1.57 V versus Ag/AgNO₃ with increasing proton concentration (Fig. 4b). This appearance indicates that hydrogen generation electrocatalyzed by 2 requires the reductions of Ni(III) (source of Scheme 2) to Ni(II) and Ni(II) to Ni(I) and protonation. With the acetic acid concentration increased from 0.0 to 6.6×10^{-3} mol L⁻¹, the onset of the catalytic wave moves positive ca. 0.39 V from -1.39 to -1.0 V versus Ag/AgNO₃. Similar to complex 1, when a different amount of acetic acid (from 0.0 to 6.6×10^{-3} mol L⁻¹) was added to the electrolyte of the complex 3, the current strength increase at -1.90 V versus Ag/AgNO₃ was increased as well as proton concentration was increased (Fig. 4c). This scene demonstrated that hydrogen generation electrocatalyzed by 3 requires the reductions of Ni(II) to Ni(I) and protonation. With the acetic acid concentration increased from 0.0 to 6.6×10^{-3} mol L⁻¹, the onset of the catalytic wave moves positive ca. 0.40 V from -1.58 to -1.18 V versus Ag/AgNO₃.

According to the above observations, analyses and literature description [28,29], we conjecture a possible catalytic cycle for the generation of hydrogen from acid mediated by 1 is depicted in Scheme 2 (Since the disulfide bond is stable in acid, it is believed that the complex structure does not change in acetic acid.). One-electron reduction of $[\text{Ni}^{\text{II}}(\text{mnt})_2] - 1$ produces a putative $[\text{Ni}^{\text{I}}(\text{mnt})_2]^{3-}$ species. Then addition of hydrogen proton (H^+) yields the $[\text{Ni}^{\text{III}}-\text{H}(\text{mnt})_2]^{2-}$. Another one-electron reduction of the $[\text{Ni}^{\text{III}}-\text{H}(\text{mnt})_2]^{2-}$ species, $[\text{H}-\text{Ni}^{\text{II}}(\text{mnt})_2]^{3-}$. Further addition of hydrogen proton (H^+) affords H_2 , and regenerates the starting 1. To complex 2 and complex 3, similar procedure is carried out.

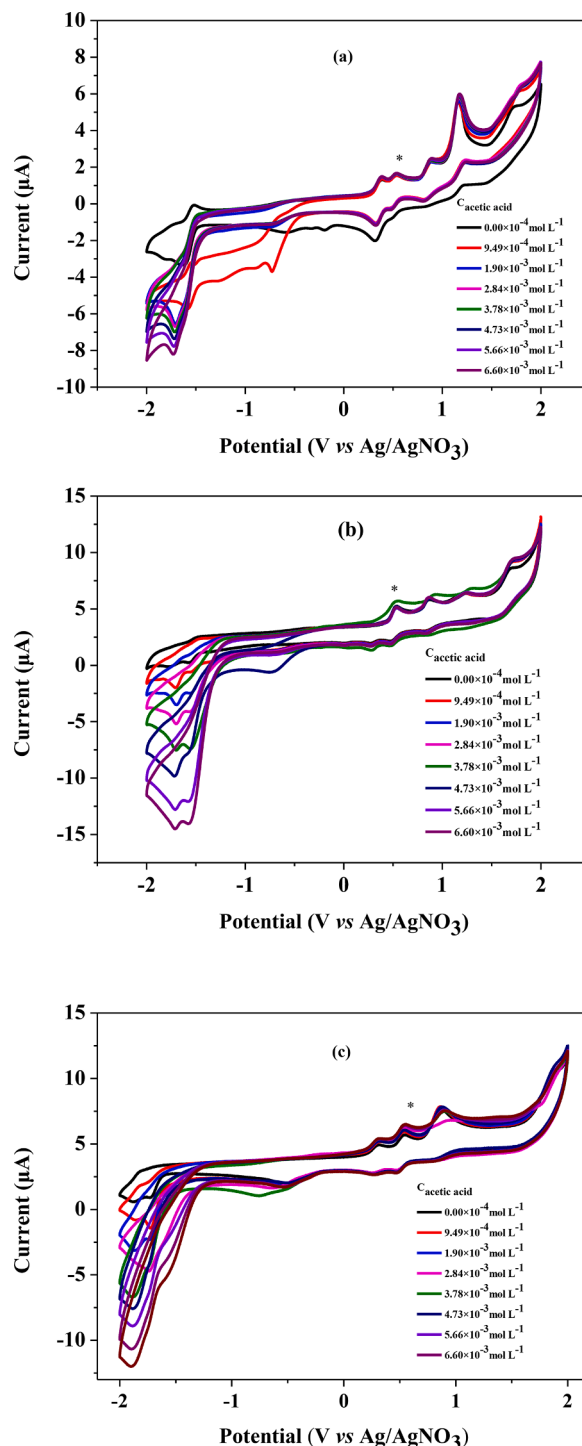
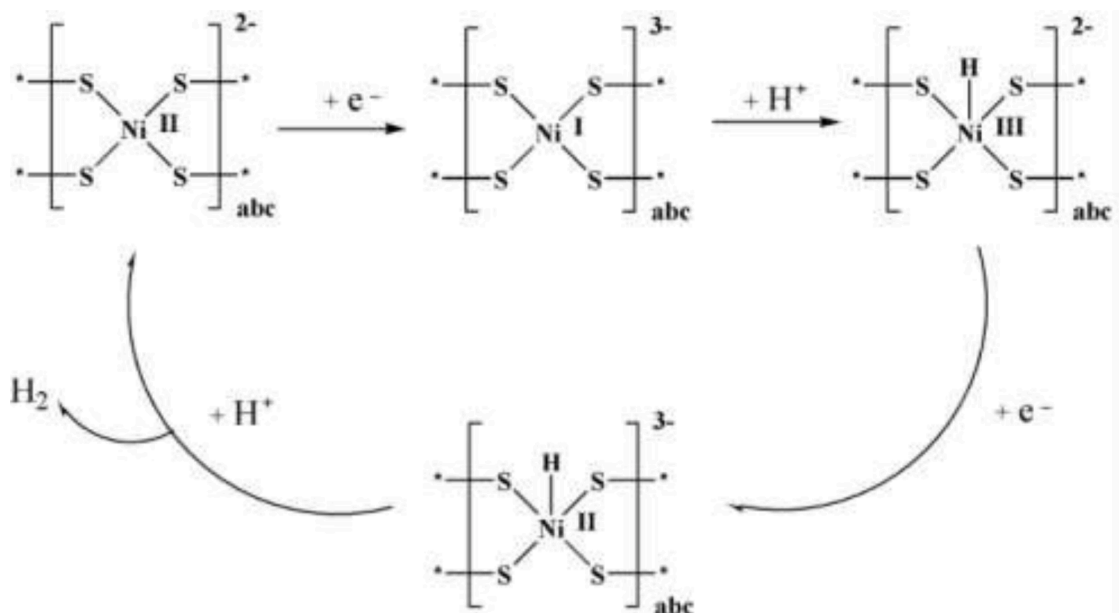


Fig. 4. CVs of a 3.31×10^{-4} mol L⁻¹ solution of complex 1 (a), complex 2 (b) and 3.03×10^{-4} mol L⁻¹ complex 3 (c) in CH₃CN with varying concentrations of acetic acid. Glassy carbon working electrode (1.0×10^{-2} m diameter), Pt counter electrode, Ag/AgNO₃ reference electrode, scan rate 0.10 V s⁻¹.

In order to further explore the catalytic activity [30], this paper was carried out in the presence of CH₃CN solutions of 1 (3.82×10^{-6} mol L⁻¹), 2 (3.82×10^{-6} mol L⁻¹) or 3 (3.82×10^{-6} mol L⁻¹) with 6.6×10^{-3} mol L⁻¹ acetic acid under varying applied potentials. Figs. S17a-c display the total charge of bulk electrolysis of 1, 2 or 3 in the presence of acetic acid, where the charge increases remarkably at increasingly negative potential. When an applied potential was -1.45 V versus Ag/AgCl, the maximum charge reaches 45 mC (by complex 1), 49



Scheme 2. The possible catalytic mechanism for proton reduction (*a*-[BzTPP]₂[Ni(mnt)₂], *b*-[BzTPP]₂[Ni(tdas)₂], *c*-[BzTPP]₂[Ni(i-mnt)₂]).

mC (by complex 2) and 90 mC (by complex 3) during 2 min of electrolysis, with accompanying evolution of a gas. A CPE experiment under -1.45 V versus Ag/AgCl without complex 1, 2 or 3 only gives a charge of 5 mC (Fig. S17d), suggesting that these three complexes do indeed serve as effective catalysts for hydrogen production under such conditions. Overpotentials are calculated by using the method of Evans, et al. [31] (Eq. (1)). On the basis of Eq. (2) [32], the TOFs are calculated to be 73.62 (by complex 1), 80.53 (by complex 2) and 149.63 (by complex 3) moles of hydrogen per mole of catalyst per hour, respectively (Eqs. (S1)-(S3) and Figs. S18). Noticeably, complex 3 exhibits a higher catalytic activity than complexes 1 and 2, indicating that the polysulfene nickel complex can constitute the better active catalyst than the dithiocarbon nickel sample. This may be because complex 3 contains more sulfur than complexes 1 and 2, which is easier for reversible electron transfer.

$$\begin{aligned} \text{Overpotential} &= \text{Applied potential} - E_{\text{HA}}^{\ominus} \\ &= \text{Applied potential} - (E_{\text{H}^+}^{\ominus} - (2.303RT/F)\text{p}K_{\text{aHA}}) \end{aligned} \quad (1)$$

$$\text{TOF} = \Delta C / (F * n_1 * n_2 * t) \quad (2)$$

Where, F is Faraday's constant, n_1 is the number of moles of electrons required to generate one mole of H_2 , n_2 is the number of moles of catalyst in solution, and t is the duration of electrolysis; ΔC is the charge from the catalyst solution minus the charge from solution without catalyst.

In methanol, complex 1 exists the same state as that in solid. This is in agreement with the result from ESI-MS measurement which exhibits one ion at a mass-to-charge ratio (m/z) of 169.4, with the mass and isotope distribution pattern corresponding to that of $[\text{Ni}^{\text{II}}(\text{mnt})_2]^{2-}$ (Fig. S6). Similarly, in methanol, complex 2 exhibits one ion at a mass-to-charge ratio (m/z) of 168.8, with the mass and isotope distribution pattern corresponding to that of $[\text{Ni}^{\text{II}}(\text{i-mnt})_2]^{2-}$ (Fig. S7). Differently, in methanol, complex 3 exhibits one ion at a mass-to-charge ratio (m/z) of 177.4 and 353.9, with the mass and isotope distribution pattern corresponding to that of $[\text{Ni}^{\text{II}}(\text{tdas})_2]^{2-}$ and $[\text{Ni}^{\text{II}}(\text{tdas})_2\text{H}]^{-}$ (Fig. S8).

3.5. Catalytic hydrogen produced from aqueous buffer

The electrochemical behaviors of complexes 1, 2 and 3 were then examined in aqueous buffer with different pH values. And Figs. 5a-c exhibit a systematic increase in i_{cat} with decreasing pH from 7.0 to 3.0 in

the presence of 1, 2 or 3, respectively. The onset of the catalytic current is clearly influenced by the solution pH, and the reduction waves are shifted to lower potentials with increasing pH values, which is consistent with a catalytic process [33]. As depicted in Figs. S19a-c, in the absence of 1, 2 or 3, a catalytic current is not apparent until a potential of -1.53 V versus Ag/AgCl is attained. Interestingly, upon addition of 1, the onset of the catalytic wave remains almost constant at ca. -1.53 V versus Ag/AgCl. But the case of adding 2 and 3 is different from 1, when add 2 or 3, the onset of the catalytic wave moves negative ca. 0.06 V from -1.53 to -1.59 V versus Ag/AgCl, and the current strength increases significantly with increasing concentrations of 1 (from 0 to 4.55×10^{-6} mol·L⁻¹), 2 (from 0 to 6.37×10^{-6} mol·L⁻¹) or 3 (from 0 to 5.83×10^{-6} mol·L⁻¹).

The electro-catalytic activities were also evaluated by bulk electrolysis of 3.82×10^{-6} mol·L⁻¹ 1 or 2 or 3.77×10^{-6} mol·L⁻¹ 3 in 0.25 mol·L⁻¹ buffer and the total charge of bulk electrolysis from a neutral buffer (pH 7.0) with and without 1, 2 and 3 were listed in Fig. 6. At an applied potential of -1.45 V versus Ag/AgCl, the buffer solution gives only 31 mC during 2 min of electrolysis in the absence of 1, 2 or 3 (Fig. 6 blank). When 1, 2 or 3 is added under the same conditions, the charge reaches 310.4 mC, 363.7 mC and 619.6 mC (Figs. 6a-c), respectively, and a large number of gas bubbles appeared, which are tested to be H_2 by gas chromatography. According to Figs. S20a-c, the activities are estimated to be 5.59×10^{-3} L (complex 1) and 10.619×10^{-3} L (complex 2) 14.528×10^{-3} L (complex 3) of H_2 during a 1 h electrolysis with a Faradaic efficiency of 101.5% (complex 1) and 98.6% (complex 2), 98.7% (complex 3) for dihydrogen, respectively (Figs. S21a-c). According to Eqs (2) and (3) [34], TOFs for electrocatalytic hydrogen production by complexes 1, 2 and 3 are calculated to be 504.76, 591.52 and 1022.93 mol of hydrogen per mole of catalyst per hour at an OP of 0.838 V, respectively (Eqs. S4-S6 and Figs. S22).

$$\begin{aligned} \text{Overpotential} &= \text{Applied potential} - E(\text{pH}) \\ &= \text{Applied potential} - (-0.059\text{pH}) \end{aligned} \quad (3)$$

From Fig. S22, the TOF of 1022.93 mol of hydrogen per mole of catalyst per hour at an OP of 0.838 V produced by complex 3 is higher than that of other molecular nickel catalysts reported in the literature for electrochemical hydrogen production from neutral water. For instance, a dinickel complex supported by macrocyclic ligand that exhibits a TOF of 160 mol of H_2 per mole of catalyst per hour at an OP of 820 mV [35],

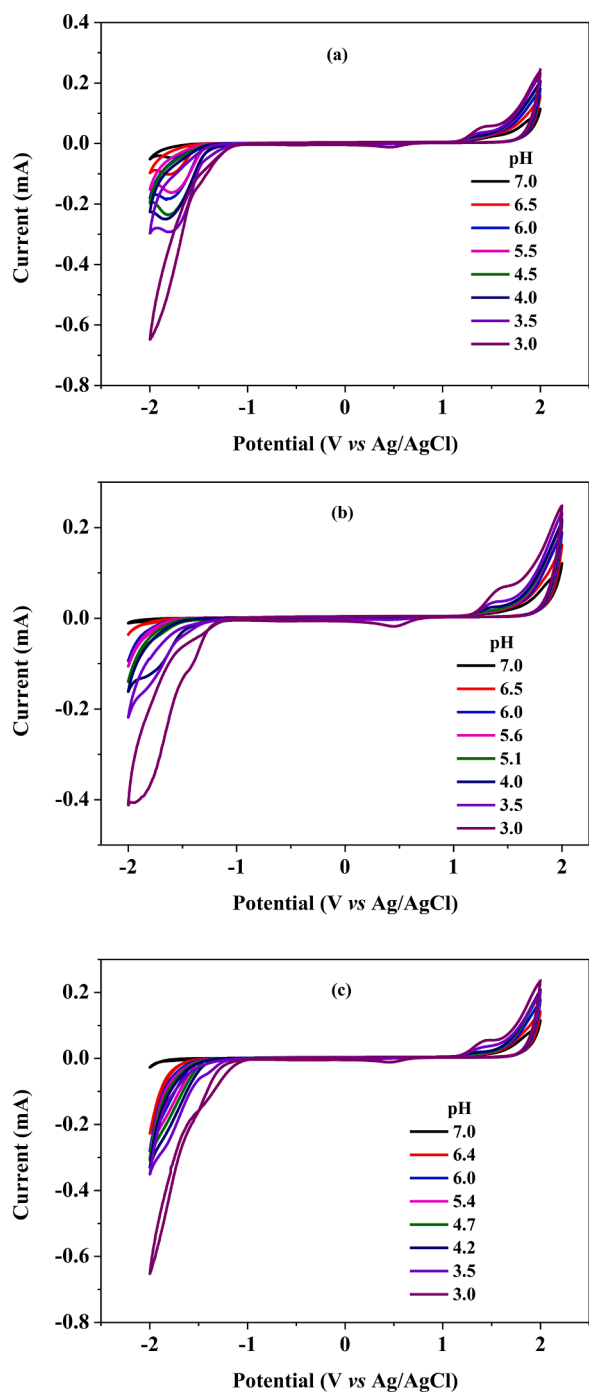


Fig. 5. CVs of $1.59 \times 10^{-5} \text{ mol}\cdot\text{L}^{-1}$ complex 1 (a), $2.23 \times 10^{-5} \text{ mol}\cdot\text{L}^{-1}$ 2 (b) and $2.04 \times 10^{-5} \text{ mol}\cdot\text{L}^{-1}$ 3 (c) in buffer with varying pH values (scan rate: $0.10 \text{ V}\cdot\text{s}^{-1}$).

and a nickel complex with 2,3-bis(2-hydroxybenzylideneimino)-2,3-butenedinitrile ion that achieves a TOF of 436 mol of H_2 per mole of catalyst per hour at an OP of 837.6 mV [7], and two nickel complex with $[\text{BzPyN}(\text{CH}_3)_2]_2[\text{Ni}(\text{mnt})_2]$, $[\text{4-ClBzPyN}(\text{CH}_3)_2][\text{Ni}(\text{mnt})_2]$ that manifestation a TOF of 282.95, 504.25 mol of H_2 per mole of catalyst per hour at an OP of 837.6 mV, respectively [36]. Similar to that in organic media, complex 3 also shows higher efficiency for hydrogen production than that of complex 2 and 1 in aqueous media. From a 72 h CPE of a natural buffer solution (pH 7.0) in the presence of complex 1, 2 or 3, we also can find that catalyst 3 is a more active species than 1 and 2. As shown in Fig. S23a, a total of 1139 C is accumulated during the

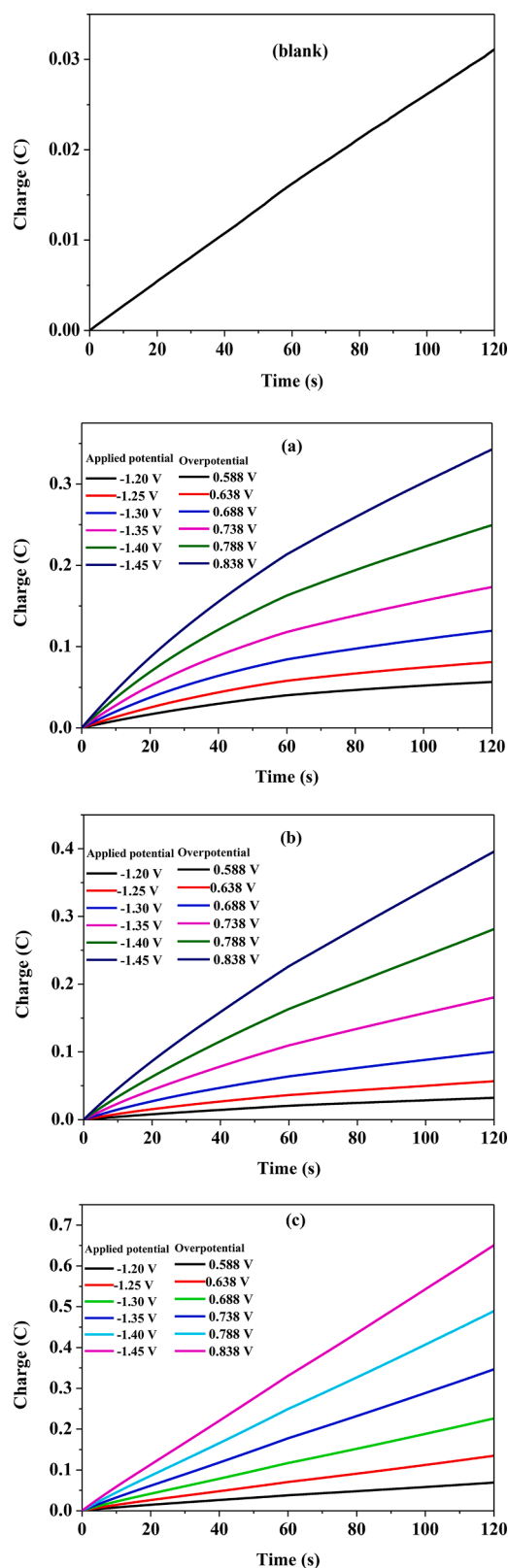


Fig. 6. Charge buildup versus time from electrolysis of a $0.25 \text{ mol}\cdot\text{L}^{-1}$ buffer solution (pH 7.0) under -1.45 V versus Ag/AgCl. Charge buildup versus time from electrolysis of $3.82 \times 10^{-6} \text{ mol}\cdot\text{L}^{-1}$ 1 (a), 2 (b) or $3.77 \times 10^{-6} \text{ mol}\cdot\text{L}^{-1}$ 3 (c) under various applied potentials at pH 7.0. All data have been deducted blank.

electrolysis catalyzed by complex 1, and in the presence of complex 2, 1390 C is passed during a 72 h electrolysis (Fig. S23b). And in the presence of complex 3, 1419 C is passed during a 72 h electrolysis (Fig. S23c).

3.6. Investigation of the stability and durability of the complexes

In order to test whether 1, 2 or 3 retains activity for water reduction for a long time, three 72 h CPE experiments were performed in a neutral buffer solution with $3.68 \times 10^{-6} \text{ mol}\cdot\text{L}^{-1}$ 1(a), $5.15 \times 10^{-6} \text{ mol}\cdot\text{L}^{-1}$ 2(b) or $3.98 \times 10^{-6} \text{ mol}\cdot\text{L}^{-1}$ 3(c) under -1.45 V versus Ag/AgCl, respectively. According to Fig. S23a, a total of 1139 C was passed during a 72 h electrolysis, and complex 1 gives a charge build-up over time, with no substantial loss in activity over the course of 30 h. After a 72 h electrolysis period, pH increased by 5.7 units (from 7.0 to 12.7), consistent with accumulation of OH^- by water reduction, $2\text{H}_2\text{O} + 2\text{e}^- \rightarrow \text{H}_2 + 2\text{OH}^-$. For complex 2, a 72 h electrolysis from complex 2 afforded 987.1 C of charge with no substantial loss in activity over the course of 72 h (Fig. S23b), which is consistent with the catalytic current experiment. For complex 3, a 72 h electrolysis from complex 3 afforded 1419 C of charge with no substantial loss in activity over the course of 72 h (Fig. S23c), which is consistent with the catalytic current experiment.

To prove complex 1, 2 or 3 acts as a homogeneous electrocatalyst, we checked dependence of the catalytic current on concentration of complexes 1, 2 and 3. According to Fig. S19, the observation of the catalytic current being dependent on concentration of 1, 2 or 3 could indicate both 1, 2 and 3 are homogeneous catalysts. And the following pieces of evidence also suggest that complexes 1, 2 and 3 are homogeneous electrocatalysts: (a) the catalytic current did not increase after several cycle CV scans (Figs. S9, S12 and S14) [37]. (b) No precipitations were found in the solution and the color of the solution did not change during cyclic voltammetry or bulk electrolysis of complexes 1, 2 and 3.

4. Conclusion

In this paper, we have studied the effect of the effect of different of metal ligands on hydrogen production electro-catalyzed by nickel complexes supported by disulfide or polysulfide ligands via electrochemical methods, including linear scan voltammetry and cyclic voltammetry. Electrochemical studies show that $[\text{Ni}^{\text{II}}(\text{mnt})_2]^{2-}$, $[\text{Ni}^{\text{II}}(\text{i-mnt})_2]^{2-}$ and $[\text{Ni}^{\text{II}}(\text{tdas})_2]^{2-}$ afford a TOF of 504.76, 591.52 and 1022.93 mol of hydrogen per mole of catalyst per hour at a OP of 0.838 V from a neutral buffer solution, respectively, indicating that the polysulfene nickel complex electrocatalyst is more active than the dithiocarbon nickel sample. This can be attributed to that $[\text{Ni}^{\text{II}}(\text{tdas})_2]^{2-}$ is more stable than $[\text{Ni}^{\text{II}}(\text{mnt})_2]^{2-}$ and $[\text{Ni}^{\text{II}}(\text{i-mnt})_2]^{2-}$. The result may offer a new chemical paradigm for the design and engineering of effective molecular catalysts for water reduction.

CRediT authorship contribution statement

Hao-Jun Yin: Conceptualization, Writing – original draft. **Zhi-Hao Gan:** Conceptualization, Writing – original draft. **Zong Wang:** Resources, Investigation, Formal analysis, Writing – original draft. **Xiao-Ting Zheng:** Resources, Investigation, Formal analysis, Writing – original draft. **Li-Yuan Huang:** Resources, Investigation, Formal analysis, Writing – original draft. **Yi-Chun Chen:** Methodology, Investigation, Validation, Writing – original draft, Data curation. **Jia-Rong Zhou:** Supervision, Methodology, Writing – review & editing, Project administration, Writing – original draft. **Chun-Lin Ni:** Methodology, Investigation, Validation, Data curation, Writing – original draft. **Wei Liu:** Supervision, Methodology, Writing – review & editing, Project administration, Writing – original draft.

Declaration of Competing Interest

The authors declare that they have no known competing financial interests or personal relationships that could have appeared to influence the work reported in the present paper.

Data availability

Data will be made available on request.

Acknowledgements

This work was supported by the National Science Foundation of China (No. 21701045), and the Science and Technology Program from Guangzhou city of China (No. 202201010559).

Supplementary materials

Supplementary material associated with this article can be found, in the online version, at doi:10.1016/j.molstruc.2023.135659.

References

- [1] Y.T. Liu, M.Y. Lu, T.P. Perng, L.J. Chen, Plasmonic enhancement of hydrogen production by water splitting with CdS nanowires protected by metallic TiN overlayers as highly efficient photocatalysts, *Nano Energy* 89 (2021), 106407.
- [2] S. Cao, L. Piao, X. Chen, Emerging photocatalysts for hydrogen evolution, *Trends Chem.* 2 (2020) 57–70.
- [3] J. Suntivich, K.J. May, H.A. Gasteiger, J.B. Goodenough, Y.A. Shao-Horn, A perovskite oxide optimized for oxygen evolution catalysis from molecular orbital principles, *Science* 334 (2011) 1383–1385.
- [4] Y. Xu, M. Kraft, R. Xu, Metal-free carbonaceous electrocatalysts and photocatalysts for water splitting, *Chem. Soc. Rev.* 45 (2016) 3039–3052.
- [5] M.D. Sampson, C.P. Kubiak, Electrocatalytic dihydrogen production by an earth-abundant manganese bipyridine catalyst, *Inorg. Chem.* 54 (2015) 6674–6676.
- [6] Y.X. Gong, J.S. Yao, P. Wang, Z.X. Li, H.J. Zhou, C.M. Xu, Perspective of hydrogen energy and recent progress in electrocatalytic water splitting, *Chin. J. Chem. Eng.* 43 (2022) 282–296.
- [7] J.P. Cao, T. Fang, L.Z. Fu, L.L. Zhou, S.Z. Zhan, A nickel molecular electro-catalyst for generating hydrogen from acetic acid or water, *Int. J. Hydrog. Energy* 39 (2014) 10980–10986.
- [8] A. Das, Z. Han, W.W. Brennessel, P.L. Holland, R. Eisenberg, Nickel complexes for robust light-driven and electrocatalytic hydrogen production from water, *ACS Catal.* 5 (2015) 1397–1406.
- [9] L. Gan, T.L. Groy, P. Tarakeshwar, S.K.S. Mazinani, J. Shearer, V. Mujica, A. K. Jones, A nickel phosphine complex as a fast and efficient hydrogen production catalyst, *J. Am. Chem. Soc.* 137 (2015) 1109–1115.
- [10] T. Fang, L.Z. Fu, L.L. Zhou, S.Z. Zhan, S. Chen, Electrochemical-driven water reduction catalyzed by a water soluble cobalt(III) complex with Schiff base ligand, *Electrochim. Acta* 178 (2015) 368–373.
- [11] A. Rodenberg, M. Oraziotti, B. Probst, C. Bachmann, R. Alberto, K.K. Baldrige, P. Hamm, Mechanism of photocatalytic hydrogen generation by a polypyridyl-based cobalt catalyst in aqueous solution, *Inorg. Chem.* 54 (2015) 646–657.
- [12] B. Kandemir, L. Kubie, Y. Guo, B. Sheldon, K.L. Bren, Hydrogen evolution from water under aerobic conditions catalyzed by a cobalt ATCUN metallopeptide, *Inorg. Chem.* 55 (2016) 1355–1357, 2016.
- [13] J.P. Cao, T. Fang, L.Z. Fu, L.L. Zhou, S.Z. Zhan, First mononuclear copper(II) electro-catalyst for catalyzing hydrogen evolution from acetic acid and water, *Int. J. Hydrog. Energy* 39 (2014) 13972–13978.
- [14] L.L. Zhou, T. Fang, J.P. Cao, Z. Zhu, X. Su, S.Z. Zhan, A dinuclear copper(II) electrocatalyst both water reduction and oxidation, *J. Power Sources* 273 (2015) 298–304.
- [15] T. Fang, L.Z. Fu, L.L. Zhou, S.Z. Zhan, A water-soluble dinuclear copper electrocatalyst, $[\text{Cu}(\text{oxpn})\text{Cu}(\text{OH})_2]$ for both water reduction and oxidation, *Electrochim. Acta* 161 (2015) 388–394.
- [16] S. Ibrahim, Y.D. Cheng, D. Zhao, M.A. Nadeem, A new insight for photocatalytic hydrogen production by a Cu/Ni based cyanide bridged polymer as a co-catalyst on titania support in glycerol water mixture, *Int. J. Hydrog. Energy* 44 (2019) 2508–2518.
- [17] S. Lin, M.W. Day, Nickel hydrides supported by a non-innocent diphosphine arene pincer: mechanistic studies of nickel-arene H-migration and partial arene hydrogenation, *J. Am. Chem. Soc.* 133 (2011) 3828–3831.
- [18] A. Das, Z.J. Han, M.G. Haghighi, R. Eisenberg, Photogeneration of hydrogen from water using CdSe nanocrystals demonstrating the importance of surface exchange, *Proc. Natl. Acad. Sci. USA* 110 (2013) 16716–16723.
- [19] S. Sproules, T. Weyhermüller, S. DeBeer, K. Wieghardt, Six-membered electron transfer series $[\text{V}(\text{dithiolene})_3]^z$ ($z = +1, 0, 1-, 2-, 3-, 4-$). An X-ray absorption

- spectroscopic and density functional theoretical study, *Chem. Rev.* 49 (2010) 5241–5261.
- [20] X. Hu, B.S. Brunschwig, J.C. Peter, Electrocatalytic hydrogen evolution at low overpotentials by cobalt macrocyclic glyoxime and tetraimine complexes, *J. Am. Chem. Soc.* 129 (2007) 8988–8998.
- [21] J.L. Fillol, Z. Codolà, I. Garcia-Bosch, L. Gómez, J.J. Pla, M. Costas, Efficient water oxidation catalysts based on readily available iron coordination complexes, *Nat. Chem.* 3 (2011) 807–813.
- [22] M. Vennampalli, G. Liang, L. Katta, C.E. Webster, X. Zhao, Electronic effects on a mononuclear Co complex with a pentadentate ligand for catalytic H₂ evolution, *Inorg. Chem.* 53 (2014) 10094–10100.
- [23] S.B. Bulgarevich, D.V. Bren, D.Y. Movshovic, P. Finocchiaro, S. Failla, Conformational investigation of *N*-aralkylpyridinium ions by cotton-mouten effect method, *J. Mol. Struct.* 317 (1994) 147–155.
- [24] H. Bian, D. Li, J.Q. Yan, S.Z. Liu, Perovskite? a wonder catalyst for solar hydrogen production, *J. Energy Chem.* 57 (2021) 325–340.
- [25] J.R. Zhou, C.L. Ni, L.L. Liang, Bis(benzyltriphenylphosphonium) bis(1,2-dicyanoethene-1,2-dithiolato)-nickel(II), *Acta Crystallogr.* 63 (2007) M1427–M1429.
- [26] X. Chen, D.H. Huang, C.Y. Huang, J.R. Zhou, H.R. Zuo, Q. Huang, Y. Hou, L.L. Yu, L.M. Yang, X.P. Liu, C.L. Ni, Q.J. Meng, Synthesis, weak hydrogen bonds and 3D crystal structure of a new iso-maleonitriledithiolate nickel ion-pair complex, *Synth. React. Inorg. M* 39 (2009) 179–182.
- [27] H.R. Zuo, J. Tian, X. Chen, Q. Huang, J.R. Zhou, X.P. Liu, C.L. Ni, X.L. Hu, Synthesis and crystal structure of a new ion-pair complex based on [Ni(tdas)₂]²⁻ anion and triphenylphosphonium cation, *J. Chem. Crystallogr.* 39 (2009) 698–701.
- [28] J.T. Muckermann, E. Fujita, Theoretical studies of the mechanism of catalytic hydrogen production by a cobaloxime, *Chem. Commun.* 47 (2011) 12456–12458.
- [29] X.Y. Liu, Y.G. Xu, Y. Jiang, M.Y. Song, Z.Y. Liu, W.W. Guo, L.F. You, J. Wu, M. Xu, Y.Z. He, Nanoarchitectonics of uniformly distributed noble-metal-free CoP in g-C₃N₄ via in-situ fabrication for enhanced photocatalytic and electrocatalytic hydrogen production, *J. Alloy Compd.* 904 (2022), 163861.
- [30] H.Q. Ye, L.Y. Shi, J.X. Zhang, Y.L. Hu, R.K. Huang, X.Z. Lv, J.R. Zhou, L.M. Yang, C. L. Ni, Syntheses, crystal structures, and magnetic properties of three new molecular solids based on bis(maleonitriledithiolate)Ni(III) monoanion and substituted chlorobenzyl-4-dimethylaminopyridinium, *Synth. Met.* 194 (2014) 137–145.
- [31] G.A.N. Felton, R.S. Glass, D.L. Lichtenberger, D.H. Evans, Iron-only hydrogenase mimics. thermodynamic aspects of the use of electrochemistry to evaluate catalytic efficiency for hydrogen generation, *Inorg. Chem.* 45 (2006) 9181–9184.
- [32] H.I. Karunadasa, E. Montalvo, Y. Sun, A molecular MoS₂ edge site mimic for catalytic hydrogen generation, *Science* 335 (2012) 698–702.
- [33] J.D. Yao, W.J. Huang, W. Fang, M. Kuang, N. Jia, H. Ren, D.B. Liu, C.D. Lv, C. T. Liu, J.W. Xu, Q.Y. Yan, Promoting electrocatalytic hydrogen evolution reaction and oxygen evolution reaction by fields: effects of electric field, magnetic field, strain, and light, *Small Methods* 4 (2020), 2000494.
- [34] Y. Sun, J.P. Bigi, N.A. Piro, M.L. Tang, J.R. Long, C.J. Chang, Molecular cobalt pentapyridine catalysts for generating hydrogen from water, *J. Am. Chem. Soc.* 133 (2011) 9212–9215.
- [35] J.P. Collin, A. Jouaiti, J.P. Sauvage, Electrocatalytic properties of (tetraazacyclotetradecane)nickel(2⁺) and Ni₂(biscyclam)⁴⁺ with respect to carbon dioxide and water reduction, *Inorg. Chem.* 27 (1988) 1986–1990.
- [36] C.N. Lin, D. Xue, Y.H. Zhou, S.Z. Zhan, C.L. Ni, The effect of oxidation state of metal on hydrogen production electro-catalyzed by nickel complexes supported by maleonitriledithiolate ligand, *J. Electroanal. Chem.* 785 (2017) 58–64.
- [37] W.T. Lee, S.B. Munoz, D.A. Dickie, J.M. Smith, Ligand modification transforms a catalase mimic into a water oxidation catalyst, *Angew. Chem. Int. Ed.* 53 (2014) 9856–9859.

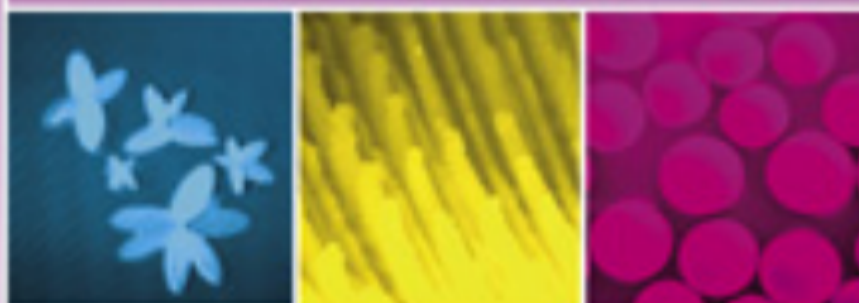


ISSN: 0926-6390

MATERIALS SCIENCE & ENGINEERING



Materials for
Biological Applications



Available online at www.sciencedirect.com


ScienceDirect


← → ↻ 🔍 <https://www.sciencedirect.com/journal/materials-science-and-engineering-c/vol/91/suppl/C> あ A ☆ ☰ ☆ 📄 📌 ...

Materials Science and Engineering: C | Supports open access

Articles & Issues ▾ 🔍 Search in this journal

Actions for 1 selected article
[Select all](#) / [Deselect all](#)

 Download PDF

 Export citation

☐ Show all article previews

Contents

Reviews

Full Length Articles


Short Communication

Erratum/Corrigendum

☐ Research article ● Full text access

Biodegradable Polyvinyl Alcohol Vascular Stents: Structural Model and Mechanical and Biological Property Evaluation


Mei-Chen Lin, Ching-Wen Lou, Jan-Yi Lin, Ting An Lin, ... Jia-Horng Lin
Pages 404-413

 [View PDF](#) Article preview ▾

☒ Research article ● Full text access

Synthesis, characterization, DNA/HSA interactions and in vitro cytotoxic activities of two novel water-soluble copper(II) complexes with 1,3,5-triazine derivative ligand and amino acids


Chun-Lian Zhang, Ya-Xian Liu, Xue-Mei Zhang, Shi Chen, ... Xue-Yi Le
Pages 414-425

 [View PDF](#) Article preview ▾

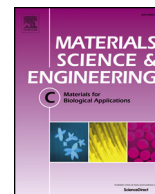
☐ Research article ● Full text access

Biodegradable shape-memory polymers using polycaprolactone and isosorbide based polyurethane blends

Yoon-Suk Joo, Jae-Ryung Cha, Myoung-Seon Gong
Pages 426-435



[FEEDBACK](#) 🗨



Synthesis, characterization, DNA/HSA interactions and in vitro cytotoxic activities of two novel water-soluble copper(II) complexes with 1,3,5-triazine derivative ligand and amino acids

ARTICLE INFO

Keywords:

Water-soluble copper(II) complexes
DNA/HSA binding
6-(pyrazin-2-yl)-1,3,5-Triazine-2,4-diamine
Amino acid
Molecular docking
Cytotoxicity

ABSTRACT

Two water-soluble copper(II) complexes of 6-(pyrazin-2-yl)-1,3,5-triazine-2,4-diamine (pzta) and amino acids, $[\text{Cu}(\text{pzta})(\text{L-ArgH})(\text{H}_2\text{O})](\text{ClO}_4)_2$ (**1**) and $[\text{Cu}(\text{pzta})(\text{L-Met})(\text{H}_2\text{O})]\text{ClO}_4 \cdot 3\text{H}_2\text{O}$ (**2**) (L-ArgH: protonated L-Arginine; L-Met: L-Methionine), were synthesized and characterized. The determined X-ray crystallographic structures of **1** and **2** exhibited distorted square-pyramidal coordination geometries. Their binding properties toward calf thymus DNA (CT-DNA) and human serum protein (HSA) were measured by spectroscopic (UV–Vis, fluorescence, circular dichroism (CD)), calorimetric (isothermal titration calorimetry (ITC)) and molecular docking technology. DNA binding experiments showed that the complexes bound to DNA through a groove binding mode, the positive ΔH and ΔS values indicated that the hydrophobic interaction was the main force in the binding between the complexes and DNA. Besides, the complexes caused the fluorescence quenching of HSA through a static quenching procedure, changed the secondary structure and microenvironment of the Trp-214 residue, and preferably bound to subdomain IIA of HSA driven by hydrophobic and hydrogen-bond interactions. These results were further verified by the molecular docking technology. Furthermore, the in vitro cytotoxicities of the complexes against three human carcinoma cell lines (A549, PC-3 and HeLa) were evaluated, which confirmed that the complexation improved the anticancer activity of the pzta ligand significantly.

1. Introduction

The discovery of the cytotoxicity of cisplatin provided enormous impetus for research into the use of metal complexes in the fight against cancers, especially for the development of transition metal Cu(II) complexes [1,2]. As an essential element in the human body, Cu(II) is distributed widely in biological systems including cells and body fluids, and may be of less toxicity than non-essential metals [3]. Copper(II) complexes with low side-effects have been considered as potential therapeutic agents for numerous diseases, and the promising alternatives to cisplatin owing to their versatile coordination modes, various oxidation states and ligand substitution kinetic [4,5]. Also, copper(II) complexes showed significantly stronger biological activity than did free ligands, related to the synergistic effect between the ligand and central copper(II) ion [6,7].

Recent studies have been occupied in the synthesis and evaluation of the biological activity of metal complexes with biologically organic

ligands, with the aim of widening the spectrum of complexes activities [8]. Some 1,3,5-triazine derivatives have been well known because of their high biological activities and widespread applications in the fields of herbicide, antibacterial and anticancer [9,10]. However, the coordination compounds from 1,3,5-triazine derivatives ligands received little attention for biological applications partly due to their limited solubility in both water and common organic solvents [11]. In order to get a suitable solubility in physiological conditions, thus enhancing the bioavailability and reducing the in vivo toxicity, amino acids could be introduced as the co-ligand [12]. Furthermore, certain amino acid complexes were found to exhibit potent antitumor and artificial nuclease activities [13]. And various side groups of amino acids were found to have a potential to recognize the specific base sequence through hydrogen bond formation with the nucleic bases in DNA [14]. L-Arginine with a guanidinium group can recognize DNA structure by forming hydrogen bonds, and L-Methionine is the primary methyl donor in cells, which plays a major role in preventing cancer

* Corresponding authors.

E-mail addresses: liuwei97@scau.edu.cn (W. Liu), lexyfu@163.com (X.-Y. Le).

<https://doi.org/10.1016/j.msec.2018.05.065>

Received 18 September 2017; Received in revised form 19 April 2018; Accepted 19 May 2018

Available online 22 May 2018

0928-4931/ © 2018 Published by Elsevier B.V.

development [15,16], hence in this work we choose *L*-Arginine and *L*-Methionine as the co-ligand to synthesis the water-soluble 1,3,5-triazine complexes.

When metal complexes are used as anticancer drugs, they can bind to carrier proteins in the blood [17]. Human serum albumin (HSA) as the most important carrier protein in the blood, has multiple binding sites to interact with many drugs [18]. Once an anticancer drug bind to carrier proteins in the blood, its solubility will increase in the blood plasma and results in deliver target position [19]. Generally, DNA is the primary intracellular target of anticancer drugs and metal complexes bind with DNA via covalent interaction or non-covalent interactions including π - π^* stacking with the DNA nucleobases, groove binding through van der Waals, hydrophobic, and hydrogen bonding interactions along the major or minor groove of the DNA helix, and external/electrostatic interaction with the phosphate groups of DNA [20,21]. These interactions can cause DNA damage, inhibition of the division of cancer cells, and finally result in cell death [22]. Therefore, studying the interactions of metal complexes toward DNA and protein will increase our understanding of the mechanism of anticancer drug cure [23,24]. Traditionally, the interactions between the metal complexes and DNA/HSA are reflected by various spectroscopic methods and molecular docking technology, but calorimetric method as an effective technique for binding investigation of biological macromolecules has been scarcely reported in these interactions [25,26]. We incorporated these techniques together to investigate the binding properties of metal complexes toward DNA/HSA so as to understand the interaction properties thoroughly.

In our previous works, the synthesis and DNA/HSA binding properties of copper(II) complexes of 6-(pyrazin-2-yl)-1,3,5-triazine-2,4-diamine (pzta) and glycine/glycylglycine have been reported [27,28]. As a continuation of this research line, in the present paper we have synthesized two new water-soluble copper(II) complexes with pzta and amino acids (Scheme 1), [Cu(pzta)(*L*-ArgH)(H₂O)](ClO₄)₂ (**1**) and [Cu(pzta)(*L*-Met)(H₂O)]ClO₄·3H₂O (**2**) (*L*-ArgH: protonated *L*-Arginine; *L*-Met: *L*-Methionine). The interactions of complexes **1** and **2** with DNA and HSA were investigated by multiple spectroscopy methods, thermal denaturation and isothermal titration calorimetry (ITC), as well as molecular docking technology. Their affinities with DNA suggested that DNA could be the target for the complexes, while their affinities with HSA suggested that the complexes could be transported by HSA in the blood. Moreover, the *in vitro* cytotoxicities of the complexes on three human carcinoma cell lines (A549, PC-3 and HeLa) were evaluated using the MTT assay.

2. Experimental

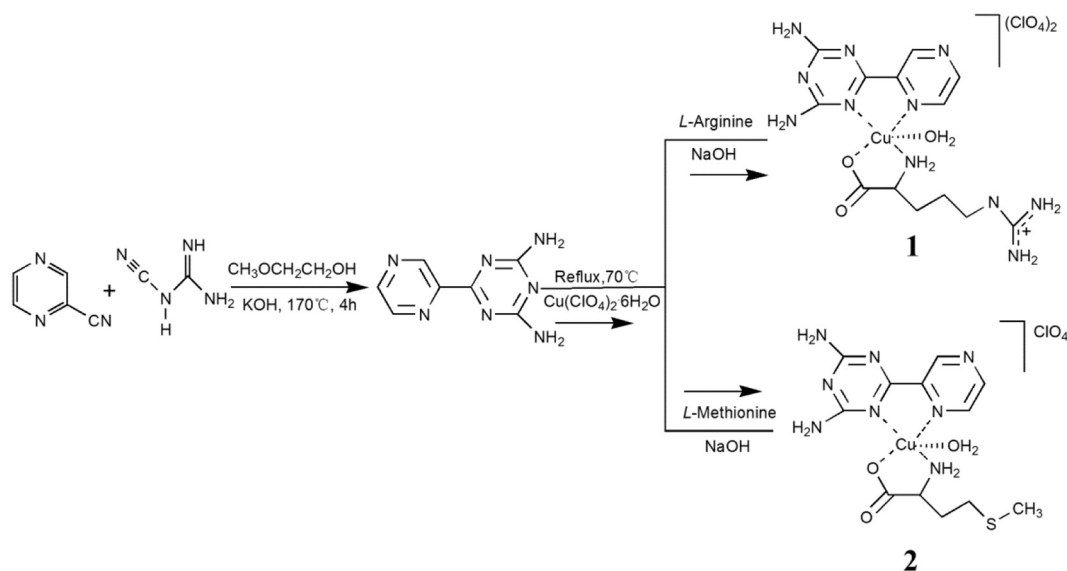
2.1. Materials and methods

All chemicals and reagents were purchased from commercial sources, and were used without further purification. *L*-Arginine, *L*-Methionine, Tris(hydroxymethyl)aminomethane (Tris) were purchased from Sinopharm Chemical Reagent Co., Ltd. (China), while Calf thymus (CT)-DNA, human serum protein (HSA), ethidium bromide (EB) and 3-[4,5-dimethylthiazol-2-yl]-2,5-diphenyl tetrazolium (MTT) were obtained from Sigma (USA). Human carcinoma cell lines of A549 (pulmonary), PC-3 (prostatic) and HeLa (cervical) were provided from the Laboratory Animal Center of Sun Yat-sen University (China). Deionized water was used throughout the experiments.

Electronic absorption spectra were recorded on a Pharmacia 2550 UV-Vis spectrophotometer (Shimadzu, Japan) equipped with a temperature controller. Fluorescence spectra were recorded with a Hitachi RF-4500 fluorescence spectrometer (Hitachi, Japan). Infrared spectra were recorded in the 4000–400 cm⁻¹ region with a Nicolet ACATAR 360 FT-IR spectrometer (Nicolet, USA) by using KBr pellet. The C, H, N and S elemental analyses were performed on a Vario EL elemental analyzer (Elementar, German). Electrospray mass spectra (ESI-MS) were investigated by API3200 triple quadrupole mass spectrometer (AB Sciex, USA). Molar conductivity measurements were made using a DDS-11A digital conductometer (Leici, China) in aqueous solution at room temperature. Isothermal titration calorimetry (ITC) experiments were performed at 25 °C using VP-ITC isothermal titration calorimeter (Microcal, Northampton, MA, USA) with a 1.48 mL sample cell, 280 μ L titration syringe, all solutions were first degassed on the MicroCal's Thermovac unit to prevent the formation of bubbles and the Origin 7.0 software provided with the instrument was used to analyze data.

2.2. Preparations

The ligand of 6-(pyrazin-2-yl)-1,3,5-triazine-2,4-diamine (pzta) was prepared according to the method in the literature for the preparation of 1,3,5-triazine-2,4-diamine derivatives [29], and complexes **1** and **2** were prepared in good yield in the following way (Scheme 1). An aqueous solution (0.5 mL) of Cu(ClO₄)₄·6H₂O (0.1850 g, 0.5 mmol) was added to an ethanol/water mixed solvent (20 mL, 3/1: v/v) of pzta (0.0945 g, 0.5 mmol) under constant stirring for 30 min. Subsequently, an aqueous solution of corresponding amino acids of *L*-Arginine (0.0871 g, 0.5 mmol)/*L*-Methionine (0.0745 g, 0.5 mmol) with equal



Scheme 1. Synthetic routes for the ligand and complexes.

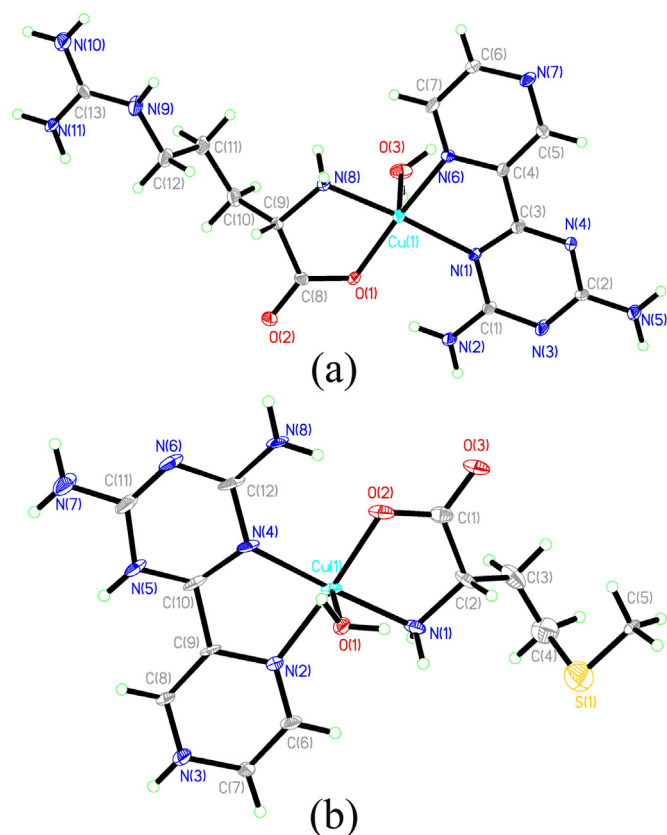


Fig. 1. Structures of **1** (a) $[\text{Cu}(\text{L-ArgH})(\text{pzta})(\text{H}_2\text{O})]^{2+}$ and **2** (b) $[\text{Cu}(\text{L-Met})(\text{pzta})(\text{H}_2\text{O})]^+$. The perchlorate ions and crystal waters were omitted for clarity.

NaOH (0.0200 g, 0.5 mmol) was added dropwise and gave a clear solution at pH 6.0. The resulting solutions were stirred for 2 h at 70 °C and then filtered, upon slowing evaporation at room temperature, well-shaped crystals suitable for X-ray diffraction analysis were obtained. The products were collected after washing with cold ethanol and water.

$[\text{Cu}(\text{pzta})(\text{L-ArgH})(\text{H}_2\text{O})](\text{ClO}_4)_2$ (**1**). Yield: 80%. Anal. Calcd for $\text{C}_{13}\text{H}_{25}\text{Cl}_2\text{CuN}_{11}\text{O}_{11}$ (MW = 645.87) (%): C, 24.25; H, 3.60; N, 23.93. Found (%): C, 24.34; H, 3.62; N, 23.80. IR (KBr, cm^{-1}): ν (OH), 3440, ν_s (NH₂) 3331, ν_{as} (NH₂) 3150, ν (COO[−]) 1657, 1381, ν (C=N) 1586. UV–Vis $\lambda_{\text{max}}/\text{nm}$ ($\epsilon/\text{M}^{-1}\text{cm}^{-1}$): π – π^* 215 (33362), 280 (9695), d – d 629 (73). Molar conductance, Λ_M (1.0×10^{-3} M, H₂O): $194.2 \text{ S}^{-1}\text{cm}^2\text{mol}^{-1}$. ESI-MS (MeOH): m/z = 425.1 $[\text{Cu}(\text{pzta})(\text{L-ArgH})]^+$.

$[\text{Cu}(\text{pzta})(\text{L-Met})(\text{H}_2\text{O})]\text{ClO}_4 \cdot 3\text{H}_2\text{O}$ (**2**). Yield: 76%. Anal. Calcd for $\text{C}_{12}\text{H}_{25}\text{ClCuN}_8\text{O}_{10}\text{S}$ (MW = 572.44) (%): C, 25.18; H, 4.40; N, 19.57; S, 5.60. Found (%): C, 25.17; H, 4.57; N, 19.25; S, 5.41. IR (KBr, cm^{-1}): ν (OH), 3435, ν_s (NH₂) 3335, ν_{as} (NH₂) 3196, ν (COO[−]) 1654, 1383, ν (C=N) 1586. UV–Vis $\lambda_{\text{max}}/\text{nm}$ ($\epsilon/\text{M}^{-1}\text{cm}^{-1}$): π – π^* 216 (33374), 278 (9589), d – d 631 (89). Molar conductance, Λ_M (1.0×10^{-3} M, H₂O): $104.6 \text{ S}^{-1}\text{cm}^2\text{mol}^{-1}$. ESI-MS (MeOH): m/z = 400.1 $[\text{Cu}(\text{pzta})(\text{L-Met})]^+$.

2.3. X-ray crystallographic studies

Suitable single crystals of complexes **1** and **2** were performed on a Bruker Smart 1000 diffractometer equipped with a CCD area detector at 173 (2) K and 100 (2) K, respectively, and graphite-monochromatized Mo-K α radiation (λ = 0.71073 Å) with the φ – ω scan technique. The data were reduced by the SAINT program and corrected for absorption using the semi-empirical multi-scan approach (SADABS). The crystal structures of the complexes were solved by direct method (SHELXL-

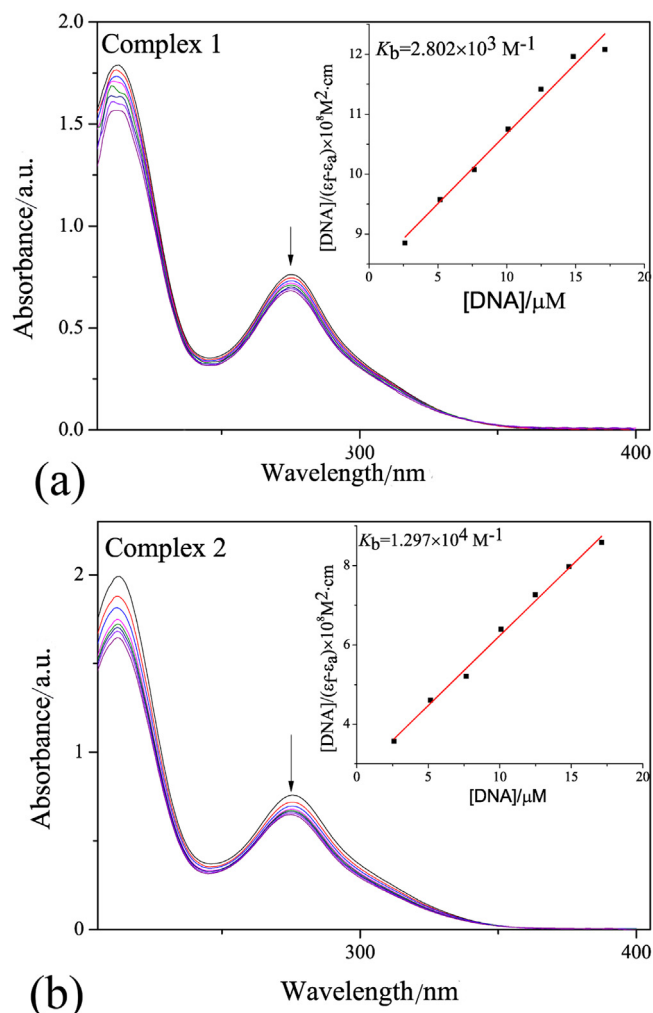


Fig. 2. Electronic absorption spectra of **1** (a) and **2** (b) in the absence and presence of CT-DNA. The arrows show the absorbance change upon increasing the DNA concentration. Inset: plots of $[\text{DNA}]/\epsilon_a - \epsilon_f$ vs. $[\text{DNA}]$.

2014), and anisotropic thermal parameters of all non-hydrogens were refined by full-matrix least-squares based on $|F|^2$ using the SHELXTL program package. Their coordinates were determined by Fourier analyses with hydrogen atoms added theoretically. In complex **2**, the contribution of the electron density by the remaining solvent molecules was removed by the SQUEEAE routine in PLATON, and the number of solvent molecules (H₂O) in **2** was obtained by element analyses [30]. Further crystallographic data and experimental details of structural analyses of **1** and **2** are summarized in Table S1. Selected bond lengths (Å) and bond angles (°) are given in Table S2. CCDC 1561104 and 1561103 for complexes **1** and **2** contain the supplementary crystallographic data for this paper. These data are provided free of charge by The Cambridge Crystallographic Data Centre.

2.4. Stability determination

The stabilities of the copper(II) complexes in buffer solutions were determined from their UV–Visible spectra. The complexes in Tris-HCl/NaCl buffer solutions at pH = 7.2 (50 mM NaCl, 5 mM Tris-HCl) or 7.4 (0.05 M Tris-HCl/0.15 mM NaCl) were incubated at room temperature for 0, 12, 24 and 48 h, respectively, and UV–Visible spectra were recorded at each time point.

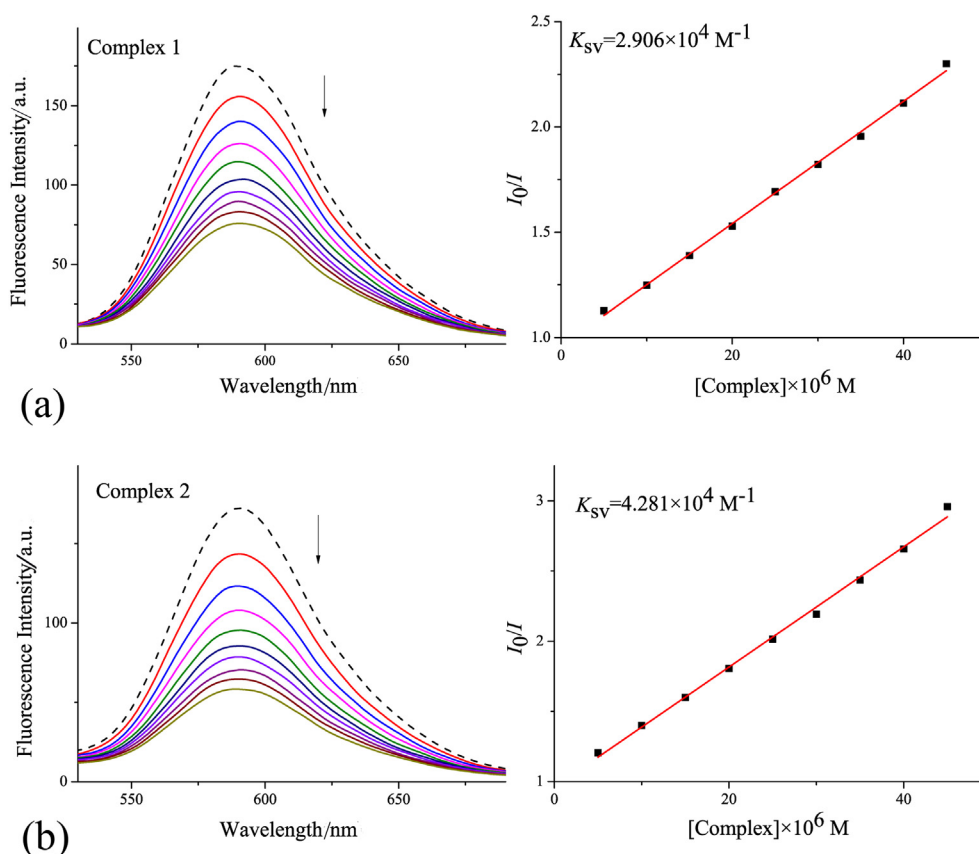


Fig. 3. Emission spectra of EB-DNA system in the absence and presence of 1 (a) and 2 (b). Inset: plots of I_0/I vs. [Complex]. Arrows show the changes in intensity with increasing concentrations of the complexes.

2.5. DNA binding studies

DNA stock solution was prepared by dilution of CT-DNA to Tris-HCl buffer (50 mM NaCl, 5 mM Tris-HCl) at pH 7.2, which was stored at 4 °C and used within 4 days. Stock solution of CT-DNA gave a ratio of UV absorbance at 260 and 280 nm (A_{260}/A_{280}) of 1.8–1.9, indicating that the DNA was sufficiently free of protein. The concentration of the DNA was calculated according to the absorbance at 260 nm by using extinction coefficient of $6600 \text{ M}^{-1} \text{ cm}^{-1}$ [31]. The complexes used in DNA-binding experiments were also prepared in Tris-HCl buffer at pH = 7.2.

Absorption titration experiments were carried out by keeping the complexes concentration constant (55 μM) and varying the concentration of CT-DNA from 0 to 17.13 μM in the spectral region of 200–400 nm. Fluorescence spectra were recorded in the range of 540 to 660 nm at room temperature with the excitation wavelength of 591 nm, by an addition of the Cu(II) complexes solutions (0–40 μM) to a sample containing EB (4.8 μM) and CT-DNA (5.5 μM). Circular Dichroic spectra of CT-DNA (3 mM) were scanned in the range of 200–320 nm by increasing the ratio of [complex] to [CT-DNA] ($r = 0, 0.2, 0.4$) at room temperature. DNA thermal denaturation experiments were carried out by monitoring the absorption intensity of CT-DNA (50 μM) at 260 nm in the temperature range from 60 to 100 °C with increments of 1 °C/min, both in the absence and presence of the copper(II) complexes (20 μM). In ITC experiments, calf thymus DNA (0.05 mM) was maintained in the sample cell and the complexes (0.2 mM) were introduced into the sample cell by means of syringes and the amount of each injection was 10 μL under continuous stirring (307 rpm), the reference power was set as 5 μcal and the duration of each injection was fixed at 10 s and the delay time between the injections was kept 120 s to achieve a complete balance.

2.6. Protein binding studies

Stock solutions of the complexes and HSA were prepared at a concentration of 0.05 M in Tris-HCl/0.15 mM NaCl buffer (pH = 7.4). The concentration of HSA was determined spectrophotometrically, using the molar absorptivity of $36,500 \text{ M}^{-1} \text{ cm}^{-1}$ at 280 nm [32]. HSA solutions were stored in the dark at 4 °C and used after no > 4 days.

Absorption titration spectra of HSA in the absence and presence of the complexes were recorded in the range of 290–500 nm. The HSA concentration was fixed at 1 μM in a quartz cell and the concentrations of the complexes were varied from 4 to 28 μM by successive additions. The fluorescence quenching and synchronous fluorescence spectra of HSA were monitored by keeping the concentration of HSA constant (5 μM), and increasing the complexes concentration (4–28 μM) at room temperature. The excitation wavelength was set to 280 nm and the fluorescence quenching spectra were recorded from 300 nm to 500 nm. The widths of the excitation and emission slits were set to 5.0 and 3.0 nm, respectively. The synchronous fluorescence spectra were recorded from 280 to 320 nm ($\Delta\lambda = 15 \text{ nm}$) and from 300 to 400 nm ($\Delta\lambda = 60 \text{ nm}$) for Tyr and Trp residues, respectively. For ITC experiments, the complexes (0.2 mM) were introduced by using a syringe into the sample cell that filled with 0.02 mM of HSA. The amount of each injection was 10 μL with a fixed stirring speed of 307 rpm. The reference power was set as 5 μcal , and the time interval between two continuous injections was set at 240 s to make sure achieve a complete balance.

2.7. Molecular docking

The binding mode and intermolecular interactions of the complexes with DNA/HSA were investigated by molecular docking technology

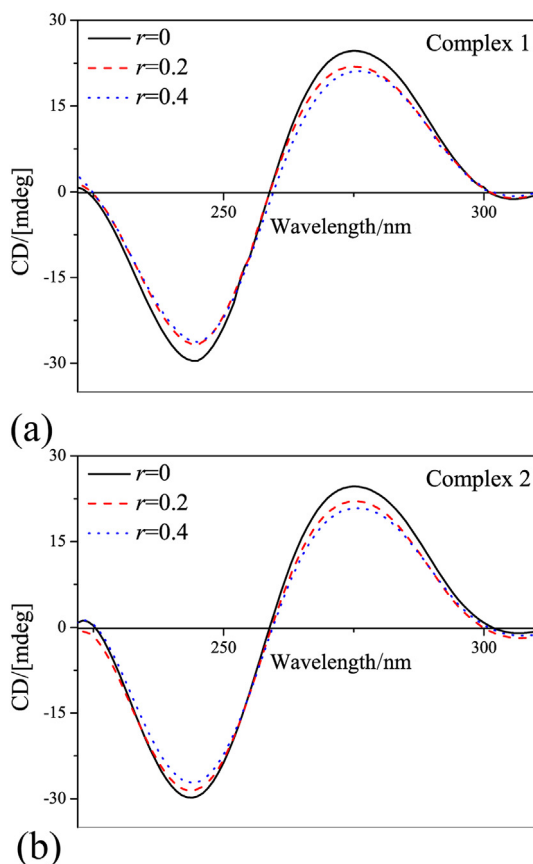


Fig. 4. CD spectra of CT-DNA in the absence and presence of **1** (a) and **2** (b) at room temperature. Conditions: $[DNA] = 1.0 \times 10^{-4} M$, $r = [complex]/[DNA] = 0, 0.2, 0.4$.

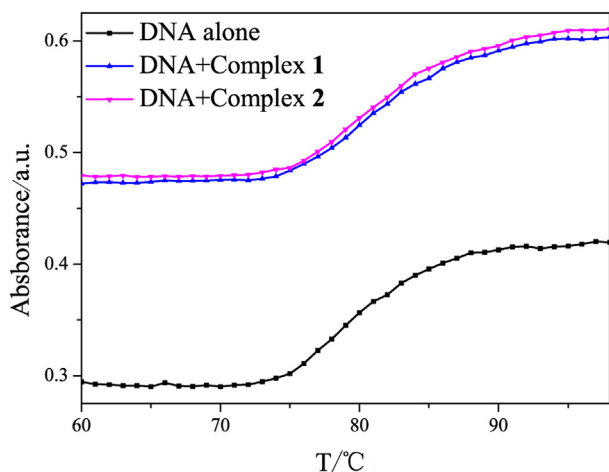


Fig. 5. Thermal melting profiles of CT-DNA in the absence and presence of complexes **1** and **2** at 260 nm.

using Autodock 4.2 program. The available crystal structures of DNA (PDB ID: 1-BNA) and HSA (PDB ID: 1H9Z) were downloaded from the PDB database [33]. The X-ray crystal structures of Cu(II) complexes were converted to PDB format using Mercury software. Before docking calculations were performed, the water molecules were removed and the polar hydrogen atoms of macromolecules were added. The binding sites were defined using a box size of $60 \times 60 \times 60 \text{ \AA}^3$ dimension with a grid-point spacing of 0.375 \AA . The complexes were centered at the coordinates $x = 14.719$, $y = 20.979$ and $z = 8.824$ at site of DNA; whereas for HSA site, the coordinates were fixed at $x = 24.986$,

$y = 9.578$ and $z = 20.079$. Docking simulation was performed using the Lamarckian genetic algorithm with local search, and with a total of 100 runs for each binding site. In each run, a population of 150 individuals with 27,000 generations and 2,500,000 energy evaluations were employed. Furthermore, the outputs from AutoDock were further analyzed using PyMOL software package [34].

2.8. In vitro cytotoxicity assays

The MTT colorimetric assays were performed to measure the cytotoxic effect of the tested compounds (pzta, $\text{Cu}(\text{ClO}_4)_2$, **1**, **2** and cis-platin). Human carcinoma cell lines of A549 (pulmonary), HeLa (cervical) and PC-3 (prostatic) were seeded in triplicate in 96-well microtiter plates with 1×10^4 cells per well and incubated overnight in a humidified atmosphere of 5% CO_2 at 37°C . Cells were treated with increasing concentrations of the complexes in RPMI 1640 medium supplemented with 10% fetal bovine serum (FBS), ranging from 3.125 to $200 \mu\text{M}$. Control wells were prepared by addition of culture medium ($100 \mu\text{L}$) and the wells containing culture medium without cells were used as blanks, then the plates were incubated in humidified atmosphere for 48 h. Subsequently, $20 \mu\text{L}$ MTT ($5 \text{ mg}\cdot\text{mL}^{-1}$) in phosphate buffer ($\text{pH} = 7.4$) was added to each well for a further 4 h, then $100 \mu\text{L}$ of DMSO was added to dissolve the formazan product formed by viable cells, the optical density (OD) of each well was then measured at 570 nm with a Tecan Infinite F200 plate reader (Switzerland). After blank subtraction, the IC_{50} values were determined by plotting the percentage viability versus the concentration on a logarithmic graph and reading off the control [35].

3. Results and discussion

3.1. Synthesis and characterization

Two ternary copper(II) complexes were prepared by reaction of copper(II) perchlorate hexahydrate with pzta and *L*-Arginine/*L*-Methionine in 75% (v/v) ethanol/ H_2O solution. The resulting complexes were stable in air and soluble in H_2O , MeOH and DMSO. The elemental (C, H, N and S) analyses confirmed the molecular formula and the number of water molecule of the complexes, and the molar conductance values of the complexes in aqueous solution indicated that complex **1** was a typical of 1:2 electrolyte, and complex **2** was a 1:1 electrolyte [36]. The ESI-MS for the complexes in methanol solution showed peaks at $m/z = 425.1$ and 400.1 , matching exactly with the coordination cations $[\text{Cu}(\text{pzta})(\text{L-Arg})]^+$ and $[\text{Cu}(\text{pzta})(\text{L-Met})]^+$, respectively.

The Single crystal X-ray analysis revealed that complexes **1** and **2** crystallized as a triclinic crystal system with the space group *P1* (Fig. 1). The distances of O (ClO_4) to central Cu(II) ions for complexes **1** and **2** were 2.728 and 2.686 \AA , respectively, which were too long to be considered as bonding, so the perchlorates were considered to be an anion [37], in accordance with the molar conductance results of the complexes. The coordination geometries around the Cu(II) center could be described as a distorted square pyramid, in which the τ values were 0.12 and 0.05 for **1** and **2**, respectively. The Cu(II) center in **1/2** exhibited a five-coordinated environment where four equatorial positions were occupied by two nitrogen atoms from the pzta ligand, the amino nitrogen and one carboxyl atom from the amino acid ligands, and a weakly coordinated oxygen atom from water molecule occupied the apical position. The distance from the axial atom to the central atom was 2.312 \AA for **1** (2.346 \AA for **2**), longer than those of the equatorial bonds (1.928–2.026 \AA for **1**, 1.959–2.016 \AA for **2**) due to the Jahn-Teller effect [38], indicating that the axial bonds was weak. The bond angles between the adjacent coordinating equatorial atoms with the central Cu(II) atom fall in the range of $80.6\text{--}97.2^\circ$ and $81.5\text{--}98.2^\circ$ for **1** and **2**, respectively. These data were similar to those of the reported mononuclear Cu(II) complexes with a distorted square pyramid

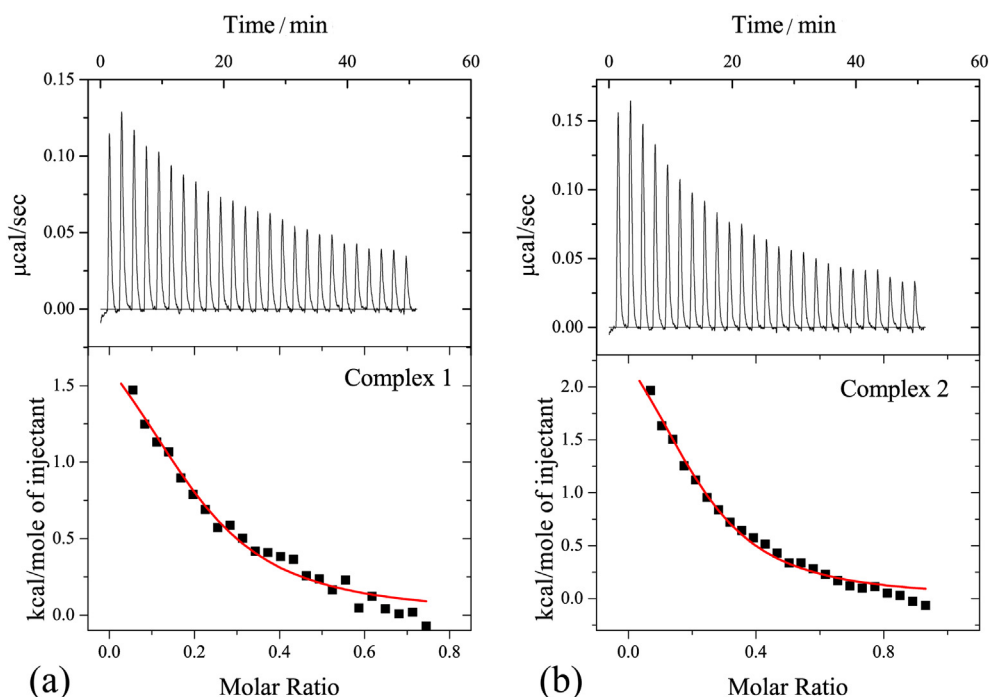


Fig. 6. ITC data for the titration of **1** (a) and **2** (b) into CT-DNA solution at 25 °C. The top panels represent the heat burst curves for successive injection of the complexes into DNA. The bottom panels represent the corresponding normalized heat signals versus molar ratio fitted to one site model.

Table 1

The thermodynamic parameters obtained by the ITC experiments for the CT-DNA binding of the complexes.

Complex	<i>n</i>	$K_b \times 10^5 \text{ (L} \cdot \text{mol}^{-1})$	$\Delta H \text{ (kcal/mol)}$	$-T\Delta S \text{ (kcal/mol)}$	$\Delta G \text{ (kcal/mol)}$
1	0.201 ± 0.0238	2.19 ± 0.533	2.273 ± 0.555	-9.570	-7.297
2	0.216 ± 0.0204	2.48 ± 0.442	3.317 ± 0.383	-10.494	-7.177

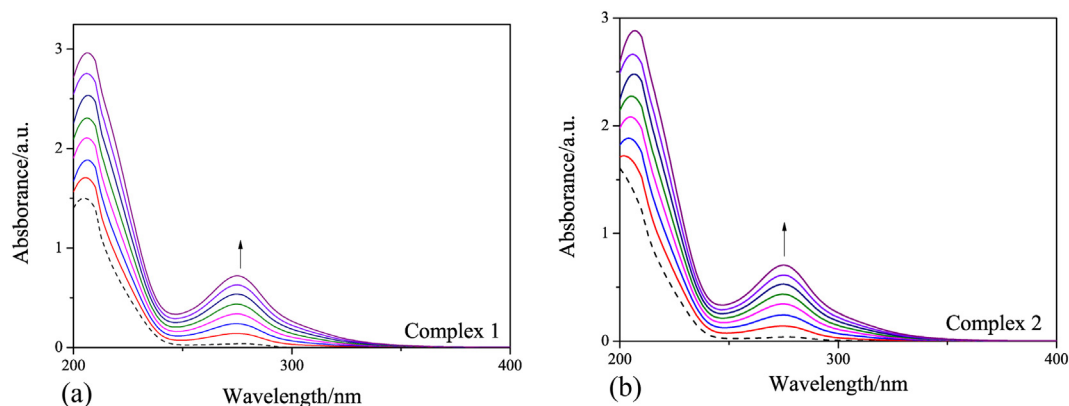


Fig. 7. UV-Vis spectra of HSA in the absence and presence of **1**(a) and **2**(b) at room temperature.

geometry [27,39,40]. In addition, the guanidinium group of *L*-Arginate side chain in complex **1** was protonated with a positive charge, being similar to the reported complexes of $[\text{Cu}(\text{L-Arg})(\text{B})\text{Cl}]\text{Cl}$ ($\text{B} = \text{bpy}/\text{phen}/\text{dpq}/\text{dppz}$) [41].

The IR spectra of complexes **1** and **2** showed a broad bands at 3440 and 3435 cm^{-1} , respectively, in agreement with the stretching vibrations ν ($-\text{OH}$) of the water molecules. The two broad bands at 3331 and 3150 cm^{-1} for **1** (3335 and 3196 cm^{-1} for **2**) were ascribed, respectively, to asymmetric ν_{as} ($-\text{NH}_2$) and symmetric ν_{s} ($-\text{NH}_2$) stretching vibrations of the coordinated and uncoordinated $-\text{NH}_2$ groups. The absence of any band in the range of 1700–1750 cm^{-1} for the complexes suggested the coordination of the COO^- groups of the amino acids to the

central copper ion. Moreover, the bands of $\nu_{\text{as}}(\text{COO}^-)$ (1657 cm^{-1} for **1**; 1654 cm^{-1} for **2**) and $\nu_{\text{s}}(\text{COO}^-)$ (1381 cm^{-1} for **1**; 1383 cm^{-1} for **2**) stretching frequencies with $\Delta\nu$ ($\nu_{\text{as}} - \nu_{\text{s}}$) values ($> 200 \text{ cm}^{-1}$), indicated monodentate nature of the carboxylate ion in the complexes [42]. Additionally, ν ($\text{C}=\text{N}$) of the coordinated pzta (1586 cm^{-1} for **1** and 1592 cm^{-1} for **2**) were shifted to lower frequencies compared to free pzta (1636 cm^{-1}) revealed the coordination of N atoms (pzta) to the central metal ion. Besides, the bands near 640 and 480 cm^{-1} were attributed to stretching vibrations of ν ($\text{Cu}-\text{O}$) and ν ($\text{Cu}-\text{N}$), respectively [43].

The electronic spectra of the complexes in aqueous solution exhibited high-energy bands (at 215 and 280 nm for **1**, at 216 and 278 nm

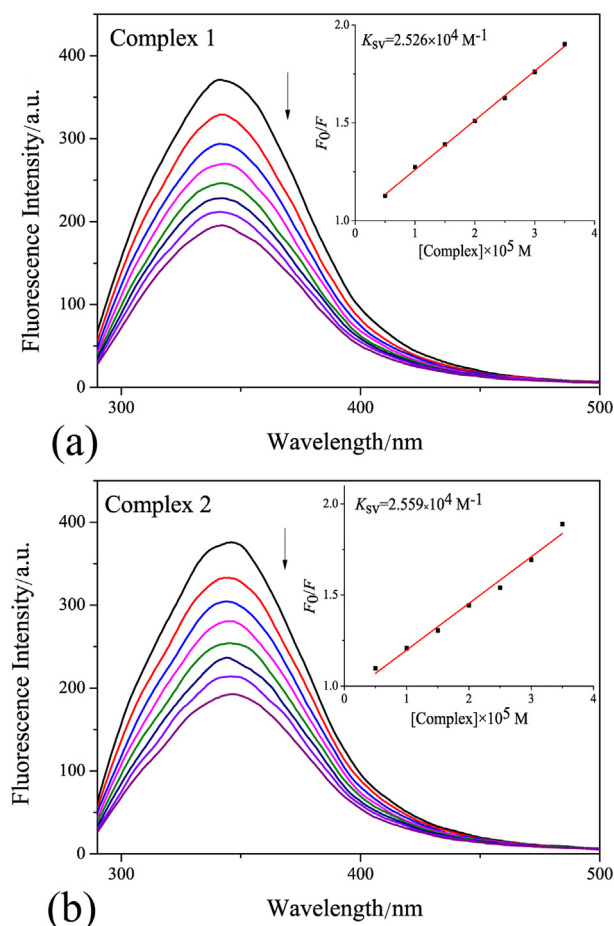


Fig. 8. Fluorescence emission spectra of HSA (5 μ M) in the absence and presence of different concentrations **1** (a) and **2** (b) in Tris-HCl buffer (pH = 7.4). Inset: The Stern-Volmer plots for fluorescence quenching of HSA by the complexes.

Table 2

The quenching constants and thermodynamic parameters of complex-HSA systems.

Complex	$K_q \times 10^{12}$ ($M^{-1}s^{-1}$)	$K_{sv} \times 10^4$ (M^{-1})	R	$K_b \times 10^4$ (M^{-1})	n	R
1	2.526	2.526	0.995	4.336	0.988	0.994
2	2.559	2.559	0.991	4.880	1.114	0.985

for **2**), which were attributed to the π - π^* transitions of the pzta ligand. The weak and broad bands (629 nm for **1** and 631 nm for **2**) observed in the lower energy regions, were attributed to the d-d transitions of the central metal Cu(II) ion and typical for Cu(II) complexes with a distorted square-pyramidal geometry [44].

In order to confirm the stabilities of the ternary copper(II) complexes, stability tests in Tris-HCl buffer (pH = 7.2 and pH = 7.4) solutions were carried out by UV-Visible spectroscopy. No obvious change could be observed for the UV-Visible spectra of **1** and **2** in Tris-HCl buffers at room temperature after 48 h incubation (Figs. S1–S2†), suggesting that the complexes were stable in buffer solutions for further experimental studies [45].

3.2. DNA-binding experiments

3.2.1. Electronic absorption titrations

Electronic absorption titration experiment is one of the convenient tools to explore the binding ability and extent of metal complexes

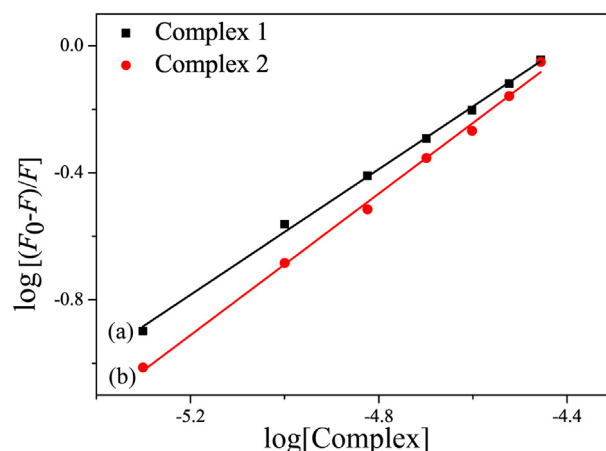


Fig. 9. The double-logarithmic plots for the fluorescence quenching of HSA by complexes **1**(a) and **2**(b).

toward DNA. The absorption spectra of the complexes in the absence and presence of CT-DNA are showed in Fig. 2. It can be found from the figure that, with increasing concentration of DNA, the intensities of the absorption bands exhibited hypochromism of 10.24% and 14.42% with negligible red shift for **1** and **2**, respectively, which was consistent with groove binding mode leading to small perturbations [46]. The observed order of hypochromism, **2** > **1**, implied that DNA binding affinity of **2** was higher than that of **1**, which might be related to the hydrophobic side chain of *L*-Methionine. The main driving force (hydrophobic interaction) of binding between the complexes and DNA was further validated by the isothermal calorimetric titration experiments. To comparing the DNA binding affinities quantitatively, the intrinsic binding constants K_b were determined using the following equation [47]:

$$[DNA]/(\varepsilon_a - \varepsilon_f) = [DNA]/(\varepsilon_b - \varepsilon_f) + 1/K_b (\varepsilon_b - \varepsilon_f) \quad (1)$$

where the apparent absorption coefficients ε_a , ε_f and ε_b correspond to $A_{obs}/[complex]$, the extinction coefficient of the complexes free in solution, and the extinction coefficient of the complexes in the fully bound form, respectively. $[DNA]$ is the concentration of CT-DNA. In the plot of $[DNA]/(\varepsilon_a - \varepsilon_f)$ versus $[DNA]$, the value of K_b is given by the ratio of slope to intercept. The binding constants were $2.802 \times 10^3 M^{-1}$ for **1** and $1.297 \times 10^4 M^{-1}$ for **2**, following the order **2** > **1**, which was the same as that for the above hypochromism. The calculated intrinsic equilibrium binding constants (K_b) were consistent well with the values (10^3 – 10^5) observed in other groove binding systems [37].

3.2.2. Ethidium bromide displacement assays

The competitive binding experiment is usually carried out by fluorescence spectral technique via monitoring the emission intensity of EB bound to DNA. The EB fluorophore emits intense fluorescence in the presence of CT-DNA due to a strong intercalation between the adjacent base pairs of DNA. The enhanced fluorescence can be quenched by the addition of a second molecule because the molecule binds to DNA at the site occupied by EB [48]. As shown in Fig. 3, the observed quenching of EB–DNA fluorescence by the complexes (up to 39.04% for **1** and 41.91% for **2**) suggested that the complexes bound to DNA by competing with EB. A quantitative estimate of this quenching behavior can be obtained by treating the data according to the Stern–Volmer equation [49]:

$$F_0/F = 1 + K_{sv} [Q] \quad (2)$$

where, I_0 and I are the fluorescence intensities in the absence and presence of the quencher, respectively. The K_{sv} is the quenching constant and $[Q]$ is the concentration of the quencher. The plot of I_0/I vs.

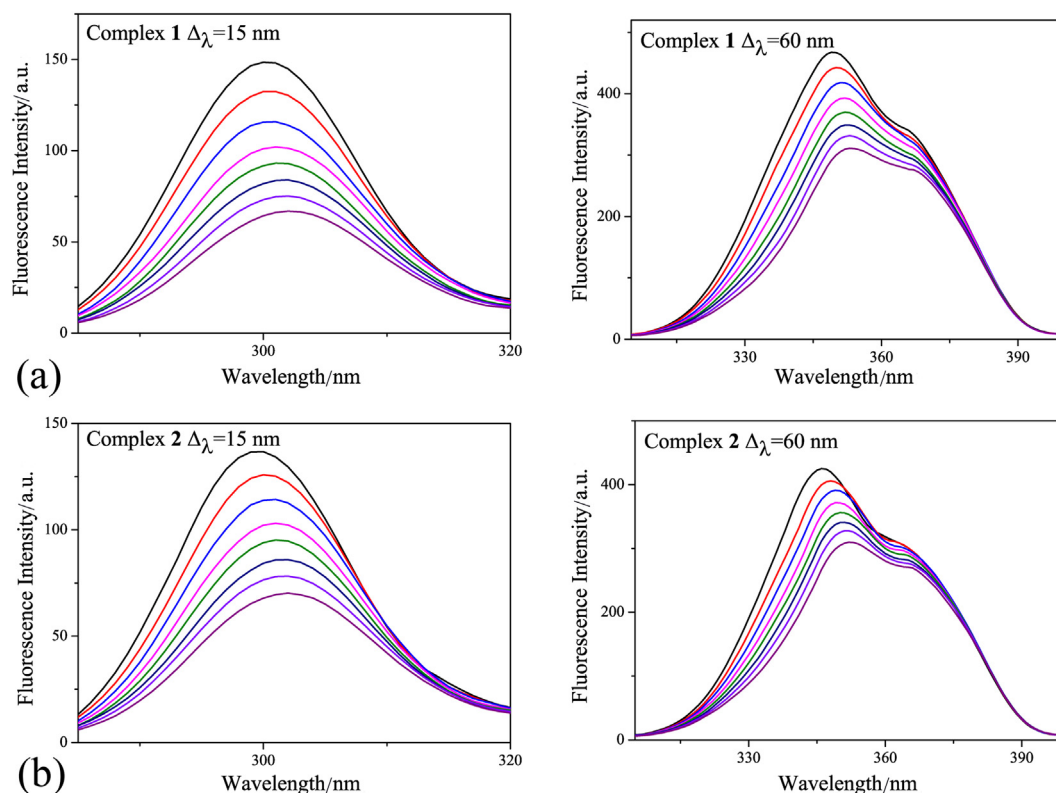


Fig. 10. Synchronous fluorescence spectra of HSA (5 μM) in Tris-HCl buffer with increasing concentration of the complexes (0–28 μM). (a): complex 1 at $\Delta\lambda = 15$ nm and $\Delta\lambda = 60$ nm. (b): complex 2 at $\Delta\lambda = 15$ nm and $\Delta\lambda = 60$ nm.

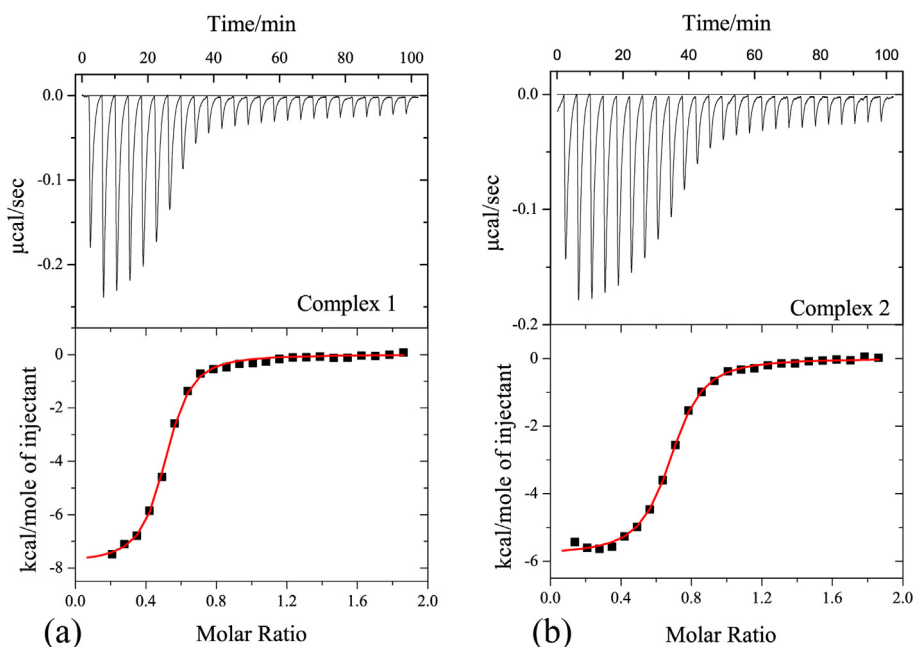


Fig. 11. ITC data for the titration of 1 (a) and 2 (b) into HSA solution at 25 °C. The top panels represent the heat burst curves for successive injection of the complexes into HSA. The bottom panels represent the corresponding normalized heat signals versus molar ratio fitted to one site model.

[Q] is of a linear relationship and K_{sv} can be calculated by the slope of this plot. The quenching constant (K_{sv}) values were calculated to be 2.906×10^4 for 1 and $4.281 \times 10^4 \text{ M}^{-1}$ for 2, following the order $2 > 1$, which was also in accord with the above absorption titration result.

3.2.3. Circular dichroism spectral studies

Circular dichroism (CD) spectroscopy is a useful technique applied for detecting any changes in the secondary structures of DNA in the presence of metal complexes. CD spectra of CT-DNA show no or very little perturbation in case of electrostatic binding or groove binding, but exhibit significant change in case of an intercalation mode [50]. As shown in Fig. 4, the observed major bands observed at 275 and 245 nm

Table 3

The thermodynamic parameters obtained by the ITC experiments for the HSA binding of the complexes.

Complex	<i>n</i>	$K_b \times 10^6$ (L·mol ⁻¹)	ΔH (kcal/ mol)	$-T\Delta S$ (kcal/ mol)	ΔG (kcal/ mol)
1	0.489 ± 0.00308	4.55 × 10 ⁶	−7.81	−1.57	−9.38
2	0.664 ± 0.00326	3.66 × 10 ⁶	−5.80	−3.43	−9.23

were corresponding to the base stacking and the helicity of normal B-DNA conformation, respectively [51]. With increasing concentration of the complexes, the intensities of the DNA bands decreased slightly and the band positions moved toward to a higher wavelength on a small scale, indicating that the secondary structures of the DNA double helix translated from B to C conformation [52]. These changes convinced that the complexes bound to DNA non-intercalatively and probably in a groove binding mode, which was consistent with the results obtained from the above electronic absorption and fluorescence spectroscopies.

3.2.4. Thermal denaturation experiments

Thermal denaturation analysis is an important method to elucidate the DNA-binding mode of metal complexes. In a thermal denaturation experiment, a duplex DNA is thermally denatured into single-strand components in the presence and absence of the complexes. The temperature at which 50% of the DNA is in the double-helical state and 50% in single stranded form, is known as melting temperature (T_m) [53]. Usually, the intercalative binding mode results in a sharp increase in melting temperature (4–8 °C), while a groove binding mode will have little effect [54]. The thermal denaturation curves of CT-DNA in the absence and presence of the complexes are shown in Fig. 5. In the absence of the complexes, the melting temperature of CT-DNA was 79.70 °C. However, the T_m values were 81.03 °C and 81.40 °C in the presence of complexes 1 and 2, respectively. The slight increases in DNA melting temperature observed in the presence of the complexes indicated that the complexes bound to DNA via a grooving binding mode, in line with the result obtained by the above spectroscopic experiments.

3.2.5. Isothermal titration calorimetry (ITC) assays

The interactions of metal complexes with DNA can be studied using isothermal titration calorimetry to gain insights into thermodynamics of the binding reaction [55]. During the calorimetric titration, the binding constant, stoichiometry, and thermodynamic parameters can be calculated directly from the changes of heat [56]. The ITC profiles of the binding of the complexes toward CT-DNA are shown in Fig. 6, in

which the upper panels represent the raw ITC curves resulting from the injection of the complexes to DNA, while the lower panels show the heats of reaction plotted against the molar ratio of the complexes to DNA after the baseline correction. Origin 7.0 program applying the one binding site model provided the best curve fitting, where the binding constants were 2.19×10^5 and $2.48 \times 10^5 \text{ M}^{-1}$ for 1 and 2, respectively. The thermodynamic parameters (Table 1) obtained by ITC suggested the spontaneous free energy ($\Delta G < 0$) and favorable entropy driven ($\Delta S > 0$) reaction, indicating the key role of the hydrophobic binding between the complexes and DNA [57]. We inferred that it might be the hydrophobic interaction that led to the binding affinities (K_b) of the complexes to DNA following the order $2 > 1$, which matched well with the results obtained by the above studies.

3.3. Interaction with HSA

3.3.1. UV–Vis absorption titrations

UV–Vis absorption titration is a simple method to predict the quenching type of HSA by metal complexes [58]. As previously reported, HSA produces two absorption bands in the UV spectrum, a strong band at 220 nm designated to the protein backbone and a weak band at 280 nm produced by the aromatic amino acids, including Trp, Tyr, and Phe [59,60]. Any interaction between the complexes and HSA can change the absorbance of the bands. Furthermore, quenching may occur either by a dynamic or static mode, in which static quenching denotes the formation of a HSA-complex system in the ground state and the absorption spectra of HSA are affected considerably, whereas dynamic quenching affects only the excited state, and thus has no effect on the absorption spectra [61]. As shown in Fig. 7, the absorbances increased with the complexes, indicating that the Cu(II) complexes interacted with HSA and the type of interaction between the complexes and HSA was mainly a static quenching process.

3.3.2. Fluorescence quenching mechanism and binding properties of HSA by the complexes

Some useful information about the interaction between metal complexes and HSA could be obtained by using fluorescence method, such as quenching mechanism, binding parameters, thermodynamic parameters and binding modes [62].

Fluorescence quenching spectra of HSA in the absence and presence of complexes 1 and 2 are shown in Fig. 8. The fluorescence emissions of the characteristic broad band at 345 nm of HSA were quenched with increasing concentrations of the complexes. The observed quenching might be attributed to possible changes in the secondary structures of HSA, indirectly indicating the binding of the complexes to HSA. The Stern-Volmer equation is usually applied for confirming the quenching

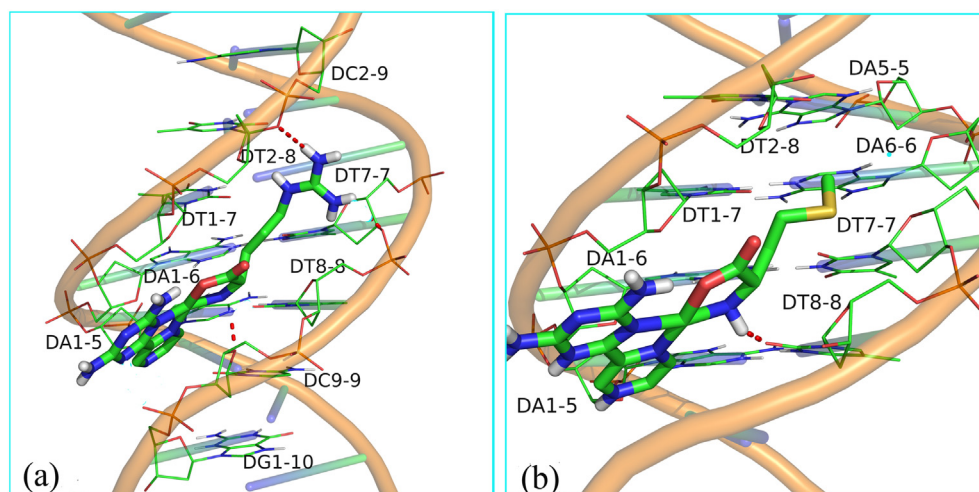


Fig. 12. Molecular docking studies of DNA-complex interactions. (a): Detailed view of the docking pose of DNA-complex 1; (b) Detailed view of the docking pose of DNA-complex 2. The hydrogen bonds between the complexes and DNA are represented using red dashed lines. (For interpretation of the references to colour in this figure legend, the reader is referred to the web version of this article.)

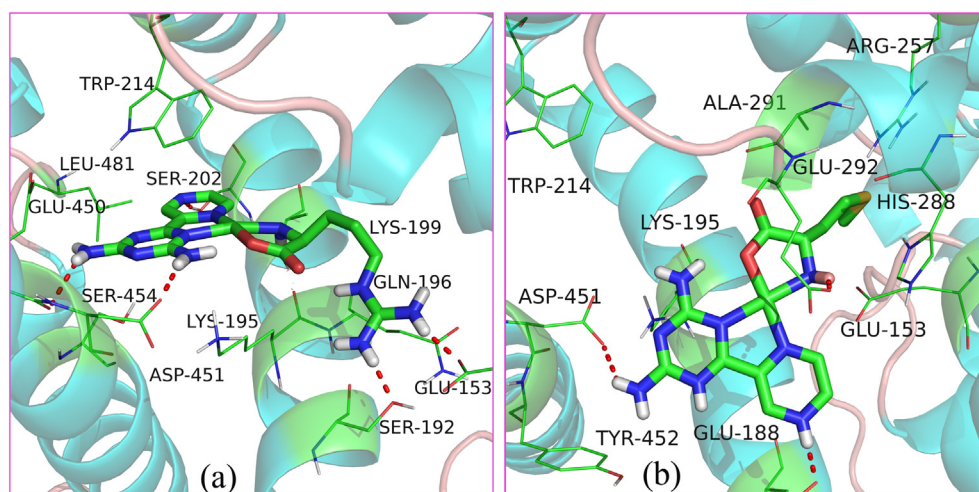


Fig. 13. Molecular docking studies of HSA-complex interactions. (a): Detailed view of the docking pose of HSA-complex 1; (b) Detailed view of the docking pose of HSA-complex 2. The hydrogen bonds between the complexes and HSA are represented using red dashed lines. (For interpretation of the references to colour in this figure legend, the reader is referred to the web version of this article.)

Table 4

The vitro cytotoxicity assays (IC_{50} values) for pzta and the complexes against A549, HeLa and PC-3 cell lines.

Compound	IC_{50} values (μM)		
	A549	HeLa	PC-3
Complex 1	89.13	131.83	85.11
Complex 2	51.29	> 200	141.25
pzta	> 200	> 200	> 200
$Cu(ClO_4)_2$	> 200	> 200	–
cisplatin	18.92	11.06	19.28
$[Cu(glygly)(pzta)]ClO_4 \cdot H_2O$ [28]	101.16	117.49	–
5-Fluorouracil [28]	61.54	124.01	–

mechanism [63]:

$$F_0/F = 1 + K_{sv}[Q] = 1 + K_q\tau_0 \quad (3)$$

where F_0 and F are the fluorescence intensities of HSA in the absence and presence of the quencher, respectively. K_{sv} is the Stern-Volmer dynamic quenching constant, and $[Q]$ is the concentration of quencher. K_q is the quenching rate constant of the biomolecule, τ_0 is the average lifetime of the biomolecule without quencher which equals 10^{-8} s. As shown in Fig. 8 (Inset), the good linearity relationship of F_0/F versus $[Q]$ showed that the quenching mechanism was only dynamic or static. The obtained bimolecular quenching constants K_q (Table 2) were in the order of magnitude at 10^{12} , which was much greater than the limiting diffusion constant K_{dif} of biomolecules ($2.0 \times 10^{10} M^{-1}s^{-1}$) [64], indicating that the fluorescence quenchings were likely to occur via a static quenching mechanism [65], which was consistent with the UV-Vis absorption titration results. For a static quenching, the binding constants (K_b) and the number of binding sites (n) could be obtained from the modified Stern-Volmer equation [63]:

$$\log[(F_0 - F)/F] = \log K_b + n \log [Q] \quad (4)$$

By the plot of $\log(F_0 - F)/F$ versus $\log [Q]$ (Fig. 9), the values of n and K_b can be obtained from the slope and the intercept of the double logarithm regression curve and the corresponding data are presented in Table 2. The K_b values at room temperature were 4.336×10^4 and $4.880 \times 10^4 M^{-1}$ for 1 and 2, respectively, indicating that the amino acid side chain in the copper(II) complexes did not have a marked effect on the association constants of the complexes toward HSA. Furthermore, the HSA-binding constants showed that HSA can be considered as a good carrier for transferring the complexes in vivo [66].

3.3.3. Synchronous fluorescence studies

Synchronous fluorescence is a very useful tool to investigate the

microenvironments around the fluorophore functional groups, which is identified as an effective method for monitoring the polarity change of amino residues by simultaneously scanning the excitation and emission wavelengths [67]. When the $\Delta\lambda$ between the excitation and emission wavelengths are 15 and 60 nm, the synchronous fluorescence spectra show characteristics of the tyrosine (Tyr) and tryptophan (Trp) residues of HSA, respectively [68]. The effects of the copper(II) complexes on HSA synchronous fluorescence spectroscopy are shown in Fig. 10. Evidently, no obvious shifts were observed in the synchronous fluorescence spectra ($\Delta\lambda = 15$ nm) of HSA with increasing concentrations of the complexes, indicating that the interactions of the complexes with HSA couldn't affect the conformation of the Tyr microenvironments. However, when $\Delta\lambda$ was 60 nm, the maximum emission wavelength of Trp residue showed obvious red shifts (from 349 to 353 nm for complex 1 and 347 to 353 nm for complex 2) after addition of the complexes, indicating that the conformation of HSA were changed by the complexes, and the hydrophobicity around Trp residue decreased, further indicating that the complexes have come to subdomain IIA of HSA where tryptophan (Trp-214: the only one tryptophan residue in HSA) residue was located [69]. Moreover, there was a large hydrophobic cavity near to Trp residue in subdomain IIA of HSA that functions as the binding site for many drugs [70].

3.3.4. Isothermal titration calorimetry assays

The isothermal titration calorimetry (ITC) experiment can determine binding constants as well as change in energetics of HSA in presence of metal complexes [71]. The ITC profiles of the binding of the complexes toward HSA are shown in Fig. 11, in which the upper panels represent the raw ITC curves resulting from the injection of the complexes to HSA, and the lower panels show the heats of reaction plotted against the molar ratio of the complexes to HSA after the baseline correction. From the ITC profiles, it was clearly found that the bindings of the complexes to HSA were exothermic, and best fitted to a single site of binding model. The binding constants, thermodynamic parameters and stoichiometries of the complex-HSA systems are summarized in Table 3. The negative ΔG values suggested the bindings of the complexes to HSA were a spontaneous process, and the negative values of ΔH and $T\Delta S$ indicated that the predominant forces in the interactions between the complexes and HSA were hydrogen-bond and hydrophobic interactions [72]. The binding constants and the thermodynamic parameters of the complexes toward HSA did not have obvious difference, which was consistent with the results of the above emission spectra.

3.4. Molecular docking study

Molecular docking technology can be used to predict the affinity and binding orientation of small molecules to their biological macromolecules such as proteins and DNA [73,74]. In this study, the synthesized complexes were subjected to molecular docking with DNA (1BNA) and HSA (1H9Z) to further confirm the results observed from the above experimental studies.

3.4.1. Molecular docking with DNA

The interactions between the complexes and DNA were confirmed by the molecular docking simulations where the complexes were docked to the crystal structure of DNA (1BNA). The optimum poses of the lowest binding energy for the complexes with DNA shown in Fig. 12 indicated that the complexes were located in the DNA major groove in the region of AT–GC residues and the binding processes were driven by hydrogen bonds and van der Waals forces, as well as hydrophobic interactions. These consequences provided a convincing complement to the above DNA binding experimental results. For complex 1 (a), two H-bonds were observed between the complex and DNA with the bond lengths of 2.119 Å (complex 1: H8A...1-BNA: DT28) and 2.025 Å (complex 1: H9A...1-BNA: DC99). Complex 2 formed only one H-bond with DNA, of which the length was 1.955 Å (complex 2: H1A...1-BNA: DT88). The calculated binding energies for 1 and 2 were -13.3 and -10.99 kcal·mol $^{-1}$, respectively, following the order of $1 > 2$, which was consistent with the number of H-bonds in the complexes.

3.4.2. Molecular docking with HSA

The complexes were also subjected to molecular docking studies with HSA to investigate their potential binding sites and energies. There are two drug binding grooves located in HSA, namely as binding site I and site II, respectively, which are present in the hydrophobic cavities of subdomain IIA and IIIA [75]. Fig. 13 showed the optimum poses of the lowest binding energy for the complexes with HSA, both the complexes were partly inserted into the hydrophobic cavity of subdomain IIA (site I) through hydrophobic interactions, resulting in the fluorescence quenching of Trp-214, which forcefully explained the above results of fluorescence spectrum experiments. It was found that, there were five hydrogen bonds between complex 1 and HSA (the interaction sites: Glu-153, Ser-192, Ser-202, Glu-450 and Asp-451 residues) with the lengths of 1.791, 1.771, 2.232, 2.215 and 1.989 Å, but there were only three H-bonds between HSA (the interaction sites: Glu 188, Glu 292 and Asp 451 residues) and complex 2 with the bond length of 1.940, 1.801 and 2.187 Å. Furthermore, the binding energies for the HSA-complex systems were -10.37 and -7.07 kcal/mol for 1 and 2, respectively.

3.5. Anticancer study

The in vitro cytotoxicities of cisplatin, pzta, Cu(ClO $_4$) $_2$ and the complexes against human tumor cell lines of A549 (pulmonary), PC-3 (prostatic) and HeLa (cervical) have been studied using MTT assays. The half maximal inhibitory concentration (IC $_{50}$) values for the cell lines incubated with the compounds after 48 h treatment are shown in Table 4. Complexes 1 and 2 showed higher cytotoxicity against the cancer cells compared with Cu(ClO $_4$) $_2$ or pzta, indicating that the chelation of the Cu(II) ion with pzta was responsible for the observed higher cytotoxic properties of the complexes. As shown in Table 4, the inhibitory rate of complex 2 was relatively high toward the A549 cell lines, but its cytotoxicities toward the HeLa and PC-3 cell lines were lower than the corresponding values of complex 1. This difference could be due to the selective inhibition of the complexes toward cancer cell lines. Though the cytotoxic activities of the complexes were lower than those of cisplatin, the complexes exhibited higher in vitro cytotoxicity against A549 compared with 5-Fluorouracil, a widely used clinical antitumor drug [28,71]. Furthermore, the complexes showed

higher cytotoxicities than the copper(II)-di-peptide complexes based on the pzta ligand reported in our previous research [28]. Therefore, the observations indicated complex 2 had the potential to act as a chemotherapeutic agent targeting A549 cell lines.

4. Conclusions

Two water-soluble copper(II) complexes of 6-(pyrazin-2-yl)-1,3,5-triazine-2,4-diamine with *L*-Arginine/*L*-Methionine were synthesized with a distorted square-pyramid geometry. In vitro DNA binding experiments clearly established the formation of groove binding systems between the complexes and CT-DNA, the binding processes were spontaneous and mainly driven by hydrophobic forces. Besides, the complexes quenched the emission intensity of HSA by static quenching and showed good binding affinities. The energetic studies performed by ITC experiments clearly showed that hydrogen-bond and hydrophobic interactions played important role in the binding of the complexes to HSA. Furthermore, the results of molecular docking studies were in good agreement with the above experimental results. Meanwhile, the chelation of copper(II) ion with pzta ligand resulted in the cytotoxicities of the complexes higher than the free ligand pzta against A549, PC-3 and HeLa cell lines. The results suggested their application as potential anticancer drugs, and may shed some light on the rational design of new potential Cu(II) anticancer agents.

Acknowledgements

We are grateful to the Program of Natural Science Foundation of Guangdong Province (2015A030313423) for generous financial support.

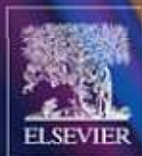
Appendix A. Supplementary data

Supplementary data to this article can be found online at <https://doi.org/10.1016/j.msec.2018.05.065>.

References

- [1] P.C. Bruijninx, P.J. Sadler, *Curr. Opin. Chem. Biol.* 12 (2008) 197–206.
- [2] K.M. Deo, B.J. Pages, D.L. Ang, C.P. Gordon, J.R. Aldrich-Wright, *Int. J. Mol. Sci.* 17 (2016) 1818–1835.
- [3] F. Tisato, C. Marzano, M. Porchia, M. Pellei, C. Santini, *Med. Res. Rev.* 30 (2009) 708–749.
- [4] C. Santini, M. Pellei, V. Gandin, M. Porchia, F. Tisato, C. Marzano, *Chem. Rev.* 114 (2014) 815–862.
- [5] C. Marzano, M. Pellei, F. Tisato, C. Santini, *Anti-Cancer Agent. Med.* 9 (2009) 185–211.
- [6] C. Rajarajeswari, M. Ganeshpandian, M. Palaniandavar, A. Riyasdeen, M.A. Akbarsha, *J. Inorg. Biochem.* 140 (2014) 255–268.
- [7] C.J. Dhanaraj, J. Johnson, *Mat. Sci. Eng. C Mater.* 78 (2017) 1006–1015.
- [8] Y. Xiao, Q. Wang, Y.M. Huang, X.L. Ma, X.N. Xiong, H. Li, *Dalton Trans.* 45 (2016) 10928–10935.
- [9] R. Shanmugakala, P. Tharmaraj, C.D. Sheela, N. Chidambaramanathan, *Med. Chem. Res.* 23 (2014) 329–342.
- [10] F. Sączewski, A. Bułakowska, *Eur. J. Med. Chem.* 41 (2006) 611–615.
- [11] R.R. Duan, Z.B. Ou, W. Wang, S. Chen, X.H. Zhou, *Spectrochim. Acta A* 151 (2015) 64–71.
- [12] K. Micskei, T. Patonay, L. Caglioti, G. Palyi, *Chem. Biodivers.* 7 (2010) 1660–1669.
- [13] T.L. Ma, J. Xu, Y. Wang, H. Yu, Y. Yang, Y. Liu, W.L. Ding, W.J. Zhu, R.H. Chen, Z.J. Ge, Y.F. Tian, L. Jia, T.F. Zhu, *J. Inorg. Biochem.* 144 (2015) 38–46.
- [14] M. Chikira, M. Inoue, R. Nagane, W. Harada, H. Shindo, *J. Inorg. Biochem.* 66 (1997) 131–139.
- [15] A.K. Patra, T. Bhowmick, S. Roy, S. Ramakumar, A.R. Chakravarty, *Inorg. Chem.* 48 (2009) 2932–2943.
- [16] N. Raman, M. Selvaganapathy, R. Senthilkumar, *Inorg. Chem. Commun.* 39 (2014) 99–105.
- [17] D. Agudelo, G. Berube, H.A. Tajmir-Riahi, *Int. J. Biol. Macromol.* 88 (2016) 354–360.
- [18] F. Kratz, *J. Control. Release* 132 (2008) 171–183.
- [19] H.Y. Cheng, T. Zou, Y.L. Xu, Y. Wang, A.B. Wu, J. Dai, Y.Z. Zhang, Y. Liu, *Luminescence* 31 (2016) 88–95.
- [20] A.M. Pizarro, P.J. Sadler, *Biochimie* 91 (2009) 1198–1211.
- [21] S.U. Rehman, T. Sarwar, M.A. Husain, H.M. Ishqi, M. Tabish, *Arch. Biochem. Biophys.* 576 (2015) 49–60.

- [22] Y.W. Jung, S.J. Lippard, *Chem. Rev.* 107 (2007) 1387–1407.
- [23] V.M. Manikandamathavan, T. Weyhermüller, R.P. Parameswari, M. Sathishkumar, V. Subramaniana, U.N. Balachandran, *Dalton Trans.* 43 (2014) 13018–13031.
- [24] M. Carreira, R. Calvo-Sanjuán, M. Sanaú, X.B. Zhao, R.S. Magliozzo, I. Marzo, M. Contel, *J. Inorg. Biochem.* 116 (2012) 204–214.
- [25] T.P. Lakshmi, M. Mondal, K. Ramadas, S. Natarajan, *Spectrochim. Acta A* 83 (2017) 90–102.
- [26] R.S.S. Muraliteal, R.S.S. Siddhardha, D.R. Babu, S. Venketesh, R. Basavaraju, G.N. Rao, *Spectrochim. Acta A* 180 (2017) 217–223.
- [27] X.M. Zhang, Z.B. Ou, S. Chen, Y.H. Xiong, X.H. Zhou, H.F. Liu, X.Y. Le, *Chinese J. Inorg. Chem.* 28 (2012) 2667–2673.
- [28] X.B. Fu, D.D. Liu, Y. Lin, W. Hu, Z.W. Mao, X.Y. Le, *Dalton Trans.* 43 (2014) 8721–8737.
- [29] F.H. Case, *J. Heterocyclic Chem.* 5 (1968) 223–226.
- [30] W.J. Lian, X.T. Wang, C.Z. Xie, H. Tian, X.Q. Song, H.T. Pan, X. Qiao, J.Y. Xu, *Dalton Trans.* 45 (2016) 9073–9087.
- [31] R. Bera, B.K. Sahoo, K.S. Ghosh, S. Dasgupta, *Int. J. Biol. Macromol.* 42 (2008) 14–21.
- [32] S. Krimm, J. Bandekar, *Adv. Protein Chem.* 38 (1986) 181–364.
- [33] M.A. Rizvi, M. Zaki, M. Afzal, M. Mane, M. Kumar, B.A. Shah, S. Srivastav, S. Srikrishna, G.M.S. Tabassum, *Eur. J. Med. Chem.* 90 (2015) 876–888.
- [34] B. Guhathakurta, A.B. Pradhan, S. Das, N. Bandyopadhyay, L.P. Lu, M.L. Zhu, J.P. Naskar, *Spectrochim. Acta A* 173 (2017) 740–748.
- [35] J.X. Qi, S.C. Liang, Y. Gou, Z.L. Zhang, Z.P. Zhou, F. Yang, H. Liang, *Eur. J. Med. Chem.* 96 (2015) 360–368.
- [36] A. Pal, S. Chaudhary, *Thermochim. Acta* 573 (2013) 200–205.
- [37] A. Draksharapu, A.J. Boersma, M. Leising, A. Meetsma, W.R. Browne, G. Roelfes, *Dalton Trans.* 44 (2015) 3647–3655.
- [38] M.J. Niu, Z. Li, H.H. Li, X. Li, J.M. Dou, S.N. Wang, *RSC Adv.* 5 (2015) 37085–37095.
- [39] D. Inci, R. Aydin, O. Vatan, D. Yilmaz, H.M. Genckal, Y. Zorlu, T. Cavas, *Spectrochim. Acta A* 1 (2015) 313–324.
- [40] F. Shen, Z.B. Ou, Y.J. Liu, W. Liu, B.F. Wang, Z.W. Mao, X.Y. Le, *Inorg. Chim. Acta* 465 (2017) 1–13.
- [41] A.K. Patra, T. Bhowmick, S. Roy, S. Ramakumar, A.R. Chakravarty, *Inorg. Chem.* 48 (2009) 2932–2943.
- [42] J.Y. Chen, X.X. Ren, Z.W. Mao, X.Y. Le, *J. Coord. Chem.* 65 (2012) 2182–2191.
- [43] Q. Gan, C.L. Zhang, B.F. Wang, Y.H. Xiong, Y.L. Fu, Z.W. Mao, X.Y. Le, *RSC Adv.* 42 (2016) 35952–35965.
- [44] S. Tabassum, S. Amir, F. Arjmand, C. Pettinari, F. Marchetti, N. Masciocchi, G. Lupidi, R. Pettinari, *Eur. J. Med. Chem.* 60 (2013) 216–232.
- [45] D. Mahendiran, R.S. Kumar, V. Viswanathan, D. Velmurugan, A.K. Rahiman, *Dalton Trans.* 45 (2016) 7794–7814.
- [46] Z.H. Xu, F.J. Chen, P.X. Xi, X.H. Liu, Z.Z. Zeng, *J. Photochem. Photobiol. A* 196 (2008) 77–83.
- [47] G. Psomas, *J. Inorg. Biochem.* 102 (2008) 1798–1811.
- [48] G.J. Chen, X. Qiao, P.Q. Qiao, G.J. Xu, J.Y. Xu, J.L. Tian, W. Gu, X. Liu, S.P. Yan, *J. Inorg. Biochem.* 105 (2011) 119–126.
- [49] R. Esteghamat-Panah, H. Hadadzadeh, H. Farrokhpour, J. Simpson, A. Abdolmaleki, F. Abyar, *Eur. J. Med. Chem.* 127 (2017) 958–971.
- [50] J. Liu, T.X. Zhang, T.B. Lu, L.H. Qu, H. Zhou, Q.L. Zhang, L.N. Ji, *J. Inorg. Biochem.* 91 (2002) 269–276.
- [51] M. Chauhan, K. Banerjee, F. Arjmand, *Inorg. Chem.* 46 (2007) 3072–3082.
- [52] S. Mahadevan, M. Palaniandavar, *Inorg. Chem.* 37 (1998) 693–700.
- [53] I. Ahmad, M. Ahmad, *Int. J. Biol. Macromol.* 79 (2015) 193–200.
- [54] A. Barve, A. Kumbhar, M. Bhat, B. Joshi, R. Butcher, U. Sonawane, R. Joshi, *Inorg. Chem.* 48 (2009) 9120–9132.
- [55] Y. Xiao, K.L. Xu, Q. Wang, X.N. Xiong, Y.M. Huang, H. Li, *RSC Adv.* 83 (2016) 80286–80295.
- [56] P. Haris, V. Mary, M. Haridas, C. Sudarsanakumar, *J. Chem. Inf. Model.* 55 (2015) 2644–2656.
- [57] I. Jelesarov, H.R. Bosshard, *J. Mol. Recognit.* 12 (1999) 3–18.
- [58] M. Muralisankar, N.S.P. Bhuvanesh, A. Sreekanth, *New J. Chem.* 40 (2016) 2661–2679.
- [59] S. Shahraki, F. Shiri, H. Mansouri-Torshizi, J. Shahraki, *J. Iran. Chem. Soc.* 13 (2016) 723–731.
- [60] M. Ishtikhar, M.S. Ali, A.M. Atta, H.A. Al-Lohedan, L. Nigam, N. Subbarao, R.H. Khan, *J. Lumin.* 167 (2015) 399–407.
- [61] S. Kathiresan, S. Magesh, M. Murugan, F. Ahamedb, J. Annaraj, *RSC Adv.* 6 (2016) 1810–1825.
- [62] D. Wu, J. Yan, J. Wang, Q. Wang, H. Li, *Food Chem.* 170 (2015) 423–429.
- [63] M. Toprak, *Spectrochim. Acta A* 154 (2016) 108–113.
- [64] G.W. Zhang, Y.D. Ma, *Food Chem.* 136 (2013) 442–449.
- [65] P.B. Kandagal, S. Ashoka, J. Seetharamappa, S.M.T. Shaikh, Y. Jadegoud, O.B. Ijare, *J. Pharmaceut. Biomed.* 41 (2006) 393–399.
- [66] A. Tarushi, C. Kakoulidou, C.P. Raptopoulou, V. Psycharis, D.P. Kessissoglou, I. Zoi, A.N. Papadopoulos, G. Psomas, *J. Inorg. Biochem.* 170 (2017) 85–97.
- [67] F.S. Mohseni-Shahri, M.R. Housaindokht, M.R. Bozorgmehr, A.A. Moosavi-Movahedi, *J. Solut. Chem.* 45 (2016) 265–285.
- [68] Y.H. Liu, A. Li, J. Shao, C.Z. Xie, X.Q. Song, W.G. Bao, J.Y. Xu, *Dalton Trans.* 45 (2016) 8036–8049.
- [69] C.Y. Liao, F.F. Li, S.S. Huang, B.Z. Zheng, J. Du, D. Xiao, *Biosens. Bioelectron.* 86 (2016) 489–495.
- [70] P.B. Kandagal, S. Ashoka, J. Seetharamappa, V. Vani, S.M.T. Shaikh, *J. Photochem. Photobiol. A* 179 (2006) 161–166.
- [71] A.A. Thoppil, S. Choudhary, N. Kishore, *BBA-Gen. Subj.* 1860 (2016) 917–929.
- [72] C. Ráfols, S. Zarza, E. Bosch, *Talanta* 130 (2014) 241–250.
- [73] P.A. Holt, J.B. Chaires, J.O. Trent, *J. Chem. Inf. Model.* 48 (2008) 1602–1615.
- [74] Z. Kazemi, H.A. Rudbari, M. Sahihi, V. Mirkhani, M. Moghadam, S. Tangestaninejad, I. Mohammadpoor-Baltork, G. Azimi, S. Gharaghani, A.A. Kajani, *J. Photochem. Photobiol. B* 163 (2016) 246–260.
- [75] S. Tayyab, M.M. Izzudin, M.Z. Kabir, S.R. Feroz, W.V. Tee, S.B. Mohamad, Z. Alias, *J. Photochem. Photobiol. B* 162 (2016) 386–394.



Volume 141 October 2021 ISSN 1567-5394

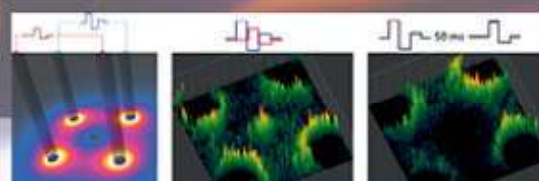
Bioelectrochemistry

Formerly Bioelectrochemistry and Bioenergetics

An international Journal Devoted to
Electrochemical Aspects of Biology and
Biological Aspects of Electrochemistry

Official Journal of the Bioelectrochemical Society

Editor in Chief:
P. Vadgama



Facile construction of ratiometric electrochemical immunosensor using hierarchical PtCoIr nanowires and porous SiO_2/Ag nanoparticles for accurate detection of septicemia biomarker

X.-Y. Wang, Y.-G. Feng, A.-J. Wang, L.-P. Mei, Xi. Luo,
Y. Xue, J.-J. Feng

Available online at www.sciencedirect.com

ScienceDirect

Actions for 1 selected article

[Select all](#) / [Deselect all](#)



Download PDF



Export citation



Show all article previews

Contents

Regular papers

Short communication

Special issue on

Electropermeabilization



[View PDF](#)

Article preview ▾



Research article ● Full text access

Cold atmospheric pressure He-plasma jet and plasma ball interactions with the Venus flytrap: Electrophysiology and side effects

Alexander G. Volkov

Article 107833



[View PDF](#)

Article preview ▾



Research article ● Full text access

Distinct biofilm formation regulated by different culture media: Implications to electricity generation

Zhixin Lin, Mingliang Long, Wei Liu, Tongxu Liu, ... Yundang Wu

Article 107826



[View PDF](#)

Article preview ▾



Research article ● Full text access

A novel tool for the adsorption of dsDNA: Electrochemical reduction of Pd nanoparticles onto reduced-keratin particles extracted from wool wastes

Meryem Kalkan Erdoğan, Gözde Aydoğdu Tığ, Mehmet Saçak

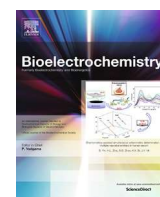
Article 107835



[View PDF](#)

Article preview ▾





Distinct biofilm formation regulated by different culture media: Implications to electricity generation



Zhixin Lin^{a,b}, Mingliang Long^{a,b}, Wei Liu^{a,*}, Tongxu Liu^b, Fangbai Li^{b,c}, Yundang Wu^{b,*}

^a College of Materials and Energy, South China Agricultural University, Guangzhou 510642, China

^b Guangdong Key Laboratory of Integrated Agro-environmental Pollution Control and Management, Institute of Eco-environmental and Soil Sciences, Guangdong Academy of Sciences, Guangzhou 510650, China

^c National-Regional Joint Engineering Research Center for Soil Pollution Control and Remediation in South China, Guangzhou 510650, China

ARTICLE INFO

Article history:

Received 2 November 2020

Received in revised form 3 April 2021

Accepted 14 April 2021

Available online 27 April 2021

Keywords:

Biofilm formation

Transcriptome

Electron mediator

Electroactive microorganism

Buffer concentration

Shewanella oneidensis MR-1

ABSTRACT

Biofilm of *Shewanella oneidensis* MR-1 is extensively studied as it can transform organic compounds directly into electricity. Although revealing the biofilm regulation mechanism is crucial for enhancing bio-current, studies regarding the mechanism by which the culture condition affects biofilm formation are still lacking. The biofilm formation of *S. oneidensis* MR-1 in two typical media with same electron donor was investigated in this study. Bio-electricity increased 1.8 times in medium with phosphate-buffered saline (PBS) than in piperazine-1,4-bisethanesulfonic acid (PIPES). Biofilm total protein has 1.5-fold of difference between two media at day 3, and biofilm structures also differed; a fluffy biofilm with curled cells was formed in medium with PBS, whereas a compact, ordered, and closely attached biofilm was formed in medium with PIPES. Transcriptome studies clarified that the expression of genes beneficial for cell aggregation [e.g., *aggA* (2.3 fold), *bpfA* (2.8 fold) and *csgB* (3.9 fold)] in medium with PIPES was significantly upregulated, thus provided an explanation for the specific biofilm structure. Buffer concentration was proved to be a critical factor impacted cell morphology and current generation. The maximum current density in 30 mM of PBS and PIPES is 165 and 159 $\mu\text{A}\cdot\text{cm}^{-2}$ respectively, but it increased to 327 and 274 $\mu\text{A}\cdot\text{cm}^{-2}$ in 200 mM of PBS and PIPES. This study provides new insights into the mechanism of medium-dependent biofilm regulation, which will be beneficial for developing simple and efficient strategies to enhance bio-electricity generation.

© 2021 Elsevier B.V. All rights reserved.

1. Introduction

Shewanella oneidensis MR-1 is an important electroactive model strain [1,2] known for its versatile electron-accepting capacity, which enables it to play a critical role for bioelectrochemical applications [3–6]. *S. oneidensis* MR-1 can transform organic wastes directly into electricity via anaerobic respiration using extracellular electron transfer (EET) [7,8], in which the electrons are transferred from the inner to the outer membrane by the soluble periplasmic cytochromes [9,10] and are subsequently transferred to an extracellular solid electron acceptor via a direct (e.g., attach) or indirect (e.g., electron shuttling) mechanism [11,12]. Formation of a mature biofilm on the electrode is the prerequisite for *S. oneidensis* MR-1 to generate high bio-current in bioelectrochemical systems (BESs) [13,14]. Hence, understanding the mechanism

underlying biofilm formation by this strain is the research focus in the field of microbial electrochemistry.

Recent studies have shown that the biofilm formation process can be regulated by simply changing the culture conditions. The biofilm biomass of *S. loihica* PV-4 increased 75-fold after addition of ethylenediamine tetraacetic acid disodium salt (EDTA-2Na); this occurred because the EDTA-2Na adsorbed on the cell membrane altered the polarity and conductivity around the outer membrane, thereby changing the interaction between the cells and the electrode [15]. Addition of the soluble electron acceptor, azo dye, to the bioelectrochemical system dissipated the proton accumulation within the biofilm, thereby increasing the biofilm thickness [16]. Although changes in culture conditions may dramatically affect the biofilm, studies regarding the mechanism by which the medium affects biofilm formation are still lacking.

Our recent study showed that exogenous electron mediators (e.g., flavin and quinone) strongly enhance the formation rate and final biomass (15–36 times) of the *S. oneidensis* MR-1 biofilm [17]. Although the effect of buffers and nutrients on current generation

* Corresponding authors.

E-mail addresses: liuwei97@scau.edu.cn (W. Liu), ydwu@soil.gd.cn (Y. Wu).

were also discussed in that study, detailed analysis regarding the mechanism was not performed. Data showed that, although electron donors are the same, the biofilm biomass and current generation were higher in medium with phosphate-buffered saline (PBS) (defined as medium A in their study) than in the medium with piperazine-1,4-bisethanesulfonic acid (PIPES) buffer and yeast extract as nutrients (defined as medium B). This strongly implies that culture media with different buffers and nutrients can alter bio-current generation by changing the biofilm formation behavior; however, why and how this is regulated still remains unclear.

Electron shuttling-mediated BESs with different media have been constructed to understand biofilm formation and the mechanism underlying current regulation in these two media. *S. oneidensis* MR-1 was used as the model strain, and flavin mononucleotide (FMN), a typical electron mediator [18,19], was added to the system to systematically study the effects of culture condition on biofilm formation and bio-current generation. The objective of this study was to monitor the bio-current generation rate, quantify the biofilm biomass, observe the biofilm morphology and structure, and analyze the electrochemical properties and transcriptome profiles of the biofilm in two different media to understand the mechanism through which the culture medium regulates current generation and biofilm formation. Our observations will provide in-depth understanding regarding the mechanism of electroactive biofilm formation and would be helpful for developing biofilm regulation strategies to enhance bio-electricity in future.

2. Materials and methods

2.1. Materials, strain, and medium

S. oneidensis MR-1 was purchased from the Marine Culture Collection of China (China). Flavin mononucleotide (FMN, 93%) was purchased from TCI (Japan). Tryptone and yeast extract were purchased from Oxoid (USA). Other chemicals were purchased from the Guangzhou Chemical Reagent Factory (China). Aerobic cultures of *S. oneidensis* MR-1 were grown in Luria Bertani (LB) medium for 16 h at 30 °C on a rotary shaker (180 rpm). Thereafter, the cultures were centrifuged, washed, and diluted for electrochemical experiments. Two different anaerobic media were used in this study, the specific compositions of which are shown in Table 1. Medium A has been used in our previous studies [20–22]. Medium B was originally used by Okamoto [23], in which yeast extract was used instead of vitamin stock solution and mineral stock solution. Although HEPES was used in Okamoto's study, PIPES was used here instead, as it has been used as a buffer in our previous study [17].

2.2. BES setup and electrochemical characterization

Each BES, equipped with a carbon cloth (2 cm × 2 cm) working electrode, titanium counter electrode, and calomel reference electrode, was incubated anaerobically for 1 to 3 days at a constant

potential of 441 mV versus standard hydrogen electrode (SHE) (Fig. S1) [22,24]. Medium A and B with the addition of 50 μM of FMN were used as the anaerobic media in the BESs. The initial cell density (OD₆₀₀) of *S. oneidensis* MR-1 was 1.0. Slow-scan cyclic voltammetry (CV, 1 mV·s⁻¹) and differential pulse voltammetry (DPV) were performed in an electrochemical workstation (CHI1040C, Chenhua Co., Ltd., USA). CV and DPV were performed at a temperature of 30 °C. The iR compensation mode was used to study the effects of uncompensated solution resistance on current generation. IR compensation experiments were conducted by a CHI760D electrochemical workstation (Chenhua Co., Ltd., USA).

2.3. Quantification of biofilm and characterization of morphology

Biofilm total protein was extracted by boiling in 0.2 M NaOH solution [20,25]. A carbon cloth sample (2 cm × 2 cm) was placed in a 50 mL centrifuge tube with 20 mL NaOH; the tube was then shaken in a 100 °C water bath at 180 rpm for 30 min. The morphologies of the biofilms on the electrodes were characterized using scanning electron microscopy (SEM; ProX, Phenom, Netherlands) after fixation, cleaning, dehydration, freeze-drying, and platinum coating. The details of biofilm sampling are shown in Fig. S2 and Table S3.

2.4. Transcriptome analysis

Biofilms on electrodes incubated in different media were collected at the end of day 3 for transcriptome analysis. The carbon cloth electrodes (2 cm × 2 cm) were cut and rapidly frozen in liquid nitrogen. Thereafter, the RNA of the electrode samples was extracted using a bacterial RNA kit (Omega Bio-Tec, R6950, USA) according to the manufacturer's protocol. RNA concentration was quantified using the Nanodrop 2000 (Thermo Scientific, USA). RNA quality was examined using a gel electropherogram (LiuYi, DYY-6C, Beijing, China). Clear RNA bands were observed (Fig. S3). Detailed information regarding the extracted RNA is shown in Table S4. The A₂₆₀/A₂₈₀ ratios of all RNA samples ranged between 1.8 and 2.0, indicating that they were highly pure. RNA reverse transcription was performed using a first strand cDNA synthesis kit (Omega, TQ2501, USA).

Transcriptome sequencing was conducted on a NextSeq 500 platform (Illumina) by Shanghai Personal Biotechnology Co. Ltd. The raw data were filtered using Cutadapt (v1.15). The reference genome and gene annotation files of *S. oneidensis* MR-1 were downloaded, and the reads were mapped using Bowtie 2. Expression was normalized using the method of fragments per kilobase of exon per million fragments mapped (FPKM). Differentially expressed mRNAs were analyzed using DESeq (v1.30.0). Transcripts with |log₂FoldChange| > 1 and P-value < 0.05 were considered differentially expressed. The Kyoto Encyclopedia of Genes and Genomes (KEGG) automatic annotation server (KAAS) was used for pathway annotation. The sequence data have been submitted to the NCBI Short Read Archive in Bioproject PRJNA668666.

3. Results and discussion

3.1. Current generation in different culture media

Current generation in the BES with different reported culture media was investigated. We have reported the use of medium A with PBS as the buffer in our previous studies [20–22,24]. Medium B containing PIPES as the buffer and yeast extract as nutrients is similar to the medium used by Okamoto (Table 1) [23]. As shown in Fig. 1a, the current in both medium A and B started increasing after a short hysteresis period, reaching a maximum value within

Table 1
Compositions of the media used in the BESs.

Medium A	Concentration	Medium B	Concentration
PBS* (pH = 7.0)	200 mM	PIPES (pH = 7.0)	30 mM
Vitamin stock solution*	5 mL·L ⁻¹	NaCl	10.0 g·L ⁻¹
Mineral stock solution*	12.5 mL·L ⁻¹	Yeast extract	0.5 g·L ⁻¹
Lactate	30 mM	Inorganic salts	Table S2**
		Lactate	30 mM

* The specific compositions of PBS, vitamin stock solution, and mineral stock solutions are shown in Table S1. ** The concentrations of inorganic salts are shown in the attached table (Table S2).

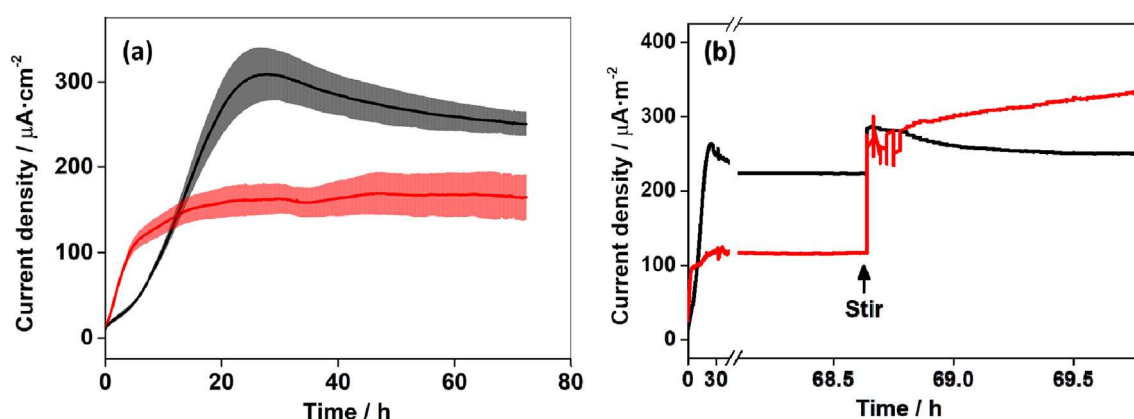


Fig. 1. (a) Current density in BESs with respect to time in different media. The values are derived from the average of biological triplicates; (b) current density in BESs with a 400 rpm of stirring. Black line: medium A; red line: medium B. Lactate (30 mM) was used as the electron donor. Voltage of 441 mV vs. SHE was poised on the electrode, and 50 μM exogenous FMN was used in both BESs.

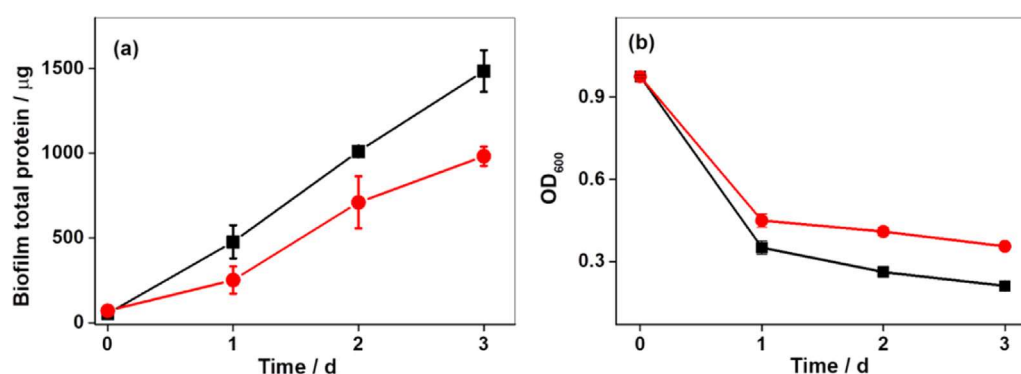


Fig. 2. (a) Biofilm total protein on electrode in BESs with two media; (b) cell density in suspension in BESs with two media. Black: medium A; red: medium B. Exogenous FMN (50 μM) was added to both treatment. Data are the values of biological triplicates.

30 h (medium A) and 20 h (medium B), respectively. The hysteresis period in medium B was about 10 h shorter than that in A. The maximum current in medium A (309 $\mu\text{A}\cdot\text{cm}^{-2}$) was 1.8 times higher than that in medium B (169 $\mu\text{A}\cdot\text{cm}^{-2}$), indicating differences in the EET ability of *S. oneidensis* MR-1 in different media. A stirring operation was conducted in two BESs at day 3 (Fig. 1b). Current in medium A increased slightly after the stirring, while current in medium B increased dramatically, indicated that mass transfer is an important factor limited the current generation, especially in medium B.

Because *S. oneidensis* MR-1 has the capacity of releasing flavin, the possible impact of changing flavin concentration on EET rates was examined. As the riboflavin released by *S. oneidensis* MR-1 is in general far < 1 μM , two more BESs with additional 1 μM of FMN, which is 51 μM , was constructed to study the effect of flavin concentration changes on EET. Result in Fig. S4 show similar current generation between the treatment with 50 and 51 μM of FMN, suggested that the influence of self-secreted flavin on the current generation in this study can be ignored.

3.2. Biofilm quantity and morphology in different media

As current in the BESs were mainly generated by biofilms on the electrodes, the biofilms were quantified after extracting the total protein. As shown in Fig. 2a, biofilm total protein in medium A increased from near 0 to 1484 μg in 3 days. Total protein in medium A at day 3 was 1.5-fold higher than that in medium B (982 μg), indicating an effect of culture medium on biofilm growth as well as

EET ability. Thus, increase in biofilm biomass could be one of the reasons behind the higher current in the BES of medium A than in that of B.

Cell density in solution was determined and shown in Fig. 2b. The OD_{600} decreased over time in both medium A and B, which is consistent with our previous study [17]. Although 50 μM of FMN was in the solution, because of the long diffusion distance from the suspension to the electrode ($\gg 1$ mm), the FMN in suspension may have been reduced at the very beginning of incubation [26]. Thus the cells in suspension away from the electrode could hardly achieve the electron acceptor, which limited their growth. The cells attached to the electrode could probably have a contribution to the cell decreasing in suspension. However, independent cell incubation experiments in medium without electron acceptor also show decreasing of cell density over time (Fig. S5). This decreasing is consistent with the decreasing in suspension of BESs, implied that the cell lysis in acceptor-limited conditions is probably a reason for the decreasing in OD value in BESs [27].

The biofilm morphology was observed using SEM and is shown in Fig. 3. Considerable differences were observed between the two biofilms. A fluffy biofilm with curled cells was formed on the electrode in medium A (Fig. 3a, b and c); however, the cells in biofilm of medium B were compact, ordered, and closely attached to the electrode (Fig. 3d, e and f), indicating a strong impact of culture medium on biofilm structure. Fluffy biofilm is probably favorable for inner biofilm mass transfer, such as diffusion of electron shuttles, which might benefit EET. The morphology pattern is consistent with the current characteristics. Current dramatically

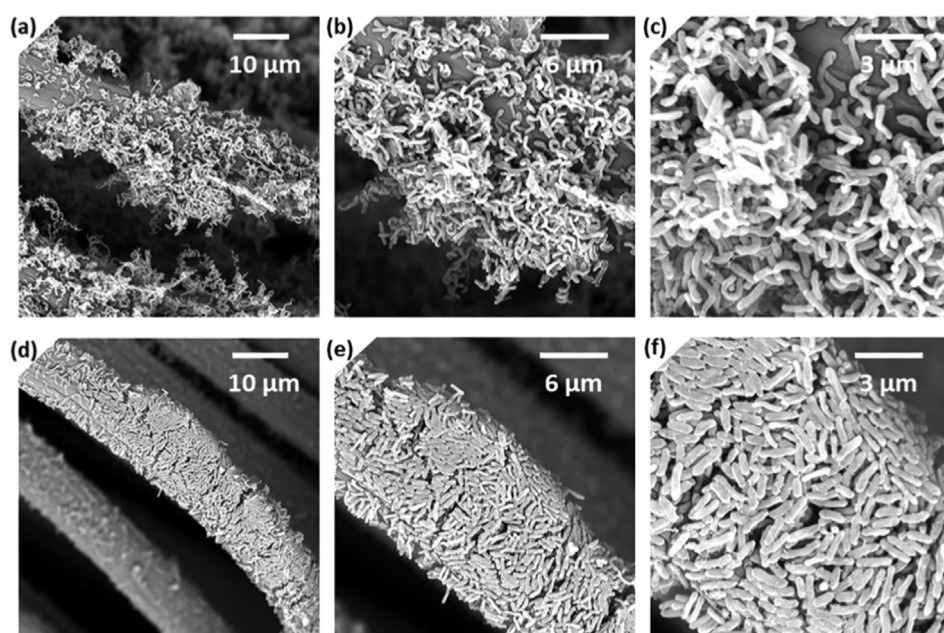


Fig. 3. Characterization of the morphology of a mature biofilm under different magnifications in medium A (a,b,c) and medium B (d,e,f); Exogenous FMN (50 μM) was added to both BESs. Biofilm was obtained after 3 days of incubation. Data are representative of the three replicates.

increased in medium B but only slightly increased in medium A after the stirring, revealing a more critical limitation of diffusion in medium B. As the disturbance of stirring to the biofilm probably has a contribution to the decreasing of current generation (Fig. 1a, black line), the SEM of biofilms after stirring was examined. But the detailed change of biofilm before and after stirring is hard to be distinguished (Fig. S6).

The deformation effect of environmental factors on cells in this study is similar to that observed in previous studies [28,29]. The length and bending of cells dramatically changed after 24 h of chromium (VI) exposure [28]; this is probably caused by cellular response of MR-1 to environmental stress. Cisplatin was reported induced elongation of *S. oneidensis* MR-1 cells, improved the microbe-electrode interactions and thereby enhancing bio-current generation [29]. Here, the length of cell in medium A is in general longer than in medium B (Fig. S7 and Fig. 3 c and f). The culture medium considerably affected the EET performance by changing the biofilm structure and biomass and thus can be potentially used for regulating biofilm formation.

As the concentration of mediator has influence on the growing of *S. oneidensis* MR-1, for comparison, the current density, biofilm morphology, and biofilm biomass was also examined in BESs with low concentration (2 μM) and without FMN (Fig. S8). Results show current profile in medium without exogenous FMN is different with the current in medium of 50 μM FMN. Extremely low current (0.3 $\mu\text{A}\cdot\text{cm}^{-2}$) was generated and very few of cells were attached onto the electrode in medium A at day 3 (Fig. S8a-d). This is consistent with our previous study, which showed biofilm of *S. oneidensis* MR-1 grows slowly without the support of electron shuttle, and electron shuttles 15–36 times promoted the biofilm formation rate [17]. But a certain intensity of current (40 $\mu\text{A}\cdot\text{cm}^{-2}$) was generated in medium B without FMN, which is probably attributed to the flavin in yeast extracts in this medium. However, in BESs with low concentration of FMN (2 μM), although no mature biofilm was formed in these BESs at day 3, results of current and total protein suggested a similar pattern to the BESs of 50 μM FMN, in which both current and biofilm biomass are higher in medium A than in medium B (Fig. S8e-h). Although differences in current were observed by changing FMN concentration, to keep the consistency

of FMN concentration in each BES, 50 μM was chosen as the typical concentration studied in this research.

3.3. Electrochemical characterization in different media

To further analyze how media affect bio-current generation and biofilm structure, electrochemical characterizations were conducted in BES with different media. Slow scan rate CV was examined at 1 $\text{mV}\cdot\text{s}^{-1}$ for the biofilm in each BES from day 1 to day 3. Sigmoidal shaped curves similar to the reported electroactive biofilm data were obtained in both systems. The maximum catalytic current in both medium A and B peaked on day 1 (Fig. 4a and b). This suggests that the early adhesion rate of biofilm on electrode in both medium A and B are rapid.

In addition, a clear two-stage increase in catalytic current was observed with the positive sweeping of potential from -200 to $+100$ mV vs. SHE in medium A (Fig. 4a, arrows), although only a one-stage increase, which is more steep than that in medium A, was obtained in medium B (Fig. 4b, arrow). First derivative analysis of CV was conducted (Fig. 4c and d), as it can be used to determine the potential at which the rate of increase of the catalytic wave is a maximum. The first derivative analysis of CVs in medium A revealed that over the scanned potential range of -459 to 441 mV, two peaks were observed between -200 to $+100$ mV. Compared to that reported previously [23,30,31], the two peaks represented the mediation process and the direct contact transport in biofilm, respectively (Fig. 4c). Nevertheless, in medium B, only one peak was observed at approximately -200 mV, the shapes of which differed completely from those of the peaks in medium A (Fig. 4d), indicating that both indirect mediation and direct attached EET performance in the two biofilms appeared to differ.

DPV was conducted to further analyze the EET performance in the biofilms. Two peaks were observed at -204 mV and -28 mV in medium A (Fig. 4e); each of these two peaks was consistent with the position of an inflection point in the biofilm CV curve. Nevertheless, only one large peak at -222 mV was obtained in the DPV of medium B (Fig. 4f), in which the peak position was consistent with the corresponding biofilm CV data. The relationship between the inflection point in CV and the peak

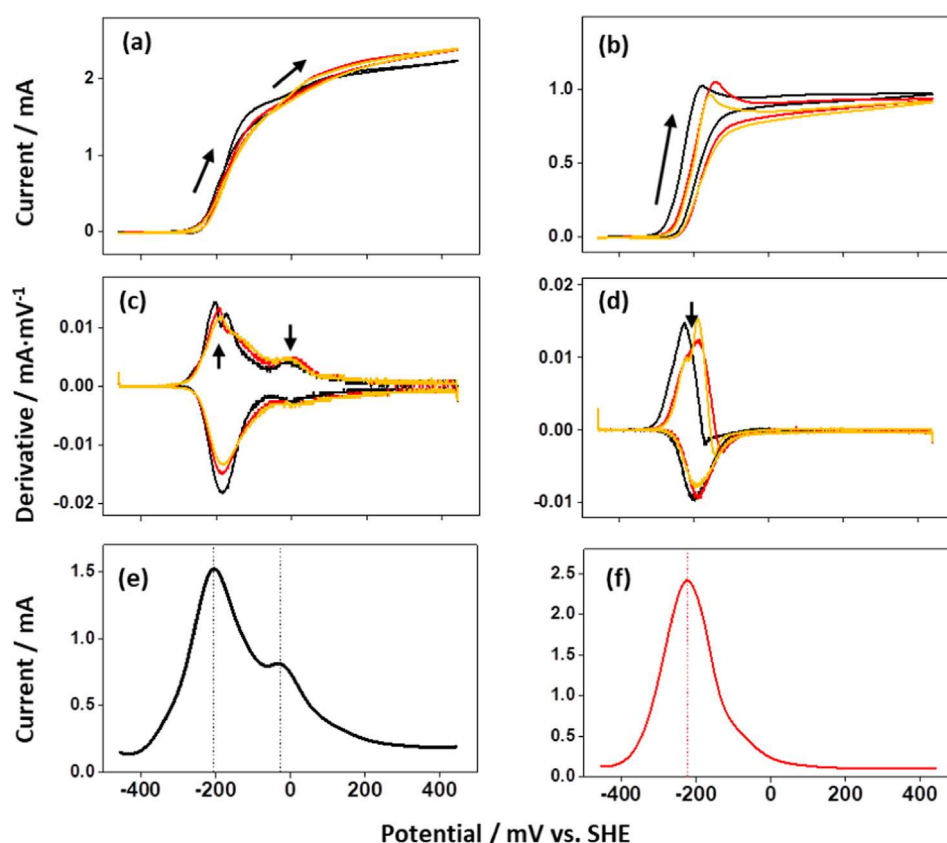


Fig. 4. Slow scan rate CV ($1 \text{ mV}\cdot\text{s}^{-1}$) of biofilm in BESs with medium A (a) and medium B (b), and the first-derivative CV traces in medium A (c) and medium B (d). Black: day 1, red: day 2, yellow: day 3. DPV of biofilm in BESs with medium A (e) and medium B (f). Exogenous FMN ($50 \mu\text{M}$) were added to all the BESs. Data are representative of the three replicates.

position in DPV indicated that the increase in catalytic current in CV curves were due to the reactions at -222 mV , -204 mV , and -28 mV .

DPV of pure FMN was measured to identify these peaks (Fig. S9). Three peaks at -332 mV , -228 mV and -85 mV were observed in medium A, but only one peak at -279 mV was obtained in medium B. Change of buffer and ionic strength influenced the electrochemical activities of the mediator [32]. The peak at -228 mV in medium A is more positive than the peak at -279 mV in medium B (Fig. S9), explained the differences of inflection points in the biofilm CV and the peaks of biofilm DPV (Fig. 4). No obvious current increase at -332 mV was observed in the corresponding biofilm CV data (Fig. 4a), probably because EET of *S. oneidensis* MR-1 cannot be mediated by redox reactions with extremely negative potentials. These results strongly suggested that the significant difference in EET in the two media was due to the differences in the electrochemical performance of FMN in the two media.

In addition, the peak at -28 mV in medium A (Fig. 4e) is probably contributed by the synergy of flavin and *c*-Cyts [33]. No such a peak was observed in medium B (Fig. 4f), implying that the culture medium also influenced the performance of *c*-Cyts. Although a previous study showed that endogenously secreted flavin can bind to *c*-type cytochromes as a cofactor and showed a peak at approximately -145 mV in DPV [30], no such a peak was observed in our BESs, probably because with the addition of high concentration of exogenous flavin ($\gg 1 \mu\text{M}$), which is several orders of magnitude higher than the level of endogenous flavin (nM), the shuttling process dominated the EET, concealing the peak of the flavin-bound *c*-type complex; this is consistent with the results of our previous study [17].

3.4. Transcriptome profiles of *S. Oneidensis* MR-1 in response to different media

The transcriptome was analyzed to further understand the physiological response of *S. oneidensis* MR-1 to the culture medium. The gene expression profiles of cells in biofilm cultured in medium A were compared to those of cells grown in medium B. Principal component analysis (PCA) showed a dramatic difference in transcriptome profiles between two media (Fig. S10). Approximately 9.1% ($n = 361$) of the total predicted *S. oneidensis* MR-1 genes ($n = 3944$) displayed at least twofold statistically significant ($P < 0.05$) change in transcript expression (Fig. S11 and Table S6). These results indicated that the physiological properties of *S. oneidensis* MR-1 differed in the two media.

The genes in Table S7 are the most up and down expressed genes related to biofilm formation in this study. Although extracellular DNA (eDNA) is a key factor influencing biofilm formation, the expression of genes related to eDNA (*endA*, *exeM*, and *exeS*) [34,35] did not differ significantly in the two media (Table S8). However, genes responsible for extracellular polymers (EPS) expression were upregulated in medium B (Table S7 and Fig. 5a). The gene cluster *mxrABCD* is crucial for exopolysaccharide biosynthesis [36], and *MxdB* transports extracellular material to form the matrix during biofilm formation; indeed, ΔmxrB mutants lost the ability to undergo transition from a cell monolayer to a three-dimensional biofilm structure [36], and the double mutants of $\Delta\text{mshA}\Delta\text{mxrB}$ completely lost initial cell attachment [37]. The expression of *mxr* genes was higher in medium B than in medium A [*mxrA* (2.0-fold), *mxrB* (2.2-fold) and *mxrC* (1.7-fold)] ($P < 0.05$). This is consistent with the order of increasing current shown in Fig. 1a, in which the hysteresis period in medium B was shorter than that

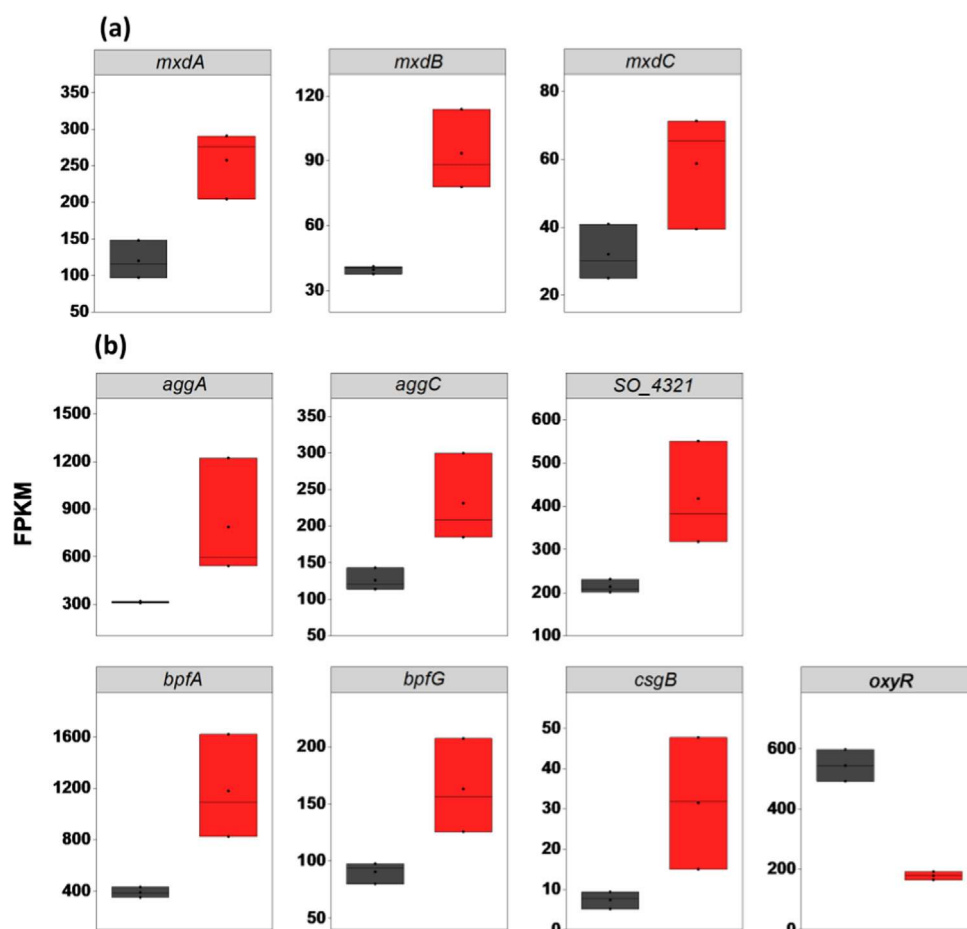


Fig. 5. Differentially expressed genes responsible for biofilm formation ($P < 0.05$). (a) Genes in *Shewanella* related to EPS; (b) other differentially expressed genes directly responsible for biofilm formation. Black: medium A, red: medium B. FPKM: Fragments Per Kilobase of transcript per Million fragments mapped. FPKM is an index represents the level of expression which has been normalized by sequencing depth and gene length. The biofilms for transcriptomic analysis were sampled in a batch of independent BESs. Biological triplicates were conducted.

in medium A, indicating an earlier cell attachment and biofilm formation in medium B than in A.

Other genes related to biofilm formation were summarized. The differentially expressed genes directly responsible for biofilm formation are listed in Table S7 and shown in Fig. 5b. The mRNA levels of six genes increased moderately but significantly ($P < 0.05$), whereas the mRNA level of one gene decreased significantly in medium B as mentioned below: *aggA* (2.3-fold), *aggC* (1.7-fold), *SO4321* (1.8-fold), *bpfA* (2.8-fold), *bpfG* (1.7-fold), *csgB* (3.9-fold), and *oxyR* (0.3-fold). *AggA* (2.3-fold) is required for autoaggregation and pellicle formation via enhancement of cell to cell and/or cell to abiotic surface attachment [38,39]. *BpfA* (2.8-fold) is secreted by a type I secretion system to the cell surface, where it is a requisite for biofilm development [40]. Both these proteins play important roles in surface attachment and biofilm formation. Increase in the expression of *aggA* and *bpfA* may probably increase the expression of extracellular proteins for stabilizing the structure of the microbial population, thus supporting the formation of a densely packed biofilm in medium B. *csgB* expression was 3.9-fold higher in medium B than in medium A. *CsgB* (3.9-fold) is an amyloid-forming biofilm protein that can form self-assembled nanofibers on solid surfaces, which may facilitate the attachment of the biofilms onto the electrode [41]. However, *oxyR* expression decreased by 0.3-fold in medium B. *OxyR* is a negative regulator of a velcro-like adhesive protein that mediates cell–cell interactions [42]. Thus, the reduction in *oxyR* expression in medium B may also enhance cell autoaggregation in the *S. oneidensis* MR-1 biofilm.

In addition to the expression of genes responsible for biofilm formation, expression of genes encoding *c*-type cytochromes and transmembrane porin in the electron transfer chain [9] also changed moderately between the two media (Table S9). The expression of genes encoding three critical membrane associated cytochromes, *mtrC* (0.4-fold), *omcA* (0.4-fold) and *mtrA* (0.5-fold), decreased substantially in medium B ($P < 0.05$), which probably decreased the EET performance of *S. oneidensis* MR-1. Other transcriptional changes included upregulation/downregulation of genes involved in amino acid metabolism and those encoding proteins required for starch and sucrose metabolism, as shown in Fig. S12, indicated that the differences in the metabolic capacities of *S. oneidensis* MR-1 also influenced the EET capacity and biofilm growth.

3.5. Determine the specific components that affect biofilm structure

Buffer and nutrient exchange experiments were performed to determine the specific culture medium component that predominantly affected EET and the biofilm. In the aforementioned experiments, PBS was the buffer in medium A and PIPES in medium B (Table 1); however, here, PIPES was used in medium A and PBS in medium B. The compositions of the new media are shown in Table S5. Results showed that, compared to the current shown in Fig. 1a (medium A > medium B), the order of current density was reversed (medium B > medium A) (Fig. 6a). Meanwhile, the maximum current in medium B with PBS as buffer ($318 \mu\text{A}\cdot\text{cm}^{-2}$) (Fig. 6a) was about 1.9 times higher than the current in medium

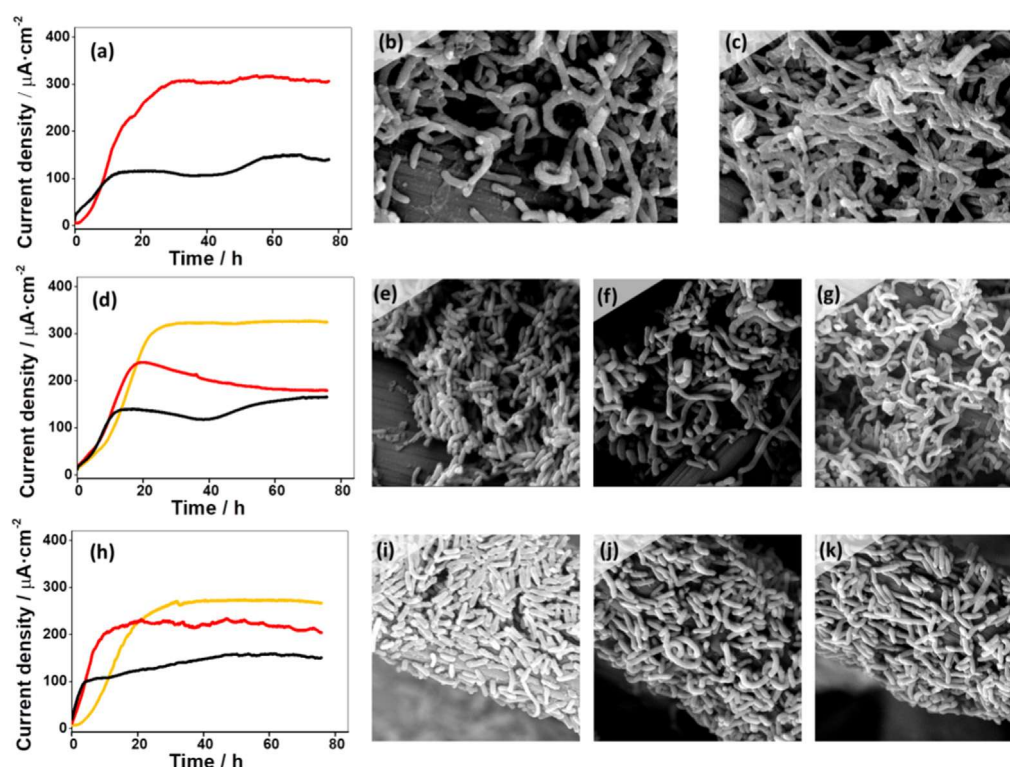


Fig. 6. (a–c) Current density and biofilm characterization after buffer and nutrient exchange. The buffer in medium A was changed to PIPES and that in medium B was changed to PBS; (d–k) Current density and biofilm morphology in medium A and B with different buffer concentration.. (a) Current generation versus time (black: medium A with PIPES as buffer; red: medium B with PBS as buffer); (b) SEM in medium B with PBS as buffer; (c) SEM in medium A with PIPES as buffer; (d) Current density in medium A (black: 30 mM, red: 100 mM, yellow: 200 mM); (e) SEM (30 mM PBS); (f) SEM (100 mM PBS); (g) SEM (200 mM PBS); (h) Current density in medium B (black: 30 mM, red: 100 mM, yellow: 200 mM); (i) SEM (30 mM PIPES); (j) SEM (100 mM PIPES); (k) SEM (200 mM PIPES). Exogenous FMN of 50 μM was used in these BESs.

B with PIPES as buffer ($169 \mu\text{A}\cdot\text{cm}^{-2}$) (Fig. 1). In other words, the current in PBS was always higher than that in PIPES, indicating a key role of the buffer in generation of high current by *S. oneidensis* MR-1. However, SEM showed that no compact, ordered, and closely attached biofilm was observed in the new media (Fig. 6b and c), indicating that specific biofilm was only formed under stringent conditions such as that of medium B with PIPES buffer.

As the concentration of buffer between medium A and B is highly different, current in BESs with different buffer concentration was examined in two media. Results show current density in both medium A and B decreased with the decreasing of concentration from 200 mM to 30 mM (Fig. 6d and h). The maximum current density in 200 mM of PBS and PIPES is 327 and $274 \mu\text{A}\cdot\text{cm}^{-2}$ respectively, but it decreased to 165 and $159 \mu\text{A}\cdot\text{cm}^{-2}$ in 30 mM of PBS and PIPES. These results implied that concentration of buffer in each medium is probably one of the most important factor impacted the current generation. SEM of biofilm in each BES with different buffer concentration was viewed and shown in Fig. 6e–g (medium A) and Fig. 6i–k (medium B). Cells in high concentration of PBS (100 and 200 mM) are in general more curly and longer than cells in 30 mM of PBS. Cells in 30 mM of PBS are short rod-like, it is more closer to what it looks like in 30 mM PIPES. In addition, biofilm in high concentration of PIPES (100 and 200 mM) is loose and porous, which is different with the compact biofilm in 30 mM of PIPES. These results strongly suggested the key role of buffer concentration buffer type on impacting biofilm morphology, which could further influence the current generation.

As the differences of uncompensated solution resistance (R_s) in different BESs could probably make anode potential to be different, thus affecting the credibility of the conclusions of this research, the R_s of the medium was analyzed. EIS in abiotic systems shows a slightly decreasing of R_s with the decreasing of buffer concentra-

tion (Figure S13a and b), and the open circuit potential also changed (Figure S13c and d). These results are consistent with a previous report [43], implying a possible influence of R_s on bio-current generation. However, the solution resistance only accounts for a small proportion (3–8%) of the total resistance in BESs [44], the slight difference in solution resistance may not have a significant effect on the bio-current. As expected, additional studies in BESs concluded that the effects of changing in R_s on the generation of bio-current and the bacteria growth are very limited. The bio-current generation in media with different buffer concentration was further examined under an iR compensation mode. This iR compensation mode can correct R_s and provide a consistent anode potential amongst different media [45]. Results in Figure S14 show very similar current output in BESs with and without iR compensation, suggested a very limited influence of R_s on the bio-current generation. The current in 200 mM of buffer is still higher than that in 30 mM of buffer, consistent with the results without iR compensation. SEM was examined too, which also shows similar morphology characteristics in BESs with and without iR compensation (Figure S15). Results after iR compensation still show a loose and porous biofilm in medium with high concentration of buffer, especially in 200 mM of PBS (Figure S15b and d), and show a compact, ordered, and closely attached biofilm in low concentration of buffer, especially in 30 mM of PIPES (Figure S14e and g). These results strongly suggested that the very limited influence of R_s on the bio-current does not affect the conclusion on the different effects of the two buffers on the biofilm morphology and biofilm biomass.

3.6. Mechanism and implications

The above results revealed a buffer-dependent biofilm regulation mechanism of *S. oneidensis* MR-1. Distinct bio-current was

generated in systems with different type and concentration of buffer due to the synergy between regulation of the biofilm structure and electrochemical activity of the biofilm. Changing of culture medium dramatically changed the EET performance, biofilm structure, and transcriptome of *S. oneidensis* MR-1. The cell elongation and curl increased the biofilm surface area thus would enhanced the bio-electricity generation. Fluffy biofilm is favorable for inner biofilm mass transfer such as the diffusion of electron shuttles, which might benefit EET too.

Electrochemical analysis of FMN showed higher peak intensity in medium A than in B, suggested that buffer could regulate the electrochemical activity of mediator in BES. The order of bio-currents reversed after exchanging the buffer (Fig. 6a), further revealed that buffer played a critical role in determining the biofilm structure and EET performance. The bio-currents decreased and cell morphology changed from curl to straight with the decreasing of buffer concentration (Fig. 6d-k), suggested the key role of buffer concentration on impacting biofilm morphology and EET.

Biofilm structure was conveniently regulated by changing culture medium in this study. Although construction of genetically modified strains can also alter biofilm properties, for example, overexpression of a bis-(3'-5')-cyclic dimeric guanosine monophosphate (c-di-GMP) biosynthesis-related gene, *ydeH*, in *S. oneidensis* MR-1 increased its biofilm formation rate [46,47], the construction of engineered bacterium is complicated. Compared to genetic methods, altering the culture medium is simple. A convenient strategy for regulating the structure of electroactive biofilms from porous to compact forms will be useful for constructing target BESs. Thus, in addition to revealing the mechanism, this study provides a simple and efficient strategy for regulating biofilm structure in artificial microbial electrochemical systems.

4. Conclusions

The mechanism by which two typical culture media influence EET was revealed in this study. The EET performance of *S. oneidensis* MR-1 in medium A, which has been used in our previous studies, and in medium B, which is similar to that used by Okamoto [23], differed considerably. Maximum current generated in medium A was 1.8 times higher than that in medium B. Higher amount of biofilm biomass was observed in medium A than that in medium B. In addition, biofilm structures in the two media differed completely. The cells in biofilm of medium B were compact, ordered, and closely attached to the electrode, whereas the biofilm in medium A was loose and porous. Transcriptome profiles showed that the expression of genes related to cell aggregation and pellicle formation in medium B was significantly upregulated [e.g., *aggA* (2.3 fold), *bpfA* (2.8 fold) and *csgB* (3.9 fold)], indicating the differences in the biofilm structure at the gene level. EPS secretion-related genes were upregulated in medium B [e.g., *mxdB* (2.0-fold), *mxdB* (2.2-fold) and *mxdB* (1.7-fold)]; this explains the rapid attachment of the cells to the electrode in this medium.

The differentiation in current generation was probably caused by the higher electrochemical activity of FMN in medium A than in medium B, the higher amount of biofilm biomass in medium A than in medium B, and the more fluffy biofilm in medium A than in medium B. Fluffy biofilm is probably favorable for inner biofilm mass transfer, such as diffusion of electron shuttles, which is possibly beneficial for EET. Buffer was proved to play a critical role in determining the biofilm structure and contributed to the difference in EET performance in two media. Increasing in buffer concentration increased the medium conductivity. This study provides new insights regarding medium-dependent biofilm regulation that will

be beneficial for developing simple and efficient strategies for regulating biofilm structure in BESs.

Declaration of competing interest

The authors declare no competing financial interests or personal relationships.

CRediT authorship contribution statement

Zhixin Lin: Dat, a curation, Investigation, Writing - original draft. **Mingliang Long:** Investigation, Validation. **Wei Liu:** Writing - review & editing, Visualization, Methodology, Funding acquisition. **Tongxu Liu:** Conceptualization, Supervision, Writing - review & editing. **Fangbai Li:** Conceptualization, Resources. **Yundang Wu:** Conceptualization, Methodology, Writing - review & editing, Project administration, Funding acquisition.

Declaration of Competing Interest

The authors declare that they have no known competing financial interests or personal relationships that could have appeared to influence the work reported in this paper.

Acknowledgments

This work was funded by the National Natural Science Foundations of China (42077020 and 21701045), the Pearl River S&T Nova Program of Guangzhou (201906010060), Guangdong Basic and Applied Basic Research Foundation (2019A1515011033), and Guangdong Foundation for Program of Science and Technology Research (Grant No.2020B1212060048)

Appendix A. Supplementary data

Supplementary data to this article can be found online at <https://doi.org/10.1016/j.bioelechem.2021.107826>.

References

- [1] J.K. Fredrickson, M.F. Romine, A.S. Beliaev, J.M. Auchtung, M.E. Driscoll, T.S. Gardner, K.H. Nealson, A.L. Osterman, G. Pinchuk, J.L. Reed, D.A. Rodionov, J.L. M. Rodrigues, D.A. Saffarini, M.H. Serres, A.M. Spormann, I.B. Zhulin, J.M. Tiedje, Towards environmental systems biology of *Shewanella*, Nat. Rev. Microbiol. 6 (2008) 592–603, <https://doi.org/10.1038/nrmicro1947>.
- [2] C.R. Myers, K.H. Nealson, Bacterial manganese reduction and growth with manganese oxide as the sole electron acceptor, Science 240 (1988) 1319–1321, <https://doi.org/10.1126/science.240.4857.1319>.
- [3] H.H. Hau, J.A. Gralnick, Ecology and biotechnology of the genus *Shewanella*, Annu. Rev. Microbiol. 61 (2007) 237–258, <https://doi.org/10.1146/annurev.micro.61.080706.093257>.
- [4] L. Zhou, Y. Jiang, Y. Wan, X. Liu, H. Zhou, W. Li, N. Li, X. Wang, Electron flow shifts from anode respiration to nitrate reduction during electroactive biofilm thickening, Environ. Sci. Technol. 54 (2020) 9593–9600, <https://doi.org/10.1021/acs.est.0c01343>.
- [5] B.E. Logan, R. Rossi, A. Ragab, P.E. Saikaly, Electroactive microorganisms in bioelectrochemical systems, Nat. Rev. Microbiol. 17 (2019) 307–319, <https://doi.org/10.1038/s41579-019-0173-x>.
- [6] C. Santoro, C. Arbizzani, B. Erable, I. Ieropoulos, Microbial fuel cells: From fundamentals to applications. A review, J. Power Sources. 356 (2017) 225–244, <https://doi.org/10.1016/j.jpowsour.2017.03.109>.
- [7] M. Li, K. Zhong, L. Zhang, S. Wang, H. Zhang, Y. Huang, S. Chen, H. Mai, N. Zhang, Cobalt-based catalysts modified cathode for enhancing bioelectricity generation and wastewater treatment in air-breathing cathode microbial fuel cells, Electroanalysis. 31 (2019) 1482–1493, <https://doi.org/10.1002/elan.201900161>.
- [8] X. Liu, W. Li, H. Yu, Cathodic catalysts in bioelectrochemical systems for energy recovery from wastewater, Chem. Soc. Rev. 43 (2014) 7718–7745, <https://doi.org/10.1039/c3cs60130g>.
- [9] L. Shi, H. Dong, G. Reguera, H. Beyenal, A. Lu, J. Liu, H.-Q. Yu, J.K. Fredrickson, Extracellular electron transfer mechanisms between microorganisms and minerals, Nat. Rev. Microbiol. 14 (2016) 651–662, <https://doi.org/10.1038/nrmicro.2016.93>.
- [10] B.M. Fonseca, C.M. Paquete, S.E. Neto, I. Pacheco, C.M. Soares, R.O. Louro, Mind the gap: Cytochrome interactions reveal electron pathways across the

- periplasm of *Shewanella oneidensis* MR-1, *Biochem. J.* 449 (2013) 101–108, <https://doi.org/10.1042/BJ20121467>.
- [11] J.A. Gralnick, D.K. Newman, Extracellular respiration, *Mol. Microbiol.* 65 (2007) 1–11, <https://doi.org/10.1111/j.1365-2958.2007.05778.x>.
 - [12] N.R. Glasser, S.H. Saunders, D.K. Newman, The colorful world of extracellular electron shuttles, *Annu. Rev. Microbiol.* 71 (2017) 731–751, <https://doi.org/10.1146/annurev-micro-090816-093913>.
 - [13] D. Sun, S. Cheng, A. Wang, F. Li, B.E. Logan, K. Cen, Temporal-spatial changes in viabilities and electrochemical properties of anode biofilms, *Environ. Sci. Technol.* 49 (2015) 5227–5235, <https://doi.org/10.1021/acs.est.5b00175>.
 - [14] Y. Yuan, S. Zhou, Y. Liu, J. Tang, Nanostructured macroporous bioanode based on polyaniline-modified natural loofah sponge for high-performance microbial fuel cells, *Environ. Sci. Technol.* 47 (2013) 14525–14532, <https://doi.org/10.1021/es404163g>.
 - [15] Y. Wang, M. Lv, Q. Meng, C. Ding, L. Jiang, H. Liu, Facile one-step strategy for highly boosted microbial extracellular electron transfer of the genus *Shewanella*, *ACS Nano*. 10 (2016) 6331–6337, <https://doi.org/10.1021/acsnano.6b02629>.
 - [16] Y. Yang, Y. Xiang, G. Sun, W.M. Wu, M. Xu, Electron acceptor-dependent respiratory and physiological stratifications in biofilms, *Environ. Sci. Technol.* 49 (2015) 196–202, <https://doi.org/10.1021/es504546g>.
 - [17] Y. Wu, X. Luo, X. Luo, X. Luo, B. Qin, F. Li, M.M. Häggblom, T. Liu, T. Liu, Enhanced current production by exogenous electron mediators via synergy of promoting biofilm formation and the electron shuttling process, *Environ. Sci. Technol.* 54 (2020) 7217–7225, <https://doi.org/10.1021/acs.est.0c00141>.
 - [18] M. Wolf, A. Kappler, J. Jiang, R.U. Meckenstock, Effects of humic substances and quinones at low concentrations on ferrihydrite reduction by *Geobacter metallireducens*, *Environ. Sci. Technol.* 43 (2009) 5679–5685, <https://doi.org/10.1021/es803647r>.
 - [19] Y. Wu, T. Liu, X. Li, F. Li, Exogenous electron shuttle-mediated extracellular electron transfer of *Shewanella putrefaciens* 200: electrochemical parameters and thermodynamics, *Environ. Sci. Technol.* 48 (2014) 9306–9314, <https://doi.org/10.1021/es5017312>.
 - [20] W. Liu, Y. Wu, T. Liu, F. Li, H. Dong, M. Jing, Influence of incubation temperature on 9,10-anthraquinone-2-sulfonate (AQS)-mediated extracellular electron transfer, *Front. Microbiol.* 10 (2019) 1–10, <https://doi.org/10.3389/fmicb.2019.00464>.
 - [21] B. Qin, Y. Wu, G. Wang, X. Chen, X. Luo, F. Li, T. Liu, Physicochemical constraints on the in-situ deposited phenoxazine mediated electron shuttling process, *Electrochim. Acta*. 339 (2020), <https://doi.org/10.1016/j.electacta.2020.135934> 135934.
 - [22] Y. Wu, W. Liu, T. Liu, F. Li, T. Xiao, Q. Wu, Y. He, Sustainable electron shuttling processes mediated by in situ-deposited phenoxazine, *ChemElectroChem*. 5 (2018) 2171–2175, <https://doi.org/10.1002/celec.201800470>.
 - [23] A. Okamoto, S. Kalathil, X. Deng, K. Hashimoto, R. Nakamura, K.H. Nealon, Cell-secreted flavins bound to membrane cytochromes dictate electron transfer reactions to surfaces with diverse charge and pH, *Sci. Rep.* 4 (2014) 5628, <https://doi.org/10.1038/srep05628>.
 - [24] Y. Wu, F. Li, T. Liu, R. Han, X. Luo, pH dependence of quinone-mediated extracellular electron transfer in a bioelectrochemical system, *Electrochim. Acta*. 213 (2016) 408–415, <https://doi.org/10.1016/j.electacta.2016.07.122>.
 - [25] L. Zhao, H. Dong, R. Kukkadapu, A. Agrawal, D. Liu, J. Zhang, R.E. Edelman, Biological oxidation of Fe(II) in reduced nontronite coupled with nitrate reduction by *Pseudogulbenkiania* sp. Strain 2002, *Geochim. Cosmochim. Acta*. 119 (2013) 231–247, <https://doi.org/10.1016/j.gca.2013.05.033>.
 - [26] Y. Wu, T. Liu, F. Li, Examination of extracellular electron transfer process mediated by c-type cytochrome in intact cells using a diffuse-transmittance spectroelectrochemical method (in Chinese), *Sci. Sin. Tech.* 49 (2019) 1473–1482, <https://doi.org/10.1360/N092018-00402>.
 - [27] T. Liu, X. Luo, Y. Wu, J.R. Reinfelder, X. Yuan, X. Li, D. Chen, F. Li, Extracellular electron shuttling mediated by soluble c-type cytochromes produced by *Shewanella oneidensis* MR-1, *Environ. Sci. Technol.* 54 (2020) 10577–10587, <https://doi.org/10.1021/acs.est.9b06868>.
 - [28] K. Chourey, M.R. Thompson, J. Morrell-Falvey, N.C. VerBerkmoes, S.D. Brown, M. Shah, J. Zhou, M. Doktycz, R.L. Hettich, D.K. Thompson, Global molecular and morphological effects of 24-hour chromium(VI) exposure on *Shewanella oneidensis* MR-1, *Appl. Environ. Microbiol.* 72 (2006) 6331–6344, <https://doi.org/10.1128/AEM.00813-06>.
 - [29] S.A. Patil, K. Górecki, C. Hägerhäll, L. Gorton, Cisplatin-induced elongation of *Shewanella oneidensis* MR-1 cells improves microbe-electrode interactions for use in microbial fuel cells, *Energy Environ. Sci.* 6 (2013) 2626–2630, <https://doi.org/10.1039/c3ee41974f>.
 - [30] A. Okamoto, K. Hashimoto, K.H. Nealon, R. Nakamura, Rate enhancement of bacterial extracellular electron transport involves bound flavin semiquinones, *Proc. Natl. Acad. Sci.* 110 (2013) 7856–7861, <https://doi.org/10.1073/pnas.1220823110>.
 - [31] S. Xu, Y. Jangir, M.Y. El-Naggar, Disentangling the roles of free and cytochrome-bound flavins in extracellular electron transport from *Shewanella oneidensis* MR-1, *Electrochim. Acta*. 198 (2016) 49–55, <https://doi.org/10.1016/j.electacta.2016.03.074>.
 - [32] R. Garjonyte, A. Malinauskas, L. Gorton, Investigation of electrochemical properties of FMN and FAD adsorbed on titanium electrode, *Bioelectrochemistry*. 61 (2003) 39–49, [https://doi.org/10.1016/S1567-5394\(03\)00058-6](https://doi.org/10.1016/S1567-5394(03)00058-6).
 - [33] D. Baron, E. Labelle, D. Coursolle, J.A. Gralnick, D.R. Bond, Electrochemical measurement of electron transfer kinetics by *Shewanella oneidensis* MR-1, *J. Biol. Chem.* 284 (2009) 28865–28873, <https://doi.org/10.1074/jbc.M109.043455>.
 - [34] J. Gödecke, M. Heun, S. Bubendorfer, K. Paul, K.M. Thormann, Roles of two *Shewanella oneidensis* MR-1 extracellular endonucleases, *Appl. Environ. Microbiol.* 77 (2011) 5342–5351, <https://doi.org/10.1128/AEM.00643-11>.
 - [35] M. Heun, L. Binnenkade, M. Kreienbaum, K.M. Thormann, Functional specificity of extracellular nucleases of *Shewanella oneidensis* MR-1, *Appl. Environ. Microbiol.* 78 (2012) 4400–4411, <https://doi.org/10.1128/AEM.07895-11>.
 - [36] J. Müller, S. Shukla, K.A. Jost, A.M. Spormann, The mxd operon in *Shewanella oneidensis* MR-1 is induced in response to starvation and regulated by ArcS/ArcA and BarA/UvrY, *BMC Microbiol.* 13 (2013) 119, <https://doi.org/10.1186/1471-2180-13-119>.
 - [37] R.M. Saville, N. Dieckmann, A.M. Spormann, Spatiotemporal activity of the *mshA* gene system in *Shewanella oneidensis* MR-1 biofilms, *FEMS Microbiol. Lett.* 308 (2010) 76–83, <https://doi.org/10.1111/j.1574-6968.2010.01995.x>.
 - [38] W. De Windt, H. Gao, W. Krömer, P. Van Damme, J. Dick, J. Mast, N. Boon, J. Zhou, W. Verstraete, AggA is required for aggregation and increased biofilm formation of a hyper-aggregating mutant of *Shewanella oneidensis* MR-1, *Microbiology*. 152 (2006) 721–729, <https://doi.org/10.1099/mic.0.28204-0>.
 - [39] G. Zhou, J. Yuan, H. Gao, Regulation of biofilm formation by BpFA, BpFD, and BpFG in *Shewanella oneidensis*, *Front. Microbiol.* 6 (2015) 1–11, <https://doi.org/10.3389/fmicb.2015.00790>.
 - [40] S. Theunissen, L. De Smet, A. Dansercoer, B. Motte, T. Coenye, J.J. Van Beeumen, B. Devreese, S.N. Savvides, B. Vergauwen, The 285 kDa Bap/RTX hybrid cell surface protein (SO4317) of *Shewanella oneidensis* MR-1 is a key mediator of biofilm formation, *Res. Microbiol.* 161 (2010) 144–152, <https://doi.org/10.1016/j.resmic.2009.12.002>.
 - [41] T. Onur, E. Yuca, T.T. Olmez, U.O.S. Seker, Self-assembly of bacterial amyloid protein nanomaterials on solid surfaces, *J. Colloid Interface Sci.* 520 (2018) 145–154, <https://doi.org/10.1016/j.jcis.2018.03.016>.
 - [42] R.M.Q. Shanks, N.A. Stella, E.J. Kalivoda, M.R. Doe, D.M. O'Dee, K.L. Lathrop, L.G. Feng, G.J. Nau, A *Serratia marcescens* OxyR homolog mediates surface attachment and biofilm formation, *J. Bacteriol.* 189 (2007) 7262–7272, <https://doi.org/10.1128/JB.00859-07>.
 - [43] F. Guo, H. Luo, Z. Shi, Y. Wu, H. Liu, Substrate salinity: A critical factor regulating the performance of microbial fuel cells, a review, *Sci. Total Environ.* 763 (2021), <https://doi.org/10.1016/j.scitotenv.2020.143021> 143021.
 - [44] E.R. Brown, D.E. Smith, Operational amplifier potentiostats employing positive feedback for IR compensation. I. Theoretical analysis of stability and bandpass characteristics, *Anal. Chem.* 40 (1968) 1411–1423, <https://doi.org/10.1021/ac60266a024>.
 - [45] F. Guo, J.T. Babauta, H. Beyenal, The effect of additional salinity on performance of a phosphate buffer saline buffered three-electrode bioelectrochemical system inoculated with wastewater, *Bioresour. Technol.* 320 (2021), <https://doi.org/10.1016/j.biortech.2020.124291> 124291.
 - [46] K.M. Thormann, K.M. Thormann, S. Duttler, R.M. Saville, R.M. Saville, M. Hyodo, M. Hyodo, S. Shukla, Y. Hayakawa, Y. Hayakawa, A.M. Spormann, A.M. Spormann, Control of formation and cellular detachment from *Shewanella oneidensis* MR-1 biofilms by cyclic di-GMP, *Microbiology*. 188 (2006) 2681–2691, <https://doi.org/10.1128/JB.188.7.2681>.
 - [47] T. Liu, Y. Yu, X. Deng, C.K. Ng, B. Cao, J. Wang, S.A. Rice, S. Kjelleberg, H. Song, Enhanced *Shewanella* biofilm promotes bioelectricity generation, *Biotechnol. Bioeng.* 112 (2015) 2051–2059, <https://doi.org/10.1002/bit.25624>.



Revealing the underestimated role of Gram-positive bacteria in iron reduction within paddy soils

Yu Huang^{a,b}, Yuquan Tan^{a,b}, Lin Shen^{b,f,g}, Chao Peng^c, Yaying Li^d, Juntao Zhang^e, Fengrong Zhang^a, Chunlin Ni^a, Wei Liu^{a,*}, Yundang Wu^{b,*}, Fangbai Li^b

^a College of Materials and Energy, South China Agricultural University, Guangzhou 510642, China

^b National-Regional Joint Engineering Research Center for Soil Pollution Control and Remediation in South China, Guangdong Key Laboratory of Integrated Agro-Environmental Pollution Control and Management, Institute of Eco-Environmental and Soil Sciences, Guangdong Academy of Sciences, Guangzhou 510650, China

^c Key Laboratory of Southwest China Wildlife Resources Conservation, College of Life Sciences, China West Normal University, Nanchong, China

^d Institute of Agricultural Resources and Environment, Guangdong Academy of Agricultural Science, Guangzhou 510640, China

^e Guangzhou Institute of Forestry and Landscape Architecture, Guangzhou 510405, China

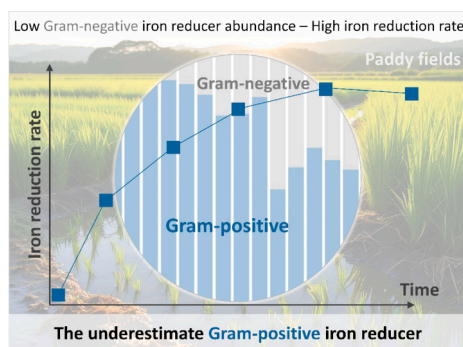
^f Guangzhou Institute of Geochemistry, Chinese Academy of Sciences, Guangzhou 510640, China

^g University of Chinese Academy of Sciences, Beijing 100049, China

HIGHLIGHTS

- Soils with over 80 % abundance of weak exoelectrogens (e.g., *Bacillus*) can still perform rapid iron reduction.
- Gram-positive iron reducers (e.g., *Bacillus*) are much more abundant than Gram-negative ones (e.g., *Geobacter*) in paddy soils.
- High abundance of Gram-positive bacteria offsets their lower reduction rates.

GRAPHICAL ABSTRACT



ARTICLE INFO

Editor: Kyle Bibby

Keywords:

Weak exoelectrogens
Iron reduction
Gram-positive bacteria
Bacillus
Clostridium

ABSTRACT

Iron reduction in paddy fields is crucial for heavy metal migration and nutrient transformation. Gram-negative iron-reducing bacteria like *Geobacter* and *Shewanella* have been widely studied due to their strong extracellular electron transfer capabilities. In contrast, Gram-positive bacteria such as *Bacillus* and *Clostridium* are often labeled as weak exoelectrogens, leading to their contributions being overlooked. But could their role in iron reduction have been underestimated? To explore this, we enriched paddy soils with glucose, resulting in a predominance of Gram-positive bacteria (e.g., *Clostridiaceae* and *Bacillaceae*) and a small presence of Gram-negative reducers (e.g., *Geobacteraceae*). Remarkably, despite the abundance of Gram-positive iron reducers being 880 times higher in the glucose system, their iron reduction rate was comparable to that of acetate and lactate systems with more Gram-negative bacteria. This suggests a significant contribution by Gram-positive bacteria to iron reduction. Pure culture experiments further revealed that the iron reduction rates of *Bacillus* and *Clostridium* are 15.4 and

* Corresponding authors.

E-mail addresses: liuwei97@scau.edu.cn (W. Liu), ydwu@soil.gd.cn (Y. Wu).

<https://doi.org/10.1016/j.scitotenv.2025.178985>

Received 10 December 2024; Received in revised form 1 February 2025; Accepted 24 February 2025

0048-9697/© 2025 Elsevier B.V. All rights are reserved, including those for text and data mining, AI training, and similar technologies.

4.0 times slower, respectively, than a Gram-negative reducer, *Geobacter*. However, even in natural paddy soil of this study, Gram-positive iron reducers are 9 times more abundant than Gram-negative ones. This gives us an unexpected insight: Considering both abundance and rate, Gram-positive weak exoelectrogens may actually contribute significantly to iron reduction. This study reveals the underestimated role of Gram-positive bacteria in paddy soils, highlighting the unique characteristics of paddy habitats and the need for further research on these weak exoelectrogens.

1. Introduction

In soil, microorganisms control the reduction and dissolution of iron, determining the toxicity and activity of contaminants on the surface of iron-bearing minerals (Dong et al., 2023). Since the discovery of *Geobacter* (Lovley et al., 1987) and *Shewanella* (Myers and Nealson, 1988), Gram-negative bacteria, which possess both an intact inner and outer membrane structure, have been regarded as the primary contributors to iron reduction, as their cell membranes contain cytochromes *c* that can transfer electrons externally, reducing extracellular iron through extracellular respiration (Bird et al., 2011; Myers and Nealson, 1988; Shi et al., 2016). However, in paddy fields rich in dissolved organic matter, Gram-positive bacteria such as *Bacillus* and *Clostridium*, which lack an outer membrane but possess a thick cell wall and have been defined as weak exoelectrogens, are abundant (Das et al., 2017; Guo et al., 2016). Particularly in paddy field that has just shifted from dry to flooded conditions, Gram-positive bacteria dominate overwhelmingly (Cui et al., 2019). From the perspective of abundance, the abundance of Gram-positive bacteria is even higher than that of Gram-negative bacteria in specific environments. This raises the question: What role do these Gram-positive bacteria play in paddy soil iron reduction?

Although Gram-positive bacteria possess thick cell walls and are unable to reduce extracellular iron through respiration, increasing evidence suggests that they have weak iron-reducing capabilities, a process defined as “fermentative iron reduction”. These bacteria are often referred to as “weak exoelectrogens” (Aiyer and Doyle, 2022; Eghtesadi et al., 2022; Qin et al., 2024). Reported examples include *Bacillus*, *Clostridium*, and *Aeromonas*, most of which are Gram-positive (Doyle and Marsili, 2018). They primarily reduce iron indirectly through metabolic products (such as H_2) released during the fermentation process (Dong et al., 2017; Zhang et al., 2020). Recent studies have indicated that certain specific Gram-positive bacteria, such as *Listeria monocytogenes*, can transfer electrons to electron shuttles like riboflavin, achieving relatively high electron transfer rates and directly reducing iron (Light et al., 2019, 2018). But in general, at the single-species level, the iron-reducing capacity of fermentative microorganisms is significantly lower than that of respiratory Gram-negative iron-reducing bacteria (Hammann and Ottow, 1974; O’Loughlin, 2008). However, some researchers believe that the role of Gram-positive bacteria in the iron reduction process may be underestimated in certain environments. For example, in the reaction system simulating the formation process of marine banded iron formations, researchers have altered conditions such as carbon source, iron type, and pH, yet the abundance of fermentative Firmicutes consistently remains dominant. Based on this, they proposed that these bacteria may play some yet unclear role (Parker et al., 2018). Paddy soil is rich in organic matter, including material produced from straw decomposition and organic matter secreted by rice roots (Neumann and Romheld, 2000; Xu et al., 2024). This organic matter serves as carbon sources for fermentative microorganisms, promoting their metabolism. In addition, they can also act as electron shuttles, thereby accelerating electron transfer between microbes and iron oxides (Klüpfel et al., 2014). Consequently, genera such as *Bacillus* and *Clostridium* are frequently found in high abundances in paddy soils (Das et al., 2017; Saxena et al., 2020). While their iron-reducing reaction rates are slower, their high abundance raises the question: Is the contribution of Gram-positive bacteria to iron reduction in paddy soil underestimated?

Paddy soil is complex, making it challenging to directly distinguish the contributions of different bacterial groups. However, by using carbohydrates as substrates to promote the significant growth of fermentative bacteria capable of carbohydrate metabolism and comparing these with systems containing lactate and acetate, we may gain insights into the roles of both Gram-negative and Gram-positive bacteria (Griffiths et al., 1998; Hernández and Hobbie, 2010). Therefore, we selected a typical iron-rich paddy soil and added three different substrates: glucose, lactate, and acetate, to observe the rates of iron reduction, substrate consumption, and changes in microbial abundance. This study aims to examine the iron reduction rate, substrate metabolism rate, and the proportions of Gram-negative and Gram-positive bacteria under different substrate conditions, thereby investigating the role of Gram-positive bacteria in iron reduction within paddy soil. This study will enhance our understanding of the underlying mechanisms of iron reduction in paddy fields and address misconceptions regarding the iron-reducing capabilities of Gram-positive bacteria, holding significant environmental and biogeochemical implications.

2. Materials and methods

2.1. Materials

The soil used in this study was collected from the rhizosphere of rice in Hainan and stored at $-20\text{ }^{\circ}\text{C}$ after being ground and sifted through a 100-mesh sieve. The physicochemical properties of the soil are shown in Table S1. 9,10-anthraquinone-2,6 disulfonic acid (AQDS) was purchased from TCI Company, Japan. Lactate, acetate, glucose, and other chemical reagents were all purchased from Guangzhou Chemical Reagent Co., Ltd.

2.2. Construction of the cultivation system

Three carbon sources, glucose, lactate, and acetate, were selected for anaerobic cultivation, with a blank control group without added carbon source. On this basis, a treatment group with the addition of electron shuttle (AQDS) (Wu et al., 2020) was set up. The carbon source concentration in the reaction system was 30 mM, the AQDS concentration was 50 μM , the reaction time was about 21 days, and the water-to-soil ratio was 10:1 (80 mL system, 8 g soil). After weighing 8 g of soil into a cleaned and dried 100 mL serum bottle, the shuttle and carbon source were added sequentially. Nitrogen was purged for 40 min to replace the oxygen inside the bottle. Then, the serum bottle was capped and sealed, mixed and shaken for 1 h before being placed in a $28\text{ }^{\circ}\text{C}$ constant temperature incubator for static cultivation. Samples were taken anaerobically with a syringe at 0, 3, 7, 11, 16, and 21 days to detect changes in the concentrations of dissolved Fe(II) and carbon source consumption. In addition, we set up a sterile soil control treatment. The soil was sterilized by gamma-ray irradiation before conducting the iron reduction experiment. The radiation source used was Co-60, and the irradiation dose was 30 kGy (Huada radiation, Guangzhou, China).

In addition, pure culture experiments with *Bacillus subtilis*, *Clostridium sporogenes*, and *Geobacter sulfurreducens* PCA were also conducted using similar anaerobic bottles. The reaction conditions were as follows: 5 mM ferrihydrite, 10 mM piperazine-*N,N'*-bis(2-ethanesulfonic acid) (PIPES) buffer (pH = 7.0), $\text{OD}_{600} = 0.5$. *Bacillus* and *Clostridium* used glucose as the carbon source, while *Geobacter* used acetate as the

carbon source. The sample was deoxygenated by flushing with nitrogen gas for 40 min. During sampling and testing, the bottle cap was opened inside the anaerobic glove box, the sample was shaken well, and then aspirated using a pipette. The sample was added to 1 M HCl solution for dissolution, and the total amount of iron(II) extracted by hydrochloric acid was measured.

2.3. Chemical analysis

I. Sampling and Analysis of Fe(II). Samples were collected using a 5 mL syringe, which was flushed with nitrogen gas prior to sampling. After thoroughly mixing the water and soil, 5 mL of the sample was extracted, and 1 mL of it was added to 2.5 mL of a sodium acetate–acetic acid (NaAc-HAc) buffer solution under nitrogen protection to prevent further oxidation of Fe(II). The sample was then filtered through a 0.22 μm membrane to remove soil particles, yielding the test sample. To determine Fe(II) concentration, 1 mL of the test sample was mixed with 2.5 mL of NaAc-HAc buffer solution and 1 mL of 0.1 % o-phenanthroline reagent, followed by a 15-min color development. Subsequently, 200 μL of the developed sample was transferred to a 96-well microplate for measurement using a microplate reader. The Fe(II) concentration was calculated based on the absorbance at 510 nm (Lu, 2000).

II. Glucose was analyzed using a Waters 2695 high-performance liquid chromatography (HPLC) system equipped with a 2414 refractive index detector. The analysis was performed on an Ultimate HILIC-NH2 column (250 mm \times 4.6 mm, 5 μm) at a column temperature of 40 $^{\circ}\text{C}$. The mobile phase consisted of 80 % acetonitrile in water, with a flow rate of 1.0 mL $\cdot\text{min}^{-1}$ and an injection volume of 10 μL (Yu and Li, 2013).

III. Both formate and butyrate were analyzed using an Agilent 1100 HPLC system. The UV detector used, operating at a wavelength of 214 nm. The analysis was performed on a C18-PAQ reversed-phase column (250 mm \times 4.6 mm, 5 μm) at a column temperature of 30 $^{\circ}\text{C}$. The injection volume is 10 μL . For formate, the mobile phase was a 20 mM phosphate buffer solution (pH = 3). The flow rate was set to 0.8 mL $\cdot\text{min}^{-1}$. For butyrate, the mobile phase was a mixture of 100 mM phosphate buffer solution (pH = 3) and methanol in a ratio of 8:2. The flow rate was set to 1.0 mL $\cdot\text{min}^{-1}$ (Li and Li, 2017).

IV. Methods for testing lactate and acetate. The Agilent 1260 Infinity II HPLC system was employed, using a C18-PAQ reverse-phase column (250 mm \times 4.6 mm, 5 μm). The injection volume was set at 10 μL , with a flow rate of 1.0 mL $\cdot\text{min}^{-1}$ and a column temperature of 30 $^{\circ}\text{C}$. The mobile phase was: 15.6 g $\cdot\text{L}^{-1}$ NaH_2PO_4 , pH adjusted to 3.1 using phosphoric acid. All mobile phases in this study need to be sonicated for 30 min to remove dissolved gases (Li and Li, 2017).

2.4. Microbial community structure analysis

DNA extraction from soil samples was performed using the Mag-Beads FastDNA Kit for Soil (MP biomedical, China). The 16S rRNA gene sequencing analysis was outsourced to Shanghai Personal Biotechnology Co., Ltd. The primers 338F (5'-ACTCCTACGGGAGGCAGCA-3') and 806R (5'-GGACTACHVGGGTWTCTAAT-3') were used to amplify the V3-V4 region of the 16S rRNA gene through PCR (Fierer et al., 2005). Sequencing of the community DNA fragments was conducted on the Illumina NovaSeq PE250 platform, with paired-end sequencing at a depth of 60,000 reads per sample. The sequencing results were aligned against the Silva database to analyze the microbial community structure in the samples. Feature tables, after removing singletons, were statistically processed to visualize the compositional distribution across six taxonomic levels: phylum, class, order, family, genus, and species. The sequence data have been submitted to the NCBI Short Read Archive in Bioproject PRJNA1192562.

2.5. Data analysis

Gram-positive bacteria were predicted using the BugBase microbiome analysis tool. First, the identified species were annotated using the Greengenes database. These annotations were then compared against the BugBase library to obtain species-level annotations corresponding to Greengenes data. Based on the annotation results, phenotypes were output to determine whether each amplicon sequence variant (ASV) belonged to Gram-positive or Gram-negative bacteria (Ward et al., 2017).

3. Results

3.1. Iron reduction under different substrate conditions

The soil iron reduction under the condition of different carbon sources was analyzed (Fig. 1a-c). Significant iron reduction occurred in all treatments within 21 days, with the production of dissolved Fe(II) gradually increasing over time. Final concentrations of Fe(II) reached 566.5 mg $\cdot\text{L}^{-1}$, 492.2 mg $\cdot\text{L}^{-1}$, and 550 mg $\cdot\text{L}^{-1}$ in the glucose, lactate, and acetate treatments, respectively. Within 11 days, the Fe(II) production in the glucose system was only slightly lower than that in the acetate and lactate systems, remaining within the same order of magnitude, indicating that glucose still exhibits a strong iron reduction capacity as a substrate (Fig. 1d). The reaction rate among the three treatments followed the order: sodium lactate (67.1 mg $\cdot\text{L}^{-1}\cdot\text{d}^{-1}$) > sodium acetate (55.8 mg $\cdot\text{L}^{-1}\cdot\text{d}^{-1}$) > glucose (37.4 mg $\cdot\text{L}^{-1}\cdot\text{d}^{-1}$) (Fig. 1d), with glucose being slightly lower than the others. No obvious Fe(II) generation was observed in the sterilization control.

Since electron shuttles can promote microbial iron reduction to some extent, we included an AQDS treatment. Results showed that AQDS significantly enhanced the iron reduction capacity in the glucose system, raising the Fe(II) production rate from 37.4 mg $\cdot\text{L}^{-1}\cdot\text{d}^{-1}$ to 66.4 mg $\cdot\text{L}^{-1}\cdot\text{d}^{-1}$ (Fig. 1a). However, only a slight increase in iron reduction capacity was observed in the lactate and acetate systems. A comparison of the Fe(II) production rate showed that the values for the three systems were very close, further confirming the strong iron reduction capacity of the glucose system.

3.2. Substrate metabolism under different conditions

To further correlate iron reduction data with substrate metabolism, we examined the kinetics of substrate metabolism under different conditions (Fig. 2). Fig. 2a-d show glucose consumption kinetics and the generation of small organic acids. Fig. 2a indicates that 30 mM of glucose was completely consumed within 7 days. Correspondingly, butyrate production occurred in the first 7 days and stopped producing afterward, confirming the depletion of glucose (Fig. 2b). Reviewing the iron reduction data in Fig. 1a, rapid iron reduction was observed both before and after day 7. In particular, during the first 3 days, the daily production of ferrous iron reached 1.3 mM, higher than the average of 0.3 mM from days 7 to 21, suggesting that rapid iron reduction occurred during glucose metabolism. Acetate was produced as a small organic acid in further reactions, as shown in Fig. 1c, with a continuous increase throughout the reaction until day 21, when acetate in the AQDS treatment decreased. This process aligns with microbial metabolism that both produces and consumes acetate. Formate, the smallest organic acid, was initially produced, then quickly consumed, and remained undetected thereafter (Fig. 1f), reflecting its rapid microbial metabolism. Comparison between treatments with and without AQDS revealed no significant difference in substrate metabolism rate, suggesting that while AQDS facilitated electron transfer to Fe(II) and accelerated iron reduction, it did not enhance microbial substrate metabolism.

Fig. 2e-h show substrate changes in the lactate and acetate system. A concentration of 30 mM lactate was fully consumed within 7 days (Fig. 2e). Correspondingly, acetate accumulated from day 0 to 3, then

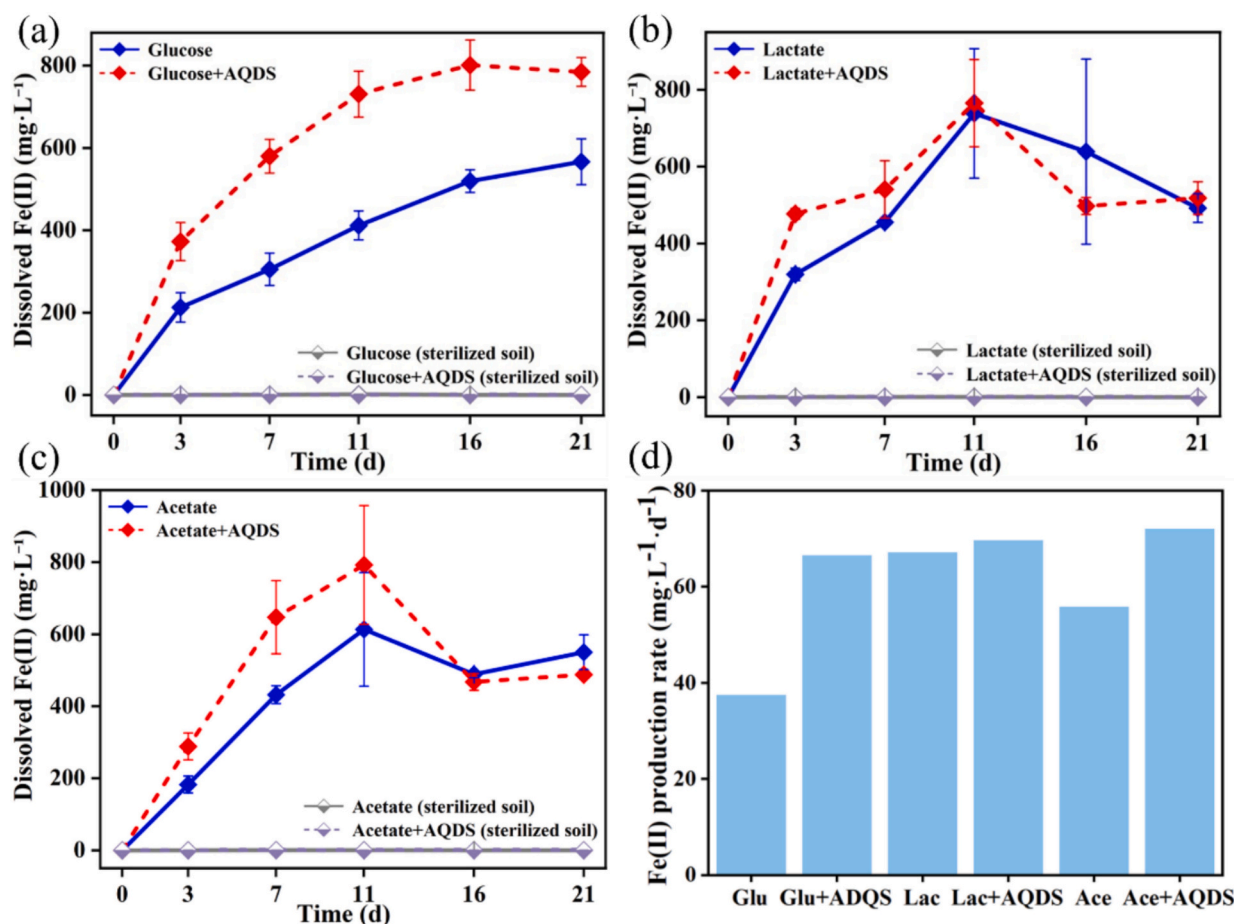


Fig. 1. Iron reduction kinetics. (a) Glucose system; (b) Lactate system; (c) Acetate system; (d) Average daily production of Fe(II), calculated over the first 11 days. Glu represents glucose, Lac represents lactate, and Ace represents acetate.

gradually decreased from day 3 to 7, nearly depleting by day 16. This acetate trend aligns with the iron reduction results in Fig. 1b, where Fe (II) ceased to increase after day 16, consistent with the depletion of acetate. Formate in Fig. 2f exhibited similar results as in the glucose system, being quickly consumed after initial production. In addition, Fig. 2h shows the acetate consumption in the acetate system, with acetate gradually depleting by day 21. Similar to glucose, the addition of AQDS in sodium lactate and sodium acetate treatments did not increase the substrate metabolism rate.

3.3. Microbial community structure under varying substrate conditions

Glucose is a carbohydrate, while lactate and acetate are small organic acids, different microorganisms have different preferences for these substrates. Thus, it is inevitable that microbial communities will differ based on the substrates they are enriched with. We analyzed the soil microbial community structure in the reaction systems using 16S rRNA gene. The beta diversity analysis in Fig. 3a shows significant changes in soil microbial community structure with different substrates, suggesting that the types of microbial communities involved in iron reduction differ across systems.

We further analyzed the specific structure of the soil microbial communities (Fig. 3b). In the initial soil, no particular microorganism holds an absolute abundance advantage, with only 5 %–8 % of total microbes comprising the top 10 % of abundant species. However, with the addition of exogenous substrates, certain dominant microbes were enriched, with different enrichment patterns across systems as follows: on day 3, Clostridiaceae and Bacillaceae were dominant in the glucose system, both primarily consisting of Gram-positive bacteria.

Clostridiaceae accounted for 69.1 % and Bacillaceae for 21.8 % of the total microbial community. In the lactate and acetate treatments, Bacillaceae also showed high abundance (53.4 %–38.2 %), this may be because the soil itself is rich in dissolved organic matter (Neumann and Romheld, 2000; Xu et al., 2024). By day 11, the total abundance of Clostridiaceae and Bacillaceae in the lactate and acetate treatments decreased to 18.1 % and 10.9 %, respectively, whereas the glucose treatment still contained 80.5 % of these families. As glucose was depleted, their abundance continued to decline by day 21 but still represented 62.9 % of the community. In contrast, by day 21, the combined abundance of Clostridiaceae and Bacillaceae in the lactate and acetate systems had dropped to 10.8 % and 6.0 %, respectively, and they were no longer the most abundant groups.

We further detailed compared the inter-group differences between the glucose and lactate treatments (Fig. 3c), as well as between the glucose and acetate treatments (Fig. 3d), which were displayed using a Manhattan plot. The results indicate that the phylum with the most differentially abundant species between the glucose and lactate (Fig. 3c) and glucose and acetate (Fig. 3d) treatments is Firmicutes, a phylum mainly composed of Gram-positive bacteria. Several major differential families, including the previously mentioned Clostridiaceae and Bacillaceae, highlight that the abundance differences in Gram-positive and Gram-negative bacteria are highly significant between the glucose and small organic acid treatments.

3.4. Analysis of the proportion of Gram-positive iron reduction bacteria

We used the Bugbase tool to identify the Gram-positive and Gram-negative bacteria in the reaction system. The results showed that in

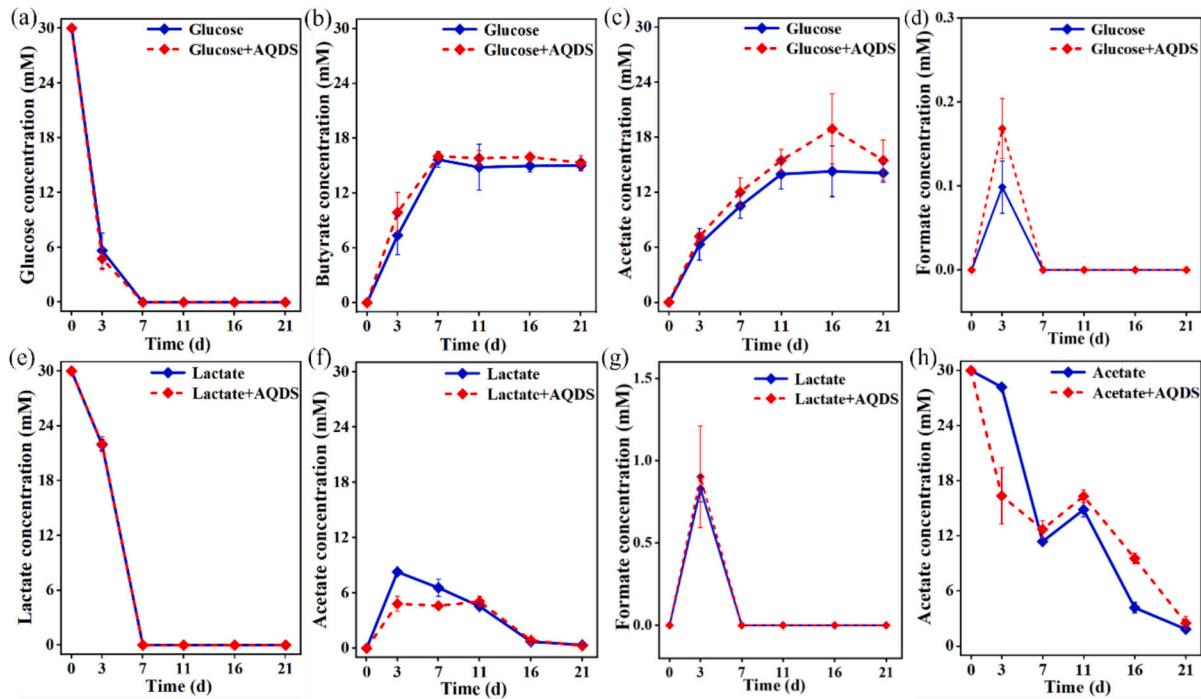


Fig. 2. Quantitative analysis of glucose, lactate, and acetate metabolites. (a–d) Substrate and metabolite consumption and production kinetics in the glucose system, including glucose, butyrate, acetate, and formate. (e–g) Substrate and metabolite consumption and production kinetics in the lactate system, including lactate, acetate, and formate. (h) Acetate consumption kinetics in the acetate system.

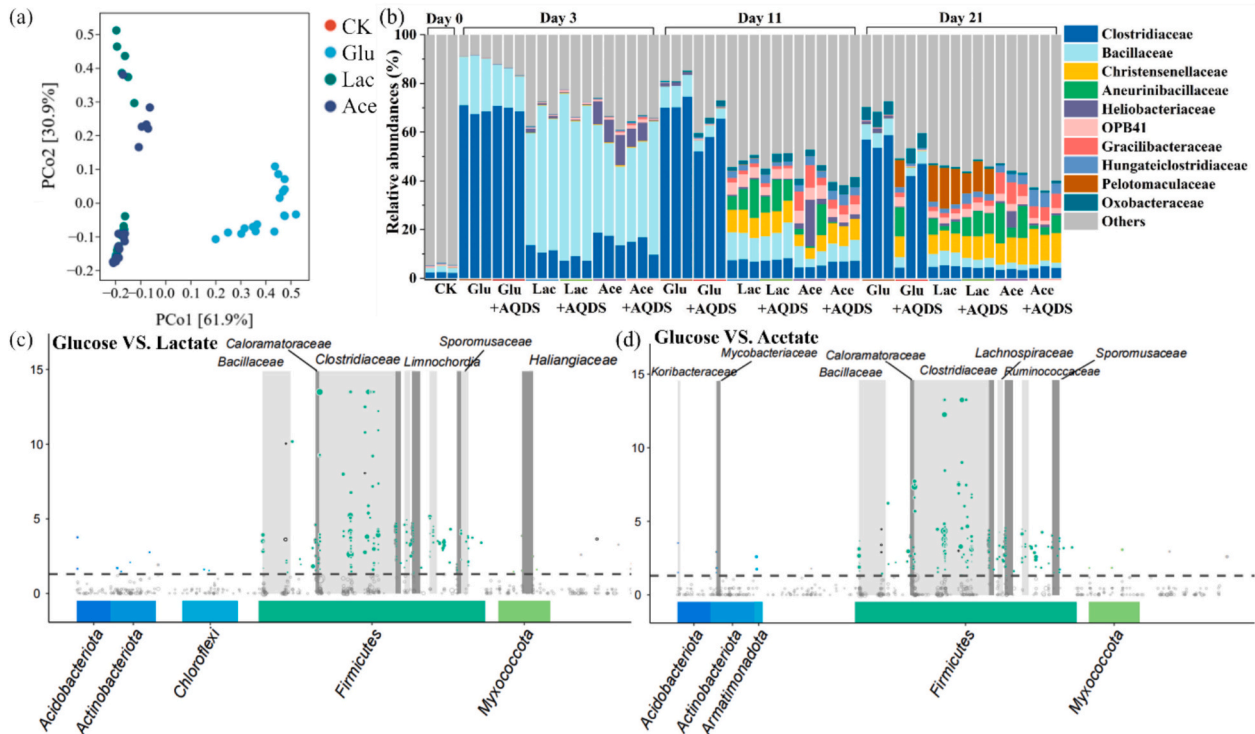


Fig. 3. (a) Beta diversity analysis; (b) Community structure at the family level; (c) Manhattan plot showing microbial differences between glucose and lactate systems; (d) Microbial differences between glucose and acetate systems. Manhattan plot explanation: Each dot represents an ASV corresponding to a bacterial species. Green dots above the gray dashed line indicate significantly different species, with dot size reflecting abundance. Dots within the same gray-shaded block belong to the same family, labeled at the top. The x-axis label indicates the species' phylum. Abbreviations: CK: before carbon addition; Glu: glucose; Lac: lactate; Ace: acetate.

the glucose treatment, the abundance of Gram-positive bacteria reached a peak of 84.8 %, with an average abundance of 76.8 % throughout the reaction, which was significantly higher than the average abundance in

the lactate (39.7 %) and acetate (55.0 %) treatments.

We further annotated the iron-reducing bacteria in the system, and distinguished whether these bacteria were Gram-positive or Gram-

negative. Since there are no specific primers to distinguish iron-reducing bacteria, we used manual classification, identifying 32 commonly reported iron-reducing genera (Table S2) (Fan et al., 2018; Ionescu et al., 2015; Lentini et al., 2012; Lovley and Holmes, 2022; Shi et al., 2024; Yang et al., 2021) and comparing them individually with the genera obtained in this study for display. In Fig. 5, gray sections represent non-iron-reducing bacteria, as they have not been reported to possess iron-reducing abilities to our knowledge. Cold-colored genera (e.g., blue) indicate Gram-positive iron-reducing bacteria, while warm-colored genera (e.g., red and yellow) represent Gram-negative iron-reducing bacteria.

The results show that in the glucose system, most iron-reducing bacteria are Gram-positive. For example, on day 3, as much as 89.8 % of the iron-reducing bacteria in the glucose system were Gram-positive, with only 0.06 % being Gram-negative. In the sodium lactate and sodium acetate treatments, Gram-negative iron-reducing bacteria were more abundant compared to the glucose system. For instance, on day 11, Gram-negative iron-reducing bacteria accounted for 0.4 % and 1.1 % of the total iron-reducing bacteria abundance in the sodium lactate and sodium acetate systems, respectively. However, Gram-positive bacteria still constituted a significant proportion.

3.5. Iron reduction rate of typical Gram-negative and Gram-positive iron-reducing bacteria

Since *Clostridium* and *Bacillus* species are the main Gram-positive iron-reducing bacteria in this study, we selected one pure culture of *Bacillus subtilis* and one strain of *Clostridium sporogenes* as representatives to further investigate their iron reduction rates, thereby providing new insights into the iron reduction process in soils. At the same time, we chose the typical Gram-negative iron-reducing bacterium *Geobacter sulfurreducens* PCA as a comparison. The results show that *Geobacter* exhibits very strong iron reduction capacity, with ferrous iron production exceeding $64.9 \text{ mg} \cdot \text{L}^{-1}$ within 72 h, which aligns with previous knowledge (Fig. 6a). Although *Bacillus subtilis* and *Clostridium sporogenes* exhibit relatively weaker iron reduction, they still produce a certain amount of iron reduction within 72 h as the reaction progresses. By calculating the iron reduction rate over 72 h, as shown in Fig. 6b, the iron reduction by *Geobacter sulfurreducens* is 4.0 times that of *Clostridium sporogenes* and 15.4 times that of *Bacillus subtilis*.

4. Discussion

4.1. Why Gram-positive bacteria deserve attention

Research on iron-reducing microorganisms originated in the United States, beginning with Derek Lovley's discovery of *Geobacter* (1997) and Kenneth Nealson's identification of *Shewanella* (1998) (Lovley et al., 1987; Myers and Nealson, 1988). In the following years, the U.S. Department of Energy funded several foundational studies, driven by the potential of these metal-reducing bacteria in the remediation of nuclear pollution (Cologgi et al., 2011; Luan et al., 2014; Pearce et al., 2012). As the importance of iron reduction in the element cycling of paddy fields became evident, many researchers turned their focus to microbial iron reduction. Nevertheless, possibly due to established thought pattern, the primary focus of the new studies remained on the same bacteria studied by American researchers, namely *Geobacter* and *Shewanella*, even though the research environment had shifted to paddy soils.

However, findings from our study suggest that these Gram-positive bacteria might play an underestimated role in paddy fields, as indicated both by iron-reducing rates (Fig. 1) and their microbial abundance (Fig. 5). More and more studies on paddy soil microbial communities suggest that *Shewanella* is not abundant in paddy soils (Sun et al., 2015), as it is more typically associated with marine sediments (Hau and Gralnick, 2007). As for *Geobacter*, although it does exist in paddy fields, its strict anaerobic nature means that the alternating anaerobic-aerobic

conditions in paddy soils limit its abundance (Kim and Liesack, 2015). In contrast, the application of organic fertilizers and straw return to paddy fields has introduced a large amount of organic matter to the soil, which benefits the growth of fermentative Gram-positive bacteria. Therefore, paddy fields host significant populations of *Clostridium* and *Bacillus* species (Das et al., 2017; Guo et al., 2016). In this study, in the original paddy soil samples we collected, *Clostridium* species accounted for approximately 2.3 % of the microbial population, while *Bacillus* species made up around 2.0 %, which is 63.3- to 57.1-fold higher than the abundance of *Geobacter* (0.04 %). These *Bacillus* and *Clostridium* have been identified as weak electron-transferring organisms with low iron-reducing capacity, yet they have received relatively little attention in the iron-reduction field. Therefore, Gram-positive bacteria are worthy of attention from researchers studying iron reduction in paddy fields.

4.2. Gram-positive bacteria abundance offsets iron reduction disadvantage

Although the iron reduction rate of fermentative Gram-positive bacteria is relatively slow, our study suggests that the differences in their rates are likely to be offset by differences in abundance.

An analysis of microbial communities showed that by day 11, the abundance of Gram-positive iron-reducing bacteria in the glucose system reached 77.2 %, which was 879.5 times higher than that of Gram-negative iron-reducing bacteria (0.09 %) (Fig. 5a). In the lactate and acetate systems, probably due to the presence of native organic matter in the soil, Gram-positive iron-reducing bacteria are 49.4 times (lactate) and 9.5 times (acetate) more abundant than Gram-negative ones, respectively (Fig. 5b and c). Even so, the iron reduction rate in the glucose system is still on the same order of magnitude as that in the lactate and acetate systems. This suggests that both Gram-positive and Gram-negative bacteria are able to successfully reduce iron.

This may be because the difference in their rates is not as significant as the difference in abundance. Research on Gram-positive bacteria has shown that *Bacillus polymyxa* can reduce approximately 0.7 mM of ferric iron within six days (Hammann and Ottow, 1974). This rate is lower compared to *Shewanella* species and *Geobacter* species, but still within two orders of magnitude. In our study, we compared the iron reduction rates of *Bacillus subtilis*, *Clostridium sporogenes*, and *Geobacter sulfurreducens*, and found that the reduction rates of the former two were 15.4 to 4.0 times lower than that of *Geobacter* (Fig. 6). If we assume that the average reaction rates of these two bacteria can represent the average iron reduction rate of all Gram-positive bacteria, once the rate is multiplied by abundance, we find that their contributions are not as vastly different as imagined. Therefore, although glucose system enriched a large number of Gram-positive fermentative bacteria (Figs. 4 and 5), its iron reduction rate was only slightly lower than in the acetate and lactate systems (Fig. 1).

Paddy soils possess distinct environmental characteristics that differentiate them from other ecosystems, including periodic flooding, alternating redox conditions, and abundant organic matter derived from rice root exudates, decaying straw, and organic amendments (Neumann and Romheld, 2000; Xu et al., 2024). These organic inputs are not only rich in carbohydrates but also contain redox-active compounds such as humic substances that are full of quinones, which can act as electron shuttles (Klöpfer et al., 2014; Lovley et al., 1996; Sahrawat, 2003). The high availability of organic carbon in paddy soils creates a selective pressure favoring fermentative Gram-positive bacteria like *Bacillus* and *Clostridium*, which thrive in environments with abundant polysaccharides and oligomers. For instance, rice straw decomposition releases cellulose and hemicellulose (Yan et al., 2019), substrates preferentially metabolized by Gram-positive fermenters, thereby promoting their dominance. The abundance advantage of Gram-positive bacteria might partially offset their slower rate, allowing them to play a substantial role in iron reduction in soil environments.

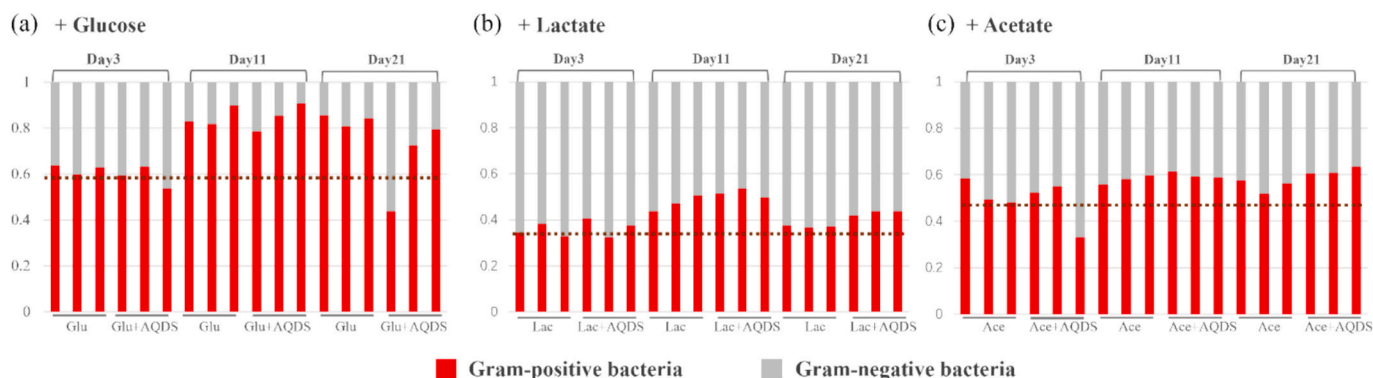


Fig. 4. Gram-positive and Gram-negative bacteria under different carbon source conditions. (a) Glucose system; (b) Lactate system; (c) Acetate system. The Gram-positive and Gram-negative phenotypes were predicted using the BugBase tool. Glu: glucose; Lac: lactate; Ace: acetate.

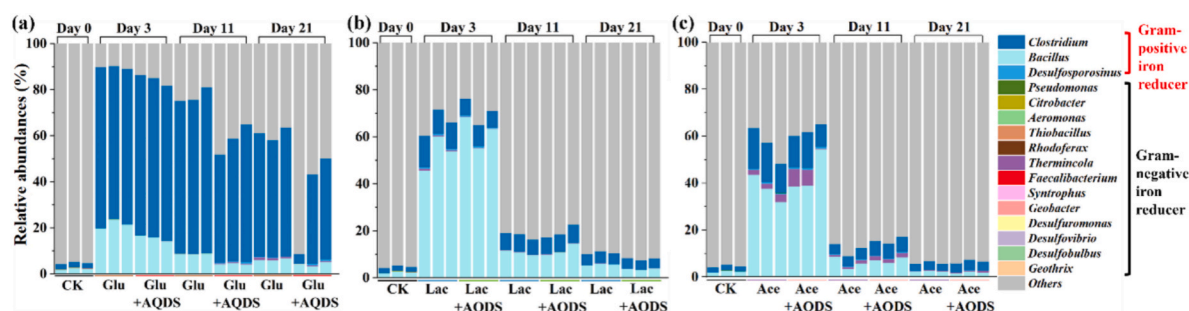


Fig. 5. Iron-reducing bacteria in the reaction system and their Gram-positive or Gram-negative classification were identified. (a) Glucose system; (b) Lactate system; (c) Acetate system. Iron reduction bacteria were selected through manual comparison with reported iron-reducing species. Gray indicates bacteria with no explicitly reported iron-reducing function. CK: sample before the addition of carbon source for cultivation; Glu: glucose; Lac: lactate; Ace: acetate. Others represent bacteria for which iron reduction has not been specifically reported.

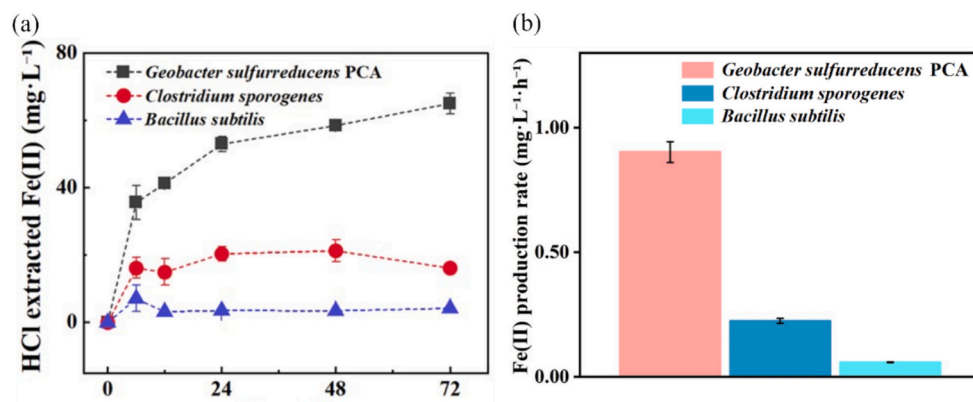


Fig. 6. Comparison of iron reduction kinetics using two typical Gram-positive iron-reducing bacteria (*Bacillus subtilis* and *Clostridium sporogenes*) and one typical Gram-negative iron-reducing bacterium (*Geobacter sulfurreducens*). (a) Fe(II) production kinetics; (b) The iron reduction rate calculated based on the amount of iron reduced over 72 h.

4.3. Gram-positive bacteria promote iron reduction by producing organic acids

Besides directly contributing to iron reduction, Gram-positive bacteria may also play an indirect role in the process. These bacteria carry out carbohydrate metabolism, producing organic acids that may serve as an important source of low-molecular-weight organic acids in paddy fields. Many Gram-positive bacteria, such as *Bacillus* and *Clostridium* species, have fermentative metabolic capabilities and can metabolize carbohydrate (Rodionov et al., 2001). In contrast, Gram-negative iron-reducing bacteria like *Geobacter* and *Shewanella* have limited ability to

metabolize glucose; only a few strains can do so (Fredrickson et al., 2008). Instead, they primarily metabolize small organic acids like lactate and acetate, using them in extracellular respiration to reduce iron. Fermentative bacteria can utilize larger organic compounds as substrates, producing small organic acids through fermentation. These organic acids, in turn, provide an energy source for iron-reducing bacteria, thus accelerating iron reduction (Liu et al., 2017).

In our study, the glucose added to the glucose-based system was fully consumed by day 7 (Fig. 2a), but iron reduction continued from days 7 to 21 (Fig. 1a). Substrate metabolism data indicate that, after day 7, a significant amount of small organic acids, such as acetate, was produced

(Fig. 2c). This suggests that these compounds likely served as substrates for other Gram-negative iron-reducing bacteria, indirectly promoting further iron reduction. This aligns with previous findings on microbial community cooperation, suggesting that one of the contributions of Gram-positive bacteria to extracellular electron transfer may be their role in enhancing substrate utilization (Richardson et al., 2015).

4.4. The indispensable role of electron shuttles in accelerating iron reduction

In addition, the abundant redox-active organic matter in paddy fields could serve as electron shuttles, potentially further enhancing the iron reduction activity of Gram-positive bacteria to some extent. Recent studies have shown that some Gram-positive bacteria, such as *Listeria monocytogenes*, possess extracellular electron transfer capabilities, and this ability can be enhanced by electron shuttles (Light et al., 2018). In our study, the iron reduction rate in the glucose system significantly increased after the addition of AQDS (Fig. 1a), while the effect of AQDS was less pronounced in the lactate and acetate systems. This may be because, although AQDS can also affect the strong exoelectrogens, its enhancing effect on the weak exoelectrogens is more noticeable, thus explaining the observed difference.

In addition, the enhancement effect of chemical materials like electron shuttles on iron reduction by Gram-positive bacteria may still have unknown aspects yet to be discovered. In recent years, the mechanisms through which chemical materials cooperate with microbial metabolism have been continuously being discovered, including nano-CdS enhancing microbial light-driven carbon fixation (Sakimoto et al., 2016), and carbon quantum dots facilitating microbial electron transfer (Yang et al., 2020). These successive new discoveries suggest that, beyond the known electron shuttles that promote extracellular electron transfer in microorganisms, it is worth further exploring whether there are other mechanisms that significantly enhance iron reduction in Gram-positive bacteria.

4.5. Environmental implications

Iron reduction plays an important role in the cycling of elements in paddy fields and is closely related to the migration and transformation of arsenic and cadmium (Tufano et al., 2008; Zhang et al., 2012). Over the past decade, researchers have conducted extensive studies on iron reduction rate (Jiang and Kappler, 2008; Shi et al., 2012), iron-reducing bacteria communities (Peng et al., 2016), and their links to pollutant transformation in paddy soils (Chen et al., 2016; Elsner et al., 2004). Despite this, research on pure cultures has focused primarily on Gram-negative bacteria such as *Geobacter* (Cai et al., 2018; Jing et al., 2020; Liu et al., 2020) and *Shewanella* (Bai et al., 2020; Liu et al., 2013; Yang et al., 2015). This is probably because these bacteria are known for their strong iron-reducing activity, and international studies provide solid evidence of their iron-reduction abilities. However, even in biofilms of iron-reducing bacteria enriched by electrochemical methods, there are many weak electron-transferring and fermentative bacteria (Fessler et al., 2022). These bacteria may perform important, yet unexplored functions that deserve further study. This study further emphasizes the importance of iron reduction by Gram-positive bacteria in paddy soils from the perspectives of abundance and habitat. In particular, the total contribution, as a product of rate and abundance, may not be overlooked.

In addition, the dissimilatory reduction of elements such as manganese and sulfur shares a similar electron transfer mechanism with iron reduction (Flynn et al., 2014; Myers and Nealson, 1988). The contribution of Gram-positive bacteria in the reduction of elements like manganese and sulfur also warrants rethinking. Furthermore, the redox cycling of iron can be coupled with the transformation of heavy metals. For instance, iron reduction can lead to the release of arsenic adsorbed on its surface, thereby increasing the bioavailability of arsenic

(Oremland and Stolz, 2003). Previous studies have often regarded Gram-negative bacteria, such as *Geobacter*, as key microorganisms responsible for arsenic release. However, the findings of this study may inspire greater attention to Gram-positive bacteria, which could also play an important role in driving the transformation of pollutants like arsenic and cadmium. These new insights provide valuable guidance for the future development of iron reduction and its related pollution control research in paddy fields. Moreover, the properties of forest soil, grassland soil, and river sediments differ from those of paddy fields (Kögel-Knabner et al., 2010). It is also worth further exploring the extent of the contribution of Gram-positive bacteria in these habitats.

5. Conclusion

It has always been believed that Gram-positive bacteria make a weak contribution to iron reduction in soil. This study suggests that, when considering their contribution from the perspective of abundance multiplied by rate, their contribution may have been underestimated. This study found that even in systems with a large enrichment of Gram-positive bacteria and a lack of Gram-negative bacteria, the iron reduction rate in the soil is still high. Although the iron reduction rate of Gram-positive iron reducer is 15.4–4.0 times lower than that of typical iron-reducing bacteria (as indicated by pure culture experiments), their abundance is 9–880 times higher in soil (data from day 11), and the combined effect of abundance and rate may contribute to their important role in soil iron reduction. This difference in abundance exists not only in enriched cultivation systems but also in natural paddy soils, where alternating aerobic and anaerobic conditions and the presence of large organic molecules contribute to this difference. Therefore, we propose that the contribution of Gram-positive bacteria to iron reduction in paddy soils may have been underestimated. This study highlights the potential for underestimating the contribution of Gram-positive bacteria. This work observing the iron reduction rates in different systems under controlled conditions. In natural soils, such high concentrations of carbon sources are not typically present, and the organic matter concentrations vary across different soil types. An important scientific challenge to address in the future is how to determine in situ the contribution of Gram-positive and Gram-negative bacteria to iron reduction in natural soil environments.

CRediT authorship contribution statement

Yu Huang: Writing – original draft, Visualization, Validation, Methodology, Investigation, Funding acquisition, Conceptualization. **Yuquan Tan:** Writing – review & editing, Investigation, Data curation. **Lin Shen:** Writing – review & editing, Methodology, Investigation. **Chao Peng:** Writing – review & editing, Investigation, Conceptualization. **Yaying Li:** Writing – review & editing, Visualization, Investigation, Data curation. **Juntao Zhang:** Writing – review & editing, Software, Formal analysis, Data curation. **Fengrong Zhang:** Methodology, Investigation, Formal analysis. **Chunlin Ni:** Writing – review & editing, Investigation, Conceptualization. **Wei Liu:** Writing – review & editing, Writing – original draft, Investigation, Funding acquisition, Conceptualization. **Yundang Wu:** Writing – review & editing, Writing – original draft, Methodology, Investigation, Funding acquisition, Conceptualization. **Fangbai Li:** Writing – review & editing, Methodology, Investigation, Formal analysis.

Declaration of Generative AI and AI-assisted technologies in the writing process

During the preparation of this work the authors used Chat GPT in order to check for grammatical errors. After using this tool, the authors reviewed and edited the content as needed and take full responsibility for the content of the publication.

Declaration of competing interest

The authors declare that they have no known competing financial interests or personal relationships that could have appeared to influence the work reported in this paper.

Acknowledgments

This work was funded by the National Natural Science Foundation of China (42077020 and 42377315), National Key Research and Development Program of China (2023YFD1902100, 2023YFD1901300), Key-Area Research and Development Program of Guangdong Province (2023B0202020001), the GDAS' Project of Science and Technology Development (2023GDASQNR-0202), Youth S&T Talent Support Program of Guangdong Provincial Association for Science and Technology (SKXRC202410), Guangdong Basic and Applied Basic Research Foundation (2024A1515010293), Guangdong Foundation for Program of Science and Technology Research (2023B1212060044), and Chemical Synthesis and Pollution Control Key Laboratory of Sichuan Province (CSPC202307).

Appendix A. Supplementary data

Supplementary data to this article can be found online at <https://doi.org/10.1016/j.scitotenv.2025.178985>.

Data availability

The data proving the results of this study are available within the paper and related supporting information.

References

- Aiyer, K., Doyle, L.E., 2022. Capturing the signal of weak electricigens: a worthy endeavour. *Trends Biotechnol.* 40, 564–575.
- Bai, Y., Sun, T., Angenent, L.T., Haderlein, S.B., Kappler, A., 2020. Electron hopping enables rapid electron transfer between quinone-/hydroquinone-containing organic molecules in microbial iron(III) mineral reduction. *Environ. Sci. Technol.* 54, 10646–10653.
- Bird, L.J., Bonnefoy, V., Newman, D.K., 2011. Bioenergetic challenges of microbial iron metabolisms. *Trends Microbiol.* 19, 330–340.
- Cai, X., Huang, L., Yang, G., Yu, Z., Wen, J., Zhou, S., 2018. Transcriptomic, proteomic, and bioelectrochemical characterization of an exoelectrogen *Geobacter soli* grown with different electron acceptors. *Front. Microbiol.* 9, 1075.
- Chen, M., Liu, C., Chen, P., Tong, H., Li, F., Qiao, J., et al., 2016. Dynamics of the microbial community and Fe(III)-reducing and dechlorinating microorganisms in response to pentachlorophenol transformation in paddy soil. *J. Hazard. Mater.* 312, 97–105.
- Cologgi, D.L., Lampa-Pastirk, S., Speers, A.M., Kelly, S.D., Reguera, G., 2011. Extracellular reduction of uranium by *Geobacter* conductive pili as a protective cellular mechanism. *Proc. Natl. Acad. Sci. USA* 108, 15248–15252.
- Cui, H.L., Duan, G.L., Zhang, H., Cheng, W., Zhu, Y.G., 2019. Microbiota in non-flooded and flooded rice culms. *FEMS Microbiol. Ecol.* 95.
- Das, Suvendu, Jeong, S.T., Das, Subhasis, Kim, P.J., 2017. Composted cattle manure increases microbial activity and soil fertility more than composted swine manure in a submerged rice paddy. *Front. Microbiol.* 8, 1702.
- Dong, H., Zeng, Q., Sheng, Y., Chen, C., Yu, G., Kappler, A., 2023. Coupled iron cycling and organic matter transformation across redox interfaces. *Nat. Rev. Earth Environ.* 4, 659–673.
- Dong, Y., Sanford, R.A., Chang, Y., McInerney, M.J., Fouke, B.W., 2017. Hematite reduction buffers acid generation and enhances nutrient uptake by a fermentative iron reducing bacterium, *Oreana metallireducens* strain Z6. *Environ. Sci. Technol.* 51, 232–242.
- Doyle, L.E., Marsili, E., 2018. Weak electricigens: a new avenue for bioelectrochemical research. *Bioresour. Technol.* 258, 354–364.
- Eghesadi, N., Olaifa, K., Perna, F.M., Capriati, V., Trotta, M., Ajunwa, O., et al., 2022. Electroactivity of weak electricigen *Bacillus subtilis* biofilms in solution containing deep eutectic solvent components. *Bioelectrochemistry* 147, 108207.
- Elsner, M., Schwarzenbach, R.P., Haderlein, S.B., 2004. Reactivity of Fe(II)-bearing minerals toward reductive transformation of organic contaminants. *Environ. Sci. Technol.* 38, 799–807.
- Fan, Y.-Y., Li, B.-B., Yang, Z.-C., Cheng, Y.-Y., Liu, D.-F., Yu, H.-Q., 2018. Abundance and diversity of iron reducing bacteria communities in the sediments of a heavily polluted freshwater lake. *Appl. Microbiol. Biotechnol.* 102, 10791–10801.
- Fessler, M., Madsen, J.S., Zhang, Y., 2022. Microbial interactions in electroactive biofilms for environmental engineering applications: a role for nonoxoelectrogens. *Environ. Sci. Technol.* 56, 15273–15279.
- Fierer, N., Jackson, J.A., Vilgalys, R., Jackson, R.B., 2005. Assessment of soil microbial community structure by use of taxon-specific quantitative PCR assays. *Appl. Environ. Microbiol.* 71, 4117–4120.
- Flynn, T.M., O'Loughlin, E.J., Mishra, B., DiChristina, T.J., Kemner, K.M., 2014. Sulfur-mediated electron shuttling during bacterial iron reduction. *Science* 344, 1039–1042.
- Fredrickson, J.K., Romine, M.F., Beliaev, A.S., Auchtung, J.M., Driscoll, M.E., Gardner, T. S., et al., 2008. Towards environmental systems biology of *Shewanella*. *Nat. Rev. Microbiol.* 6, 592–603.
- Griffiths, B.S., Ritz, K., Ebbelwhite, N., Dobson, G., 1998. Soil microbial community structure: effects of substrate loading rates. *Soil Biol. Biochem.* 145–153.
- Guo, L., Zheng, S., Cao, C., Li, C., 2016. Tillage practices and straw-returning methods affect topsoil bacterial community and organic C under a rice-wheat cropping system in central China. *Sci. Rep.* 6, 33155.
- Hammann, R., Ottow, J.C.G., 1974. Reductive dissolution of Fe₂O₃ by saccharolytic Clostridia and *Bacillus polymyxa* under anaerobic conditions. *Z. Pflanzenernähr. Bodenkd.* 137, 108–115.
- Hau, H.H., Gralnick, J.A., 2007. Ecology and biotechnology of the genus *Shewanella*. *Ann. Rev. Microbiol.* 61, 237–258.
- Hernández, D.L., Hobbie, S.E., 2010. The effects of substrate composition, quantity, and diversity on microbial activity. *Plant Soil* 335, 397–411.
- Ionescu, D., Heim, C., Polerecky, L., Ramette, A., Haessler, S., Bizic-Ionescu, M., et al., 2015. Diversity of iron oxidizing and reducing bacteria in flow reactors in the Åspö Hard Rock Laboratory. *Geomicrobiol. J.* 32, 207–220.
- Jiang, J., Kappler, A., 2008. Kinetics of microbial and chemical reduction of humic substances: implications for electron shuttling. *Environ. Sci. Technol.* 42, 3563–3569.
- Jing, X., Yang, Y., Ai, Z., Chen, S., Zhou, S., 2020. Potassium channel blocker inhibits the formation and electroactivity of *Geobacter* biofilm. *Sci. Total Environ.* 705, 135796.
- Kim, Y., Liesack, W., 2015. Differential assemblage of functional units in paddy soil microbiomes. *PLoS ONE* 10, e0122221.
- Klüpfel, L., Piepenbrock, A., Kappler, A., Sander, M., 2014. Humic substances as fully regenerable electron acceptors in recurrently anoxic environments. *Nat. Geosci.* 7, 195–200.
- Kögel-Knabner, I., Amelung, W., Cao, Z., Fiedler, S., Frenzel, P., Jahn, R., Kalbitz, K., Köhl, A., Schloter, M., 2010. Biogeochemistry of paddy soils. *Geoderma* 157, 1–14.
- Lentini, C.J., Wankel, S.D., Hansel, C.M., 2012. Enriched iron(III)-reducing bacterial communities are shaped by carbon substrate and iron oxide mineralogy. *Front. Microbiol.* 3.
- Li, Y., Li, X., 2017. Determination of short-chain fatty acids in Rancimat measuring cell water by reversed-phase high-performance liquid chromatography. *China Oils Fats* 126–128.
- Light, S.H., Su, L., Rivera-Lugo, R., Cornejo, J.A., Louie, A., Iavarone, A.T., et al., 2018. A flavin-based extracellular electron transfer mechanism in diverse Gram-positive bacteria. *Nature* 562, 140–144.
- Light, S.H., Méheust, R., Ferrell, J.L., Cho, J., Deng, D., et al., 2019. Extracellular electron transfer powers flavinylated extracellular reductases in Gram-positive bacteria. *PNAS* 116, 26892–26899.
- Liu, X., Jing, X., Ye, Y., Zhan, J., Ye, J., Zhou, S., 2020. Bacterial vesicles mediate extracellular electron transfer. *Environ. Sci. Technol. Lett.* 7, 27–34.
- Liu, X.W., Sun, X.F., Chen, J.J., Huang, Y.X., Xie, J.F., Li, W.W., et al., 2013. Phenothiazine derivative-accelerated microbial extracellular electron transfer in bioelectrochemical system. *Sci. Rep.* 3, 1616.
- Liu, Y., Ding, M., Ling, W., Yang, Y., Zhou, X., Li, B., et al., 2017. A three-species microbial consortium for power generation. *Energy Environ. Sci.* 10, 1600–1609.
- Lovley, D.R., Holmes, D.E., 2022. Electromicrobiology: the ecophysiology of phylogenetically diverse electroactive microorganisms. *Nat. Rev. Microbiol.* 20, 5–19.
- Lovley, D.R., Stolz, J.F., Nord, G.L., Phillips, E.J.P., 1987. Anaerobic production of magnetite by a dissimilatory iron-reducing microorganism. *Nature* 330, 252–254.
- Lovley, D.R., Coates, J.D., Blunt-Harris, E.L., Phillips, E.J.P., Woodward, J.C., 1996. Humic substances as electron acceptors for microbial respiration. *Nature* 382, 445–448.
- Lu, R., 2000. Soil Agrochemical Analytical Methods. China agricultural science and technology press, Beijing.
- Luan, F., Gorski, C.A., Burgos, W.D., 2014. Thermodynamic controls on the microbial reduction of iron-bearing nontronite and uranium. *Environ. Sci. Technol.* 48, 2750–2758.
- Myers, C.R., Nealson, K.H., 1988. Bacterial manganese reduction and growth with manganese oxide as the sole electron acceptor. *Science* 240, 1319–1321.
- Neumann, G., Romheld, V., 2000. The release of root exudates as affected by the Plant's physiological status. The Release of Root Exudates as Affected by the Plant's Physiological Status. *The Rhizosphere* 41–93.
- O'Loughlin, E.J., 2008. Effects of electron transfer mediators on the bioreduction of lepidocrocite (γ-FeOOH) by *Shewanella putrefaciens* CN32. *Environ. Sci. Technol.* 42, 6876–6882.
- Oremland, R.S., Stolz, J.F., 2003. The ecology of arsenic. *Science* 300, 939–944. <https://doi.org/10.1126/science.1081903>.
- Parker, C.W., Auler, A.S., Barton, M.D., Sasowsky, I.D., Senko, J.M., Barton, H.A., 2018. Fe(III) reducing microorganisms from iron ore caves demonstrate fermentative Fe (III) reduction and promote cave formation. *Geomicrobiol. J.* 35, 311–322.

- Pearce, C.I., Wilkins, M.J., Zhang, C., Heald, S.M., Fredrickson, J.K., Zachara, J.M., 2012. Pore-scale characterization of biogeochemical controls on iron and uranium speciation under flow conditions. *Environ. Sci. Technol.* 46, 7992–8000.
- Peng, Q., Shaaban, M., Wu, Y., Hu, R., Wang, B., Wang, J., 2016. The diversity of iron reducing bacteria communities in subtropical paddy soils of China. *Appl. Soil Ecol.* 101, 20–27.
- Qin, B., Huang, Y., Liu, T., Wu, Y., Li, F., 2024. Dissolved organic matter (DOM) enhances the competitiveness of weak exoelectrogens in a soil electroactive biofilm. *Carbon Res.* 3, 34.
- Richardson, A.R., Somerville, G.A., Sonenshein, A.L., 2015. Regulating the intersection of metabolism and pathogenesis in gram-positive bacteria. *Microbiol. Spectr.* 3, 3.3.11.
- Rodionov, D.A., Mironov, A.A., Gelfand, M.S., 2001. Transcriptional regulation of pentose utilisation systems in the *Bacillus/Clostridium* group of bacteria. *FEMS Microbiol. Lett.* 205, 305–314.
- Sahrawat, K.L., 2003. Organic matter accumulation in submerged soils. In: *Advances in Agronomy*. Elsevier, pp. 169–201.
- Sakimoto, K.K., Wong, A.B., Yang, P., 2016. Self-photosensitization of nonphotosynthetic bacteria for solar-to-chemical production. *Science* 74–77.
- Saxena, A.K., Kumar, M., Chakdar, H., Anuroopa, N., Bagyaraj, D.J., 2020. *Bacillus* species in soil as a natural resource for plant health and nutrition. *J. Appl. Microbiol.* 128, 1583–1594.
- Shi, L., Dong, H., Reguera, G., Beyenal, H., Lu, A., Liu, J., et al., 2016. Extracellular electron transfer mechanisms between microorganisms and minerals. *Nat. Rev. Microbiol.* 14, 651–662.
- Shi, T., Peng, C., Lu, L., Yang, Z., Wu, Y., Wang, Z., et al., 2024. Response of Fe(III)-reducing kinetics, microbial community structure and Fe(III)-related functional genes to Fe(III)-organic matter complexes and ferrihydrite in lake sediment. *Biogeochemistry* 1–13.
- Shi, Z., Zachara, J.M., Shi, L., Wang, Z., Moore, D.A., Kennedy, D.W., et al., 2012. Redox reactions of reduced flavin mononucleotide (FMN), riboflavin (RBF), and Anthraquinone-2,6-disulfonate (AQDS) with ferrihydrite and lepidocrocite. *Environ. Sci. Technol.* 46, 11644–11652.
- Sun, M., Xiao, T., Ning, Z., Xiao, E., Sun, W., 2015. Microbial community analysis in rice paddy soils irrigated by acid mine drainage contaminated water. *Appl. Microbiol. Biotechnol.* 99, 2911–2922.
- Tufano, K.J., Reyes, C., Saltikov, C.W., Fendorf, S., 2008. Reductive processes controlling arsenic retention: revealing the relative importance of iron and arsenic reduction. *Environ. Sci. Technol.* 42, 8283–8289.
- Ward, T., Larson, J., Meulemans, J., Hillmann, B., Lynch, J., Sidiropoulos, D., et al., 2017. BugBase Predicts Organism-level Microbiome Phenotypes.
- Wu, Y., Luo, X., Qin, B., Li, F., Häggblom, M.M., Liu, T., 2020. Enhanced current production by exogenous electron mediators via synergy of promoting biofilm formation and the electron shuttling process. *Environ. Sci. Technol.* 54, 7217–7225.
- Xu, S., Eisenhauer, N., Zeng, Z., Mo, X., Ding, Y., Lai, D.Y.F., Wang, J., 2024. Drivers of soil organic carbon recovery under forest restoration: a global meta-analysis. *Carbon Res.* 3, 80.
- Yan, C., Yan, S.-S., Jia, T.-Y., Dong, S.-K., Ma, C.-M., Gong, Z.-P., 2019. Decomposition characteristics of rice straw returned to the soil in northeast China. *Nutr. Cycl. Agroecosyst.* 114, 211–224.
- Yang, C., Aslan, H., Zhang, P., Zhu, S., Xiao, Y., Chen, L., et al., 2020. Carbon dots-fed *Shewanella oneidensis* MR-1 for bioelectricity enhancement. *Nat. Commun.* 11, 1379.
- Yang, L., Jiang, M., Zou, Y., Qin, L., Chen, Y., 2021. Geographical distribution of iron redox cycling bacterial community in peatlands: distinct assemble mechanism across environmental gradient. *Front. Microbiol.* 12, 674411.
- Yang, Y., Ding, Y., Hu, Y., Cao, B., Rice, S.A., Kjelleberg, S., et al., 2015. Enhancing bidirectional electron transfer of *Shewanella oneidensis* by a synthetic flavin pathway. *ACS Synth. Biol.* 4, 815–823.
- Yu, L., Li, X., 2013. Simultaneous determination of monosaccharide and oligosaccharides by RP-HPLC-RID in *Huai-Radix Rehmanniae*. *Chin. J. Pharm. Anal.* 33, 977–982.
- Zhang, C., Ge, Y., Yao, H., Chen, X., Hu, M., 2012. Iron oxidation-reduction and its impacts on cadmium bioavailability in paddy soils: a review. *Front. Environ. Sci. Eng.* 6, 509–517.
- Zhang, Y., Xiao, L., Hao, Q., Li, X., Liu, F., 2020. Ferrihydrite reduction exclusively stimulated hydrogen production by *Clostridium* with community metabolic pathway bifurcation. *ACS Sustain. Chem. Eng.* 8, 7574–7580.

Actions for 1 selected article

Select all / Deselect all



Download PDF



Export citation



Show all article previews

Martin Pivokonsky, Katerina Novotna, Lenka Pivokonska, Lenka Cermakova, ... Ondrej Lacina
Article 174913



View PDF

Article preview ▾



Research article • Full text access

Anthropogenic impact of rare earth elements on groundwater and surface water in the watershed of the largest freshwater lake in China

Haiyan Liu, Huaming Guo, Olivier Pourret, Zhen Wang

Article 175063



View PDF

Article preview ▾



Research article • Full text access

Hematite enhances microbial autotrophic nitrate removal in carbonate and phosphate-rich environments by increasing Fe(II) activity

Mingliang Long, Jiayi Zhu, Xinxin Wang, Shiwen Hu, ... Fangbai Li

Article 175002



View PDF

Article preview ▾



Research article • Full text access

Long-term effects of conventional cultivation on soil cation exchange capacity and base saturation in an arid desert region

Dengke Ma, Zhibin He, Wenzhi Zhao, Rui Li, ... Wenliang Ju

Article 175075



View PDF

Article preview ▾



Research article • Open access

The hospitalisation risk of chronic circulatory and respiratory diseases associated with coal mining in the





Volume 287 (2019) November 2019

ISSN 0273-3285

POLYHEDRON

The international journal for research in inorganic chemistry



Editors
D.R. Deeney, C.E. Anzures & G.H. Bunting

Available online at www.sciencedirect.com
ScienceDirect

Actions for 1 selected article

Select all / Deselect all



Download PDF



Export citation



Show all article previews

Article preview ▾



Research article ○ Abstract only

Construction of four new d^{10} metal ion coordination polymers: Synthesis, characterization and structural diversity

Anupam Maiti, Arijit Halder, Susanta Dinda, Goutam Pahari, Debajyoti Ghoshal
Article 116144

Article preview ▾



Research article ○ Abstract only

A solid state Ag(I) complex with excellent stability, luminescent and sensing properties

Cong-Cong Chen, Wei-Quan Lin, Yu-Wei Wen, Shi-Yang Wang, ... Wei Liu
Article 116148

Article preview ▾



Research article ○ Abstract only

Alkane hydroxylation by *m*-chloroperbenzoic acid catalyzed by nickel(II) complexes of linear N₄-tetradentate ligands

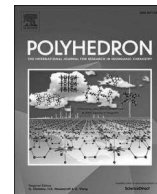
Takuma Wada, Hideki Sugimoto, Yuma Morimoto, Shinobu Itoh
Article 116150

Article preview ▾



Research article ○ Abstract only





A solid state Ag(I) complex with excellent stability, luminescent and sensing properties

Cong-Cong Chen^a, Wei-Quan Lin^b, Yu-Wei Wen^a, Shi-Yang Wang^a, Hao-Jun Yin^a, Jin-Yan Li^c, Chun-Lin Ni^{a,*}, Wei Liu^{a,*}

^a College of Materials and Energy, South China Agricultural University, Guangzhou 510640, China

^b School of Chemistry and Chemical Engineering/Institute of Clean Energy and Materials/Guangzhou Key Laboratory for Clean Energy and Materials, Guangzhou University, Guangzhou Higher Education Mega Center, Guangzhou 510006, China

^c School of Chemical and Environmental Engineering, Hanshan Normal University, Chaozhou, Guangdong 521041, China

ABSTRACT

In the current study, a novel luminescent dinuclear coordination compound was prepared by the solution method and named $[\text{Ag}(\text{aca})(\mu\text{-}3,3'\text{-abpt})]_2$ (**1**) (3, 3'-abpt = 4-amino-3,5-bis(3-pyridyl)-1,2,4-triazole and Haca = 9-anthracene carboxylic acid). Structural analysis showed that the compound has a zero-dimensional (0D) fundamental structure, comprising several intermolecular interactions resulting in a tightly packed three-dimensional (3D) framework. In addition, powder X-ray diffraction, elemental analysis, infrared (IR), and luminescence property were performed to further characterize the compound. The compound exhibited excellent stability in aqueous solution. Moreover, it showed favourable luminescence emission under ultraviolet (UV) light irradiation at room temperature. These findings show that the compound can be used as luminescent sensor for detection of Fe^{3+} and $\text{Cr}_2\text{O}_7^{2-}$ in aqueous solution with high selectivity, sensitivity, and good anti-interference ability. The possible sensing mechanisms were also investigated. Such an effective detection method may provide inspiration for the detection of other kinds of orange-yellow substances such as dye molecules.

1. Introduction

Previous studies have widely explored the coordination compounds obtained from intriguing framework construction. These compounds have distinctive properties and can be applied in several areas including gas storage/separations [1–4], luminescence [5–7], catalysis [8–11], magnetic applications [12–15] and sensing [16–19], etc. These compounds can be applied in luminescence sensing owing to their unique advantages including high selectivity, good anti-interference performance, high sensitivity, quick response and operability [20–23]. To customize coordination compounds for chemical sensing, it is important to design and select suitable organic linker and metal containing units [24,25]. Currently, lack of water stability limits application of coordination compounds [26–28]. Therefore, there is need to develop new fluorescence compounds with good water resistance.

In recent years, fluorescence active coordination compounds have been applied in the biological field and detection of pollutants [29–31]. Notably, identification of pollutants is of greater significance for improving environmental safety and human health. Although several functional fluorescence complexes have been synthesized for detection of divalent transition metal ions, such as Cu^{2+} and Pb^{2+} , only a few

studies have focused on developing sensors of trivalent metal ions [32]. Fe^{3+} plays a crucial role in the metabolic processes of most mammals and is also widely used in industries. Abnormal levels of Fe^{3+} can lead to the development of serious diseases. For instance, low levels of Fe^{3+} can cause anaemia, reduced resistance and irritability whereas excessive Fe^{3+} in living cells can damage nucleic acids and proteins by promoting production of reactive oxygen species [33]. In addition, Fe^{3+} is a major factor contributing to Alzheimer's disease development [34–36]. On the other hand, the anion pollutant, for example $\text{Cr}_2\text{O}_7^{2-}$, which has been proverbially used in the field of metallurgy, dyestuff, leather industry and timber preservation. It is one of most common heavy metal pollutants present in water, and can cause critical damage to the environment as well as humans at low concentrations, has become an increasingly severe problem [37,38]. Thus, the World Health Organization (WHO) guidelines stipulate that the concentration of $\text{Cr}_2\text{O}_7^{2-}$ in groundwater should be limited to $50 \mu\text{g L}^{-1}$ [39]. Currently, several detection techniques, including inductively coupled plasma (ICP) mass spectrometry [40], atomic absorption spectroscopy [41], voltammetry [42] and spectrophotometry [43], are used for detection of these ions. However, high cost and complex instrument and other factors limit development of detection compounds. Therefore, cheaper and effective techniques for

* Corresponding authors.

E-mail addresses: niclchem@scau.edu.cn (C.-L. Ni), liuwei97@scau.edu.cn (W. Liu).

<https://doi.org/10.1016/j.poly.2022.116148>

Received 2 May 2022; Accepted 15 September 2022

Available online 21 September 2022

0277-5387/© 2022 Elsevier Ltd. All rights reserved.

rapid and selective detection to trace Fe^{3+} and $\text{Cr}_2\text{O}_7^{2-}$ ions should be investigated.

Synthesis of solvent-free and neutral structure is an effective strategy to achieve structural stability [44]. In the current study, two ligands including 3,3'-abpt (4-amino-3,5-bis(3-pyridyl)-1,2,4-triazole) and Haca (9-anthracene carboxylic acid) were chosen as organic linkers owing to their unique advantages. The advantages include: (i) 3,3'-abpt is a good candidate that possesses versatile coordination sites, which helps to construct multiple structures; (ii) Haca is a rigid carboxylate ligand that is conducive for construction of neutral structure when connecting metal cations; (iii) the two ligands have several electrons with favorable electron-transferring ability. A novel OD luminescent Ag(I) complex, namely, $[\text{Ag}(\text{aca})(\mu\text{-}3,3'\text{-abpt})]_2$ (**I**) was successfully synthesized and characterized using these ligands. The complex exhibited excellent stability in aqueous solutions. In addition, luminescence analysis showed that this compound could detect Fe^{3+} and $\text{Cr}_2\text{O}_7^{2-}$ in aqueous solution with high selectivity, sensitivity, and had good anti-interference ability owing to the quenching effect. And thus, it can be a potential material used as a fluorescent probe to detect orange-yellow substances (Fe^{3+} and $\text{Cr}_2\text{O}_7^{2-}$) in aqueous solution.

2. Experimental section

2.1. Materials and measurements

Except that the 3,3'-abpt ligand was prepared according to the literature [45], all reagents as well as solvents were obtained from commercial suppliers and made use of without further purification. Elemental analysis (C, H and N) were conducted on a Vario EL Cube elemental analyser. Powder X-ray diffraction (PXRD) intensities were carried out on an Ultima IV diffractometer ($\text{Cu K}\alpha$, $\lambda = 1.54056 \text{ \AA}$) in the scanning range of $2\theta = 5\text{--}50^\circ$ with a step of $0.2^\circ/\text{s}$ at room temperature. Thermogravimetric analysis (TGA) was recorded in a TG 209 F1 Libra TM with a heating rate of $10 \text{ K}\cdot\text{min}^{-1}$ from 30 to 900°C under the flowing air atmosphere, in which an empty Al_2O_3 crucible was used as reference. Infrared spectra were performed by using a Nicolet IS10 spectrometer in the range $4000\text{--}400 \text{ cm}^{-1}$ with a pressed KBr pellet. UV–vis absorption spectra were measured on UV-2550 spectrophotometer. The solid fluorescence spectra and emission decay curve were measured on an Edinburgh FLS920 spectrofluorometer. The liquid fluorescence spectra were measured on a Hitachi F-7000 fluorescence spectrometer.

2.2. X-ray structure determination

X-ray single-crystal diffraction data of the compound was acquired on a Bruker D8 QUEST diffractometer equipped with $\text{Mo K}\alpha$ radiation ($\lambda = 0.71073 \text{ \AA}$) at 100 K . The structure was solved by direct methods using SHELXTL 2014 and Olex2 program package [46,47], and refined by full-matrix least-squares technique on F^2 . All non-hydrogen atoms were refined using anisotropic thermal parameters, and hydrogen atoms from the organic ligands were generated geometrically by the riding mode. A summary of the crystal data for this compound is listed in Table S1. CCDC 2069519 contains the supplementary crystallographic data for this paper. The data can be obtained free of charge from The Cambridge Crystallographic Data Centre via www.ccdc.cam.ac.uk/data_request/cif.

2.3. Synthesis of $[\text{Ag}(\text{aca})(\mu\text{-}3,3'\text{-abpt})]_2$ (**I**)

The mixture resulting from the continuous addition of 3,3'-abpt (12 mg, 0.05 mmol), 9-anthracene carboxylic acid (22 mg, 0.1 mmol), fresh $\text{NH}_3\cdot\text{H}_2\text{O}$ ($0.1 \text{ mol}\cdot\text{L}^{-1}$, 2 mL) and Ag_2O (12 mg, 0.05 mmol) to ethanol (10 mL) was stirred for 30 min. After that, the resulting colorless solution was filtered and kept undisturbed for slow evaporation in dark environment. Pale yellow cluster crystal was obtained three days later

with ca. 64 % yield based on 3, 3'-abpt. Anal. Calcd (%) for $\text{C}_{27}\text{H}_{19}\text{AgN}_6\text{O}_2$: C, 57.16; H, 3.38; N, 14.81. Found: C, 57.12; H, 3.18; N, 14.86. IR (KBr, cm^{-1}): 3437w, 3249m, 3129w, 3057w, 1557s, 1479w, 1461m, 1428m, 1391m, 1317s, 1278w, 1194w, 1134w, 1015w, 973m, 887m, 863m, 817m, 795m, 767s, 740s, 704s, 652w, 638w, 560m.

3. Results and discussion

3.1. Crystal structure

Single-crystal X-ray diffraction analysis reveals that the compound crystallizes in the monoclinic space group $P2_1/n$ with an asymmetric unit containing one crystallographically independent Ag(I) atom, one 3,3'-abpt and one aca^- . Each Ag(I) atom is planar coordination geometry ligated by one carboxylate oxygen atoms from aca^- and two nitrogen atoms from two different 3,3'-abpt ligands, which are all in the opposite direction respectively, thus forming a binuclear complex based on charge balance (Fig. 1a). As portrayed in Fig. 1b, the dinuclear silver molecules are linked by the abundant intermolecular $\pi\text{-}\pi$ interactions between aromatic rings of aca^- with the distance of $3.6079(1) \text{ \AA}$, $3.6572(1) \text{ \AA}$, $3.6654(1) \text{ \AA}$ and $3.8658(1) \text{ \AA}$, respectively, as well as $\text{N}\cdots\text{H}\cdots\text{O}$ hydrogen bonds with the distance of $2.8957(84) \text{ \AA}$ and $2.9554(91) \text{ \AA}$, that further composing a 3D close-packed supramolecular structure along the $\langle 001 \rangle$ direction (Fig. 1c). Furthermore, IR spectra customarily exhibit characteristic peaks attributable to each component of the compound. For the compound, the characteristic peaks of carboxylic acid groups arisen at 1557 cm^{-1} and 1317 cm^{-1} , which were attributed to asymmetric stretching vibration and symmetric stretching vibrations,

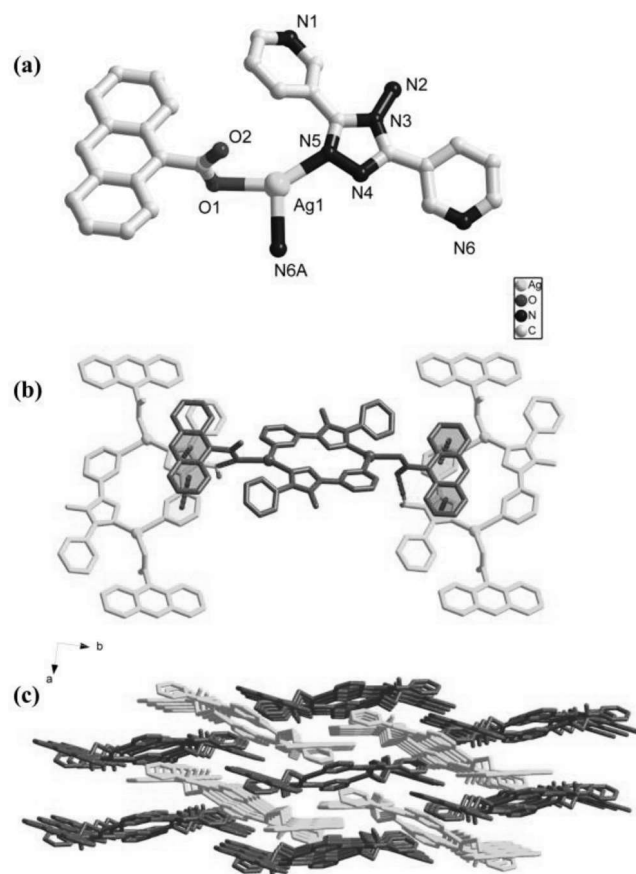


Fig. 1. (a) Coordination environments of Ag(I) center of **I**. (b) The intermolecular $\pi\text{-}\pi$ stacking interactions (purple dashed lines) and $\text{N}\cdots\text{H}\cdots\text{O}$ hydrogen bonds (red dashed lines). (c) The close-packed 3D framework formed by rich weak interactions. And only H atoms involved in the interactions are shown for clarity.

respectively [48].

3.2. Stability characterization

Thermogravimetric analysis (TGA) and powder X-ray diffraction (PXRD) were performed to explore the stability of compound **I**. TGA was carried out using crystalline sample to explore the thermal stability in air (Fig. S1). The findings showed that the compound had excellent thermal stability under temperature up to 540 K. All peak positions of the as-synthesized PXRD patterns were consisted with the simulated ones, indicating the pure-phase of corresponding material (Fig. S2). The compound also maintained the original frame structure even after immersion in different pH solutions (pH 6–12) for 24 h, as showed by analysis of PXRD patterns (Fig. 2). Notably, excellent stability is important for extending the compound to practical applications [49].

3.3. Luminescent properties

D¹⁰ metal coordination compounds have been widely explored owing to their excellent luminescence properties and can be used as chemical sensors or optical devices [16,50]. The photoluminescence spectra of compound **I** at room temperature is presented in Fig. 3. Intense emission bands were observed at 435 and 460 nm upon excitation of compound **I** at 393 nm. The emission bands resemble π - π^* transition bands (395, 415 and 437 nm) observed at low concentrations of Haca (Fig. S4). To assign the emission bands for **I**, molecular orbital (MO) calculations were performed on the [Ag(aca)(μ -3,3'-abpt)]₂ species and the free ligands. The HOMOs and LUMOs, and the orbital energies were presented as contour plots as shown in Fig. S5. Analysis of Haca and [Ag(aca)(μ -3,3'-abpt)]₂ showed that the HOMOs were associated with the π -bonding orbital whereas the LUMOs were mainly ascribed to the π -antibonding orbital from the anthracene rings. This finding indicates that the emission of **I** is a ligand centered state possibly originating from the intraligand π - π^* transitions of the anthracene ring in Haca.

The bright blue emission color of **I** was recorded under the excitation wavelength of 365 nm UV irradiation (Fig. S6). The luminescent decay curve of **I** was obtained at room temperature (Fig. S7), and the lifetime τ was 1.19 ns at the 435 nm emission peak. Therefore, complex **I** may be a potential luminescent material.

3.4. Sensing metal ions

The potential sensing ability toward the metal ions was performed in aqueous solution based on the photoluminescent property and

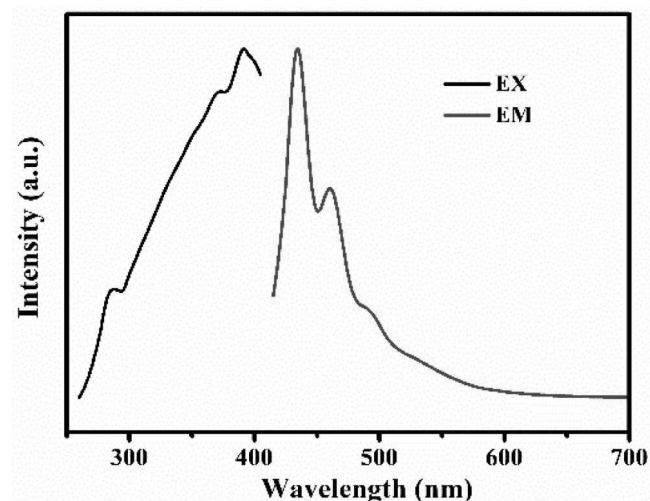


Fig. 3. The photoluminescence spectra of complex **I** in the solid state recorded at room temperature.

framework stability of **I**. A suspension of the sample incorporated with metal ions was prepared by dispersing the ground crystalline sample (3 mg) into 0.01 mol/L aqueous solution containing the same concentration of M(NO₃)_n (5 mL, M = K⁺, Na⁺, Cd²⁺, Zn²⁺, Co²⁺, Mg²⁺, Ni²⁺, Ag⁺, Cu²⁺ and Fe³⁺) for liquid fluorescence analysis after carrying out ultrasound for 30 min. Analysis of intensity of emission spectra showed different intensities resting with the feature of metal ions, especially for Fe³⁺ ion (Fig. 4a and Fig. S8). The intensity decreased significantly compared with that obtained without adding the compounds, indicating that the compound exhibits an excellent quenching effect. In addition, the color changes before and after the fluorescence quenching of compound **I** in response to the presence of Fe³⁺ could be seen by naked eyes under 365 nm UV light (Fig. S9). These findings indicate that compound **I** is a potential fluorescent sensor with high selectivity. Notably, chemosensors feasible in practical applications require good anti-interference ability. The fluorescence intensity of compound **I** was significantly quenched in presence of Fe³⁺, although other competitive metal ions were added into the solution (Fig. 4b). Therefore, this compound can be used to sense Fe³⁺ in complex substances in real environments.

A series of concentration-dependent luminescent analysis based on the Fe³⁺ ion concentrations were carried out to further explore the sensitivity of compound **I** for Fe³⁺ in aqueous solution. The findings showed that luminescence intensities significantly decreased with increase in concentration of Fe³⁺ ions in the range of 0.12–5.16 mM (Fig. 5a). Luminescence was almost quenched at a concentration of 5.16 mM. The quenching efficiency can be calculated quantitatively using the Stern–Volmer equation: $I_0/I = 1 + K_{SV}[Q]$, where I_0 and I are the fluorescence intensities of compound **I** before and after adding Fe³⁺ respectively, $[Q]$ represents the corresponding concentration of Fe³⁺ ion, and K_{SV} is the quenching constant [51]. The Stern – Volmer plot is almost linear for low concentrations of Fe³⁺ ions (Fig. 5b). The quenching constant, K_{SV} value is approximately $2.19 \times 10^3 \text{ M}^{-1}$. Furthermore, the calculated detection limit for Fe³⁺ ion following the $3\sigma/\text{slope}$ can be as low as $3.92 \times 10^{-5} \text{ M}$. This value is similar to values of compounds reported previously and this compound shows a better performance, indicating that compound **I** exhibits a significantly high detection sensitivity towards Fe³⁺ [17,52–54].

3.5. Sensing anions

To expand the application field of sensing properties of **I** to anions, solid sample (3 mg) was, respectively, dispersed in diverse potassium salt aqueous solutions with concentrations of 0.01 mol/L, including

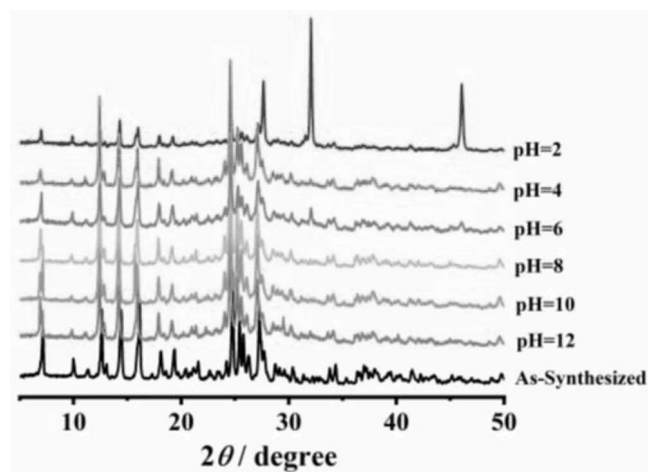


Fig. 2. PXRD patterns immersed in aqueous solutions (pH 2–12) for 24 h at room temperature.

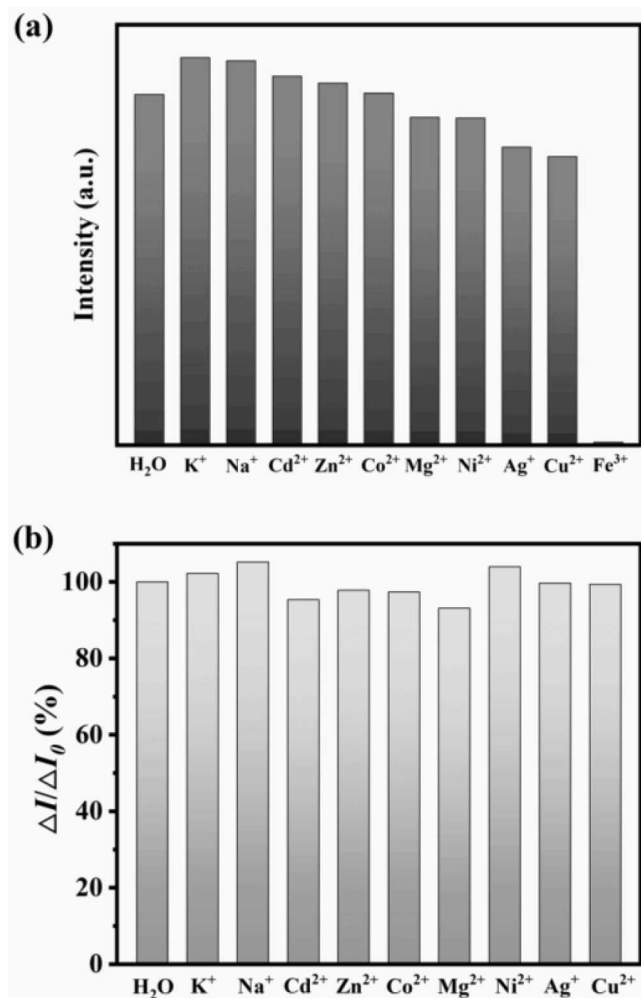


Fig. 4. (a) Luminescence intensity after treatment with different metal ions for I. (b) Fluorescence changes ratio $\Delta I/\Delta I_0$ (%) histograms of I in the presence of aqueous Fe³⁺ and various interfering substances.

CH₃COO[−], SO₄^{2−}, Br[−], Cl[−], I[−], OH[−], H₂PO₄[−], NO₃[−] and Cr₂O₇^{2−}. These results showed that the luminescence of I largely depends on anionic species, especially at the existence of Cr₂O₇^{2−}, which presented distinct fluorescence quenching (Fig. 6a). Meanwhile, the color changes with the addition of Cr₂O₇^{2−} in solvents could be seen by the naked eyes under 365 nm UV light (Fig. S9). Furthermore, the good anti-interference ability as chemical sensors is also very important in practical applications. As showed in Fig. 6b, the luminescence intensity was almost completely quenched only by the addition a certain amount of Cr₂O₇^{2−} in spite of the presence of other interfering anions. Therefore, benefiting from high selectivity and anti-interference, it is expected that the detection of Cr₂O₇^{2−} in complex substances has great potential in the real environment.

To investigate the sensitivity of luminescence quenching character for Cr₂O₇^{2−} further, emissive response of I was recorded by gradually increasing the concentrations of Cr₂O₇^{2−} ions. As illustrated in Fig. 7a, the luminescence intensity gradually weakens with the increase of Cr₂O₇^{2−} concentrations in the range of 0.05–1.22 mM, and the luminescence of the solution is completely quenched when the concentration of Cr₂O₇^{2−} reaches 1.22 mM. The calculated K_{sv} value was $4.55 \times 10^3 \text{ M}^{-1}$ at low concentrations (Fig. 7b), and the detection limit was $1.16 \times 10^{-5} \text{ M}$, which is comparable to or even better than those of other compounds, showing that I have tremendous potential application value for detecting Cr₂O₇^{2−} ions [53,55,56].

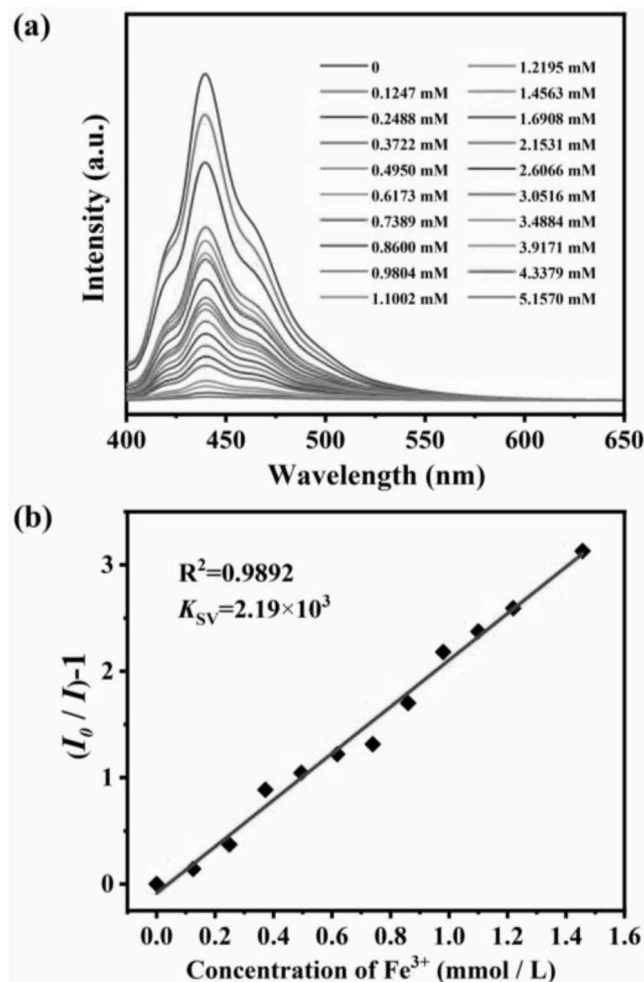


Fig. 5. (a) Emission spectra of I with diverse concentrations of Fe³⁺ ions in aqueous solution. (b) Stern-Volmer plot of $(I_0/I) - 1$ vs the concentration of Fe³⁺ at low range.

3.6. Sensing mechanism

Analysis of the PXRD pattern of the recovered sample that was soaked in Fe³⁺ and Cr₂O₇^{2−} aqueous solution for 24 h showed that the crystal structure of I was consistent with the original structure (Fig. S3). This result shows that the luminescence quenching is not attributed to the framework change of compound I. Notably, cationic exchange of Ag⁺ center with the Fe³⁺ ion is challenging to achieve in neutral framework of compound I. The mechanism of the quenching effect was further explored through UV-vis absorption spectra analysis. Analysis of the spectra of Fe³⁺ aqueous solution (Fig. S12) showed a broad absorption band from 240 to 500 nm. It was observed that the band partially overlapped with the excitation spectrum of I. The other metal ions showed no palpable overlap with the excitation spectrum. For these anions, only the UV-visible absorption spectrum solution of Cr₂O₇^{2−} overlaps with the excitation spectrum of I (Fig. S13). A batch of UV-Vis absorption spectra with various concentrations for Fe³⁺ and Cr₂O₇^{2−} were determined in aqueous solutions (Fig. S14 and S15). The results show that absorption intensity decreased in concentration of Fe³⁺ and Cr₂O₇^{2−} ions. These findings indicate that Fe³⁺ and Cr₂O₇^{2−} solution can absorb the energy of the excitation wavelength of I, resulting in luminescence quenching [57].

4. Conclusion

In the current study, a novel Ag(I) complex with OD-structure was

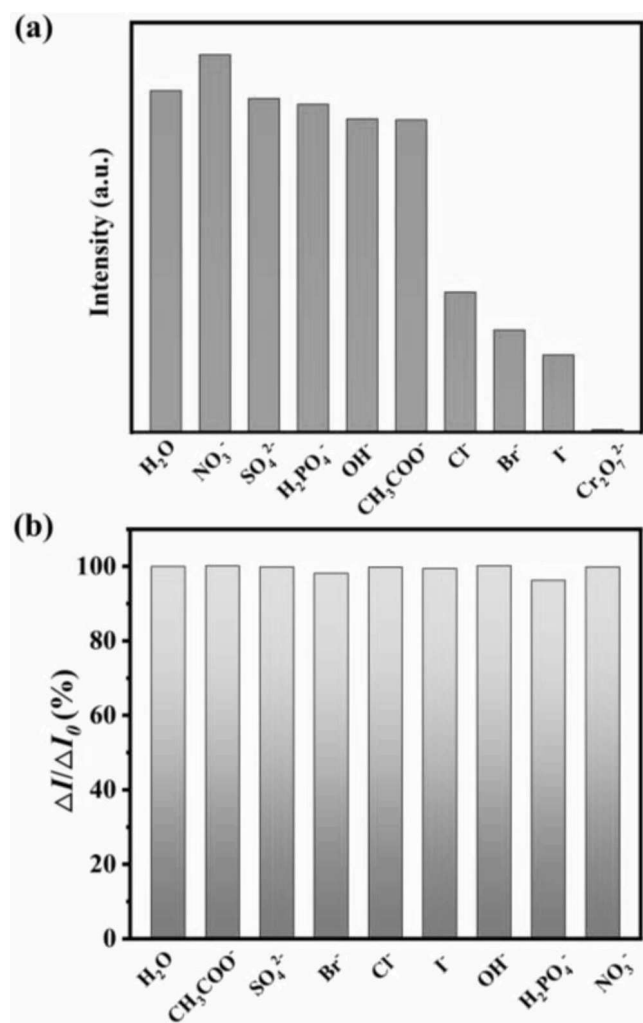


Fig. 6. (a) Luminescence intensity after treatment with different anions for I. (b) Fluorescence changes ratio $\Delta I/\Delta I_0$ (%) histograms of I in the presence of aqueous $\text{Cr}_2\text{O}_7^{2-}$ and various interfering substances.

successfully synthesized based on 3,3'-abpt and anthracene-contained carboxylate ligand. The structural stability and solid-state luminescence properties of I were determined at room temperature. Compound I showed significant fluorescence quenching effect after introduction of Fe^{3+} and $\text{Cr}_2\text{O}_7^{2-}$ ion. The findings on anti-interference and fluorescence titration indicate that the compound can be used as an effective probe for detection of Fe^{3+} and $\text{Cr}_2\text{O}_7^{2-}$ in aqueous solution with high selectivity, sensitivity, and good anti-interference ability. Therefore, I can be used as a stable functional material to develop economical and effective luminescent sensors for detecting orange-yellow substances (Fe^{3+} and $\text{Cr}_2\text{O}_7^{2-}$) in aqueous solution in practical applications.

CRedit authorship contribution statement

Cong-Cong Chen: Investigation, Validation, Writing – original draft. **Wei-Quan Lin:** Software. **Yu-Wei Wen:** Validation. **Shi-Yang Wang:** Software. **Hao-Jun Yin:** Visualization. **Jin-Yan Li:** Writing – review & editing. **Chun-Lin Ni:** Supervision. **Wei Liu:** Funding acquisition, Supervision.

Declaration of Competing Interest

The authors declare that they have no known competing financial interests or personal relationships that could have appeared to influence

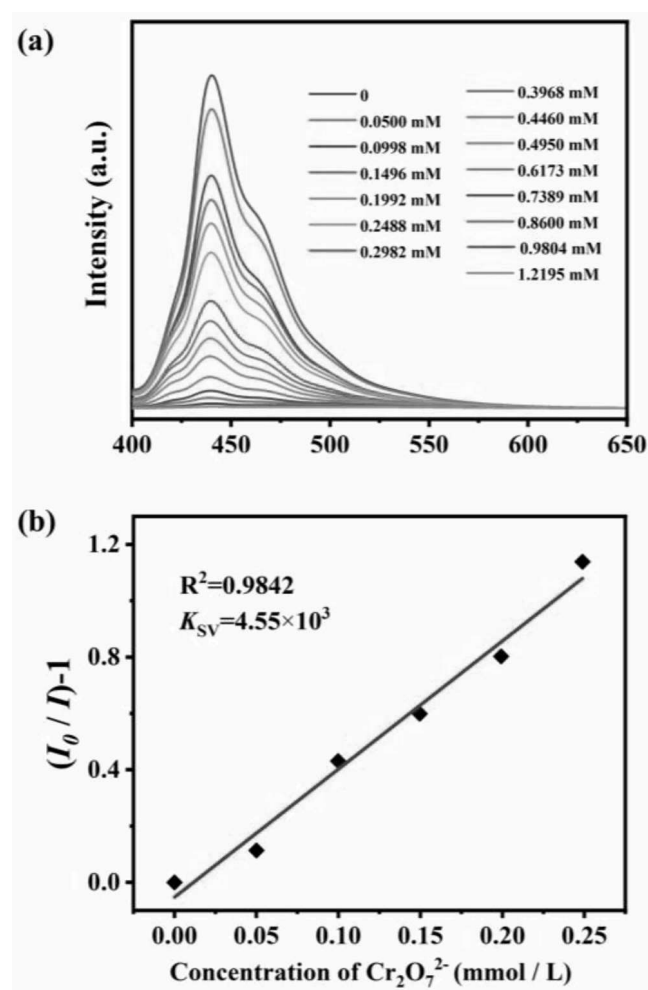


Fig. 7. (a) Emission spectra of I with diverse concentrations of $\text{Cr}_2\text{O}_7^{2-}$ ions in aqueous solution. (b) Stern–Volmer plot of $(I_0/I) - 1$ vs the concentration of $\text{Cr}_2\text{O}_7^{2-}$ at low range.

the work reported in this paper.

Data availability

Data will be made available on request.

Acknowledgements

This work was supported by the National Natural Science Foundation of China (Grant no. 21701045, 21701066) and Guangdong Basic and Applied Basic Research Foundation (No. 2019A1515011359).

Appendix A. Supplementary data

Supplementary data to this article can be found online at <https://doi.org/10.1016/j.poly.2022.116148>.

References

- [1] F. Gándara, H. Furukawa, S. Lee, O.M. Yaghi, J. Am. Chem. Soc. 136 (2014) 5271–5274.
- [2] S. Roy, A. Chakraborty, T.K. Maji, Coord. Chem. Rev. 273–274 (2014) 139–164.
- [3] P. Liao, N. Huang, W. Zhang, J. Zhang, X. Chen, Science 356 (2017) 1193–1196.
- [4] A. Cadiou, K. Adil, P.M. Bhatt, Y. Belmabkhout, M. Eddaoudi, Science 353 (2016) 137–140.
- [5] W. Liu, C. Chen, L. Mao, S. Wu, L. Wang, M. Tong, CrystEngComm 21 (2019) 6446–6451.

- [6] J. Jia, Q. Li, Y. Chen, J. Liu, M. Tong, *Coord. Chem. Rev.* 378 (2019) 365–381.
- [7] M. Cui, A. Wang, Y. Liu, H. Xiao, F. Li, L. Zhou, S. Fang, X. Li, *RSC Adv.* 10 (2020) 39359–39365.
- [8] G. Yuan, H. Jiang, L. Zhang, Y. Liu, Y. Cui, *Coord. Chem. Rev.* 378 (2019) 483–499.
- [9] K. Manna, T. Zhang, W. Lin, *J. Am. Chem. Soc.* 136 (2014) 6566–6569.
- [10] Y. Kang, Y. Lu, K. Chen, Y. Zhao, P. Wang, W. Sun, *Coord. Chem. Rev.* 378 (2019) 262–280.
- [11] A. Misale, S. Niyomchom, M. Luparia, N. Maulide, *Angew. Chem. Int. Ed.* 53 (2014) 7068–7073.
- [12] Z. Ni, J. Liu, M.N. Hoque, W. Liu, J. Li, Y. Chen, M. Tong, *Coord. Chem. Rev.* 335 (2017) 28–43.
- [13] Q. Liu, C. Deng, N. Sun, *Nanoscale* 10 (2018) 12149–12155.
- [14] P. Zhang, L. Zhang, C. Wang, S. Xue, S. Lin, J. Tang, *J. Am. Chem. Soc.* 136 (2014) 4484–4487.
- [15] J.D. Rinehart, J.R. Long, *Chem. Sci.* 2 (2011) 2078–2085.
- [16] M. Zhang, G. Feng, Z. Song, Y. Zhou, H. Chao, D. Yuan, T.T.Y. Tan, Z. Guo, Z. Hu, B.Z. Tang, B. Liu, D. Zhao, *J. Am. Chem. Soc.* 136 (2014) 7241–7244.
- [17] X. Zhao, S. Wang, L. Zhang, S. Liu, G. Yuan, *Inorg. Chem.* 58 (2019) 2444–2453.
- [18] Z. Sun, J. Sun, L. Xi, J. Xie, X. Wang, Y. Ma, L. Li, *Cryst. Growth Des.* 20 (2020) 5225–5234.
- [19] C. Chen, Y. Cai, L. Wang, Y. Wu, H. Yin, J. Zhou, C. Ni, W. Liu, *Inorg. Chem.* 60 (2021) 5463–5473.
- [20] Z. Li, X. Li, Y. Yan, L. Hou, W. Zhang, Y. Wang, *Cryst. Growth Des.* 18 (2018) 2031–2039.
- [21] R. Lv, H. Li, J. Su, X. Fu, B. Yang, W. Gu, X. Liu, *Inorg. Chem.* 56 (2017) 12348–12356.
- [22] Z. Ran, S. Cao, Q. Peng, X. Liu, J. Zhou, *Inorg. Chem.* 61 (2022) 5957–5964.
- [23] Y.E. Yu, Y. Wang, H. Yan, J. Lu, H. Liu, Y. Li, S. Wang, D. Li, J. Dou, L. Yang, Z. Zhou, *Inorg. Chem.* 59 (2020) 3828–3837.
- [24] S.D. Burd, S. Ma, J.A. Perman, B.J. Sikora, R.Q. Snurr, P.K. Thallapally, J. Tian, L. Wojtas, M.J. Zaworotko, *J. Am. Chem. Soc.* 134 (2012) 3663–3666.
- [25] T.M. McDonald, W.R. Lee, J.A. Mason, B.M. Wiers, C.S. Hong, J.R. Long, *J. Am. Chem. Soc.* 134 (2012) 7056–7065.
- [26] R.J. Marshall, Y. Kalinovsky, S.L. Griffin, C. Wilson, B.A. Blight, R.S. Forgan, *J. Am. Chem. Soc.* 139 (2017) 6253–6260.
- [27] X. Zhu, K. Zhang, Y. Wang, W. Long, R. Sa, T. Liu, J. Lü, *Inorg. Chem.* 57 (2018) 1060–1065.
- [28] J. Aguilera-Sigalat, D. Bradshaw, *Chem. Commun.* 50 (2014) 4711–4713.
- [29] M.A. Fik, A. Gorczyński, M. Kubicki, Z. Hnatejko, A. Fedoruk-Wyszomirska, E. Wyszko, M. Giel-Pietraszuk, V. Patroniak, *Eur. J. Med. Chem.* 86 (2014) 456–468.
- [30] A. Adamski, M.A. Fik, M. Kubicki, Z. Hnatejko, D. Gurda, A. Fedoruk-Wyszomirska, E. Wyszko, D. Kruska, Z. Dutkiewicz, V. Patroniak, *New J. Chem.* 40 (2016) 7943–7957.
- [31] Y. Huang, P. Chuang, J. Wu, *Inorg. Chem.* 59 (2020) 9095–9107.
- [32] J. Zhao, Y. Wang, W. Dong, Y. Wu, D. Li, Q. Zhang, *Inorg. Chem.* 55 (2016) 3265–3271.
- [33] Z. Chen, Y. Sun, L. Zhang, D. Sun, F. Liu, Q. Meng, R. Wang, D. Sun, *Chem. Commun.* 49 (2013) 11557–11559.
- [34] E. András, É. Farkas, H. Scheibler, A. Réffy, L. Bezúr, *Arch. Gerontol. Geriatr.* 21 (1995) 89–97.
- [35] N. Solov'yev, A.H. El-Khatib, M. Costas-Rodríguez, K. Schwab, E. Griffin, A. Raab, B. Platt, F. Theuring, J. Vogl, F. Vanhaecke, *J. Biol. Chem.* 296 (2021).
- [36] N. Kim, H.J. Lee, *Int. J. Mol. Sci.* 22 (2021) 7697.
- [37] E.A. Katayev, Y.A. Ustynyuk, J.L. Sessler, *Coord. Chem. Rev.* 250 (2006) 3004–3037.
- [38] M. Reynolds, L. Stoddard, I. Bespalov, A. Zhitkovich, *Nucleic Acids Res.* 35 (2007) 465–476.
- [39] Y. Zhang, Q. Wang, J. Lu, Q. Wang, Y. Cong, *Chemosphere* 162 (2016) 55–63.
- [40] A. Ohashi, H. Ito, C. Kanai, H. Imura, K. Ohashi, *Talanta* 65 (2005) 525–530.
- [41] K. Akatsuka, J.W. McLaren, J.W. Lam, S.S. Berman, *J. Anal. Atom. Spectrom.* 7 (1992) 889–894.
- [42] V.A. Elrod, K.S. Johnson, K.H. Coale, *Anal. Chem.* 63 (1991) 893–898.
- [43] Z.O. Tesfaldet, J.F. van Staden, R.I. Stefan, *Talanta* 64 (2004) 1189–1195.
- [44] A.V. Desai, S. Sharma, S. Let, S.K. Ghosh, *Coord. Chem. Rev.* 395 (2019) 146–192.
- [45] L. Cheng, W. Zhang, B. Ye, J. Lin, X. Chen, *Inorg. Chem.* 46 (2007) 1135–1143.
- [46] G.M. Sheldrick, *Acta Crystallogr., Sect. C: Struct. Chem.* 71 (2015) 3–8.
- [47] O.V. Dolomanov, L.J. Bourhis, R.J. Gildea, J.A.K. Howard, H. Puschmann, *J. Appl. Crystallogr.* 42 (2009) 339–341.
- [48] M. Zhang, Y. Zheng, M. Liu, Y. Ren, Z. Wang, J. Cao, J. Wang, *RSC Adv.* 9 (2019) 21086–21094.
- [49] J.J. Low, A.I. Benin, P. Jakubczak, J.F. Abrahamian, S.A. Faheem, R.R. Willis, *J. Am. Chem. Soc.* 131 (2009) 15834–15842.
- [50] H. Wang, W. Yang, Z. Sun, *Chem. Asian J.* 8 (2013) 982–989.
- [51] H. He, Y. Song, F. Sun, Z. Bian, L. Gao, G. Zhu, *J. Mater. Chem. A* 3 (2015) 16598–16603.
- [52] B. Hou, D. Tian, J. Liu, L. Dong, S. Li, D. Li, Y. Lan, *Inorg. Chem.* 55 (2016) 10580–10586.
- [53] Y. Zhang, V.A. Blatov, T. Zheng, C. Yang, L. Qian, K. Li, B. Li, B. Wu, *Dalton Trans.* 47 (2018) 6189–6198.
- [54] Z. Liu, Y. Zhao, X. Zhang, Y. Kang, Q. Lu, M. Azam, S.I. Al-Resayes, W. Sun, *Dalton Trans.* 46 (2017) 13943–13951.
- [55] W. Tong, W. Liu, J. Cheng, P. Zhang, G. Li, L. Hou, Y. Wang, *Dalton Trans.* 47 (2018) 9466–9473.
- [56] S. Xu, J. Shi, B. Ding, Z. Liu, X. Wang, X. Zhao, E. Yang, *Dalton Trans.* 48 (2019) 1823–1834.
- [57] J. Dong, H. Xu, S. Hou, Z. Wu, B. Zhao, *Inorg. Chem.* 56 (2017) 6244–6250.

References

Electrocatalysis

 Springer

© 2000 Blackwell Science Ltd
Journal of Internal Medicine 247: 101–107

Synthesis of a New Nanocomposite Based on Natural Asphalt and Its Application as a High-Performance and Eco-friendly Platform for the Electrochemical Determination of Deferiprone

Somayeh Farokhi, Mahmoud Roushani ... Mohammad Soleiman-Beigi

Research | 03 June 2023 | Pages: 732 – 740



[Articles](#) →

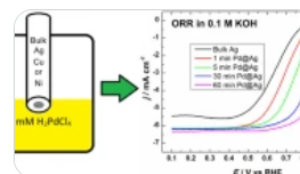
[Volumes and issues](#) →

[Collections](#) →

Oxygen Reduction Reaction Studies on Pd Coatings Prepared by Galvanic Exchange of Silver, Nickel and Copper

Audris Mihailovs, Markus Otsus ... Kaido Tammeveski

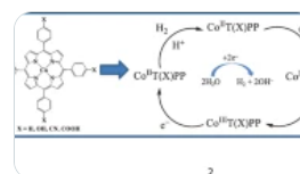
Research | 06 June 2023 | Pages: 741 – 751



Cobalt-based Metalloporphyrins As Efficient Electro-catalysts for Hydrogen Evolution From Acetic Acid and Water

Zong Wang, Yin Liu ... Wei Liu

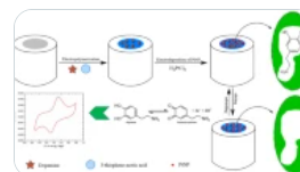
Research | 06 June 2023 | Pages: 752 – 762



Dopamine Electrochemical Sensor Based on Molecularly Imprinted Polymer on Carbon Electrodes with Platinum Nanoparticles

İzzet Koçak & Berrin Gürler Akyüz

Research | 07 June 2023 | Pages: 763 – 775





Cobalt-based Metalloporphyrins As Efficient Electro-catalysts for Hydrogen Evolution From Acetic Acid and Water

Zong Wang¹ · Yin Liu¹ · Ting Li¹ · Yong-Zhen He¹ · Er-Chen Han¹ · Yan-Lin Chen¹ · Xin-Yi Jiang¹ · Chun-Lin Ni¹ · Le-Min Yang¹ · Wei Liu¹

Accepted: 20 May 2023

© The Author(s), under exclusive licence to Springer Science+Business Media, LLC, part of Springer Nature 2023

Abstract

Four molecular electrocatalysts based on cobalt complexes, CoT(X)PP (X = H (**1**), OH (**2**), CN (**3**), COOH (**4**)), were prepared from *meso*-tetra-*p*-X-phenylporphyrin (H₂T(X)PP, X = H, OH, CN, COOH) by reaction with cobalt acetate to be used for electrolytic proton or water reduction. The electrochemical properties and the corresponding catalytic activities of these four catalysts were investigated by cyclic voltammetry. Controlled potential electrolysis with gas chromatography analysis confirmed that the turn-over frequencies (TOF) per mol of catalyst per hour were 42.4, 38.6, 55.5, and 70.1 mol H₂ at an overpotential of 941.6 mV (in DMF) in the acetic acid solution containing catalyst. In neutral buffered aqueous solution (pH 7.0), these four molecular catalysts had TOF per mol of catalyst per hour of 352.53, 313.7, 473.4, and 714.6 mol H₂, respectively, with an overpotential of 837.6 mV, indicating that complex **4** had better activity than complexes **1**, **2**, and **3**. The Faraday efficiencies of complexes **1–4** were 99.1, 99.6, 100.4, and 99.0% at 72 h of consecutive reduction on a glassy carbon electrode, respectively. These results indicate that the electronic properties of the ligands play a crucial role in determining the catalytic activity of the cobalt complex and are consistent with the phenomenon that the catalytic activity of the benzene porphyrins is significantly increased in the presence of electron-withdrawing groups, and the CoT(COOH)PP is the most active catalyst.

Keywords Cobalt(II) porphyrin complexes · Molecular electrocatalysts · Proton and water reduction · Hydrogen evolution

Introduction

Finding alternative clean and renewable energy sources is crucial given the diminishing fossil fuels and the significant environmental pollution issues [1–4]. Due to its abundant supply, lack of pollution, and increased calorific value, hydrogen has drawn a lot of attention. Currently, the electro- and photocatalytic separation of water into hydrogen and oxygen is the focus of the study [5–7]. However, the development of effective catalysts with reduced overpotential, superior stability, and a high rate of turnover for the water reduction reaction is the primary problem for water decomposition [8, 9]. Consequently, a substantial

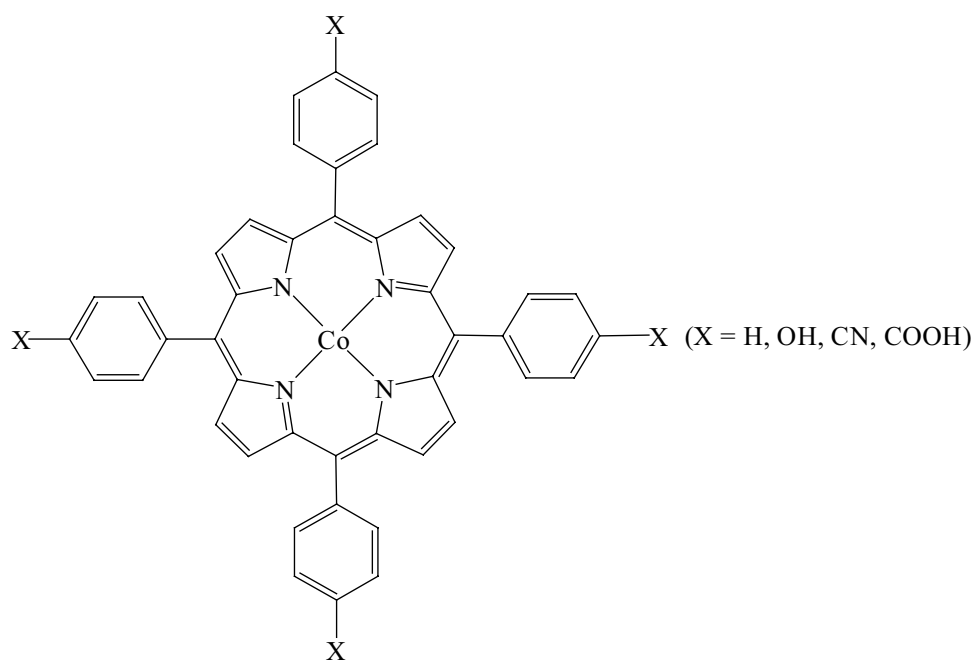
amount of investigational work has been dedicated to the exploitation of efficient catalysts of transition metal complexes based on cobalt [10, 11, 20], molybdenum [12], manganese [13–16], copper [17–19], nickel [20–24] and iron [25, 26] for the reduction of protons or water to form H₂. Macrocyclic complexes of cobalt have been broadly studied and reported as electrocatalysts for hydrogen production since the seminal research work of Sutin [27–29]. Cobalt porphyrins were also demonstrated to be a catalyst with high Faraday efficiency in homogeneous solutions [30–33]. Spiro and colleagues were the first to report that water-soluble cationic cobalt porphyrins could generate hydrogen by electrocatalysis [30], but this report displayed that hydrogen release occurred only at a very low turnover rate and high-potential acidity. Subsequently, a large number of related studies were reported. Nevertheless, the majority of reports utilized acid or organic solvent buffers in water to deliver the proton source. In this paper, we present an efficient bimolecular porphyrin cobalt catalyst for the reduction of water to hydrogen in phosphate buffer

✉ Chun-Lin Ni
niclchem@scau.edu.cn

✉ Wei Liu

¹ College of Materials and Energy, South China Agricultural University, Guangzhou 510642, P. R. China

Scheme 1 Molecular structure of cobalt porphyrin under study



solutions. It possesses higher Faraday efficiency, turnover, and reversal rates compared to the first reported porphyrins [33]. Whereas, the donor type and electronic properties of the ligands perform a crucial role in determining the structure and reactivity of the corresponding metal complexes [27, 34, 35]. We are continuously studying different substituted ligands and their complexes with cobalt [36–39]. Our group has already investigated the electrocatalytic hydrogen production of two cobalt(II) complexes [40], designated CoT(4-Cl)PP and CoT(4-OMe)PP. In this context, we proceeded to investigate the electrocatalytic properties of the subsequent four cobalt complexes, CoT(X)PP (X = H (**1**), OH (**2**), CN (**3**), COOH (**4**)), and the implications of the four tetravalent ligand modifications on the catalytic properties of this four cobalt (II) complexes (Scheme 1).

Experimental

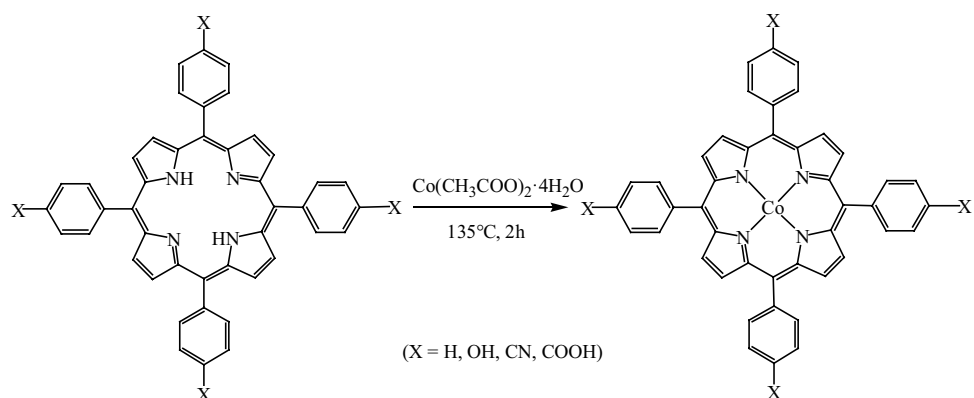
Materials

Pyrrole, benzaldehyde, 4-hydroxybenzaldehyde, 4-cyanobenzaldehyde and 4-carboxybenzaldehyde were purchased from Aldrich and Macorin without further purification. Tetrabutylammonium perchlorate $[(n\text{-Bu})_4\text{N}]\text{ClO}_4$ was recrystallized from anhydrous ethanol and dried in a vacuum oven. $\text{H}_2\text{T(X)PP}$ and CoT(X)PP were synthesized in accordance with the literature procedures [41, 42].

Syntheses of Complexes 1-4

CoTPP was prepared as described in Scheme 2. H_2TPP (0.5106 g, 1 mmol) and $\text{Co}(\text{CH}_3\text{COO})_2 \cdot 4\text{H}_2\text{O}$ (1.7436 g, 7

Scheme 2 Synthesis of complexes 1-4



mmol) were dissolved in 80 mL DMF solution, refluxed at 135°C for 2 h, quickly poured into 500 mL ice water, filtered, washed with distilled water and anhydrous ethanol, and dried under vacuum at 70°C for 8 h. Yield: 83.1%.

Complexes **2**, **3**, and **4** were prepared by replacing H₂TPP with H₂T(4-OH)PP, H₂T(4-CN)PP, and H₂T(4-COOH)PP, respectively, according to the method used for the synthesis of complex **1**. Yields were 85.1, 84.6, and 87.2%, respectively.

Physical Measurements

Infrared spectra in the range of 400–4000 cm^{−1} were recorded on a Nicolet Avatar 360 FT-IR spectrophotometer with samples in the form of KBr pellets. The absorption spectra of the samples in DMF solution were measured with a Shimadzu UV-2550 double-beam spectrophotometer in the vertical incident light range of 200–800 nm. The ESI-MS spectra of the four complexes were measured on an AB SCIEX, API3200.

Electrochemical Methods

Cyclic voltammograms (CVs) were as well obtained on a CHI-660E electrochemical analyzer under N₂ using a three-electrode cell with a glassy carbon electrode as the operating electrode, saturated Ag/AgNO₃ or Ag/AgCl electrode as the reference electrode, as well as a platinum wire as the auxiliary electrode. In organic media, a ferrocene/ferrocene (1+) couple was used as an internal standard and 0.10 M [(n-Bu)₄N]ClO₄ was utilized as a supporting electrolyte. Controlled potential electrolysis (CPE) in aqueous media was undertaken using a hermetically sealed glass double chamber cell separated by a glass frit. The working compartment was instrumented with a glassy carbon plate and an Ag/AgCl reference electrode. The auxiliary compartment was installed with a platinum gauze electrode. The working compartment and the auxiliary compartment contained 40 mL of phosphate buffer. The CVs were documented after the addition of cobalt complexes. After electrolysis, 0.50 mL of the headspace sample was withdrawn and exchanged with 0.50 mL of CH₄. The headspace sample was injected into a gas chromatograph (GC). The GC experiments were executed using an Agilent Technologies 7890A gas chromatograph.

Result and Discussion

Characterizations

In the FT-IR spectra of complexes **1–4** (Fig. S1), the N–H stretching vibrational bands of **1** and **3** are located at 3309 and 3313 cm^{−1}, respectively, while the N–H stretching vibrational bands of **2** and **4** are covered by their –OH at 3430 cm^{−1}

and –COOH stretching vibrational bands at 3436 cm^{−1}, respectively. The N–H bending vibrational bands were located at 966, 962, 966, and 960 cm^{−1}, whereas when the free base porphyrins are converted to cobalt (II) complexes, the vibrational bands of N–H disappear and a new vibrational band appearance near 1000 cm^{−1}, which is the characteristic band of N–Co bond, signifying that the hydrogen atoms on the nitrogen atoms are substituted by metal ions to form metalloporphyrins [43].

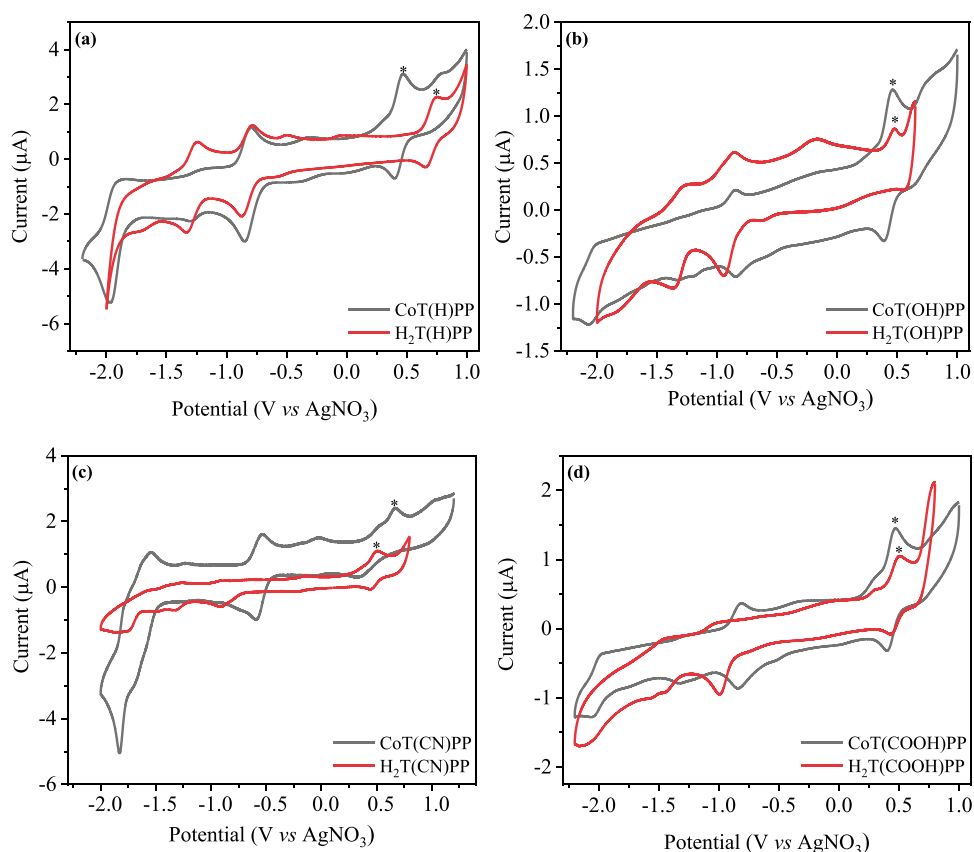
The UV-Vis spectra of complexes **1–4** dissolved in DMF are demonstrated in Fig. S2. The intense absorption peak near 412–421 nm belongs to the Soret band and the weak absorption at 500–700 nm to the Q band, which accounts for the $\pi \rightarrow \pi^*$ leap in the porphyrin ring ($a_{2u}-e_g^*$ leap and $a_{1u}-e_g^*$). While, the four characteristic peaks near 515, 550, 590 and 648 nm in the Q-band of the free base porphyrins were reduced to one peak near 530 nm, confirming the formation of the cobalt(II) complex [43].

The ESI-MS spectra of complexes **1–4** in CH₃OH solution exhibited in Fig. S3 with the characteristic bands of cation mass spectra of 671.2, 735.0, 771.0, and 847.1, corresponding to the theoretical values of 671.6, 735.6, 771.7, and 847.7. The experimental values generally corresponded to the theoretical values, confirming the synthesis of metalloporphyrins.

Cyclic Voltammetry Studies

To explore the electrochemical properties of four molecular catalysts, CVs were measured in DMF with 0.10 M [(n-Bu)₄N]ClO₄ as the supporting electrolyte as shown in Fig. 1. Complex **1–4** both exhibit two redox waves and followed the order **1** (−0.85 and −1.97 V verse Ag/AgNO₃) → **2** (−0.85 and −2.07 V verse Ag/AgNO₃) → **3** (−0.78 and −1.90 V verse Ag/AgNO₃) → **4** (−1.34 and −2.05 V verse Ag/AgNO₃), respectively. As illustrated in Fig. 1a, the CV of 0.89 mM complex **1** exhibits two reversible peaks at −0.85 V and −1.97 V verse Ag/AgNO₃, respectively. For comparison, CV of H₂T(4-H)PP was measured in a similar condition, H₂T(4-H)PP exhibits one reversible peak at −0.78 V verse Ag/AgNO₃. The first reduction wave of **1** at −0.85 V, being close to the first reduction of the free ligand, is assigned to H₂T(4-H)PP. The second redox peak can be assigned to Co^{II}/Co^I couple. From Fig. 1b, complex **2** also shows two reversible peaks at −0.85 V and −2.07 V verse Ag/AgNO₃, respectively. H₂T(4-OH)PP exhibits one reversible peak at −0.86 V verse Ag/AgNO₃. The first reduction wave of **2** at −0.85 V, being close to the first reduction of the free ligand, is assigned to H₂T(4-OH)PP. The second redox peak can be assigned to Co^{II}/Co^I couple. From Fig. 1c, complex **3** also shows two reversible peaks at −0.78 V and −1.90 V verse Ag/AgNO₃, respectively. H₂T(4-CN)PP exhibits one reversible peak at −0.91 V verse Ag/AgNO₃. The first reduction wave

Fig. 1 (a) Cyclic voltammogram (CV) of 0.89 mM complex **1** and H₂T(H)PP (0.91 mM) in DMF. (b) CV of 0.82 mM complex **2** and H₂T(OH)PP (0.88 mM) in DMF. (c) CV of 0.78 mM complex **3** and H₂T(CN)PP (0.84 mM) in DMF. (d) CV of 0.71 mM complex **4** and H₂T(COOH)PP (0.76 mM) in DMF. Conditions: 0.10 M [n-Bu₄N]ClO₄ as supporting electrolyte, glassy carbon working electrode (1 mm diameter), Pt counter electrode, Ag/AgNO₃ reference electrode, scan rate 100 mV/s, Ferrocene internal standard (*)



of **3** at -0.78 V, being close to the first reduction of the free ligand, is assigned to H₂T(4-CN)PP. The second redox peak can be assigned to Co^{II}/Co^I couple. From Fig. 1d, complex **4** also shows two reversible peaks at -1.34 V and -2.05 V verse Ag/AgNO₃, respectively. H₂T(4-COOH)PP exhibits one reversible peak at -1.04 V verse Ag/AgNO₃. The first reduction wave of **4** at -1.34 V, being close to the first reduction of the free ligand, is assigned to H₂T(4-COOH)PP. The second redox peak can be assigned to Co^{II}/Co^I couple. The Potential of Co^{II}/Co^I is shifted by 100, 70, and 80 mV correspondingly since H at the para-position of the benzene ring is superseded by hydroxyl, cyano, and carboxyl groups, respectively.

Catalytic Hydrogen Evolution From Acetic Acid in DMF

The performance of hydrogen evolution for acetic acid in DMF solution was investigated by cyclic voltammetry test, as depicted in Fig. 2a–e. As depicted in Fig. 2a, the significant voltammetric current emerges at -1.99 V with the addition of different concentrations of acetic acid (from 0.0 to 5.56 mM) and significantly increases with the proton concentration. The results indicated that **1** electrocatalytic hydrogen evolution required the reduction of Co(II) to Co(I) and the protonation reaction. Interestingly, the catalytic wave onset of Ag/AgNO₃ remained almost constant at about -1.75 V as the acetic acid concentration proceeded

to increase from 0.0 to 5.56 mM (Fig. 2a). complex **2** increased significantly with the change of acetic acid concentration (from 0.00 to 6.30 mM) around -2.04 V, and the initiation point of the catalytic peak remained almost around -2.04 V compared to Ag/AgNO₃ (Fig. 2b). Along with the change in acetic acid concentration (from 0.00 to 7.78 mM), complex **3** exhibited a significant increase around -1.82 V, and the catalytic peak onset remained almost at -1.49 V compared to Ag/AgNO₃ (Fig. 2c). A systematic peak also emerges at -2.03 V with varying acetic acid concentration (from 0.00 to 6.30 mM) compared to the previous complexes of complex **4** (Fig. 2d). Following the above observations, only the Co^{II}/Co^I couple was engaged in the proton reduction. As the acetic acid concentration increased, the Co^{II}/Co^I reduction peak current gradually enhanced. All the complexes exhibited a significant positive shift in the starting reduction potential, diminishing the energy required for electron transfer.

In accordance with the existing literature [44–46] and the mentioned analytical work, the potential mechanism of acid-mediated catalytic cycling for hydrogen production is described in Scheme 3. The single-electron reduction of [Co^{II}T(X)PP] provides a [Co^IT(X)PP][−] species. The addition of protons produces Co^{III}-H, a potentially highly reactive intermediate [43]. Further reduction of Co^{III}-H generates H₂ reconstitutes the initiating complex [CoT(X)PP].

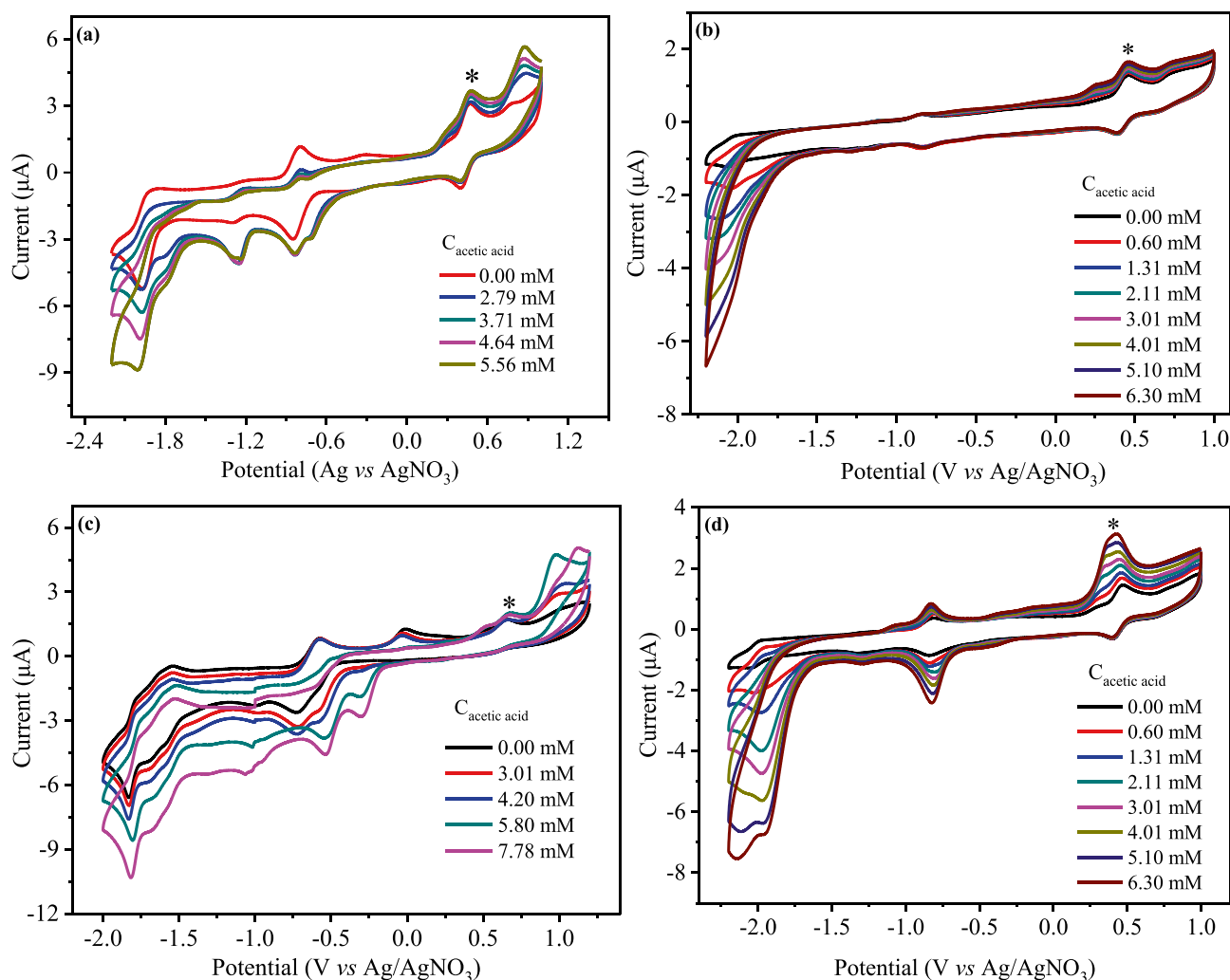


Fig. 2 (a) CVs of a 0.89 mM solution of complex 1, with varying concentration of acetic acid in DMF. (b) CVs of a 0.82 mM solution of complex 2, with varying concentration of acetic acid in DMF. (c) CVs of a 0.78 mM solution of complex 3, with varying concentration of acetic acid in DMF; (d) CVs of a 0.71 mM solution of com-

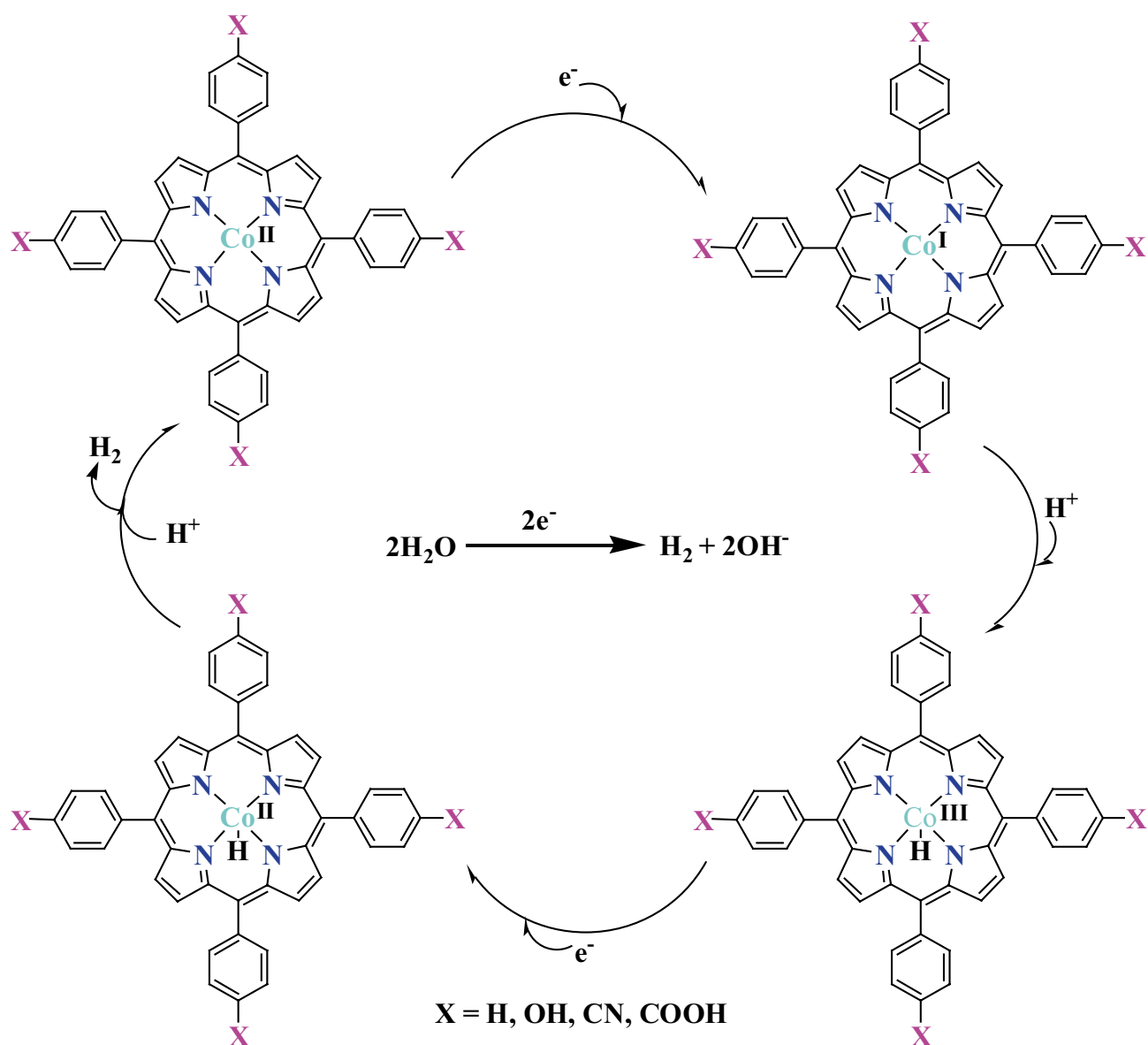
plex 4, with varying concentration of acetic acid in DMF. Conditions: 0.10 M [n-Bu₄N]ClO₄ as supporting electrolyte, scan rate: 100 mV/s, glassy carbon working electrode (1 mm diameter), Pt counter electrode, Ag/AgNO₃ reference electrode, Fc internal standard (*)

To develop a further assessment of the catalytic performance of complexes **1–4**, bulk electrolysis was carried out in DMF solution using glassy carbon plate electrodes in acetic acid at mutually variable applicative potentials. Fig. 3a–d illustrate the aggregate overall electrolytic charge of complexes **1–4** in the existence of acid. While the applied potential was -1.45 V, the maximum charges reached 57.8 mC, 45.8 mC, 52.3 mC and 71.8 mC in 2 min. The CPE experiment without complex **1–4** at the same potential has a charge of a mere 8.7 mC (Fig. 4), indicating that these four complexes in the presence of such conditions are effective in hydrogen production indeed. Assuming that each of the catalyst molecules is exclusively distributed on the electrode surface and that each electron is used for the reduction of protons, complexes **1**, **2**, **3** and **4** provide 42.4, 38.6, 55.5 and 70.1 moles of

hydrogen (Eqs. S1–S4) per mole of catalyst in the 941.6 mV OP in accordance with equations (1) [47] and (2) [48]. It is remarkably that complexes **1**, **3** and **4** are significantly more active than complex **2**, which is in agreement with the apparently higher catalytic activity in the presence of the electron-withdrawing group relative to the activity of the electron-donating group. In the presence of hydrogen, hydroxyl or carboxyl radicals on the porphyrin benzene ring, *meso*-tetra-*p*-carboxyphenylporphyrin is a superior active catalyst. Increasing the Co^{II}/Co^I redox potential, the decrease in the hydrogen-producing activity of the cobalt complexes.

$$\text{TOF} = \Delta C / (F \times n_1 \times n_2 \times t) \quad (1)$$

$$\text{Overpotential} = \text{Applied potential} - E_{\text{HA}}^{\ominus}$$



Scheme 3 The possible catalytic mechanism for proton reduction by Co[T(4-X)PP]

$$= \text{Applied potential} - (E^\ominus_{\text{H}^+} - (2.303RT/F) \text{pK}_{\text{aHA}}) \quad (2)$$

Note that ΔC is the charge from the catalyst solution during CPE minus the charge from solution without catalyst during CPE, F is Faraday's constant, n_1 is the number of moles of electrons required to generate one mole of H_2 , n_2 is the number of moles of catalyst in solution, and t is the duration of electrolysis.

Catalytic Hydrogen Evolution From Aqueous Buffer

We conducted further investigations on the electrochemical properties of these four complexes in buffered aqueous

solutions at pH 3.5–7.0, the pH range associated with catalytic water reduction. As indicated in Fig. 5a, in the absence of complex **1**, the catalytic current is not obvious until the potential is up to -1.50 V versus Ag/AgCl. On the addition of complex **1**, the catalytic current emerges at around -1.37 V relative to Ag/AgCl, indicating that the addition of complex **1** can reduce the potential. Furthermore, the current intensity increased significantly as the concentration of complex **1** increased from 0.72 to 1.67 μM , where the peak current is up to 23.6 μA and the initial reduction potential of Ag/AgCl is positively shifted by 130 mV. It is apparent from Fig. 5b that the initiation of the catalytic current is influenced by the pH of the solution, and the imposed potential

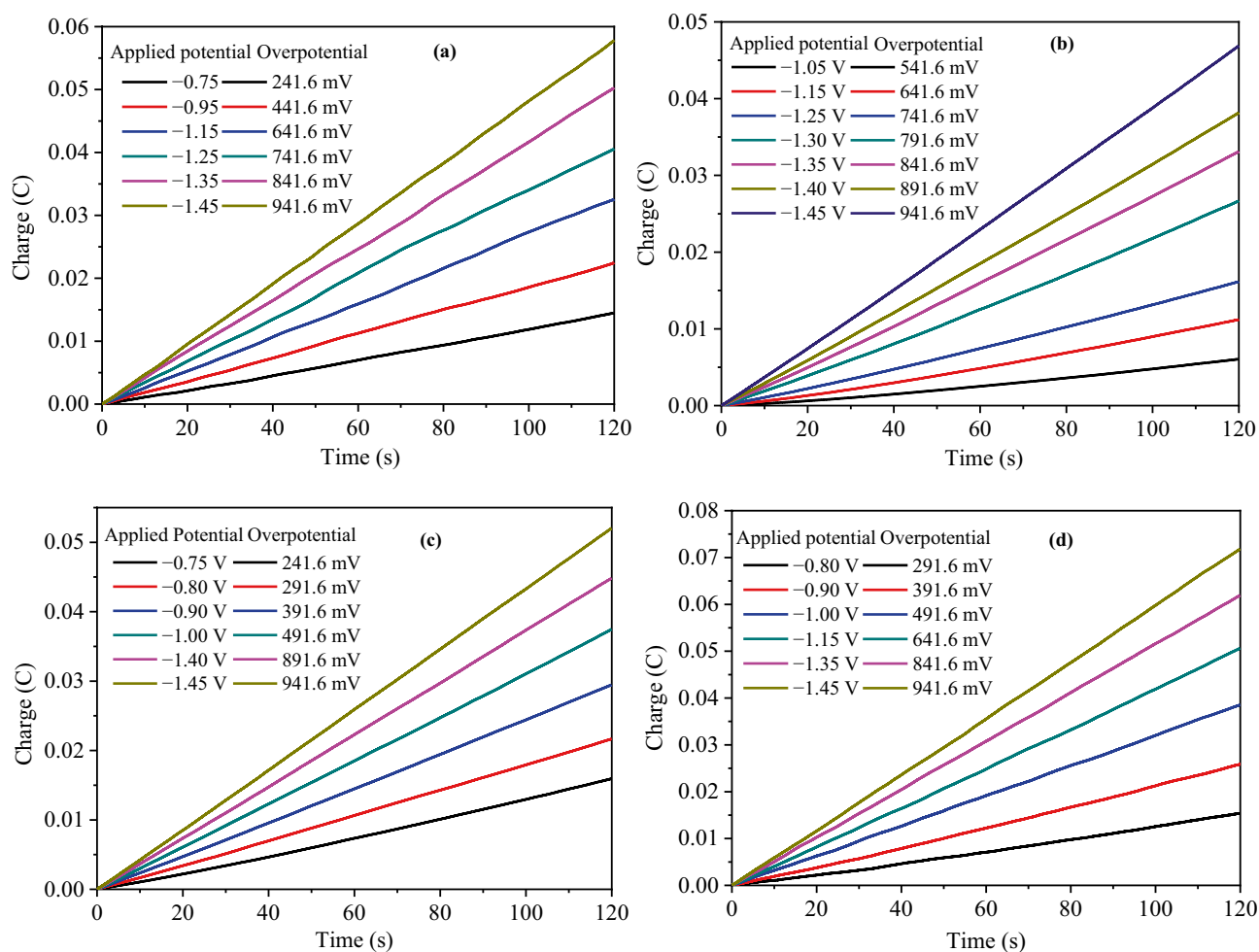


Fig. 3 (a) Charge buildup versus time from electrolysis of 5.42 mM acetic acid with 6.01 μM complex 1 in DMF; (b) Charge buildup versus time from electrolysis of 5.42 mM acetic acid with 4.98 μM complex 2 in DMF; (c) Charge buildup versus time from electrolysis of

5.42 mM acetic acid with 3.33 μM complex 3 in DMF; (d) Charge buildup versus time from electrolysis of 5.42 mM acetic acid with 4.66 μM complex 4 in DMF; All data have been deducted blank

decreases with increasing pH, demonstrating the involvement of protons in the initial stage of electrochemical catalysis.

Among the same conditions, as illustrated in Figs. 6a, S4a, and S5a, while no catalyst **2-4** was an addition, the catalytic current was not evident until the potential reached -1.50 V for Ag/AgCl. When catalyst **2-4** was added, the catalytic current increased significantly, demonstrating that the addition of complex **2-4** can diminish the potential as well. As the concentration of complex **2-4** increased from 0.07 to 1.55 μM , 0.05 to 0.86 μM , and 0.45 to 3.02 μM , respectively, the current intensity was significantly increased and the peak currents were up to 14.3, 24.6, and 18.7 μA , as the initial reduction potentials of Ag/AgCl were positively shifted by 144, 128, and 168 mV, respectively. From Figs. 6b, S4b, and S5b, it is clear that The starting potential of the catalytic current is regulated by the pH of the solution, and the applied potential decreases with increasing pH, which confirms the

involvement of protons in the initial stage of electrochemical catalysis.

The results indicated that the addition of the complex can reduce the potential current when the pH is determined, as well as the current intensity increases with the concentration, and there is a saturation concentration. At a constant catalyst concentration, along with the decrease of pH, the proton in the system increases, and the peak current gradually increases, with a positive shift of the starting reduction potential amount.

To investigate further the electrocatalytic activity of complexes **1-4** in aqueous media, the bulk electrolysis of complexes **1-4** with an aqueous solution of 0.25 M buffer solution (pH 7.0) was evaluated at variable potentials using a glassy carbon electrode in a double-chamber cell. As can be observed in Fig. S6e, in the absence of complex **1**, the maximum charge for 2 min of electrolysis was

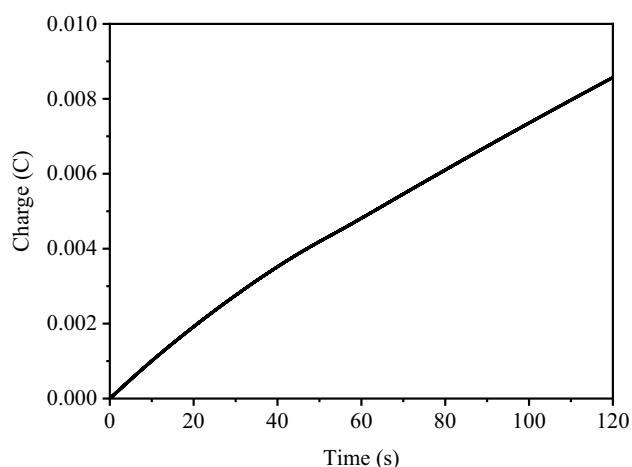


Fig. 4 Charge buildup versus time from electrolysis of 0.10 mM [n-Bu₄N]ClO₄ in DMF

solely 32 mC when the external potential was -1.45 V versus Ag/AgCl. The electrolysis in the presence of **1** under the same conditions for 2 min resulted in a charge

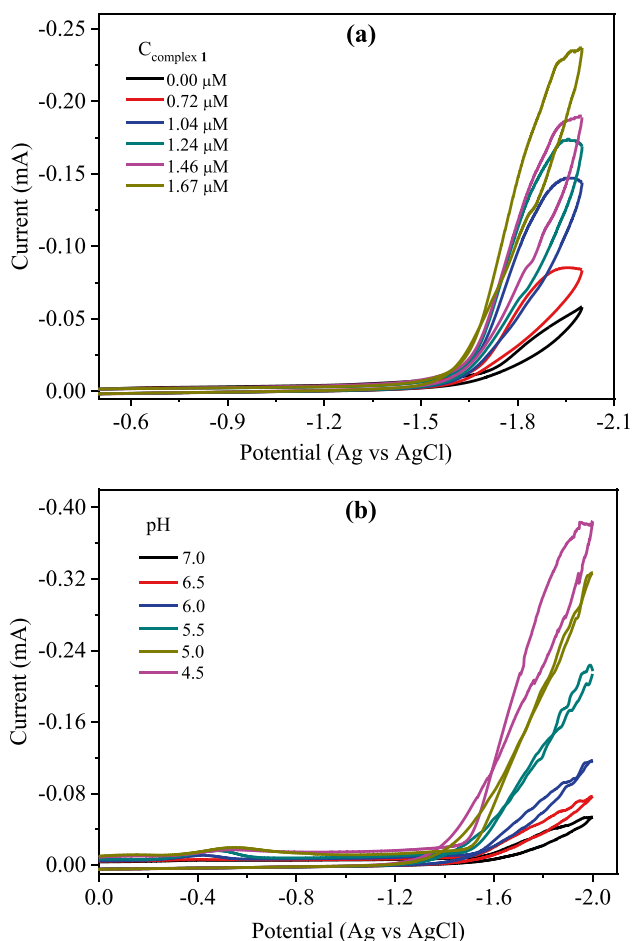


Fig. 5 (a) CVs of complex **1** in different concentration; (b) CVs of 1.67 mM complex **1**, showing the variation in catalytic current with pH (scan rate: 100 mV/s) Conditions: 0.25 M phosphate buffered solution at pH 7.0, glassy carbon working electrode (1 mm diameter), Pt wire counter electrode, Ag/AgCl reference electrode

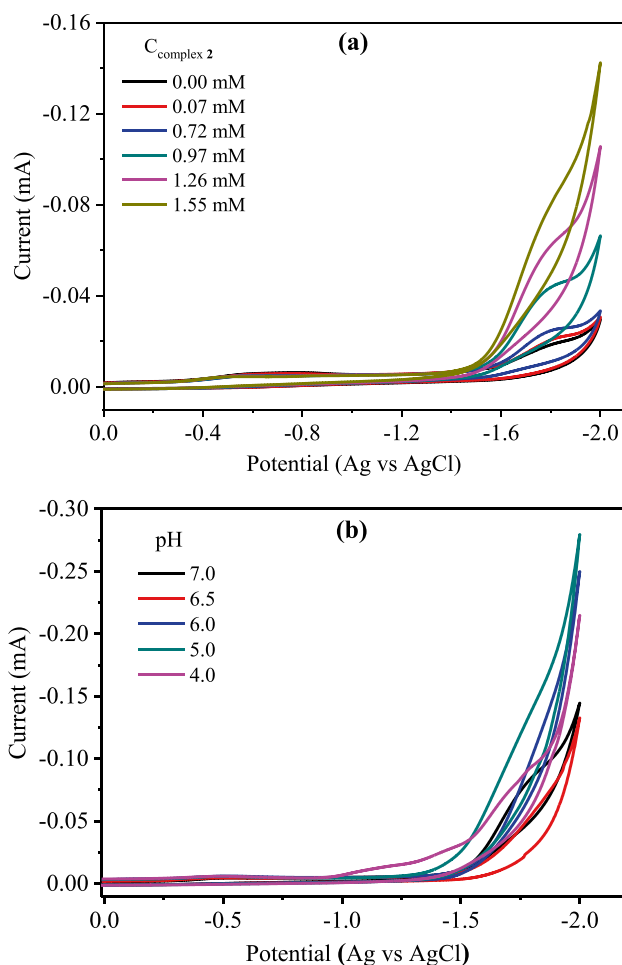


Fig. 6 (a) Cyclic voltammograms of complex **2** in different concentration; (b) CVs of 1.55 μ M complex **2**, showing the variation in catalytic current with pH (scan rate: 100 mV/s) Conditions: 0.25 M phosphate buffered solution at pH 7.0, glassy carbon working electrode (1 mm diameter), Pt wire counter electrode, Ag/AgCl reference electrode

of 330 mC (Fig. S6a), accompanied by the appearance of a large number of bubbles, which was confirmed by gas chromatography as H₂ (Fig. S7a). An electrolysis time of 1 h yielded about 3.62 mL of H₂ with a Faraday efficiency of 99.13% of H₂ (Fig. S7b). Following Eqs. (1) and (3) [49], we calculate the TOF of the catalyst as 352.53 mol of hydrogen per mol of catalyst per hour at a maximum overpotential of 836.7 mV (Eq. S5),

$$\begin{aligned} \text{Over potential} &= \text{Applied potential} - E(\text{pH}) \\ &= \text{Applied potential} - (-0.059 \text{ pH}) \end{aligned} \quad (3)$$

where

As it can be seen in Fig. S6b, at an applied potential of -1.45 Vs Ag/AgCl, the maximum charge generated by electrolysis for 2 min verse was 258.1 mC, while the generated gas was verified by gas chromatography to be hydrogen (Fig. S8a), and the electrolysis cycle for 1 h produced 3.24 mL of hydrogen with a Faraday efficiency of 99.6% (Fig. S8b).

Table 1 TOF values of Co[T(4-X)PP] from aqueous buffer*

X	Cl	OMe	1 (H)	2 (OH)	3 (CN)	4 (COOH)
TOF(h ⁻¹)	632.9	120.1	352.53	313.7	473.4	714.6
References	Ref [40]	Ref [40]	This work	This work	This work	This work

*Applied potential (Ag/AgCl) = −1.45 V

According to Eqs. (1) and (3), complex **2** furnished a TOF of 313.7 mol of hydrogen per hour per mole of catalyst and an OP of 837.6 mV (Eq. S6). From Fig. S6c, the maximum charge production for 2 min of electrolysis was 521.2 mC when the applied potential was −1.45 V versus Ag/AgCl, while the generated gas was identified by gas chromatography as hydrogen (Fig. S9a), the electrolytic cycle for 1 h generated 5.11 mL of hydrogen with a Faraday efficiency of 100.4% (Fig. S9b). Based on Eqs. (1) and (3), complex **3** yields a TOF of 473.4 mol of hydrogen per mol of catalyst per hour and an OP of 837.6 mV (Eq. S7). It is noted from Fig. S6d that the maximum charge generated by electrolysis for 2 min was 741.7 mC when the applied potential was −1.45 V versus Ag/AgCl, whereas the generated gas was identified by gas chromatography as hydrogen gas, as observed in Fig. S10a. In the 1 h electrolysis cycle 8.56 mL of hydrogen was produced with a Faraday efficiency of 99.0% (Fig. S10b). Under Eqs. (1) and (3), the TOF of complex **4** is 714.6 mol of hydrogen per mol of catalyst per hour and the OP is 837.6 mV (Eq. S8).

It is clear from the above experimental data that the complexes examined in this paper have excellent catalytic properties. The catalytic performance of complex **4** was significantly superior to the other three complexes, which may be due to the enhanced electron absorption ability of complex **4** than the tetradentate ligand of complex **3**. The catalytic activity of complex **1** was higher than that of complex **2**, which may be since the tetradentate ligand of complex **2** is an electron-donating group, and the electron-donating group decreased the activity of the complex. In these results, it is suggested that the presence of ligands is a crucial structural feature of proton or water reduction catalysis and has a substantial influential effect on its catalytic performance.

It is well known that the catalytic efficiency of different electrocatalytic systems varies with different experimental conditions, which makes it difficult to compare the hydrogen evolution performance of the reported electrocatalytic systems based on cobalt porphyrins under the same conditions. Our group has studied the catalytic properties of cobalt complexes CoT(4-Cl)PP and CoT(4-OMe)PP. On this basis, we have carried out a more systematic study, under the same test conditions to compare, the results show that: **4** has higher activity than the reported tetra-*p*-Cl cobalt porphyrin complex (TOF = 632.9 in neutral phosphate buffer solution) [40]. In a neutral phosphate buffer solution, the

TOF of complex **4** was equal to 714.6 mol, and the applied potential was 1.45 V versus Ag/AgCl (Table 1). As presented in Fig. S11, the four catalysts had a powerful charge accumulation capacity in 0.25 M buffer solution (pH = 7) under the action of −1.40 V against Ag/AgCl with no remarkable loss of activity in 72 h.

Conclusions

We have successfully synthesized four electrocatalysts based on *meso*-tetra-*p*-X-phenylporphyrin cobalt complexes. The potentially higher the Co^(II/I) redox potential the quieter the hydrogen production activity of the cobalt complexes. Electrochemical investigations demonstrated that the four complexes could generate hydrogen not only from acetic acid but also in buffer solutions without acetic acid. The electrochemical studies indicated that the four complexes had excellent catalytic properties for hydrogen production, and their catalytic activities (TOF) were in descending order: **4** (714.6) → **3** (473.4) → **1** (352.5) → **2** (313.7). The results are concordant with the results that the catalytic activity is significantly enhanced with the presence of electron-withdrawing groups on the phenol counterpart of the ligand.

Supplementary Information The online version contains supplementary material available at <https://doi.org/10.1007/s12678-023-00832-z>.

Authors' Contributions Zong Wang and Yin Liu wrote the main manuscript text. Ting Li, Yong-Zhen He, Yan-Lin Chen prepared all figures in text. Er-Chen Han, Xin-Yi Jiang and Le-Min Yang prepared all figures in SI. Wei Liu and Chun-Lin Ni are supervisors with writing-review and editing. All authors reviewed the manuscript.

Funding This work was supported by the National Science Foundation of China (No. 21701045) and the Science and Technology Project (No.2016A010103025) from Guangdong Science and Technology Department.

Availability of Data and Materials No datasets are used, and the data and materials will be provided if necessary.

Declarations

Ethical Approval The work is not applicable for both human and/or animal studies.

Conflict of Interests The authors declare no competing interests.

References

- H. Lei, X. Li, J. Meng, H. Zheng, W. Zhang, R. Cao, Structure effects of metal corroles on energy-related small molecule activation reactions. *ACS Catal.* **9**, 4320–4344 (2019)
- W. Zhang, W. Lai, R. Cao, Energy-related small molecule activation reactions: oxygen reduction and hydrogen and oxygen evolution reactions catalyzed by porphyrin- and corrole-based systems. *Chem. Rev.* **117**, 3717–3797 (2017)
- D. Zhao, Z. Zhuang, X. Cao, C. Zhang, Q. Peng, C. Chen, Y. Li, Atomic site electrocatalysts for water splitting, oxygen reduction and selective oxidation. *Chem. Soc. Rev.* **49**, 2215–2264 (2020)
- C.X. Zhao, J.N. Liu, B.Q. Li, D. Ren, X. Chen, J. Yu, Q. Zhang, Multiscale construction of bifunctional electrocatalysts for long-lifespan rechargeable zinc-air batteries. *Adv. Funct. Mater.* **30**, 2003619 (2020)
- X. Li, H. Lei, J. Liu, X. Zhao, S. Ding, Z. Zhang, X. Tao, W. Zhang, W. Wang, X. Zheng, R. Cao, Carbon nanotubes with cobalt corroles for hydrogen and oxygen evolution in pH 0–14 solutions. *Angew. Chem. Int. Ed.* **57**, 15070–15075 (2018)
- M.Z. Jacobsen, Review of solutions to global warming, air pollution, and energy security. *Energy Environ. Sci.* **2**, 148–173 (2009)
- M.G. Walter, E.L. Warren, J.R. McKone, S.W. Boettcher, Q.X. Mi, E.A. Santori, N.S. Lewis, Solar water splitting cells. *Chem. Rev.* **110**, 6446–6473 (2010)
- J. Suntivich, K.J. May, H.A. Gasteiger, J.B. Goodenough, Y. Shao-Horn, A perovskite oxide optimized for oxygen evolution catalysis from molecular orbital principles. *Science* **334**, 1383–1385 (2011)
- J. Barber, Photosynthetic energy conversion: natural and artificial. *Chem. Soc. Rev.* **38**, 185–196 (2009)
- L. Tong, R. Zong, R.P. Thummel, Visible light-driven hydrogen evolution from water catalyzed by a molecular cobalt complex. *Chem. Soc. Rev.* **136**, 4881–4884 (2014)
- W.M. Singh, T. Baine, S. Kudo, S. Tian, X.A. Ma, H. Zhou, N.J. DeYonker, T.C. Pham, J.C. Bollinger, D.L. Baker, B. Yan, C.E. Webster, X. Zhao, Electrocatalytic and photocatalytic hydrogen production in aqueous solution by a molecular cobalt complex. *Angew. Chem. Int. Ed.* **51**, 5941–5944 (2012)
- C. Wang, Y.T. Shan, W.H. Zheng, M. Zhang, Z.M. Su, Two-dimensional graphdiyne analogue containing mo-coordinated porphyrin covalent organic framework as a high-performance electrocatalyst for nitrogen fixation. *Appl. Surf. Sci.* **580**, 152359 (2022)
- R. Peng, A. Offenhäusser, Y. Ermolenko, Y. Mourzina, Biomimetic sensor based on Mn(III) meso-tetra(n-methyl-4-pyridyl) porphyrin for non-enzymatic electrocatalytic determination of hydrogen peroxide and as an electrochemical transducer in oxidase biosensor for analysis of biological media. *Sensor Actuat B-Chem* **321**, 128437 (2020)
- Y.G. Mourzina, A. Offenhäusser, Electrochemical properties and biomimetic activity of water-soluble meso-substituted Mn(III) porphyrin complexes in the electrocatalytic reduction of hydrogen peroxide. *J Electroanal Chem* **866**, 114159 (2020)
- A. Patel, R. Sadasivan, Modified Mn substituted POMs: synthetic strategies, structural diversity to applications. *Prog. Mater. Sci.* **118**, 100759 (2021)
- M. Jokazi, L.S. Mpeti, T. Nyokong, Electrocatalytic activity of manganese tetra 4-aminophenyl porphyrin in the presence of graphene quantum dots. *J Electroanal Chem* **901**, 115748 (2021)
- L.L. Zhou, T. Fang, J.P. Cao, Z.H. Zhu, X.T. Su, S.Z. Zhan, A dinuclear copper(II) electrocatalyst both water reduction and oxidation. *J. Power Sources* **273**, 298–304 (2015)
- J.P. Cao, T. Fang, L.Z. Fu, L.L. Zhou, S.Z. Zhan, First mononuclear copper(II) electro-catalyst for catalyzing hydrogen evolution from acetic acid and water. *Int. J. Hydrogen Energy* **39**, 13972–13978 (2014)
- T. Fang, L.Z. Fu, L.L. Zhou, S.Z. Zhan, A water-soluble dinuclear copper electrocatalyst, [Cu(oxpn)Cu(OH)₂] for both water reduction and oxidation. *Electrochim. Acta* **161**, 388–394 (2015)
- L. Lu, Q. Li, J. Du, W. Shi, P. Cheng, Bimetallic cobalt-nickel coordination polymer electrocatalysts for enhancing oxygen evolution reaction. *Chinese Chem. Lett.* **33**, 2928–2932 (2022)
- H. Lee, X. Wu, L. Sun, Homogeneous electrochemical water oxidation at neutral pH by water-soluble Ni(II) complexes bearing redox non-innocent tetraamido macrocyclic ligands. *ChemSusChem* **13**, 3277–3282 (2020)
- A. Das, Z. Han, W.W. Brennessel, P.L. Holland, R. Eisenberg, Nickel complexes for robust light-driven and electrocatalytic hydrogen production from water. *ACS Catal.* **5**, 1397–1406 (2015)
- X. Jin, X. Li, H. Lei, K. Guo, B. Lv, H. Guo, D. Chen, W. Zhang, R. Cao, Comparing electrocatalytic hydrogen and oxygen evolution activities of first-row transition metal complexes with similar coordination environments. *J Energy Chem* **63**, 659–666 (2021)
- L. Gan, T.L. Groy, P. Tarakeswar, S.K. Mazinani, J. Shearer, V. Mujica, A.K. Jones, A nickel phosphine complex as a fast and efficient hydrogen production catalyst. *J. Am. Chem. Soc.* **137**, 1109–1115 (2015)
- L. Xie, X.P. Zhang, B. Zhao, P. Li, J. Qi, X. Guo, B. Wang, H. Lei, W. Zhang, U.P. Apfel, R. Cao, Enzyme-inspired iron porphyrins for improved electrocatalytic oxygen reduction and evolution reactions. *J. Am. Chem. Soc.* **60**, 7576–7581 (2021)
- M.L. Pegis, D.J. Martin, C.F. Wise, A.C. Brezny, S.I. Johnson, L.E. Johnson, N. Kumar, S. Rauegi, J.M. Mayer, The mechanism of catalytic O₂ reduction by iron tetraphenylporphyrin. *J. Am. Chem. Soc.* **141**, 8315–8326 (2019)
- X. Hu, B.S. Brunshwig, J.C. Peters, Electrocatalytic hydrogen evolution at low overpotentials by cobalt macrocyclic glyoxime and tetraimine complexes. *J. Am. Chem. Soc.* **129**, 8988–8998 (2007)
- V. Artero, M. Chavarot-Kerlidou, M. Fontecave, Splitting water with cobalt. *Angew. Chem. Int. Ed.* **50**, 7238–7266 (2011)
- V.S. Thoi, Y. Sun, J.R. Long, C.J. Chang, Complexes of earth-abundant metals for catalytic electrochemical hydrogen generation under aqueous conditions. *Chem. Soc. Rev.* **42**, 2388–2400 (2013)
- R.M. Kellett, T.G. Spiro, Cobalt(I) porphyrin catalysis of hydrogen production from water. *Inorg. Chem* **24**, 2373–2377 (1985)
- M. Natali, A. Luisa, E. Iengo, F. Scandola, Efficient photocatalytic hydrogen generation from water by a cationic cobalt(II) porphyrin. *Chem. Commun* **50**, 1842–1844 (2014)
- D. Huang, J. Lu, S. Li, Y. Luo, C. Zhao, B. Hu, M. Wang, Y. Shen, Fabrication of cobalt porphyrin. electrochemically reduced graphene oxide hybrid films for electrocatalytic hydrogen evolution in aqueous solution. *Langmuir* **30**, 6990–6998 (2014)
- J.G. Kleingardner, B. Kandemir, K.L. Bren, Hydrogen evolution from neutral water under aerobic conditions catalyzed by cobalt microperoxidase-11. *J. Am. Chem. Soc.* **136**, 4–7 (2014)
- B.B. Beyene, S.B. Mane, C.H. Hung, Highly efficient electrocatalytic hydrogen evolution from neutral aqueous solution by a water-soluble anionic cobalt(II) porphyrin. *Chem. Commun.* **51**, 15067–15070 (2015)
- J.L. Fillol, Z. Codola, I. Garcia-Bosch, L. Gomez, J.J. Pla, M. Costas, Efficient water oxidation catalysts based on readily available iron coordination complexes. *Nat. Chem.* **3**, 807–813 (2011)
- J. Chu, Q.y. Lv, J.P. Cao, X.h. Xie, S. Zhan, Synthesis and electrocatalytic properties of a dinuclear triazenido-palladium complex. *Inorg. Chem. Commun.* **36**, 245–248 (2013)
- J. Chu, Q.Y. Lv, X.H. Xie, W. Li, S. Zhan, Synthesis and electrocatalytic properties of a dinuclear palladium(I) 1-[(2-bromo)benzene]-3-[(2-carboxymethyl)benzene]triazene complex. *Transit Met Chem* **38**, 843–847 (2013)
- J.P. Cao, T. Fang, L.Z. Fu, L.L. Zhou, S. Zhan, A nickel molecular electro-catalyst for generating hydrogen from acetic acid or water. *Int J Hydrogen Energy* **39**, 10980–10986 (2014)

39. J.P. Cao, T. Fang, Z.Q. Wang, Y.W. Ren, S. Zhan, A dinuclear triazenido-copper complex: a new molecular electro-catalyst for generating hydrogen from acetic acid or water. *J. Mol. Catal. A: Chem* **391**, 191–197 (2014)
40. Y. Liu, L.Z. Fu, L.M. Yang, X.P. Liu, S.Z. Zhan, C.L. Ni, The impact of modifying the ligands on hydrogen production electrocatalyzed by meso-tetra-p-X-phenylporphin cobalt complexes, CoT(X)PP. *J. Mol. Catal. A: Chem* **417**, 101–106 (2016)
41. A.D. Adler, F.R. Longo, J.D. Finarelli, J. Goldmacher, J. Assour, L. Korsakoff, A simplified synthesis for meso-Tetraphenylporphin. *J. Org. Chem.* **32**, 476 (1967)
42. A.D. Adler, F.R. Longo, F. Kampas, On the preparation of metalloporphyrins. *J. Inorg. Nucl. Chem.* **32**, 2443–2453 (1970)
43. J. Jing, J. Yang, W. Li, Z. Wu, Y. Zhu, Construction of interfacial electric field via dual-porphyrin heterostructure boosting photocatalytic hydrogen evolution. *Adv Mater* **34**, 2106807 (2022)
44. J.T. Muckerman, E. Fujita, Theoretical studies of the mechanism of catalytic hydrogen production by a cobaloxime. *Chem. Commun.* **47**, 12456–15458 (2011)
45. J. Xie, Q. Zhou, C. Li, W. Wang, Y. Hou, B. Zhang, X. Wang, An unexpected role of the monodentate ligand in photocatalytic hydrogen production of the pentadentate ligand-based cobalt complexes. *Chem. Commun.* **50**, 6520–6522 (2014)
46. A.E. King, Y. Surendranath, N.A. Piro, J.P. Bigi, J.R. Long, C.J. Chang, A mechanistic study of proton reduction catalyzed by a pentapyridine cobalt complex: evidence for involvement of an anation-based pathway. *Chem. Sci.* **4**, 1578–1587 (2013)
47. L.Z. Fu, L.L. Zhou, L.Z. Tang, Y.X. Zhang, S.Z. Zhan, Electrochemical and photochemical-driven hydrogen evolution catalyzed by a dinuclear Co^{II}-Co^{II} complex. *J. Power Sources* **280**, 453–458 (2015)
48. G.A.N. Felton, R.S. Glass, D.L. Lichtenberger, D.H. Evans, iron-only hydrogenase mimics. thermodynamic aspects of the use of electrochemistry to evaluate catalytic efficiency for hydrogen generation. *Inorg. Chem.* **45**, 9181–9184 (2006)
49. H.I. Karunadasa, C.J. Chang, J.R. Long, A molecular molybdenum-oxo catalyst for generating hydrogen from water. *Nature* **464**, 1329–1333 (2010)

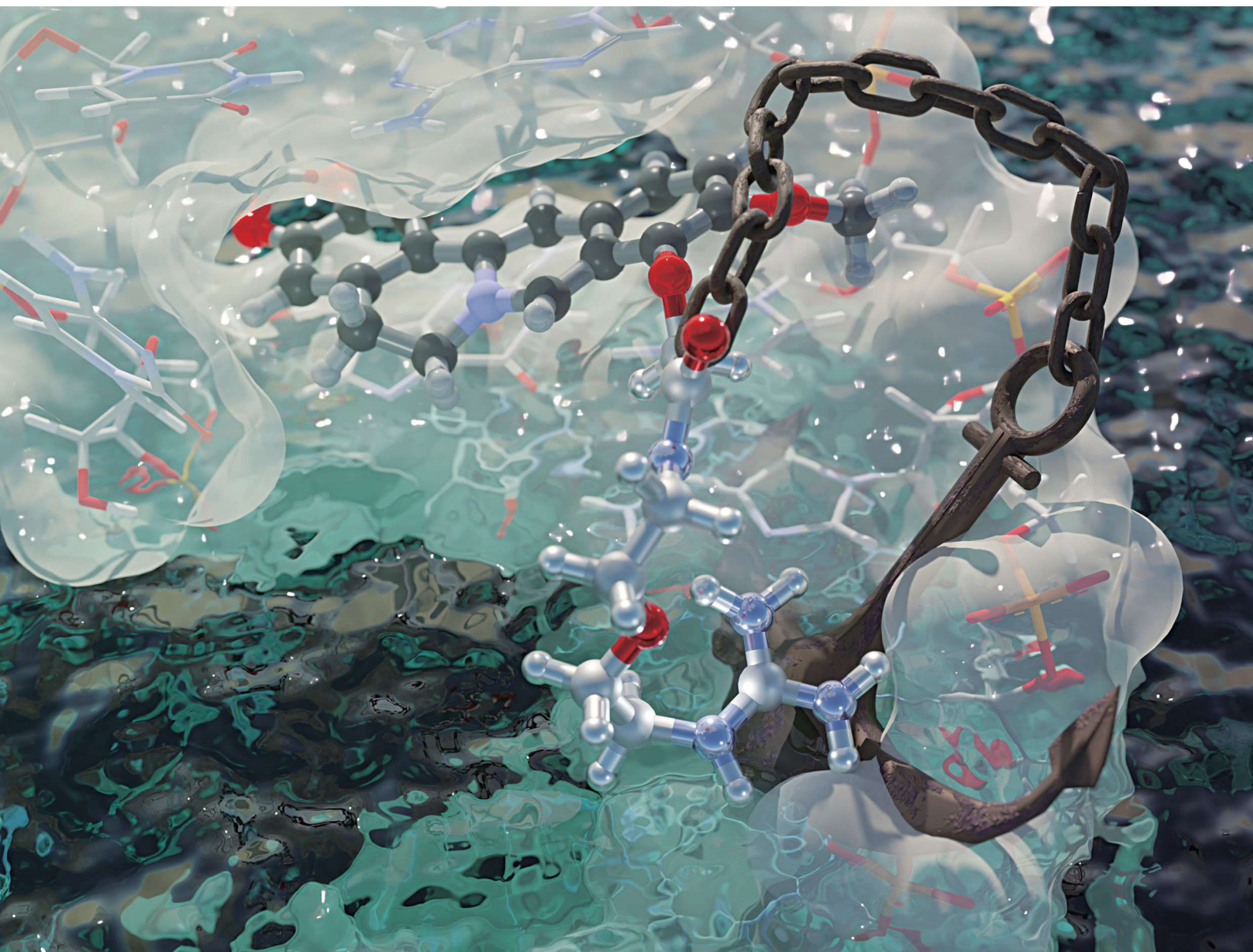
Publisher's Note Springer Nature remains neutral with regard to jurisdictional claims in published maps and institutional affiliations.

Springer Nature or its licensor (e.g. a society or other partner) holds exclusive rights to this article under a publishing agreement with the author(s) or other rightsholder(s); author self-archiving of the accepted manuscript version of this article is solely governed by the terms of such publishing agreement and applicable law.

NJC

New Journal of Chemistry
rsc.li/njc

A journal for new directions in chemistry



ISSN 1144-0546

COMMUNICATION

Tamaki Endoh, Naoki Sugimoto *et al.*
Guanidine modification improves functions of natural
RNA-targeting alkaloids

The article was first published on 15 Apr 2024
New J. Chem., 2024, **48**, 8860–8867
<https://doi.org/10.1039/D4NJ00351A>

Download PDF

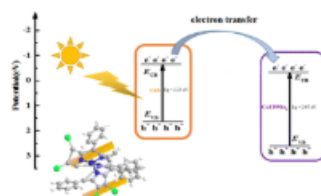
Article HTML

Paper

Enhancing the photocatalytic hydrogen production performance of CdS by introducing a co-catalyst CoTPPBr₄ (7,8,17,18-tetrabromo-5,10,15,20-tetraphenylporphyrin)

Zong Wang, Xinxin Wang, Kelai Chen, Haojun Yin, Huangsheng Su, Yundang Wu, Chunlin Ni and Wei Liu

This study developed an efficient photocatalyst for hydrogen production, consisting of CdS nanorods and the CoTPPBr₄ co-catalyst.



The article was first published on 29 Mar 2024
New J. Chem., 2024, **48**, 8868–8876
<https://doi.org/10.1039/D4NJ00372A>

Download PDF

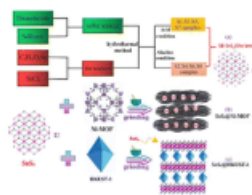
Article HTML

Paper

Facile grinding method synthesis of SnS₂@HKUST-1 and SnS₂@Ni-MOF for electrocatalytic hydrogen evolution

Hongtao Cui, Lige Gong, Hongyan Lv, Limin Dong, Jihua Wang, Jingyu Zhang, Yitong Mu, Yunhao Gu, Hui Li, Binghe Yang and Meijia Wang

The synthesis of SnS₂@Ni-MOF and SnS₂@HKUST-1 with high HER performance.



The article was first published on 14 Apr 2024
New J. Chem., 2024, **48**, 8877–8885
<https://doi.org/10.1039/D4NJ05571J>

Download PDF

Article HTML



Cite this: DOI: 10.1039/d4nj00372a

Enhancing the photocatalytic hydrogen production performance of CdS by introducing a co-catalyst CoTPPBr₄ (7,8,17,18-tetrabromo-5,10,15,20-tetraphenylporphyrin)[†]

Zong Wang,^a Xinxin Wang,^{ab} Kelai Chen,^a Haojun Yin,^a Huangsheng Su,^a Yundang Wu,^b Chunlin Ni^{*a} and Wei Liu^{id} ^{*a}

This study developed an efficient photocatalyst for hydrogen production, consisting of CdS nanorods and the CoTPPBr₄ co-catalyst. The synthesized photocatalyst was characterized using a suite of techniques including X-ray diffraction (XRD), X-ray photoelectron spectroscopy (XPS), scanning electron microscopy (SEM), high-resolution transmission electron microscopy (HR-TEM), photoluminescence (PL) spectroscopy, and ultraviolet-visible diffuse reflectance spectroscopy (UV-Vis DRS). Additionally, transient photocurrent response and electrochemical impedance spectroscopy (EIS) were carried out to further probe the material's properties. Our findings demonstrate that the CoTPPBr₄ co-catalyst significantly enhances the photocatalytic H₂ evolution efficiency under visible light irradiation. Notably, among the tested photocatalysts, a 12.5% CoTPPBr₄/CdS composite exhibited the most superior photocatalytic performance, achieving a hydrogen production rate of 41.3 mmol g⁻¹ h⁻¹, which is 4.1 times higher than that of pristine CdS. The introduction of CoTPPBr₄ effectively facilitates charge transfer within CdS, enhances the separation efficiency of light-induced electron-hole pairs, and boosts the surface H₂-evolution kinetics. This research not only introduces a promising photocatalyst for visible light-driven hydrogen production but also provides a way for the development of highly efficient and stable CdS-based hybrid semiconductor nanocomposites suitable for diverse photocatalytic applications.

Received 23rd January 2024,
Accepted 26th March 2024

DOI: 10.1039/d4nj00372a

rsc.li/njc

1. Introduction

In the quest for sustainable and clean energy solutions, harnessing solar power for hydrogen production through photocatalysis has emerged as a critical pathway.¹ The catalytic process of hydrogen production involves a series of light-induced reactions that take place on the surface of a photocatalyst. The key steps in the photocatalytic process include light absorption, generation of photoexcited charge carriers, and subsequent redox reactions.^{2,3} Nevertheless, photocatalytic hydrogen production encounters challenges, including a relatively limited quantum efficiency and a low utilization rate of visible light.⁴

Therefore, developing new efficient photocatalytic materials is a hot topic in this field.

Previously, a significant number of materials with photocatalytic properties have been developed. These include inorganic non-metallic materials,^{5,6} inorganic metallic materials,⁷ and organic metal-organic framework materials.⁸ Among them, CdS stands out as a high-performance II-VI semiconductor. It exhibits typical characteristics of an n-type direct band gap semiconductor, featuring a band gap of approximately 2.4 eV. Due to its highly negative conduction band potential (*E*_{CB}) and outstanding absorption of visible light, CdS can serve as an effective photocatalyst driven by visible light.^{9,10} However, the photo-generated electron-hole pairs in CdS semiconductors undergo significant recombination, affecting their photocatalytic performance.¹¹ The pursuit of enhanced catalytic performance through the modification of CdS is a focal point in this field.

The development of co-catalysts is a commonly employed strategy and method for enhancing the catalytic activity of semiconductor materials.¹² Some organic compounds, characterized by a large macrocyclic structure,¹³ exhibit unique properties that contribute to their effectiveness in catalytic

^a College of Materials and Energy, South China Agricultural University, Guangzhou 510642, China. E-mail: niclchem@scau.edu.cn, liuweiy97@scau.edu.cn; Fax: +86 20 87024123; Tel: +86 20 87025180

^b National-Regional Joint Engineering Research Center for Soil Pollution Control and Remediation in South China, Guangdong Key Laboratory of Integrated Agro-environmental Pollution Control and Management, Institute of Eco-environmental and Soil Sciences, Guangdong Academy of Sciences, Guangzhou 510650, China

[†] Electronic supplementary information (ESI) available. See DOI: <https://doi.org/10.1039/d4nj00372a>

processes. Among these compounds, porphyrin, serving as an environmentally friendly biomimetic ligand, possesses a conjugated structure with excellent photoelectric properties.^{14,15} Porphyrin compounds are currently the most extensively studied tetrapyrrole compounds, exhibiting large molar absorption coefficients, high fluorescence quantum yields, excellent thermal stability, and broad spectrum absorption.¹⁶ The band structure and electronic properties of porphyrin derivatives can be fine tuned by the introduction of central metal ions or functional groups, thereby imparting excellent reaction selectivity to the material.^{17,18} Additionally, porphyrin is non-planar, demonstrating S₄ symmetry.¹⁹ Introduction of transition metals such as Co, Fe, Ni, and Zn into porphyrin induces a transition to planarity, thereby further enhancing its symmetry.²⁰ Transition metalloporphyrins exhibit elevated binding energy, electron affinity, and ionization potential, leading to notable catalytic activity and unique photoelectrochemical properties.²¹ Therefore, among them, cobalt porphyrin, with low electron affinity, demonstrates high

conductivity and stability and could probably hold significant promise in the field of photocatalytic catalysis.^{22,23}

In this study, we synthesized a β -substituted cobalt tetrabromotetraphenyl porphyrin (CoTPPBr₄). This compound was used as a photosensitizer to encapsulate CdS nanorods on their surfaces, resulting in the formation of a CoTPPBr₄/CdS composite material. This composite material not only enhances the ability to respond to visible light but also facilitates the separation and transfer of photogenerated carriers, enabling it to serve as a photocatalyst for the hydrogen precipitation reaction. The composite material exhibits outstanding performance and maintains good long-term stability, which are of significant scientific value.

2 Experimental

2.1 Preparation of cocatalysts and catalysts

A schematic of the synthesis of CdS/CoTPPBr₄ is shown in Fig. 1. The specific method is described as follows:

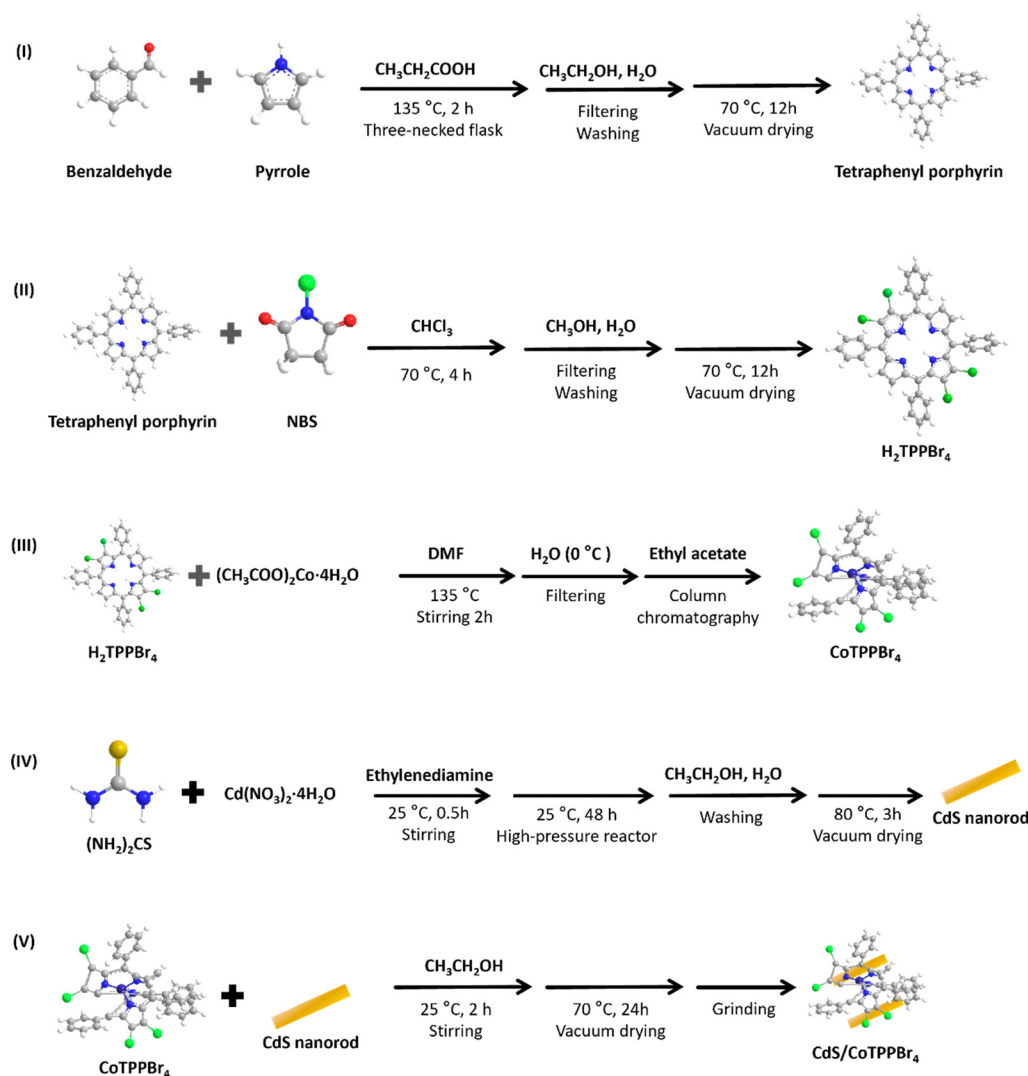


Fig. 1 A schematic of the synthesis of CdS/CoTPPBr₄.

I. Preparation of tetraphenylporphyrin^{24,25}. Tetraphenylporphyrin was synthesized using the Adler method. A mixture of 0.03 mol of benzaldehyde and 0.03 mol of distilled pyrrole was dissolved in 80 mL of propionic acid, which served as the solvent. The solution was refluxed at 135 °C in a three-necked flask for 2 hours to maintain a consistent temperature. Following refluxing, 20 mL of anhydrous ethanol was added, and the mixture was cooled overnight. Ethanol was subsequently employed for washing, and the compound was dried by extraction filtration.

II. Preparation of 7,8,17,18-tetrabromo-5,10,15,20-tetraphenylporphyrin, H₂TPPBr₄²⁶. A solution containing 0.5 g of tetraphenylporphyrin in 100 mL of chloroform, supplemented with 620 mg of NBS, was refluxed at approximately 70 °C for 4 hours. Subsequently, the solution volume was reduced to 30 mL using vacuum distillation. Following the addition of methanol, the mixture was filtered, rinsed with methanol, and subsequently dried under vacuum conditions. The XRD results of the obtained H₂TPPBr₄ crystals confirm that the material has been successfully synthesized (Fig. S1, ESI†).

III. Preparation of CoTPPBr₄²⁷. A mixture of 0.5 g of tetrabromotetraphenyl porphyrin and 1 g of cobalt acetate was dissolved in 80 mL of DMF. The solution was then heated and reacted at 135 °C for 2 hours. Following the reaction, the mixture was swiftly transferred into 500 mL of ice water for extraction, followed by vacuum drying. CoTPPBr₄ was purified by column chromatography. The sample was dissolved in chloroform and separated by column chromatography using 100–200 mesh silica gel, with ethyl acetate as the eluent. The first fraction was collected, evaporated, and recrystallized to obtain the CoTPPBr₄ sample. The nuclear magnetic resonance (NMR) hydrogen spectrum results of the obtained CoTPPBr₄ confirm that the material has been successfully synthesized (Fig. S2, ESI†).

IV. Preparation of CdS²⁸. A solution comprising 0.006 mol of cadmium nitrate tetrahydrate and 0.018 mol of thiourea was dissolved in 40 mL of ethylenediamine and stirred for 30 minutes. This mixture was then transferred into a PTFE-lined container and subjected to a reaction at 200 °C for 48 hours in an oven. After the reaction, the resultant mixture was filtered, rinsed with anhydrous ethanol, and subsequently dried in the oven at 80 °C for 3 hours.

V. Preparation of CoTPPBr₄/CdS. 0.5 g of CdS and 0.0625 g of CoTPPBr₄ were taken. They were placed in a beaker with 20 mL of ethanol and stirred in the dark for 2 hours. Subsequently, the mixture was transferred to a vacuum drying oven following natural evaporation.

2.2 Characterization

CdS, CoTPPBr₄, and CoTPPBr₄/CdS were analyzed by X-ray powder diffraction with an Ultima IV model. The scanning angles ranged from 5° to 80°, and the results were cross-referenced with a crystallography database. The morphology of the composite was observed using a scanning electron microscope (SEM) (FEL Verios 460), while the microstructural characteristics of the complexes were elucidated using a

transmission electron microscope (TEM) (JEM 2100 F).²⁹ X-ray photoelectron spectroscopy (XPS) (AXIS SUPRA+) was used to analyze the surface properties of the aforementioned materials.³⁰ Ultraviolet-visible diffuse reflectance spectra (UV-Vis DRS) were recorded using a UV1780 ultraviolet-visible spectrophotometer (Shimadzu UV1780). The photocurrent and impedance measurements were carried out using an electrochemical workstation (Autolab PGSTAT 302N). The photoluminescence (PL) spectra were recorded using a fluorescence spectrometer (Edinburgh Instruments, FS5).

2.3 Photocatalytic activity of the prepared samples

The photocatalytic activity of the samples was evaluated using gas chromatography.³¹ Specifically, 18 mL of water was subjected to photolysis, with 2 mL of lactic acid serving as the sacrificial agent to provide electrons. Prior to the experiment, oxygen was purged from the water for 5 minutes using nitrogen, and subsequently, 2 mL of methane was introduced as the standard gas to quantify hydrogen production. The sample was irradiated with full light intensity for 8 hours. After exposure, a 400 µL sample was extracted for analysis using gas chromatography.

2.4 Electrochemical characterization

Preparation of the working electrode: 5 mg of the photocatalyst was added to 1 mL of anhydrous ethanol and sonicated for 30 minutes. Then, 100 mL of the resulting suspension was uniformly drop-cast onto a fluorine-doped tin oxide conductive glass (FTO) electrode (2 × 2 cm). After drying under an infrared lamp, the drop-casting process was repeated 10 times. Subsequently, the electrode was annealed at 150 °C under a nitrogen atmosphere for 1 hour to obtain the working electrode.

The photoelectrochemical tests were conducted using an electrochemical workstation (CH Instruments Ins. CHI-660E) equipped with a standard three-electrode system, with a platinum electrode as the working electrode, Ag/AgCl (saturated KCl solution) as the reference electrode, and 0.2 M Na₂SO₄ aqueous solution as the electrolyte. A 300 W xenon lamp with a UV filter ($\lambda > 400$ nm) was used as the light source, and transient photocurrent curves (*i*-*t*) were recorded under bias voltage. Electrochemical impedance spectroscopy (EIS) spectra of the samples were recorded in the frequency range of 0.01–10⁵ Hz with an amplitude of 5 mV. Mott-Schottky (M-S) curves of the samples were recorded at different frequencies (500 Hz, 1000 Hz, 1500 Hz).

3 Results and discussion

3.1 Morphological and structural characterization

The detailed morphology of the as-prepared catalysts was studied using SEM. It shows that the original CdS has a good crystalline nanorod morphology (Fig. 2a), and the original CoTPPBr₄ is micrometer-level and crystalline rod-like (Fig. 2b). After the formation of CoTPPBr₄/CdS, it can be seen from Fig. 2c that the nanostructure of the CdS nanorods is well

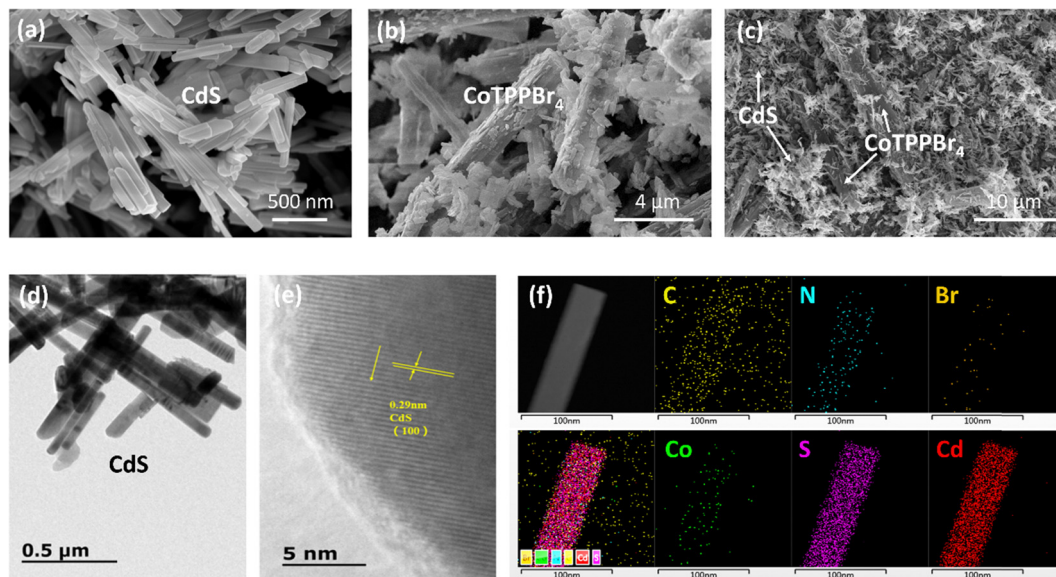


Fig. 2 Morphology and surface topography of the as-prepared composite samples: (a) SEM images of CdS; (b) SEM images of CoTPPBr₄; (c) SEM images of 12.5% CoTPPBr₄/CdS; (d) TEM images of 12.5% CoTPPBr₄/CdS; (e) HRTEM images of 12.5% CoTPPBr₄/CdS; and (f) elemental mapping images of 12.5% CoTPPBr₄/CdS.

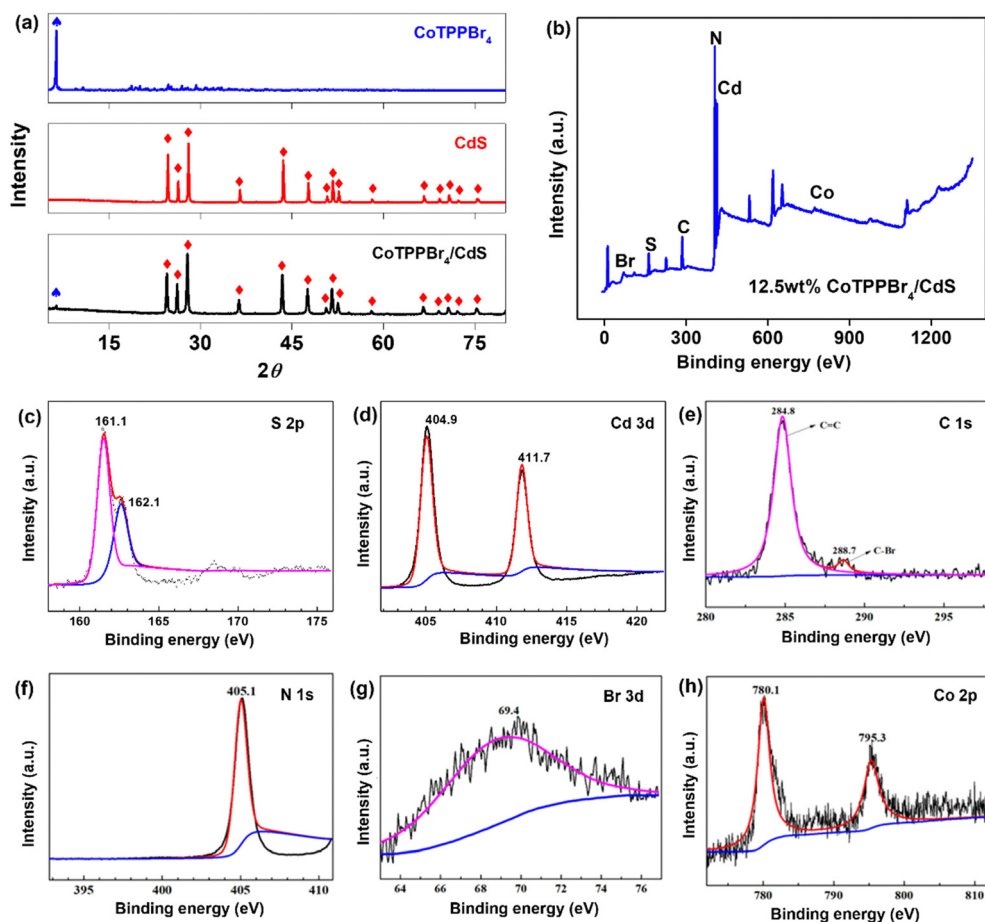


Fig. 3 (a) XRD patterns of the as-prepared composite samples. (b)–(h) XPS patterns of 12.5% CoTPPBr₄/CdS. (b) survey spectrum; (c) Cd 3d; (d) S 2p; (e) C 1s; (f) N 1s; (g) Br 3d; and (h) Co 2p.

preserved. A composite of micrometer-scale CoTPPBr_4 and nanometer-scale CdS has been formed.

The TEM image of 12.5% $\text{CoTPPBr}_4/\text{CdS}$ is presented in Fig. 2d, and the HRTEM image in Fig. 2e shows a lattice spacing of 0.29 nm corresponding to the (100) plane of CdS .³² In order to obtain more detailed information about the $\text{CoTPPBr}_4/\text{CdS}$ composite, the elemental mapping images of the $\text{CoTPPBr}_4/\text{CdS}$ complex were obtained as shown in Fig. 2f; elements C, N, Br, Co, Cd and S were detected. From the images, it is evident that C, N, Br and Co can be detected on the CdS nanorods, indicating that some CoTPPBr_4 may have adhered to the surface of CdS . To further quantify the composition of each element in the composite catalyst, the content of each element was measured by energy dispersive X-ray spectroscopy (EDX) and the results are shown in Fig. S3 (ESI†). The ratio of C, N, Co, and Br is 21.25%, which is higher than the expected $\text{CoTPPBr}_4/\text{CdS}$ composition. This discrepancy may be attributed to the selection of test fields and the material's heterogeneity.

The X-ray diffraction patterns of CdS , CoTPPBr_4 and 12.5% $\text{CoTPPBr}_4/\text{CdS}$ are shown in Fig. 3a. All XRD spectra show obvious diffraction peaks, indicating that these samples have a good crystalline state. The characteristic peaks at 24.8° , 26.5° , 28.2° , 36.6° , 43.7° , 47.8° and 51.82° belong to the (1 0 0), (0 0 2), (1 0 1), (1 0 2), (1 1 0), (1 0 3) and (1 1 2) lattice planes of CdS , respectively (JCPDS Card No. 41-1049). This suggests that the prepared CdS nanorods are well crystallized in the hexagonal crystal phase, since the intensity of the (103) plane can only be assigned to the hexagonal phase of CdS .³³ CoTPPBr_4 has a characteristic absorption peak at 6.36° , which is still visible in the 12.5% $\text{CoTPPBr}_4/\text{CdS}$ composite, indicating the presence of both CoTPPBr_4 and CdS . The peak at 6.36° has a lower intensity, which may be related to the ratio between CdS and CoTPPBr_4 . The above results suggest the successful preparation of the $\text{CoTPPBr}_4/\text{CdS}$ composite catalyst.

XPS was further used to analyze the elemental valence states of the $\text{CoTPPBr}_4/\text{CdS}$ composition and study the surface chemical formation of the complex. Fig. 3b shows a survey spectrum, indicating that the $\text{CoTPPBr}_4/\text{CdS}$ composite catalyst contains C, N, Co, Br, Cd and S elements. Fig. 3b–g show high-resolution XPS images of S 2p, Cd 3d, C 1s, N 1s, Co 2p, and Br 3d respectively. In Fig. 3c, the peak at 161.5 eV belongs to S

$2p_{3/2}$, and the peak at 162.1 eV belongs to S $2p_{1/2}$. The main peaks at 404.9 eV and 411.7 eV (Fig. 3d) belong to Cd $3d_{5/2}$ and Cd $3d_{3/2}$, which are consistent with the previously reported data for CdS . In Fig. 3e, the peaks at 284.8 eV and 288.7 eV correspond to the C=C bond and C–Br, respectively, while N and Br have only one form shown in 405.1 eV (N 1s) and 69.4 eV (Br 3d) respectively (Fig. 3f and g). The peak at 780.1 eV belongs to Co $2p_{3/2}$, and the other peak at 795.3 eV belongs to Co $2p_{1/2}$ (Fig. 3h). The above surface results are consistent with the structure of CoTPPBr_4 . Therefore, XPS further confirms that 12.5% $\text{CoTPPBr}_4/\text{CdS}$ is a composite material formed from CoTPPBr_4 and CdS .

3.2 Photocatalytic H_2 production activity

To elucidate the H_2 production performance of the composite catalyst we prepared, we assessed the photocatalytic H_2 evolution activities of CdS , CoTPPBr_4 , and $\text{CoTPPBr}_4/\text{CdS}$ from a lactic acid water solution (10%, V/V) under visible light irradiation under a standard atmosphere at room temperature (Fig. 4a). Specifically, $\text{CoTPPBr}_4/\text{CdS}$ samples with varying CoTPPBr_4 contents (ranging from 10% to 20%) were employed to investigate the H_2 evolution kinetics. As illustrated in Fig. 4a, CoTPPBr_4 alone exhibited negligible H_2 production, whereas CdS nanorods autonomously produced H_2 at a moderate rate (78.9 mmol g^{-1}). Remarkably, upon introducing CoTPPBr_4 onto CdS nanorods, the H_2 production capability of the $\text{CoTPPBr}_4/\text{CdS}$ composite catalyst saw a significant enhancement. The H_2 evolution over an 8-hour period showed an increment from 10% to 12.5% CoTPPBr_4 content, peaking at 12.5% with a value of 330.4 mmol/g . This represents an approximately 4.1-fold improvement over pure CdS . However, a further increase in the CoTPPBr_4 content (from 12.5% to 20%) led to a decline in H_2 evolution activity, likely attributed to the excessive CoTPPBr_4 doping diminishing light absorption. We compiled recent photocatalytic studies related to CdS and compared them with the material used in this study, as shown in Fig. S4 and Table S1 (ESI†). 12.5% CoTPPBr_4 used in this study exhibited remarkably excellent hydrogen production performance, indicating the superiority of this material.

Furthermore, the hydrogen production stability of the 12.5% $\text{CoTPPBr}_4/\text{CdS}$ composite was assessed through recycling

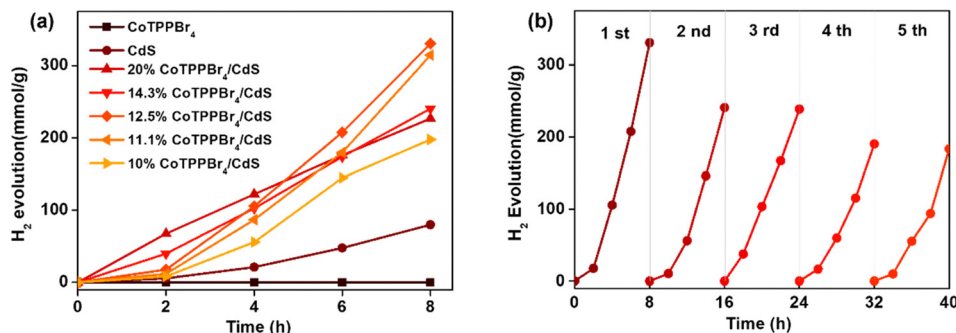


Fig. 4 (a) Time evolution profiles of H_2 production for $\text{CoTPPBr}_4/\text{CdS}$ with varying CoTPPBr_4 concentrations, alongside pure CoTPPBr_4 and CdS . (b) Photocatalytic cyclic tests of 12.5% $\text{CoTPPBr}_4/\text{CdS}$.

experiments, as depicted in Fig. 4b. After each cycle, the catalyst was retrieved *via* centrifugation and subsequently employed in a repeated hydrogen production experiment. The results revealed that the H_2 evolution over an 8-hour span decreased from an initial 330 mmol g^{-1} to 182 mmol g^{-1} after 5 cycles. Nevertheless, this performance remains 2.28 times superior to that of CdS as shown in Fig. 4a. To investigate whether CoTPPBr₄ would detach from CdS during the reaction, we characterized the materials after 3 and 5 cycles of reaction by XRD, SEM, and TEM (Fig. S5, ESI†). The XRD results showed that the characteristic peaks hardly changed with the progression of cycles. SEM still observed CoTPPBr₄ attached to the surface of CdS, while TEM also observed rod-shaped CoTPPBr₄. This indicates that the material possesses a certain degree of structural stability.

3.3 Photoelectrochemical properties and the photocatalytic mechanism

To elucidate the potential mechanisms behind the enhanced photocatalytic activities, we characterized the photoelectrochemical properties of the composite. Initially, the photocurrent responses of both CdS and 12.5% CoTPPBr₄/CdS were examined (Fig. 5a) to delineate the influence of CoTPPBr₄ on CdS regarding light absorption and electron transfer.³⁴ The results revealed a pronounced photocurrent response in the 12.5% CoTPPBr₄/CdS system, with a current density exceeding that of pure CdS by more than double. Additionally, the photocurrent response of the 12.5% CoTPPBr₄/CdS composite exhibited reversibility and stability, evidenced by a swift current recovery upon light exposure. Conversely, the photocurrent of

CdS decreased with increasing cycles, indicating a diminished stability compared to the composite.³⁵ The amplified photocurrent suggests that the introduction of CoTPPBr₄ on the CdS surface enhances the electron transfer and charge separation efficiency. To delve deeper into the electron transfer dynamics, electrochemical impedance spectroscopy was employed (Fig. 5b). Observations indicated a reduced semicircular diameter for 12.5% CoTPPBr₄/CdS post-introduction of CoTPPBr₄, signifying a decline in interface resistance. This impedance reduction likely mitigates the electron transfer resistance, thereby facilitating the separation of photogenerated carriers.

As photogenerated electron-hole pairs recombine and emit light, the likelihood of this recombination increases with the emission intensity.³⁶ Consequently, the photoluminescence (PL) spectrum serves as a valuable tool to investigate the charge separation efficiency. In this study, we meticulously analyzed the PL spectra of both 12.5% CoTPPBr₄/CdS and CdS. As illustrated in Fig. 5c, CdS exhibited a distinct peak at 525 nm. However, this peak was noticeably decreased in the 12.5% CoTPPBr₄/CdS composite, indicating an enhanced charge separation efficiency in the composite compared to pure CdS. This enhancement is likely attributed to CoTPPBr₄ on the CdS surface, which facilitates the capture of photogenerated electrons. This, in turn, promotes electron transfer from the catalyst to H^+ , amplifying photocatalytic H_2 production. Furthermore, we obtained the UV-visible spectra of the composite. As depicted in Fig. 5d, there was a significant rise in absorption between 500 and 600 nm following the incorporation of CoTPPBr₄. This suggests that the modification led to an increased absorption of visible light. The alteration in the

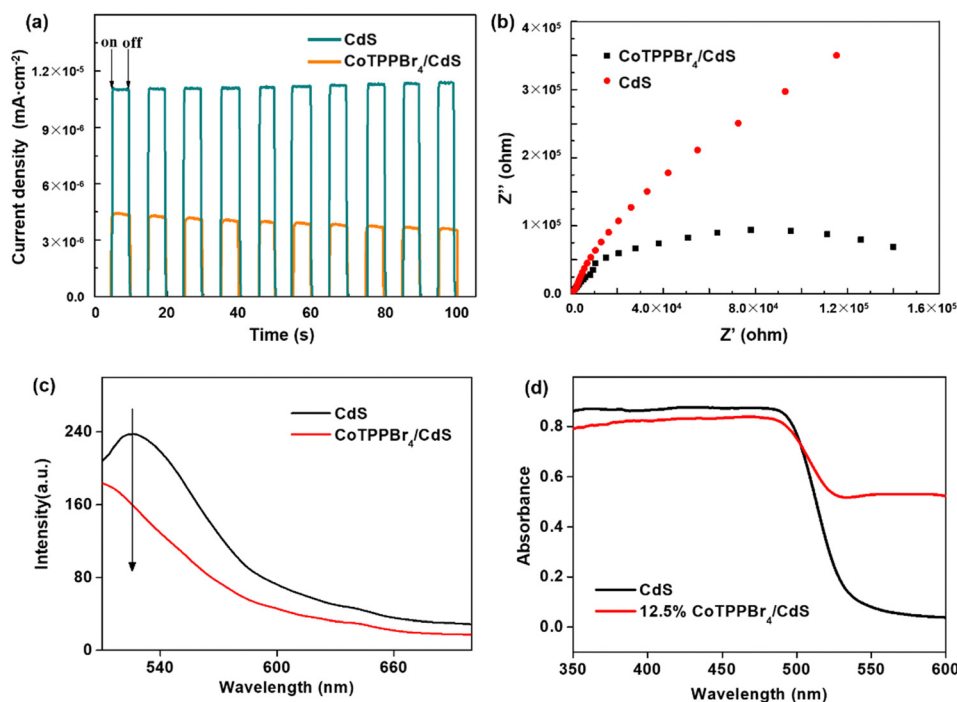


Fig. 5 (a) Transient photocurrent curves of CdS and 12.5%CoTPPBr₄/CdS; (b) EIS Nyquist plots of pure CdS and 12.5% CoTPPBr₄/CdS; (c) the PL spectra of CdS and 12.5% CoTPPBr₄/CdS; and (d) UV-visible spectra of the composite.

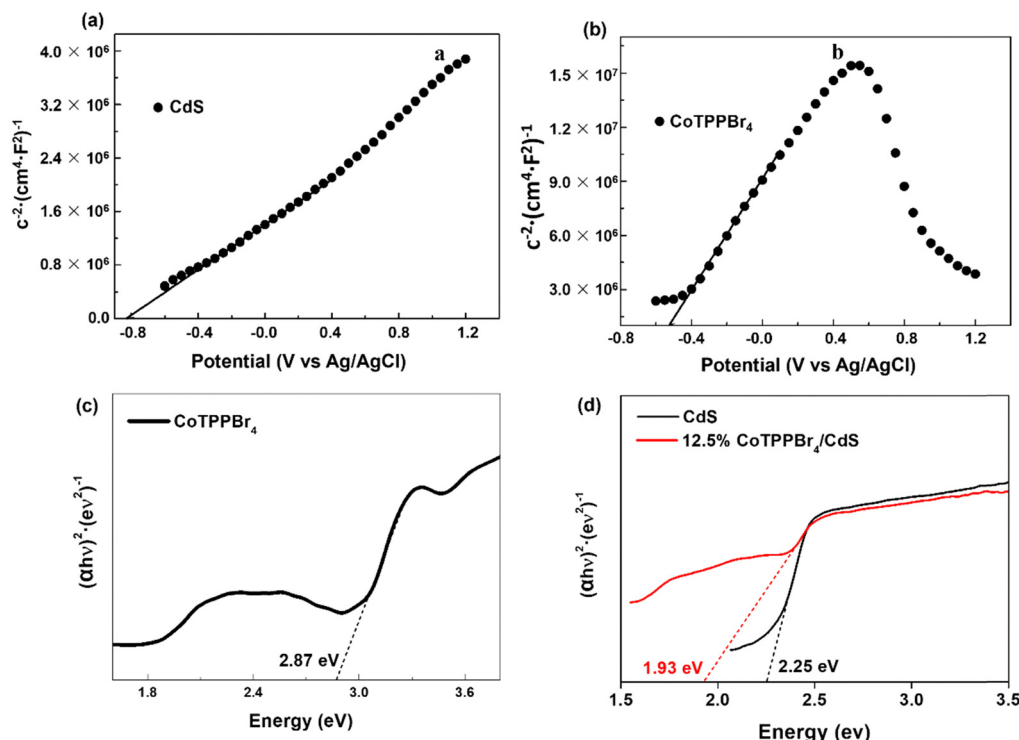


Fig. 6 The Mott–Schottky plots for (a) CdS and (b) CoTPPBr₄. (c) (d) The relationship between $(\alpha h\nu)^2$ and photon energy. This is derived from the UV-Vis DRS spectra of CoTPPBr₄, CdS and 12.5% CoTPPBr₄/CdS.

catalyst's color due to the introduction of CoTPPBr₄ likely enhanced its visible light absorption capacity, which is beneficial for the photocatalytic process.³⁷ This underscores that the modified light absorption capability is a crucial factor contributing to the enhanced photocatalytic performance.

To further elucidate the charge transfer pathway and understand the underlying photocatalytic mechanism, we analyzed the energy band structure. Mott–Schottky plots for both CdS and CoTPPBr₄ were recorded at varying frequencies to determine the flat band potential (E_{FB}) (Fig. 6a and b). The E_{FB} values were deduced from the x -axis intercepts and were found to be -0.83 eV for CdS and -0.53 eV for CoTPPBr₄, respectively. Notably, the positive slopes of these curves for both materials—CdS and CoTPPBr₄—suggest that they exhibit n -type semiconductor behavior. The bandgap can be calculated using the Tauc plot function:^{38,39}

$$(\alpha h\nu)^{1/n} = A(h\nu - E_g)$$

where α is the light absorption index, h is Planck's constant, ν is the frequency, A is a constant, E_g is the semiconductor bandgap width, and the index n is directly related to the semiconductor type (for a direct bandgap semiconductor, $n = 1/2$ and for an indirect bandgap semiconductor, $n = 2$). The n value is 0.5 as CdS and CoTPPBr₄ are direct bandgap semiconductors. As shown in Fig. 6c and d, the band gap (E_g) values of CdS and CoTPPBr₄ were calculated to be 2.25 eV and 2.87 eV respectively. The test value of E_g for CoTPPBr₄ is relatively consistent with the result obtained from density functional theory (DFT) calculations (2.829 eV) (Fig. S6, ESI†). The band gap of the

composite catalyst was estimated to be 1.93 eV as shown in Fig. 6d, which is lower than that of pure CdS (2.25 eV).

Based on the photoelectrochemical characterization and energy band structure analysis, the possible photocatalytic mechanism of the composite was figured out and is shown in Fig. 7. The introduction of CoTPPBr₄ changed the color of CdS, thus enhancing its visible light absorption capacity, which is beneficial for the photocatalytic process. In addition, the band gap of the composite catalyst was estimated to be 1.93 eV, which is lower than that of pure CdS (2.25 eV). This decrease in band gap significantly decreased the energy required for charge separation, thus enhancing the photocatalytic ability under visible light conditions. The LUMO of CoTPPBr₄ could capture the photogenerated electrons from CdS thus enhancing the charge separation efficiency, leading to a prohibition in charge recombination. Therefore, the introduction of CoTPPBr₄ as a

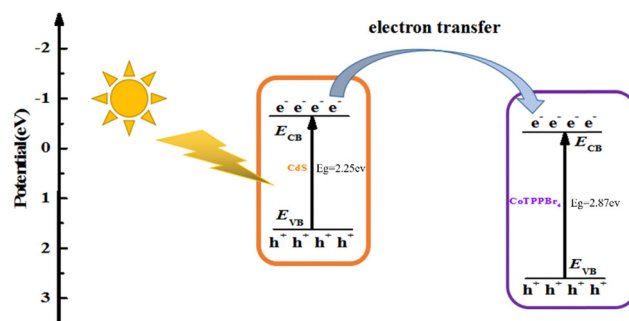


Fig. 7 The possible photocatalytic mechanism of CoTPPBr₄/CdS.

co-catalyst dramatically enhanced the hydrogen production by improving the charge separation efficiency.

4 Conclusion

In this study, we successfully synthesized a high-performance photocatalytic CoTPPBr₄/CdS catalyst. We examined the H₂ evolution activity of the catalysts prepared with varying concentrations of CoTPPBr₄ (ranging from 10% to 20%). Remarkably, the catalyst comprising 12.5% CoTPPBr₄ exhibited an optimal H₂ evolution performance of 330.4 mmol g⁻¹. This value is approximately 4.1 times greater than that of pure CdS. The PL spectrum revealed that the presence of CoTPPBr₄ enhanced the H₂ evolution activity due to its improved charge separation efficiency. This observation was further supported through energy band analysis. Specifically, the band gap of our composite catalyst was estimated to be 1.93 eV, a value lower than that of pure CdS (2.25 eV). This reduced band gap suggests a diminished energy requirement for charge separation. Consequently, our catalyst demonstrates enhanced photocatalytic performance, particularly under visible light conditions.

Author contributions

Zong Wang: data curation, investigation, and writing – review & editing; Xinxin Wang: investigation and validation; Kelai Chen: investigation, writing – original draft, visualization, and methodology; Haojun Yin: investigation and validation; Huangsheng Su: investigation; Yundang Wu: conceptualization and supervision; Chunlin Ni: conceptualization, resources, and writing – review & editing; Wei Liu: conceptualization, methodology, writing – review & editing, project administration, and funding acquisition.

Conflicts of interest

The authors declare no competing financial interests or personal relationships.

Acknowledgements

This work was funded by the Guangzhou Basic and Applied Basic Research Project (202201010559), the Guangdong Basic and Applied Basic Research Foundation (2019A1515011033), and the National Natural Science Foundation of China (42077020).

References

- 1 F. Dawood, M. Anda and G. M. Shafiullah, *Int. J. Hydrogen Energy*, 2020, **45**, 3847–3869.
- 2 V. Preethi and S. Kanmani, *Mater. Sci. Semicond. Process.*, 2013, **16**, 561–575.
- 3 T. Van Gerven, G. Mul, J. Moulijn and A. Stankiewicz, *Chem. Eng. Process.*, 2007, **46**, 781–789.
- 4 J. Yang, H. Yan, X. Wang, F. Wen, Z. Wang, D. Fan, J. Shi and C. Li, *J. Catal.*, 2012, **290**, 151–157.
- 5 P. Wang, Z. Guan and Q. Li, *et al.*, *J. Mater. Sci.*, 2018, **53**, 774–786.
- 6 Y. Liu, M. Tayyab, W. Pei, L. Zhou, J. Lei, L. Wang, Y. Liu and J. Zhang, *Small*, 2023, 2208117.
- 7 G. L. Chiarello, M. V. Dozzi and E. Selli, *J. Energy Chem.*, 2017, **26**, 250–258.
- 8 D. A. Reddy, Y. Kim, M. Gopannagari, D. P. Kumar and T. K. Kim, *Sustainable Energy Fuels*, 2021, **5**, 1597–1618.
- 9 Q. Li, B. Guo, J. Yu, J. Ran, B. Zhang, H. Yan and J. R. Gong, *J. Am. Chem. Soc.*, 2011, **133**, 10878–10884.
- 10 Q. Wang, J. Li, Y. Bai, J. Lian, H. Huang, Z. Li, Z. Lei and W. Shangguan, *Green Chem.*, 2014, **16**, 2728–2735.
- 11 R. B. Wei, Z. L. Huang, G. H. Gu, Z. Wang, L. Zeng, Y. Chen and Z. Q. Liu, *Appl. Catal., B*, 2018, **231**, 101–107.
- 12 K. Chang, X. Hai and J. Ye, *Adv. Energy Mater.*, 2016, 1502555.
- 13 S. Grau, M. Schilling, D. Moonshiram, J. Benet-Buchholz, S. Luber, A. Llobet and C. Gimbert-Suriñach, *ChemSusChem*, 2020, **13**, 2745–2752.
- 14 J. S. O'Neill, L. Kearney, M. P. Brandon and M. T. Pryce, *Coord. Chem. Rev.*, 2022, 467.
- 15 H. Sheng, J. Wang, J. Huang, Z. Li, G. Ren, L. Zhang, L. Yu, M. Zhao, X. Li, G. Li, N. Wang, C. Shen and G. Lu, *Nat. Commun.*, 2023, **14**, 1528.
- 16 Y. Zhu, D. Zhu, Y. Chen, Q. Yan, C. Y. Liu, K. Ling, Y. Liu, D. Lee, X. Wu, T. P. Senftle and R. Verduzco, *Chem. Sci.*, 2021, **12**, 16092–16099.
- 17 V. Nikolaou, G. Charalambidis, K. Ladomenou, E. Niko-udakis, C. Drivas, I. Vamvasakis, S. Panagiotakis, G. Landrou, E. Agapaki, C. Stangel, C. Henkel, J. Joseph, G. Armatas, M. Vasilopoulou, S. Kennou, D. M. Guldi and A. G. Coutsolelos, *ChemSusChem*, 2021, **14**, 961–970.
- 18 S. Shanmugam, J. Xu and C. Boyer, *J. Am. Chem. Soc.*, 2015, **137**, 9174–9185.
- 19 C. J. Kingsbury and M. O. Senge, *Coord. Chem. Rev.*, 2021, 431.
- 20 S. Wang, Z. Liu, Y. Ye, X. Meng, P. Yang, Z. Zhang, Y. Qiu and J. Lei, *New J. Chem.*, 2022, **47**, 421–427.
- 21 F. Leng, H. Liu, M. Ding, Q. P. Lin and H. L. Jiang, *ACS Catal.*, 2018, **8**, 4583–4590.
- 22 Q. Luo, K. Zhu, S. Z. Kang, L. Qin, S. Han, G. Li and X. Li, *J. Porphyrins Phthalocyanines*, 2018, **22**, 877–885.
- 23 B. Bhavani, N. Chanda, V. Kotha, G. Reddy, P. Basak, U. Pal, L. Giribabu and S. Prasanthkumar, *Nanoscale*, 2022, **14**, 140–146.
- 24 J.-Z. Zou, Z. Xu, M. Li and X.-Z. You, *Acta Crystallogr., Sect. C: Cryst. Struct. Commun.*, 1995, **51**, 760–761.
- 25 A. Bettelheim, B. A. White, S. A. Raybuck and R. W. Murray, *Inorg. Chem.*, 1987, **26**, 1009–1017.
- 26 H. Duval, V. Bulach, J. Fischer, M. W. Renner, J. Fajer and R. Weiss, *JBIC, J. Biol. Inorg. Chem.*, 1997, **2**, 662–666.
- 27 Z. Jian-Zhong, L. Ming, X. Zheng and Y. Xiao-Zeng, *Acta Chim. Sin.*, 1994, 683–692.
- 28 T. Zhai, X. Fang, L. Li, Y. Bando and D. Golberg, *Nanoscale*, 2010, **2**, 168–187.

- 29 J. F. Han, C. Liao, L. M. Cha, T. Jiang, H. M. Xie, K. Zhao and M. P. Besland, *J. Phys. Chem. Solids*, 2014, **75**, 1279–1283.
- 30 G. Hota, S. B. Idage and K. C. Khilar, *Colloids Surf., A*, 2007, **293**, 5–12.
- 31 J. Yu, Y. Yu, P. Zhou, W. Xiao and B. Cheng, *Appl. Catal., B*, 2014, **156–157**, 184–191.
- 32 M. F. Kotkata, A. E. Masoud, M. B. Mohamed and E. A. Mahmoud, *Phys. E*, 2009, **41**, 1457–1465.
- 33 C. Zhu, C. Liu, Y. Fu, J. Gao, H. Huang, Y. Liu and Z. Kang, *Appl. Catal., B*, 2019, **242**, 178–185.
- 34 Y. Chen, G. Mao, Y. Tang, H. Wu, G. Wang, L. Zhang and Q. Liu, *Chin. J. Catal.*, 2020, **42**, 225–234.
- 35 H. Liu, J. Chen, W. Guo, Q. Xu and Y. Min, *J. Colloid Interface Sci.*, 2022, **613**, 652–660.
- 36 I. A. Shkrob and M. C. Sauer, *J. Phys. Chem. B*, 2004, **108**, 12497–12511.
- 37 D. Li and W. Shi, *Chin. J. Catal.*, 2016, **37**, 792–799.
- 38 J. B. Coulter and D. P. Birnie, *Phys. Status Solidi B*, 2017, 1700393.
- 39 H. Shirzadi, A. Nezamzadeh-Ejhieh and M. Kolahdoozan, *Inorg. Chem. Commun.*, 2023, **150**, 110464.

证书号第 4468268 号



发明专利证书

发明名称：一种多功能性荧光识别 Ag 配位聚合物及其制备方法与应用

发明人：刘维;陈丛丛;吴云当;倪春林;张静;徐奕琳;陈克来

专利号：ZL 2020 1 0979587.0

专利申请日：2020 年 09 月 17 日

专利权人：华南农业大学;广东省科学院生态环境与土壤研究所

地址：510642 广东省广州市天河区五山路 483 号

授权公告日：2021 年 06 月 08 日

授权公告号：CN 112126073 B

国家知识产权局依照中华人民共和国专利法进行审查，决定授予专利权，颁发发明专利证书并在专利登记簿上予以登记。专利权自授权公告之日起生效。专利权期限为二十年，自申请日起算。

专利证书记载专利权登记时的法律状况。专利权的转移、质押、无效、终止、恢复和专利权人的姓名或名称、国籍、地址变更等事项记载在专利登记簿上。



局长
申长雨

申长雨



第 1 页 (共 2 页)

其他事项参 99 续页

证书号第 4468268 号



专利权人应当依照专利法及其实施细则规定缴纳年费。本专利的年费应当在每年 09 月 17 日前缴纳。未按照规定缴纳年费的，专利权自应当缴纳年费期满之日起终止。

申请日时本专利记载的申请人、发明人信息如下：

申请人：

华南农业大学, 广东省科学院生态环境与土壤研究所

发明人：

刘维, 陈丛丛, 吴云当, 倪春林, 张静, 徐奕琳, 陈克来

证书号第 3787287 号



发明专利证书

发明名称：配位聚合物晶体材料及其制备方法与荧光应用

发明人：刘维;陈丛丛;周家容;倪春林;张静;牛志成;董正南
甘智豪;李婷

专利号：ZL 2019 1 0361620.0

专利申请日：2019 年 04 月 30 日

专利权人：华南农业大学

地址：510642 广东省广州市天河区五山路 483 号

授权公告日：2020 年 05 月 08 日

授权公告号：CN 110078933 B

国家知识产权局依照中华人民共和国专利法进行审查，决定授予专利权，颁发发明专利证书并在专利登记簿上予以登记。专利权自授权公告之日起生效。专利权期限为二十年，自申请日起算。

专利证书记载专利权登记时的法律状况。专利权的转移、质押、无效、终止、恢复和专利权人的姓名或名称、国籍、地址变更等事项记载在专利登记簿上。



局长
申长雨

申长雨



第 1 页 (共 2 页)

其他事项参阅续页

证书号第 3787287 号



专利权人应当依照专利法及其实施细则规定缴纳年费。本专利的年费应当在每年 04 月 30 日前缴纳。未按照规定缴纳年费的，专利权自应当缴纳年费期满之日起终止。

申请日时本专利记载的申请人、发明人信息如下：

申请人：

华南农业大学

发明人：

刘维；陈丛丛；周家容；倪春林；张静；牛志成；董正南；甘智豪；李婷

证书号第 4353198 号



发明专利证书

发 明 名 称：一种温度诱导的三维自旋交叉配位聚合物及其制备方法和应用

发 明 人：刘维;陈丛丛;吴云当;倪春林;张静;徐奕琳;陈克来

专 利 号：ZL 2020 1 0977427.2

专利申请日：2020 年 09 月 17 日

专 利 权 人：华南农业大学;广东省科学院生态环境与土壤研究所

地 址：510642 广东省广州市天河区五山路 483 号

授权公告日：2021 年 04 月 09 日

授权公告号：CN 112029110 B

国家知识产权局依照中华人民共和国专利法进行审查，决定授予专利权，颁发发明专利证书并在专利登记簿上予以登记。专利权自授权公告之日起生效。专利权期限为二十年，自申请日起算。

专利证书记载专利权登记时的法律状况。专利权的转移、质押、无效、终止、恢复和专利权人的姓名或名称、国籍、地址变更等事项记载在专利登记簿上。



局长
申长雨

申长雨



第 1 页 (共 2 页)

其他事项参阅续页

203

证书号第 4353198 号



专利权人应当依照专利法及其实施细则规定缴纳年费。本专利的年费应当在每年 09 月 17 日前缴纳。未按照规定缴纳年费的，专利权自应当缴纳年费期满之日起终止。

申请日时本专利记载的申请人、发明人信息如下：

申请人：

华南农业大学；广东省科学院生态环境与土壤研究所

发明人：

刘维；陈丛丛；吴云当；倪春林；张静；徐奕琳；陈克来

证书号第 4520600 号



发明专利证书

发明名称：一种新型 Ag 配位聚合物晶体材料及其制备方法与应用

发明人：刘维;陈丛丛;吴云当;倪春林;张静;徐奕琳;陈克来

专利号：ZL 2020 1 0982006.9

专利申请日：2020 年 09 月 17 日

专利权人：华南农业大学;广东省科学院生态环境与土壤研究所

地址：510642 广东省广州市天河区五山路 483 号

授权公告日：2021 年 07 月 02 日

授权公告号：CN 112142990 B

国家知识产权局依照中华人民共和国专利法进行审查，决定授予专利权，颁发发明专利证书并在专利登记簿上予以登记。专利权自授权公告之日起生效。专利权期限为二十年，自申请日起算。

专利证书记载专利权登记时的法律状况。专利权的转移、质押、无效、终止、恢复和专利权人的姓名或名称、国籍、地址变更等事项记载在专利登记簿上。



局长
申长雨

申长雨



第 1 页 (共 2 页)

其他事项参见续页

证书号第 4520600 号



专利权人应当依照专利法及其实施细则规定缴纳年费。本专利的年费应当在每年 09 月 17 日前缴纳。未按照规定缴纳年费的，专利权自应当缴纳年费期满之日起终止。

申请日时本专利记载的申请人、发明人信息如下：

申请人：

华南农业大学, 广东省科学院生态环境与土壤研究所

发明人：

刘维, 陈丛丛, 吴云当, 倪春林, 张静, 徐奕琳, 陈克来

证书号第7543101号



专利公告信息

发明专利证书

发明名称：一种四氯合钴复合双季磷盐、缓释薄膜材料及其制备方法和应用

专利权人：华南农业大学;广州美颂化妆品有限公司

地址：510642 广东省广州市天河区五山路483号

发明人：刘维;张紫晗;王晓斌;朱妙婷;温智敏;高珊珊;王宗;倪春林

专利号：ZL 2022 1 0972155.6

授权公告号：CN 115304639 B

专利申请日：2022年08月15日

授权公告日：2024年11月22日

申请日时申请人：华南农业大学;广州美颂化妆品有限公司

申请日时发明人：刘维;张紫晗;王晓斌;朱妙婷;温智敏;高珊珊;王宗;倪春林

国家知识产权局依照中华人民共和国专利法进行审查，决定授予专利权，并予以公告。
专利权自授权公告之日起生效。专利权有效性及专利权人变更等法律信息以专利登记簿记载为准。

局长
申长雨

申长雨





荣誉证书

陈丛丛、尹浩均、文雨薇、甘丹同学

在广东第十届大学生材料创新大赛金属材料分赛区中荣获

三等奖

特发此证，以资鼓励。

作品名：基于多吡啶基配体的 Ag(I) 配位聚合物的构筑及荧光传感研究

指导老师：刘维

主办单位：

广东省材料研究学会



承办单位：

广东工业大学材料与能源学院



麦克赛迪·琮卡杯第五届广东省大学生金相技能大赛暨琮卡杯第十三届全国大学生金相技能大赛复赛（广东赛区）

荣誉证书

HONORARY CREDENTIAL

华南农业大学 郑璐瑶 同学

荣获第五届广东省大学生金相技能大赛——金相大会（第二赛道）

二等奖

指导教师：刘维、钟礼韬

广东省本科高校材料类专业教学指导委员会
(南方科技大学代章)



广东省大学生金相技能大赛组委会
(广东工业大学代章)



2024年6月23日
广东·广州市



获奖证书

蒋妍、李香玲、胡宝怡、李欣然 同学

在第十四届“华港杯”广东大学生材料创新大赛中，荣获

三等奖

特发此证，以资鼓励。

作品名称：《四溴合铜(II)酸取代苄基哌啶晶态材料的制备、结构及其性能研究》

指导教师：刘维

承办单位：

华南农业大学材料与能源学院



主办单位：

广东省材料研究学会



二〇二五年十一月

“麦克奥迪·徕卡杯”第六届广东省大学生金相技能大赛
暨徕卡杯第十四届全国大学生金相技能大赛复赛（广东赛区）



荣誉证书

华南农业大学 梁锐政 同学

荣获第六届广东省大学生金相技能大赛

三等奖

指导教师：张殿武、刘维



广东省材料研究学会 广东省本科高校材料类专业教学指导委员会 广东省大学生金相技能大赛组委会



2025年6月8日

广东·汕头

“麦克奥迪·徕卡杯”第六届广东省大学生金相技能大赛
暨徕卡杯第十四届全国大学生金相技能大赛复赛（广东赛区）



荣誉证书

华南农业大学 钟文杰 同学

荣获第六届广东省大学生金相技能大赛

一等奖

指导教师：刘维、董汉武

广东省本科高校材料类专业教学指导委员会 广东省大学生金相技能大赛组委会

汕头大学
2025年6月8日
广东·汕头



全国大学生金相技能大赛

教育部高等学校材料类专业教学指导委员会指导

荣誉证书

徕卡杯第十四届全国大学生金相技能大赛
(全国大学生金相技能大赛第一赛道)

个人三等奖

获奖选手

李柔娴

(华南农业大学)

指导教师

刘 维、董汉武

(证书编号: JXDS-14G-0646)



全国大学生金相技能大赛竞赛委员会

2025年7月30日
成都工业学院 承办





全国大学生金相技能大赛

教育部高等学校材料类专业教学指导委员会指导

荣誉证书

徕卡杯第十四届全国大学生金相技能大赛
(全国大学生金相技能大赛第一赛道)

个人二等奖

获奖选手

张文冬

(华南农业大学)

指导教师

胡 航、刘 维

(证书编号: JXDS-14G-0643)



全国大学生金相技能大赛竞赛委员会

2025年7月30日

成都工业学院 承办





荣誉证书

刘维 同志：

在广东省第七届高校本科青年教师教学大赛理科小组中表现优异，荣获一等奖。

特发此证，以资鼓励。



二〇二四年十二月



高等农林院校
课程思政联盟

获奖证书

刘维 老师：

您主讲的课程思政教学案例在第四届全国高等农林院校课程思政联盟研讨会
案例征集评选中被评为优秀案例。

特发此证，以资鼓励。

课程名称：物理化学

案例名称：克拉佩龙方程

所在高校：华南农业大学

获奖组别：视频案例

全国高等农林院校课程思政联盟

(华中农业大学代章)

二〇二四年十二月

荣誉证书

HONORARY CREDENTIAL

刘维 老师：

被评为 2023 年度华南农业大学
十佳教师。

特发此证，以资鼓励！


华南农业大学
2024 年 9 月 5 日

荣誉证书

刘维：

被评为华南农业大学2022-2024年度“十佳
本科生班主任”。

特发此证，以资鼓励。



荣誉证书

刘 雍：

被评为2018-2020年度华南农业大学
优秀班主任。

特发此证，以资鼓励。



华南农业大学文件

华南农教〔2021〕25号

关于公布华南农业大学第二批卓越青年教师 百人计划人选的通知

各学院、部处、各单位：

为贯彻落实《华南农业大学高水平本科教育实施意见》（华南农办〔2019〕62号），进一步加强我校青年教师队伍建设，重点培育一批卓越青年教师，整体提升我校青年教师教育教学能力，根据《华南农业大学卓越青年教师百人计划实施方案》，学校开展了第二批卓越青年教师百人计划遴选工作，经教师自愿报名、单位推荐、学校资格审查、校内公示无异议等程序，共遴选出王小龙等42位教师入选第二批卓越青年教师百人计划（详见附件），现予以公布。

附件：华南农业大学第二批卓越青年教师百人计划人选名单

华南农业大学
2021年5月12日

- 1 -

附件

华南农业大学第二批卓越青年教师 百人计划人选名单

序号	单位名称	姓名	序号	单位名称	姓名
1	农学院	王小龙	22	水利与土木工程学院	杨雨冰
2	农学院	金 晶	23	水利与土木工程学院	卢小圣
3	植物保护学院	郑 正	24	材料与能源学院	刘 维
4	植物保护学院	徐春玲	25	材料与能源学院	袁 腾
5	植物保护学院	孔广辉	26	材料与能源学院	刘海峰
6	植物保护学院	刘家莉	27	数学与信息学院、软件学院	王雪琴
7	植物保护学院	陈少华	28	数学与信息学院、软件学院	金玲玉
8	林学与风景园林学院	吴道铭	29	数学与信息学院、软件学院	李娇娇
9	林学与风景园林学院	单体江	30	数学与信息学院、软件学院	周 燕
10	林学与风景园林学院	李 培	31	经济管理学院	董 莹
11	园艺学院	赵杰堂	32	公共管理学院	曾永辉
12	动物科学学院	谭成全	33	公共管理学院	王 枫
13	动物科学学院	蔺文成	34	公共管理学院	徐 强
14	动物科学学院	李耀坤	35	公共管理学院	曲 霞
15	动物科学学院	孙宝丽	36	人文与法学学院	李 颖
16	资源环境学院	李荣华	37	外国语学院	林 绿
17	资源环境学院	张 池	38	外国语学院	郭圣琳
18	海洋学院	黄玉妹	39	外国语学院	侯丽娴
19	海洋学院	孙红岩	40	艺术学院	栾志弘
20	海洋学院	曾 芳	41	艺术学院	欧阳文昱
21	食品学院	宋明月	42	马克思主义学院	梁 娟

公开方式：主动公开

华南农业大学党政办公室

2021 年 5 月 12 日印发

荣誉证书

刘维：

被评为华南农业大学2025年“七一”表彰
优秀共产党员。

特发此证，以资鼓励。



验签二维码

证书编码： 2025033105

中共华南农业大学委员会

2025年6月

年度考核结果通知书

刘维 同志：

你在 2018 年年度考核中，被确定为优秀等次，

特此通知。



2019 年 4 月 18 日

年度考核结果通知书

刘维 同志：

你在 2020 年 年度考核中，考核结果为 优秀等次，
特此通知。



年度考核结果通知书

刘维 同志：

你在 2022 年 年度考核中，考核结果为 优秀等次 ，
特此通知。



2023 年 6 月 10 日

教职工业绩成果报表

姓 名	刘维	工 号	30004294	所在单位	材料与化学工程学院		
年 龄	38	职 称	讲师	学 历	博士研究生 毕业	学 位	理学博士学位
岗位类别	专业技术	一级分类	教师	二级分类	教学科研型	岗位级别	专业技术岗 位10级
年度考核结果		2016年：不定等次； 2017年：合格； 2018年：优秀； 2019年：合格； 2020年：优秀； 2021年：合格； 2022年：优秀； 2023年：合格； 2024年：优秀； 2025年：合格					

荣誉证书

刘维 老师：

在华南农业大学 2019-2020 学年青年教师
教学优秀奖评选中荣获“三等奖”。

特发此证，以资鼓励！

华南农业大学

2021年1月19日

荣誉证书

HONORARY CREDENTIAL

刘 维 老师:

在华南农业大学 2022-2023 学年青年教师教学优秀奖
奖评选中荣获

二等奖

特发此证，以资证明！


华南农业大学
2024 年 1 月 4 日



获奖证书

刘维 老师

在第十四届“华港杯”广东大学生材料创新大赛中，荣获

优秀指导教师

特发此证，以资鼓励。

单位：华南农业大学

承办单位：

华南农业大学材料与能源学院



主办单位：

广东省材料研究学会



二〇二五年十一月

奖状

刘维老师:

荣获华南农业大学材料与能源学院 2022 年度教
学效果优秀奖一等奖。

特发此证，以资鼓励！

华南农业大学材料与能源学院

2023 年 9 月 7 日

奖状

刘 维 老师:

获得华南农业大学材料与能源学院 2020 年度教学
效果优秀奖, 一 等奖。

特发此证, 以资鼓励!

华南农业大学材料与能源学院

2021 年 9 月 16 日

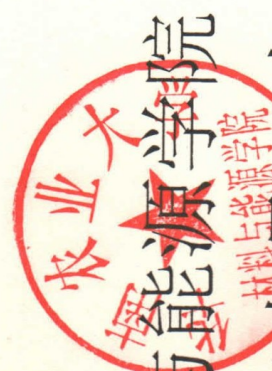


奖状

刘 维 老师

荣获材料与能源学院第二届青年教师教学
观摩竞赛 一等奖。

特发此证，以资鼓励！



材料与能源学院

二〇一七年十月二十七日

奖 状

刘 维 老师:

荣获华南农业大学材料与能源学院 2022 年度教
学效果优秀奖 一 等奖。

特发此证，以资鼓励！

华南农业大学材料与能源学院

2023 年 9 月 7 日



奖状

刘瑾

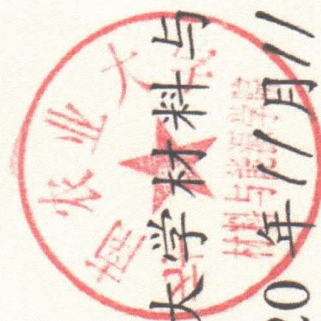
老师：

在华南农业大学材料与能源学院第五届青年
教师教学观摩竞赛中获得二等奖。

特发此证，以资鼓励！

华南农业大学材料与能源学院

2020年11月11日



荣誉证书

HONORARY CREDENTIAL



刘维 老师：

在华南农业大学材料与能源学院 2020 届本科
毕业生就业工作中表现突出，被评为：就业工作
积极分子。特发此证，以资鼓励。

材料与能源学院
二〇二〇年十二月十五日



生产实践单位证明

姓 名	刘维	性别	女	出生年月	1988 年 9 月
学历学位	博士研究生	专业技术职务		讲师（首聘副教授）	
工作单位	华南农业大学材料与能源学院				
生产实践单位	佛山市铁人环保科技有限公司				
生产实践形式	生产观摩与技术咨询	生产实践时间		2017.06-2017.08 2018.06-2018.08	
个人实践总结	<p>本人在佛山市铁人环保科技有限公司为期六个月的科技服务实践工作中，通过生产观摩与技术咨询形式的生产实践，认真学习了该企业在土壤重金属污染治理与光触媒方面研发、生产与市场推广工作。通过这的生产实践，让我深深感受到科研探讨与实际应用应紧密联系在一起，做到用理论去指导实践，用实践去证明理论，让所掌握的技术与知识运用到实践中去，才能体现出这些技术与知识的价值。</p> <p style="text-align: right;">签 名：  日 期：2018年 9 月 1 日</p>				
实践单位评价	<p>刘维博士在本公司科技服务过程中，态度认真，踏实上进，充分利用专业优势，积极对本公司相关产品的质量和推广工作都提出建设性意见和建议。</p> <p style="text-align: right;">单位盖章  日 期：2018年 9 月 1 日</p>				